Science Instrument (SI) Calibration Report for the AXAF CCD Imaging Spectrometer (ACIS)

Version 2.20 - January 15, 1999
Copy printed January 13, 1999
Final Pre-launch Calibration Report

Marshall W. Bautz
Co-Editor
Massachusetts Institute of Technology

John A. Nousek
Co-Editor
Pennsylvania State University

Approved by:

Gordon P. Garmire
ACIS Instrument PI
Pennsylvania State University

Prepared exclusively for:
George C. Marshall Space Flight Center
National Aeronautics and Space Administration
Marshall Space Flight Center, AL 35812

Prepared by:

Center for Space Research
Massachusetts Institute of Technology
Cambridge, MA 02139

Dept. of Astronomy & Astrophysics
Pennsylvania State University
University Park, PA 16802

Contents

List of Tables

List of Figures

Chapter 1

Preface

The task of AXAF calibration, and ACIS calibration in particular, was the combination of the tremendous effort by many individuals and organizations. It is not practical to include the names of everyone who contributed, but the ACIS instrument team is extremely grateful for the superlative effort and great technical competence shown by the many people in Huntsville and at their home institutions who worked for many years to make the six months of twenty-four hour days of AXAF calibration at XRCF a success.

Some teams which gave support which cries out for recognition were: MSFC Project Science, the TRW Test Directors, the ASC Calibration group and third floor staff, the Gratings Science teams, the MST HXDA team, and the XRCF staff and second floor operators.

This report is a collective effort by the entire ACIS team. Prime responsibility for the authorship of the sections is as follows:

2	Introduction	M. Bautz, J. Nousek
3	Data Products	K. Glotfelty (ASC) P. Broos, B. LaMarr
4	ACIS CCD Performance	M. Bautz, F. Baganoff, T. Isobe S. Jones, B. LaMarr, S.Kissel H. Manning, M. Pivovaroff, G. Prigozhin
5	ACIS OBF Performance	G. Chartas, L. Townsley, G. Garmire
6	ACIS/HRMA Performance Prediction	G. Chartas, L. Townsley J. Nousek, R. Sambruna, A. Garmire
7	Calibration products	P. Broos, B. LaMarr

The ASC provided extensive support of CCD subassembly calibration; the efforts of K. Glotfelty, P. Plucinsky, N. Schulz, J. Woo, B. McNamara and A. Estes all made significant contributions, as did Kaori Nishikida and Catherine Grant of PSU. J. Woo collaborated on the measurement of X-ray absorbtion fine structure using thin-film replicas of the CCD gate structure. The absolute response detection efficiency measurements would not have been possible without the collaboration of G. Ulm, R. Thornagel and F. Scholze at the PTB laboratory at the BESSY synchrotron. ACIS filter measurements depended upon synchrotron support provided by Jim MacKay and Dale Graessle.

Chapter 2

Introduction

2.1 Purpose

The purpose of this document is to provide a final pre-launch report on the analysis of data collected for the calibration of the AXAF CCD Imaging Spectrometer (ACIS). The goal of the calibration is to provide an accurate measurement of the performance of the ACIS/HRMA instrument. Through calculation of the effects of finite source distance and gravitationaly loading on the HRMA mirror assembly it will be possible to predict the in-orbit performance of the ACIS/HRMA instrument. This will allow precise evaluation of astrophysical X-ray source models and their errors.

2.2 Scope

This document should be perceived as an index and consolidation of the complete pre-launch calibration of ACIS. It shall contain documentation describing the calibration, the location and form of data products, and the results of analysis to date. The data and analysis covered will include sub-assembly calibration data (collected at MIT for the CCD chips, and at synchrotrons for the filters and reference CCDs), integrated HRMA and flight ACIS data (collected at XRCF), ACIS flat-field data (collected at XRCF) and integrated HRMA-CCD chip data (collected at XRCF using the 2C camera).

2.3 Overview of calibration

2.3.1 Lab calibration

The CCD chips received extensive calibration at MIT in the process of selecting the flight chips. After the chips were selected a standard calibration process was applied to all chips. The process and the results of the analysis of the data collected are provided in Chapter 4.

2.3.2 BESSY calibration

Various measurements were made at the Berlin synchrotron facility, BESSY, on flight-like CCDs. Because the absolute photon flux is very well known at the BESSY facility these measurements provide the opportunity to apply absolute quantum efficiency calibration to the ACIS CCDs. Every flight CCD chip was cross calibrated against a CCD with a BESSY calibration in the same chamber and at the same time. Details of the BESSY measurements and analysis of the data are also provided in Chapter 4.

2.3.3 Filter calibration

Our Optical Blocking Filter (OBF) calibration plan consisted of five stages. At the University of Wisconsin Synchrotron Radiation Center (SRC) we mapped the transmission of all flight-like filters and many of their witness samples at five energies using a beam of 0.76 mm $\times$0.76 mm. At the National Synchrotron Light Source at Brookhaven National Laboratory (BNL) we measured filter witness samples at hundreds of energies, but only two positions per filter. At Denton Vacuum, Inc., using a UV/visible/IR spectrophotometer, we measured the optical/UV leakage through witness samples to refine the optical constants for polyimide. At Penn State, we measured changes to the transmission in filter witness samples as a function of temperature.

The SRC data are critical as they are the only measurements of the flight filters as separate entities, before the filter response is convolved with the response from the CCDs and the AXAF mirrors. These data allow us to search for any large light leaks or manufacturing defects, to measure spatial variations, and to make normalizing bulk thickness measurements to carry over to the high-resolution BNL energy data, which in turn provide detailed transmission models including the effects of EXAFS (Extended X-ray Absorption Fine Structure).

2.3.4 HRMA/ACIS calibration

The ACIS team collected calibration data utilizing the HRMA telescope during three data collection intervals. Following the XRCF nomenclature these occured during Phases F, G and H. During Phases F and G the HRMA focussed X-rays were collected on two flight-like CCDs (one front side illuminated (FI), and one back side illuminated (BI)) in a camera utilizing electronics very similar to the MIT CSR lab cameras. This camera, named the ACIS-2C, served as a proxy to enable data collection while the ACIS flight instrument finished the final stages of certification and thermal vacuum testing.

The ACIS-2C camera, using chips of identical design and fabricated in the same lots at Lincoln Lab as the flight ACIS chips, has differing processing electronics and does not hold the chips in the same orientation as the flight unit. Thus these ACIS-2C data are useful for understanding the chip level interaction between the mirror effects and the CCDs, but do

not fully calibrate the effect of the flight electronic processing and flight array orientation effects. (It should be noted that the ACIS-2C chips were significantly worse in cosmetic quality than the flight chips. We designed the 2C tests such that only a small portion of the chip area was used, to minimize the effect of the poor portions of the 2C chips.)

Measurements were collected using the flight ACIS instrument and the HRMA at XRCF for eight days during Phase H (see Table 2.1 for the times of ACIS data collection). These data are the most directly relevant data as they use the flight mirrors and detectors, but must still be adjusted for the effects of finite conjugate distance, gravitational loading on the mirrors and a slightly differing CCD temperature operating point than planned for flight (-115 C vs. -120 C).

Following the departure of the HRMA mirrors to meet the schedule of assembly into the spacecraft, the XRCF was used to collect data with ACIS without any focussing optics. These data, collected during Phase I, fit naturally into the sub-assembly lab calibration data, and act as a gross calibration with the beam monitor counter, and are discussed there.

For completeness, it is worth mentioning that data were collected at XRCF during September, 1996, using the ACIS-2C camera and the TMA (Test Mirror Assembly). Data from these tests are still available, and they have not been used in the ACIS calibration. The primary purpose of this testing was to serve as a rehearsal of the true AXAF calibration.

Table 2.1: XRCF Data Collection Phases Involving ACIS

Phase	Detector	Mirror	Start Date*	End Date
F	ACIS-2C	HRMA	12:11 22 Feb 1997	17:52 10 Mar 1997
G	ACIS-2C	HRMA	9:57 10 Apr 1997	8:41 12 Apr 1997
H	Flight	HRMA	23:56 17 Apr 1997	6:00 26 Apr 1997
I	Flight	none	6:45 7 May 1997	0:04 18 May 1997
R	ACIS-2C	TMA	7:00 30 Sep 1996	13:28 5 Oct 1996

* Times are given in local (Central) time. Note these refer to the start and end of ACIS data collection intervals, not necessarily to the start and end of the XRCF Phase.

2.4 Version History

Version 1.0 - Preliminary version submitted to Marshall Space Flight Center, October 13, 1997.

Version 1.5 - Draft of final pre-launch version for review by Marshall Space Flight Center and AXAF team, July 15, 1998.

Version 2.0 - Final pre-launch calibration report submitted to Marshall Space Flight Center, October 15, 1998.

Version 2.2 - Final pre-launch calibration report after full ACIS team internal review, January 15, 1999.

Chapter 3

Data Products

3.1 XRCF Calibration

Two methods of data acquisition were used to collect ACIS event data at the XRCF: the *high-speed tap pipeline* and the *telemetry pipeline*.

3.1.1 High-speed Tap Pipeline

The high-speed tap (HST) pipeline acquired raw, complete CCD frames directly from the camera using a secondary data pathway that is available only on the ground. Having this independent data pathway allows a direct check on the fidelity of the flight processing electronics and software.

The CCD frame data emerging from the camera high-speed tap were captured by the ACIS EGSE workstation and written to disk as FITS images. Software running on the ACIS EGSE processed these images to correct for bias and to extract events, producing FITS event lists. This process and the format of the high-speed tap event lists are described in Section 3.2.

The high-speed tap was used in all phases of ACIS calibration at the XRCF. During the ACIS-2C calibration only high-speed tap data was available because the 2C camera did not support the event extraction and telemetry formatting functions of the flight ACIS experiment. An archive of event lists is maintained by the Calibration Group at the AXAF Science Center and is available on the web at http://hea-www.harvard.edu/acis/xrcf_archive/.

3.1.2 Telemetry Pipeline

The telemetry pipeline acquired events that were recognized by the ACIS flight software and telemetered through the RCTU and CTUE. The telemetry data analyzed at PSU were captured by the ACIS EGSE computer and saved to disk as binary files, each containing one AXAF major telemetry frame. The ATICA (ACIS Telemetry Interpreter for Calibration

Analysis) program extracted x-ray events from this telemetry stream, saving them as FITS event list tables.

3.1.2.1 Science Run Archive

ATICA organized the events it extracted in the same way that the flight software organizes science data – by *science runs* which are defined in Ford & Francis (1997). ATICA creates a directory for each science run, named for the mode and start time of the run, e.g. the run *tefwb_111:07:17* was a Timed Exposure Faint With Bias run that started at IRIG time 111:07:17. Within that directory the event list is arbitrarily divided into files of about 100,000 events each. ATICA was not able to organize the data by TRW ID because the flight software and thus the telemetry knew nothing about that concept. Unfortunately it was necessary to schedule multiple TRW ID's within one ACIS science run so a single ATICA output directory will contain data from several TRW ID's.

The FITS binary tables used to store the event lists consist of the following columns.

- TIME: A timestamp for the CCD frame, expressed as an IRIG time in seconds, i.e. the number of seconds since 1997.0.
- CHIPX/CHIPY: The 1-based position of the event. Note that the flight software telemeters event positions in a 0-based system.
- TDETX/TDETY: The position of the event in the "tiled coordinate system AXAF-ACIS-2.2" defined by Jonathan McDowell at the ASC (McDowell, 1997).
- CCD_ID: The CCD that detected the event. (See Table 3.1.)

Table 3.1: Conversion table from CCD_ID to ACIS array location.

CCD_ID	Chip	Serial #	CCD_ID	Chip	Serial #	CCD_ID	Chip	Serial #
0	I0	w203c4r	4	S0	w168c4r	8	S4	w457c4
1	I1	w193c2	5	S1	w140c4r	9	S5	w201c3r
2	I2	w158c4r	6	S2	w182c4r			
3	I3	w215c2r	7	S3	w134c4r			

- AMP_ID: The amplifier, numbered 0,1,2,3, associated with the central pixel of the event.
- EXPOSURE: The exposure sequence number as telemetered by the flight software.
- PHAS: For most modes this is a 9 element vector containing the event island pixel values NOT corrected for bias. The relationship between this 9-vector and the 3x3 event island is shown in Figure 3.1.

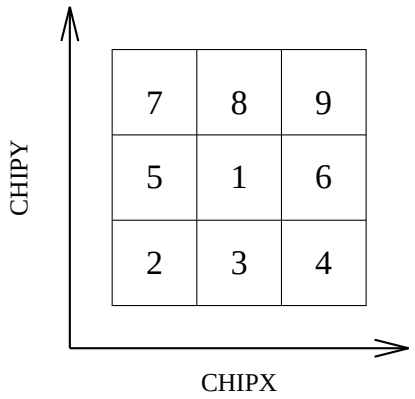

Figure 3.1: Ordering of the elements of the PHAS and BIAS Vectors

- BIAS: A vector of the same form as PHAS, containing the BIAS values used for processing this event.
- OVRCLK: The overclock value associated with the amp in AMP_ID for this exposure.[1]

3.1.2.2 Post Production Archive

A set of *Post Production* activities were performed on the science run archive produced by ATICA:

- An 8-bit quality code (QUALCODE) was computed for each event.
  - The flight software marks pixel locations that appear in the on-board "bad pixel list" with the bias flag value 4095, and marks pixel locations where the bias has been corrupted (by a memory fault) by the bias flag value 4094. An event whose island contains either of these BIAS values has bit 0 in QUALCODE set.
  - A BIAS value of zero indicates that ATICA was unable to recover a bias for that location. Such events have bit 1 in QUALCODE set.
  - CCD pixels whose charge exceeds the dynamic range of the flight electronics end up with a DN value of 4095. Events whose central pixel have this value have bit 2 in QUALCODE set.

  For most analyses, events with non-zero quality codes should be ignored.
- The bias correction $PHAS = PHAS - BIAS - OVRCLK$ is applied.
- The events that belong to each of the phase H tests are identified and are saved in files named by the TRW ID of the test. This is the most important step in Post

[1] A bias-corrected event island would be computed as $PHAS - BIAS - OVRCLK$.

Production since it segments the long science runs (the instrument's view of what happened) into TRW ID's (the scientist's view of what happened).

- The as-requested CMDB table was edited to reflect the tests that were actually performed, based on what was seen in the data stream and what was written in various logs at the XRCF, producing the beginning of an as-run CMDB table. See http://www.astro.psu.edu/xray/axaf/xrcf for the Penn State version of the as-run CMDB.

The FITS event lists that comprise the Post Production archive consist of the following binary table columns: TIME, CHIPX, CHIPY, TDETX, TDETY, CCD_ID, AMP_ID, EXPOSURE, PHAS, & QUALCODE.

The only filtering performed during Post Production was the extraction of a single segment of time around the test. These time boundaries were liberally chosen to include a few frames before and after the test – thus one can usually still see the rise of the light curve at the beginning of the test and the fall at the end. **Analysis of Post Production data will typically require additional filtering by time, elimination of non-zero QUALCODES, grade filtering, etc.**

3.2 ACIS-2C HST Products

3.2.1 Raw data

The raw data output by the ACIS-2C EGSE are FITS images. The dimensions of these images vary depending on the different clocking modes which are described below; however they all share some common characteristics.

3.2.1.1 Quadrants and Nodes

Under normal operation, each ACIS CCD is read out in parallel through four output nodes that split the CCD into quadrants. Each node has its own set of electronics, thus the gain and noise varies from quadrant to quadrant.

The output nodes are commonly referred to as nodes 0 through 3, and the quadrants are commonly named A through D. Thus someone talking about node 0, or 'c0', and quadrant A are talking about the same data. [Footnote: It is actually possible to read the CCDs out through only 2 output nodes. Then the idea of quadrants and nodes becomes more confusing.]

3.2.1.2 READ vs. CHIP coordinates

Due to the physical location of the readout nodes on the CCD, quadrants B and D are read out of the CCD from right to left while quadrants A and C are read out from left to right.

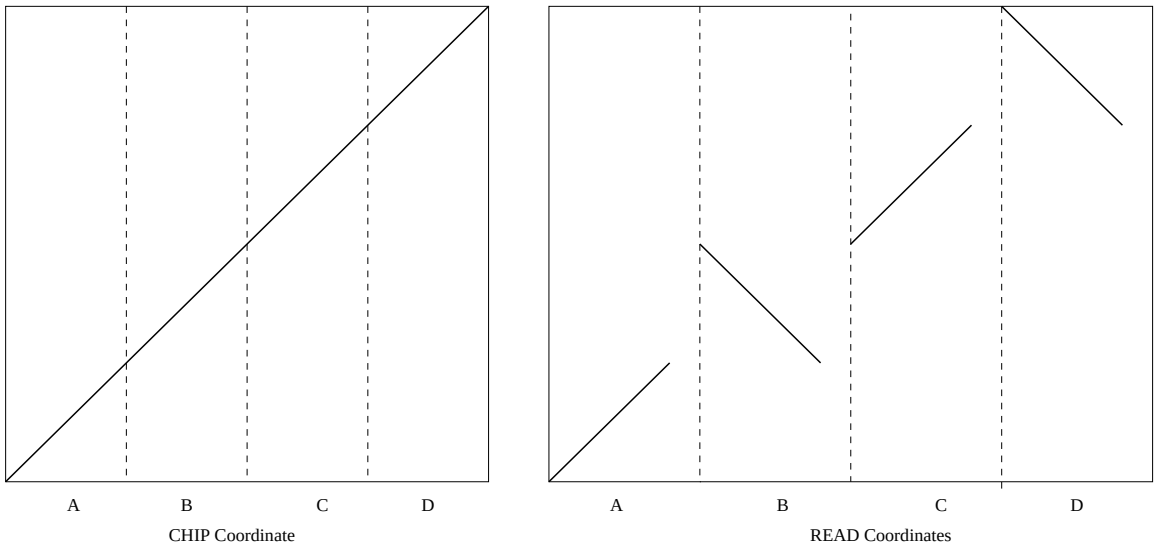

Figure 3.2: CHIP vs. READ coordinates

This gives rise to two coordinate systems, 'READ' and 'CHIP' coordinates.

- CHIP coordinates are physical pixel units on the CCD.
- READ coordinates are virtual pixel units that describe how the pixels were read from the CCD.

The raw FITS images that the ACIS-2C EGSE outputs are in READ coordinates.

Below is an example illustrating the difference between CHIP and READ coordinates. Suppose charge was physically distributed along a diagonal line from the bottom left edge of quadrant A to the top right of quadrant D (Figure 3.2) it would be read out of the CCD in READ coordinates as shown. Note that the gaps in the right ends of the straight lines are real; they indicate the presence of overclock pixel data in the chip readouts, which don't appear in the CHIP coordinate system.

The transformation from READ to CHIP coordinates includes the 'flipping' of quadrants B and D and the removal of overclocks as described below.

3.2.1.3 Overclocks

After all the physical pixels have been read out from each row of each quadrant, the electronics continue to cycle. These cycles create additional overclock 'pixels' which are simply reading out the electronics' noise+bias values. These overclock pixels are virtual pixels in that they do not really exist but are recorded in the raw FITS image in the same way as real pixels are. The FITS keywords IxMINCOL, IxMAXCOL, IxMINROW,

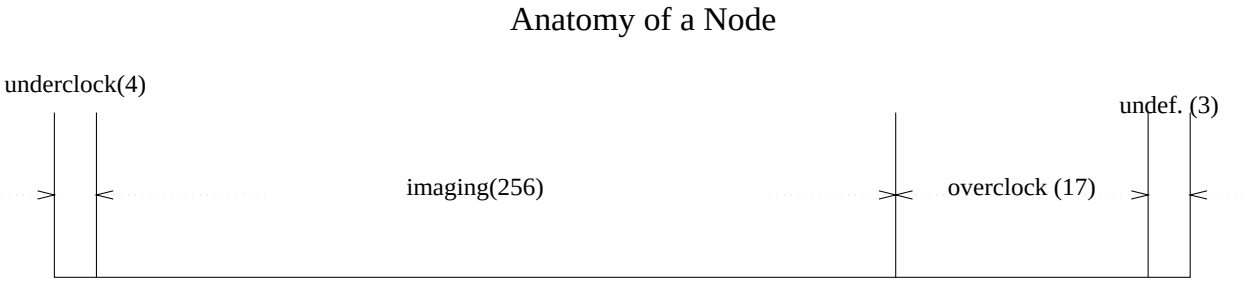

Figure 3.3: Which pixels are which in READ coordinates for each output node.

IxMAXROW (where x is A, B, C, or D) tell us where the real pixels are located in the image.

The number of overclock pixels can be changed by adjusting the electronic sequencers. The number of overclock pixels per row for ACIS-2C is currently set at 17.

The overclock pixels are used to make adjustments to the bias level on small temporal scales. Thus if the bias level changes uniformly across the entire CCD (e.g., if the CCD temperature fluctuates), we use the average overclock level to adjust for this without having to capture a new bias image.

3.2.1.4 Other pixels

In addition to overclock pixels, there are two other kinds of virtual pixels in the raw FITS image:

- 'underclock' pixels are read out before the first real pixel is read out.
- 'undefined parallel transfer' pixels are read out as the next row is shifted down in the frame store array

These pixels are currently not used when creating an event list. The total makeup of each quadrant in the raw FITS image is shown in Figure 3.3.

3.2.1.5 Full Frame

Full frames are written when the entire 1024x1024 image region is transferred to the frame store region in one step. The minimum integration time is then the amount of time it takes to read the data out of the frame store array, roughly 6 seconds with the ACIS-2C electronics.

3.2.1.6 Continuous Clocking

In continuous clocking mode, as soon as a row is read from the output node, the next row of pixels is shifted down to be read out. The minimum integration time is then limited by

the time to read out a single row which is on the order of 6 msec (for the 2C cameras; for the flight ACIS this is about 2.6 msec). The cost of being able to read out this quickly is the loss of all spatial resolution in the parallel transfer, or FAM 'Y', direction. (Again this is explicitly for the ACIS 2C. The flight ACIS chip transfer directions in FAM coordinates are a function of which chip is being referred to.)

3.2.1.7 Staggered Frames

Staggered Frames mode is a mixture of Continuous Clocking and Full Frame modes. Similar to continuous clocking, pixels are continuously transferred to the frame store array; however, instead of going 1 row at a time, groups of rows are transferred. The result is a kind of moving window across the CCD. The integration time is then the amount of time to read out the group of rows.

This mode trades off the advantages and disadvantages of Full Frame and Continuous clocking. You have spatial resolution on a scale as big as the window you are using; however, the bigger the window the longer the integration time. There were several window sizes to choose from so the planners chose which parameter is the most important and designed XRCF tests accordingly.

In the raw FITS images of the Staggered Frames mode data, there is 2-pixel-wide spacer row between each window. These are ignored by the event finding routine.

3.2.1.8 Summary of Staggered Data Modes

The following was provided by S. Kissel (MIT) about the size and timing information for each of the various staggered data modes:

Table 3.2: Staggered Mode Size and Timing for 2C Data

Rows	Int. time (msec)	Window/frame	Raw FITS image size
1	5.712	1024	1120x1024
18	113.87	51	1120x1020
38	227.70	25	1120x1000
54	318.77	18	1120x1008
114	660.27	9	1120x1044
1024	6000.	1	1120x1024

3.2.2 Average Bias

As part of the start up procedure for each test, a set of unexposed raw frames were captured. These raw bias frames were used to determine the nominal offset that was subtracted from

each pixel during event detection.

The algorithm used to compute the average bias image (or map) is the 'mean bias clip' algorithm that J. Woo developed, which is described below:

1. Find the median and standard deviation of every pixel through all n raw bias frames.

$$\tilde{p}(x,y) = \text{median}_n(p(x,y,n)) \tag{3.1}$$

$$\hat{p}(x,y) = \frac{1}{N}\sum_{n=1}^{N} p(x,y,n) \tag{3.2}$$

$$\sigma^2(x,y) = \frac{1}{N-1}\sum_{n=1}^{N} \left(\hat{p}(x,y) - p(x,y,n)\right)^2 \tag{3.3}$$

2. Compute the average value of every pixel, $\hat{p}(x,y)$, discarding pixels that are 3 times the standard deviation above the median value.

$$\mathcal{S}(x,y) = \{n : p(x,y,n) \leq \tilde{p}(x,y) + 3\sigma(x,y)\} \tag{3.4}$$

$$\mathcal{N}(x,y) = \{\text{num}(p(x,y,n)) : p(x,y,n) \leq \tilde{p}(x,y) + 3\sigma(x,y)\} \tag{3.5}$$

$$\bar{p}(x,y) = \frac{1}{\mathcal{N}(x,y)}\sum_{n\in\mathcal{S}(x,y)} p(x,y,n) \tag{3.6}$$

This algorithm does a very good job at removing cosmic ray events which can be present in the bias images. It does however suffer from being computationally and memory intensive. The average bias image is written as a FITS image in READ coordinates.

3.2.3 Events & Event lists

Events are any occasion in which there is a signal remaining in a CCD pixel above the event recognition threshold after bias subtraction. Thus an event may be produced by X-ray photons, charged particles, noisy electronics, stray optical light or defective CCD pixels, just to name a few. It is part of the scientist's analysis task to determine how to maximize the utility of the data by appropriately selecting events so as to maximize the signal and minimize the background.

Before events are extracted, each raw FITS image is bias and overclock corrected. This is done in three steps.

1. First the average bias image is subtracted from every pixel in the raw FITS image (image, $\mathcal{I}$, and overclock, $\mathcal{O}$, pixels).

$$\acute{p}(x,y,n) = p(x,y,n) - \bar{p}(x,y) \quad \forall (x,y) \in \{\mathcal{I},\mathcal{O}\} \tag{3.7}$$

2. Then the overclock pixels associated with each quadrant, q, are averaged

$$o(q,n) = \frac{1}{n(q)} \sum_{(x,y)\in\mathcal{O}(q)} \acute{p}(x,y,n) \quad \forall q = \{\mathrm{A},\mathrm{B},\mathrm{C},\mathrm{D}\} \tag{3.8}$$

   where $n(q)$ is the number of overclock pixels in each quadrant

3. And finally the overclock correction is added back

$$\grave{p}(q,n) = \acute{p}(x,y,n) + o(q,n) \quad \forall (x,y) \in \mathcal{I}(q) : q = \{\mathrm{A},\mathrm{B},\mathrm{C},\mathrm{D}\} \tag{3.9}$$

These bias corrected pixel values are then used for event detection and subsequent extraction. Note that the reason for the overclock pixels is to allow removal of short term drift in the electronic baseline on the timescale of CCD row readout.

Depending on the flux of the source, events can be extracted in one of two ways: *photon counting* mode and *integration* mode. Both of these are described in detail below.

3.2.3.1 Photon Counting

In photon counting mode the basic idea is to search every bias corrected image for a local maximum; any local maximum above some user set *event threshold* is called an event. In addition to its pulse height, every event is given a time tag and a position tag. Also, since the physics of X-ray CCDs dictates that charge from a single X-ray photon can spread into more than one pixel, a pixel island or neighborhood is generally extracted about the local maximum to collect all the charge.

Events are stored in an *event list* which is a FITS binary table with the following columns:

1. TIME: The chosen unit of time for the ACIS 2C data is in seconds since 1994.0. (For flight instrument ACIS data collected at XRCF the unit is in seconds from 1997.0.) Since there is always ambiguity about the exact arrival time of every photon, which is equal to the integration time (one doesn't know if a photon arrived at the beginning or end of the exposure), the time assigned to photons within a single frame, t_{photon} is the start time of the frame, T_{start} plus half the integration time, Δt.

$$t_{photon} = T_{start} + 0.5\Delta t \tag{3.10}$$

In staggered frame mode (see above), the time tag is assigned to each photon within a staggered window based on which window it appeared in. Note that because the entire active area of the chip was open to X-rays it is possible that some events are misassigned in time, but the great majority of X-rays arrive within the focussed HRMA image spot. The time tag for staggered mode data is:

$$t_{photon} = T_{start} + \frac{\Delta t}{N}(n + 0.5) \tag{3.11}$$

where N is the total number of windows in each raw FITS image (see table above) and n is which window the event was recorded in.

2. READX: The location of the event in the serial transfer direction. Quadrants B and D are reversed from 'normal' and overclock pixels are counted.

3. READY: The location of the event in the parallel transfer direction. In full frame mode, this is the same as CHIPY.

4. CHIPX: The physical location of the event in the X direction. Nodes have been flipped and overclock pixels removed.

5. CHIPY: The pseudo physical location of the event in the Y direction. In full frame mode this is the true Y location; however, in Staggered Frames mode, this is the location within the subframe. CHIPY goes from 1 to the size of the window.

6. LABX: This is the same as CHIPX. 'LAB' is a left-over reference to subassembly applications.

7. LABY: This is similar to CHIPY, except it is centered on the CCD. So LABY goes from 512-(r/2) to 512+(r/2), where r is the number of rows per window.

8. FRAME: Frames are counted sequentially for all raw FITS images and windows. So in full frame mode and continuous clocking, the FRAME number is the number of raw FITS files in the data set. In Staggered mode multiple images (equivalent to CCD frames but with fewer rows) appear in a single FITS file. In this case the raw FITS image number is equal to the FRAME number divided by number of windows per frame, N:

$$\text{raw FITS image number} = \left\lfloor \frac{FRAME}{N} \right\rfloor + 1 \tag{3.12}$$

9. pulse height(s): The pulse height channel column varies in size depending on the data extraction mode; however all modes share some common bases. The pulse height(s) are stored in a vector (a vector of 1 is still a vector). The first element of the vector is

always the bias corrected pulse height of the local maximum. The other pixel values (if present) are arranged in a specific order as detailed below.

10. NODE: Simply the CCD output node from which the data were extracted, 0 through 3.

The number of pixels, in the vicinity of a local maximum, which are processed to extract information about the X-ray events varies. The different formats are described below.

3.2.3.1.1 Standard 3x3 Standard event processing is based on 3x3 pixel neighborhood event detection and extraction. A local maximum is specifically defined as any pixel, p_0, that meets the following comparison rules.

$p_0 > p_6$	$p_0 > p_7$	$p_0 > p_8$
$p_0 \geq p_4$	$p_0 \geq$threshold	$p_0 > p_5$
$p_0 \geq p_1$	$p_0 \geq p_2$	$p_0 \geq p_3$

where the pixels are in READX and READY coordinates. Any event that meets the above comparison rules is written into the event list as a 9 pixel vector with the pixels arranged from p_0 to p_8 as illustrated above.

In the ACIS-2C processing, events are ignored if they occur at quadrant boundaries (i.e., the pixel which forms the local maximum signal value falls on the boundaries between regions read by a single output node). Therefore there will always be a 2 pixel gap in images where nodes meet (one pixel on each side of the node). Events are also not detected at the edges of windows or full-frames. Note that in the flight instrument events are recorded as recognized events, even if the local maximum pixel falls on a quadrant boundary (but no effort is made to adjust for differential gain between output nodes; the effect of gain differences should only be modest changes in the event grade distributions).

3.2.3.1.2 BI–(5x5) island Due to the poor CTE of the backside CCD in ACIS-2C, an extended pixel island is being extracted from the raw data. Events are still detected on a 3x3 pixel island using the rules described above; however, an extra pixel is extracted from all sides to perhaps aid in the analysis. Events are written to the event list as a 25 pulse height vector in the order illustrated below:

p_{20}	p_{21}	p_{22}	p_{23}	p_{24}
p_{18}	p_6	p_7	p_8	p_{19}
p_{16}	p_4	p_0	p_5	p_{17}
p_{14}	p_1	p_2	p_3	p_{15}
p_9	p_{10}	p_{11}	p_{12}	p_{13}

This was done so that software that was written to only look for 3x3 pixel islands can still get that information without any change to the code.

Events are still not recorded if they occur at the frame and node boundaries; however, the spacing is now bigger. There is now a two pixel boundary around each quadrant, leading to a four pixel gap in images at quadrant boundaries.

3.2.3.2 Continuous Clocking

In continuous clocking mode, events are defined to lie in a single row. Therefore the events extracted and written to the event list have the following structure:

$p_0 \geq p_1$	$p_0 \geq$threshold	$p_0 > p_2$

In continuous clocking mode, the CHIPY position is always equal to 1 and LABY is set at 512. Events are still not detected at quadrant boundaries (1 pixel on each side of node); however, they are detected at the top and bottom row of the frame.

3.2.3.3 Integration Mode

In integration mode, the source flux is intentionally increased to the point where multiple photons are hitting the CCD during a single integration time. The charge from the photons accumulates (integrates) in each pixel. This mode can be used to quickly determine centroid locations, but is not applicable for spectral measurements where we need to know the energy of every single photon. (Note that this mode works in the same way as CCDs in the optical regime.)

The problem with this mode is that normal event detection fails. There is typically no local maximum except at the very center of the image, so all the photons on the gradient leading up to the peak would be lost. A different way of extracting data is therefore needed.

Integration mode data are extracted in two ways: event list and postage stamps. The two methods were chosen to satisfy differing requirements of the ACIS team and the ASC. Both methods have advantages and disadvantages which will be discussed below.

3.2.3.3.1 Event List The integration mode event list is very similar to the photon counting event list as far as the FITS format goes; however the criteria of what an event list is has changed. In integration mode, any pixel in the bias subtracted image that is above some user set threshold is output to the event list. This is simply a way to encode the images as an event list. The differences in the event list are

- Long integer. The pulse height column is a single long integer, instead of multiple short integers. This is to accommodate the ACIS-2C electronics that read data out in the range from 0-65535. *Any pixel that has a value of 65535 was pinned at the A/D converter limit and should be rejected.*

- Extra "Grade" column. To make this data format compatible with ASCDS (ASC Data Systems) software, an extra column was added to the event list. This is simply a column of 0's ...as in integration mode, the event list is treated as events with flight grades assigned.

  The advantage of this format is that every frame is recorded individually, resulting in a much finer time scale. The disadvantage is that this is a difficult format to understand ... basically we are simply changing an image into an event list.

3.2.3.3.2 Postage Stamps In Staggered Frame mode, there are multiple windows containing data in a single raw FITS file. This information has to be transferred to the AQLC efficiently. Instead of sending the entire FITS file, a postage stamp is extracted from each raw FITS file for the AQLC to use. Only 1 postage stamp is extracted for each raw FITS file regardless of the number of windows that file may contain. The following is a summary of the steps involved in creating the postage stamp files:

1. Read in average bias and convert to long integer. Saturated pixels are converted to NaN's
2. Read in raw FITS image and convert to long integer. Saturated pixels are converted to NaN's
3. Subtract bias from raw image and do over-clock correction as in photon counting event list.
4. Sum all the windows together.
5. Apply gain corrections for each node (convert to real numbers).
6. Extract a region about the user input centroid (program can determine/adjust centroid if desired).
7. Write out a FITS postage stamp image.
8. At end, write out a total postage stamp image from all the data.

The advantage is that these images give a quick turn around on the quality of the data and are good for computing centroids. The disadvantage is that the time scale for each image is the total time of the raw FITS image (about 6sec), and if the user selects too small a postage stamp to extract, useful data may be lost.

3.2.3.4 Overclock status file

The overclock correction value and the overclock noise value (standard deviation of bias corrected overclock pixels) are written to an ASCII file. These can be useful to diagnose the electronics to see if there were significant jumps during any of the runs.

3.2.3.5 Housekeeping file

The housekeeping file contains information about the electronic voltage and current settings. It is not of interest to the general user.

Chapter 4

CCD Detector Calibration and Modelling

4.1 Basic CCD Model Components and Measurement Strategy

The fundamental strategy for calibration of the ACIS instrument is to make measurements which constrain free parameters of mathematical models of the system. This approach was followed in calibration of the CCD detectors themselves, and the reader must therefore understand the detector models in order to understand the detector calibration.

In this section we describe some principles of X-ray CCD detector operation and describe the parameters of the (simplified) CCD model which we have fit to the data. In section 4.2, we present an overview of the measurements made to constrain those parameters.

4.1.1 A Brief Description of ACIS CCDs

The ACIS focal plane contains ten MIT Lincoln Laboratory CCID17 charge-coupled detectors. The CCID17 (Burke et al., 1997) is a three-phase, frame transfer imager with 1026 rows of 1024 columns in each of the imaging and framestore areas. The 2 rows nearest the framestore section are ignored by the ACIS digital electronics. The pixels in the imaging area are 24 microns square. Each device is served by four output nodes which are (usually) operated in parallel. The architecture is illustrated in Figure 4.1.

ACIS flight detectors are fabricated of high-resistivity silicon ($\rho > 6500\Omega$-cm) to maximize depletion depth and, therefore, high-energy X-ray detection efficiency. The devices are three-side-abuttable to minimize inter-chip gaps in the flight focal plane. Flight CCDs have been fabricated in both front-illuminated and back-illuminated configurations. Other characteristics of the detectors are listed in Table 4.1.

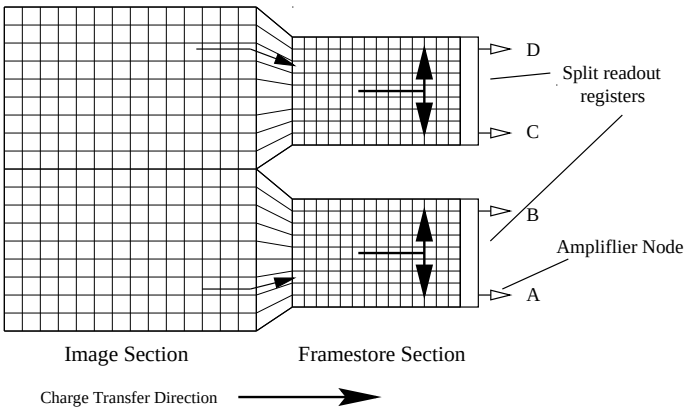

Figure 4.1: Layout of the ACIS CCID17 detector, showing framestore architecture and four output nodes. Ten such devices comprise the ACIS focal plane.

Parameter	Value
Architecture	3-phase, frame-transfer, 3-side-abuttable
Format	1024 columns by 1026 rows, image array
	2x 512 columns by 1026 rows, framestore
Pixel Size	24 x 24 μm, image array
	21(H) x 13.5(V), μm, framestore
Output Nodes	4
Readout Rate	100 kpix s^{-1} at each of output four nodes
	400 kpix s^{-1} total per CCD
Operating Temperature	-120C (nominal)
Readout Noise:	
CCD	$< 2e^-$ RMS, typical
System	2 - 3 e^- RMS
Charge Transfer Inefficiency:	
(Low-illumination, 5.9 keV)	
FI Devices	$< 3 \times 10^{-6}$ per pixel transfer
BI Devices	$< 1 - 3 \times 10^{-5}$ per pixel transfer
Mean Dark Current (-120C)	$< 5 \times 10^{-2} e^- s^{-1}$ pixel^{-1}

Table 4.1: Some Characteristics of the ACIS CCD (MIT Lincoln Laboratory CCID17)

4.1.2 X-ray CCD Detection Efficiency: Processes, Models and Parameters

A cross-section of a generic, front-illuminated CCD is shown in Figure 4.2. In this figure, X-rays incident from the top must pass through a number of "dead" layers which make up

the gate structure before entering the photosensitive volume of the device. The function of the gate structure is to allow charge collected in the device to be moved (transferred) from the vicinity of the photon interaction site to an output amplifier which converts the charge to a measurable electrical signal. The direction of charge transfer is indicated in the figure. The gate structure consists of overlapping strips of highly-doped, conductive polysilicon, interlarded with insulating silicon dioxide, and undergirded by relatively thin, uniform insulating layers of silicon nitride and silicon dioxide. Although the gate structure is not completely insensitive to X-rays, (see section 4.14 below) for present purposes we assume it to be so.

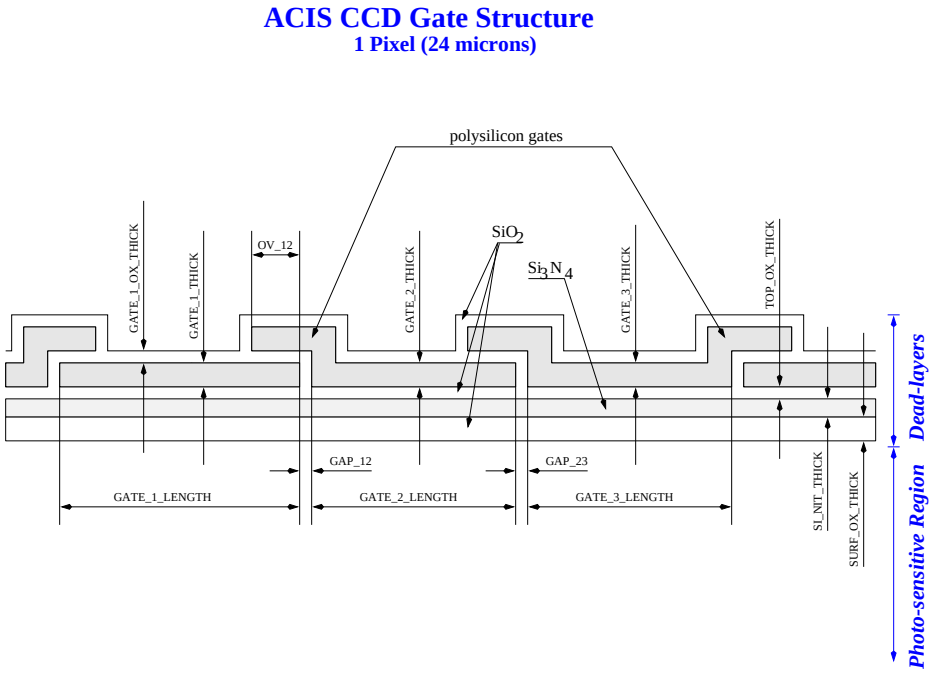

Figure 4.2: Cross-section through a front-illuminated CCD. X-rays are incident from the top. The gate structure poses a deadlayer; only the depletion region region is usefully photosenstive. Calibration data must constrain the physical dimensions of these and other regions shown in the figure.

A section of the CCD in a plane orthogonal to that shown in figure 4.2, would reveal a set of structures called the channel stops. (The channel stops are illustrated and discussed in great detail in section 4.5 below). The channel stops function to isolate adjacent CCD columns from one another, and present additional dead and partially dead layers which affect CCD detection efficiency.

Back-illuminated CCDs differ from front-illuminated devices in two crucial ways. First,

back-illuminated devices are thinned; essentially all of the material shown "below" the depletion region in Figure 4.2 is removed during device fabrication. In fact, to ensure a sufficiently strong electric field at the back surface, some of the putative depletion region is removed during the thinning. Therefore, a back-illuminated device is thinner than the depleted region of a front-illuminated device. Second, the device is mounted so that the X-rays are incident from the bottom in Figure 4.2. As a result, the gate structure does not function as a deadlayer in a back-illuminated device. A very thin deadlayer of silicon dioxide (of order $\sim$ 500 Angstroms thick) does exist on the back (illuminated) surface of the back-illuminated devices.

The total thickness of the gate structure is of order 0.5 microns. Deadlayers associated with the channel stops are somewhat thicker, but cover a relatively small fraction of the device (see section 4.5, below). In any event, the deadlayer thicknessses (rather than, say, electronic noise) largely determines the low-energy limit of the response of the front-illuminated CCD. By construction the gate structures and channel stops are not deadlayers for the back-illuminated CCD, and the "low-energy limit" of these devices is much lower than that of the front-illuminated detectors.

X-rays penetrating the gate structure may be absorbed photoelectrically by the silicon below. If the X-ray is absorbed, the resulting primary photoelectron produces secondary ionization within a volume which is very small compared to the scale of 1 CCD pixel (generally much less than 1 micron in radius for X-rays in the 0.1- 10 keV bandpass of interest). Auger relaxation of the absorbing silicon atom will also contribute to the charge produced. The volume immediately below the gates (for the first 60 - 75 μm) is depleted of free charge carriers. The residual negative fixed charge provided by the ionized acceptor impurities (the substrate is very lightly doped p-type), together with the charge induced on the gates when they are biased, produces a relatively strong electric field in the depletion region. This field sweeps photo-liberated electrons up to the charge transfer channel very rapidly (on timescales of nsec or less). Once in the transfer channel, the charge may be transferred to the CCD output node by application of proper voltage waveforms to the various gates, and then measured.

The depletion region of a typical front-illuminated ACIS flight device is between 65 and 75 microns thick; the back-illuminated devices have photosensitive volumes which are 30 to 40 microns thick. These thicknesses essentially determine the high-energy detection efficiency limit.

In simplest terms, then, the CCD detection efficiency is the probability than an incident X-ray will interact (photoelectrically) in the depletion region, rather than being absorbed in the gate structure or passing entirely through the depletion region without interaction. This is in principle a straightforward problem requring that one find the spatially averaged transmission of the gate structure, and the transmission of the (assumed uniformly thick) depletion region as functions of incident X-ray energy. If the relevant mass absorption coefficients are known, (except near edges, where, as discussed in section 4.6.4, below, we have measured the mass absorbtion coefficients, we adopt the values published by Henke

in 1993) the problem reduces to one of determining dimensions.

In practice, even this simple model is rather more complex than the one we have fit to the data. Specifically, all analysis presented in this report will assume that each gate structure layer is uniform along the charge transfer direction shown in Figure 4.2, and piecewise uniform in the direction normal to the page of the figure. The quantum efficiency model then has only the seven gate structure parameters listed in Table 4.2; the thickness of the depletion region is the eighth and final model parameter.

Parameter/Description	Typical Value (μm)
Pixel Width	24.0
Silicon Gate Thickness	0.25 - 0.30
SiO_2 Insulator Thickness	0.20 - 0.35
Si_3N_4 Insulator Thickness	0.02 - 0.04
Channel Stop Width	4.1
Channel Stop Silicon Implant Thickness	0.35
Channel Stop SiO_2 Thickness	0.45

Table 4.2: Parameters for "Slab and Stop" Model of CCD Gate Structure

While this model oversimplifies the three-dimensional gate structure, it is worth noting that it is exactly correct to first order in the gate structure optical depth. Thus it is least accurate at energies where the gate optical depth is large (e.g., at energies immediately above those of the K absorption edges of oxygen and, to a lesser extent, of nitrogen and silicon). Our detection efficiency model also neglects the influence of charge collection efficiency (described below) on detection efficiency; fortunately, we have found that by judicious choice of event selection criteria, that the latter effects are independent of energy. We discuss this point further in the following paragraphs. Finally, it is worth stressing that the depletion approximation is just that; in adopting this approximation by fitting for the "depletion depth" parameter (see section 4.6.2), we have ignored the fact that the electric field does not drop linearly to zero in the substrate. The remarkable accuracy of this approximation is a consequence of the fact that the depletion region is quite large compared to the amount the initial charge cloud diameter changes over the energy band.

Although to date we have used only the simplified detection efficiency model described in this section to predict ACIS detector quantum efficiency, we have developed a more detailed model for use in future analysis. This model is described in some detail in section 4.14. We must rely on the sub-pixel structure measurements described in section 4.5, together with (destructive) electron micrographs of sibling devices produced by Lincoln Laboratory,

to estimate typical values for some of the parameters (gate overlaps, phase-to-phase gate thickness variations, and channel stop dimensions) of the detailed gate structure model.

4.1.3 Spectral Redistribution: Processes, Models and Parameters

A spectral redistribution function describes the probability of an instrument response in each pulse-height channel to photons of any particular energy. In this section we discuss the spectral redistribution function and its models.

To guide this discussion, a typical spectral redistribution function for a front-illuminated CCD (the response of a flight-like detector to a radioactive ^{55}Fe source) is shown in Figure 4.3. The main components of the redistribution function are indicated: in addition to the two primary photopeaks at 5.9 and 6.4 keV (from the Kα and Kβ lines of the manganese daughter of the radioactive decay), one sees Si-K escape and flourescence peaks, an assymetrical shoulder on the low-energy side of the photopeaks, a low-energy continuum, and an upturn (tail) at very low energies. (The Manganese L lines from the source are also visible). The off-nominal features (everything except the primary photopeaks) together contribute about 2% of the integrated area under the response function at this energy. The task of modelling the spectral response function is to predict this curve in sufficient detail to meet AXAF calibration requirements.

We divide our discussion into three parts: the energy scale (or "gain"); the spectral resolution (essentially the width of the photopeak); and the off-nominal features (everything else).

Consider first the first moment of the spectral redistribution function, that is, the variation of the mean response (essentially the centroid of the primary photopeak) with incident energy. To high accuracy, the output of an ACIS front-illuminated detector (and its associated detector electronics) is a highly linear function of the *charge* generated in the detector. In the absence of pileup, the photon induced charge is, in turn, a highly linear function of the input photon energy. This linear relationship between input energy and the output pulseheight is sometimes referred to as the energy scale or "gain" relation. While the linearity of the energy scale rests on the well-understood physics discussed briefly below, (not to mention nearly-ideal detectors and meticulous electrical engineering), the program of the energy scale calibration is the empirical one of determining the slope and intercept of this relationship for each of the forty CCD output nodes as a function of focal plane and detector electronics temperatures. Results of this determination are presented in sections 4.3.1 and 4.9.2. It is worth noting, that, as is shown in section 4.3.1, the back-illuminated detectors exhibit significant non-linearity that we have not yet modelled in physical terms.

The second moment of the redistribution function (the detector's "spectral resolution", as measured by the width of the photopeak) is, in the case of front-illuminated detectors,

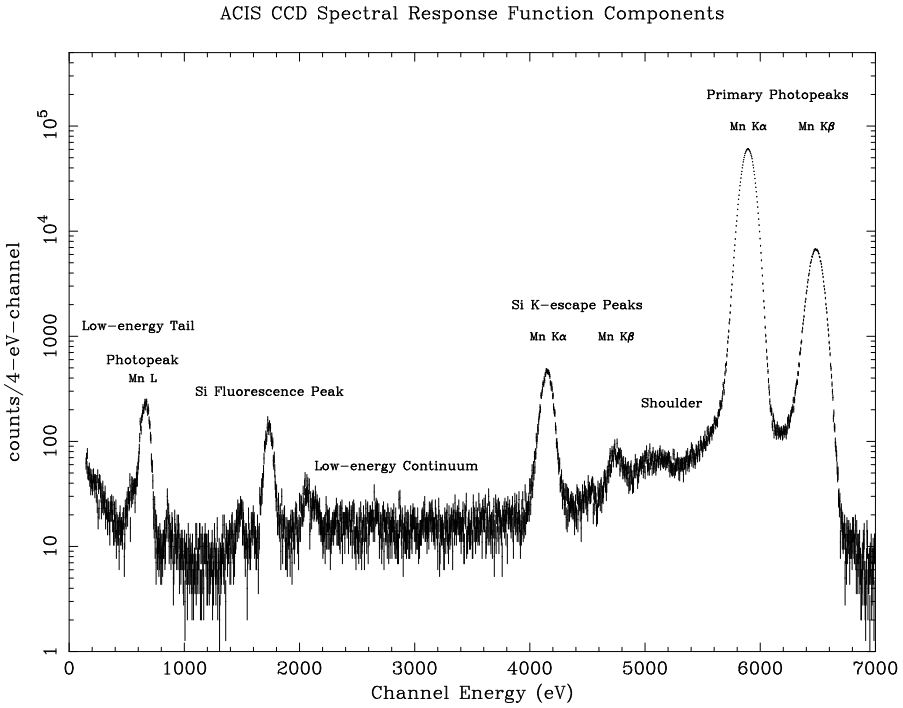

Figure 4.3: Principal components of the CCD spectral response function. The (asymmetric) primary photopeaks, silicon K-escape and fluorescence features, and the extended low-energy tail are indicated. Note that the upturn in the tail at very low energies (E< 400 eV) is not due to electronic noise, but is a characteristic of the detector itself. Note that the ordinate is logarithmic.

equally amenable to simple modelling. In the mean, the quantity of charge liberated by an X-ray interacting in the CCD is proportional to the energy of the incident X-ray:

$$N_e = \frac{E}{w} \tag{4.1}$$

where N_e is the number electrons liberated, E is the photon energy and $w \approx 3.7eV/e^-$, the mean ionization energy per electron-hole pair, is a function of the temperature of the silicon.

The two most important factors affecting the spectral resolution of the CCD are readout noise and the stochastic nature of the ionization process. The readout noise characterizes the accuracy with which one can measure the quantity of charge deposited in any given pixel. For ACIS detectors, the readout noise is found to be a normally distributed, zero mean random deviate (see, e.g., (Pivovaroff et al., 1996)) of standard deviation $\sigma_r \sim$ 2-3

electrons, RMS, per read. The variance σ_N^2 on the charge liberated N_e, is

$$\sigma_N^2 = F \times N_e = F \times \frac{E}{w} \tag{4.2}$$

where F, the Fano factor, has the value $F = 0.135$, and is characteristic of crystalline silicon. Using the room-temperature measurement of (Scholze et al., 1996), *viz.*, $w = 3.64 \pm 0.03 eV/e^-$ and the temperature dependence reported by (Canali et al., 1972), who find that w increases linearly with temperature between 77K to 300 K, and we expect that $w = 3.71 eV/e^-$ at the CCD operating temperature of $T = 153K$.

The effect of these two processes alone, then, is that the primary photopeak produced in response to a beam of monochromatic incident photons of energy E will be a Gaussian distribution with mean proportional to E and standard deviation, expressed on the input energy scale, given by

$$\sigma_E = \sqrt{(w\sigma_r)^2 + (F \times w \times E)} \tag{4.3}$$

The form of equation 4.3 is an accurate model of the spectral resolution of front-illuminated ACIS detectors, as is shown in section 4.3.1. This accuracy is the more remarkable in light of the fact that equation 4.3 neglects the summation of multiple pixels to compute the event amplitude (see below). The insensitivity of the spectral resolution to multi-pixel summation arises because the readout noise σ_r is low enough, and the depletion depth large enough, that $\sigma_N^2 \gg \sigma_r^2$ at all energies where a significant fraction of events must be summed. Note also that equation 4.3 implies that the the spectral resolution can be computed from i) a measurement of the readout noise and ii) knowledge of w and F. As discussed in section 4.3.1, the best fit model parameters differ significantly from the values expected on this basis. Finally, the resolution of the back-illuminated devices deviates considerably from the predictions of equation 4.3. This deviation has yet to be modelled in detail.

As Figure 4.3 shows, a number of processes complicate the CCD spectral redistribution function. In addition to the K-escape and fluorescence phenomena common to all photoelectric X-ray detectors, the CCD response function is influenced by incomplete charge collection and, to a more limited extent, by photoelectric interactions in the gates and channel stops.

The amplitude of the K-escape peak may be modelled reasonably accurately through straightforward simulation of photon transport in the detector. With somewhat less accuracy, the (lower) amplitude of the silicon flourescence line can also be modelled; see section 4.3.2, below. The locations and widths of these peaks are also modelled in the obvious way.

In practice, then our model of the portion of the spectral redistribution function discussed to this point consists of a sum, for each incident energy, of a set of Gaussian distributions of fixed relative centroid locations, with absolute locations, relative amplitudes and widths constrained by fits to measurements. Together, these components account for all but about 1% of the spectral redistribution function for the front-illuminated devices.

Finally, we come to the remaining off-nominal features: the shoulder, low-energy continuum and low-energy tail. The physical origin of these features is believed to be well-understood, but their amplitude is not easily desribed analytically.

In spite of the relatively small volume occupied by initial the photoelectric charge cloud, there is a non-zero probability that charge can be shared among multiple pixels, because events can occur near pixel boundaries. Although the event amplitude computation algorithm sums together pixels in which signficant charge is detected, a pixel is only included in the sum if it exceeds a so-called split-event threshold, typically set at 15 electrons (equivalent to about 55 eV). The split-event threshold excludes empty (but noisy) pixels from the event amplitude summation, but has the undesirable consequence of excluding some bonafide photo-ionization from the sum. As a result, the spectral redistribution function can contain a low-energy shoulder.

Moreover, some charge from events which interact below the depletion region (in front-illuminated devices) will diffuse to the back of the device and will never be collected in the charge transfer channel. Events of this sort can generally be identified because the charge that is collected must diffuse large distances, and hence can occupy several pixels (more than 3). Charge can also be lost when photons interact in the channel stops and gate structure. These processes produce a "low-energy continuum" tail on the spectral response function. A more detailed account of this model, developed at MIT by Prigozhin et al. (1998), is given in section 4.3.2.

4.1.4 De-coupling Detection Efficiency and Spectral Resolution by Choice of Event Selection Criteria

The charge diffusion and charge loss processes just described also affect the effective detection efficiency of the CCD. This coupling operates mainly by way of the "event-shape-based" event selection criteria which, as discussed above, are used to reject events for which charge collection is so poor that the event amplitude is a poor measure of the incident photon energy. If each and every event rejected on grounds of shape resulted from interactions outside the depletion region, then the effect of the selection criteria could be modelled in a straightforward "geometrical" way. In fact, the selection criteria are not perfectly efficient; they accept a fraction of events occuring outside the depletion region, and reject a fraction of events occuring in the depletion region.

While the ultimate CCD model will predict this coupling by accurate simulation of the details of the charge diffusion process, for present purposes we have attempted to avoid the problem by choosing event selection criteria that minimize the influence of charge collection effects on detection efficiency. Specifically, we elect to compute the response of the CCD for ASCA event grades 0, 2, 3, 4 and 6, with a split event threshold of 15 electrons. (This criterion accepts all 1- and 2-pixel events, as well as "L-shaped" 3-pixel events and square or "Quad-shaped" 4-pixel events. More precisely, our standard grade selection

criterion accepts events in accordance with the following ACIS grade map: 0x1d05 0x0047 0x0004 0x0047 0x1133 0x0003 0x1100 0x0000 0x1d04 0x0000 0x0004 0x0000 0x0000 0x0003 0x0000 0x0000. Readers without decoder rings may see the ACIS Software Requirements Specification for an interpretation.

This criterion also turns out to produce a response function which is relatively insensitive to the precise value of the split-event threshold.

In principle, the event selection criteria we've adopted represent the high-detection efficiency extreme of detection efficiency-*vs.*-spectral resolution tradeoff. However, in practice, the readout noise of the ACIS detectors is so low, and the depletion depth so large, that, at least for front-illumianted detectors, there is little sacrifice in spectral resolution entailed by this choice. As is discussed elsewhere in this report, the situation is not so clear for the back-illuminated detectors.

4.2 Overview of Detector Calibration Measurements

As has been indicated in the introduction to this report, the calibration of the ACIS instrument has been performed at several levels. Figure 4.4 provides a summary of the various calibration stages.

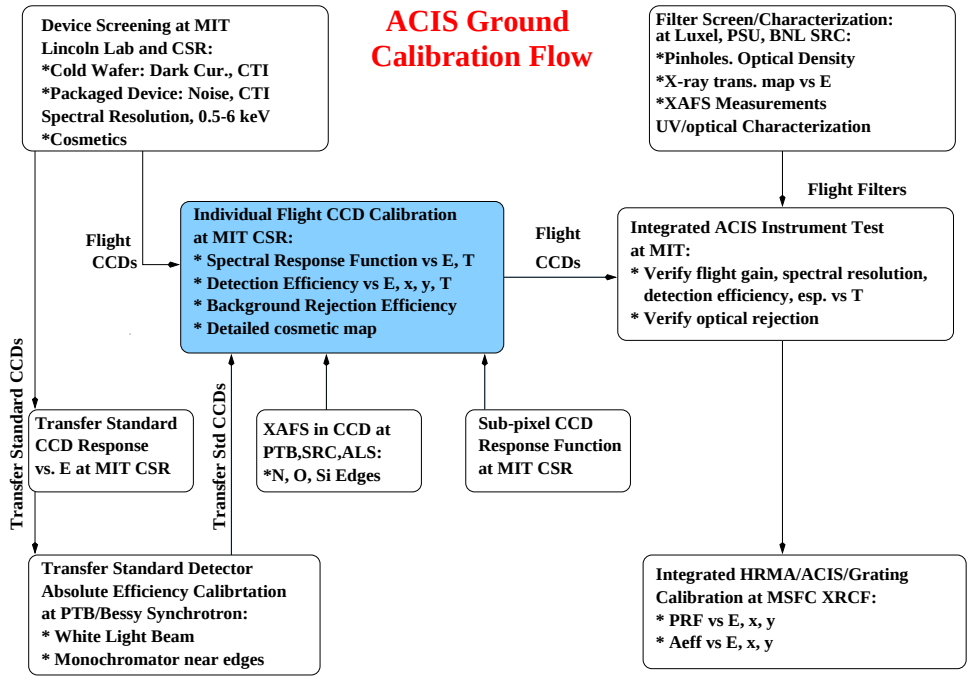

Figure 4.4: ACIS ground calibration flow.

In nearly every stage of this process, data were obtained that constrain the response

of the CCDs themselves. Moreover, a number of ancillary measurements, not shown in Figure 4.4, were made to address particular calibration issues. These include measurement of X-ray Absorption Fine Structure near the relevant edges in the detector response, measurement of structure within a single CCD pixel, and measurement of pileup effects for a variety of source spectral and spatial distributions. At this writing, not all of these data have been analyzed.

Here we summarize the objectives and some salient characteristics of each type of measurement that bears directly on CCD performance calibration. It is intended that this summary serve as a guide to the analysis presented in the remainder of this chapter, as well as an indication of what additional data remain to be analyzed.

Specifically, spectral response function measurements are discussed in section 4.3, and pileup effects and sub-pixel structure are considered in sections 4.4 and 4.5, respectively. Absolute quantum efficiency measurements are described in section 4.6, while comparison of the flight detectors to absolutely calibrated standards is discussed in section 4.7.

It should be noted that the confidence we may ultimately place in the ACIS calibration will depend critically on the extent to which the elements of this large, overlapping measurement set can be compared, one to another. The power of this intercomparison is illustrated, for example, in section 4.7.3, which compares relative detection efficiency measurements made at MIT subassembly calibration with those made using the integrated instrument at XRCF. It is clear at present, that much work remains to be done if we are to achieve a calibration that is as accurate as this vast data set allows.

ACIS Detector Response Function Measurements are summarized by objective in Table 4.3.

4.3 Energy Scale and Spectral Redistribution Function

4.3.1 Energy Scale and Spectral Resolution

4.3.1.1 Purpose

The purpose of this section is to present the correct response from incident X-ray energy to detected pulse height for the ACIS flight instrument. Also presented is the spectral resolution of the ACIS flight devices.

4.3.1.2 Measurements

The XRCF energy scale and spectral resolution results presented here have been based on phase I telemetry data. XRCF phase I was performed with the ACIS flight instrument, but without the High Resolution Mirror Assembly or the gratings. The full ACIS focal plane was illuminated with X-rays from either the Electron-Impact Point Source or the Double

Measurement Objective	Site	Spectral Content†	Spatial Distrib.	Energies (keV)	Flight Devices?	Analysis Status	Remarks
Spectral Response	MIT	Mon.	Diffuse	0.2-1.5(cont)	yes	TBD	HIREFS,IFM
		QM.	Diffuse	0.5 - 9.9 (15 energies)	yes	Done	
	PTB/ BESSY	Mono.	Diffuse	0.2-1.5	no	Done	SX-700 grating mon.
		Mono.	Diffuse	1.5-6	no	Done	KMC 2-crys. mono.
	XRCF(I)	Mon.,QM.	Diffuse	0.3 - 8.1 (7 energies)	yes	In prog.	4.3
Detection Efficiency (Primary Std.)	PTB/ BESSY	Continuum	Diffuse	0.2 -4	no	Done	sec. 4.6.1
		Undisp. S. R.		0.2-12	no	Done	WLS; 4.6.1
		Mono.	Diffuse	0.2-1.5	no	Done	SX-700; FI and BI
Detection Efficiency (Secondary. Std.)	MIT	QM	Diffuse	0.2-8.0 (8 energies)	yes	Done	2×10^6 phot/energy sec 4.7.2
	XRCF(F,G)	QM,Mon.	HRMA	0.3 - 10	no	In Prog.	ACIS 2C
	XRCF(H)	QM,Mon.	HRMA	0.3 - 8	yes	In Prog.	Flight Instr.
	XRCF(I)	QM,Mon.	Diffuse	0.3 - 8.0	yes	In Prog.	Flight Instr. sec. 4.7.3
XAFS	ALS,UW/SRC PTB/BESSY	Mon.	Diffuse	N-K,O-K,Si-L,K	no	Done	Thin Films sec. 4.6.4
Sub-pixel	MIT	QM	Mesh(4μm)	0.5 -2	no	In Prog.	sec. 4.5
Structure/ Spatial Lin.	XRCF(F)	QM,Mon.	HRMA	0.3 - 8	no	In Prog.	ACIS 2C
	XRCF(H)	QM,Mon.	HRMA	0.3 - 8	yes	In Prog.	Flight Instr.
Pileup/	MIT	QM	Diffuse	0.2-8.0	no	In Prog.	sec. 4.4
Count Rate	PTB/BY	Cont. S.R.	Diffuse	0.2 -4	no	In Prog.	sec. 4.4
Linearity	XRCF(F,G)	QM,Mon.	HRMA	0.3 - 10	no	In Prog.	ACIS 2C
	XRCF(H)	QM,Mon.	HRMA	0.3 - 8	yes	In Prog.	Flight Instr.

†:
Mon.: monochromatic;$\frac{E}{\Delta E} > 100$;.
QM: quasi-monochromatic (electron-impact or photon-fluor.;
S.R: Synchrotron Radiation

Table 4.3: ACIS CCD Response Function Measurement Summary

Crystal Monochromator. During XRCF phase I, the detector electronics temperature was 13° C and the focal plane temperature was −110° C.

ACIS was run in the full frame timed exposure mode, with a 3.34 second exposure time. During most science runs, six of the CCDs were read out simultaneously. A single science run included a number of TRW IDs, and in a few cases multiple energies as well. Subarrays of various sizes were used to avoid telemetry saturation. Table 4.4 describes each of the science runs used in this section.

4.3.1.3 Data Processing

The ACIS FEP processing mode was timed exposure faint 3x3 with an event threshold of 38 ADU for the front illuminated devices and 20 ADU for the back illuminated devices.

Science Run	Source	Energy	FI Window	BI Window	CCDs	TRW IDs
		eV	Rows	Rows		
69	EIPS O-K	525	500	156	s0 s2 s4-5	
70	EIPS O-K	525	250	78	s0-5	I-IAS-EA-2.001 - 2.006
71	EIPS O-K	525	250	78	i0-3 s2-3	I-IAI-EA-1.001 - 1.004
72	EIPS Si-K	1740	56	50	s0 s2 s4-5	I-IAS-EA-2.013 - 2.018
75	EIPS Si-K	1740	56	50	i0-3 s2	I-IAI-EA-1.009 - 1.012
77	EIPS Fe-K	6399	46	46	i0-3 s3	
78	EIPS Fe-K	6399	46	46	i0-1 i3 s3	I-IAI-EA-1.025 - 1.028
83	EIPS Fe-K	6399	46	46	i0-2 s2-3	I-IAI-EA-1.028
84	EIPS Fe-K	6399	46	46	s0-5	I-IAS-EA-2.037 - 2.042
91	EIPS Cu-K	8040	30	30	i0-3 s2-3	I-BND-BU-2.004
92	EIPS Cu-K	8040	20	30	i0-3 s2-3	I-IAI-EA-1.029 - 1.032
93	EIPS Cu-K	8040	20	30	s0-5	I-IAS-EA-2.043 - 2.048
96	EIPS C-K	277	1024	512	s0-5	I-BND-BU-2.037
97	EIPS C-K	277	512	1024	s0-5	I-IAS-EA-2.049 - 2.050
100	EIPS Ti-K	4509	28	24	s0-5	I-IAS-EA-2.032, 2.034
104	EIPS Ti-K	4509	28	24	i0-3 s2-3	I-IAI-EA-1.024
111	EIPS Al-K	1487	24	20	s0-5	I-IAS-EA-2.029 - 2.031
112	EIPS Al-K	1487	24	20	i0-3 s2-3	I-IAI-EA-1.017 - 1.020
114	EIPS Si-K	1740	28	26	i0-3 s2	I-IAI-EA-5.003 - 5.004
115	EIPS O-K	525	250	78	i0-3 s2-3	I-IAI-EA-5.001 - 5.002
116	EIPS O-K	525	250	78	s0-5	I-IAS-EA-2.101 - 2.106
117	EIPS O-K	525	250	78	i0-3 s2-3	I-IAI-EA-1.101 - 1.104
120	EIPS Ti-K	4509	28	24	s0-5	I-IAS-EA-2.131 - 2.132, 2.134
122	EIPS Ti-K	4509	28	24	s0-5	I-IAS-EA-2.133, 2.135 - 2.136
123	EIPS Ti-K	4509	28	24	i0-3 s2-3	I-IAI-EA-1.121 - 1.124
128	DCM	1380	1024	1024	i3 s1 s3	I-IAI-EA-1.204 - 1.206
131	DCM	1770	512	512	i3 s1 s3	I-IAI-EA-1.213 - 1.215
132	DCM	4500	1024	1024	i3 s1 s3	I-IAI-EA-1.222 - 1.224
149	DCM	2035	1024	1024	i0-3 s2-3	I-IAI-EA-1.225

Table 4.4: XRCF Phase I ACIS Science Run Descriptions

The split threshold was 13 ADU for all measurements.

The ACIS BEP processing mode was timed exposure Faint mode with a window filter. The size of the windows varied depending on the flux rate, from as tiny as 20 rows to as many as the full 1024. In all cases, the windowing was split into two strips, one toward the top of the CCD and one toward the bottom of the CCD. Because of the differences in the quantum efficiency of the front illuminated devices from the back illuminated devices, different window sizes were used for the front illuminated and back illuminated devices. The window sizes used in each data set are listed in Table 4.4.

The flight software telemetry packets were converted to FITS format average bias files and ERV format event lists using PSCI (for a description of the formats and the PSCI program see http://acis.mit.edu/ttools/psci.html).

The average bias and the ERV format event lists were combined and converted to ARV format event lists using an IDL script. The IDL script subtracted the delta overclock value and the average bias values for each pixel of each event.

Each ARV format event list was then summarized using an IDL script. This IDL script fit a gaussian to the main peak of the spectrum. Only events in ACIS grade bit map 0x1d05 0x0047 0x0004 0x0047 0x1133 0x0003 0x1100 0x0000 0x1d04 0x0000 0x0004 0x0000 0x0000 0x0003 0x0000 0x0000 (ASCA grades 02346) were considered. Using the fit parameters, the position of the peak, full width half max of the peak (defined to be 2.35 times the fitted sigma), and total number of counts under the peak are determined. The number of counts

under the peak is taken to be $\sqrt{2\pi}\sigma N_{max}$, where N_{max} is the number of counts in the peak channel. The IDL script computes the flux in counts per centimeter squared per second assuming a frame time of 3.34 seconds and an input window size. All of these values are written to a text format file.

Finally, the text format summary files are read by another IDL script which uses the peak location and peak width values at each energy to tabulate and plot the linear energy scale and spectral resolution values. This script also applies a pileup correction and the filter efficiency to the counts under the peak. See Section 4.4 for a description of pileup.

4.3.1.4 Results

The slope, intercept, and RMS deviation of a linear fit of the energy scale of the ACIS flight devices are listed in Table 4.5. Pulse height as a function of energy is fit to the relation $PH(ADU) = Slope \times Energy(eV) + Intercept$.

CCD	Quadrant A			Quadrant B			Quadrant C			Quadrant D		
	Slope	Intercept	RMS	Slope	Intercept	RMS	Slope	Intercept	RMS	Slope	Intercept	RMS
	ADU/eV	ADU	eV	ADU/eV	ADU	eV	ADU/ev	ADU	eV	ADU/eV	ADU	eV
i0	0.2636	0.81	3.75	0.2573	0.65	4.03	0.2662	0.77	3.52	0.2582	0.60	4.06
i1	0.2622	0.38	3.50	0.2559	-0.09	3.97	0.2596	0.36	4.34	0.2616	0.07	3.80
i2	0.2731	-0.98	3.10	0.2839	-1.07	3.35	0.2825	0.07	3.59	0.2745	0.43	3.67
i3	0.2582	1.19	4.68	0.2588	1.25	4.65	0.2542	1.25	4.51	0.2592	1.09	4.55
s0	0.2725	-0.12	4.69	0.2677	-0.54	3.35	0.2574	0.13	4.02	0.2565	-0.34	3.40
s1	0.2359	-22.00	14.80	0.2182	-27.07	22.37	0.2234	-24.86	20.23	0.2297	-25.33	18.84
s2	0.2602	0.03	3.75	0.2715	0.15	5.27	0.2640	-0.51	4.25	0.2692	-0.54	6.33
s3	0.2262	-17.33	11.16	0.2158	-19.88	13.99	0.2186	-19.65	13.18	0.2273	-22.80	13.66
s4	0.2328	-1.09	3.80	0.2272	-0.58	6.16	0.2301	-0.72	5.76	0.2391	-0.96	4.55
s5	0.2534	-0.16	3.09	0.2576	-0.13	3.18	0.2601	0.18	2.70	0.2114	0.46	4.32

Table 4.5: Energy Scale for ACIS Flight Devices

The residual errors from the linear energy scale fit for the front illuminated devices are shown in Figure 4.5. The residual errors from the linear energy scale fit for the back illuminated devices are shown in Figure 4.6. Note that Figure 4.5 and Figure 4.6 are on different vertical scales. Random errors for the line center locations are much less than 1 eV.

The FWHM for the ACIS flight devices is shown in Figure 4.7. In Figure 4.7 the points for the front illuminated devices are the average of the four quadrants, while the points for the back illuminated devices show each quadrant separately. The values for the front illuminated devices are listed in Table 4.6. The values for the back illuminated devices are listed in Table 4.7. The "NA" indicates that a data point is not available. The 277 eV measurement was made only for the S-array. Many of the DCM energies were taken with only i3, s1 and s3 on. One of the DCM sets was taken with only the I-array.

The spectral resolution as a function of energy for the front illuminated devices is shown

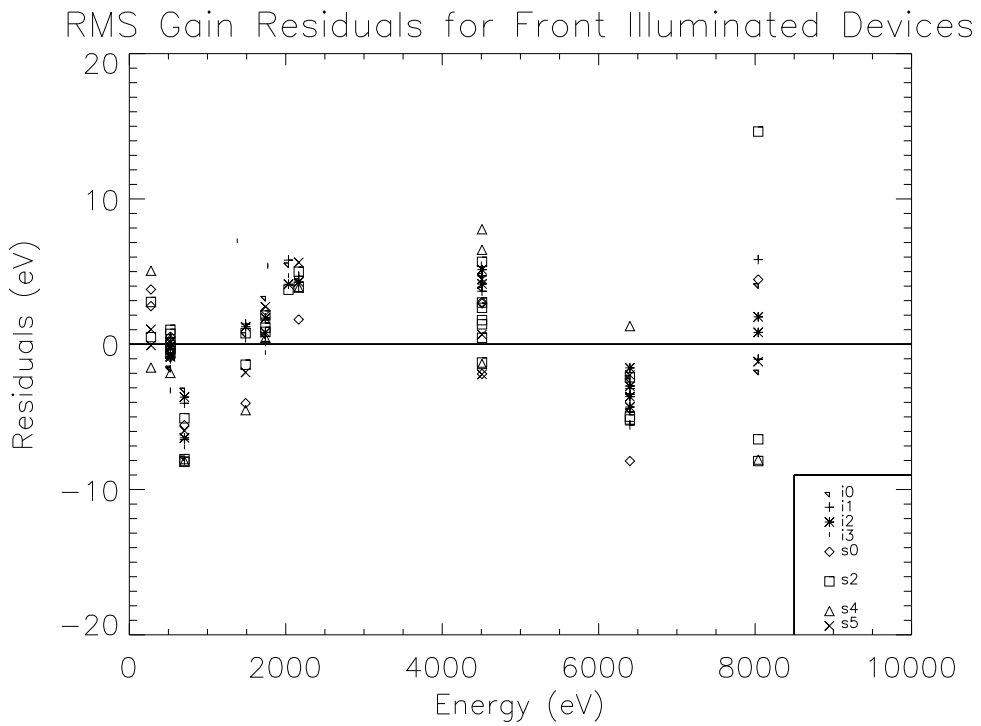

Figure 4.5: Linear Energy Scale Residuals for the Front Illuminated Devices

Energy	277	525	1380	1487	1740	1770	2035	4500	4509	6399	8040
Source	C-K	O-K	DCM	Al-K	Si-K	DCM	DCM	DCM	Ti-K	Fe-K	Cu-K
i0	NA	50.8	NA	73.7	83.7	NA	81.8	NA	120.4	145.9	169.5
i1	NA	50.9	NA	73.3	83.1	NA	80.7	NA	119.9	145.1	169.7
i2	NA	53.7	NA	77.8	89.4	NA	85.6	NA	128.7	155.2	179.1
i3	NA	49.6	67.0	71.8	81.8	77.4	79.7	114.5	118.6	144.0	168.2
s0	45.8	54.9	NA	77.3	86.7	NA	NA	NA	123.5	149.8	175.7
s2	39.6	52.0	NA	74.6	84.6	NA	82.7	NA	122.6	149.0	172.2
s4	37.3	49.8	NA	69.5	78.9	NA	NA	NA	111.3	134.9	159.9
s5	38.8	48.4	NA	69.2	79.3	NA	NA	NA	113.3	137.3	161.4

Table 4.6: Average FWHM (eV) for Front Illuminated Devices

as a solid line in Figure 4.7 and is described by

$$FWHM(E) = \sqrt{(FWHM_0)^2 + 2.35^2 Fano \times w \times E} \tag{4.4}$$

Note that here we treat $FWHM_0$ as an empirical parameter. In the simplest model for

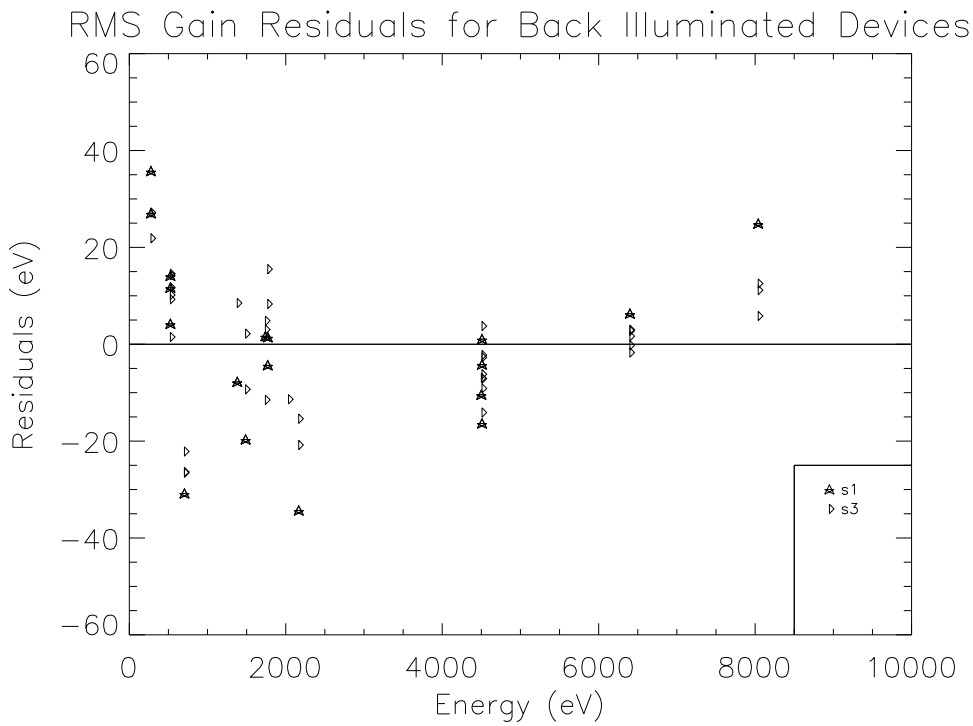

Figure 4.6: Linear Energy Scale Residuals for the Back Illuminated Devices

	Energy	277	525	1380	1487	1740	2035	4500	4509	6399	8040
	Source	C-K	O-K	DCM	Al-K	DCM	DCM	DCM	Ti-K	Fe-K	Cu-K
s1	A	92.8	139.6	143.8	150.3	154.0	NA	205.9	209.0	232.8	242.1
	B	82.6	128.6	135.9	140.5	147.8	NA	205.3	208.6	225.3	234.5
	C	84.9	130.1	135.5	138.2	146.4	NA	210.5	207.5	229.5	234.0
	D	99.5	152.9	159.0	162.3	170.1	NA	233.5	235.0	264.6	275.8
s3	A	73.7	104.5	96.5	105.3	103.9	115.0	141.0	147.4	167.0	180.9
	B	72.1	101.3	95.8	102.6	102.2	110.4	145.1	150.8	170.8	185.5
	C	70.0	102.1	94.9	102.5	102.1	112.9	140.0	143.6	161.3	176.5
	D	89.0	131.2	124.5	135.1	134.5	149.0	193.5	199.4	227.7	241.3

Table 4.7: FWHM (eV) for Back Illuminated Devices

spectral resolution (see section 4.1) one expects

$$FWHM_0 = 2.35 \times \sigma \times w \tag{4.5}$$

The expected value of $Fano \times w$ in silicon detectors at -120 ° C is $0.135 \times 3.73 = 0.504$.

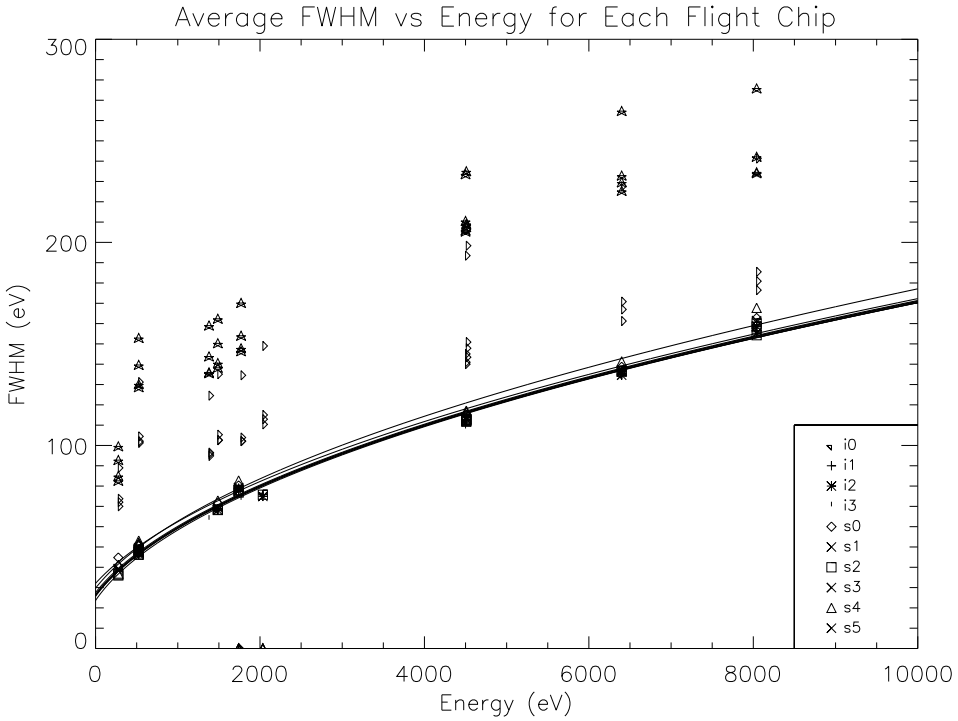

Figure 4.7: Average FWHM versus Energy

$FWHM_0$ and $Fano \times w$ for each quadrant of each front illuminated device is shown in Table 4.8.

Chip	$FWHM_0$	$Fano \times w$
i0	26.56	0.516
i1	26.49	0.517
i2	26.02	0.513
i3	23.77	0.514
s0	32.09	0.519
s2	25.88	0.509
s4	29.73	0.552
s5	27.56	0.518

Table 4.8: Average Front Illuminated Devices $FWHM_0$ and $Fano \times w$

4.3.1.5 CSR Energy Scale Linearity and Spectral Response Valid Data Summary

In addition to the data taken at XRCF, spectral resolution data was collected at CSR. These sets were taken with laboratory electronics identical in design to the flight DEA, but with gains different from the flight electronics. These data should be useful for future analyses of energy scale linearity and spectral response function shape. The data sets are listed in Tables 4.9 through 4.18.

The column labeled "Directory" is the location of the dataset from /ohno/di/database on the local CSR network.

In the column labeled "Rejected Frames" the letter "b" following the number indicates that the majority of the rejected frames were rejected due to pixels above the event threshold in the overclock region. The letter "n" following the number indicates that the majority of the rejected frames were rejected due to standard deviation of the overclocks exceeding the noise threshold.

The column labeled "Counts per Frame" contains the total number of G02346 events under the main peak for the data set.

Each data set included has been checked for by visual inspection of the data products and for consistency with other data sets.

Chip	Target/Energy	Directory eV	Accepted Frames	Rejected Frames	Frame Time (seconds)	Counts per Frame
w203c4r/I0	al/1487	w203c4r/beavis/al/03jan97/2213	547	2b	3.277	4564.4
w203c4r/I0	cl/2622	w203c4r/beavis/cl/05jan97/0895	546	4b	3.277	2383.6
w203c4r/I0	v/4949	w203c4r/beavis/v/05jan97/0931	495	5b	3.277	4746
w203c4r/I0	v/4949	w203c4r/beavis/v/05jan97/1150	49	0n	3.276	4745.6
w203c4r/I0	fe/6399	w203c4r/beavis/fe/03jan97/2249	570	5b	3.277	4139.6
w203c4r/I0	co/6925	w203c4r/beavis/co/05jan97/1017	626	4b	3.277	3815.6
w203c4r/I0	ni/7471	w203c4r/beavis/ni/05jan97/1210	645	4b	3.277	3333.6
w203c4r/I0	ni/7471	w203c4r/beavis/ni/05jan97/1255	100	0n	3.277	3338
w203c4r/I0	zn/8630	w203c4r/beavis/zn/05jan97/1312	642	2b	3.277	2648.4
w203c4r/I0	zn/8630	w203c4r/beavis/zn/05jan97/1359	245	0n	3.277	2679.6
w203c4r/I0	ge/9875	w203c4r/beavis/ge/30dec96/2200	596	2b	3.277	2020.8
w203c4r/I0	ge/9875	w203c4r/beavis/ge/30dec96/2250	596	2b	3.277	2011.2

Table 4.9: w203c4r/I0 CSR Spectral Resolution Data Sets

The data products in each directory are summarized in Table 4.19. See MIT ACIS memo PS-71 dated 4 May 1995, by J. Woo (which can be found at http://acis.mit.edu/ttools/acis-analysis.html) for a detailed description of the file formats.

Chip	Target/Energy	Directory eV	Accepted Frames	Rejected Frames	Frame Time (seconds)	Counts per Frame
w193c2/I1	al/1487	w193c2/butthead/al/22nov96/1819	646	2b	3.277	4577.2
w193c2/I1	p/2015	w193c2/butthead/p/27nov96/2228	174	1b	3.277	1705.2
w193c2/I1	cl/2622	w193c2/butthead/cl/25nov96/1921	648	1n	3.277	2425.6
w193c2/I1	cl/2622	w193c2/butthead/cl/25nov96/2002	324	0n	3.277	2422.8
w193c2/I1	v/4949	w193c2/butthead/v/22nov96/2001	644	6b	3.277	4806.4
w193c2/I1	fe55/5894	w193c2/butthead/fe55/30nov96/1214	594	1b	3.297	3360.8
w193c2/I1	fe/6399	w193c2/butthead/fe/22nov96/1913	644	1b	3.277	4170
w193c2/I1	co/6925	w193c2/butthead/co/29nov96/2002	644	2n	3.277	3840
w193c2/I1	co/6925	w193c2/butthead/co/29nov96/2041	97	2n	3.277	3836
w193c2/I1	ni/7471	w193c2/butthead/ni/29nov96/2300	150	0n	3.277	3426.8
w193c2/I1	ni/7471	w193c2/butthead/ni/29nov96/2323	643	3b	3.279	3404.8
w193c2/I1	zn/8630	w193c2/butthead/zn/22nov96/2050	633	6b	3.278	2501.6
w193c2/I1	zn/8630	w193c2/butthead/zn/22nov96/2141	490	2b	3.279	2496.8
w193c2/I1	ge/9875	w193c2/butthead/ge/25nov96/2027	635	5b	3.278	1982.4
w193c2/I1	ge/9875	w193c2/butthead/ge/25nov96/2108	650	NA	3.277	1983.6
w193c2/I1	ge/9875	w193c2/butthead/ge/25nov96/2148	191	1n	3.276	1998.8

Table 4.10: w193c2/I1 CSR Spectral Resolution Data Sets

Chip	Target/Energy	Directory eV	Accepted Frames	Rejected Frames	Frame Time (seconds)	Counts per Frame
w158c4r/I2	al/1487	w158c4r/butthead/al/03nov96/1340	569	5b	3.277	3822.8
w158c4r/I2	al/1487	w158c4r/butthead/al/05nov96/0938	70	0n	3.279	3752.4
w158c4r/I2	si/1740	w158c4r/butthead/si/05nov96/1241	572	7b	3.322	1693.6
w158c4r/I2	cl/2622	w158c4r/butthead/cl/03nov96/0844	668	6b	3.277	2408.4
w158c4r/I2	cl/2622	w158c4r/butthead/cl/03nov96/0950	299	1b	3.277	2416.4
w158c4r/I2	cl/2622	w158c4r/butthead/cl/05nov96/0955	99	0n	3.277	2370.4
w158c4r/I2	fe55/5894	w158c4r/butthead/fe55/27oct96/1921	788	4b	3.277	2820.8
w158c4r/I2	fe/6399	w158c4r/butthead/fe/03nov96/1416	646	4b	3.277	4259.2
w158c4r/I2	co/6925	w158c4r/butthead/co/03nov96/1250	99	1b	3.277	3800
w158c4r/I2	co/6925	w158c4r/butthead/co/03nov96/1301	646	4b	3.277	3813.6
w158c4r/I2	ni/7471	w158c4r/butthead/ni/03nov96/1032	591	6b	3.278	3229.6
w158c4r/I2	ni/7471	w158c4r/butthead/ni/03nov96/1108	136	4b	3.277	3229.2
w158c4r/I2	zn/8630	w158c4r/butthead/zn/03nov96/1527	516	4b	3.278	2474.8
w158c4r/I2	zn/8630	w158c4r/butthead/zn/03nov96/1558	647	3b	3.278	2469.6
w158c4r/I2	ge/9875	w158c4r/butthead/ge/03nov96/1121	659	6b	3.277	1952.4
w158c4r/I2	ge/9875	w158c4r/butthead/ge/03nov96/1158	651	NA	3.277	1963.2
w158c4r/I2	ge/9875	w158c4r/butthead/ge/03nov96/1234	184	1b	3.277	1966.8

Table 4.11: w158c4r/I2 CSR Spectral Resolution Data Sets

Chip	Target/Energy	Directory eV	Accepted Frames	Rejected Frames	Frame Time (seconds)	Counts per Frame
w215c2r/I3	al/1487	w215c2r/beavis/al/06jan97/2044	550	0n	3.277	4578.8
w215c2r/I3	cl/2622	w215c2r/beavis/cl/06jan97/2002	547	2b	3.277	2423.6
w215c2r/I3	ti/4509	w215c2r/beavis/ti/11jan97/1109	561	6b	3.329	5134.8
w215c2r/I3	v/4949	w215c2r/beavis/v/06jan97/2212	497	3b	3.277	4760.4
w215c2r/I3	v/4949	w215c2r/beavis/v/10jan97/2250	25	0n	3.277	4717.2
w215c2r/I3	fe/6399	w215c2r/beavis/fe/06jan97/2136	564	6b	3.277	4187.6
w215c2r/I3	fe/6399	w215c2r/beavis/fe/10jan97/2233	25	0n	3.277	4148.4
w215c2r/I3	co/6925	w215c2r/beavis/co/06jan97/0106	622	0n	3.277	3788.4
w215c2r/I3	co/6925	w215c2r/beavis/co/10jan97/2258	25	0n	3.277	3815.6
w215c2r/I3	ni/7471	w215c2r/beavis/ni/06jan97/0056	100	0n	3.277	3342
w215c2r/I3	ni/7471	w215c2r/beavis/ni/06jan97/2356	648	2b	3.277	3371.6
w215c2r/I3	zn/8630	w215c2r/beavis/zn/06jan97/2254	645	4b	3.277	2580.4
w215c2r/I3	zn/8630	w215c2r/beavis/zn/10jan97/2150	299	1b	3.277	2678.8
w215c2r/I3	ge/9875	w215c2r/beavis/ge/06jan97/1812	598	1b	3.277	1925.6
w215c2r/I3	ge/9875	w215c2r/beavis/ge/06jan97/1922	596	4b	3.277	1984
w215c2r/I3	ge/9875	w215c2r/beavis/ge/12jan97/1359	74	1b	3.277	1954

Table 4.12: w215c2r/I3 CSR Spectral Resolution Data Sets

Chip	Target/Energy	Directory eV	Accepted Frames	Rejected Frames	Frame Time (seconds)	Counts per Frame
w168c4r/S0	o/525	w168c4r/beavis/o/15dec96/1247	595	5b	7.149	3372
w168c4r/S0	al/1487	w168c4r/beavis/al/14dec96/1914	574	1b	3.277	4483.2
w168c4r/S0	al/1487	w168c4r/beavis/al/20dec96/2018	542	4b	3.277	4524
w168c4r/S0	cl/2622	w168c4r/beavis/cl/14dec96/2027	545	4b	3.277	2347.6
w168c4r/S0	cl/2622	w168c4r/beavis/cl/20dec96/2059	546	1b	3.277	2376.4
w168c4r/S0	v/4949	w168c4r/beavis/v/21dec96/1052	499	1b	3.277	4701.6
w168c4r/S0	v/4949	w168c4r/beavis/v/21dec96/1732	98	2b	3.277	4772.8
w168c4r/S0	fe/6399	w168c4r/beavis/fe/14dec96/2119	573	1b	3.274	4135.6
w168c4r/S0	co/6925	w168c4r/beavis/co/21dec96/1136	611	5b	3.278	3735.2
w168c4r/S0	co/6925	w168c4r/beavis/co/21dec96/1651	100	0n	3.277	3678.4
w168c4r/S0	ni/7471	w168c4r/beavis/ni/21dec96/1219	647	0n	3.277	3203.2
w168c4r/S0	ni/7471	w168c4r/beavis/ni/21dec96/1401	147	2b	3.277	3213.6
w168c4r/S0	zn/8630	w168c4r/beavis/zn/21dec96/1420	647	2b	3.277	2587.6
w168c4r/S0	zn/8630	w168c4r/beavis/zn/21dec96/1814	456	3b	3.277	2653.6
w168c4r/S0	ge/9875	w168c4r/beavis/ge/14dec96/2212	398	0n	3.277	1947.6
w168c4r/S0	ge/9875	w168c4r/beavis/ge/21dec96/0909	592	9b	3.277	1927.2
w168c4r/S0	ge/9875	w168c4r/beavis/ge/21dec96/0956	647	3b	3.277	1900.8

Table 4.13: w168c4r/S0 CSR Spectral Resolution Data Sets

Chip	Target/Energy	Directory eV	Accepted Frames	Rejected Frames	Frame Time (seconds)	Counts per Frame
w140c4r/S1	al/1487	w140c4r/butthead/al/20jan97/2041	647	2b	3.277	5247.6
w140c4r/S1	cl/2622	w140c4r/butthead/cl/20jan97/2131	647	1b	3.277	2819.2
w140c4r/S1	v/4949	w140c4r/butthead/v/24jan97/2106	650	0n	3.277	4092.8
w140c4r/S1	fe55/5894	w140c4r/butthead/fe55/24jan97/1901	645	3b	3.277	2444.8
w140c4r/S1	fe/6399	w140c4r/butthead/fe/23jan97/0752	649	1b	3.277	4294.4
w140c4r/S1	co/6925	w140c4r/butthead/co/24jan97/2157	649	1b	3.277	2689.6
w140c4r/S1	co/6925	w140c4r/butthead/co/28jan97/0916	321	4b	3.277	2720.8
w140c4r/S1	ni/7471	w140c4r/butthead/ni/28jan97/1003	646	4b	3.277	4086.4
w140c4r/S1	ni/7471	w140c4r/butthead/ni/28jan97/1051	649	1b	3.277	4068.8
w140c4r/S1	zn/8630	w140c4r/butthead/zn/28jan97/1147	640	8b	3.277	3149.6
w140c4r/S1	zn/8630	w140c4r/butthead/zn/28jan97/1234	648	2b	3.277	3197.2
w140c4r/S1	ge/9875	w140c4r/butthead/ge/23jan97/0837	646un	nun	0un	3004un
w140c4r/S1	ge/9875	w140c4r/butthead/ge/23jan97/0920	644un	nun	0un	3008.4un

Table 4.14: w140c4r/S1 CSR Spectral Resolution Data Sets

Chip	Target/Energy	Directory eV	Accepted Frames	Rejected Frames	Frame Time (seconds)	Counts per Frame
w182c4r/S2	al/1487	w182c4r/butthead/al/21dec96/1948	561	10b	3.277	4655.2
w182c4r/S2	cl/2622	w182c4r/butthead/cl/21dec96/2029	634	6b	3.277	2390.8
w182c4r/S2	cl/2622	w182c4r/butthead/cl/21dec96/2115	315	4b	3.277	2392.4
w182c4r/S2	v/4949	w182c4r/butthead/v/02jan97/1321	521	4b	3.277	5554
w182c4r/S2	fe/6399	w182c4r/butthead/fe/21dec96/2146	627	5n	3.277	4386.4
w182c4r/S2	co/6925	w182c4r/butthead/co/02jan97/1503	644	4b	3.277	3538
w182c4r/S2	co/6925	w182c4r/butthead/co/02jan97/1802	149	1b	3.277	4058.4
w182c4r/S2	ni/7471	w182c4r/butthead/ni/02jan97/1548	642	8b	3.277	3430.8
w182c4r/S2	ni/7471	w182c4r/butthead/ni/02jan97/1755	148	2b	3.277	3455.2
w182c4r/S2	zn/8630	w182c4r/butthead/zn/02jan97/1631	645	3b	3.277	2708
w182c4r/S2	zn/8630	w182c4r/butthead/zn/02jan97/1718	519	3b	3.277	2707.2
w182c4r/S2	ge/9875	w182c4r/butthead/ge/02jan97/1234	639	9b	3.277	2118.8
w182c4r/S2	ge/9875	w182c4r/butthead/ge/02jan97/1359	645	5b	3.277	2096

Table 4.15: w182c4r/S2 CSR Spectral Resolution Data Sets

Chip	Target/Energy	Directory eV	Accepted Frames	Rejected Frames	Frame Time (seconds)	Counts per Frame
w134c4r/S3	f/677	w134c4r/butthead/f/03feb97/1151	587	0n	7.148	5260
w134c4r/S3	al/1487	w134c4r/butthead/al/01feb97/1941	646	2b	3.277	5342.4
w134c4r/S3	cl/2622	w134c4r/butthead/cl/01feb97/2024	649	1b	3.277	2907.6
w134c4r/S3	v/4949	w134c4r/butthead/v/05feb97/1840	646	4b	3.277	4664
w134c4r/S3	fe/6399	w134c4r/butthead/fe/01feb97/2110	648	2b	3.277	3615.6
w134c4r/S3	fe/6399	w134c4r/butthead/fe/05feb97/1811	100	0n	3.277	3603.6
w134c4r/S3	co/6925	w134c4r/butthead/co/05feb97/1923	641	2b	3.277	4505.6
w134c4r/S3	ni/7471	w134c4r/butthead/ni/05feb97/1457	644	2b	3.277	4457.2
w134c4r/S3	zn/8630	w134c4r/butthead/zn/05feb97/1547	647	1b	3.277	3623.2
w134c4r/S3	zn/8630	w134c4r/butthead/zn/05feb97/1825	99	0n	3.277	3618.8
w134c4r/S3	ge/9875	w134c4r/butthead/ge/01feb97/2152	647	3b	3.277	1733.2
w134c4r/S3	ge/9875	w134c4r/butthead/ge/05feb97/1638	649	1b	3.277	3394.8
w134c4r/S3	ge/9875	w134c4r/butthead/ge/05feb97/1749	100	0n	3.277	3453.6

Table 4.16: w134c4r/S3 CSR Spectral Resolution Data Sets

Chip	Target/Energy	Directory eV	Accepted Frames	Rejected Frames	Frame Time (seconds)	Counts per Frame
w457c4/S4	al/1487	w457c4/beavis/al/02dec96/1024	544	6b	3.277	4634.8
w457c4/S4	cl/2622	w457c4/beavis/cl/02dec96/1155	547	3b	3.277	2405.2
w457c4/S4	v/4949	w457c4/beavis/v/02dec96/0128	49	0n	3.277	4830.8
w457c4/S4	v/4949	w457c4/beavis/v/02dec96/0135	48	1b	3.285	4878.4
w457c4/S4	v/4949	w457c4/beavis/v/02dec96/1424	498	1b	3.277	4807.2
w457c4/S4	fe/6399	w457c4/beavis/fe/02dec96/1236	566	4b	3.277	4151.6
w457c4/S4	co/6925	w457c4/beavis/co/02dec96/1500	624	6b	3.277	3995.6
w457c4/S4	ni/7471	w457c4/beavis/ni/02dec96/1638	639	5b	3.278	3516.8
w457c4/S4	ni/7471	w457c4/beavis/ni/02dec96/1832	98	2b	3.277	3544.4
w457c4/S4	zn/8630	w457c4/beavis/zn/02dec96/1726	644	4b	3.277	2906
w457c4/S4	zn/8630	w457c4/beavis/zn/02dec96/1813	249	1b	3.277	2916
w457c4/S4	ge/9875	w457c4/beavis/ge/02dec96/1318	596	1n	3.277	2144.8
w457c4/S4	ge/9875	w457c4/beavis/ge/02dec96/1547	596	4b	3.277	2234.8

Table 4.17: w457c4/S4 CSR Spectral Resolution Data Sets

Chip	Target/Energy	Directory eV	Accepted Frames	Rejected Frames	Frame Time (seconds)	Counts per Frame
w201c3r/S5	al/1487	w201c3r/beavis/al/13dec96/0945	648	2b	3.277	4487.2
w201c3r/S5	cl/2622	w201c3r/beavis/cl/13dec96/1026	642	5b	3.278	2405.6
w201c3r/S5	v/4949	w201c3r/beavis/v/13dec96/1400	636	2b	3.277	4812.4
w201c3r/S5	fe/6399	w201c3r/beavis/fe/13dec96/1106	627	4b	3.278	4324
w201c3r/S5	co/6925	w201c3r/beavis/co/13dec96/1463	647	3b	3.277	3965.2
w201c3r/S5	ni/7471	w201c3r/beavis/ni/13dec96/1531	649	1b	3.277	3521.2
w201c3r/S5	ni/7471	w201c3r/beavis/ni/13dec96/1613	298	2b	3.277	3526
w201c3r/S5	zn/8630	w201c3r/beavis/zn/13dec96/1655	649	1b	3.277	2868.8
w201c3r/S5	zn/8630	w201c3r/beavis/zn/13dec96/1735	300	0n	3.277	2873.6
w201c3r/S5	ge/9875	w201c3r/beavis/ge/13dec96/1147	645	5b	3.277	2192
w201c3r/S5	ge/9875	w201c3r/beavis/ge/13dec96/1229	649	0n	3.277	2177.2

Table 4.18: w201c3r/S5 CSR Spectral Resolution Data Sets

Data File	Description
*_rt.evlist	ACIS RV format eventlist
*_rt_bias_avg.fits	mean bias frame
*_bias.000?.fits	sample bias frames
*_frame.000?.fits	sample data frames
*.mca.summary	ascii file summarizing the dataset
*.mca.data	IDL save file including average overclock level, average overclock noise, total number of events, peak location, peak width, and number of events under the peak as a function of frame number.
*.mca.spec	IDL save file including number of events as a function of energy, quadrant, and grade, and an image of the g02346 events under the peak in 32x32 pixel bins.
products/*g0234_img.fits	number density map of detected events in g0234.
products/*g0.qdp	for each quadrant, the pulse height histogram of g0 events.
products/*g0234.qdp	for each quadrant, the pulse height histogram of g0234 events.
products/*g0234_lightcv.qdp	for each quadrant, g0234 count rate as a function of frame number.
prodcuts/*pcf.qdp	for each quadrant, pulse height histograms of each grade.
products/*neighborhist*.qdp	for each quadrant, histograms of corner, top, bottom, left, and right pixel distributions of detected events.

Table 4.19: CSR Database Products

4.3.2 Physics of low energy tail in the CCD response function

A response of the frontside illuminated CCDs to monochromatic X-rays shows a noticeable low energy tail in addition to the well understood main peak and escape and fluorescence features. It is generally assumed for silicon detectors that the tail's origin is due to dead layer on the surface of the device (Scholze and Ulm, 1994; Lechner and Struder, 1995). We have studied the response of the CCD to the monochromatic synchrotron X-rays at BESSY in a wide range of energies and have discovered an unknown feature in the very low energy part of the response function (Prigozhin et al., 1998a; Jones et al., 1997). Examining changes in its behavior as a function of energy of incoming radiation we came to the conclusion that it originates from the photons interacting in the gate insulator, which is not a dead layer as was previously thought. We have developed a model that explains the shape of this newly discovered feature as well as the shape of entire low energy tail in the CCD response function.

4.3.2.1 Experimental

Experimental data were acquired at the electron storage ring BESSY (Berlin), where device cooled down to -120^o C was illuminated with monochromatized synchrotron X-rays. The data were taken at the KMC (Krystal MonoChromator) beamline in a wide range of energies from 1487 eV to 5898 eV with the emphasis on the understanding of the device behavior around silicon absorption K edge (1836 eV). That explains the choice of the energy data points for this measurement having higher density around silicon K edge: 1487, 1700, 1740, 1800, 1825, 1832, 1835, 1836.5, 1838, 1840, 1842, 1845, 1847, 1855, 1870, 1900, 2015, 2309, 2622, 3313, 3691, 4090, 4510, 4952, 5414, and 5898 eV. A typical exposure time at each energy was 4000 seconds, with 5 times that amount for the 2015 eV measurement.

Device was clocked by the ACIS electronics with serial register clock frequency of 100 kHz, total system noise at this frequency being about 2 electrons *rms*. Very low system noise was the crucial factor that allowed us to observe the low energy features discussed below.

4.3.2.2 Escape and fluorescence peaks

At X-ray energies greater than silicon K absorption edge, which we have measured for crystalline silicon to be 1839 eV, the response function of the device shows two distinct peaks in addition to the primary one. One of them at energy $E_f = 1739$ eV is due to the silicon fluorescent photons that have escaped far enough from the original site of interaction to be detected as a separate event. The other peak centered at energy $E_e = E_0 - E_f$, where E_0 is energy of the incident photon, is called an escape peak. It is formed by the electron clouds that are left when the flourescent photon carrying away energy E_f leaves silicon substrate or, again, is stopped far enough to be detected separately. The behavior of these peaks is reasonably well described by the model developed as a part of ACIS calibration

program and is discussed in more detail in section 4.14. The relative amplitudes of these peaks as a function of energy, both experimentally measured and simulated, are shown in Fig. 4.128.

4.3.2.3 Low energy peak

On Fig. 4.8 is shown the histogram of the CCD response to the monochromatic flux of 1700

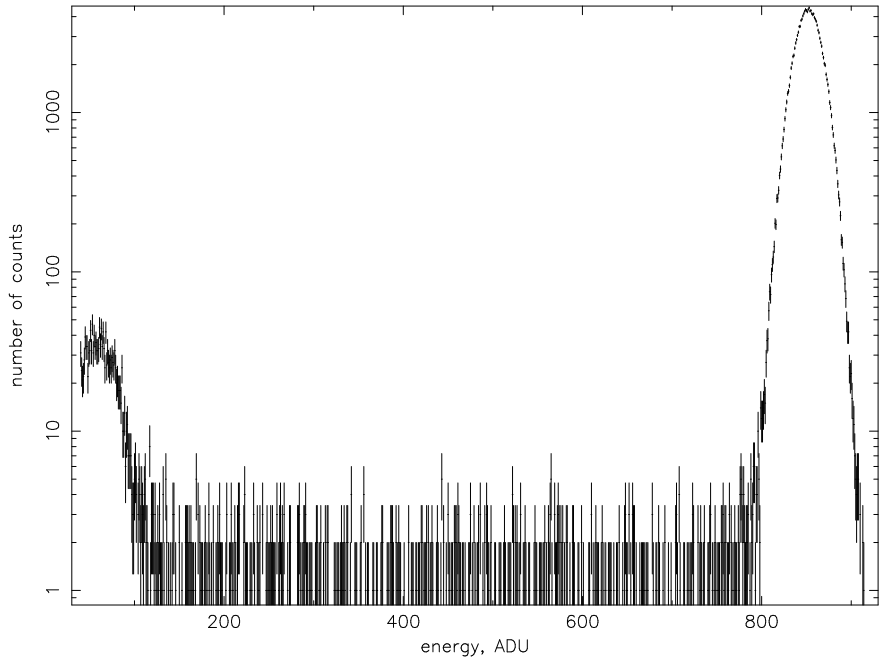

Figure 4.8: Histogram of the CCD response to 1700 eV X-rays.

eV X-rays, this histogram is typical for the device response at energies below the silicon absorption K edge (1841 eV). It has two distinct peaks - the main one which corresponds to the energy of the incoming photons, and the second one at energy which constitutes 7% of the main peak energy. Notice that since 1700 eV is below the silicon K absorption edge energy, silicon fluorescence does not play any role here.

The shape of the low energy peak is not quite gaussian, though it is possible to make a gaussian fit of reasonable quality. Having done that at different energies we found that the centroid of the low energy peak moves approximately proportionally to the centroid of the main peak (which is known to be a linear function of the energy of irradiating photons), as it is shown in Fig. 4.9. Such behavior is different, for instance, from the silicon escape peak for which energy shift is exactly the same as for the main peak.

Another important observation is that total number of counts in the low energy peak is consistent with the number of calculated photon interactions within the gate isolator.

If we assume that the gate insulator consists of a layer of SiO_2 with thickness d_{ox} and characteristic absorption length λ_{ox}, the number of photons per unit area N_{ox} absorbed in

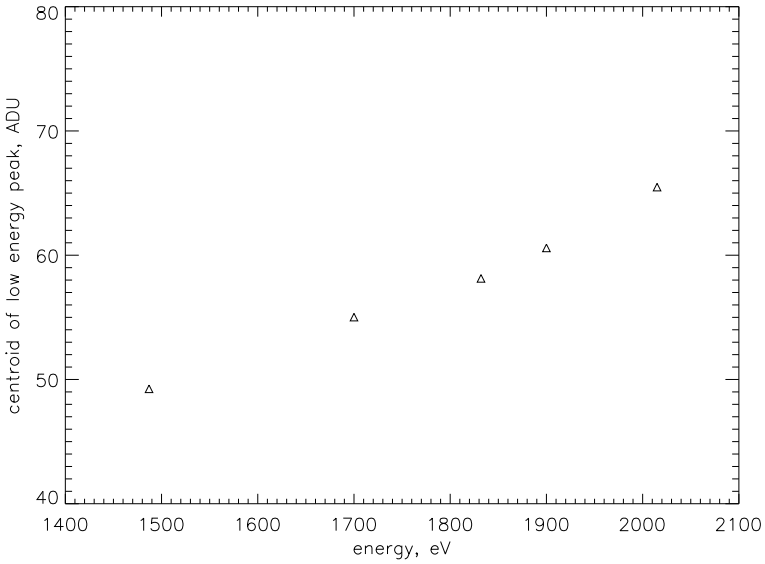

Figure 4.9: Centroid of the low energy peak as a function of energy.

it is

$$N_{ox} = N_0(1 - \exp(-\frac{d_{ox}}{\lambda_{ox}})) \tag{4.6}$$

where N_0 is photon flux enetering SiO_2 layer. The number of photons N_{si} that are absorbed inside the volume of silicon and form the main peak in the histogram equals simply entire flux of photons entering silicon in the case when thickness of the depleted layer of silicon d_d is big compared to the characteristic absorption length in silicon λ_{si}. Due to attenuation in the gate oxide $N_{si} = N_0 \exp(-\frac{d_{ox}}{\lambda_{ox}})$. This gives the ratio of the intensities for the two peaks:

$$\frac{N_{ox}}{N_{si}} = (e^{\frac{d_{ox}}{\lambda_{ox}}} - 1) \tag{4.7}$$

In the case $d_{ox} \ll \lambda_{ox}$ which is definitely true at energies below silicon absorption K edge, formula (4.7) comes to

$$\frac{N_{ox}}{N_{si}} = \frac{d_{ox}}{\lambda_{ox}} \tag{4.8}$$

In Fig. 4.10 is shown the ratio of the number of events in the low energy peak to the number of events in the main peak as a function of energy. The dashed line in this Figure is the result of the calculation according to equation 4.7. The dependence of λ_{ox} on energy comes from our high precision experimental measurement (Prigozhin et al., 1998c) and includes all the details of the near edge absorption structure. The relative number of counts in the low energy peak jumps up sharply at the energy corresponding to the silicon K absorption edge, in full agreement with the prediction of the formula 4.7.

The most remarkable feature of this plot is that the jump occurs at the energy corresponding to the silicon absorption edge in SiO_2, which is different from the silicon absorption edge in the crystalline silicon. We have shown in (Prigozhin et al., 1998c) that there exists a 6 eV shift between the silicon absorption edge energies in Si and SiO_2. Three data points on Fig. 4.10 in between the two edges staying at the same level as the points below the edge in Si prove most reliably that the low energy peak originates in the SiO_2 layer.

Unlike diode-type detectors such as Si(Li) (Scholze and Ulm, 1994) or $p-n$ junction CCD (Lechner and Struder, 1995), buried channel CCDs have an electric field in the gate oxide covering silicon surface. In Fig. 4.11 is shown a distribution of the potential in the gate structure of the buried channel CCD. It is clear from this figure that electrons generated in the SiO_2 layer adjacent to the silicon substrate will be travelling towards the collecting potential well of the CCD. Charge created in the Si_3N_4 and other layers sitting on the top of it will be lost. The mobility of the electrons in silicon dioxide, although lower than in silicon by roughly an order of magnitude, is still high enough to allow the photogenerated charge to get collected in a frame time.

All these facts lead to the unambiguous conclusion that the low energy peak's origin is due to the photons absorbed inside the gate insulator.

When an X-ray photon interacts with a material of the gate oxide layer, it generates a cloud of electron-hole pairs. Since the bandgap of SiO_2 is approximately 9 eV (as opposed to 1.12 eV in silicon), the amount of electrons created by one photon is approximately an order of magnitude lower than for silicon-absorbed photons. As a result the corresponding peak in a histogram is seen at very low energy.

So far we have discussed only data taken at energies around silicon K edge. The picture

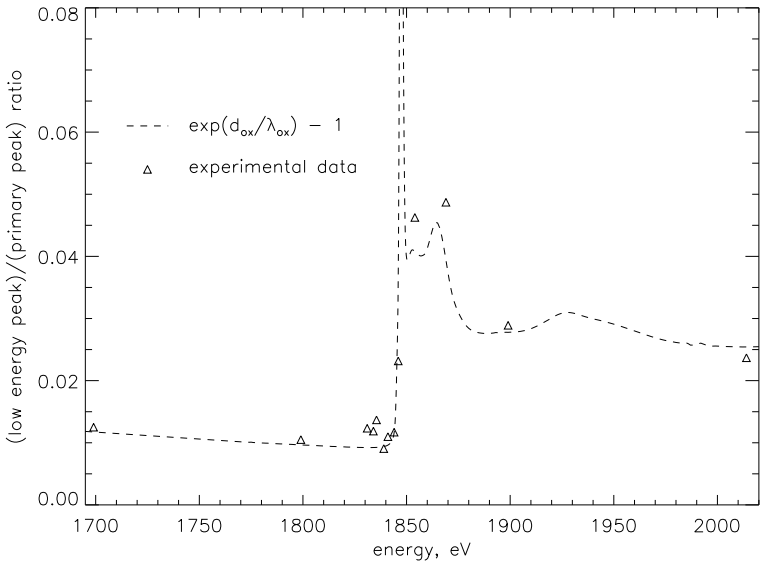

Figure 4.10: Ratio of number of counts in low energy peak and in the primary peak as a function of energy, calculated (dashed line), and measured (triangles).

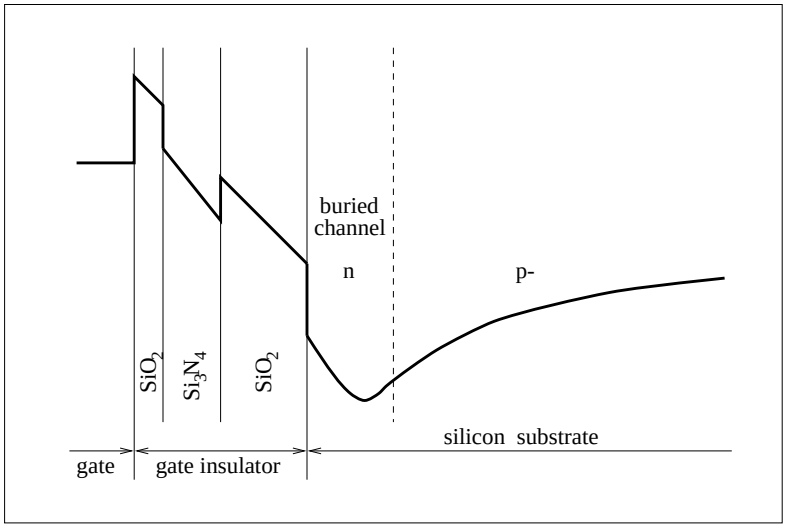

Figure 4.11: Potential distribution in the buried channel CCD.

is very different at higher energies. At 5414 eV (a histogram of the device response is shown on Fig. 4.12) instead of the well-defined low energy peak shifted further up from what we see at 1700 eV histogram, there is a broad elevation which goes all the way down to the noise peak (not shown) without reaching a maximum. We believe that the reason

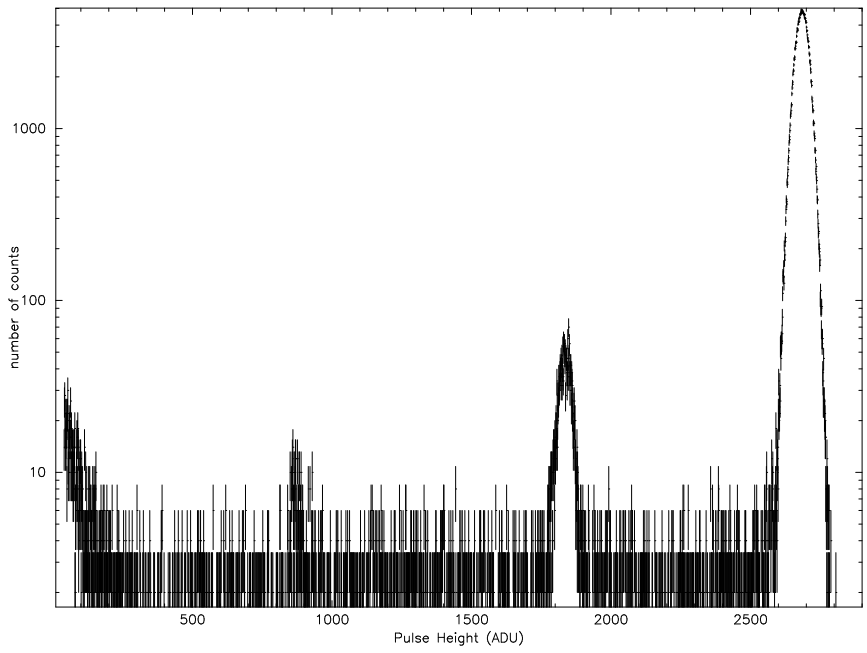

Figure 4.12: Histogram of the CCD response to 5414 eV X-rays.

for such behavior is an increased electron cloud size at higher energies. It is known that the

diameter of an electron cloud generated by a photon increases with energy and according to various authors could be tens or even hundreds of nanometers at several keV (Scholze and Ulm, 1994; Lechner and Struder, 1995; Janesick et al., 1986). The gate oxide layer is very thin, approximately 70 nm and its thickness is comparable to the cloud size. When the cloud diameter exceeds the oxide thickness, for any cloud originated in silicon dioxide part of the charge will end up either in silicon, or in silicon nitride and the amount of that charge depends on the photon's depth of interaction. There exists a potential barrier for the electrons that are moving from Si_3N_4 into SiO_2 (see Fig. 4.11), which means that part of the cloud that enters Si_3N_4 will be almost entirely lost. For the events that originate in Si_3N_4 only electrons with sufficiently high enough energy can overcome the potential barrier.

Thus, even small changes in the depth of interaction of the original photon in the SiO_2 layer lead to significant changes in the total number of electrons collected, and as a result the low energy peak is washed out into a much broader feature without an extremum.

4.3.2.4 Shape of the entire low energy tail

A similar phenomenon - splitting of the electron cloud between silicon and silicon dioxide - should obviously take place for any cloud which originates within the distance R from the $Si - SiO_2$ interface, where R is the cloud radius. Since the number of the electron-hole pairs generated per eV of the incoming photon energy is significantly higher in silicon than in silicon dioxide, the amplitude of such events will change gradually from the primary peak down to the low energy peak, as the center of the cloud moves from silicon into oxide. This is schematically shown in Fig. 4.13, which explains how the low energy tail of the spectral redistribution function is formed. Fig. 4.14 provides evidence that the entire low energy tail comes from the photons interacting within a small distance from the silicon interface. This figure shows the fraction of the events in the tail as a function of the characteristic absorption length λ_{si} in silicon. In order to produce this plot events in the fluorescent and in the escape peaks were ignored, as well as the low energy (oxide) peak events discussed above. Each point in this plot corresponds to a measurement at a particular energy, and the points are connected sequentially in energy ascending order, starting at the lowest energy point labeled 1487 eV. The plot demonstrates that for widely separated energies (for instance, 1487, 1836, and 3600 eV) with the similar valaues of λ_{si} the fraction of events in the tail is similar. Moreover, immediately above the silicon edge, at very small λ_{si}, the tail intensity goes up sharply. If one makes a very crude assumption that the cloud radius R is constant (or slowly changing function of energy in the range of interest), then an approximately $1/\lambda_{si}$ dependence is an indication that the flat part of the tail results from the the photons interacting in a shallow region near the surface, whose thickness $2R$ is small compared to λ_{si}.

If all the events in the flat part of the low energy tail come from the electron clouds formed within a distance R from the $Si - SiO_2$ interface, the fraction of the events in the

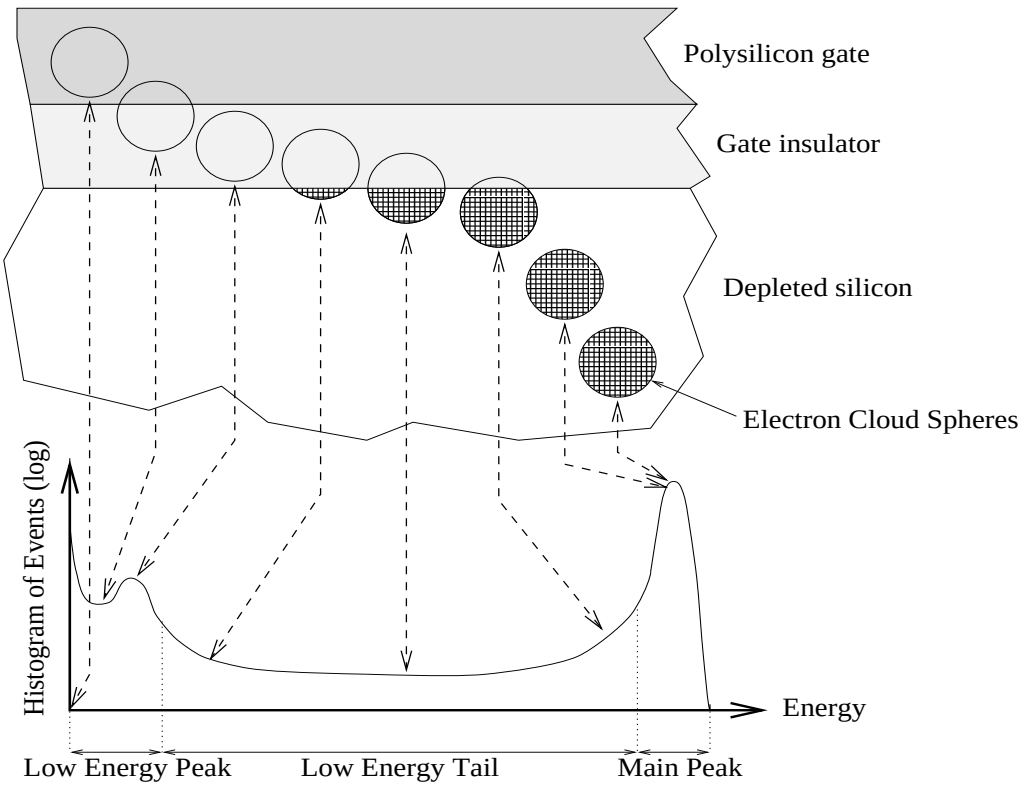

Figure 4.13: Scheme of forming low energy tail from the electron clouds generated close to $Si - SiO_2$ interface.

flat part of the tail can be used to determine the electron cloud size. The results of such calculations are shown on Fig. 4.15. The values of cloud sizes are significantly lower than 150 – 200 nm (Scholze and Ulm, 1994; Lechner and Struder, 1995). They also are much smaller than cloud sizes in the bulk silicon extracted from our mesh experiments (Pivovaroff et al., 1998). We believe the reason for this large discrepancy is the presence of a potential barrier for electrons at the $Si - SiO_2$ interface.

Electron cloud generation starts with emission of relatively high energy primary photo- and Auger electrons which dissipate their energy in an ionization cascade. The range of electrons in the initial stages of the cascade is roughly consistent with the cloud radius in our model. It is the low energy, nearly thermalized electrons with sharply increased mean free path (of an order of 100 nm), that are responsible for the large cloud sizes quoted in Scholze and Ulm (1994) and Lechner and Struder (1995). In the MOS structure analyzed here a "potential wall" at the $Si-SiO_2$ interface prevents the low energy electrons from penetrating into the SiO_2 for the clouds centered at a distance greater than R from this interface. Only hot electrons in the initial stages of cascading (for which the range is very small) can participate in the cloud splitting between the silicon and the silicon dioxide.

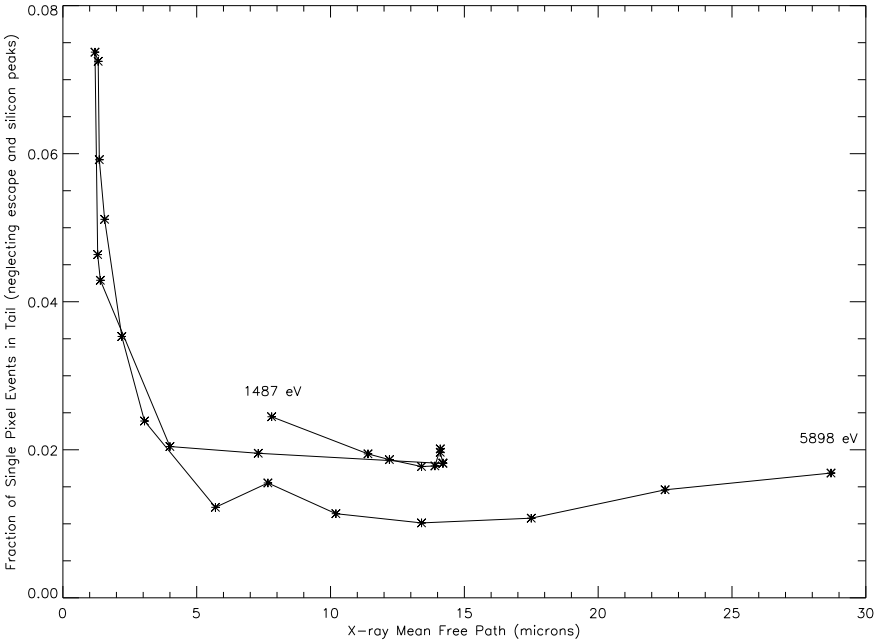

Figure 4.14: Fraction of single pixel events in tail as a function of characteristic absorption length in silicon.

This feature of the buried channel MOS X-ray CCDs is very beneficial for the spectrometric properties of the frontside illuminated CCDs, since it results in larger fraction of counts going into the main peak instead of the tail, and, hence, better energy resolution and quantum efficiency.

The precise shape of the tail depends on the density distribution of charge in the cloud and this distribution in principle can be extracted. We have not accomplished this task yet, because it requires much higher number of counts than we were able to obtain during the limited time at the synchrotron facility.

We have developed a model based on the scheme shown at Fig. 4.13. The basic assumption is that each electron cloud is a sphere and when the sphere crosses the silicon interface, the number of electrons produced in each material is proportional to the volume of the corresponding segment of the sphere. Each material is assumed to have different electron-hole creation energy. This is equivalent to assuming that electrons have the same mean free path in both materials. This may be not such a bad approximation, especially for high energy electrons in the original stages of cascading. As discussed above, electrons liberated in the oxide contribute to the total charge collected. From the low energy peak position (see Fig. 4.9) we deduce an effective electron-hole pair creation energy w_{ox} in SiO_2 of approximately 52 eV. This value includes recombination losses and hence differs significantly from the reported value of 17 eV/pair. We have made no attempt here to decouple

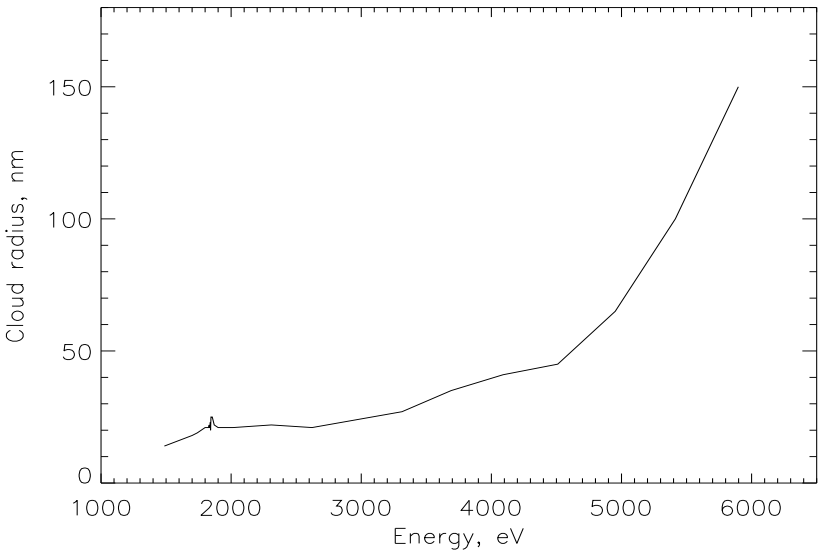

Figure 4.15: Cloud radius in silicon as a function of energy.

the true value of w_{ox} and the losses. This matter is clearly worth pursuing, because it will allow to produce a more accurate model of the device response.

In Fig. 4.16 - 4.19 are shown the results of the best fit of the model to the data at several energies.

The results of this section are used as the basis for the model of the CCD described in section 4.14 to produce a response matrix for the flight devices.

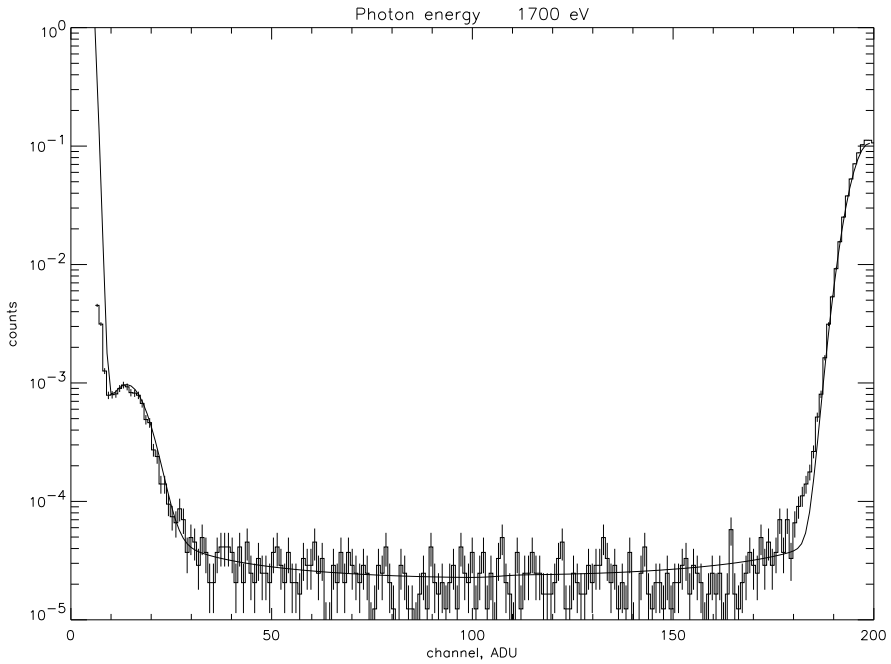

Figure 4.16: Response of the CCD to 1700 eV photons and the model prediction.

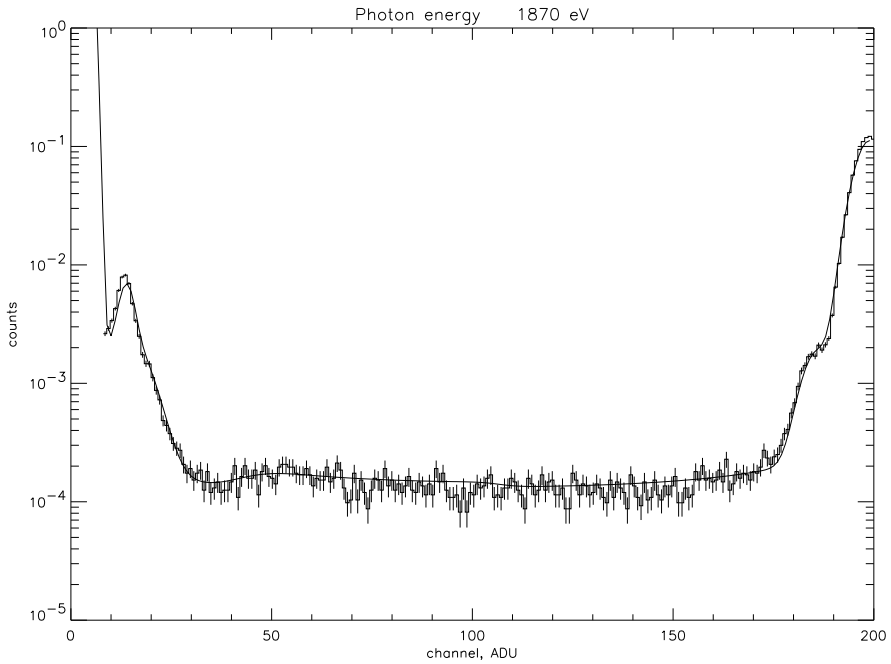

Figure 4.17: Response of the CCD to 1870 eV photons and the model prediction.

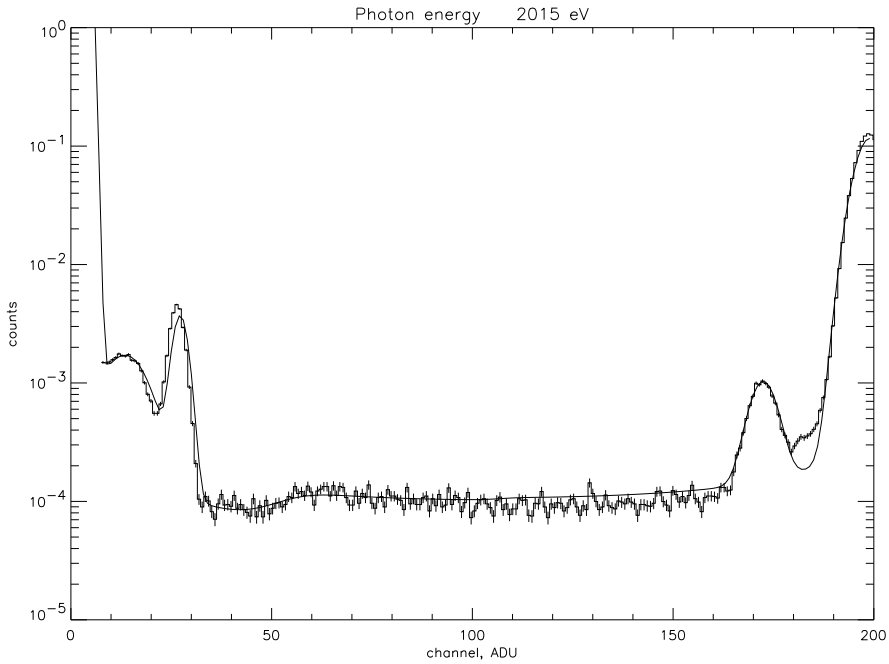

Figure 4.18: Response of the CCD to 2015 eV photons and the model prediction.

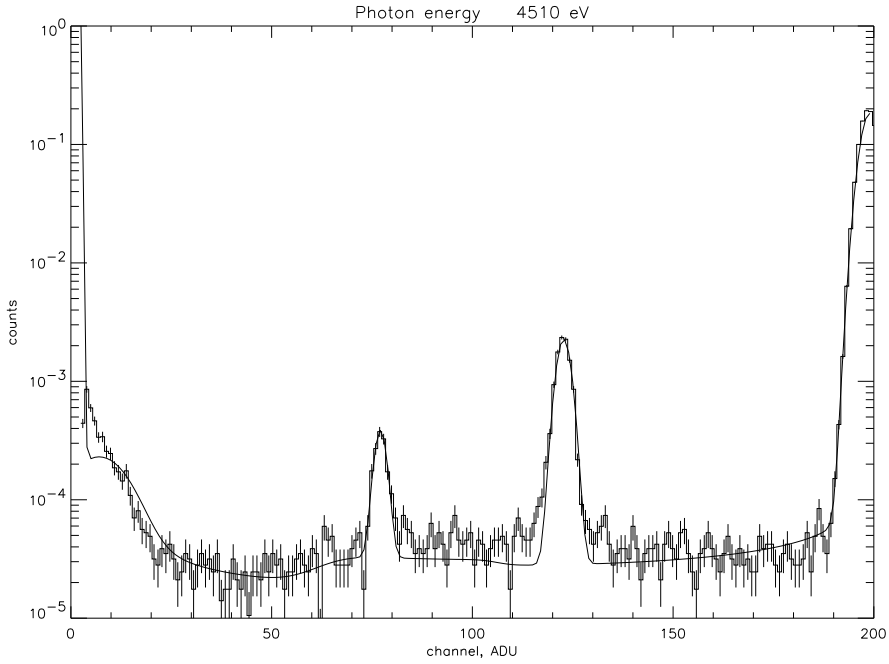

Figure 4.19: Response of the CCD to 4510 eV photons and the model prediction.

4.4 Pileup Measurements and Modelling

4.4.1 Introduction

In the low flux limit x-rays incident on a CCD are assumed to be independently detectable. That is, the detection of any one x-ray is not affected by the x-ray flux incident on the detector. At sufficiently high flux this approximation breaks down as "pileup" occurs. In a CCD the piled-up x-rays do not directly interact with each other, but their electron charge clouds, which form in the depleted region of the CCD, merge or even overlap. All isolated x-rays produce charge clouds whose detection pattern varies strongly with (1) the x-ray energy, (2) the sub-pixel location of the initial photoelectric interaction, (3) the depth of the interaction, and (4) the detector electronics. All detections, or events, can be categorized by (1) the shape (grade) and (2) the magnitude (energy) of their charge cloud pattern. Figure 4.20 represents a matrix of the possible grade-energy combinations for which a single x-ray can be detected. The x-ray counts for a timed exposure will divide among the categories. In the low flux limit, the probability of a single x-ray to produce an event in any category approaches a "pileup-free" value characterisitic of the detector and the spectral content of the source. However, the probability of producing an event in any category is a function of the incident flux, and the the essential problem of pileup characterization is to determine this functional relationship. The effect of pileup is to redistribute the counts in each category, as exemplified by the arrows in the figure.

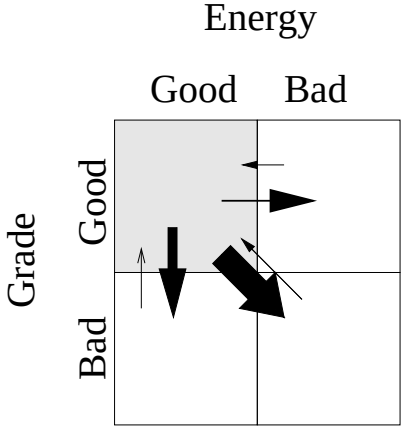

Figure 4.20: Possible redistributions of detected x-rays due to pileup

The largest effect of merging charge clouds is to reduce the number of detected "good" x-ray events. Here by "good" we mean that the event satisfies both of the following conditions: i) the event amplitude is in the spectral band of interest and ii) that the event grade (shape) is in the grade set of interest. The merged cloud resulting from pileup will most likely be detected as a single x-ray event with either a different grade (e.g. if the two x-rays landed in adjacent pixels) or a different energy (e.g. if the two x-rays landed in the same pixel). Many cases will appear as mixtures of these types of pileup. In either case, as a second good x-ray event is produced near a first good x-ray event, not only is the second event undetected, but the first x-ray is removed from detection as a good event. These major redistributions are represented by the heavy arrows in Fig. 4.20. The smaller redistributions shown by the light arrows occur very infrequently for quasi-monochromatic x-ray beams and are not considered here.

There are two complications in a general pileup analysis. The first concerns spatial distribution of the incident flux. We note that, in general, pileup effects are a function of fluence (number of events per unit area within a given CCD readout or exposure), and if the incident fluence varies with position on the detector, the pileup effects will also vary. Thus, in general, pileup can change the apparent spatial distribution of detected flux. In particular, the apparent HRMA/ACIS point-response function can be changed by pileup effects. The discussion in this section is based on experimental data with uniform illumination, and we do not specifically address effects of pileup on the point response function. We note, however, that the pileup "cross-sections" we report below are prerequisites for understanding the effects of pileup on spatial flux distribution measurements. A short discussion at the end of this section considers some aspects of pileup in the limit of a perfectly focussed point source.

The second complication for pileup analysis is the spectral distribution of the incident flux. Here there are two limits, those of a monochromatic source and a continuum source, respectively. The strategy followed in this discussion is to examine a monochromatic source first to understand the redistribution of events as a function of energy. Then, an approximation technique will be discussed to apply these results to a more general spectral distribution.

The remainder of this section is organized as follows. The next subsection details a simple pileup model for a quasi-monochromatic source. This approach only considers the effect of pileup on the number of detected counts at one major line in the spectrum. The strategy is to develop a theory based on fundamental pileup processes which can be applied for any CCD. The following subsection describes pileup experiments which when analyzed in the context of the preceeding theory provide generally applicable cross sections for pileup processe as a function of incident X-ray energy. The final section extends the simple model to include any arbitrary spectrum, specifically including spectral redistribution.

4.4.2 Simple model of pileup for a quasi-monochromatic incident spectrum

The simple model starts by defining any x-ray event detected with the desired energy and grade to be "good". All other events (i.e., those with different energy or grade) are defined as "bad". Most practical x-ray line sources are not monochromatic, and are typically a mixture of a monochromatic line, other spectral features, and some continuum. The pileup model quantifies this aspect by defining that for every "good" x-ray event there are α "bad" events. Alternatively, if, in the absence of pileup, the number of good incident x-rays is N_i out of a total number of events N_T, then the fraction f_B of good x-ray events is $f_B = N_i/N_T = 1/(1+\alpha)$. This model of a quasi-monochromatic beam is a good representation of the x-ray sources used in the ACIS quantum efficiency calibration.

Although for any CCD exposure the time history of event interactions is unknown, for

the purposes of analysis we can picture the x-rays incident in one exposure as striking the CCD serially. The goal is to describe a function $N_d(N_i)$ which represents the number of detected good x-rays as a function of the number of incident good x-ray events. By inverting this function, we can determine N_i from an experimental measurement of N_d. We begin construction of this function by examining the effect of a single x-ray.

Let ϵ be the effective area of the CCD affected by the occurrence of a "good" x-ray event (typically the desired energy is that of a K_α line the desired shapes are ASCA grades 0,2,3,4 and 6). In general, $\epsilon = \epsilon(E)$ will be a function of energy; the energy dependence is described in detail later. Similarly, $\epsilon^{'}$ is the average effective area corresponding to any other x-rays, i.e. those with different energies and grades. The physical meaning of ϵ is that if a second x-ray is absorbed near a prior x-ray event such that the center of the second photoelectric absorption occurs within the area ϵ centered on the first x-ray, then an interaction occurs. Specific interaction effects are described mathematically below. We can derive the minimum size for ϵ commensurate with our event detection criteria. All (standard) event discrimination is based on the 3x3 pixel subarray surrounding a local maximum of detected charge. Thus, any second x-ray landing within the subarray invokes an interaction, and the area of 9 pixels forms a lower limit for ϵ. In all that follows, we express ϵ and $\epsilon^{'}$ in units of the area of one quadrant of an ACIS CCID17 detector. In these units, a nine-pixel "island" has an area of 3.4×10^{-5}.

The mathematical model begins by schematically dividing the area of a CCD as shown in Fig. 4.21. In our units, the total surface area of the detector (one quadrant of a CCID17) is normalized to unity. Let A_1 be the total area occupied by all good x-ray events (A_1 can also be interpreted as a probability or cross section for interaction; however the interpretation as an area is useful for developing a model). The number of detected events is taken to be $N_d = A_1/\epsilon$. This assumption is approximate since two good x-ray events could lie close enough together so that their ϵs overlap while they do not interact. Let A_2 be the total area occupied by charge produced by all other events. Then $1 - A_1 - A_2$ is the CCD area unblemished by any interaction. The probability for an incident x-ray to land on a previous good x-ray event is A_1; the probability for an incident x-ray to land on a previous bad x-ray event is A_2, and the probability for an incident x-ray to land and be detected in unperturbed pixels is $1 - A_1 - A_2$. The effect of an incident x-ray landing in A_1 is removal of one previous x-ray from A_1 while adding some area $\epsilon^{''}$ to A_2, which must be between 1 and 2 times ϵ. We assume that any x-ray landing in A_2 does not change either A_1 or

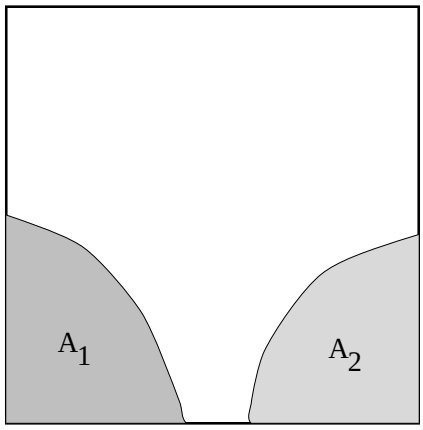

Figure 4.21: Regions of CCD for pileup model

A_2. Finally, we assume that A_1 can increase only by good interactions in the unperturbed region $1 - A_1 - A_2$. Then the change of A_1 and A_2 with per unit change in N_i can be described by the following pair of ordinary differential equations:

$$\frac{dA_1}{dN_T} = (1 - A_1 - A_2) f_B \epsilon - A_1 \epsilon \tag{4.9}$$

$$\frac{dA_2}{dN_T} = (1 - A_1 - A_2)(1 - f_B)\epsilon^{'} + A_1 \epsilon^{''} \tag{4.10}$$

The solution is obtained by combining the two equations to separate variables. This results in a second order differential equation with the following solution,

$$A_1 = \epsilon/\beta \exp(-\hat{\epsilon} N_i) \sin(\beta N_i) \tag{4.11}$$

or

$$N_d = f_B N_T e^{-\hat{\epsilon} f_B N_T} \mathrm{sinc}(f_B \beta N_T) \tag{4.12}$$

where

$$\hat{\epsilon} = \epsilon \left[1 + \alpha(1 + \epsilon^{'}/\epsilon) \Big/ 2\right], \tag{4.13}$$

$$\beta = \sqrt{(1+\alpha)(\alpha\epsilon\epsilon^{'} + \epsilon\epsilon^{''}) - \hat{\epsilon}^2} \tag{4.14}$$

and

$$A_1 = \epsilon N_d, f_B = N_i/N_T \tag{4.15}$$

Equation 4.12 has the desired asymptotic limit of $N_i = N_d$ for low flux, with the following useful expansion for the logarithm of the ratio:

$$\log(\frac{N_d}{N_i}) = -\hat{\epsilon} N_i - \beta^2 N_i^2/6 \tag{4.16}$$

In the limit where $\epsilon^{'} \sim \epsilon$ and $\epsilon^{''} \sim 3/2\epsilon$ then

$$\beta = \hat{\epsilon}/\sqrt{2(1+\alpha)} \tag{4.17}$$

Solutions to Eqn. 4.12 are plotted in Fig. 4.22 for two different flux ranges and for $\hat{\epsilon}$=0, 2, 4, ... 40 ($\times 10^5$) using $\epsilon^{''} = 3/2\epsilon$. Specifically, the cross-section $\hat{\epsilon}$ equals the fractional area of a CCD region of interest, and N_d and N_i are the corresponding counts in that region. Note that $\hat{\epsilon} = 10 \times 10^{-5}$ corresponds to a area of 26.2 pixels. The deviation from the line $N_i = N_d$ increases as $\hat{\epsilon}$ increases. All the curves bend over for significantly high pileup and should assymtote to 0 for high enough N_i. This high pileup limit corresponds to severe charge cloud overlap so that very few x-rays satisfy the event selection criteria.

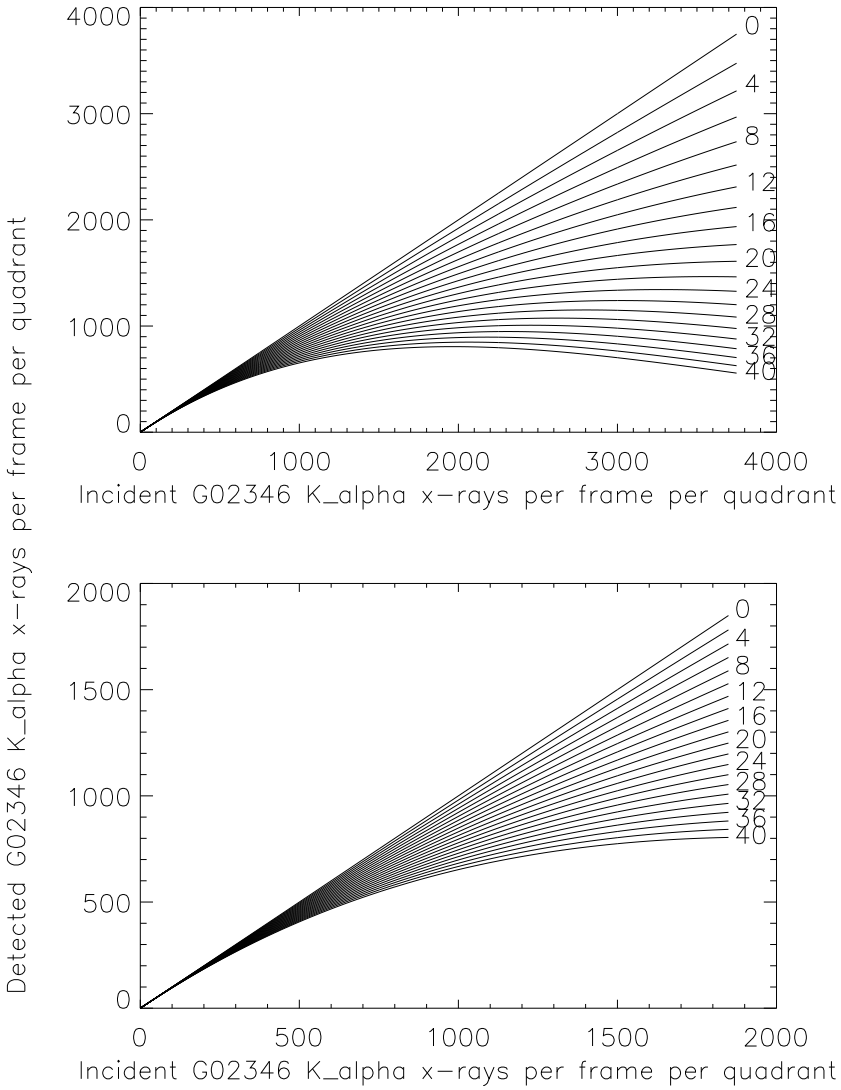

Figure 4.22: Predicted relationship between detected and incident flux parameterized by the assumed value of $\epsilon \times 10^5$. For example, the curve labeled 4 is the prediction for $\epsilon = 4 \times 10^{-5} = 10.5$ pixels.

4.4.3 Pileup experiments and determination of $\hat{\epsilon}$ and ϵ

The experimental technique to measure ϵ and $\hat{\epsilon}$ used the High Energy X-ray Source (HEXS) at MIT's CCD Calibration Facility. HEXS is the same source used for the ACIS quantum efficiency calibration, so careful measurements of pileup using that source are particularly important for the AXAF program. The HEXS source uses fluorescence from 12 different

targets ranging from Al to Ge as shown in Table 4.20. The fluorescence spectrum is generated by the bremsstrahlung spectrum from a commercial electron impact x-ray tube using a Mo target. The tube current and voltage are independently adjustable and are temporally stable to within one percent over relevant measurement periods. The maximum tube power is 9 W, with a maximum voltage of 30 kV.

Target	Energy (eV)	X-ray mfp in Si (μm)
Al	1487	8.0
Si	1740	12.4
P	2015	1.6
Cl	2622	3.1
Ti	4508	13.6
V	4949	17.7
Fe	6399	36.9
Co	6925	46.4
Ni	7471	57.8
Cu	8040	71.6
Zn	8630	88.0
Ge	9874	130.7

Table 4.20: HEXS targets, energies, and x-ray penetration depths.

All detectors used for this analysis are flight-like ACIS CCDID-17s, produced by MIT Lincoln Laboratories, which have a 1024 column by 1026 row array of 24 μm square pixels. As mentioned above, each CCD is divided into 4 readout quadrants of 256x1026 pixels. Since the gain from each quadrant can be different, most analysis is conducted on a quadrant basis rather than on the entire CCD. Each CCD was flight qualified for ACIS although only w140c4r was selected for the flight focal plane.

A series of 11 pileup measurements were conducted using various CCDs, HEXS configurations, electronics and exposure times. The different configurations are listed in Table 4.21 . For each configuration, the CCD was exposed to x-rays from most of the 12 available targets. For each target, a sequence of exposures was taken with 4 or 5 different x-ray fluxes generated by using different tube currents (the tube voltage was held constant at 15 kV). The range of fluxes covered an approximately even spread up to twice the nominal flux used during the ACIS calibration.

An important assumption for the process is that the x-ray flux from HEXS varies linearly with the x-ray tube current. This was checked two different ways. First, the actual tube current was measurered using three different current meters and compared to the front

CCD	Date	Electronics	Exposure Time	Comments
			(secs)	
w103c4	03jun96	Lbox	7.22	Early HEXS configuration
w103c4	16jan97	Lbox	7.22	
w103c4	12feb97	Lbox	7.22	
w140c4r	22jan97	DEA	3.28	Back sided CCD
w163c3	27sep96	DEA	3.28	
w190c3	26nov96	DEA	3.28	
w203c2	07may97	DEA	3.28	
w203c2	08may97	DEA	7.15	Lbox exposure time
w203c4r	16jan97	DEA	3.28	
w210c3r	12may97	DEA	3.28	
w210c3r	12may97	DEA	7.15	Lbox exposure time

Table 4.21: Pileup measurement configurations.

panel display. All agreed within error. Secondly, the total electron charge detected by the CCD was found to be linear with tube current. The total charge is a reliable quantity since is does not depend on any event selection criteria. The data are presented in the next subsection.

4.4.3.1 Determination of $\hat{\epsilon}$ and ϵ

An example of experimental pileup data is shown in Figs. 4.23 - 4.26. The CCD w203c2 was used with a 7 second exposure on all 12 x-ray targets. The data for each target is presented with two graphs forming two columns . The left hand column plots the number of detected counts in the K_α per frame per quadrant and is normalized to the x-ray tube current (in units of μA) versus the x-ray tube current. The counts are determined by fitting a three parameter gaussian curve to the K_α peak and using the fitted coefficients to determine the total counts. The four grade selections displayed are G0 (triangles), G0234 (stars), G02346 (squares), and G01234567 = All (diamonds). The value for each quadrant is plotted independently. The lines result from a least squares polynomial fit to Eqn. 4.16. The fit for each quadrant is plotted independently. The zero current intercept averaged for all four quadrants is listed in the first column within each figure, and the zero current slope is listed in the second column. The third column is the slope normalized by the square of the intercept and multiplied by 10^5, which is called the rate. This number provides a configuration-independent slope which only depends on the number of detected x-rays, not on the x-ray tube current. The units for the rate are $(\text{Counts/Frame/Qd})^{-1}$. The fourth column displays the error for the rate.

In an ideal detector with no pileup effects, a horizontal lines would result. The non-zero slope of all the lines clearly indicates the presence of pileup. The presence of a non-linear slope for high Z indicates higher order pileup events, for which the quadratic correction of Eqn. 4.16 becomes important.

In the righthand column are similar plots for the number of pixels above the threshold (diamonds) and the total charge collected (triangles). Printed underneath the values of intercept and slope are the respective errors. The fact that the normalized charge doesn't vary significantly with x-ray tube current is good evidence for linearity of the x-ray flux with tube current.

Figures 4.27 and 4.28 are parallel to Figs. 4.23 - 4.26, except the analysis uses *all* x-rays in the spectrum, not just those in the K_α peak. A useful number from these plots is the intercept value from a linear fit to the x-ray fluxes from all grades. From this number the pileup-corrected branching ratios can be computed.

For our pileup analysis, the most significant number presented in each figure is the rate and error for the G02346 grade set, the set used most commonly for the ACIS calibration. These figures were produced for all 11 test configurations, although the other 10 configuration's figures are not included for space reasons. A summary for the G02346 rate values for all configurations is presented in Figs. 4.29 and 4.30. Figure 4.29 shows the rate for the first targets elements. The graph for each target shows the rate value with errors for each test configuration. Not every configuration has a value for every element since due to some experimental problems and time constraints. A mean value has been determined for the front sided data (i.e. not including w140c4r), excluding any suspicious data points. The mean value is plotted as the horizontal dashed line and is printed in the upper right of each figure. Figure 4.30 corresponds to Fig. 4.29, but shows results for the other six targets.

Figure 4.31 presents a summary of the mean rate values, both as a function of the K_α energy (top) and the x-ray penetration length (bottom) in silicon. With the exception of the Cl line at 2621 eV, the rate is roughly a constant at low energies, and increases quickly at high energies. The Cl line is a known exception since the target source is actually KCl and the K line competes with the Cl, causing more relative pileup than the other targets.

An example of pileup corrections for an ACIS CCD is shown in Table 4.22. Typical detected flux rates for the CCD w215c2r (which presently is located in the I3 position of the ACIS flight focal plane) are listed in the second column for the 13 different K_α x-rays listed in the first column (Mn K_α has now been included, whose source is radioactive Fe^{55}). The third column lists the mean values for $\hat{\epsilon}$ presented in Figs. 4.29 and 4.30. The fourth column lists the corresponding incident fluxes as determined by Eqn. 4.16, and the next column is the ratio N_i/N_d. These measurements were conducted with a 3.28 s exposure time. The last column lists the corresponding ratio if a 7.15 second exposure time had been used for the same incident flux.

The previous analysis is directly specific to the spectra emitted by HEXS. That is, $\hat{\epsilon}$(E) includes all the effects of spectral impurities particular to the HEXS source. While this is useful for computing pileup effects on HEXS data, a more general analysis requires ϵ, which

K_α X-ray	Detected Flux	$\hat{\epsilon}$	Incident Flux	Correction Factor	Correction Factor
	(G02346)	(10^5)	(G02346)	(3.28 sec)	(7.15 sec)
Al	1145	6.69	1246±15	1.088	
Si	1310	4.88	1404±17	1.072	1.186
P	1120	7.15	1225±13	1.094	1.257
Cl	605	11.1	651 ±6	1.076	
Ti	1285	4.62	1370±8	1.066	1.169
V	1180	4.57	1251±8	1.059	
Mn	880	7	938±6	1.060	1.174
Fe	1040	8.07	1143±10	1.099	
Co	950	10.3	1062 ±11	1.118	
Ni	840	13.5	959 ±19	1.142	
Cu	700	18.2	815 ±22	1.164	1.643
Zn	660	26.4	829 ±46	1.256	
Ge	480	46.9	662 ±87	1.379	

Table 4.22: Example of pileup correction factors for typical detection fluxes in w215c2r

is independent of the spectra. Equation 4.13 gives the relation between $\hat{\epsilon}$ and ϵ in terms of α (the number of bad events per good event) and $\epsilon^{'}$ (the average ϵ associated with the "out-of-band" portion of the spectrum). Mathematically, a direct solution for ϵ(E) from the 12 different energies is complicated since $\epsilon^{'}$ depends on ϵ, and we use an iterative approximation described as follows. Using interept values for G02346 and G01234567 from the left hand column in Figs. 4.23 - 4.28, we compute f_B or α. Plots of α for each target from every data set are presented in Figs. 4.32 and 4.33. Using initial guesses for ϵ, spectrally averaged values of $\epsilon^{'}$ are computed. Together with α, new values of ϵ are generated according to Eqn. 4.13, and the process is repeated until the values become self-consistent. Plots of $\epsilon^{'}$ for all targets and data sets are shown in Figs. 4.34 and 4.35. Figures 4.36 and 4.37 display the final values of ϵ, as computed by Eqn. 4.13. These values of the pileup cross section as a function of energy for a monochromatic incident beam, which are summarized in Fig. 4.38, represent the major result of the pileup experiments.

Notice that the low energy values are close to the theoretical minimum of $\epsilon = 3.4 \times 10^{-5}$. Recall this value corresponds to a cross-sectional area of 9 pixels in one quadrant (viz, 9/262144). We do not yet understand why the value of ϵ has a slight increase at the lowest energies. The discrepancy is no more than about one standard deviation. A comparison with Fig. 4.32 suggests that spectral impurities may be the cause since the 1740 eV Si point (which is most spectrally pure) lies near the minimum while the 2622 eV Cl point (which is most spectrally impure due to a potassium line) lies far from the minimum. The 1487 eV

Al source is also known to be very spectrally impure.

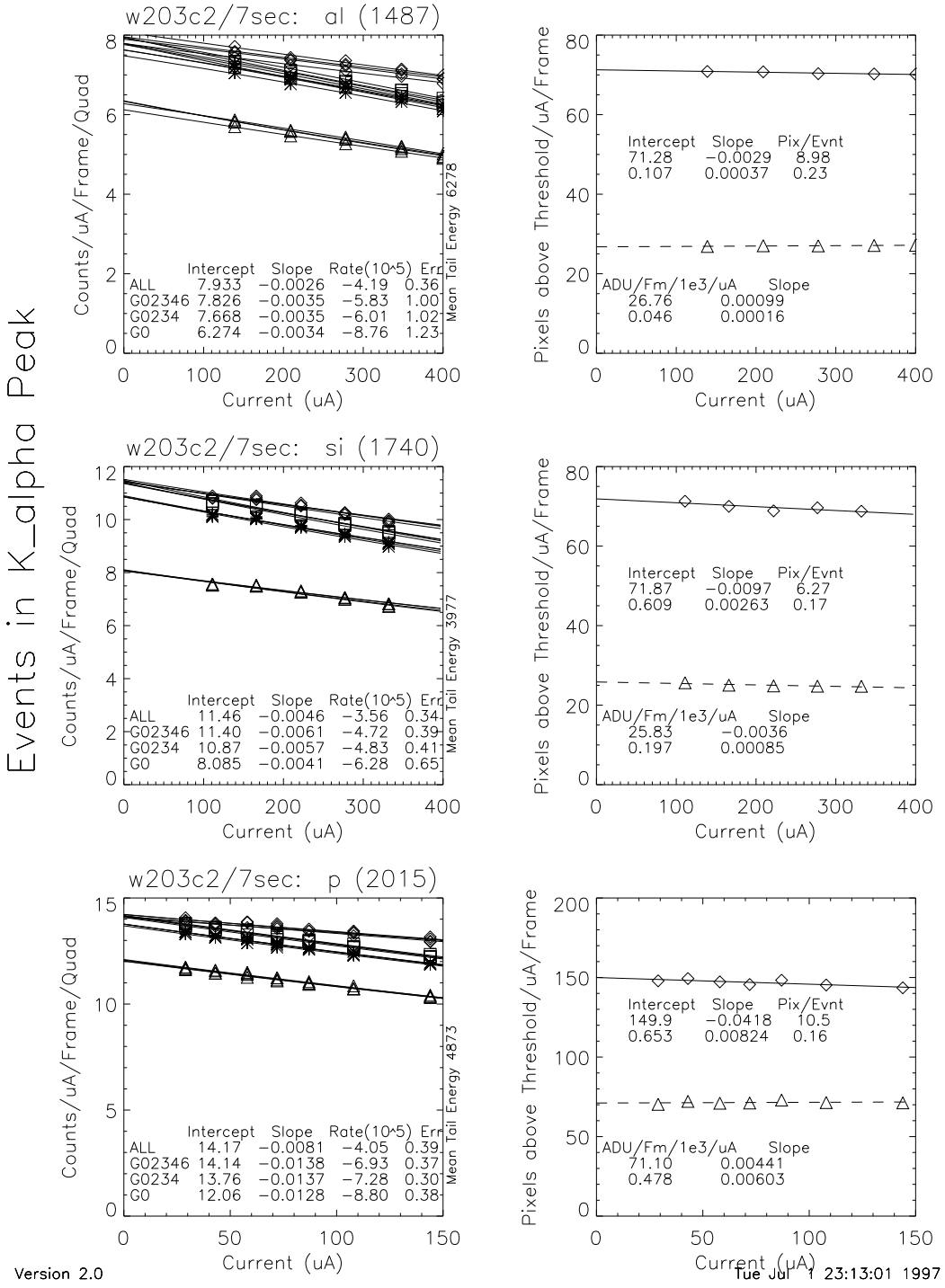

Figure 4.23: Raw HEXS pileup data for detector w203c2 with a 7 second exposure for characteristic K lines from Al,Si, and P targets, with best-fit model for various ASCA event grade sets. triangles:G0; stars:G0234; squares: G02346; G01234567: diamonds. Points for each detector quadrant are shown. Best-fit model parameters are shown in each panel. See text for details.

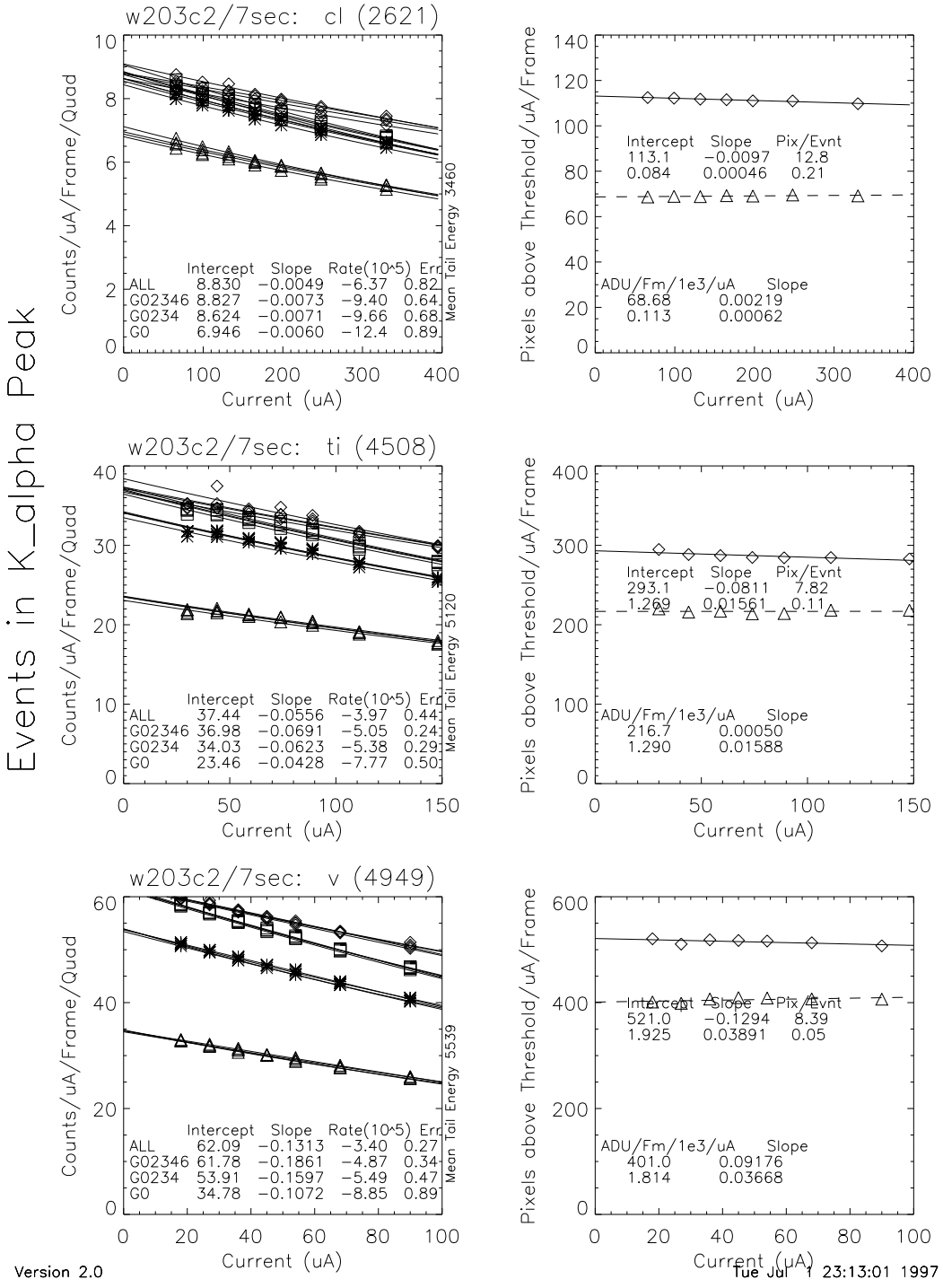

Figure 4.24: Raw HEXS pileup data for K_α for detector w203c2 with a 7 second exposure for characteristic K lines from Cl,Ti, and V targets, with best-fit model for various ASCA event grade sets. triangles:G0; stars:G0234; squares: G02346; G01234567: diamonds. Points for each detector quadrant are shown. Best-fit model parameters are shown in each panel. See text for details.

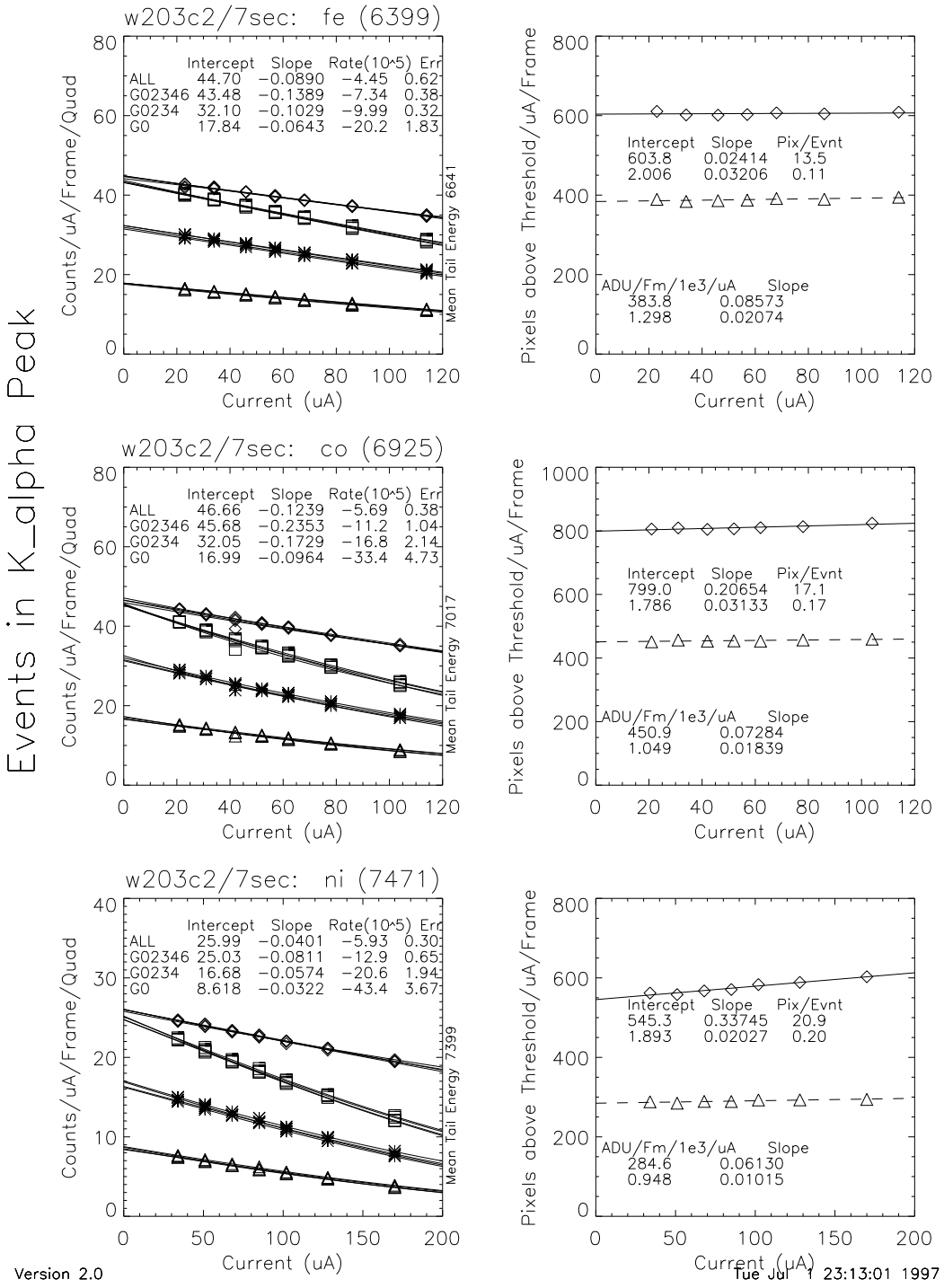

Figure 4.25: Raw HEXS pileup data for K_α for w203c2 with a 7 second exposure for Fe,Co, and Ni targets

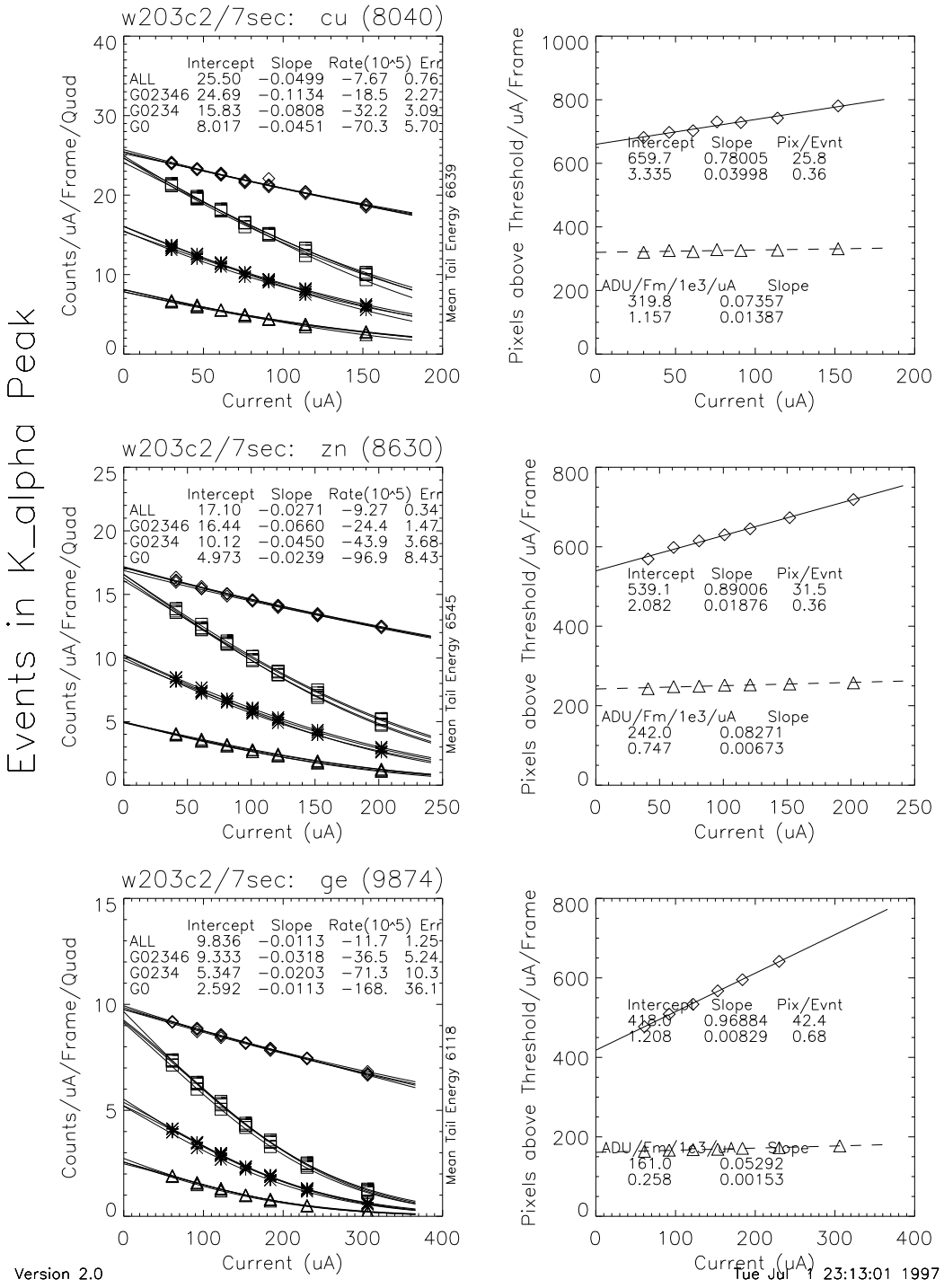

Figure 4.26: Raw HEXS pileup data for K_α for w203c2 with a 7 second exposure for Cu, Zn, and Ge targets

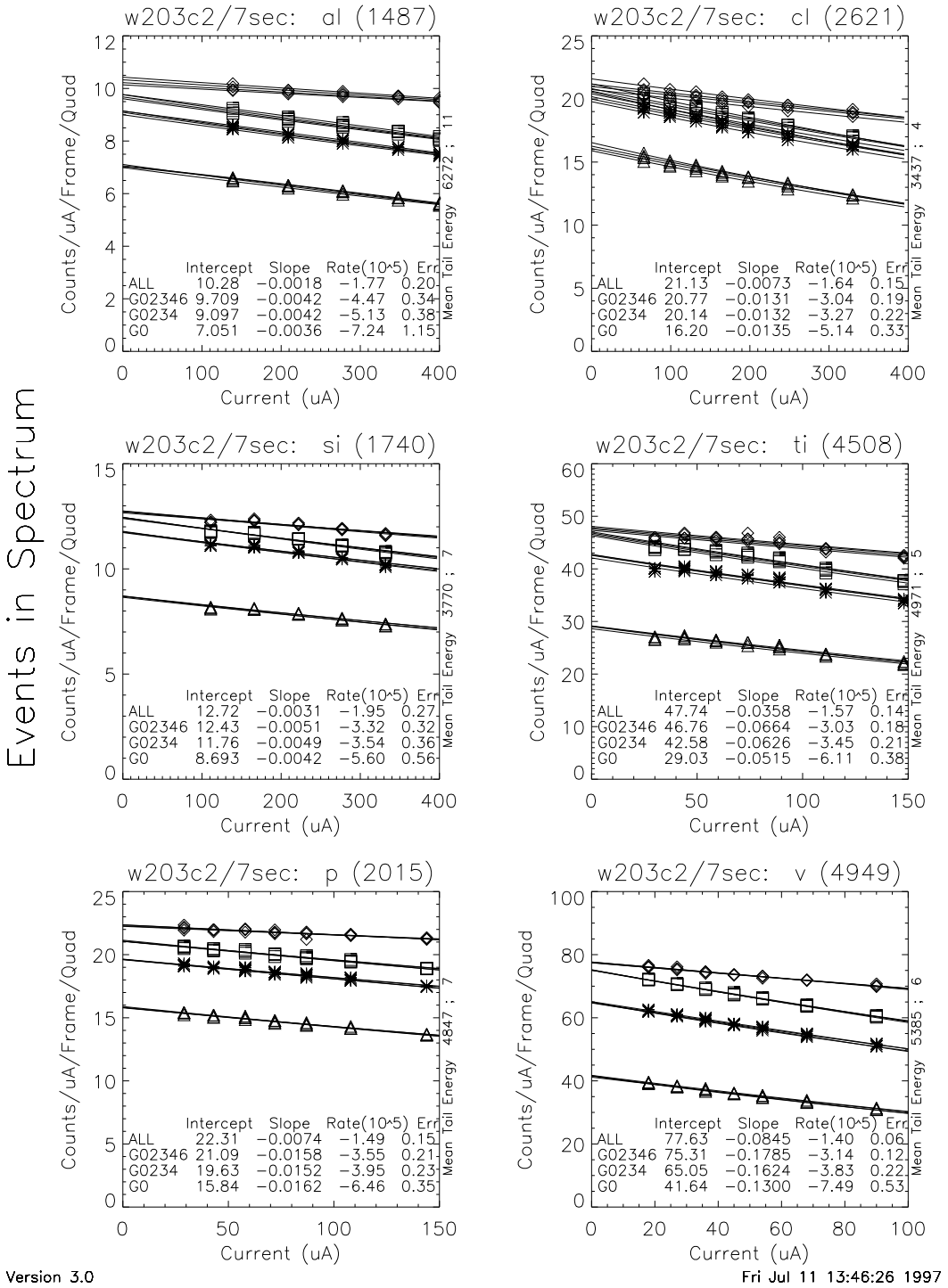

Figure 4.27: Raw HEXS pileup data for entire spectrum for w203c2 with a 7 second exposure for Al, Si, P, Cl,Ti, and V targets

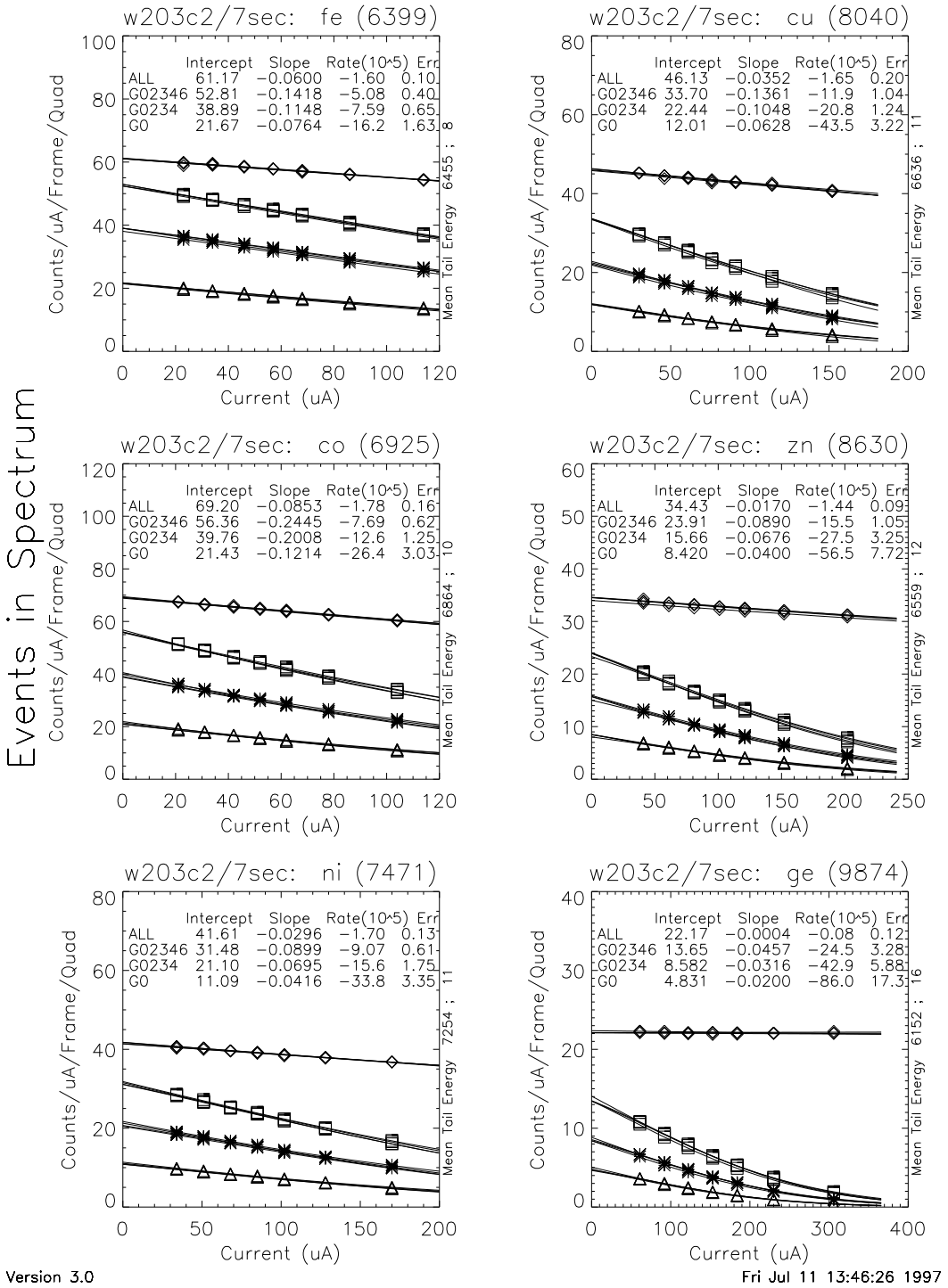

Figure 4.28: Raw HEXS pileup data for entire spectrum for w203c2 with a 7 second exposure for Fe, Co, Ni, Cu, Zn, and Ge targets

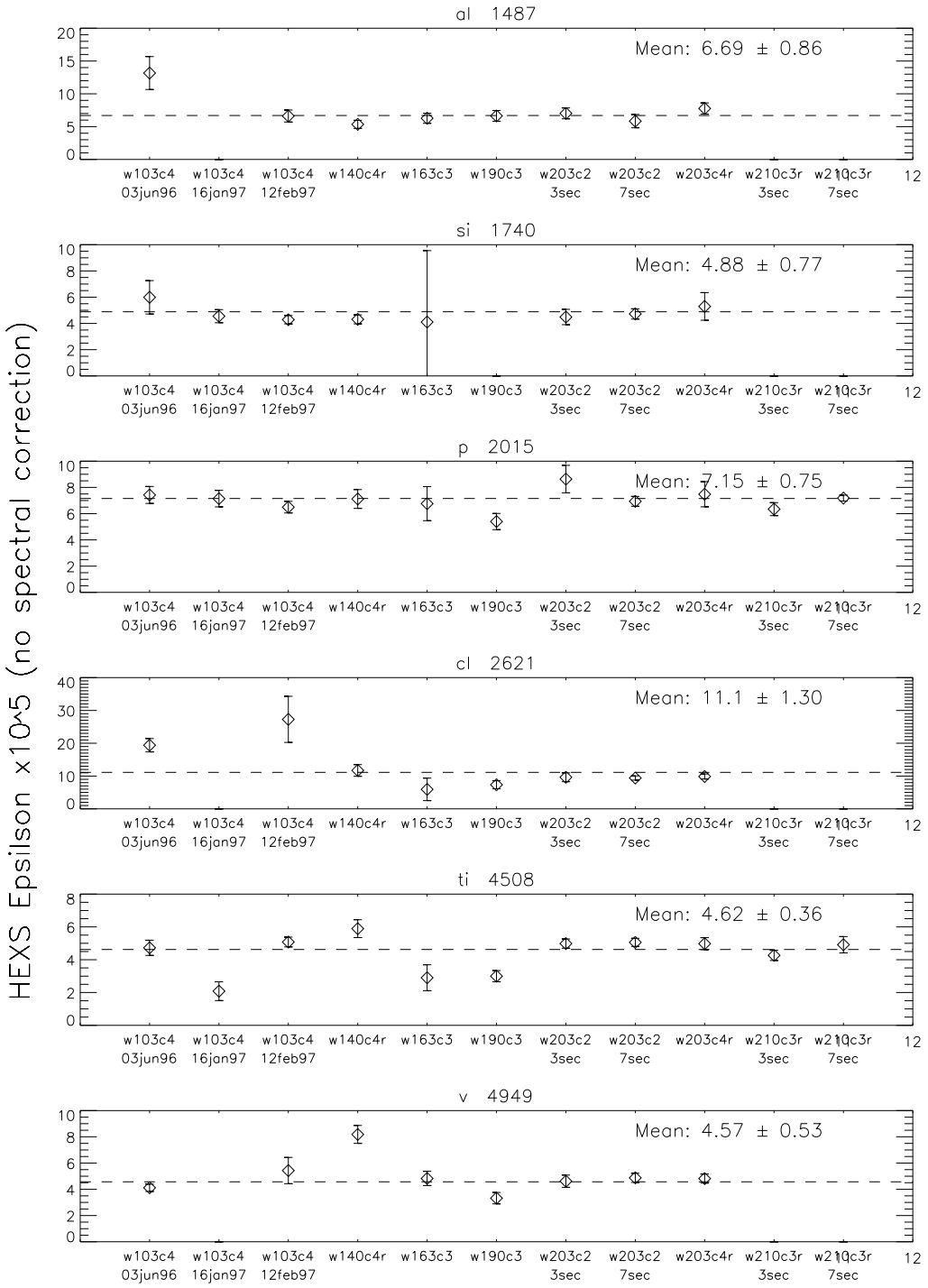

Figure 4.29: Mean g02346 epsilon for all data sets with no spectral correction (Al - V)

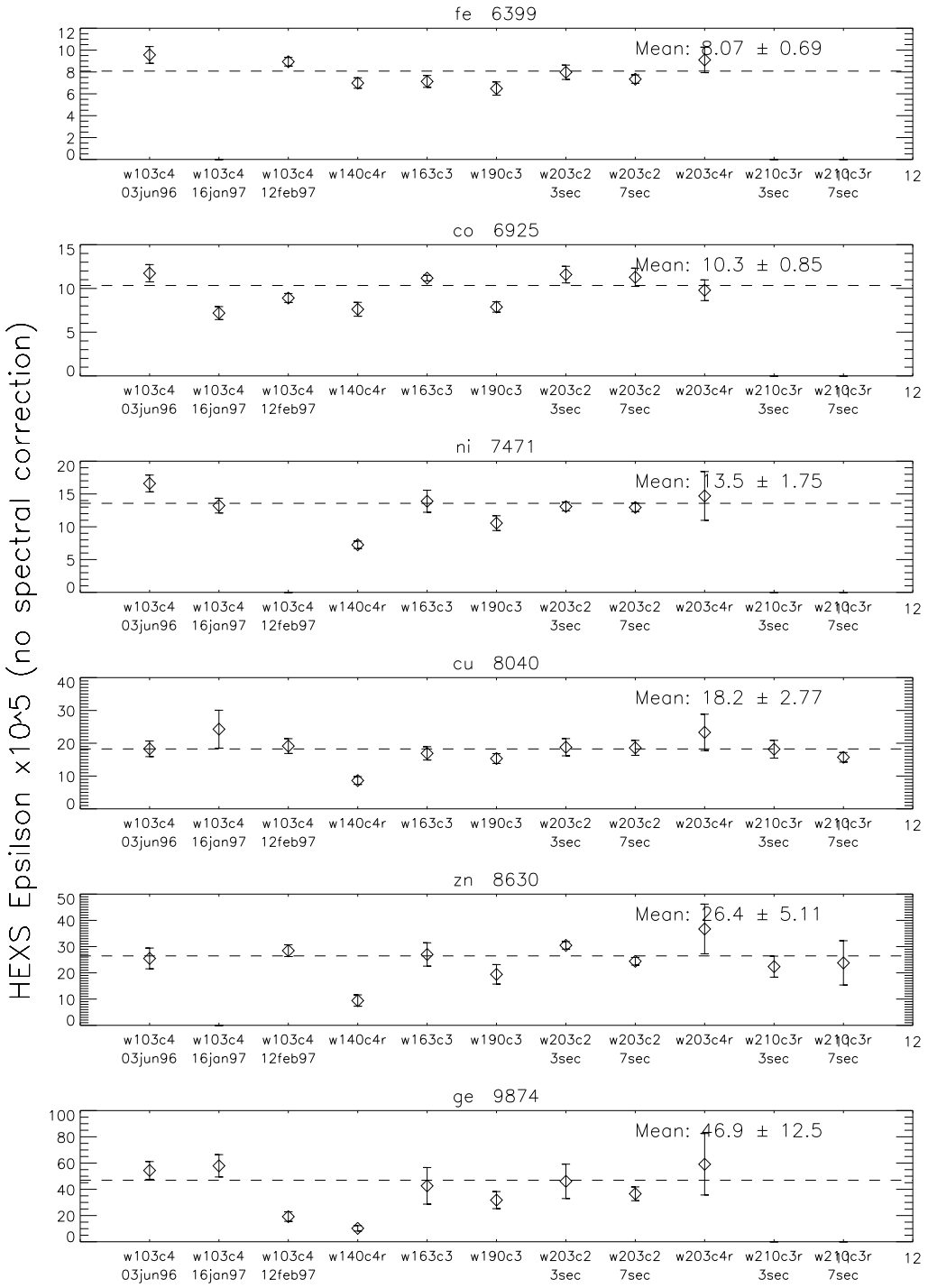

Figure 4.30: Mean g02346 epsilon for all data sets with no spectral correction (Fe - Ge)

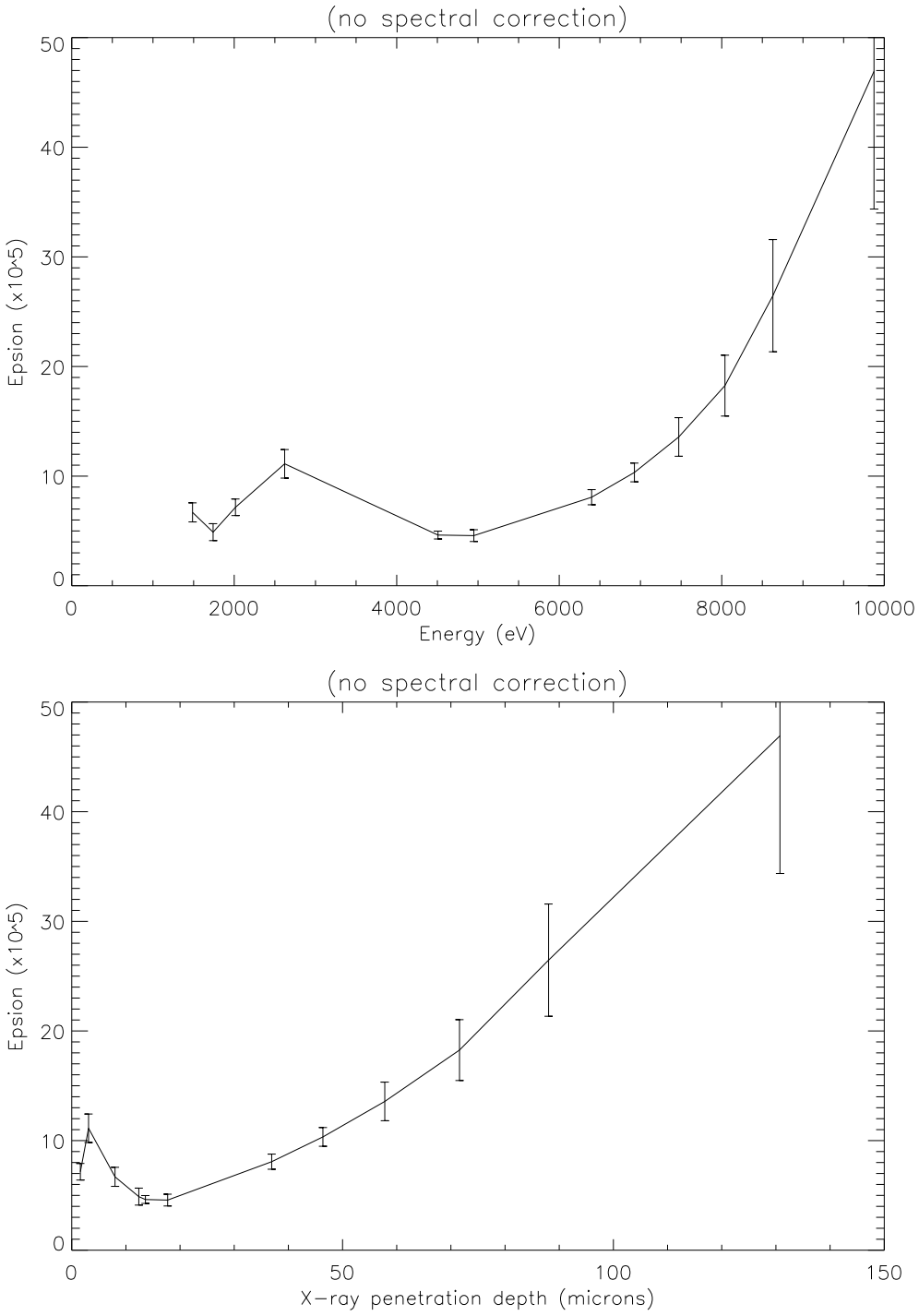

Figure 4.31: Variation of epsilon with Si penetration depth for raw HEXS data

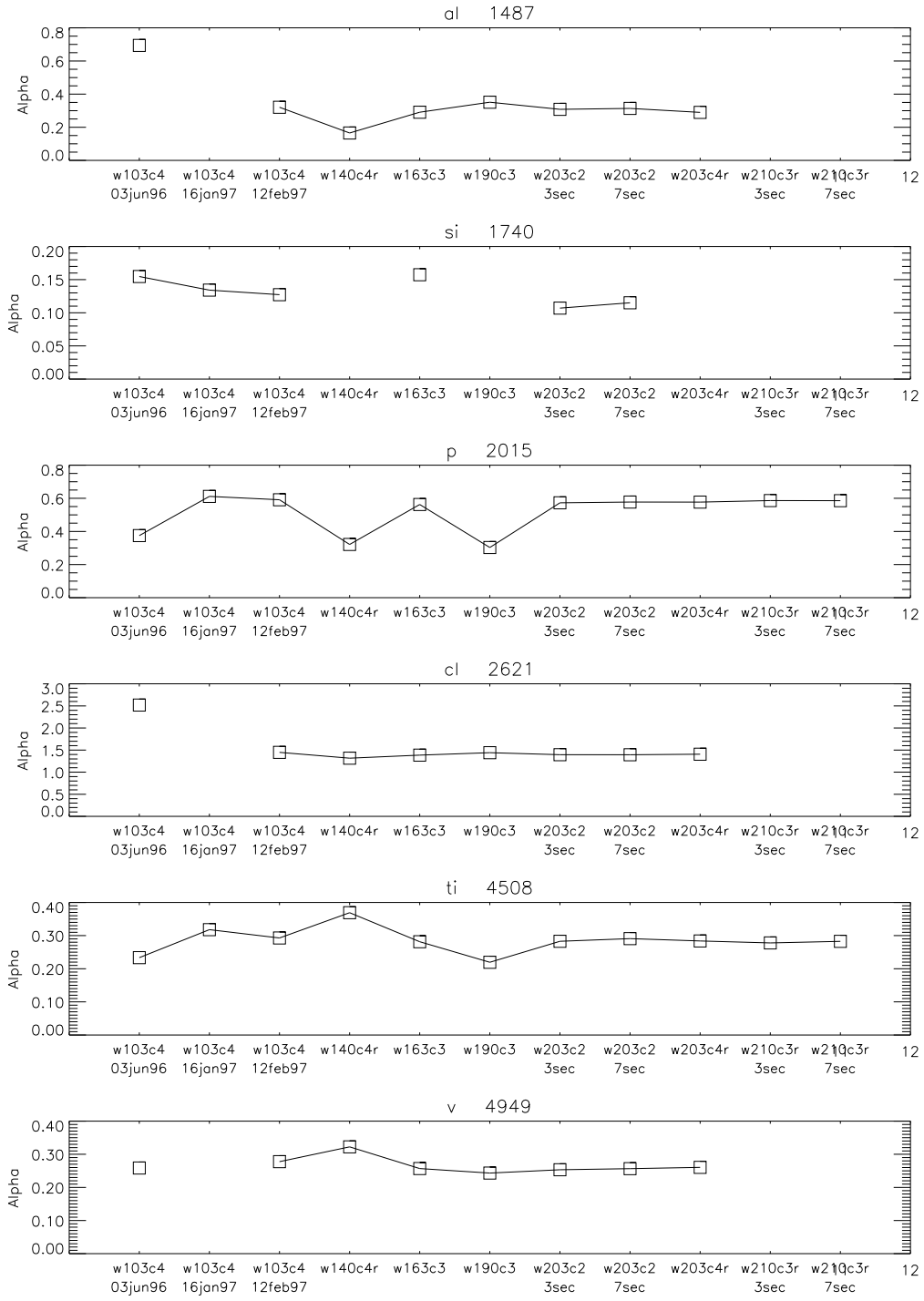

Figure 4.32: Variation of alpha, the ratio of bad to good x-ray events, for Al to V

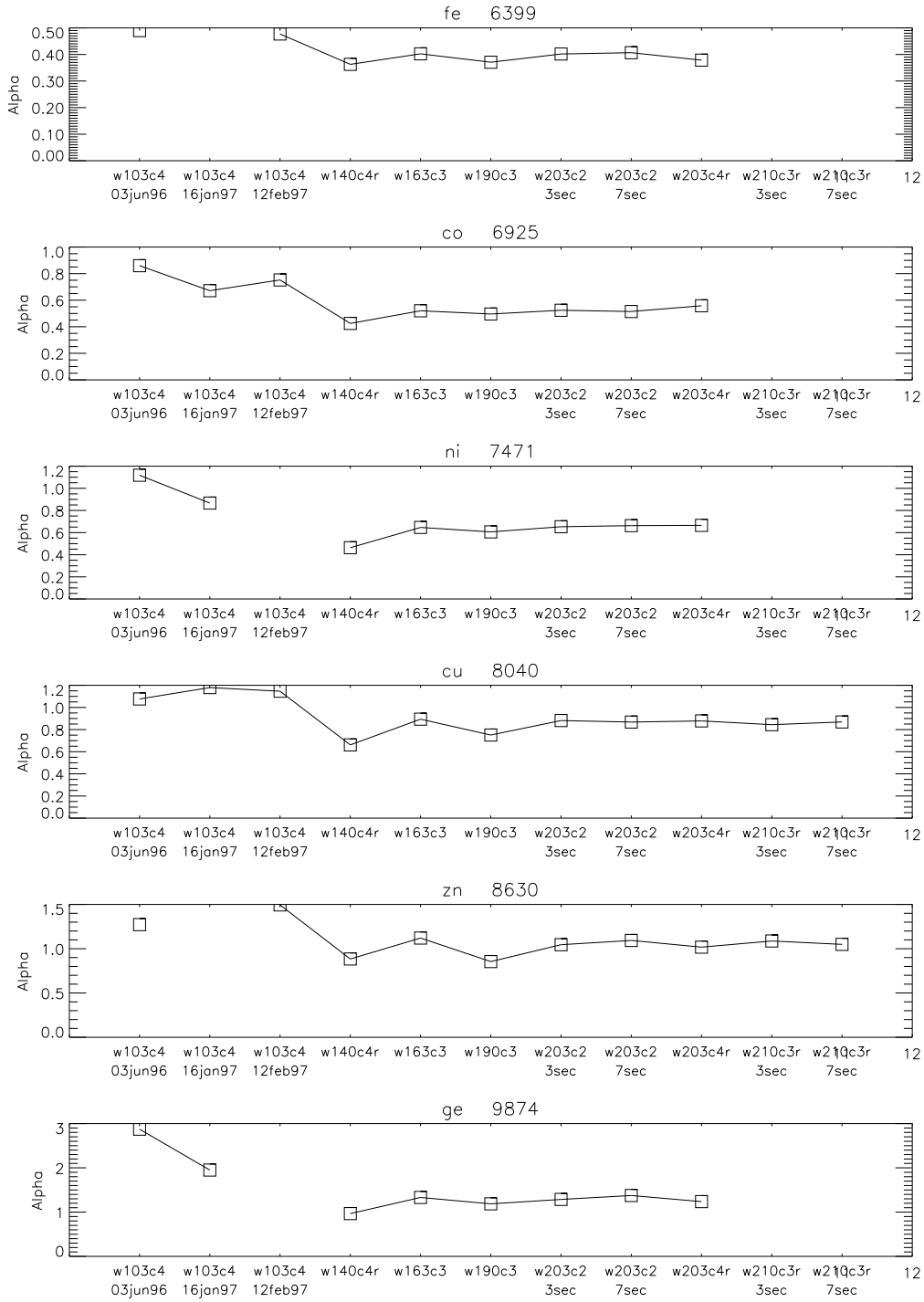

Figure 4.33: Variation of alpha, the ratio of bad to good x-ray events for Fe to Ge

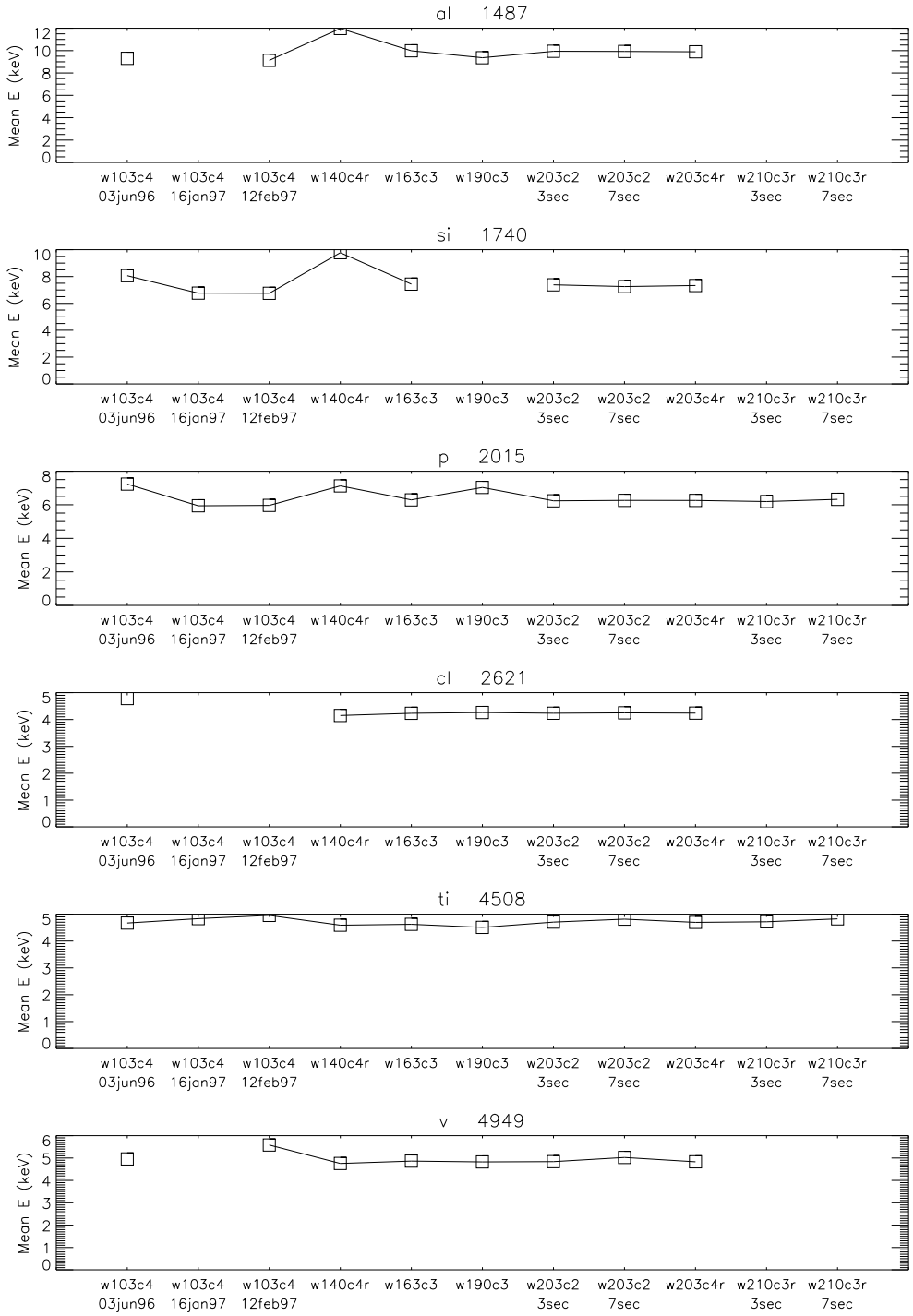

Figure 4.34: Variation of spectrally averaged epsilon (ϵ') for Al to V

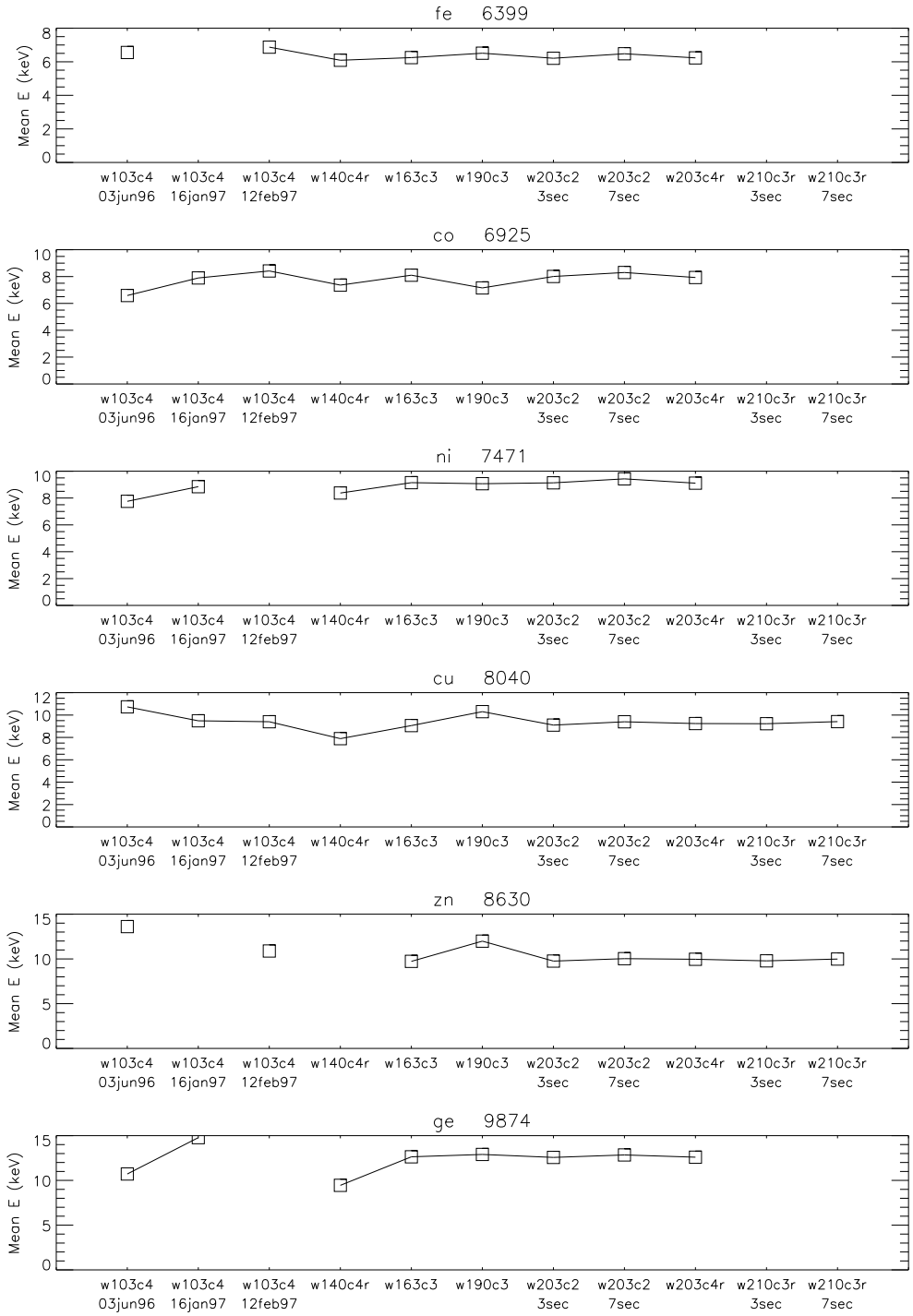

Figure 4.35: Variation of spectrally averaged epsilon ($\epsilon^{'}$) for Fe to Ge

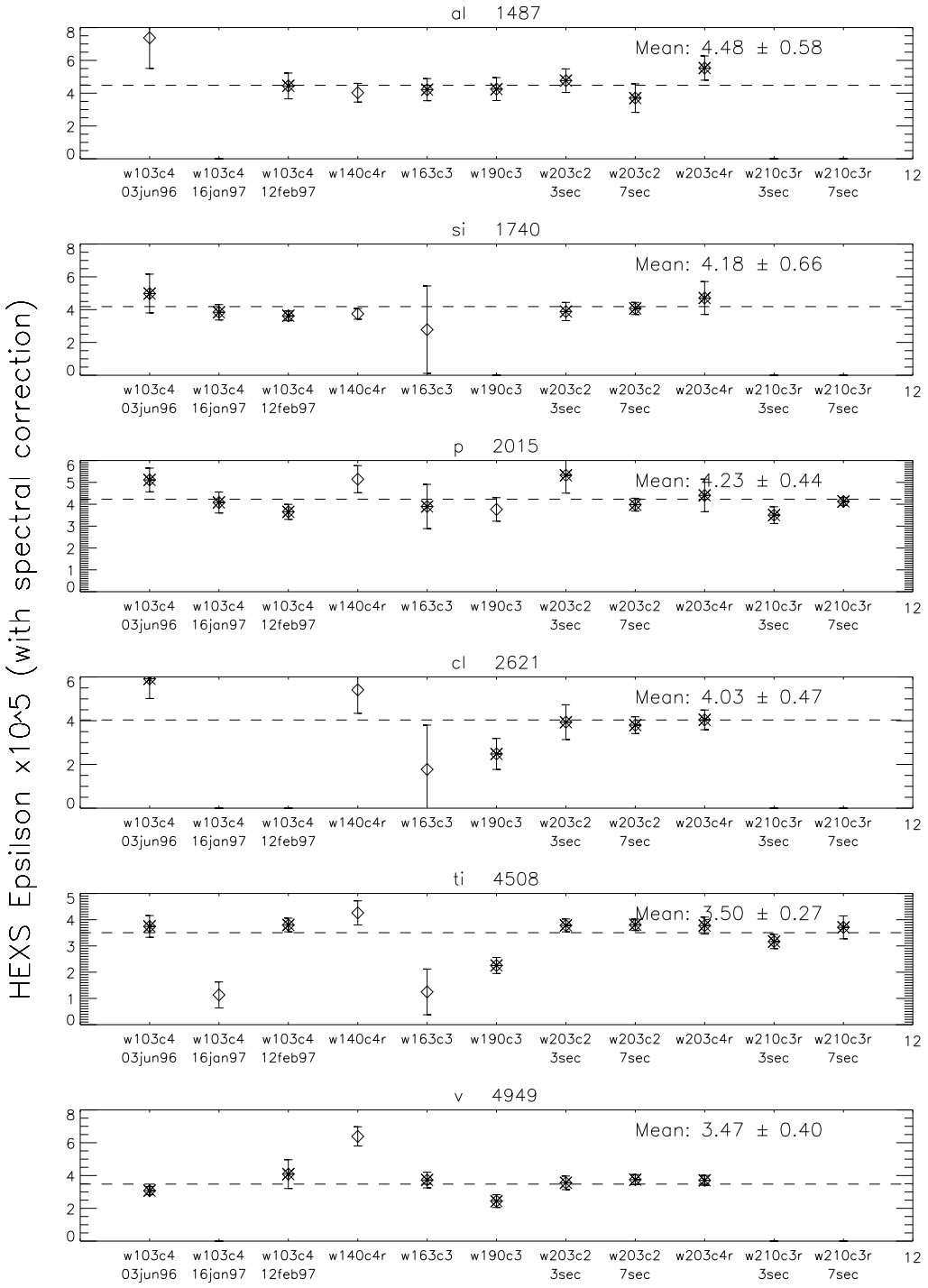

Figure 4.36: Mean g02346 epsilon for all data sets including a spectral correction (Al - V)

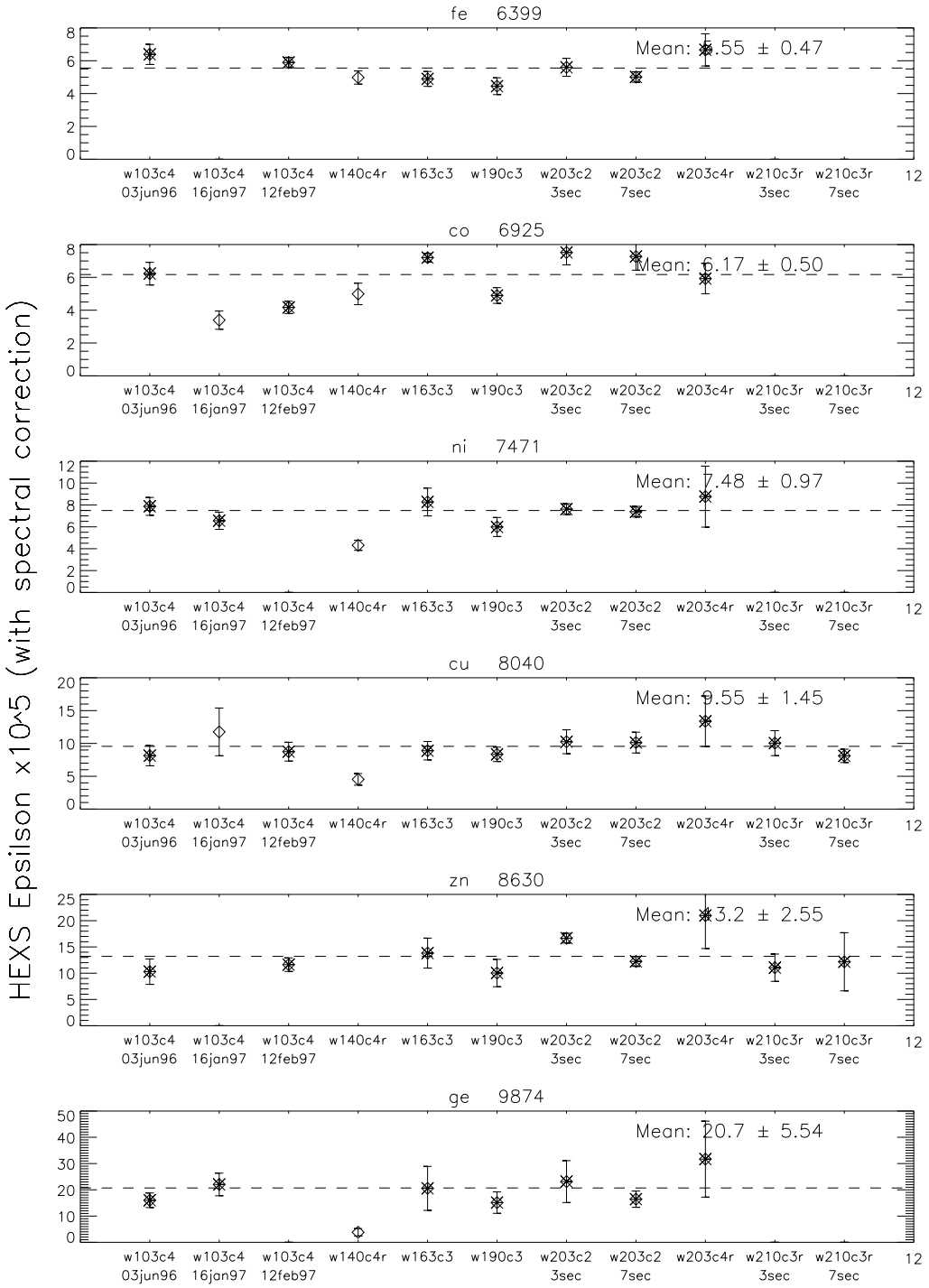

Figure 4.37: Mean g02346 epsilon for all data sets including a spectral correction (Fe - Ge)

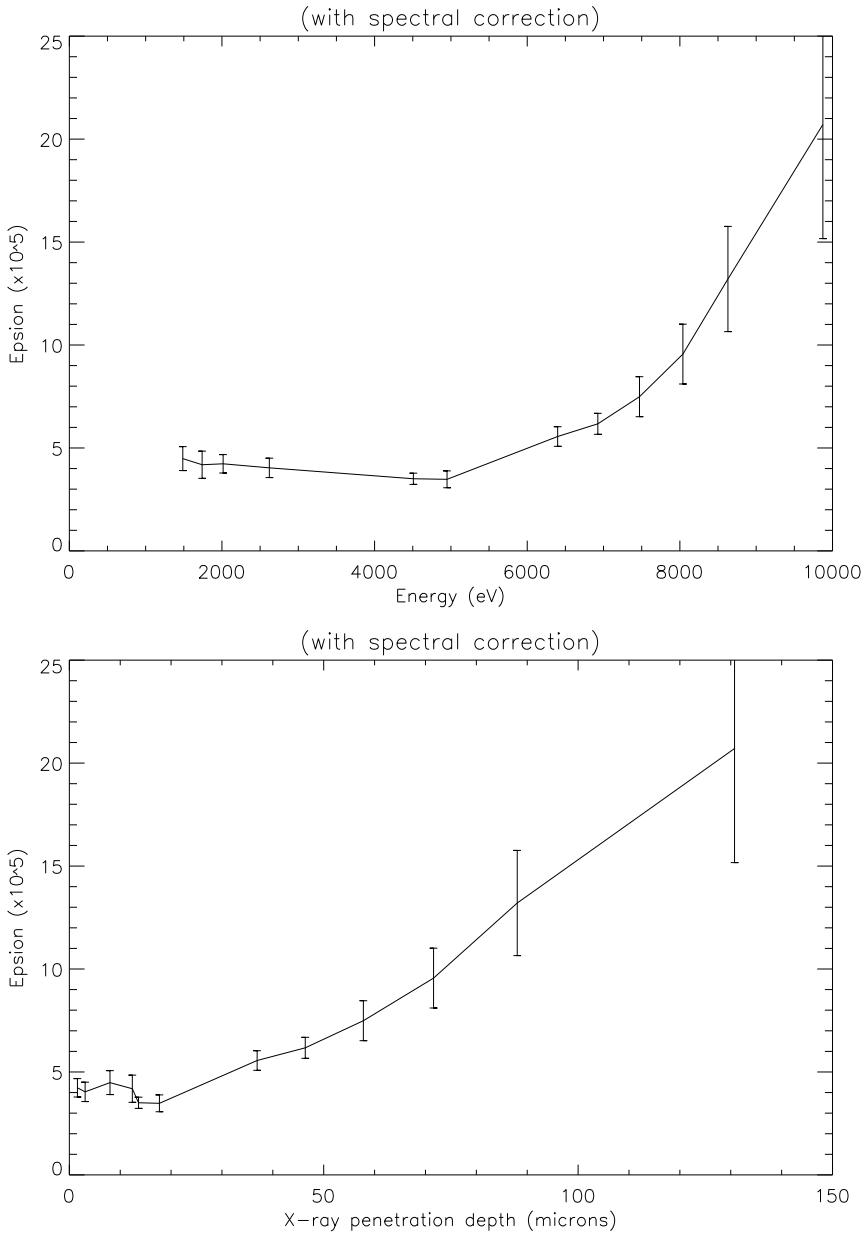

Figure 4.38: Variation of epsilon including corrections for spectral impurities

4.4.4 Redistribution of X-rays by Pileup

Pileup can effect event detection in two ways, event-extinction and event-redistribution. Up to this point, only event-extinction has been modeled since its occurance rate is nearly a factor of ten less than event-redistribution. This difference is nicely displayed by reanalyzing the experimental pileup data from section 3 as follows. For a series of energy spectra at different source fluxes (i.e. different x-ray tube currents), the spectra are normalized to the total exposure time and incident flux. Since the CCD output electronics use an A to D converter, the energy scale is discretized into intervals. For each energy interval, a plot is made of the spectral intensity versus the incident flux. If there was no pileup effect, the points would lie along a horizontal line, that is the normalized spectral intensity would not vary with incident flux at that energy. For weak pileup in the linear regime, the points actually lie on a linear line with a negative slope. In effect, this procedure results in plots similar to Figs. 4.23-4.26, except now there is a plot for every energy bin (in our case there were 4096 energy bins). The intercept of this line represents the intensity observed at that energy if pileup effects did not occur. Plotting all 4096 intercepts together versus energy results in a new spectrum which can be considered the spectrum observed if the detector had no pileup effects. Correspondingly, in addition to the intercept, the slope of each line represents a quantitative measure of the pileup effect at that energy. Plotting all 4096 slopes together versus energy results in a new spectrum reflecting the spectral change caused by pileup.

Figures 4.39-4.40 show the spectral change for all 12 energies as observed by w203c2 during 7 second exposures. The most prominant feature for each (target) energy is the large negative spike which represents x-ray extinction of the K_α peak. For example, in V, the K_α line at 4949 eV looses about 0.02 x-rays/μA^2 in each energy bin. Associated with each K_α extinction spike is the K_β extinction spike, usually about ten times smaller. Small negative spikes also result from the Si escape peak, the fluorescence peak, and the L peak (best seen in spectra from higher Z, e.g. Cu). Aside from negative extinction spikes, there are positive redistribution spikes. The largest such positive peak always occurs at twice the K_α energy. This peak represents the pileup of two K_α x-rays such that they appear as a single x-ray at twice the energy. One nice example of additive redistribution is the Cl plot which shows a series of three positive peaks, each representing pileup from all three combinations of K_α and K_β x-rays. Redistribution in the continuum can also be seen, but is too small to be observed on the displayed scale. These events represent the slight overlap of two x-rays appearing as one x-ray, but without the total inclusion of the sum all their charges (or energy). The collected energy lies anywhere between that of one memeber of the incident pair of x-rays and that of the sum of the pair. The number of these redistributed "continuum" events is a small fraction (about 10%) of redistributed events with no energy loss. This observation forms an important conclusion: the largest effect of spectral redistribution is the simple energy summation of two x-rays.

Other minor redistribution effects are observed around the base of the K_α peak. The

net effect appears as a slight line shift, caused by pileup moving a few events from the low energy side of the K_α peak to the high energy side. However, this detail was not regularly observed under all conditions.

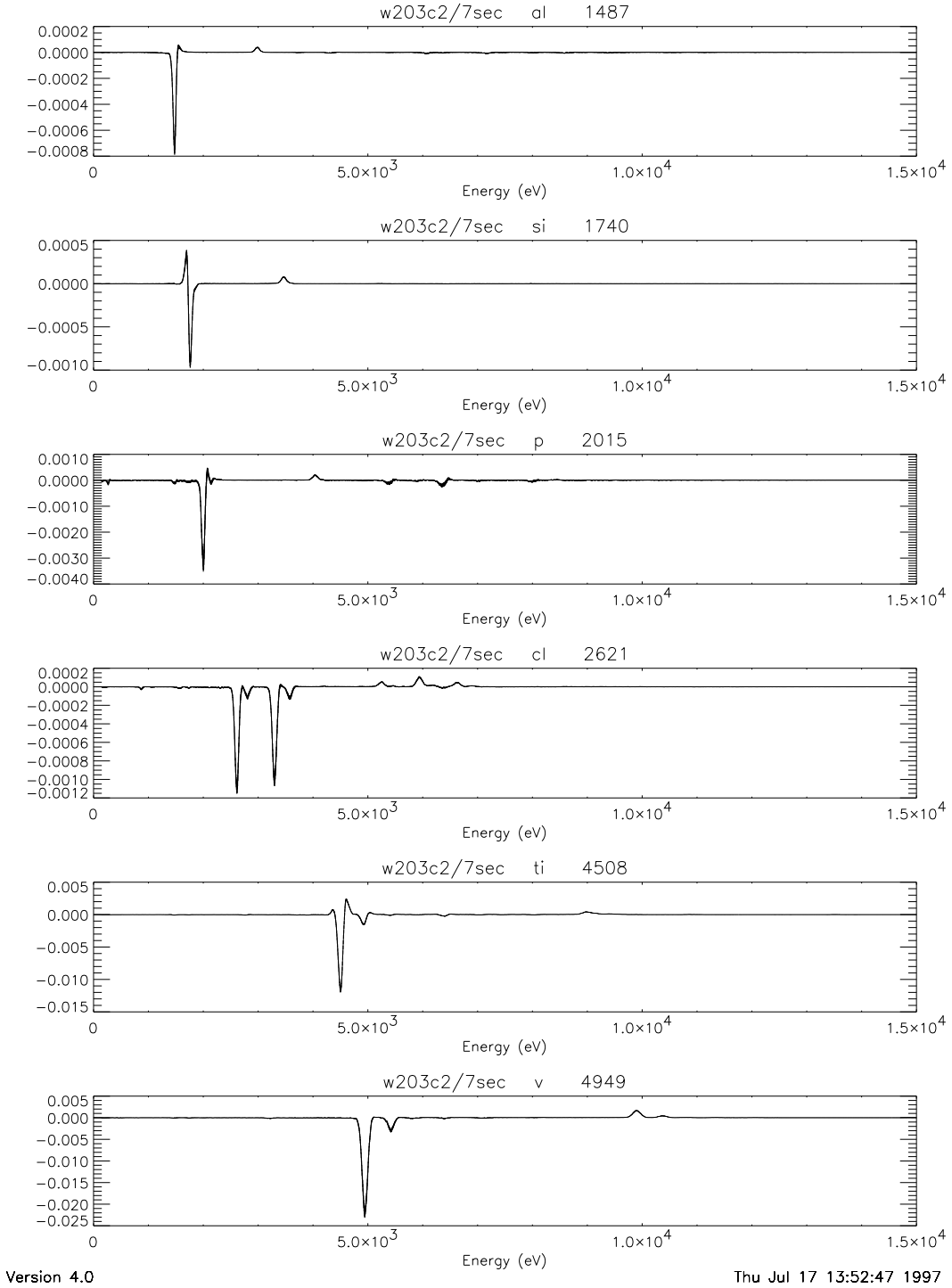

Figure 4.39: Redistribution of G02346 events in w203c2 during 7 second exposures due to pileup for Al, Si, P, Cl, Ti, and V HEXS targets

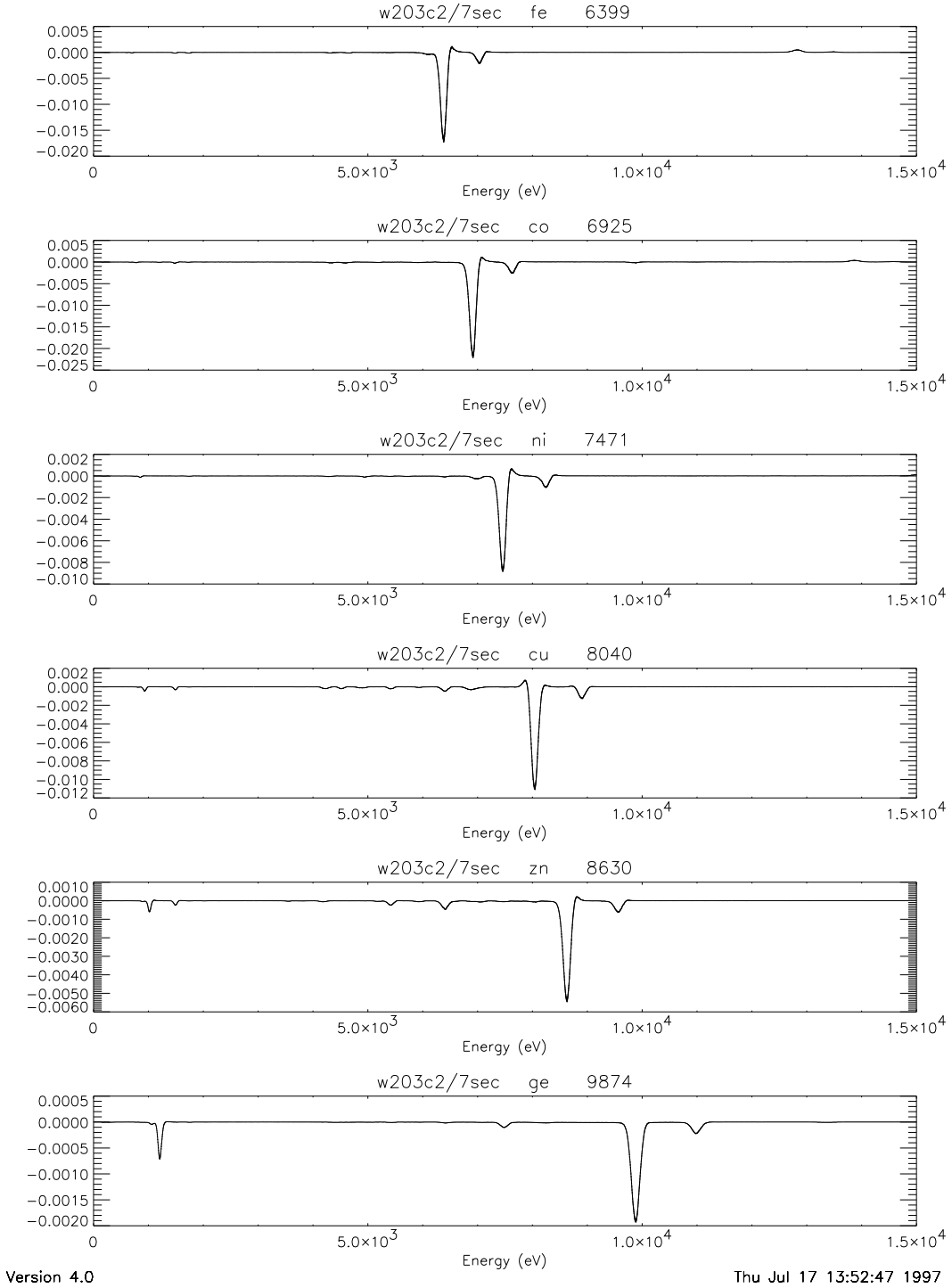

Figure 4.40: Redistribution of G02346 events in w203c2 during 7 second exposures due to pileup for Fe, Co, Ni, Cu, Zn, Ge HEXS targets

4.4.5 Branching Ratio Variation with Flux

Branching ratios can be defined as the number of x-rays detected in one grade selection divided by the total number of x-rays detected. The branching ratio is not only energy dependent but is flux dependent. The laboratory pileup data can be used to compute the effect of flux on the branching ratios. These "branching ratio epsilons" are presented in Figs. 4.41 and 4.42, which show some variation between the various CCDs. These numbers are relative correction factors to the branching ratio per detected g02346 x-ray per quadrant. For example, if the BR eps equals 4×10^{-5}, and there are 1000 x-rays per quadrant per frame, then the relative correction to the branching ratio is 4%. The numbers in Figs. 4.41 and 4.42 are specfically the number of G02346 events in the K_α peak divided by all events in the peak. The effect of pileup on branching ratio has a direct effect on methods which use the branching ratio to determine the depletion depth. An example of this method is discussed in section 4.6.2.

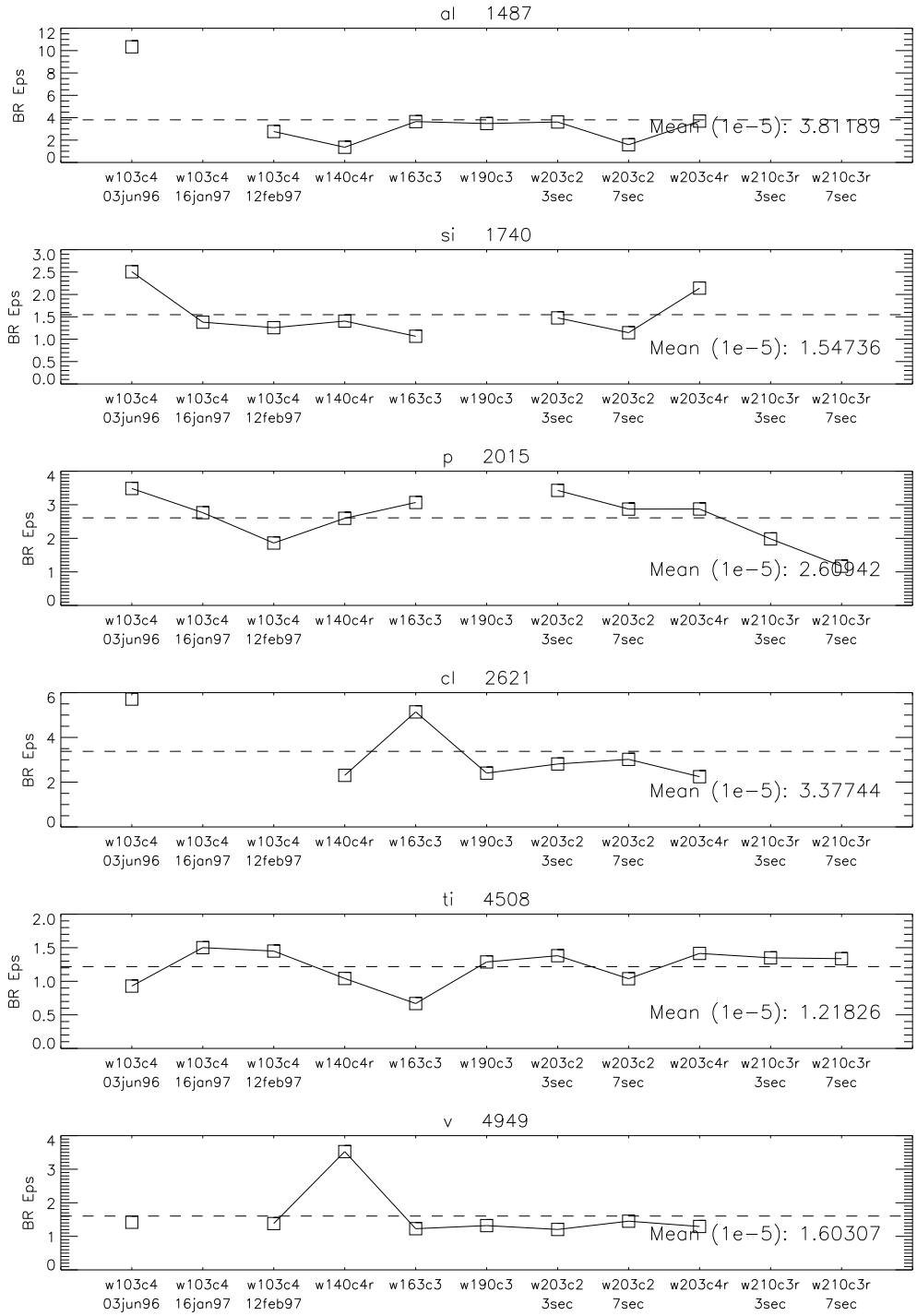

Figure 4.41: Branching ratio epsilons from data set for elements Al - V

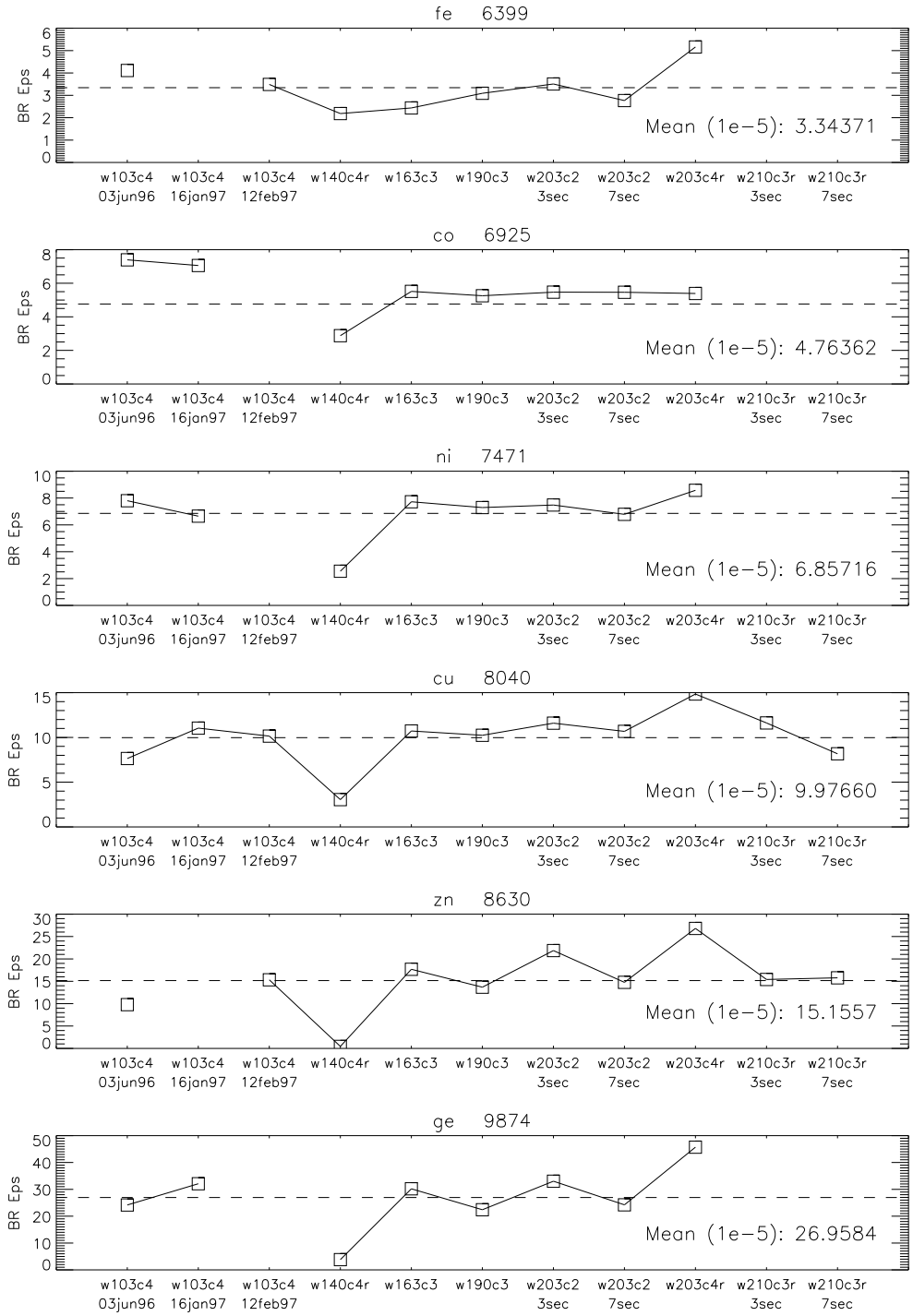

Figure 4.42: Branching ratio epsilons from data set for elements Fe - Ge

4.4.6 Single Pixel Pileup

As an imaging x-ray telescope, AXAF focuses a point source onto the CCD. Since the point response function FWHM is comparable to the size of one pixel, pileup from a strong point source is a particular problem.

All pileup cross sections presented so far are evaluated in terms of detected x-rays per quadrant per frame. However, it is often useful to describe pileup in units of x-rays per pixel per frame. The factors are translated multiplying ϵ by $256 \times 1024 = 2.62 \times 10^5$. Thus, if $R_{nopileup}$=incident x-ray rate per pixel per frame for a monochromatic beam, then to first approximation the detected rate $R_{nopileup}$ is given by the transcendental equation

$$R_{pileup} = R_{nopileup} \exp\left(2.62 \times 10^5 R_{nopileup} \epsilon\right) \tag{4.18}$$

From another viewpoint, pileup in a single pixel with a monochromatic source is easily understood as a simple Poisson process. That is, if the probability for an x-ray to interact with a pixel during one exposure is λ, then the probability that N x-rays interact during one exposure is

$$P_N = \frac{\lambda^N e^{-\lambda}}{n!} \tag{4.19}$$

Consider an entire observation of N_{frames} frames. If there was no pileup, the total incident flux of $N_i = N_{frames}\lambda$ x-rays would be detected. The effect of pileup is manifest as several (or many) x-rays which add during one exposure. Let

$$N_0 = N_{nframes} e^{-\lambda} \equiv \text{number of frames with no interaction.} \tag{4.20}$$

Combining these two equations yields,

$$\frac{N_i}{N_{frames}} = -\log\left(\frac{N_0}{N_{frames}}\right) \tag{4.21}$$

For example, if out of 1000 frames, x-rays from a point source are present in 100 frames, then

$$N_i = -1000 \log(900/1000) = 105 \tag{4.22}$$

Thus, pileup accounted for an apparent reduction in the incident flux of 5%.

This method differs from the first method developed in this chapter by treating every incident x-ray as a valid event, including the coincidence of two or many x-rays. This method has use in high pileup situations where Eqn. 4.16 presents ambiguity. For example, the shape of the graphs in Fig. 4.22 show that for a given value of the detected flux, there are *two* possibilities for the incident flux. Without additional information it is impossible to discriminate between the low and high flux solution. Although most astrophysical point sources should not be so strong, the ambiguity of strong sources can be resolved by application of the method described above.

4.5 CCD Subpixel Structure

4.5.1 Introduction and Motivation

The low energy (< 4 keV) quantum efficiency of a front side (FI) CCD is intimately related to the dimensions of the sub-pixel structures. The sub-pixel structures in question include the polysilicon gates and insulating layers, as well as channel stops: implanted p^+ channels and their insulating layers. The gates run the length of the CCD, and are responsible for clocking the charge out of the device. The ACIS CCDs employ a three phase read-out scheme to transfer charge, so the gate structure is actually comprised of three different gates that differ slightly in dimension from one to another (Burke et al., 1993). Three neighboring gates define one pixel, with the boundary location dependent on the voltages applied to the gates. Figure 4.43 is an idealized schematic of a CCD cross section revealing the structure of the gates. Figure 4.44 is a SEM cross section of a CCD showing the over lap of gate B with gate A. The rectangular, black regions are the polysilicon gates. The white material over and between the gates is insulating SiO_2.

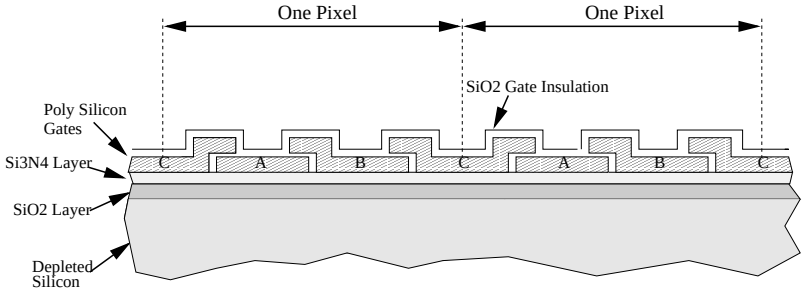

Figure 4.43: Gate structure of a CCD.

The embedded channel stops run perpendicular to and lie beneath the gates. These structures help confine the charge clouds created by a photoelectric absorption and define the horizontal boundaries of a pixel. Figure 4.45 is a picture of a 2×2 array of pixels and shows the orientation of the gates and channel stops to one another. To fabricate the channel stops, a portion of the insulating Si_3N_4 layer is etched away. A p^+ dopant is then implanted into the bulk silicon. Finally, the silicon is oxidized creating an insulating layer of SiO_2 between the channel stop and the gate structure. The gate structure is then grown on top of the silicon after this process. Figure 4.46 is a SEM measurement of a channel stop. The black and white bands at the top of the image are the polysilicon gates and insulating oxide, respectively. The elongated, hexagonal structure is the SiO_2 insulator between the p^+ channel (not visible in this image) and the gates. The thin white structure between the gates and hexagonal insulator is the Si_3N_4.

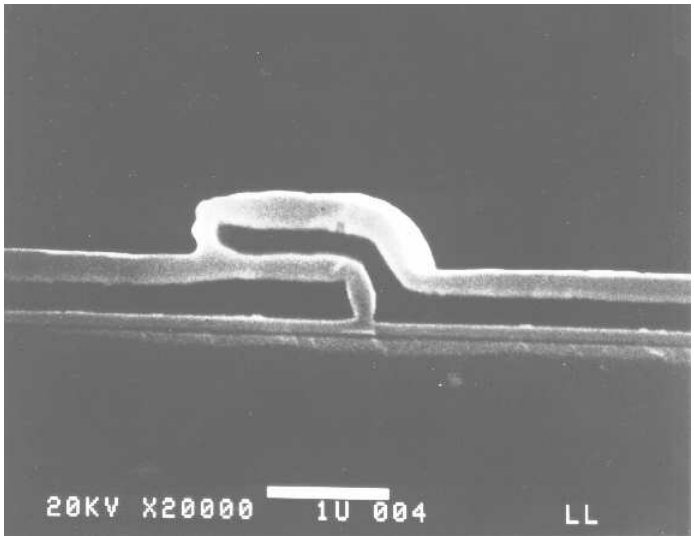

Figure 4.44: SEM photo of the CCD gate structure. Gate B is shown overlapping gate A. The bar above the text in the photo is 1 μm.

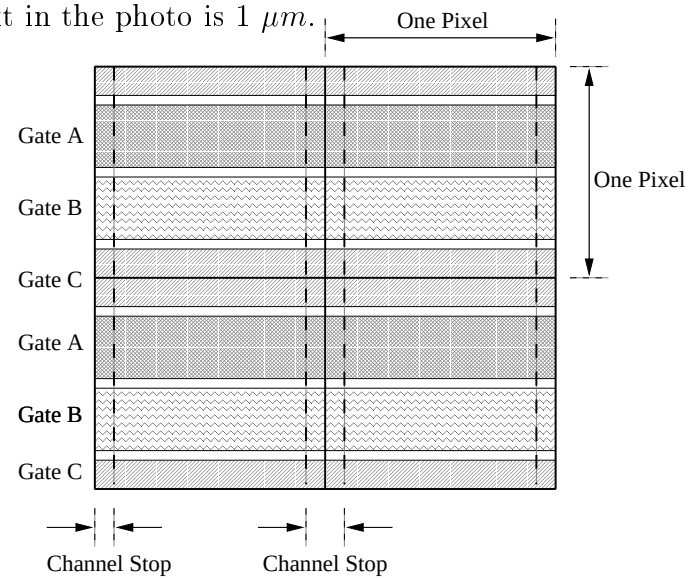

Figure 4.45: Schematic of a 2×2 array of pixels showing the orientation of the gates and channel stops. The channel stops are beneath the gates.

When modeling the quantum efficiency of an ACIS CCD, the complicated gate structure can accurately be approximated as uniform slabs of material that cover the entire CCD. This model assumes that the charge created by a photon interaction in one of these layers is not collected by the device (i.e. the layer is "dead"). This model–The Slab and Stop model–was first developed by Keith Gendreau during calibration of the ASCA SIS

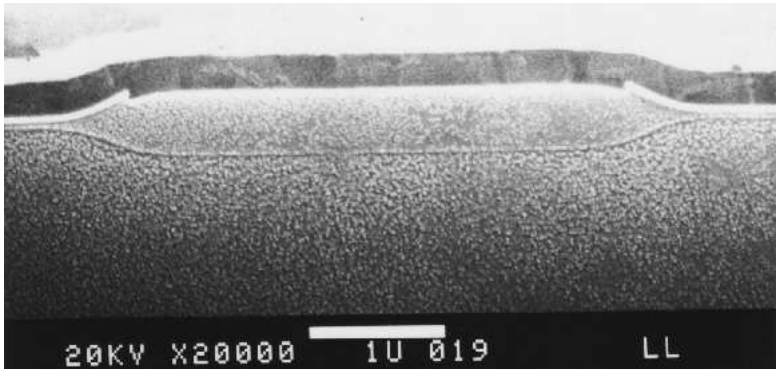

Figure 4.46: SEM measurement of a channel stop

CCDs (Gendreau, 1995). The Stop part of the model refers to treating the hexagonal insulator structure and implanted p^+ as rectangular regions of dead SiO_2 and Si, respectively. The absolute calibration of the reference standards involves fitting the data obtained at the BESSY facility with the Slab and Stop Model. While the BESSY measurements determine the thicknesses of the gate slabs, they prove insufficient for constraining the channel stop parameters[1]. Construction of a highly accurate CCD model, then, requires determination of this information in some other fashion.

4.5.2 Description of Mesh Experiments

One possible method for determining the sub-pixel structure is illuminating a pixel with a very narrow beam of monochromatic X-ray and observing how the CCD response changes as the beam is rastered across the pixel. Unfortunately, obtaining a well focused X-ray beam is difficult, and even if it were trivial, the experiment would require too much time to acquire enough data to make the results statistically significant. One possible solution to both of these problems is using a metal film with relatively small holes (4 μm holes compared to the 24 μm size of a pixel) placed in a regular fashion (Tsunemi et al., 1997). When this mesh is placed close to the CCD surface and rotated with respect to the axes defined by the gate structure and channel stops, a moiré pattern is formed when the device/mesh combination is illuminated with X-rays. Below, we summarize the experimental technique and our initial results. Interested readers are referred to the paper by Pivovaroff *et al.* for details (Pivovaroff et al., 1998).

Figure 4.47 shows a section of the mesh, and Figure 4.48 shows the fixture used to hold the mesh tight and close to the surface of the CCD. The resulting moiré pattern contains the CCD's response to a 4 μm X-ray beam that was uniformly rastered across the pixel

[1]See Section 4.6.1 for details.

area. The smaller the relative angle between the mesh's orientation and the CCD axes, the more pixels are required to make a moiré cell, and the finer resolution of the CCD's response[2]. Typical measurements were performed with angles on order of 5°, and moiré cell dimensions of 61 pixels.

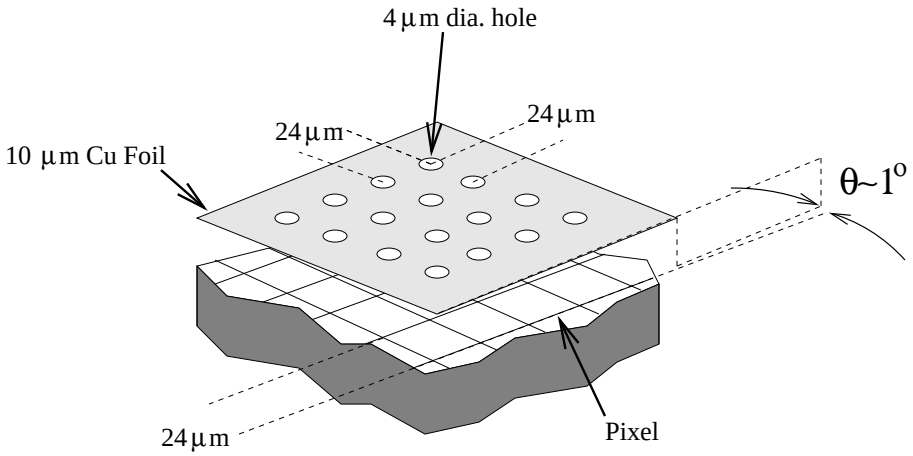

Figure 4.47: Schematic of the mesh showing its orientation to the CCD

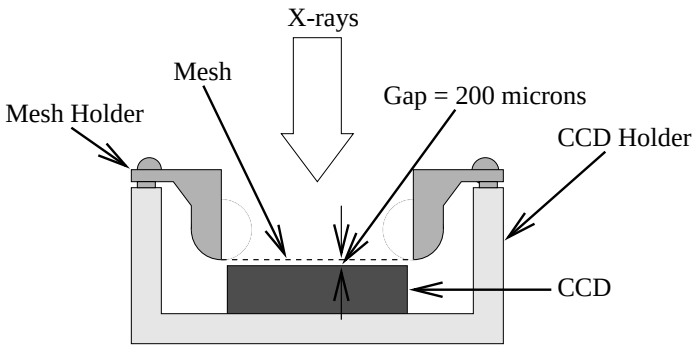

Figure 4.48: Fixture used to hold the mesh close to the CCD surface

Analysis of the data begins with selecting suitable grade events (single pixel and horizontally or vertically split events) from the photo-peak of the monochromatic line to build the moiré cells, rotating the moiré cells, and summing individual cells into one representative

[2]Readers are referred to the paper by Tsunemi (Tsunemi et al., 1997) for the analytic derivation of these relationships.

pixel (hereafter RP) for the entire CCD. Figure 4.49 shows a sample of the unrotated, raw moiré cells that are a direct output of the illumination of the mesh/CCD system and the RP, repeated in a 3×3 array to make it easy to see the boundary regions of the pixel. With the RP generated, determination of the sub-pixel structure can proceed. By compressing the RP in one direction, the attenuating affect of the channel stops or the gates can be modeled. For the rest of this review, we concentrate only on the channel stops, although the same techniques can be applied to measure the gates.

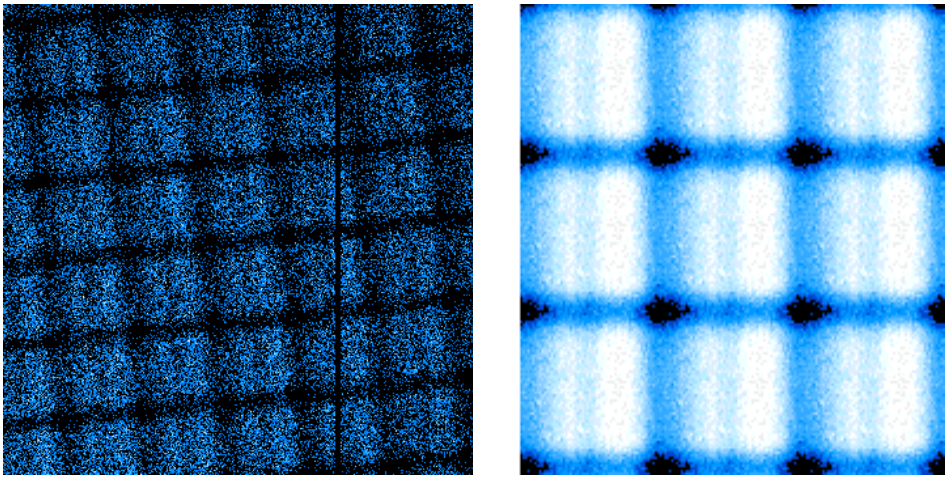

Figure 4.49: Left: Raw data showing the moiré cells. Right: The representative pixel (RP) repeated in a 3×3 array.

The approach for determining the channel stop dimensions is quite straightforward. The attenuation in detected photons expected from the channel stop (recall that the Slab and Stop Model assumes that any photon interacting in the sub-pixel structure will not be detected) is convolved with the PSF of the mesh holes. The resultant convolution is compared to the experimental data, and the channel stop model parameters are allowed to vary, using a χ^2 fit statistic to determine the best-fit parameters. Figure 4.50 shows the five parameters used to describe the channel stop. Compare the model to the SEM photo of an actual channel stop in Figure 4.46.

In addition to constructing a realistic channel stop model, the success of this technique depends on providing an accurate PSF for the mesh and accounting for additional processes that effectively broadens the PSF (i.e. diffraction, diffusion of the charge cloud, distortions to the PSF caused by using a non-parallel X-ray source). Producing such an analytic aperture function (hereafter AF) is a daunting task. Fortunately, the AF can be ascertained from the mesh data itself. Horizontal and vertical split events come from photons that interact within an electron cloud size diameter of the pixel boundary. Analysis of BESSY

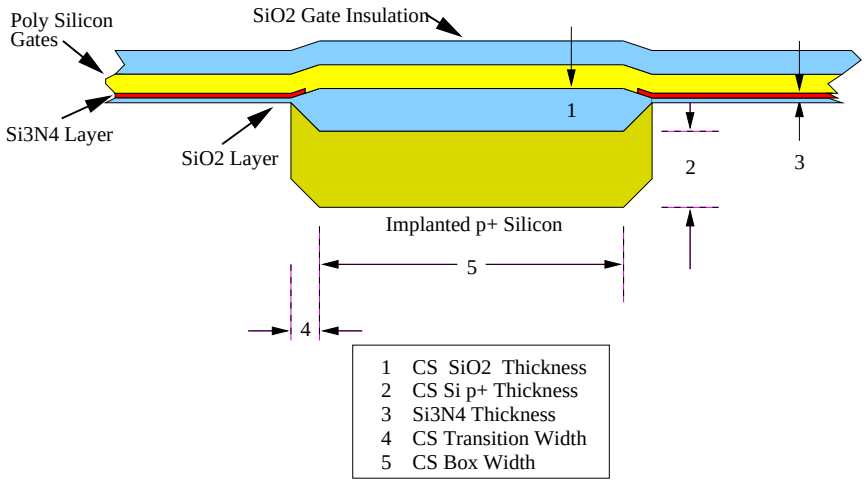

Figure 4.50: Five parameter channel stop model.

KMC data performed by Jones and Prigozhin (Jones et al., 1997) indicate that cloud sizes range between 10 and 100 nm. The distribution of the horizontal and vertical split events ($\Delta_{split\ events}$), then, is the convolution of a 10-100 nm step function (Θ) with the AF.

$$AF \otimes \Theta = \Delta_{split\ events} \tag{4.23}$$

The projection of the mesh holes on the surface of the CCD are at least 4.5 μm in diameter, so Θ can be approximated as a δ function. Equation 4.23 then becomes

$$AF \otimes \Theta \approx AF \otimes \delta = AF = \Delta_{split\ events} \tag{4.24}$$

4.5.3 First Results

Two different X-ray sources were used to perform measurements at six different energies. A monochromator produced photons corresponding to the O Kα line, and the HEXS electron impact source (Jones et al., 1996) produced Al, Si, P, Cl and K Kα lines. Table 4.23 shows the number of photons collected at each of the energies. Figure 4.51 shows the relative amount of attenuation caused by the channel stops, modulated with the mesh AF. The amount of attenuation is governed entirely by the characteristic attenuation lengths of the Kα photons in Si, SiO_2, and Si_3N_4 and does not simply monotonically decrease with increasing photon energy.

K_α	Energy (eV)	total counts
O	525	4.5×10^5
Al	1487	8.4×10^4
Si	1740	6.8×10^4
P	2035	2.2×10^5
Cl	2622	5.5×10^4
K	3312	7.7×10^4

Table 4.23: Summary of Mesh Measurements

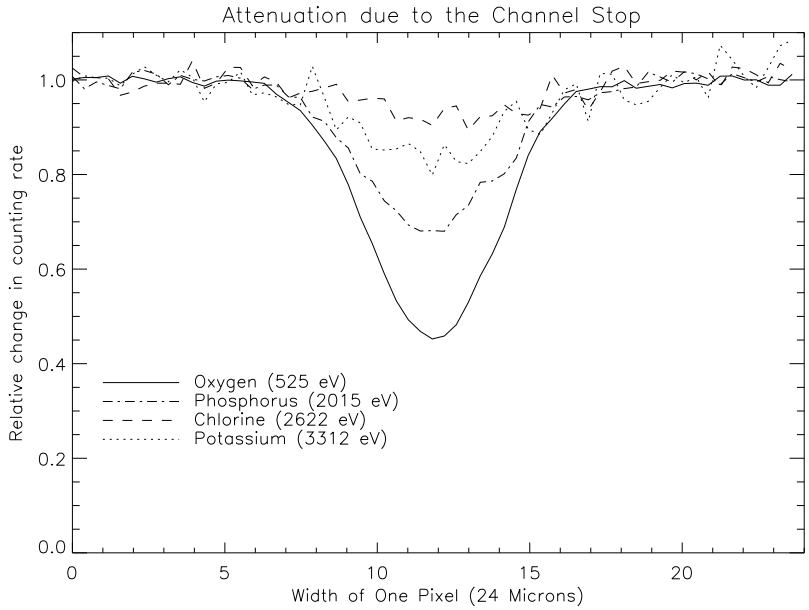

Figure 4.51: Variation in detection efficiency due to the channel stop

Fitting the channel stop model to data from only one Kα line results in degeneracies in the model. Effectively, the five parameters reduce to two: the total width of the stop and the total attenuation. These are given by:

$$\text{Width}_{Total} = 2 \times \text{Width}_{wing} + \text{Width}_{box}$$
$$\text{Atten}_{Total} = \text{Atten}_{Si} \times \text{Atten}_{SiO_2} \times \text{Atten}_{Si_3N_4}$$

The upper two panels of figure 4.52 show the χ^2 confidence plots for the O Kα data set and the P Kα data sets. The contours are for the 68%, 90% and 99% confidence levels. The box and wing parameters have great uncertainty, but the constant slope of the contours

does indicate some bound to the total width. The situation is similar for the thicknesses of the Si p^+ channel and the insulating SiO_2. By simultaneous fitting multiple data sets, a tighter constraint can be placed on the model. The bottom panels of figure 4.52 show the χ^2 contours for the five HEXS data sets (Al,Si,P,Cl, and K). Taken together, these data still do not tightly constrain the width parameters, but do provide estimations for thicknesses of the p^+ and SiO_2. Table 4.24 lists the parameter, the range of parameter space and grid sized used, and the derived best fit-value (90% confidence levels) from the simultaneous fitting.

	parameter space data		
parameter	search range	step size	best fit-value
box width	3.1-4.5 μm	0.16 μm	$4.2^{+.3}_{-.4}$ μm
wing width	0.12-1.2 μm	0.12 μm	$.35^{+.19}_{-.12}$ μm
Si thickness	0.12-1.2 μm	0.12 μm	$.35^{+.06}_{-.03}$ μm
SiO_2 thickness	0.12-1.2 μm	0.12 μm	$.71^{+.17}_{-.11}$ μm
Si_3N_4 thickness	0.0-0.05 μm	0.01 μm	insensitive

Table 4.24: Information from Simultaneous Fitting to all Five HEXS Data Sets

Unfortunately, the O Kα χ^2 contours do not overlap the the HEXS data χ^2 contours. Figure 4.53 shows the experimental data and the model with the best-fit values derived from combining all five HEXS measurements. The difference between the oxygen data and the model is quite severe, and no set of acceptable HEXS parameters yield a reasonable fit to the oxygen data. A number of possibilities have been explored to explain the discrepancy. The oxygen data was obtained with a different X-ray/vacuum system than the HEXS data and scattering may have been present. Scattering would have the effect of introducing a false background to the system and thus influence the measure of relative attenuation. The monochromator data also had a steep position dependent intensity gradient. In order to add the moiré cell data to produce the RP, a correction had to be applied to the raw data to normalize the flux across the CCD imaging area. This correction also could have introduced an error into the data.

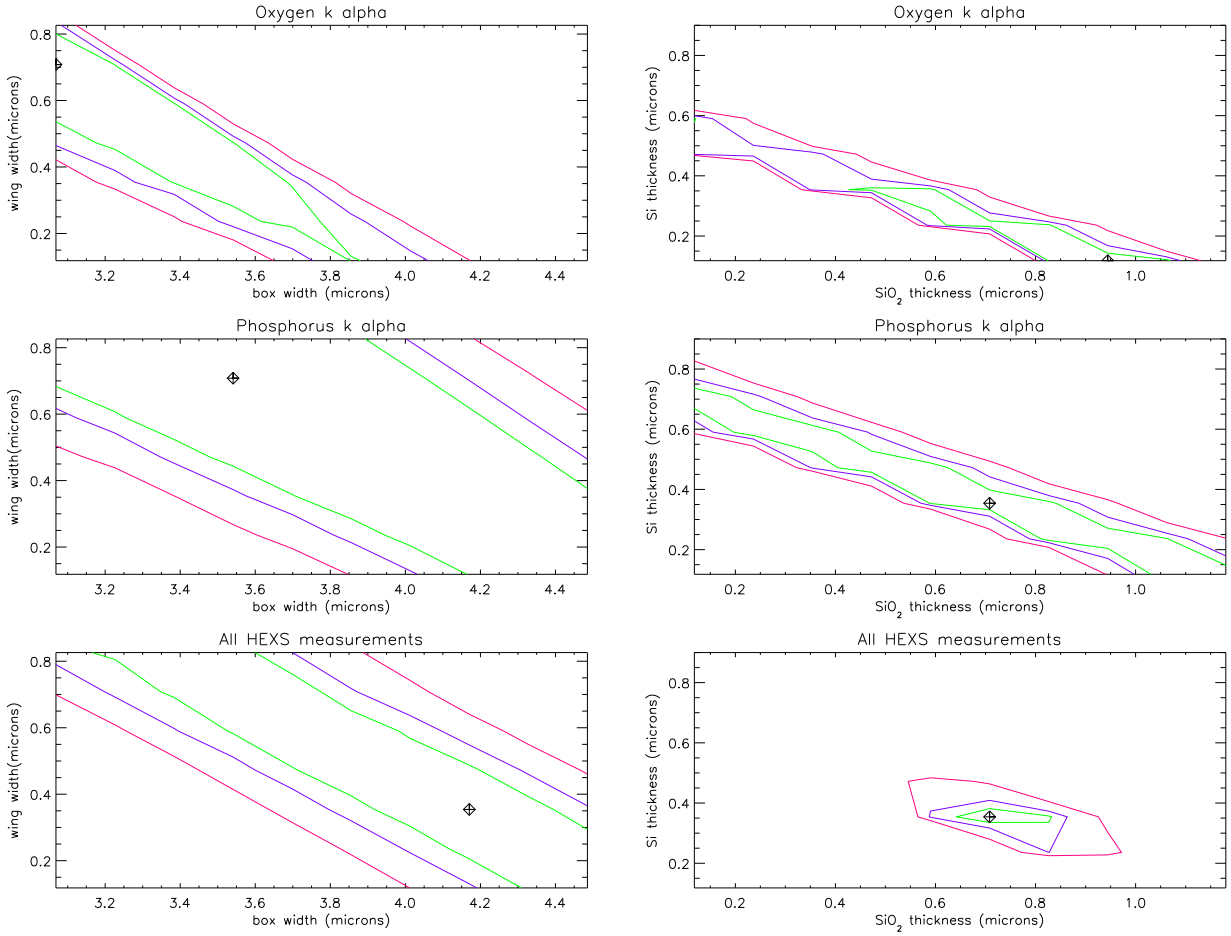

Figure 4.52: χ^2 contour plots for box width vs. wing width and Si p^+ depth vs. SiO_2 depth. Contours are the 68%, 90%, and 99% confidence levels.

In addition to the suspected problems with O Kα data, there is a disagreement between the best-fit parameters and other, independent measures of the channel stop dimensions. The manufacturers of the CCDs, MIT Lincoln Laboratories, reports that about one μm of p^+ dopant is implanted to make the channels, not 0.35 μm as determined by the mesh experiments. Many SEM measurements were performed on chips identical to the CCDs. These photos, exactly like Figure 4.46, show that the SiO_2 thickness is about 0.45 μm, not 0.70 μm. The same SEM studies, however, do show that the box and wing parameters obtained by the mesh studies agree with physical reality.

The discrepancy between the dimensions obtained from the experiments and those known

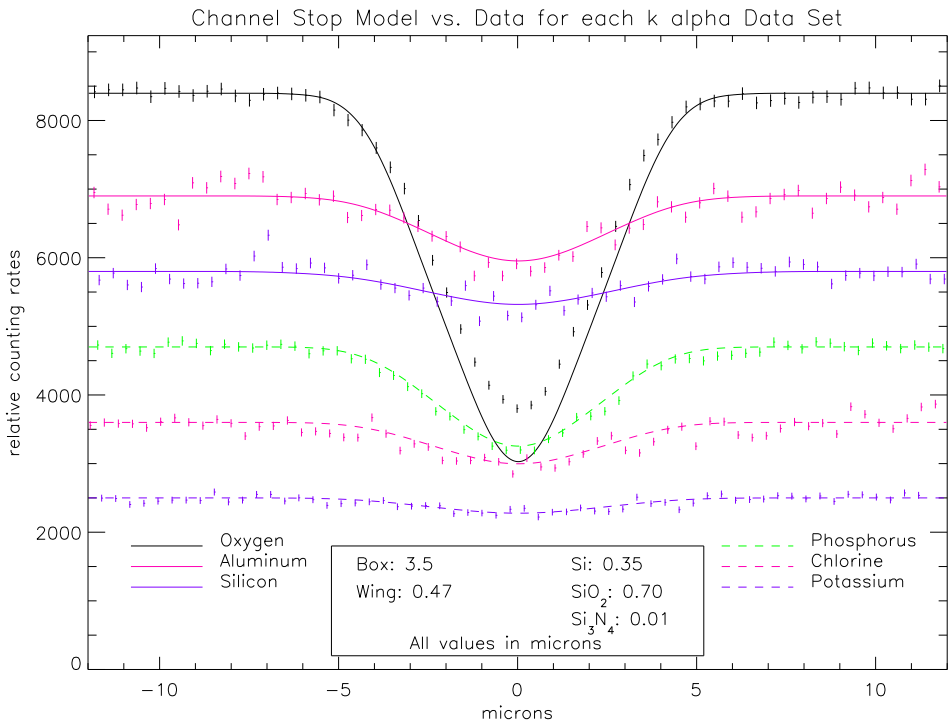

Figure 4.53: Best-fit HEXS channel stop model compared to experimental data.

either from the fabrication process or from direct measurement indicate flaws in the experimental technique or an incorrect model. As part of our attempt to understand our results, we have begun a series of new investigations that show great promise in explaining the inconsistencies. The key refinement to the experimental technique is the use of a mesh with square holes $\sim$1.4μm on a side. The smaller hole size allows the sub-pixel structure to be probed with significantly greater detail. Figure 4.54 shows g0 event pixel maps at O Kα (525 eV) made with the 4μm mesh and the new, 1.4μm mesh. The marked improvement in resolution offers the possibility of not only increasing the accuracy of the channel stop parameters, but also studying the small scale structures in the gates (i.e. gate overlaps). See Section 4.14 for the model predictions.

There also exists the distinct possibility that the Slab-and-Stop model is too simplistic and does not properly account for all the physical processes occurring inside the device. In fact, we have recently achieved a significant breakthrough in our understanding of the charge loss mechanism. We are currently exploring the details of these processes and will report on these results once our investigations are complete.

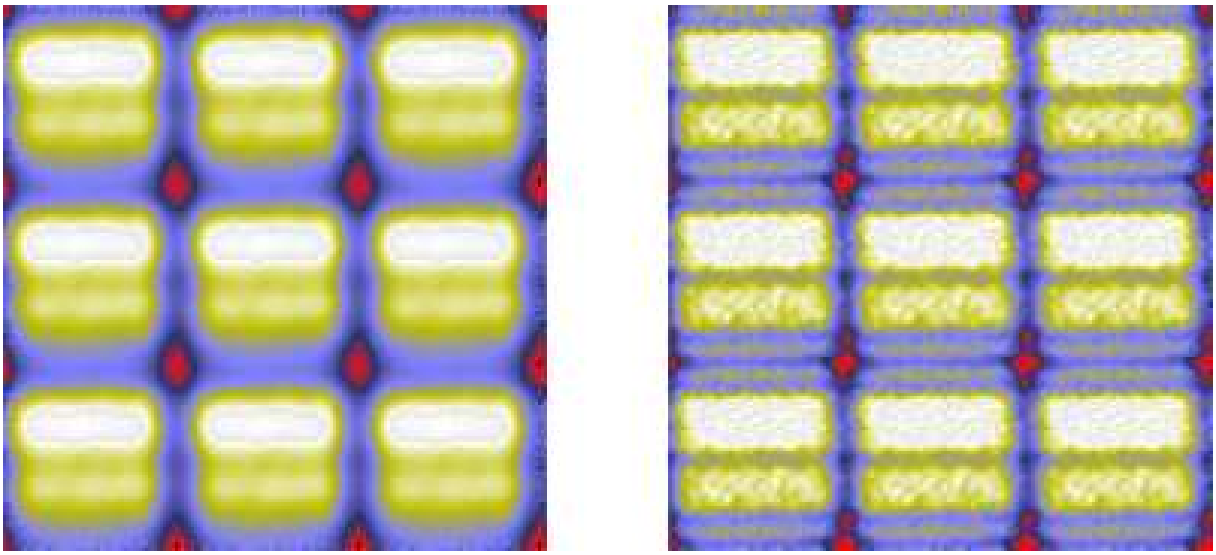

Figure 4.54: Intensity of grade 0 events at O Kα. **Left:** Results from the 4μm mesh. **Right:** Results from the 1.4μm mesh. Data has been smoothed with a boxcar function approximating the mesh aperture. The new mesh provides significant resolution of the sub-pixel structures.

4.5.4 Prospects for sub-pixel resolution

In addition to revealing the dimensions of sub-pixel structures, the mesh experiments also hint at the possibility of improving the spatial resolution of the CCD beyond that of a 24 μm pixel device. Before continuing, a short digression on event grades is necessary. The CCD registers an event when the charge cloud created by a photoelectric absorption is pulled into the potential of one of the gates. Some fraction of the time, the charge is divided into multiple pixels. Theoretically, this fraction, the branching ratio, depends on what depth in the silicon the interaction took place and where it occurs with respect to the pixel boundaries. According to this scheme, single pixel events (ASCA grade 0) come from photons that land in the center of the pixel, vertically split events (ASCA grade 2) come from photons that land near the vertical boundary of the two pixels, horizontally split events (ASCA grades 3 and 4) come from photons that land near the horizontal boundary of two pixels, and three and four pixel events (ASCA grade 6) come from photons that land in the corner of a pixel. The mesh experiments, for the first time, have conclusively proven that this simple picture is in fact correct. Figure 4.55 shows the 3×3 RP arrays from the O Kα data for grade 0, grade 2, grade 3 and 4, and grade 6 events. It is obvious that the horizontal and vertical split events come from the boundary regions and that the multiple pixel events come from the corner regions. At the same time, the single pixel RP events occur only in the center of the pixel.

The confinement of certain event grades to a specific area of the CCD is effectively like having smaller pixels inside a 24 μm pixel and is the key to obtaining sub-pixel resolution. The branching ratios are a strong function of energy and penetration of the photon into the device. As the percentage of multiple pixel events increase, these mini-pixels will increase in size. Figure 4.56 shows two 3×3 pixel grids. Both grids show a geometric area (computed from the branching ratios) for the different event grades discussed above, one for Si Kα photons (1.740 keV) and one for Cu Kα photons (8.040 keV). Superimposed on each of these grids are the 33% and 66% enclosed energy curves for the HRMA. A full, mathematical investigation has not been performed, but the hope is that by comparing the branching ratios from an astronomical observation with ground calibration data, the source location can be determined to better than one pixel.

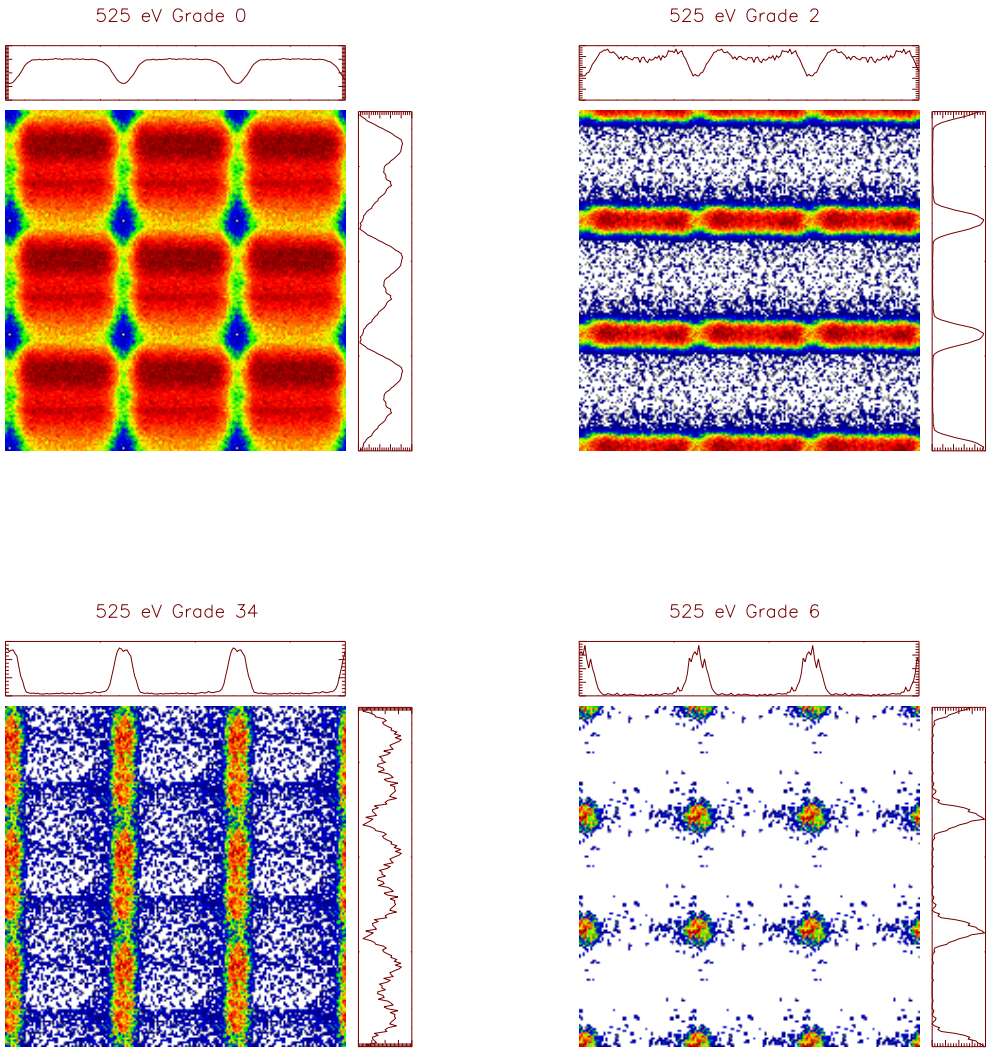

Figure 4.55: O Kα Representative Pixels for grade 0, grade 2, grades 3 and 4, and grade 6 events.

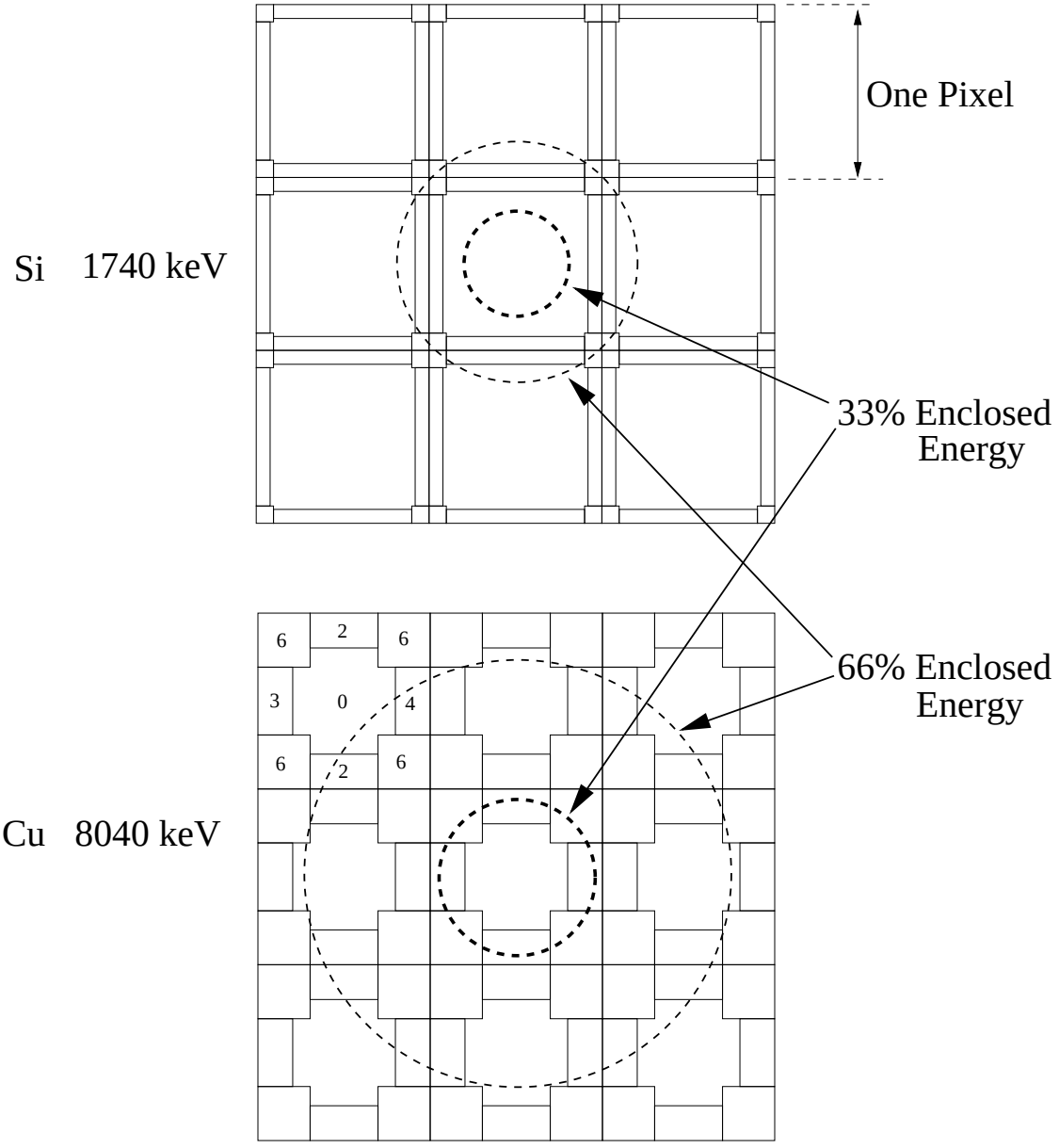

Figure 4.56: HRMA encircled energy surfaces projected onto a schematic of sub-pixel locations

4.6 Measurement of Absolute Quantum Detection Efficiency of Reference Detectors

4.6.1 Absolute Calibration of Reference Detectors with Undispersed Synchrotron Radiation

4.6.1.1 Methodology

The absolute calibration of the reference standards–detectors used for ACIS quantum efficiency measurements–was performed using the Physikalisch-Technische Bundesanstalt (PTB) laboratory in the BESSY electron storage ring. Undispersed synchrotron radiation was used as the primary flux standard. Using the `XSPEC` fitting routine, a response matrix, constrained by spectral response measurements at MIT, was convolved with the known incident spectrum. The CCD gate structure parameters were then adjusted to minimize the χ^2 measure of fit. The quality of the resulting quantum efficiency model hinges on the accuracy of our knowing the synchrotron radiation. The spectral flux can be calculated with relative errors below 1% from the physical geometry of the detector with respect to the orbital plane of the electrons and other storage ring parameters: electron energy, ring current and magnetic field of the bending magnets (Arnold and Ulm, 1992).

Figure 4.57 illustrates the experimental set-up at the PTB laboratory. A standard MIT vacuum chamber, modified to hold two CCDs simultaneously was mounted to the PTB beamline via a ceramic electro-isolator to eliminate electrical interference between the CCD electronics and the BESSY facility. A gate valve and turbo pump located between the CCDs and the storage ring allowed the chamber to be connected and pumped down to the requisite vacuum without compromising the integrity of the storage ring. The CCDs were operated at the nominal flight temperature of -120 C°.

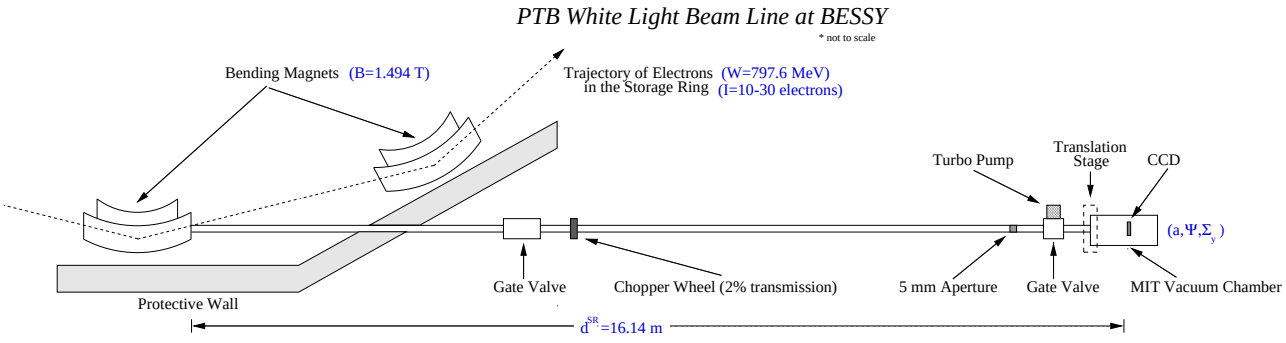

Figure 4.57: Sketch of the PTB laboratory

Even with just a single electron in the storage ring, the incident photon flux would

have caused significant pileup (defined as multiple photons landing in the same pixel or neighboring pixels during one integration time) in the CCDs and corrupted the absolute calibration. Two measures were taken to reduce the flux to an acceptable level. First, a chopper wheel with a 2.00% transmission cycle was inserted into the beam line to reduce the incident flux. Second, only 256 rows of the CCD were read out. This readout mode reduced the integration time by a factor of four. The storage ring was usually operated with currents between 10 and 30 electrons, although measurements with as few as 5 electrons and as many as 50 electrons were performed to determine pileup effects.

The process of reading out 256 rows of the CCD limited the amount of the detector that could be calibrated during one measurement. To ensure that all the incident photons would fall on an active area of the detector (a necessary requirement for the determination of absolute quantum efficiency) a five mm high aperture was placed in the beam line and carefully centered on the electron orbital plane. The five mm slit produced an illumination pattern 208 pixels tall, and the CCD columns were nominally aligned perpendicular to the orbital plane. A two dimensional translation stage was incorporated into the section of the PTB beamline that the MIT chamber mounted to. To calibrate an entire chip, the chamber was moved an appropriate distance in the y direction, a 256-row swath of the CCD was read out, and the image was visually inspected to check that all the photons hit the active area. This procedure was repeated four or five times to calibrate the entire chip. The chamber was then moved in the horizontal direction to illuminate a second CCD inside the chamber. By placing two chips inside the chamber, the overhead associated with thermally cycling the CCD, venting the chamber, switching CCDs, re-evacuating the chamber and finally cooling the CCDs was eliminated. This configuration allowed calibration of as many as four chips in a single 48 hour user shift.

Given a well located electron beam, the synchrotron radiation from a storage ring can be derived from Schwinger's equation (Riehle and Wende, 1986; Schwinger, 1949):

$$E(\lambda)^{SR} = E^{SR,\parallel}(\lambda) + E^{SR,\perp}(\lambda) = \frac{2e\rho^2 I}{3\varepsilon_0 \lambda^4 \gamma^4 a d^{SR}} \left\{ \int_{\psi_0-\psi'}^{\psi_0+\psi'} [1+(\gamma\psi)^2]^2 K_{\frac{2}{3}}^2(\xi) d\psi + \int_{\psi_0-\psi'}^{\psi_0+\psi'} [1+(\gamma\psi)^2]^2 (\gamma\psi)^2 K_{\frac{1}{3}}^2(\xi) d\psi \right\} \quad (4.25)$$

with

$$\gamma = \frac{W}{m_0 c^2}, \qquad \xi = \frac{2\pi}{3\gamma^3\lambda}[1+(\gamma\psi)^2]^{\frac{2}{3}}, \qquad \rho = \frac{W}{ecB}, \qquad \psi' = \frac{a}{2d^{SR}}$$

W, e and m_0 are the energy, charge and rest mass of the electrons and I is the current of the electrons in the storage ring. B is the magnetic induction of the bending magnets tangent to the observation point. a is the measure of the height of the beam, d^{SR} is the distance from the beam to the observation point, and ψ is the opening angle between the orbital plane and the observation point. c and ε_0 are fundamental constants, and K_x is the modified Bessel function, order x, of the the second kind. Thus, the spectral photon flux

can be expressed in terms of seven measurable quantities:

$$\Phi_E = \Phi_E(E; W, B, I, \Sigma_y, d^{SR}, a, \psi) \tag{4.26}$$

where Σ_y characterizes the vertical position and divergence of the electrons at the observation point and the other quantities are the same as above. W and B were measured once for each run, and I was monitored continually. Horizontal variation of Φ_E is less than 10^{-3} over the width of the CCD (Riehle and Wende, 1986). Due to its dependence on the opening angle ψ, Φ_E varies strongly as the observation point moves out of the orbital plane of the electrons. Figure 4.58 shows how the BESSY spectrum softens as the height above the orbital plane increases. The calculated Φ_E is for one electron in the storage ring with no chopper wheel. For typical integration times and ring currents, no flux above 4 keV was detected by the CCDs.

Similar measurements were also performed using the PTB Wavelength Shifter (WLS) beamline. Additional magnets are introduced into the normal storage ring configuration, thus boosting the energy of the electrons and shifting the energy of the synchrotron radiation. Figure 4.58 also shows how the WLS spectrum changes as a function of height above the orbital plane. Although the spectrum extends beyond 20 keV, the low high energy quantum efficiency of the devices limits the detection of photons to below 14 keV. The WLS experiments will be discussed in greater detail in Section 4.6.1.3.

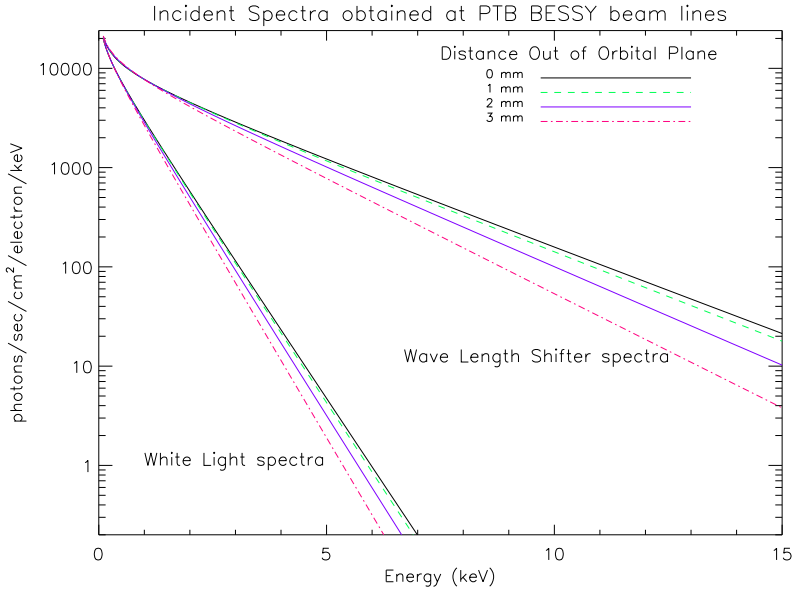

Figure 4.58: White Light and WLS BESSY spectra as a function of height above the orbital plane

4.6.1.2 Analysis

Before discussing how to reduce the BESSY data, we review the assumptions that go into generating the CCD response function. The spectral redistribution function (or matrix) contains all the information (e.g. gain, fluorescence and escape peak amplitudes, FWHM vs. energy) necessary to perform modeling of a pulseheight distribution. Refer to Section 4.1 for a full description of the relevant quantities and their determination. The tool that generates the redistribution matrix (hereafter RM) is `rspgen`, written by A. Rasmussen (Rasmussen, 1995b). `rspgen` uses a description of the CCD's response to monochromatic X-ray sources over a range of energies. Table 4.25 lists the options used to create RMs for the analysis of BESSY data.

When invoked, the unity command normalizes all redistribution function to unity at each energy. This is equivalent to assuming the branching ratios are not a function of energy. Although this is generally incorrect, by limiting the analysis to a specific energy range (0.3−4 keV) and to a particular subset of events (ASCA grades 0,2,3,4,6), the assumption is valid. The threshold values are matched to those used in the extraction of events from the CCD output. Although the same CCD/electronics combination was used for the BESSY calibration, the energy scale and noise conditions can vary slightly between the two measurements. The gain, offset, and broadening options account for the differences in the operating conditions and modifies the RM accordingly.

Option	Flag	Units	Remarks
unity	u	N/A	assumes unity branching ratios
split threshold	p	ADU	standard MIT values; depends on CCD electronics
event threshold	v	ADU	standard MIT values; depends on CCD electronics
grid spacing	E	keV	defines the energy grid that `rspgen` uses
gain	g	N/A	scales the ECD data
offset	o	ADU	offsets the ECD data
broadening	b	ADU	decreases or increases the ECD in quadrature
tailing	t	N/A	scales the low energy redistribution

Table 4.25: Summary of Adjustments to *rspgen* required for BESSY data

The purpose of the BESSY experiments is to obtain an absolute calibration for the reference detectors. This goal is achieved by multiplying a model of the CCD quantum efficiency with the RM, convolving the model response with the input spectrum, and comparing the results to the data. The parameters of the CCD QE model are adjusted to the find the best fit to the data. The current CCD model is the Slab and Stop Model synthesized by K. Gendreau (Gendreau, 1995). It approximates the gate structure as piecewise-uniform layers of Si, SiO_2, and Si_3N_4 and the channel stop as layers of Si and SiO_2 with finite width.

The final two CCD parameters are the width of the pixel and the depletion depth. The model assumes that the gate and channel stop are dead, and only those photons interacting in the depleted silicon will be detected.

Fitting the BESSY data with this model does not constrain all the parameters. The channel stops occupy a small area compared to the gate structure. This reduces the role of the channel stop parameters on the overall fit and leads to degeneracy in these three best-fit parameters[3]. Rather than determining these dimensions from BESSY data, we have measured the channel stops by other methods and frozen the parameters at these values. For the energy range of the White Light calibrations (E $<$ 4 keV), the quantum efficiency is mainly determined by the gate parameters and is insensitive to the depletion depth. Therefore, this parameter is also frozen at a value determined by another method (see Section 4.6.2 for details). Table 4.26 gives the parameters names, describes it and states whether or not it is fixed.

Parameter Name	Description	Status
Dead	Si gate thickness	free
SiOx	SiO_2 gate thickness	free
SiNit	Si_3N_4 gate thickness	free
Depl	Depletion depth	frozen–determined by branching ratio method†
CSWidth	Channel Stop width	frozen–determined by SEM measurements‡
CSSiOx	SiO_2 stop thickness	frozen–determined by SEM measurements‡
CSSi	Si p^+ thickness	frozen–determined by mesh experiments‡
Pix	Pixel width	frozen at 24 μm

†: see Section 4.6.2

‡: see Section 4.5

Table 4.26: CCD Model Parameters for BESSY absolute measurements

A total of eleven devices were characterized at BESSY during six separate 48 hour shifts[4]. Table 4.27 shows when each CCD was calibrated, how many data sets were taken, and the number of CCD positions illuminated. A typical measurement consisted of acquiring 2000 frames. Integration times ranged from 0.83−1.53 seconds, depending on which readout electronics were used. Storage ring currents ranged from 2 to 50 electrons, but typically the ring current was adjusted to either 10 or 20 electrons (again, this depended on readout electronics) in order to provide 350 counts/frame/quadrant. For a typical measurement, this yields on order of 3×10^6 counts in the 0.3−4.0 keV band over the illuminated part of the CCD.

[3]Equally good χ^2 values can be achieved for a range of channel stops widths and thicknesses. The gate thicknesses and overall normalizations change with the values of the channel stop parameters used.

[4]The last measurement were done on Wavelength Shifter beamline.

Reduction of the data begins by extracting events from the raw data and saving the location, pulse-height value, and frame number of each event in an event list. The storage ring current is monitored by the BESSY facility, and this data stream is searched for the loss of electrons from the storage ring during our measurements. If such a loss occurred, the event list is temporal filtered. Pileup effects are very dependent on the initial flux rate, and limiting the data to a single ring current allows the most accurate correction. Finally, the event list is further filtered by event grade selection and a `XSPEC` compatible PHA file is produced. At this time, the data from an entire quadrant is averaged together in a 5mm $\times$ 6mm spatial bin.

Chip	**Date**	**Data Sets**	**Chip Positions**	**Electronics**
w34c3	Mar 95	7	4	acis 3
w34c3	Apr 95	17	4	acis 3
w34c3	May 95	6	5	acis 6
w34c3	Aug 95	3	1	acis 3
w103c1	Mar 95	7	4	acis 3
w102c3	May 95	6	5	acis 6
w103c2	May 95	5	5	acis 6
w103c4	May 95	6	5	acis 6
w103c4	Aug 95	5	5	acis 3
w147c3 (BI)	Aug 95	15	5	acis 3
w148c4 (BI)‡	Aug 95	6	5	acis 3
w190c1	Jun 96	10	5	dea-sn014
w190c1	Dec 96†	6	5	dea-sn017
w190c3	Jun 96	10	5	dea-sn014
w168c2	Dec 96†	5	5	dea-sn017
w203c2	Dec 96†	19	5	dea-sn017

†: Wavelength Shifter Measurement
‡: ACIS-2C device

Table 4.27: Summary of synchrotron measurements made with PTB beamlines at BESSY.

The `rspgen`-generated RM, an "atable" model of the incident synchrotron radiation spectrum, the CCD model, and the PHA file are loaded into `XSPEC`. The atable model (*/usr/acis/atable/bessy_new.mod*) has two parameters, an overall normalization factor and another parameter that exists for historical reasons but is no longer used. The data is rebinned, the energy range limited to 0.3-4.0 keV and the model parameters are left free or frozen according to Table 4.26. If pileup is significant, two techniques are available to correct the data. One method developed by A. Rasmussen utilizes a mtable model that is

compatable with `XSPEC`. This empirical model simulates the effects of pileup from BESSY data and relies on the incident flux levels being sufficiently low (Rasmussen, 1995a). It has one phenomenological parameter that corresponds to the incident flux rate. `XSPEC` then fits for gate thicknesses, the source normalization and the pileup parameter. The other method developed by S. Jones (see Section 4.4) utilizes extensive laboratory data from incident flux–count rate linearity studies. The pulse-height spectrum is directly corrected, and this corrected PHA file is then read directly into `XSPEC`.

Figure 4.59, Figure 4.60, and Figure 4.61 show the best fit models with the data for individual quadrants of detectors w190c3, w190c1, and w103c4. The RMs used for the fit can be found in:

/ohno/d9/mjp/BESSY/XSPEC/w190c3/t0852/c1.rsp
/ohno/d9/mjp/BESSY/XSPEC/w190c1/t2347/tmp_memo.rsp
/ohno/d9/mjp/BESSY/XSPEC/w103c4/t1414/tmp_c1.rsp

Pileup corrections have been applied to the data for all three devices. The Rasmussen method was used for devices w190c1 and w190c3, while the Jones method was used for w103c4. To check the consistency of each method, w190c3 was also corrected using the Jones method. Normalization values from the two techniques differed by $\sim 0.1\%$, indicating excellent agreement between the two correction methods. Table 4.28 shows the best-fit parameters, the RMS error, and the normalization accuracy for each reference detector as well as listing the values of the frozen parameters.

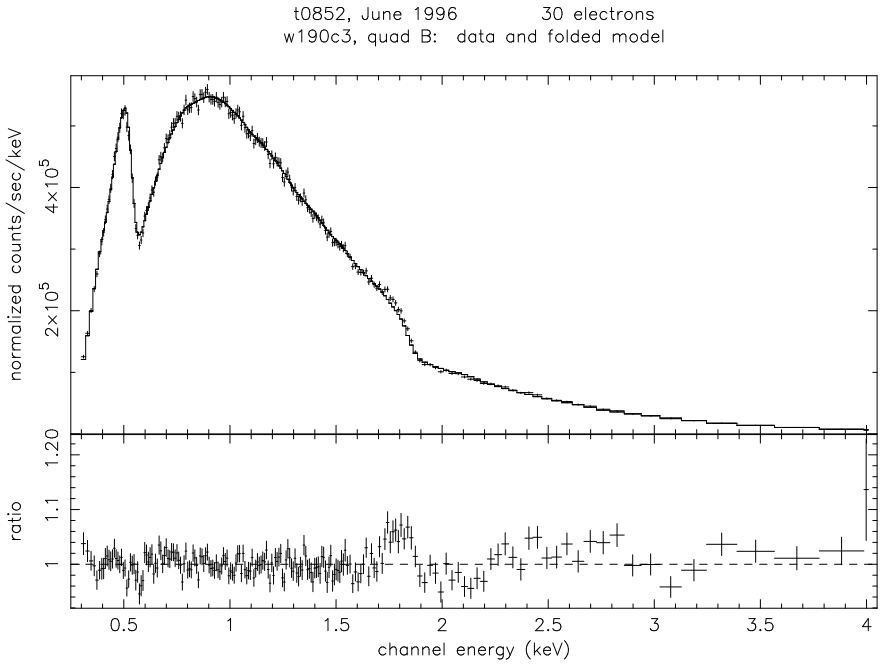

Figure 4.59: w190c3, quad B: BESSY data vs. model

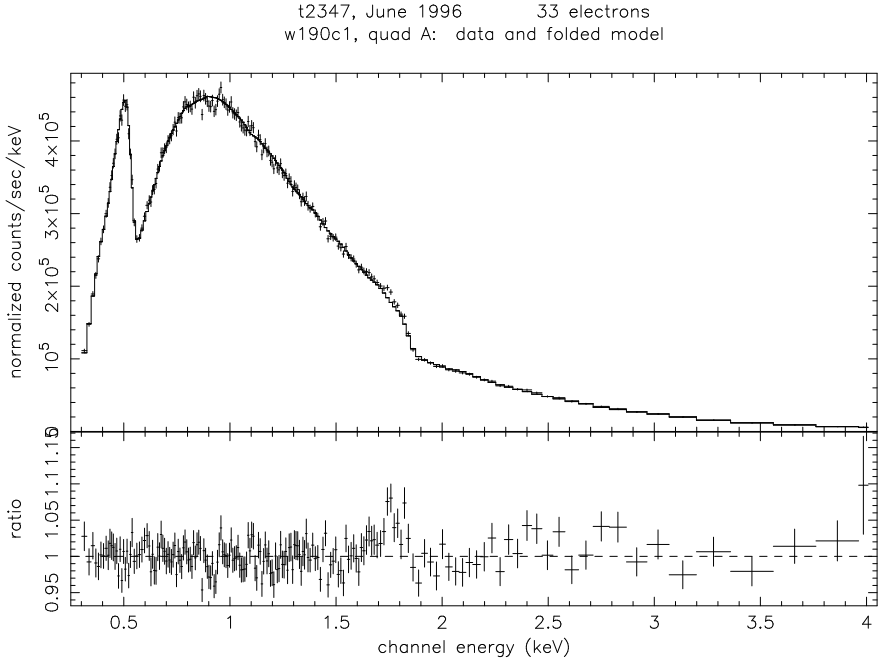

Figure 4.60: w190c1,quad A: BESSY data vs. model

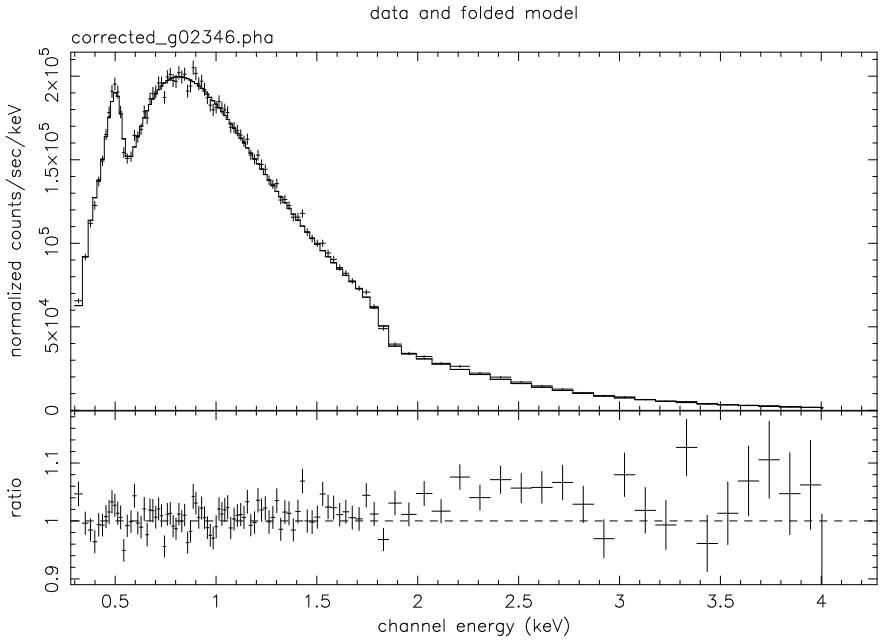

Figure 4.61: w103c4, quad B: BESSY data vs. model

	CCD Parameters (in μm)							(0.3-4 keV) RMS	
	Free			Fixed					
Chip	Si†	SiO_2‡	Si_3N_4	CS Si	CS SiO_2	CS Width	Depletion Depth	Deviation of Fit	Best Fit Normalization
w190c3	0.259	0.354	0.031	0.35	0.45	4.1	71.3	2.54%	$1.000 \pm .003$
w190c1	0.261	0.358	0.029	0.35	0.45	4.1	70.6	2.24%	$0.994 \pm .003$
w103c4	0.291	0.202	0.030	0.35	0.45	4.1	57.9	3.88%	$0.956 \pm .003$

†: typical 90% confidence error is ± 0.008 μm

‡: typical 90% confidence error is ± 0.011 μm

Table 4.28: CCD model parameter fit results from synchrotron radiation measurements

As a whole, the model fits for detectors w190c1 and w190c3 are quite good. In both cases the data:model ratio shows two deviation from unity: a narrow feature around 1.8 keV and a systematic underestimation of the flux above 2.2 keV. An underestimation of the Si Kα fluorescence could help contribute to the narrow feature. Analysis of the response function data indicates that the fluorescence yields in the current response matrices are too low (see Section 4.14). Another probable source of error is the use of the Henke optical constants. Our EXAFS measurements (see Section 4.6.4) show large deviations from the tabulated Henke values around both the O Kα and Si Kα absorption edges. In the future we will incorporate these optical constant measurements in our model. The excess above 2.2 keV results from the good, but not exact, correction for pileup. The best-fit normalizations are within 1% of the calculated value, but could change with an improved pileup algorithm and inclusion of more accurate fluorescence data. Another measure of the goodness of fit for these two devices is the comparison of the derived gate thicknesses. w190c1 and w190c3 came from the same wafer, and hence, underwent the exact same fabrication process. The differences between the derived thickness for the Si, SiO_2, and Si_3N_4 layers are well within the errors.

The fit for reference detector w103c4 is noticeably worse than the other two devices. The RMS error is higher, and the best-fit normalization is nearly 6% too low. Above 2 keV, the model underestimates the data by almost 10%. The deviation from unity illustrates the importance of correcting the data for pileup. At the same time, however, the best-fit values for the three gate layers are reliable. Studies with devices w190c1 and w190c3 indicate that neglecting pileup influences the RMS error and normalization but has only small effects on the best-fit gate thicknesses. This behavior is consistent with the low level pileup model discussed in Section 4.4. To first order, pileup shifts events out of the acceptable grades (this explains the low best-fit normalization) and deposits some small fraction of these events' charge into non-physical, higher energy events (this accounts for the excess of counts above 2 keV).

Extensive measurements at MIT CSR have shown that the QE of front-illuminated

CCDs have little spatial variation over bin sizes of 0.77 mm^2. Because the intensity and shape of the BESSY spectrum changes over the illumination pattern, similar measures of fine spatial uniformity are non-trivial. Our current spectral fitting procedure is to integrate all the data into 5mm × 6mm spatial bins. Table 4.29 shows the average counting rate (cts/sec/e^- ring current) normalized to the y001 position for each quadrant of w103c4 at five different CCD positions. Data is from the August 95 shift. The counting rates for y768 are expected to be higher than those for any other quadrants since the beam current was lower for this measurement and pileup effects should be smaller. Statistical errors for the data sets are less than 0.002. Finally, on average there is one bad column per quadrant that does not extend the length of the CCD. This analysis does not account for the reduction of the active area caused by the bad column, and this introduces an uncertainty on order of 0.004 to the ratios.

CCD Position	Ring Current	Quad A	Quad B	Quad C	Quad D
y001	19 e^-	1.0000	1.0000	1.0000	1.0000
y209	19 e^-	1.0069	1.0087	1.0056	1.0049
y417	19 e^-	1.0069	1.0062	1.0080	1.0025
y625	19 e^-	1.0031	1.0050	1.0043	0.99938
y768	18 e^-	1.0056	1.0019	1.0025	1.0012

Table 4.29: Average counting rate (cts/sec/e^- ring current) for w103c4 normalized to CCD position y001. Statistical errors for all measurements are below .002. No pileup corrections have been applied.

A final check of the BESSY data is a comparison of the relative quantum efficiency measurements made at MIT CSR. Reference standards w190c3 and w103c4 were calibrated with respect to one another at discrete energies using the HEXS (see Section 4.7.1 for details). The model fitting to the BESSY data yields absolute efficiencies for both devices. Dividing these continuous curves by one another provides an independent check of both the MIT CSR measurements and the quality of the CCD model. The upper panel of Figure 4.62 shows the absolute quantum efficiencies determined from the synchrotron data. The higher efficiency of w103c4 is easily understood as it has a thinner gate oxide layer than w190c3. The bottom panel of Figure 4.62 shows the discrete relative measurements made at MIT CSR *vs.* the continuous BESSY-derived relative quantum efficiencies. The errors associated with the MIT CSR values are systematic and currently estimated at 2%[5].

[5]Statistical errors for these data are negligible.

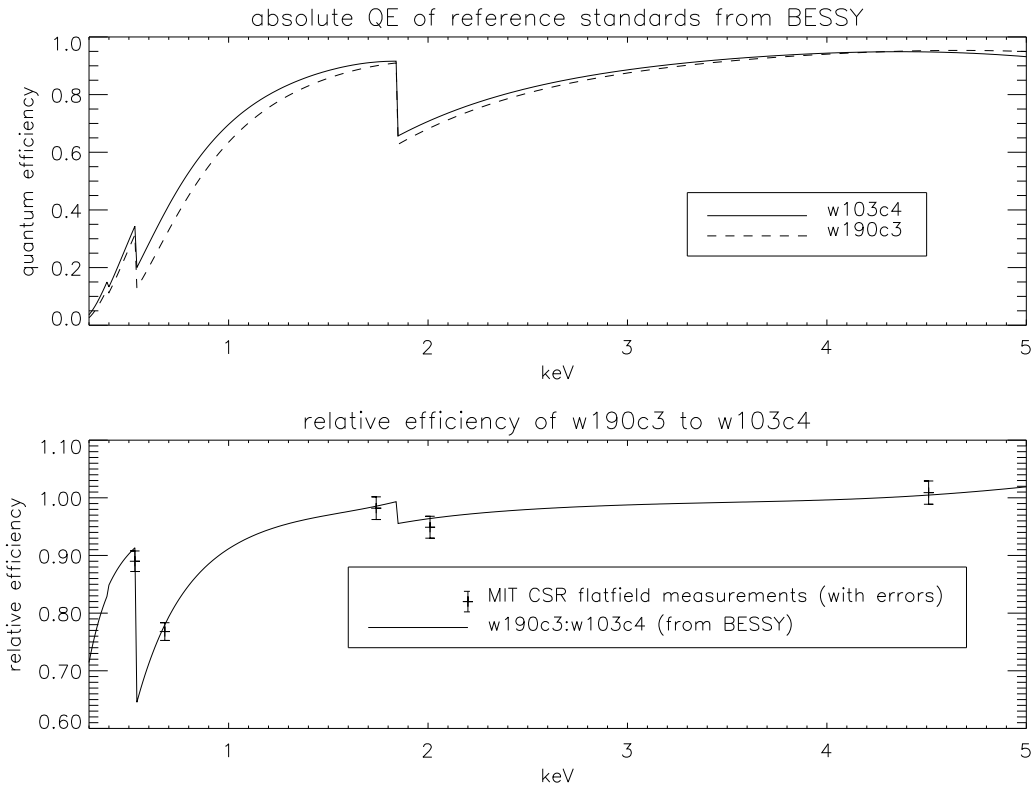

Figure 4.62: BESSY absolute efficiencies vs. MIT CSR relative efficiencies for reference detectors w190c3 and w103c4.

4.6.1.3 Preliminary Assessment of Wavelength Shifter Data

The measurements made during the December 96 user shift were performed with the PTB Wavelength Shifter (WLS) beamline. With the incident radiation going well beyond 15 keV, it was hoped the measurements would extend the absolute calibration of the reference standards up to the high energy limit of the AXAF observatory. Another goal of this measurement was to provide an independent determination of the depletion depths. Unlike the White Light beamline which can only constrain the low energy quantum efficiency dominated by the gate thicknesses, the harder spectra of the WLS beamline produces photons that easily transverse the length of depleted silicon–the requisite condition to accurately model the high energy quantum efficiency and the depletion depth.

Initial analysis of the WLS data reveals two potential problems with the quality of the data. Reduced data products indicate that the electronics were performing sub-optimally during half of the measurements. The problems can be simply characterized as a spatial and temporal variation in the bias levels (Pivovaroff, 1997b). Techniques do exist to correct for such effects, but it is unclear how well they will work. It was known that the WLS would produce many more photons than the White Light beam for a given ring current.

Anticipating problems with pileup, the storage ring currents were reduced from typical White Light operating conditions by at least a factor of two. Unfortunately, the extent that pileup influences high energy spectra has only recently been fully appreciated. Given the way the BESSY data was collected, it is quite possible that the data may prove difficult to accurately correct for pileup [6]. Initial `XSPEC` fitting indicate that pileup is much more severe than for the White Light data.

4.6.2 High-Energy Quantum Efficiency from Grade Branching Ratios

4.6.2.1 Introduction

In a number of ACIS memos issued by K. Gendreau and G. Prigozhin some years ago numerous techniques were suggested for determining a depletion depth of a CCD. All of the suggested techniques were very complicated and not too accurate. Described here is the most simple, efficient and stable technique. It is not sensitive to the way the events are counted (for example, reasonably small changes in thresholds do not affect the result), does not require any assumptions about the potential profile, and, probably, the most important, depletion depth can be extracted from just one dataset of Fe^{55} data (no need to step through the range of voltages, for instance).

4.6.2.2 Description of the technique

This technique makes use of the following idea. Let us assume that CCD is illuminated with a monochromatic source of X-ray photons whose characteristic absorption length λ is smaller than, but comparable to the depletion depth. If an interaction of the photon with Si occurres in the depleted region of the CCD, the created electron cloud will be drawn into the potential wells by the electric field and all the charge will be collected (see Fig. 4.63).

Depending on where relative to pixel boundaries the photon landed the resulting event can be either a single-pixel or a split one (can be either horizontally or vertically split, or grade 6), but the sum of the amplitudes of the pixels containing a signal charge should account for all the charge generated by the photon, and, hence, be part of the main peak in the response histogram. On the other hand, if an interaction occurred in an undepleted bulk of the semiconductor, the charge cloud diffuses more or less uniformly in all directions. Part of the cloud drifting towards the back side of the device will be lost. Electrons moving towards the front surface enter the depletion region and being pulled by an electric field end up in the potential wells of the CCD. Due to initial diffusion of charge the registered event in this case is a widespread multipixel cloud. According to the ASCA grading scheme this is a grade 7 event and, since part of the initial charge is lost to the backside junction,

[6] The beating of the chopper wheel with the readout time of the CCDs leads to different pileup conditions for some fraction of the data (Pivovaroff, 1997a).

the amplitude is lower than the peak energy even if all the pixels of the event are summed together.

If we denote N_d the number of interactions in the depleted region and N_{und} the number of events in the undepleted bulk, then, due to exponential distribution of the of the number of interacting photons as as a function of depth, a simple equation holds (see Fig. 4.64 for a better understanding):

$$N_{und} = (N_d + N_{und}) \exp(-\frac{d_d}{\lambda}) \tag{4.27}$$

where d_d is the depletion depth of the device.

This implies the following algorithm of the depletion depth calculation.

1. Sum the the intensities of the grades 0,1,2,3,4,6 and determine what is the number of events N_d in the main peak. Find the peak center E_c and width σ, and then count how many events are within the $\pm 3\sigma$ interval from the peak center.
2. Count what is the total number of events N_{und} in the grade 7 below $E_c - 3\sigma$.
3. Calculate the depletion depth d_d according to the formula derived from (4.27):

$$d_d = \lambda \ln(\frac{N_d}{N_{und}} + 1) \tag{4.28}$$

The logarithmic function in the above equation makes the result very insensitive to small changes in both N_d and N_{und} caused by statistical uncertainties or, say, choosing different set of grades for the peak counts calculation. At the same time, small changes of the depletion depth cause changes in the N_d and N_{und} to go in the opposite directions (because the sum $N_d + N_{und} = const$, see Fig. 4.64), thus amplifying the change in the result.

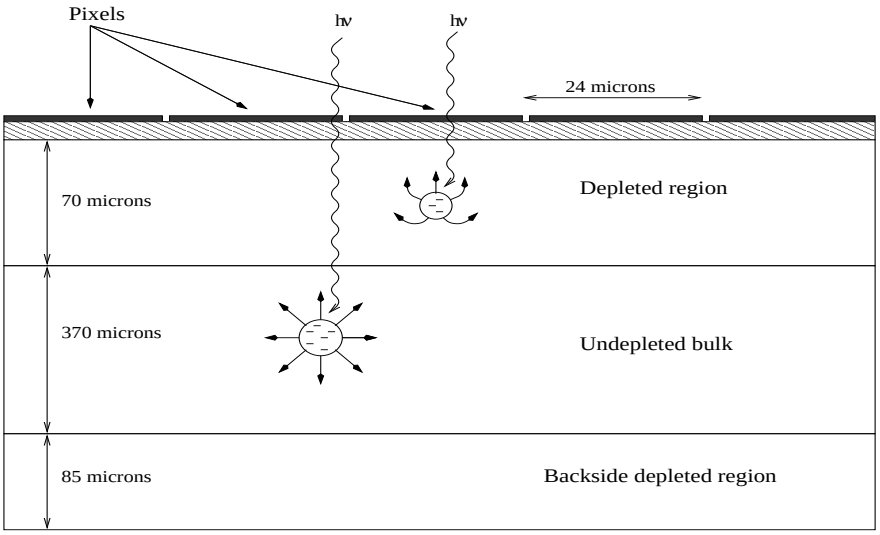

Figure 4.63: Schematic of the CCD depleted layers.

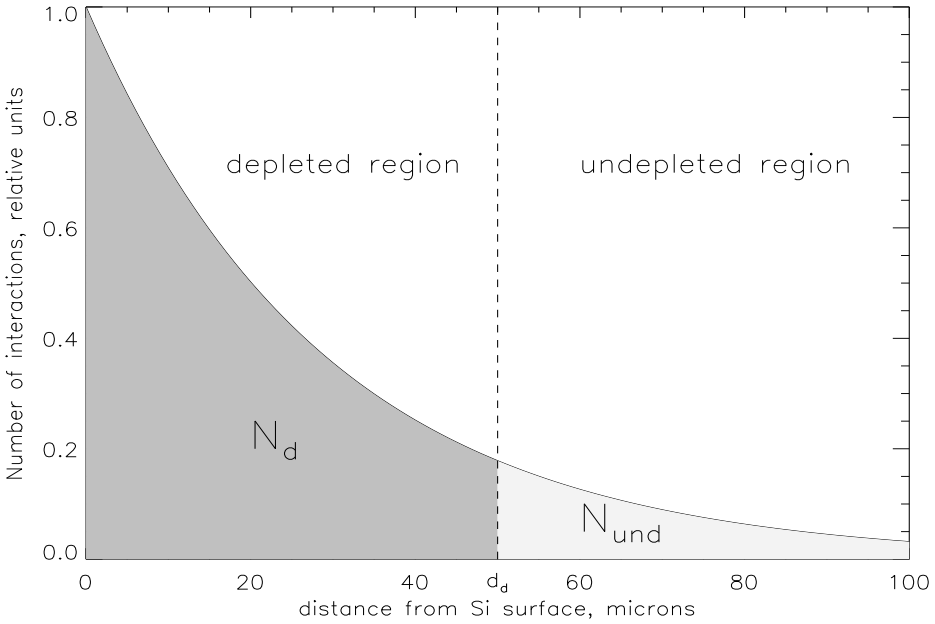

Figure 4.64: Exponential distribution of the number of interacting photons as a function of distance from the surface.

Sharp sensitivity of the result to the changes of the depletion depth has been confirmed by experiment where the gate voltage was stepped from 0 to +10 Volts.

4.6.2.3 A typical example and possible sources of errors

a. Statistical errors

Here is an exemplary calculation of depletion depth for the ACIS flight device $w193c2$. The dataset */ohno/di/database/w193c2/butthead/fe55/30nov96/1713/* represents 416 frames of Fe^{55} X-rays taken in Butthead at -120^o C with standard imaging array voltages of +1 and +11 Volts. The average count rate is 1110 $counts/sector/frame$. The calculation is made for the chip sector 2.

In Fig. 4.65 is shown a standard set of histograms of different grades. The number of counts in the K_α peak of combined grades 0 1 2 3 4 6 histogram within the $\pm 3\sigma$ interval is 355719 ± 596 (an error is calculated as a square root of number of counts). The number of counts in grade 7 histogram below $E_c - 3\sigma$ is 33092 ± 182 (again assuming an error being the square root although, strictly speaking, it may not be the right estimate because this is not the gaussian distribution). This results in the depletion depth of 70.9 microns. Assuming the worst case of statistical errors going in the opposite directions we get the limits for d_d from 70.69 to 71.07 microns, which means that the statistical accuracy for the standard dataset is better than 0.3%.

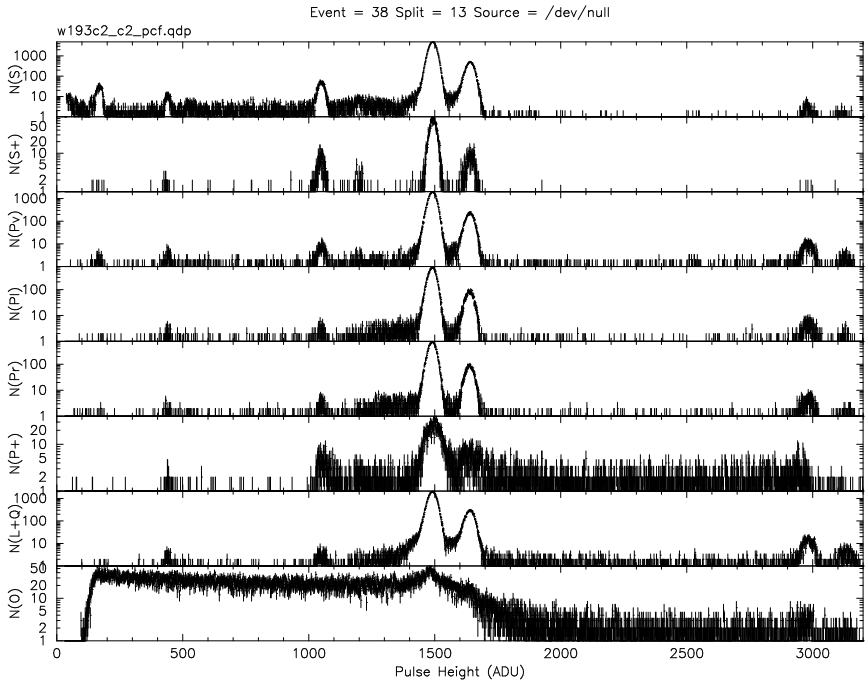

Figure 4.65: Histograms of different grades for Fe^{55} X-rays. Eight panels (from top to bottom) correspond to ASCA grades 0 through 7.

b. K_β line induced error

There is a source of systematic error associated with the nonmonochromatic nature of the Fe^{55} radioactive source. Presence of the K_β line in the spectrum leads to underestimation of the depletion depth because the characteristic absorption length at 6.4 keV ($\lambda_\beta = 38.0$ microns) is bigger than at 5.89 keV ($\lambda_\alpha = 28.77$ microns) and, hence, K_β line produces a larger share of events in the undepleted bulk. To calculate the error introduced by the K_β line let us rewrite equation (4.27) separately for both lines:

$$N_{und\alpha} = (N_{d\alpha} + N_{und\alpha}) \exp(-\frac{d_d}{\lambda_\alpha}) \tag{4.29}$$

$$N_{und\beta} = (N_{d\beta} + N_{und\beta}) \exp(-\frac{d_d}{\lambda_\beta}) \tag{4.30}$$

Quantities $N_{d\alpha}$ and $N_{d\beta}$ can be determined from the experimental data as the number of counts in each of the corresponding peaks, whereas $N_{und\alpha}$ and $N_{und\beta}$ cannot be separated. But, since the sum $N_{und\alpha} + N_{und\beta}$ is known (it is number of counts in the grade 7 tail), equations (4.29) and (4.30) can be solved numerically after transforming them into the following:

$$\frac{N_{d\alpha}}{\exp(\frac{d_d}{\lambda_\alpha}) - 1} + \frac{N_{d\beta}}{\exp(\frac{d_d}{\lambda_\beta}) - 1} - (N_{und\alpha} + N_{und\beta}) = 0 \tag{4.31}$$

The Newton-Rafson method was implemented to solve (4.31). For the above example (number of counts in the K_β peak equals 45709) the corrected solution gives $d_d = 73.8$ microns, or, 4% increase of d_d.

c. Pileup

One other source of error can be pileup. It throws events out of the main peak into events with higher amplitude. The most simple first order correction would be to assume that all the events in the pileup peak (located at the energy $2E_c$) originates from two main peak photons landed on the top of each other, and that the "high energy tail" of grade 7 distribution (events to the right from the K_β peak) comes from one main peak photon and one grade 7 event piled up together. After adding the corresponding number of counts to the main peak and to the grade 7, the corrected depletion depth (using formula (4.28)) becomes 69.64 microns.

d. Interactions beyond detection limit

Some photons interact so deep in the bulk of silicon that the portion of charge collected in one pixel is too small to be detected. An event will not be registered by the data analysis software if the charge in each pixel falls below the event threshold. To determine the distance from the depletion region border beyond which the charge will stay undetected. S. Jones' code was used to implement the solution of diffusion equation as described in the Hopkinson's paper (Hopkinson, 1987). The solid line on Fig. 4.66 shows charge collected in the pixel for 5.89 keV photon stopped in the field free region as a function of distance from the cloud center to the depletion region boundary. A dotted line in the plot shows the same thing calculated on the simple assumption that charge diffuses uniformly in all directions. This approach is attractive since the result can be expressed by a single analytical formula. In this case charge Q_{pix} collected in one pixel is proportional to the solid angle under which the pixel is seen from the center of the cloud. Solving the stereometry quiz in the case of cloud center located at the pixel center line results in the following:

$$Q_{pix} = \frac{Q_{tot}}{4\pi}(8 \arcsin \sqrt{\frac{2{d_c}^2 + a^2}{4{d_c}^2 + a^2}} - 2\pi) \tag{4.32}$$

where a is a pixel size, d_c is the distance from the center of the charge cloud to the depletion region border, Q_{tot} is total electron charge created by the photon. As expected, both curves in Fig. 4.66 converge at large distances, when the influence of the boundary becomes negligible. At small d_c simplified approach results in the collected charge approximately factor of 2 smaller than the full solution, which also makes sense. In the middle range of distances smaller than 140 microns, though, the difference is surprisingly big to justify the use of the simple approach.

For the data analyzed above the event threshold is 38 ADU, or, multiplied by gain, 35 electrons. From the above plot (solid line) one can determine critical distance $d_c = 59$ microns beyond which a photon is not detected. It means that 1.1% of all the events stay undetected (the ones that are deeper than $70.9 + 59$ microns from surface) instead of being

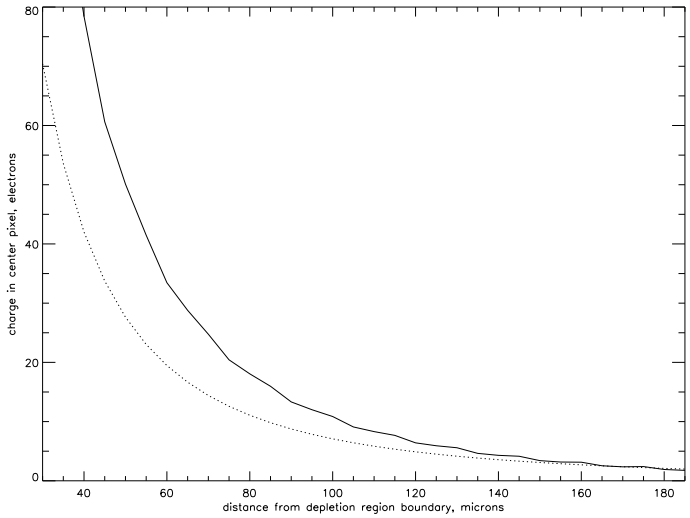

Figure 4.66: Charge collected in the center pixel from the Fe^{55} photon landing in the neutral bulk as a function of distance from depletion region boundary.

counted as grade 7 events.

In order to calculate the correction for the depletion depth introduced by the undetected photons the equation (4.27) should be modified into

$$N_{und} + N_{lost} = (N_d + N_{und} + N_{lost}) \exp(-\frac{d_d}{\lambda}) \tag{4.33}$$

and supplemented by a similar equation for the region beyond the depletion boundary:

$$N_{lost} = (N_{und} + N_{lost}) \exp(-\frac{d_c}{\lambda}) \tag{4.34}$$

where we introduced N_{lost} – number of interactions beyond the detection border located at the distance $d_d + d_c$ from the silicon surface.

These two equations can be converted into the corrected formula for the depletion depth

$$d_d = \lambda \ln(\frac{N_d}{N_{und}(\frac{1}{1-\exp(-\frac{d_c}{\lambda})})} + 1) \tag{4.35}$$

For the above analyzed example the corrected depletion depth according to (4.35) is 67.3 microns, which constitutes a 5% correction. It is clear from this analysis that reducing the event threshold will significantly improve the accuracy of the original formula (4.28).

e. Simultaneous correction for both K_β and undetected photons

It is possible to apply the formalism developed above to describe simulteneously both mechanisms that distort the result of the measurement. In order to do that, equations

(4.33) and (4.34) have to be written separately for the K_α and K_β lines. Notice that the critical distance d_c from the depleted layer boundary is different at different energies and we need to use two parameters $d_{c\alpha}$ and $d_{c\beta}$ instead. Combining the following four equations together:

$$N_{und\alpha} + N_{lost\alpha} = (N_{d\alpha} + N_{und\alpha} + N_{lost\alpha}) \exp(-\frac{d_d}{\lambda_\alpha}) \quad (4.36)$$

$$N_{lost\alpha} = (N_{und\alpha} + N_{lost\alpha}) \exp(-\frac{d_{c\alpha}}{\lambda_\alpha}) \quad (4.37)$$

$$N_{und\beta} + N_{lost\beta} = (N_{d\beta} + N_{und\beta} + N_{lost\beta}) \exp(-\frac{d_d}{\lambda_\beta}) \quad (4.38)$$

$$N_{lost\beta} = (N_{und\beta} + N_{lost\beta}) \exp(-\frac{d_{c\beta}}{\lambda_\beta}) \quad (4.39)$$

one can arrive to the equation somewhat similar to (4.31):

$$N_{d\alpha} \frac{1 - \exp(-\frac{d_{c\alpha}}{\lambda_\alpha})}{\exp(\frac{d_d}{\lambda_\alpha}) - 1} + N_{d\beta} \frac{1 - \exp(-\frac{d_{c\beta}}{\lambda_\beta})}{\exp(\frac{d_d}{\lambda_\beta}) - 1} - (N_{und\alpha} + N_{und\beta}) = 0 \quad (4.40)$$

The C program *~gyp/het/dep_Kbeta_corrected* implements the Newton-Rafson method to solve (4.40) numerically for d_d when other parameters are known.

f. Summary of error estimates

The conclusion is that statistical errors for the depletion depth determination using standard set of Fe^{55} frames are negligible (less than 0.3%). The biggest sources of systematic errors are K_β line photons and photons interacting deep in the bulk of the silicon. Corrections from those two factors go in the opposite directions and tend to compensate each other because the K_β photons increase number of events counted as grade 7, whereas undetected ones diminish this number. For the analyzed example they almost entirely cancelled each other, although, undetected photons seem to pull d_d down a little stronger. As a result, a calculation made with the simple formula (4.28) seems to overestimate depletion depth by about 2% due to pileup and the detection limit. To get a more accurate result a very detailed modeling is necessary.

4.6.2.4 Results for the flight devices.

The technique described above was applied to all frontside illuminated flight devices. Depletion depths were extracted from the Fe^{55} data sets taken at the HIREFS spectrometer chamber. These data have lower flux rate than other chambers, and, hence, very low level of pileup. The computation of the depletion depth included correction for the presence of the K_β line in the source spectrum as well as correction for the undetected photons according to equation (4.40). No pileup correction was made because the level of pileup in these data is low. Results are summarized in Table 4.30.

For standard image section voltages (+2,+10 Volts) every measurement was made at three different temperatures, namely, -130, -120, and -110 degrees C. Since depletion depths should not depend on temperature (at least in the narrow temperature range), for every quadrant of every chip the results were averaged over three measurements. Typical standard deviation of the result is 0.35 microns. As can be seen in Table 4.30, some of the chips show quadrant-to-quadrant variations of the depletion depth on the order of 1.5 microns. Such variations exceed statistical error and, most likely, are real and caused by nonuniformity of the substrate resistivity. They translate into approximately 2% variations of QE at 8.4 keV and provide an explanation why spatial variation of QE at this energy is much larger than at lower energies.

4.6.3 Comparison Between Measured & Modeled Relative Quantum Efficiency above 5 keV

At energies above 4–5 keV quantum efficiency of the device depends entirely on the depletion depth. Consequently, the results of the depletion depth measurements described in Section 4.6.2 can be checked against the results of the quantum efficiency measurements of the flight devices relative to the reference chips. Since depletion depths were extracted from the data taken in the HIREFS chamber, the results of the two measurements are completely independent. Absolute QE numbers at two energies - 5.898 KeV (Manganese K_α line) and 8.047 keV (Copper K_α line) were calculated for both flight and reference

Device	Location	Depletion Depth, μm								Remarks
		Φ PI = +2,+10V (standard)				Φ PI = -5,+5V (reduced dark current)				
		c0	c1	c2	c3	c0	c1	c2	c3	
w203c4r	I0	66.4	66.9	66.8	66.4	47.6	48.1	48.0	48.7	
w193c2	I1	67.4	66.5	67.8	66.6	48.3	47.4	47.5	47.9	
w158c4r	I2	66.8	67.2	66.5	66.3	47.7	47.9	47.8	47.4	
w215c2r	I3	66.1	67.3	66.5	66.2	48.7	47.8	48.5	47.9	
w168c4r	S0	64.8	65.5	65.5	65.3	44.9	45.8	45.5	45.4	
w182c4r	S2	79.5	79.1	80.6	79.9	57.7	58.2	58.1	58.3	
w457c4	S4	73.3	74.2	73.9	73.6	53.4	53.5	53.0	53.4	
w201c3r	S5	73.0	74.4	74.7	74.4	52.1	53.4	52.9	53.2	
w198c1	ref.	73.7	73.9	74.7	72.8	52.3	51.6	52.2	51.3	
w461c4	ref.	81.2	81.3	80.2	80.6	59.2	58.9	58.2	58.4	
w203c2	ref.	68.1	68.1	67.0	67.2	48.0	49.0	48.9	47.8	

Table 4.30: Depletion Depth Estimated from 5.9 keV branching ratio

devices based on the assumption that any photon interacting within the depleted layer will be detected. Table 4.31 shows the results of these calculations along with the results of the relative QE measurements in the big chambers. Both results are in good agreement.

Device	Loc.	Deplet. depth, μm	Absolute QE (calculated)		Relative QE (calculated)		Relative QE (measured)		Rel. QE difference (meas.-calc.)		Reference device
			5.9 keV	8.05 keV	5.9 keV	8.05 keV	5.9 keV	8.05 keV	5.9 keV	8.05 keV	
w203c4r	I0	64-65	0.875	0.594	1.039	1.086	1.031	1.106	-0.008	0.02	w103c4
w193c2	I1	64-65	0.875	0.594	1.039	1.086	1.033	1.087	-0.006	0.001	w103c4
w158c4r	I2	64-65	0.875	0.594	1.039	1.086	1.030	1.096	-0.009	0.01	w103c4
w215c2r	I3	64-65	0.871	0.588	0.974	0.94	0.986	0.932	0.012	-0.008	w190c3
w168c4r	S0	63-64	0.867	0.583	0.970	0.93	0.974	0.919	0.004	-0.011	w190c3
w182c4r	S2	75-76	0.905	0.646	1.07	1.18	1.068	1.211	-0.002	0.031	w103c4
w457c4	S4	70-72	0.894	0.626	1.00	1.00	1.000	1.003	0.000	0.003	w190c3
w201c3r	S5	71-72	0.894	0.626	1.00	1.00	1.001	1.008	0.001	0.008	w190c3
w103c4	ref	57	0.842	0.547							
w190c3	ref	71	0.894	0.626	1.062	1.145	1.058	1.164	-0.004	0.019	w103c4
mean									-0.0013	0.008	
σ									0.0066	0.014	

Table 4.31: Comparison of relative QE measured directly and calculated from the results of depletion depth measurement

4.6.4 Near edge structure of X-ray absorption in the CCD response

4.6.4.1 Introduction

In order to produce an accurate model of CCD quantum efficiency it is very important to know precisely the optical constants of the materials comprising the gate structure of the device. Widely used Henke data are quite inaccurate at energies close to the absorption edges. We undertook an effort to measure the transmission of the corresponding films in order to to fill in this gap.

The CCD gate structure contains three different materials: silicon dioxide, silicon nitride (Si_3N_4), and polycrystalline silicon, which is heavily doped with phosphorus. All the X-ray absorption edges of these materials, namely, silicon L (100 eV), nitrogen K (400 eV), oxygen K (532 eV), and silicon K (1840 eV) are within the range of interest for ACIS.

In the course of technology development for manufacturing backside CCD, Lincoln Lab implemented a technique for etching away the thick silicon substrate, leaving only a thin layer of material at the surface of the wafer. This technology turned out to be exceptionally well suited for making thin films supported by a rigid frame, allowing them to be handled easily. Usually, at low energies the transmission of a material is derived from the results of the measurement of total electron yield. With the Lincoln Lab technology it is possible to make extremely thin free standing films and measure transmission directly. We used synchrotron radiation to measure the transmission of these materials as a function of energy. There is no single beamline which can cover such a wide range of energies, and for this reason measurements were performed at three different synchrotrons.

4.6.4.2 Sample preparation

All the samples were prepared in a similar manner. A film was grown on the silicon substrate and then silicon from the back side of the wafer was etched away in a circular opening approximately 0.5 centimeter in diameter. The etching stops when the film is reached. This results in an extremely thin film sitting on the top of the silicon frame. The cross section of such structure is shown in Fig. 4.67.

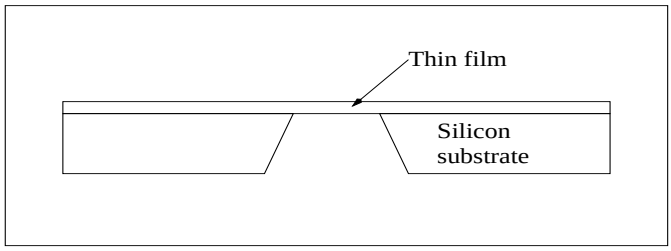

Figure 4.67: Cross section of the thin film sample.

The following samples were prepared at Lincoln Lab for the transmission measurements:
1. Thin SiO_2 film (dry oxidation of Si wafer at 1000^o C, a process identical to the one used for CCD gate oxide growth), nominally 0.14 microns thick.
2. Thick SiO_2 film (wet oxidation at 1000^o C, a process used for channel stop oxide growth), approximately 1.5 microns thick.
3. A sandwich of $SiO_2 + Si_3N_4 + SiO_2$, a copy of the CCD gate insulator structure, nominal thicknesses 0.06 + 0.03 + 0.015 microns.
4. Phosphorus doped polycrystalline silicon, 0.6 microns thick.
5. The same polycrystalline silicon film partially oxidized, nominally 0.46 + 0.2 microns of $Si + SiO_2$ respectively.

4.6.4.3 Measurement details

X-ray transmission measurements of samples 1 and 3 at low energies (60 eV – 900 eV) were performed at the Advanced Light Source (Lawrence Berkeley National Lab), beamline number 6.2.3, which is equipped with a grating monochromator with superb energy resolution (resolving power 7000). Three different gratings are needed to cover the entire energy range. For each grating the interval is further divided into two or three subranges due to the necessity of using different filters to suppress higher orders. For this reason a dataset for each sample consists of 8 separate subsets. It should be noted that changing of the grating requires realignment of the beam.

Only samples 1 and 3 were characterized at ALS. Three other samples were too thick for the measurement in this energy range, being opaque at energies below 300 – 400 eV and above the O K edge (SiO_2 sample). The energy step in the region from 360 to 580 eV containing nitrogen and oxygen edges was set to 0.25 eV, to 0.5 eV for energies below 180 eV (around the Si L edge), and 1 eV for the rest of the energy range.

Transmission at energies around the silicon K edge was measured at two other synchrotrons: at BESSY (Berlin) and at the Synchrotron Radiation Center (Madison, Wisconsin). The Canadian Double Crystal Beamline at the SRC has a double crystal monochromator with a resolution of 0.9 eV. It utilizes a pair of InSb(111) crystals (instead of the more commonly used in this range silicon), which is important for this measurement in order to avoid silicon edge "steps" in the incoming flux. Due to the low energy of electrons in the storage ring (800 MeV) and the double crystal arrangement of the monochromator, this beamline has very low higher order light penetration (below 0.2%). The data were taken in the range from 1770 to 2500 eV. The energy step was 0.25 eV around Si edge (from 1830 to 1860 eV), and 1 eV for the rest of the range. The accuracy and reproduceability of the SRC data is better than 0.1%, the noise being hardly noticeable.

At BESSY measurement were made over a wider range, from 1300 eV to 3000 eV. In general BESSY results are much noisier, but they are very valuable since they span a wider range and this helps to constrain the thickness of the films more reliably.

Since the X-ray flux emitted by a storage ring is continuously changing, it is necessary to normalize the output intensity to the input flux. This requires two detectors for any measurement - one in front, and one behind the sample. A solid state X-ray detector was installed downstream from the sample to register the output flux. At all three beamlines it was an uncovered Hamamatsu GaAsP photodiode G1127-02. Again, this was one of the precautions taken to avoid silicon absorption edges anywhere in the measurement system. Upstream from the sample a transparent beam normalization detector monitored the input flux. At ALS and BESSY this was a metal mesh whose electron yield was measured. At SRC a gas ionization chamber served as the beam normalization detector.

Each measurement consisted of two passes through the energy range – one with the sample in the beam, another one with the sample out. The ratio of the two normalized fluxes is the transmission of the film.

4.6.4.4 Measurement results.

a. Silicon L, nitrogen and oxygen K edges

In Fig. 4.68 the solid line shows the transmission of the thin SiO_2 film at energies

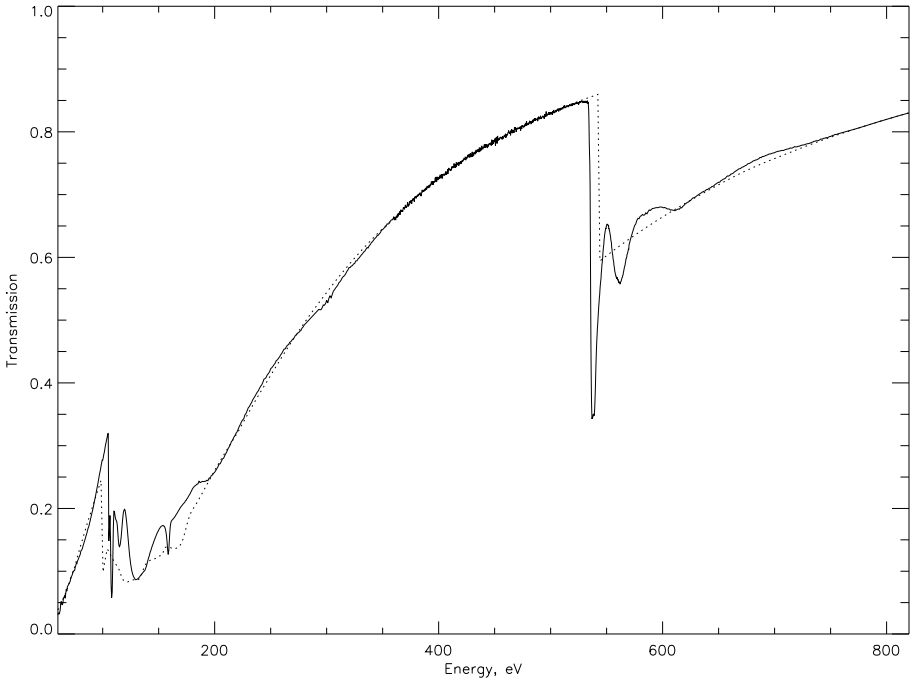

Figure 4.68: Transmission of the thin SiO_2 film as a function of energy (solid line). Dotted line represents standard Henke data.

below 800 eV. Very strong near-edge oscillations can be seen at energies above the silicon L and oxygen K absorption edges. In the areas where near-edge structure does not play a significant role, a fit to the standard Henke data was made with a thickness of the film as a free parameter. The best fit thickness was found to be 0.157 microns, and the corresponding transmission curve is shown on Fig. 4.68 as a dotted line. The deviation of the measured transmission from the Henke data is very strong above the absorption edges, and the edges themselves are shifted. The structure above 100 eV corresponds to silicon L_1, L_2, and L_3 edges at 158, 107, and 105 eV respectively. At the oxygen edge a very strong resonant absorption peak is found at 538 eV.

A transmission curve for the $SiO_2 + Si_3N_4 + SiO_2$ sandwich (which is an exact copy of the CCD gate isolator) is shown on the Fig. 4.69. In addition to the silicon and oxygen edges this plot shows a prominent nitrogen K edge, also shifted from the tabulated atomic value. The transmission of this sandwich was modeled as a combination of the Henke-derived Si_3N_4 transmission and the experimentally measured transmission of SiO_2. The best fit (thicknesses of both materials being free parameters) is shown in Fig. 4.69 as the dotted line.

b. Silicon K edge

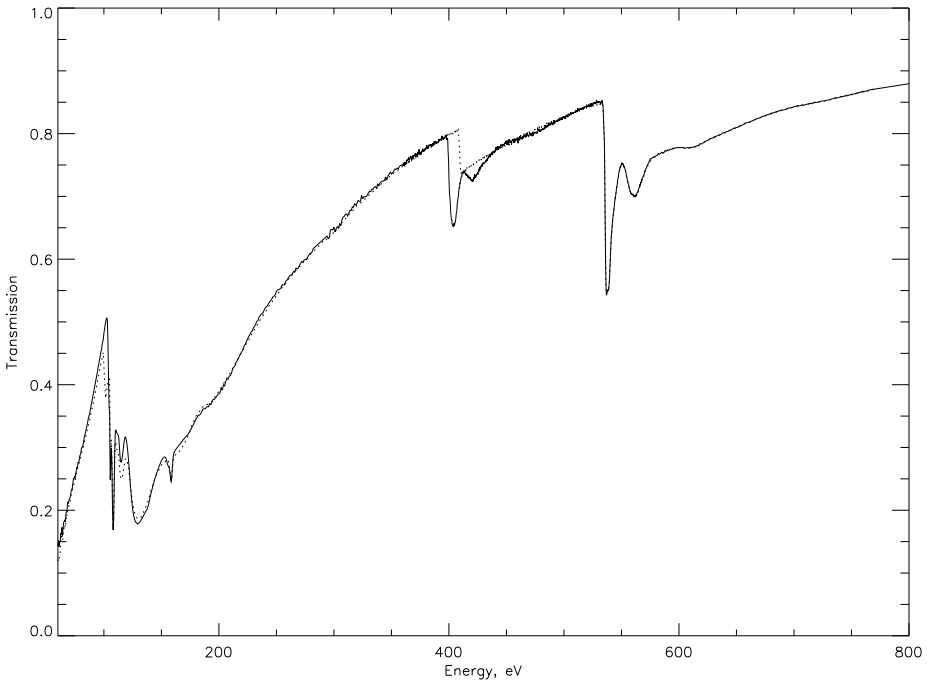

Figure 4.69: Transmission of the sandwich (solid line).

Fig. 4.70 contains absorption curves (not transmission!) of polysilicon, SiO_2, and the $SiO_2 + Si_3N_4 + SiO_2$ sandwich in the close vicinity of the silicon K edge. Each sample shows a sharp resonant peak right above the edge. Due to chemical shifts each of the three materials exhibits the silicon K-edge at slightly different energy. For polysilicon the peak is at 1841 eV; for SiO_2 it is at 1847.3 eV. The $SiO_2 - Si_3N_4 - SiO_2$ sandwich shows two distinct peaks which, although are not well-resolved, can be determined to be at 1847.3 and 1844.7 eV. The first one can obviously be attributed to SiO_2, while the second one originates from Si_3N_4. Polysilicon absorption shows a lot of structure due to its crystalline and ordered nature, whereas silicon dioxide has fewer peaks because it is amorphous and uncorrelated interference from remote atoms smears out the features.

The difference between the edge and resonant peak energies of polysilicon and SiO_2 can be seen very nicely in the oxidized polysilicon sample transmission in Fig. 4.71. A dashed line in this plot represents the result of fitting to this data the product of the transmissions of the separate films of polysilicon and SiO_2. The quality of the fit is so good that the dashed line can hardly be seen under the solid line.

In order to fill a gap in the data (no measurements were made in the range from 900 to 1300 eV), and also to extend the results to higher energies, we used Henke data (which should be adequate at energies far enough from the edges).

For each of the materials standard Henke data were used to fit the transmission at energies below the edge and far above the edge, where the near edge oscillations become weak. This procedure allows us to define the thickness of each film. The results are slightly

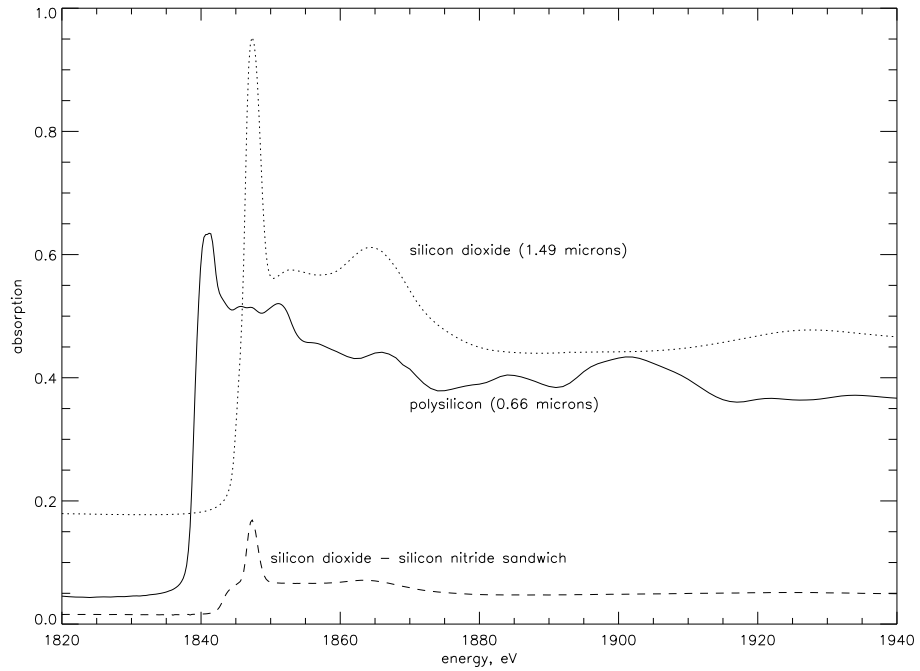

Figure 4.70: Absorption of the thin films of polysilicon (solid line), silicon dioxide (dotted line) , and $SiO_2 - Si_3N_4$ (dashed line) sandwich.

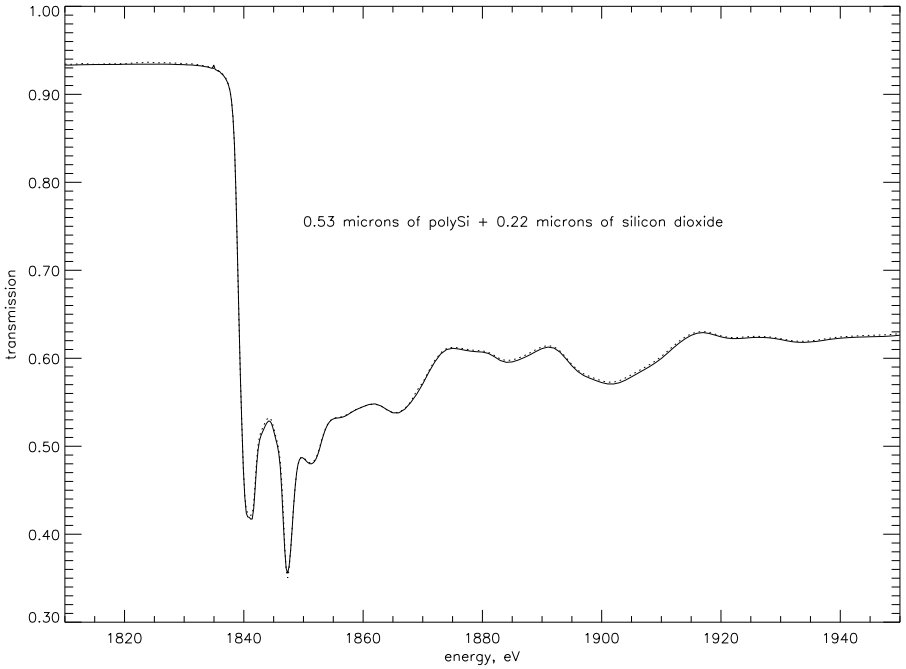

Figure 4.71: Transmission of the oxidized polysilicon film (solid line) and result of the best fit to it of the product of the polysilicon and SiO_2 transmissions (dotted line).

different from the nominal values and are reflected in the labels in the above Figures. The densities of the materials used for those calculations were 2.19, 2.33 and 3.44 g/cm^3 for SiO_2, polysilicon and Si_3N_4, respectively. For both polysilicon and SiO_2 near-edge measurements were combined with Henke atomic scattering factors for silicon and oxygen, and mass absorption coefficient were produced in the range from 60 eV to 15 keV.

We encountered some difficulties in our attempt to separate optical constants of the Si_3N_4 film from the other components of the sandwich, most likely due to deviations from stoichiometry in one or more constituent layers. Because of that, for further applications we used a transmission of the sandwich as a whole unit, instead of deriving a mass absorption coefficient for each component.

4.6.4.5 CCD quantum efficiency.

Having all the absorption coefficients in hand it is possible to calculate the quantum efficiency of the CCD taking into account transmission of all the layers in the gate structure of the frontside CCD. In this model we accounted for the overlaps between the gates of the CCD, and assumed triangular edges of the channel stop oxide layer (which is a good approximation for the so-called "bird's beak" shape of those edges). Thicknesses of the layers were taken from the results of Scanning Electron Microscope (SEM) measurement of a sibling device cross section (see Fig 4.46). In Fig. 4.72 is shown a plot of quantum efficiency as a function of energy for the frontside illuminated device. The dashed line in

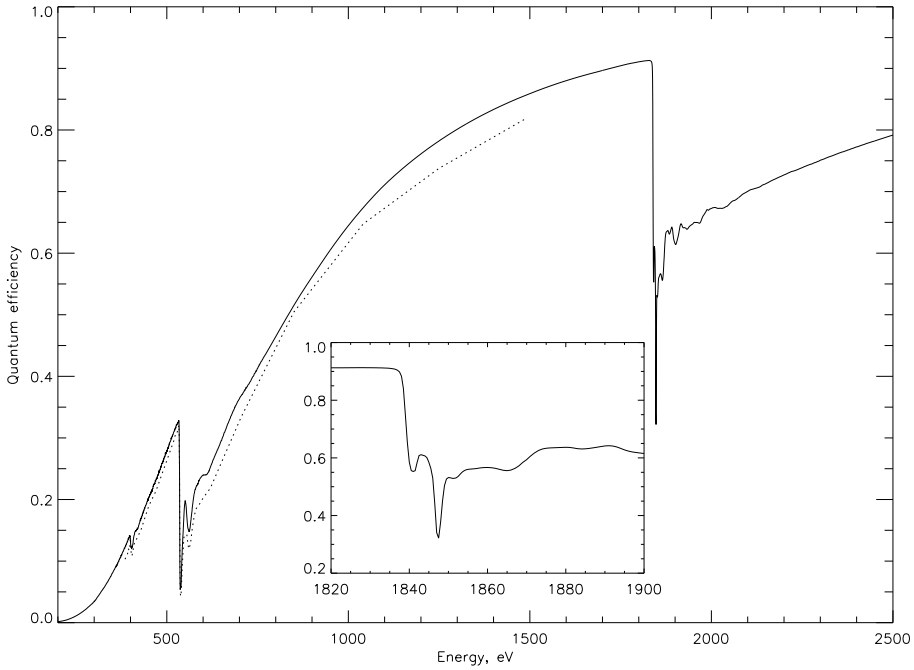

Figure 4.72: Quantum efficiency of the frontside illuminated CCD. Dashed line is the result of the QE measurement at SX700 line at BESSY.

the Figure represents results of the quantum efficiency measurement of the frontside CCD at the SX700 beamline at BESSY. No fitting of the model to the data has been made for this plot. The deviation of the experimental points from the model at higher energies can be explained by the known second order light penetration of the SX700 monochromator at higher energies. In the analysis of the SX700 results the second order light counts are excluded in the CCD, while the reference photodiode cannot discriminate between orders. This results in the underestimation of the QE values for the CCD. It should also be mentioned that the above model accounts only for the transmission losses in all the layers (in great detail, though) and does not deal with the redistribution of counts into the low energy tail. This should not be a very significant factor for the frontside illuminated CCDs.

A similar plot for the backside illuminated device is shown in Fig. 4.73. Triangular points show the results of experimental measurements of the quantum efficiency of the backside illuminated device at the SX700 beamline at BESSY. The plot extends to very low energies around the silicon L edges, although the device loses its ability for spectral resolution below 250 eV. It still can be used for imaging, and its QE can be high enough, as can be seen from the Figure. The best agreement of experimental data with the transmission model was

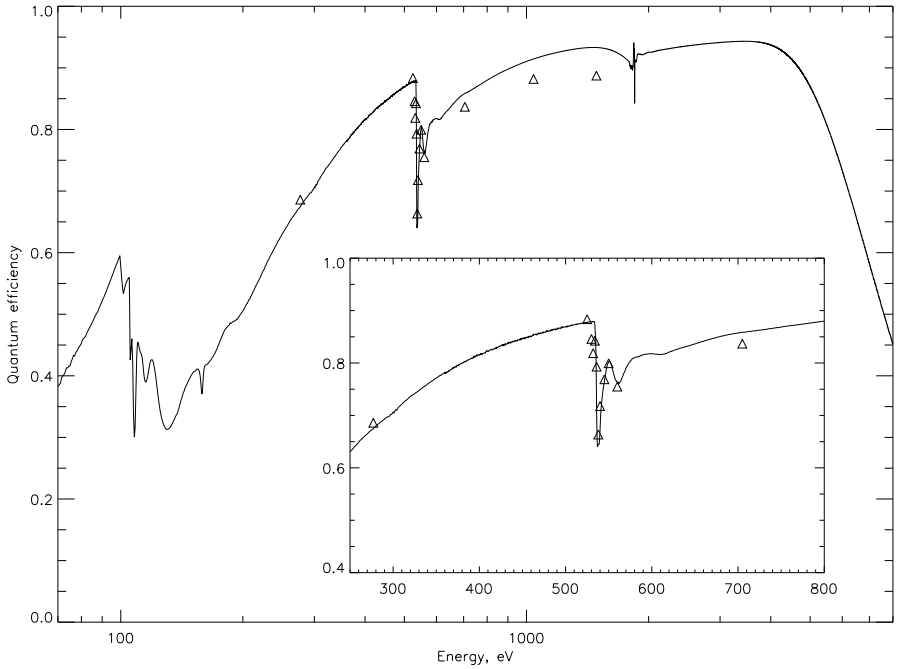

Figure 4.73: Quantum efficiency of the backside illuminated CCD. Triangles mark experimental results from SX700 at BESSY.

reached assuming a surface thickness of oxide layer of 0.055 microns, whereas the nominal thickness specified by Lincoln Lab is 0.035 microns. Besides that, we had to multiply the calculated QE by a factor of 0.96 to obtain an agreement with the experiment. This is expected, since for the backside devices a noticeable fraction of events is lost to the low

energy tail. A more sophisticated model is necessary to account for this effect. As in the case with the frontside devices, a discrepancy at higher energies is attributed to second order light contamination.

4.6.5 Validation of High Speed Tap Data Acquired at XRCF

4.6.5.1 Purpose

The purpose of this section is to show that the High Speed Tap event lists can be used to determine absolute quantum efficiency of the ACIS instrument.

4.6.5.2 The Data Set

During flat field calibration operations at the XRCF in May of 1997, telemetry data and High Speed Tap data were taken simultaneously for a number of sources for all ten of the flight devices. The standard procedure was to begin a science run, then use the High Speed Tap to collect raw data frames for each of the chips being operated. After some processing, the event list generated from the raw High Speed Tap data frames can be directly compared with the events telemetered by the flight software. The data set chosen for this comparison is TRW ID I-IAS-EA-2.017. The chip is s4 (aka. w457c4). The anode is silicon. The data set was captured on 09 May 1997 at 22:12 GMT.

4.6.5.3 The Telemetry Data Processing

The telemetry event list is from Science Run 72, which began on 09 May 1997 at 17:48 GMT as TRW ID I-IAS-SG-2.008. The parameter block used was xfaint_win_s.te. xfaint_win_s.te is full frame, faint telemetry, trickle bias, with a window. The window block used was xsik56b50.2d. For the s4 chip, this has two windows. The first window begins at row 9 (counting from 0) and is 28 rows high. The second window begins at row 972 and is 28 rows high. All 1024 columns were telemetered. The first event for the science run was on 09 May 1997 at 18:03 GMT. The last event for the science run was on 09 May 1997 at 23:49 GMT.

An ERV event list and fits format average bias frame for this science run were created from the ACIS telemetry using PSCI. For a description of PSCI and the ERV format see http://acis.mit.edu/ttools/psci.html. The ERV format event list was converted to ACIS RV format using an IDL program which combines the fits format average bias file and the ERV format event list. For a description of the ACIS RV format see http://acis.mit.edu/ttools/acis-analysis.html.

To directly compare the telemetry event list with the High Speed Tap event list, events which the telemetry includes but the High Speed Tap does were removed. There are three types of events that the High Speed Tap event list does not include; events on quadrant

boundaries, events taken before (22:17 GMT) or after (23:00 GMT) the High Speed Tap data were captured, and events in frames that the High Speed Tap dropped.

4.6.5.4 The High Speed Tap Data Processing

The High Speed Tap event list used was taken as TRW ID I-IAS-EA-2.017, which began on 09 May 1997 at 22:12 GMT. The first event was at 22:17 and the last event was at 23:00 GMT. An RV format event list was created from the fits format bias frames (taken with the gate valve shut, immediately prior to the data) and the FITS format data frames using "xrcf_find_events".

To directly compare the High Speed Tap event list to the telemetry event list the High Speed Tap times and coordinates were converted to telemetry times and coordinates, and events not included in the telemetry event list were removed. The times had to be converted because the telemetry times are given in seconds from the beginning of 1997 while the High Speed Tap times are given in seconds from the beginning of 1994. The coordinates needed to be converted because the telemetry row and column coordinates are given in chip coordinates while the High Speed Tap coordinates are given in readout coordinates.

There are two types of events that the High Speed Tap event list includes that the telemetry event list does not; events that occur outside of the telemetry window, and events in frames that the telemetry dropped.

4.6.5.5 Event List Comparison

Both of the event lists in the comparison contain events from 755 frames. The average number of events per frame in the 56 rows of the comparison is 56.6 events per frame. The total number of events in the filtered telemetry event list is 42738. There are 42768 events in the filtered High Speed Tap event list.

4.6.5.6 Spectral Resolution Comparison

After subtracting the average bias and delta-overclocks, the event amplitudes in the two event lists can be directly compared. The spectra for ACIS grade bit map 0x1d05 0x0047 0x0004 0x0047 0x1133 0x0003 0x1100 0x0000 0x1d04 0x0000 0x0004 0x0000 0x0000 0x0003 0x0000 0x0000 (ASCA grades 02346) for both the High Speed Tap and telemetry event lists are shown in Figure 4.74.

The peak and sigma fit to the data for each of the four quadrants is the same for each of the event lists.

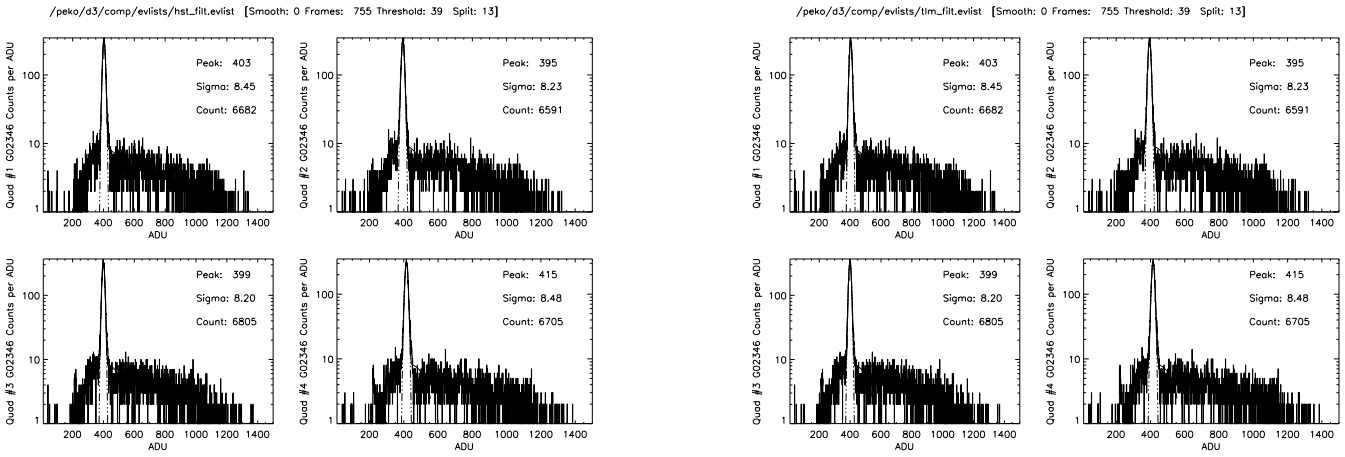

Figure 4.74: Telemetry and High Speed Tap Spectra

4.6.5.7 Event Timing Comparison

The total number of events in each frame is shown in Figure 4.75 for both the telemetry event list and the High Speed Tap event list as well as the difference between the two.

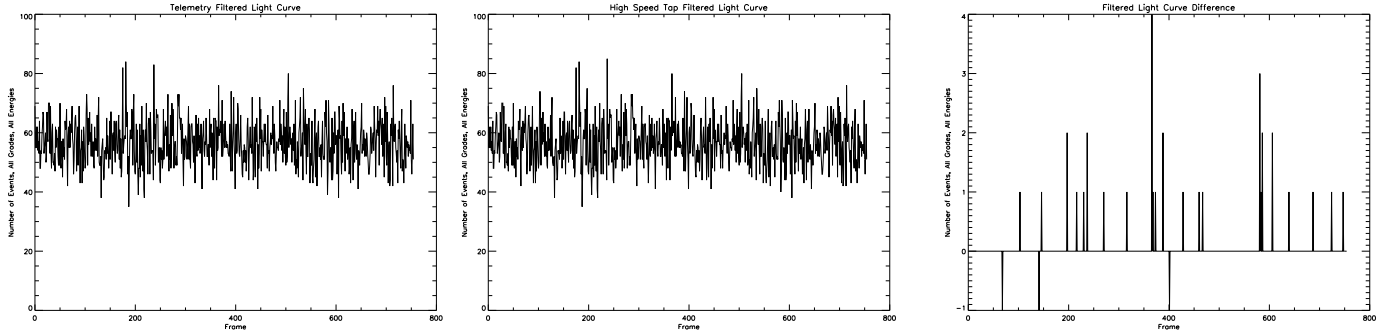

Figure 4.75: Telemetry, High Speed Tap, and Difference Light Curves

4.6.5.8 Position Comparison

Subtracting the event list images for the two files shows that there are 124 pixels for which the total number of events is different. Ninety-six of the differences are due to split events which, because to differences in the biases or processing order, have a difference in the position of one row or column.

Table 4.32 is an example of an event found in the exposure taken at 22:45.558 GMT (frame 502 for the High Speed Tap, frame 5075 for the telemetry). Due to the 3 ADU

difference in the bias levels, the peak of this split event was found at two different positions.

	Telemetry				High Speed Tap				Difference			
r/c	169	170	171	172	169	170	171	172	169	170	171	172
9		1	1	4	2	2	3		-2	-1	-2	+2
10		124	125	-4	2	127	126		+1	-3	-1	-3
11		65	96	-3	1	66	97		-2	-1	-1	+2

Table 4.32: Event Position Comparison

The remaining events which don't appear in both lists are events which are, due to the variations in the bias, either below the threshold, or are no longer the local maximum.

4.6.6 ACIS High Speed Tap Count Rates During XRCF Phase I: Towards Absolute Efficiency Measurements from XRCF Data

4.6.6.1 Purpose

The purpose of this section is to present the measured counting rate and inferred photon fluxes during XRCF phase I measurements.

Also presented is the ratio of ACIS detected counts (corrected for pileup and filter efficiencies) to the flux detected by the Beam Normalization Detector (corrected for source to detector distance). This information, combined with the absolute efficiency of the Beam Normalization Detector (which is not available to us at this time) can be used to determine the the absolute quantum efficiency of the ACIS CCDs.

4.6.6.2 Measurement Description

XRCF phase I was performed with the ACIS flight instrument, but without the HRMA or the gratings. The full ACIS focal plane was illuminated with X-rays from either the EIPS or the DCM.

ACIS was run in the full frame timed exposure mode, with a 3.34 second exposure time. During most science runs, six of the CCDs were read out simultaneously. During each science run, the high speed tap was cycled through each of the devices that was on. As the high speed tap was changed, so was the TRW ID.

There are two reasons why high speed tap data are used here in favor of telemetry data. Without the limitations of the telemetry, the entire full frames can be captured, not just the events from a small window. Also, because a single science run contains data from may

TRW IDs, a time filter must be applied when comparing the telemetry data to the Beam Normalization Detector data. Using High Speed Tap data eliminates this complication.

The tables presented in this section identify the data used by science run number, not TRW ID. A single science run is all of the data taken between sending the "Start Run" and "Stop Run" commands to the ACIS instrument and often includes several TRW IDs. Table 4.33 lists the relevant TRW IDs for the data used in this section.

Science Run	Energy eV	i0 I-IAI-EA-	i1 I-IAI-EA-	i2 I-IAI-EA-	i3 I-IAI-EA-	s0 I-IAS-EA-	s1 I-IAS-EA-	s2 I-IAS-EA-	s3 I-IAS-EA-	s4 I-IAS-EA-	s5 I-IAS-EA-
70 71	525	1.001	1.002	1.003	1.004	2.001	2.002	2.003	2.004	2.005	2.006
88 89	705	1.005	1.006	1.007	1.008	2.007	2.008	2.009	2.010	2.011	2.012A
111 112	1487	1.017	1.018	1.019	1.020	2.026	2.027	2.028	2.029	2.030	2.031
72 75	1740	1.009	1.010	1.011	1.012	2.013	2.014	2.015	2.016	2.017	2.018
107 108	2166	1.013	1.014	1.015	1.016	2.019	2.020	2.021	2.022	2.023	2.024
120 122 123	4509	1.121	1.122	1.123	1.124	2.131	2.132	2.133	2.134	2.135	2.136
77 78 83 84	6399	1.025	1.026	1.027	1.028	2.037	2.038	2.039	2.040	2.041	2.042
92 93	8040	1.029	1.030	1.031	1.032	2.043	2.044	2.045	2.046	2.047	2.048

Table 4.33: TRW IDs

4.6.6.3 Data Processing

Event finding was performed on each raw data frame with an event threshold of 38 ADU for the front illuminated devices and 20 ADU for the back illuminated devices. The split threshold was 13 ADU for all measurements. The event finding was performed using an IDL script which output an ARV format event list.

Each ARV format event list was then summarized using an IDL script. This IDL script fit a gaussian to the main peak of the spectrum. Only events in ACIS grade bit map 0x1d05 0x0047 0x0004 0x0047 0x1133 0x0003 0x1100 0x0000 0x1d04 0x0000 0x0004 0x0000 0x0000 0x0003 0x0000 0x0000 (ASCA grades 02346) were considered. Using the fit parameters, the position of the peak, width of the peak, and total number of counts under the peak are determined assuming the line response is Gaussian. All of these values are written to a text format file.

Finally, the text format summary files are read by another IDL script which uses the counts per frame versus energy to correct for pileup, the filter efficiency versus energy to correct for filter effects, and the CSR calculated s2 quantum efficiency. This IDL script also reads in a SSD 5 flux rate.

4.6.6.4 Results

The absolute flux at the ACIS filter in photons per second per centimeter squared is shown in Table 4.34. The statistical error of the flux rates presented is generally 0.1 percent, with a worse case of 0.5 percent.

Science Runs	Energy	i0	i1	i2	i3	s0	s1	s2	s3	s4	s5
70 71	525	18.1	18.3	18.2	17.3	18.6	26.2	18.9	24.6	18.1	18.0
88 89	705	23.7	23.3	23.5	23.8	23.6	40.0	24.4	39.9	25.7	23.8
111 112	1487	171.7	171.7	172.2	172.4	171.7	172.7	172.5	174.5	173.1	172.4
72 75	1740	39.5	39.6	39.8	39.7	39.6	41.4	39.5	41.7	39.6	39.3
107 108	2166	73.2	73.6	73.8	73.6	73.2	76.3	74.4	78.9	73.6	74.3
120 122 123	4509	64.7	66.0	65.0	65.9	76.8	68.6	74.0	75.1	70.8	69.3
77 78 83 84	6399	78.3	79.1	79.5	79.4	79.5	73.4	79.0	76.1	78.8	78.5
92 93	8040	242.9	244.4	240.4	245.7	254.1	230.9	246.4	233.2	243.4	247.8

Table 4.34: Estimated High Speed Tap Flux at ACIS Focal Plane Corrected for Pileup, Filter Efficiency, and CCD Efficiency in photons per second per centimeter squared in the line.

The relative efficiencies of the ACIS flight devices compared to s2 are shown in Table 4.35.

Science Runs	Energy	i0	i1	i2	i3	s0	s1	s2	s3	s4	s5
70 71	525	0.755	0.805	0.825	0.887	0.922	3.311	1.000	3.216	0.843	0.807
88 89	705	0.559	0.867	0.684	0.652	0.851	3.193	1.000	3.173	0.914	0.854
111 112	1487	0.967	0.949	0.962	0.972	0.978	1.076	1.000	1.161	0.984	0.975
72 75	1740	0.965	0.967	0.976	0.971	0.948	0.672	1.000	1.042	0.956	0.943
107 108	2166	0.944	0.957	0.970	0.958	0.964	1.282	1.000	1.328	0.975	0.964
120 122 123	4509	1.002	1.007	0.995	0.999	0.998	0.843	1.000	0.969	1.003	0.994
77 78 83 84	6399	0.949	0.950	0.957	0.954	0.951	0.604	1.000	0.750	0.992	0.976
92 93	8040	0.901	0.906	0.891	0.911	0.936	0.489	1.000	0.638	0.990	0.976

Table 4.35: High Speed Tap Based Quantum Efficiencies Relative to the s2 Detector

The ratio of ACIS counts to SSD 5 counts is shown in Table 4.36. The SSD 5 count rates used are from "flux_d3" column of ftp://es81-server1.msfc.nasa.gov/xrayastronomy/QE_energy_total.rdb, which was last updated August 13, 1997.

4.6.6.5 Warnings

The pileup correction applied to the data are based on CSR spectra, not XRCF spectra.

Science Runs	Energy	i0	i1	i2	i3	s0	s1	s2	s3	s4	s5
70 71	525	3.621	3.862	3.960	4.256	4.422	15.887	4.798	15.430	4.044	3.870
88 89	705	0.790	1.224	0.966	0.921	1.201	4.508	1.412	4.479	1.290	1.205
111 112	1487	0.977	0.958	0.972	0.982	0.988	1.087	1.010	1.173	0.994	0.985
72 75	1740	1.156	1.158	1.169	1.163	1.135	0.805	1.198	1.249	1.145	1.129
107 108	2166	0.782	0.793	0.804	0.794	0.799	1.063	0.829	1.100	0.808	0.799
120 122 123	4509	0.785	0.789	0.780	0.783	0.782	0.661	0.784	0.760	0.787	0.780
77 78 83 84	6399	0.792	0.793	0.799	0.796	0.793	0.504	0.834	0.626	0.828	0.815
92 93	8040	0.617	0.620	0.610	0.624	0.641	0.335	0.685	0.437	0.678	0.668

Table 4.36: ACIS Count Rate Divided by SSD 5 Count Rate

4.7 Quantum Efficiencies of ACIS Flight Detectors Relative to Reference Detectors

4.7.1 Measurement Method, Analysis Techniques, and Data Products

4.7.1.1 Calibration Strategy

The quantum detection efficiency of each ACIS flight CCD was calibrated relative to one or more reference CCDs at the CCD Laboratory in MIT's Center for Space Research. The reference CCDs used as calibration transfer standards for the flight CCDs are of the same design and are essentially identical to the flight CCDs except for small manufacturing variations. The reference CCDs were previously calibrated using the facilities of the Physikalisch-Technishe Bundesanstalt (PTB) laboratory at the Berlin Electron Storage ring BESSY(Arnold and Ulm, 1992), as well as via comparison to a Si(Li) solid state detector at energies above 3 keV. The calibrations performed at PTB-BESSY are described in Section 4.6.1.

The strategy adopted to measure the relative quantum detection efficiency of flight CCDs vs. reference CCDs consisted of alternately moving one flight CCD and one reference CCD into a stable quasi-monochromatic X-ray beam at each of several energies, spanning the spectral range of 0.3–10 keV. Two special vacuum chambers were built for this purpose, containing mounts for two CCDs attached to X-Y translation stages, X-ray sources, and alignment systems employing LEDs and pinholes(Jones et al., 1996). The pinholes illuminated the CCDs with small spots, coaxial with the X-ray sources, whose centroids were determined to the nearest pixel in order to alternately position each CCD at the same X-Y location for the calibration measurements.

Both radioactive (^{55}Fe) and fluorescent X-ray sources were used to illuminate the CCDs, providing a range of discrete emission lines to cover the energy band. Two fluorescent sources were used, one with a tritium source whose beta particles excite low-Z targets (for C, O, and F lines), and one employing a Mo-anode commercial X-ray tube to excite higher-Z targets (Al, Si, P, K, Cl, Ti, V, Fe, Co, Ni, Cu, Zn, and Ge targets were available). These sources have been described in detail elsewhere(Jones et al., 1996). The carbon source was only used with back-illuminated (BI) CCDs, as front-illuminated (FI) CCDs have very poor efficiency at 277 eV. The sources used for relative QE calibration and the energies of their K_α lines are shown below:

Element	(C)	O	F	Si	P	Ti	Mn	Cu
Energy (keV)	.277	.525	.677	1.74	2.02	4.51	5.89	8.04

To analyze the relative quantum efficiency (QE) data, a Gaussian fit to the main X-ray line was made to the cumulative spectra (for each CCD quadrant); then all counts within 3 sigma of that peak were counted towards the detected flux rate in that line. Both the flight and reference CCDs (containing 1024 × 1024 pixels) were divided into 1024 "superpixels" (32×32 pixel square regions). The calibration measurements collected approximately 10000 counts per superpixel for 1% accuracy (in counting statistics) at the superpixel level. This goal required collecting over ten million counts in each CCD for each energy of interest, a process requiring typically 10 days, with two shifts of data operators per day, per flight CCD candidate. [Counting re-flexed CCDs, almost 40 devices have undergone this process since Jan. 1996.] Smaller sets of data were also taken at the energies not used for quantum efficiency analysis in order to fully characterize the spectral response (gain and FWHM vs. energy).

The alignment process ensured that each reference CCD superpixel viewed the same X-ray flux as the corresponding flight CCD superpixel, even for non-uniform source radiation patterns (C, O, and F were most sharply peaked on axis—the higher energies were relatively flat). It is estimated that the flight and reference CCDs were positioned at the same location in the X-Y (translation stage) plane to within two pixels. The raw relative QE (uncorrected for pileup) for each superpixel pair was taken to be the ratio of the flight CCD count rate (counts/sec/superpixel) to the reference CCD count rate.

This yielded 1024 values of the QE ratio, with typically a Gaussian distribution. By fitting a Gaussian to this histogram of ratios, we obtained a fitted centroid, representing the nominal QE ratio for the two CCDs, and a width (sigma) which represents the spatial variations. A simple average of the 1024 ratios was also calculated, along with the standard deviation. The standard deviation is quite sensitive to outlying values that can originate from bad pixels, hot columns, or edge effects (particularly shadows along one edge attributed to the framestore covers attached to each CCD).

Images and histograms of the spatial uniformity of the superpixel ratios at each energy are presented in Figures 4.77–4.86 in section 4.7.2.

4.7.1.2 Pileup Corrections To Relative Quantum Efficiency Values

The average count rate for each CCD is used to estimate pileup correction factors, which are then used to obtain corrected nominal values of the QE ratio and the sigma value. The pileup correction is typically very close to unity when both the flight and reference CCD have the same exposure time. Larger corrections were found in several cases where the reference CCD used older (and slower) electronics than the flight CCD and therefore recorded higher counts/frame and pileup values. Also, data comparing FI CCDs to BI CCDs can be affected by slight differences in pileup behavior exhibited by the two types of detector.

The pileup model and parameters are explained in Section 4.4; flux scaling studies were used to fit typical FI and BI pileup model parameters at energies above 1.5 keV. These studies consisted of recording data from fluorescent targets at different current values on the commercial X-ray tube (at constant voltage); analysis of total charge collected indicates that the X-ray flux is linear with respect to this current. For energies below 1.5 keV (O and F data), parameters measured with the Al source were employed. A more refined treatment for these energies is planned later. Note, however, that empirically fit pileup parameters were typically independent of energy below 3 keV. For a given flux level, pileup is greatest for high energy photons because their charge clouds typically spread to more pixels, especially if the X-ray is energetic enough to penetrate below the depletion layer of the CCD before initiating a photoelectric interaction.

Pileup effects may be expressed for one measurement in terms of a correction factor (f), defined as the ratio of counting rate (corrected) to counting rate (raw). Typical correction factors (f) and errors in the correction are shown in Table 4.37 for the relative QE calibration of flight CCD I1 (w193c2) vs. reference CCD w103c4. This is an example in which the reference CCD used the older electronics and was limited to a 7.15 second exposure time, whereas the flight CCD using engineering versions of the flight electronics was capable of running with 3.28 second exposures if the flux was high enough to warrant it.

Pileup correction factors applied to the MIT CSR measurements of relative quantum efficiency are presented below in Section 4.7.2.

4.7.1.3 Relative Quantum Efficiency Error Sources

Several factors contribute to the uncertainty in the relative QE measurements. Photon statistics contribute $\sim 1.4\%$ for the 1024 individual superpixel quantum efficiency ratios, but only $\sim 0.04\%$ to the full CCD nominal value (assuming spatially uniform QE), where the nominal value is taken to be the centroid of the Gaussian fit to the histogram of 1024 values.

Reproducibility of relative QE measurements made after moving the CCDs out of and then back into the chamber is typically within 1%, but is observed to be as poor as 3%

Energy	I1 f	I1 exp	Ref f	Ref exp	f ratio	+/-
.525	1.061	7 sec	1.071	7 sec	0.991	0.013
.677	1.031	7 sec	1.041	7 sec	0.990	0.001
1.74	1.046	3 sec	1.109	7 sec	0.943	0.016
2.02	1.022	3 sec	1.051	7 sec	0.972	0.009
4.51	1.027	3 sec	1.059	7 sec	0.969	0.006
5.89	1.065	3 sec	1.146	7 sec	0.930	0.014
8.04	1.068	3 sec	1.144	7 sec	0.934	0.012

Table 4.37: Pileup correction factors f for the relative quantum efficiency calibration of ACIS detector I1 (w193c2) versus reference detector w103c4. The correction factors are defined by f =(Corrected count rate)/(Raw count rate). The corrected relative QE is the raw relative QE multiplied by the f ratio of the two CCDs.

at Cu (8.04 keV), possibly due to relatively high uncertainty in the pileup factor for the reference CCD caused by a high count rate at high energy.

It should also be noted that the pileup correction parameters are generally similar from one FI CCD to another, but they do seem to be slightly different for one older reference CCD (w103c4) used to calibrate some flight CCDs. Because older electronics were used for this CCD, the depletion depth is thought to be smaller, which would exert some influence on the pileup rate. This difference has not yet been incorporated into the correction codes.

A further test of the accuracy of the relative quantum efficiency measurements is described in Section 4.7.3.

4.7.1.4 Data Products and Valid Data Summary

The data used for relative quantum efficiency measurements are listed in Tables 4.38 through 4.50.

The column labeled "Directory" is the location of the dataset from /ohno/di/database on the local CSR network.

In the column labeled "Rejected Frames" the letter "b" following the number indicates that the majority of the rejected frames were rejected due to pixels above the event threshold in the overclock region. The letter "n" following the number indicates that the majority of the rejected frames were rejected due to standard deviation of the overclocks exceeding the noise threshold.

The column labeled "Counts per Frame" contains the total number of G02346 events under the main peak for the data set.

Each data set included has been checked by visual inspection of the data products and for consistency with other data sets.

Chip	Target/Energy eV	Directory	Accepted Frames	Rejected Frames	Frame Time (seconds)	Counts per Frame
w203c4r/I0	o/525	w203c4r/beavis/o/31dec96/2351	322	3b	7.149	2847.2
w203c4r/I0	o/525	w203c4r/beavis/o/31dec96/2203	647	3b	7.148	2844.4
w203c4r/I0	o/525	w203c4r/beavis/o/31dec96/1654	647	3b	7.148	2869.2
w203c4r/I0	o/525	w203c4r/beavis/o/31dec96/1509	644	6b	7.148	2869.6
w203c4r/I0	o/525	w203c4r/beavis/o/31dec96/1207	646	4b	7.148	2893.2
w203c4r/I0	o/525	w203c4r/beavis/o/31dec96/1040	647	3b	7.148	2902
w190c3/REF	o/525	w190c3/beavis/o/31dec96/2033	647	3b	7.148	2947.6
w190c3/REF	o/525	w190c3/beavis/o/31dec96/1908	645	5b	7.148	2949.2
w190c3/REF	o/525	w190c3/beavis/o/31dec96/1337	629	16b	7.149	2968.4
w190c3/REF	o/525	w190c3/beavis/o/31dec96/0904	648	2b	7.148	2996.4
w190c3/REF	o/525	w190c3/beavis/o/01jan97/2115	648	2b	7.148	2996.4
w203c4r/I0	f/677	w203c4r/beavis/f/01jan97/1647	647	3b	7.148	3888.4
w203c4r/I0	f/677	w203c4r/beavis/f/01jan97/1520	646	4b	7.148	3893.2
w203c4r/I0	f/677	w203c4r/beavis/f/01jan97/1213	645	5b	7.148	3898.8
w203c4r/I0	f/677	w203c4r/beavis/f/01jan97/1045	645	5b	7.148	3896.4
w190c3/REF	f/677	w190c3/beavis/f/01jan97/1950	649	1b	7.148	3911.6
w190c3/REF	f/677	w190c3/beavis/f/01jan97/1825	647	3b	7.148	3907.2
w190c3/REF	f/677	w190c3/beavis/f/01jan97/1342	645	5b	7.148	3912
w190c3/REF	f/677	w190c3/beavis/f/01jan97/0917	648	2b	7.148	3913.6
w203c4r/I0	si/1740	w203c4r/beavis/si/02jan97/1440	640	5b	3.276	5382.4
w203c4r/I0	si/1740	w203c4r/beavis/si/02jan97/1338	647	3b	3.277	5386
w203c4r/I0	si/1740	w203c4r/beavis/si/02jan97/1159	649	1b	3.277	5390.8
w190c3/REF	si/1740	w190c3/beavis/si/02jan97/1527	645	5b	3.277	5389.6
w190c3/REF	si/1740	w190c3/beavis/si/02jan97/1246	647	3b	3.277	5385.6
w190c3/REF	si/1740	w190c3/beavis/si/02jan97/1108	641	8b	3.277	5390.8
w203c4r/I0	p/2015	w203c4r/beavis/p/02jan97/2116	247	2b	3.277	4594
w203c4r/I0	p/2015	w203c4r/beavis/p/02jan97/2033	649	1b	3.277	4596
w203c4r/I0	p/2015	w203c4r/beavis/p/02jan97/1853	645	4b	3.277	4587.6
w203c4r/I0	p/2015	w203c4r/beavis/p/02jan97/1714	648	1b	3.277	4610.4
w190c3/REF	p/2015	w190c3/beavis/p/02jan97/2139	223	2b	3.277	4637.2
w190c3/REF	p/2015	w190c3/beavis/p/02jan97/1947	646	3b	3.277	4643.2
w190c3/REF	p/2015	w190c3/beavis/p/02jan97/1806	648	2b	3.277	4635.6
w190c3/REF	p/2015	w190c3/beavis/p/02jan97/1625	647	1b	3.277	4662.8
w203c4r/I0	ti/4508	w203c4r/beavis/ti/03jan97/2035	324	1b	3.277	4900
w203c4r/I0	ti/4508	w203c4r/beavis/ti/03jan97/1956	646	2b	3.277	4897.2
w203c4r/I0	ti/4508	w203c4r/beavis/ti/03jan97/1827	645	5b	3.277	4896.8
w203c4r/I0	ti/4508	w203c4r/beavis/ti/03jan97/1746	648	1b	3.277	4892
w190c3/REF	ti/4508	w190c3/beavis/ti/03jan97/2140	323	1b	3.277	4905.2
w190c3/REF	ti/4508	w190c3/beavis/ti/03jan97/2100	647	3b	3.277	4906.8
w190c3/REF	ti/4508	w190c3/beavis/ti/03jan97/1914	645	5b	3.277	4902.4
w190c3/REF	ti/4508	w190c3/beavis/ti/03jan97/1646	647	2b	3.277	4895.6
w203c4r/I0	fe55/5894	w203c4r/beavis/fe55/03jan97/1549	320	5b	3.277	3517.2
w203c4r/I0	fe55/5894	w203c4r/beavis/fe55/03jan97/1508	642	7b	3.277	3520
w203c4r/I0	fe55/5894	w203c4r/beavis/fe55/03jan97/1337	650	0n	3.277	3518
w203c4r/I0	fe55/5894	w203c4r/beavis/fe55/03jan97/1151	639	4b	3.277	3523.6
w203c4r/I0	fe55/5894	w203c4r/beavis/fe55/03jan97/1011	645	4b	3.277	3527.2
w190c3/REF	fe55/5894	w190c3/beavis/fe55/03jan97/1619	322	3b	3.277	3582.8
w190c3/REF	fe55/5894	w190c3/beavis/fe55/03jan97/1425	640	9b	3.277	3584.4
w190c3/REF	fe55/5894	w190c3/beavis/fe55/03jan97/1238	648	2b	3.277	3584.4
w190c3/REF	fe55/5894	w190c3/beavis/fe55/03jan97/1059	646	3b	3.277	3582.4
w190c3/REF	fe55/5894	w190c3/beavis/fe55/03jan97/0921	647	3b	3.277	3584.8
w203c4r/I0	cu/8040	w203c4r/beavis/cu/04jan97/1939	325	0n	3.277	2850
w203c4r/I0	cu/8040	w203c4r/beavis/cu/04jan97/1815	647	2b	3.277	2848
w203c4r/I0	cu/8040	w203c4r/beavis/cu/04jan97/1650	645	5b	3.277	2829.2
w203c4r/I0	cu/8040	w203c4r/beavis/cu/04jan97/1541	643	4b	3.277	2846
w203c4r/I0	cu/8040	w203c4r/beavis/cu/04jan97/1419	648	2b	3.277	2836.8
w203c4r/I0	cu/8040	w203c4r/beavis/cu/04jan97/1241	553	3b	3.285	2827.6
w190c3/REF	cu/8040	w190c3/beavis/cu/04jan97/2119	324	1n	3.277	2998
w190c3/REF	cu/8040	w190c3/beavis/cu/04jan97/2003	650	0n	3.277	2995.6
w190c3/REF	cu/8040	w190c3/beavis/cu/04jan97/1733	650	0n	3.277	2984
w190c3/REF	cu/8040	w190c3/beavis/cu/04jan97/1457	645	5b	3.277	3008.4
w190c3/REF	cu/8040	w190c3/beavis/cu/04jan97/1325	648	2b	3.277	2999.6
w190c3/REF	cu/8040	w190c3/beavis/cu/04jan97/1158	641	7b	3.277	2986.4

Table 4.38: w203c4r/I0 CSR Quantum Efficiency Data Sets

Chip	Target/Energy eV	Directory	Accepted Frames	Rejected Frames	Frame Time (seconds)	Counts per Frame
w193c2/I1	o/525	w193c2/butthead/o/23nov96/2100	645	5b	7.148	3278.8
w193c2/I1	o/525	w193c2/butthead/o/23nov96/1934	648	2n	7.148	3295.2
w193c2/I1	o/525	w193c2/butthead/o/23nov96/1426	645	5b	7.15	3289.2
w193c2/I1	o/525	w193c2/butthead/o/23nov96/1009	649	1b	7.15	3283.2
w103c4/REF	o/525	w103c4/butthead/o/23nov96/2239	295	4b	7.224	3748.4
w103c4/REF	o/525	w103c4/butthead/o/23nov96/1800	587	8b	7.225	3712.8
w103c4/REF	o/525	w103c4/butthead/o/23nov96/1633	551	37b	7.225	3706.4
w103c4/REF	o/525	w103c4/butthead/o/23nov96/1137	566	32b	7.224	3719.6
w103c4/REF	o/525	w103c4/butthead/o/23nov96/0842	573	24b	7.225	3724.8
w193c2/I1	f/677	w193c2/butthead/f/24nov96/2049	644	3n	7.15	1755.6
w193c2/I1	f/677	w193c2/butthead/f/24nov96/1703	647	3b	7.15	1754.4
w193c2/I1	f/677	w193c2/butthead/f/24nov96/1324	613	4n	7.15	1760.4
w193c2/I1	f/677	w193c2/butthead/f/24nov96/1108	581	7n	7.148	1756.4
w103c4/REF	f/677	w103c4/butthead/f/24nov96/2225	589	8b	7.224	2281.6
w103c4/REF	f/677	w103c4/butthead/f/24nov96/1842	595	14b	7.225	2279.2
w103c4/REF	f/677	w103c4/butthead/f/24nov96/1528	586	14b	7.224	2282.4
w103c4/REF	f/677	w103c4/butthead/f/24nov96/0954	575	11b	7.225	2284.4
w193c2/I1	f/677	w193c2/butthead/f/25nov96/1605	699	1b	7.15	1747.2
w193c2/I1	f/677	w193c2/butthead/f/25nov96/1433	692	8b	7.15	1749.6
w193c2/I1	f/677	w193c2/butthead/f/25nov96/1147	597	2b	7.15	1754
w193c2/I1	f/677	w193c2/butthead/f/25nov96/1019	598	2b	7.15	1753.2
w103c4/REF	f/677	w103c4/butthead/f/25nov96/1738	580	12b	7.225	2281.6
w103c4/REF	f/677	w103c4/butthead/f/25nov96/1311	489	14n	7.225	2281.2
w103c4/REF	f/677	w103c4/butthead/f/25nov96/0859	582	10b	7.224	2276.4
w193c2/I1	si/1740	w193c2/butthead/si/29nov96/1830	661	4n	3.277	2500.8
w193c2/I1	si/1740	w193c2/butthead/si/29nov96/1744	678	1b	3.277	2499.6
w193c2/I1	si/1740	w193c2/butthead/si/29nov96/1358	642	6b	3.277	2504.8
w193c2/I1	si/1740	w193c2/butthead/si/29nov96/1315	647	3b	3.277	2505.6
w193c2/I1	si/1740	w193c2/butthead/si/29nov96/1233	647	2b	3.277	2503.2
w193c2/I1	si/1740	w193c2/butthead/si/29nov96/1013	649	0n	3.277	2503.2
w103c4/REF	si/1740	w103c4/butthead/si/29nov96/1616	547	27n	7.226	5382.4
w103c4/REF	si/1740	w103c4/butthead/si/29nov96/1449	13	17n	7.224	5427.6
w103c4/REF	si/1740	w103c4/butthead/si/29nov96/1101	581	14b	7.224	5388.4
w193c2/I1	p/2015	w193c2/butthead/p/27nov96/2248	647	1b	3.277	1701.2
w193c2/I1	p/2015	w193c2/butthead/p/27nov96/2149	645	4b	3.277	1704
w193c2/I1	p/2015	w193c2/butthead/p/27nov96/2110	588	2n	3.277	1703.6
w193c2/I1	p/2015	w193c2/butthead/p/27nov96/1907	642	3n	3.277	1718.8
w193c2/I1	p/2015	w193c2/butthead/p/27nov96/1825	646	2n	3.277	1721.6
w193c2/I1	p/2015	w193c2/butthead/p/27nov96/1541	617	5n	3.277	1719.2
w193c2/I1	p/2015	w193c2/butthead/p/27nov96/1502	647	3b	3.277	1717.2
w193c2/I1	p/2015	w193c2/butthead/p/27nov96/1233	648	2b	3.277	1720.8
w193c2/I1	p/2015	w193c2/butthead/p/27nov96/1142	596	3b	3.277	1718.8
w103c4/REF	p/2015	w103c4/butthead/p/27nov96/2313	293	NA	7.227	3776
w103c4/REF	p/2015	w103c4/butthead/p/27nov96/1950	584	15b	7.224	3779.2
w103c4/REF	p/2015	w103c4/butthead/p/27nov96/1654	589	8b	7.225	3802
w103c4/REF	p/2015	w103c4/butthead/p/27nov96/1318	579	13b	7.225	3796.8
w103c4/REF	p/2015	w103c4/butthead/p/27nov96/1006	583	11b	7.225	3800
w193c2/I1	ti/4508	w193c2/butthead/ti/01dec96/2018	313	2n	3.277	2184.4
w193c2/I1	ti/4508	w193c2/butthead/ti/01dec96/1939	547	2n	3.277	2183.6
w193c2/I1	ti/4508	w193c2/butthead/ti/01dec96/1745	610	1n	3.277	2182.4
w193c2/I1	ti/4508	w193c2/butthead/ti/01dec96/1514	649	0n	3.277	2186
w193c2/I1	ti/4508	w193c2/butthead/ti/01dec96/1431	644	6b	3.277	2189.2
w193c2/I1	ti/4508	w193c2/butthead/ti/01dec96/1348	620	4n	3.277	2179.6
w193c2/I1	ti/4508	w193c2/butthead/ti/01dec96/1137	618	3n	3.277	2178.8
w193c2/I1	ti/4508	w193c2/butthead/ti/01dec96/1054	625	5n	3.277	2184.8
w103c4/REF	ti/4508	w103c4/butthead/ti/01dec96/2042	214	9b	7.225	4634
w103c4/REF	ti/4508	w103c4/butthead/ti/01dec96/1826	533	12b	7.225	4634.8
w103c4/REF	ti/4508	w103c4/butthead/ti/01dec96/1622	533	12b	7.225	4640
w103c4/REF	ti/4508	w103c4/butthead/ti/01dec96/0943	125	19n	7.225	4620
w193c2/I1	fe55/5894	w193c2/butthead/fe55/30nov96/1713	416	2n	3.277	3362.4
w193c2/I1	fe55/5894	w193c2/butthead/fe55/30nov96/1520	640	6b	3.277	3362
w193c2/I1	fe55/5894	w193c2/butthead/fe55/30nov96/1435	639	2b	3.28	3360
w193c2/I1	fe55/5894	w193c2/butthead/fe55/30nov96/1124	647	3b	3.277	3363.6
w103c4/REF	fe55/5894	w103c4/butthead/fe55/30nov96/1749	541	38b	7.225	6646.8
w103c4/REF	fe55/5894	w103c4/butthead/fe55/30nov96/1321	362	184b	7.225	6631.6
w103c4/REF	fe55/5894	w103c4/butthead/fe55/30nov96/0905	554	15b	7.225	6638.8
w193c2/I1	cu/8040	w193c2/butthead/cu/02dec96/1746	645	4b	3.277	1313.2
w193c2/I1	cu/8040	w193c2/butthead/cu/02dec96/1702	650	0n	3.277	1311.2
w193c2/I1	cu/8040	w193c2/butthead/cu/02dec96/1426	646	2b	3.277	1334.4
w193c2/I1	cu/8040	w193c2/butthead/cu/02dec96/1224	647	3b	3.277	1293.6
w193c2/I1	cu/8040	w193c2/butthead/cu/02dec96/1136	644	5b	3.277	1294.8
w193c2/I1	cu/8040	w193c2/butthead/cu/02dec96/1035	638	2b	3.279	1310.8
w103c4/REF	cu/8040	w103c4/butthead/cu/02dec96/2201	571	12b	7.225	2427.2
w103c4/REF	cu/8040	w103c4/butthead/cu/02dec96/1525	482	102b	7.225	2448
w103c4/REF	cu/8040	w103c4/butthead/cu/02dec96/1312	492	77b	7.224	2478
w103c4/REF	cu/8040	w103c4/butthead/cu/02dec96/0856	558	10b	7.225	2501.2

Table 4.39: w193c2/I1 CSR Quantum Efficiency Data Sets

Chip	Target/Energy eV	Directory	Accepted Frames	Rejected Frames	Frame Time (seconds)	Counts per Frame
w158c4r/I2	o/525	w158c4r/butthead/o/26oct96/1826	595	5b	7.148	3732
w158c4r/I2	o/525	w158c4r/butthead/o/26oct96/0158	299	1b	7.15	3720.4
w103c4/REF	o/525	w103c4/butthead/o/26oct96/1706	588	9b	7.225	4059.2
w103c4/REF	o/525	w103c4/butthead/o/26oct96/0114	298	2b	7.224	4060.8
w158c4r/I2	o/525	w158c4r/butthead/o/31oct96/2018	137	0n	7.149	3620.4
w158c4r/I2	o/525	w158c4r/butthead/o/31oct96/1849	663	7b	7.15	3543.2
w158c4r/I2	o/525	w158c4r/butthead/o/31oct96/1724	667	3b	7.15	3511.2
w158c4r/I2	o/525	w158c4r/butthead/o/31oct96/1417	664	6b	7.15	3599.6
w158c4r/I2	o/525	w158c4r/butthead/o/31oct96/1256	593	7b	7.15	3538.4
w103c4/REF	o/525	w103c4/butthead/o/31oct96/2222	194	6b	7.225	3951.6
w103c4/REF	o/525	w103c4/butthead/o/31oct96/2050	588	12b	7.224	3928.8
w103c4/REF	o/525	w103c4/butthead/o/31oct96/1554	571	29b	7.225	3820.4
w103c4/REF	o/525	w103c4/butthead/o/31oct96/1123	588	12b	7.224	3876.4
w103c4/REF	o/525	w103c4/butthead/o/31oct96/0951	590	10b	7.224	3956.8
w158c4r/I2	f/677	w158c4r/butthead/f/01nov96/1853	643	7b	7.15	1830.8
w158c4r/I2	f/677	w158c4r/butthead/f/01nov96/1730	642	8b	7.15	1832.8
w158c4r/I2	f/677	w158c4r/butthead/f/01nov96/1232	695	5b	7.15	1830.8
w158c4r/I2	f/677	w158c4r/butthead/f/01nov96/1038	342	2b	7.149	1831.6
w103c4/REF	f/677	w103c4/butthead/f/01nov96/2030	590	8b	7.224	2268.4
w103c4/REF	f/677	w103c4/butthead/f/01nov96/1609	587	10b	7.224	2270.4
w103c4/REF	f/677	w103c4/butthead/f/01nov96/1444	584	11b	7.225	2272
w103c4/REF	f/677	w103c4/butthead/f/01nov96/0901	588	11b	7.225	2276.4
w158c4r/I2	f/677	w158c4r/butthead/f/06nov96/1935	647	3b	7.148	1817.2
w158c4r/I2	f/677	w158c4r/butthead/f/06nov96/1631	648	2b	7.15	1818
w158c4r/I2	f/677	w158c4r/butthead/f/06nov96/1453	648	2b	7.15	1818.8
w103c4/REF	f/677	w103c4/butthead/f/06nov96/2130	588	7b	7.227	2257.2
w103c4/REF	f/677	w103c4/butthead/f/06nov96/1807	582	16b	7.226	2263.2
w103c4/REF	f/677	w103c4/butthead/f/06nov96/1311	550	NA	7.225	2247.6
w158c4r/I2	si/1740	w158c4r/butthead/si/29oct96/2059	425	3b	3.277	1701.2
w158c4r/I2	si/1740	w158c4r/butthead/si/29oct96/2018	641	9b	3.277	1700
w158c4r/I2	si/1740	w158c4r/butthead/si/29oct96/1920	653	0n	3.278	1698.4
w158c4r/I2	si/1740	w158c4r/butthead/si/29oct96/1840	647	3b	3.277	1699.2
w158c4r/I2	si/1740	w158c4r/butthead/si/29oct96/1213	647	3b	3.277	1698
w158c4r/I2	si/1740	w158c4r/butthead/si/29oct96/1123	648	2b	3.277	1692.8
w103c4/REF	si/1740	w103c4/butthead/si/29oct96/2133	559	13b	7.224	3688.8
w103c4/REF	si/1740	w103c4/butthead/si/29oct96/1722	540	17b	7.225	3686.8
w103c4/REF	si/1740	w103c4/butthead/si/29oct96/0943	560	33b	7.225	3678.8
w158c4r/I2	si/1740	w158c4r/butthead/si/05nov96/1535	643	3b	3.277	1686.4
w158c4r/I2	si/1740	w158c4r/butthead/si/05nov96/1449	642	8b	3.277	1690.4
w158c4r/I2	si/1740	w158c4r/butthead/si/05nov96/1201	640	4b	3.274	1688.4
w103c4/REF	si/1740	w103c4/butthead/si/05nov96/1625	563	7b	7.225	3668.8
w103c4/REF	si/1740	w103c4/butthead/si/05nov96/1323	536	11b	7.225	3671.6
w103c4/REF	si/1740	w103c4/butthead/si/05nov96/1017	534	15b	7.225	3666
w158c4r/I2	p/2015	w158c4r/butthead/p/30oct96/2029	646	3b	3.279	1733.2
w158c4r/I2	p/2015	w158c4r/butthead/p/30oct96/1940	644	4b	3.277	1735.2
w158c4r/I2	p/2015	w158c4r/butthead/p/30oct96/1602	646	4b	3.277	1732
w158c4r/I2	p/2015	w158c4r/butthead/p/30oct96/1459	649	1b	3.277	1730.8
w158c4r/I2	p/2015	w158c4r/butthead/p/30oct96/1252	645	4b	3.277	1732
w158c4r/I2	p/2015	w158c4r/butthead/p/30oct96/1155	642	8b	3.278	1730.4
w158c4r/I2	p/2015	w158c4r/butthead/p/30oct96/1105	644	6b	3.277	1730.8
w103c4/REF	p/2015	w103c4/butthead/p/30oct96/1825	434	111b	7.225	3776
w103c4/REF	p/2015	w103c4/butthead/p/30oct96/1338	499	43b	7.225	3773.2
w103c4/REF	p/2015	w103c4/butthead/p/30oct96/0930	529	20b	7.225	3771.2
w158c4r/I2	p/2015	w158c4r/butthead/p/05nov96/2112	633	2b	3.277	1699.6
w158c4r/I2	p/2015	w158c4r/butthead/p/05nov96/2030	646	4b	3.277	1695.2
w158c4r/I2	p/2015	w158c4r/butthead/p/05nov96/1950	646	2b	3.278	1698
w158c4r/I2	p/2015	w158c4r/butthead/p/05nov96/1909	641	8b	3.277	1700.4
w103c4/REF	p/2015	w103c4/butthead/p/05nov96/2219	560	13b	7.224	3703.2
w103c4/REF	p/2015	w103c4/butthead/p/05nov96/2159	100	NA	7.225	3698.4
w103c4/REF	p/2015	w103c4/butthead/p/05nov96/1746	561	12b	7.225	3702.4
w158c4r/I2	ti/4508	w158c4r/butthead/ti/04nov96/2011	643	1b	3.28	2226
w158c4r/I2	ti/4508	w158c4r/butthead/ti/04nov96/1915	648	2b	3.277	2222.8
w158c4r/I2	ti/4508	w158c4r/butthead/ti/04nov96/1834	647	2b	3.277	2222
w158c4r/I2	ti/4508	w158c4r/butthead/ti/04nov96/1559	647	3b	3.277	2225.2
w158c4r/I2	ti/4508	w158c4r/butthead/ti/04nov96/1455	649	NA	3.277	2222
w158c4r/I2	ti/4508	w158c4r/butthead/ti/04nov96/1238	648	1b	3.277	2224.4
w158c4r/I2	ti/4508	w158c4r/butthead/ti/04nov96/1146	647	3b	3.277	2225.6
w103c4/REF	ti/4508	w103c4/butthead/ti/04nov96/2145	565	7b	7.225	4705.2
w103c4/REF	ti/4508	w103c4/butthead/ti/04nov96/1657	569	6b	7.225	4699.6
w103c4/REF	ti/4508	w103c4/butthead/ti/04nov96/1324	558	17b	7.225	4707.2
w103c4/REF	ti/4508	w103c4/butthead/ti/04nov96/1016	584	12b	7.225	4701.2
w158c4r/I2	fe55/5894	w158c4r/butthead/fe55/27oct96/2044	631	7b	3.28	3438.8
w158c4r/I2	fe55/5894	w158c4r/butthead/fe55/27oct96/2003	643	4b	3.277	3437.6
w158c4r/I2	fe55/5894	w158c4r/butthead/fe55/27oct96/1655	648	2b	3.277	3441.2
w158c4r/I2	fe55/5894	w158c4r/butthead/fe55/27oct96/1414	648	2b	3.277	3442.8
w103c4/REF	fe55/5894	w103c4/butthead/fe55/27oct96/2128	506	50b	7.225	6798
w103c4/REF	fe55/5894	w103c4/butthead/fe55/27oct96/1753	550	10b	7.224	6801.6
w103c4/REF	fe55/5894	w103c4/butthead/fe55/27oct96/1238	555	15b	7.225	6801.2

Table 4.40: w158c4r/I2 CSR Quantum Efficiency Data Sets - continued on next page

Chip	Target/Energy eV	Directory	Accepted Frames	Rejected Frames	Frame Time (seconds)	Counts per Frame
w158c4r/I2	cu/8040	w158c4r/butthead/cu/02nov96/2018	649	1b	3.277	1300.4
w158c4r/I2	cu/8040	w158c4r/butthead/cu/02nov96/1920	642	6b	3.277	1303.6
w158c4r/I2	cu/8040	w158c4r/butthead/cu/02nov96/1817	644	6b	3.277	1300.4
w158c4r/I2	cu/8040	w158c4r/butthead/cu/02nov96/1720	648	2b	3.277	1300.8
w158c4r/I2	cu/8040	w158c4r/butthead/cu/02nov96/1436	595	5b	3.277	1301.6
w158c4r/I2	cu/8040	w158c4r/butthead/cu/02nov96/1355	596	3b	3.277	1304.8
w103c4/REF	cu/8040	w103c4/butthead/cu/02nov96/2104	558	9b	7.225	2442.4
w103c4/REF	cu/8040	w103c4/butthead/cu/02nov96/1552	558	12b	7.225	2444.4
w103c4/REF	cu/8040	w103c4/butthead/cu/02nov96/1056	548	17b	7.225	2448.8

Table 4.41: w158c4r/I2 CSR Quantum Efficiency Data Sets - continued from previous page

Chip	Target/Energy eV	Directory	Accepted Frames	Rejected Frames	Frame Time (seconds)	Counts per Frame
w215c2r/I3	o/525	w215c2r/beavis/o/07jan97/2013	149	1b	7.148	2756.4
w215c2r/I3	o/525	w215c2r/beavis/o/07jan97/1848	647	3b	7.148	2764
w215c2r/I3	o/525	w215c2r/beavis/o/07jan97/1724	648	2b	7.148	2768.4
w215c2r/I3	o/525	w215c2r/beavis/o/07jan97/1417	646	4b	7.148	2771.6
w215c2r/I3	o/525	w215c2r/beavis/o/07jan97/1118	649	1b	7.148	2781.2
w190c3/REF	o/525	w190c3/beavis/o/07jan97/2210	247	3b	7.148	2752.4
w190c3/REF	o/525	w190c3/beavis/o/07jan97/2045	645	3n	7.148	2754
w190c3/REF	o/525	w190c3/beavis/o/07jan97/1551	606	37b	7.148	2762
w190c3/REF	o/525	w190c3/beavis/o/07jan97/1247	610	22n	7.148	2765.6
w190c3/REF	o/525	w190c3/beavis/o/07jan97/0949	641	5n	7.148	2775.2
w215c2r/I3	o/525	w215c2r/beavis/o/08jan97/1216	246	4b	7.148	2758.8
w215c2r/I3	o/525	w215c2r/beavis/o/08jan97/1050	645	5b	7.148	2753.6
w190c3/REF	o/525	w190c3/beavis/o/08jan97/1307	250	0n	7.148	2748.8
w190c3/REF	o/525	w190c3/beavis/o/08jan97/0854	648	2b	7.148	2756.4
w215c2r/I3	f/677	w215c2r/beavis/f/08jan97/1948	648	2b	7.148	3954.4
w215c2r/I3	f/677	w215c2r/beavis/f/08jan97/1647	647	3b	7.148	3957.2
w215c2r/I3	f/677	w215c2r/beavis/f/08jan97/1522	648	2b	7.148	3962.4
w190c3/REF	f/677	w190c3/beavis/f/08jan97/2115	648	2b	7.148	3884.4
w190c3/REF	f/677	w190c3/beavis/f/08jan97/1816	649	1b	7.148	3885.2
w190c3/REF	f/677	w190c3/beavis/f/08jan97/1345	647	3b	7.148	3891.6
w215c2r/I3	f/677	w215c2r/beavis/f/09jan97/0944	648	2b	7.149	3959.6
w190c3/REF	f/677	w190c3/beavis/f/09jan97/1112	396	4b	7.148	3884.4
w190c3/REF	f/677	w190c3/beavis/f/09jan97/0856	297	3b	7.148	3883.2
w215c2r/I3	si/1740	w215c2r/beavis/si/10jan97/1301	645	3b	3.277	5251.6
w215c2r/I3	si/1740	w215c2r/beavis/si/10jan97/1120	646	4b	3.277	5254
w215c2r/I3	si/1740	w215c2r/beavis/si/10jan97/1036	646	1b	3.277	5253.2
w190c3/REF	si/1740	w190c3/beavis/si/10jan97/1358	645	5b	3.277	5243.2
w190c3/REF	si/1740	w190c3/beavis/si/10jan97/1202	646	4b	3.277	5250.4
w190c3/REF	si/1740	w190c3/beavis/si/10jan97/0938	650	0n	3.277	5246.8
w215c2r/I3	p/2015	w215c2r/beavis/p/10jan97/1957	521	3b	3.277	4482.4
w215c2r/I3	p/2015	w215c2r/beavis/p/10jan97/1918	646	3b	3.277	4484
w215c2r/I3	p/2015	w215c2r/beavis/p/10jan97/1721	644	3b	3.277	4486
w215c2r/I3	p/2015	w215c2r/beavis/p/10jan97/1555	646	2b	3.277	4488
w190c3/REF	p/2015	w190c3/beavis/p/10jan97/2044	522	0n	3.277	4513.2
w190c3/REF	p/2015	w190c3/beavis/p/10jan97/1828	646	4b	3.277	4508.8
w190c3/REF	p/2015	w190c3/beavis/p/10jan97/1638	645	4b	3.277	4503.2
w190c3/REF	p/2015	w190c3/beavis/p/10jan97/1453	642	6b	3.277	4518.4
w215c2r/I3	ti/4508	w215c2r/beavis/ti/11jan97/1339	648	1b	3.277	5136.4
w190c3/REF	ti/4508	w190c3/beavis/ti/11jan97/1456	647	2b	3.277	5140
w190c3/REF	ti/4508	w190c3/beavis/ti/11jan97/1203	646	2b	3.277	5138.4
w190c3/REF	ti/4508	w190c3/beavis/ti/11jan97/1024	522	102b	3.277	5129.2
w215c2r/I3	fe55/5894	w215c2r/beavis/fe55/11jan97/2146	199	1b	3.277	3529.2
w215c2r/I3	fe55/5894	w215c2r/beavis/fe55/11jan97/2106	647	2b	3.277	3518
w215c2r/I3	fe55/5894	w215c2r/beavis/fe55/11jan97/2025	644	5b	3.277	3516.4
w190c3/REF	fe55/5894	w190c3/beavis/fe55/11jan97/2204	391	48b	3.277	3572
w190c3/REF	fe55/5894	w190c3/beavis/fe55/11jan97/1930	622	6n	3.277	3578.8
w215c2r/I3	cu/8040	w215c2r/beavis/cu/09jan97/2047	373	2b	3.277	2808.4
w215c2r/I3	cu/8040	w215c2r/beavis/cu/09jan97/1958	640	9b	3.277	2800.8
w215c2r/I3	cu/8040	w215c2r/beavis/cu/09jan97/1826	648	1b	3.277	2780
w215c2r/I3	cu/8040	w215c2r/beavis/cu/09jan97/1659	646	4b	3.277	2795.2
w215c2r/I3	cu/8040	w215c2r/beavis/cu/09jan97/1525	645	4b	3.277	2800
w215c2r/I3	cu/8040	w215c2r/beavis/cu/09jan97/1349	648	2b	3.277	2801.2
w190c3/REF	cu/8040	w190c3/beavis/cu/09jan97/2129	150	0n	3.277	2967.2
w190c3/REF	cu/8040	w190c3/beavis/cu/09jan97/1911	647	3b	3.277	2967.2
w190c3/REF	cu/8040	w190c3/beavis/cu/09jan97/1743	648	2b	3.277	2940
w190c3/REF	cu/8040	w190c3/beavis/cu/09jan97/1614	647	3b	3.277	2964
w190c3/REF	cu/8040	w190c3/beavis/cu/09jan97/1434	645	5b	3.277	2970.4
w190c3/REF	cu/8040	w190c3/beavis/cu/09jan97/1306	649	1b	3.277	2975.2

Table 4.42: w215c2r/I3 CSR Quantum Efficiency Data Sets

Chip	Target/Energy eV	Directory	Accepted Frames	Rejected Frames	Frame Time (seconds)	Counts per Frame
w168c4r/S0	o/525	w168c4r/beavis/o/15dec96/1108	598	2b	7.15	3596
w168c4r/S0	o/525	w168c4r/beavis/o/15dec96/1540	647	3b	7.149	3588.8
w190c3/REF	o/525	w190c3/beavis/o/15dec96/0915	596	4b	7.149	3410.8
w190c3/REF	o/525	w190c3/beavis/o/15dec96/1409	644	6b	7.149	3409.6
w190c3/REF	o/525	w190c3/beavis/o/15dec96/2136	647	3b	7.149	3394.8
w168c4r/S0	o/525	w168c4r/beavis/o/16dec96/1609	593	1b	7.149	3610.4
w168c4r/S0	o/525	w168c4r/beavis/o/16dec96/1942	649	1b	7.15	3601.2
w168c4r/S0	o/525	w168c4r/beavis/o/16dec96/2113	325	NA	7.15	3603.2
w190c3/REF	o/525	w190c3/beavis/o/16dec96/0930	548	2b	7.149	3394.4
w190c3/REF	o/525	w190c3/beavis/o/16dec96/1217	549	1b	7.149	3390.8
w190c3/REF	o/525	w190c3/beavis/o/16dec96/1344	648	2b	7.149	3388.4
w190c3/REF	o/525	w190c3/beavis/o/16dec96/1803	649	1b	7.149	3393.2
w190c3/REF	o/525	w190c3/beavis/o/16dec96/2200	323	2b	7.149	3380.4
w168c4r/S0	f/677	w168c4r/beavis/f/17dec96/1135	648	2b	7.15	3886.4
w168c4r/S0	f/677	w168c4r/beavis/f/17dec96/1300	600	0n	7.15	3882
w168c4r/S0	f/677	w168c4r/beavis/f/17dec96/1608	647	3b	7.15	3884.4
w168c4r/S0	f/677	w168c4r/beavis/f/17dec96/1757	648	2b	7.149	3875.6
w168c4r/S0	f/677	w168c4r/beavis/f/17dec96/1926	199	1b	7.15	3875.2
w190c3/REF	f/677	w190c3/beavis/f/17dec96/1007	645	5b	7.148	3583.6
w190c3/REF	f/677	w190c3/beavis/f/17dec96/1429	648	2b	7.149	3575.6
w190c3/REF	f/677	w190c3/beavis/f/17dec96/2002	648	2b	7.149	3579.6
w190c3/REF	f/677	w190c3/beavis/f/17dec96/2126	648	2b	7.148	3578.4
w190c3/REF	f/677	w190c3/beavis/f/17dec96/2250	200	0n	7.148	3582.8
w168c4r/S0	si/1740	w168c4r/beavis/si/18dec96/1100	647	3b	3.277	5247.2
w168c4r/S0	si/1740	w168c4r/beavis/si/18dec96/1227	645	2b	3.277	5247.6
w168c4r/S0	si/1740	w168c4r/beavis/si/18dec96/1306	647	3b	3.277	5243.2
w190c3/REF	si/1740	w190c3/beavis/si/18dec96/1013	648	2b	3.277	5218.8
w190c3/REF	si/1740	w190c3/beavis/si/18dec96/1144	649	1b	3.277	5218.4
w190c3/REF	si/1740	w190c3/beavis/si/18dec96/1350	647	1b	3.277	5222
w168c4r/S0	p/2015	w168c4r/beavis/p/18dec96/1722	645	5b	3.277	4562.8
w168c4r/S0	p/2015	w168c4r/beavis/p/18dec96/1854	644	6b	3.277	4558
w168c4r/S0	p/2015	w168c4r/beavis/p/18dec96/1939	645	5b	3.277	4560.4
w168c4r/S0	p/2015	w168c4r/beavis/p/18dec96/2022	638	6b	3.277	4553.2
w190c3/REF	p/2015	w190c3/beavis/p/18dec96/1459	646	4b	3.277	4494.4
w190c3/REF	p/2015	w190c3/beavis/p/18dec96/1617	646	3b	3.277	4494.4
w190c3/REF	p/2015	w190c3/beavis/p/18dec96/1809	646	3b	3.277	4494.4
w190c3/REF	p/2015	w190c3/beavis/p/18dec96/2106	646	3b	3.277	4494.4
w168c4r/S0	ti/4508	w168c4r/beavis/ti/19dec96/1802	646	2b	3.277	5186.4
w168c4r/S0	ti/4508	w168c4r/beavis/ti/19dec96/1947	646	3b	3.277	5182.4
w168c4r/S0	ti/4508	w168c4r/beavis/ti/19dec96/2034	648	2b	3.277	5184
w190c3/REF	ti/4508	w190c3/beavis/ti/19dec96/1713	647	3b	3.277	5186.8
w190c3/REF	ti/4508	w190c3/beavis/ti/19dec96/1850	649	1b	3.277	5193.6
w190c3/REF	ti/4508	w190c3/beavis/ti/19dec96/2157	648	2b	3.277	5195.6
w168c4r/S0	fe55/5894	w168c4r/beavis/fe55/19dec96/0952	640	3b	3.277	3592.8
w168c4r/S0	fe55/5894	w168c4r/beavis/fe55/19dec96/1307	647	3b	3.277	3593.6
w168c4r/S0	fe55/5894	w168c4r/beavis/fe55/19dec96/1349	645	4b	3.277	3592
w168c4r/S0	fe55/5894	w168c4r/beavis/fe55/19dec96/1502	647	3b	3.277	3595.2
w168c4r/S0	fe55/5894	w168c4r/beavis/fe55/19dec96/1546	224	1b	3.277	3589.6
w190c3/REF	fe55/5894	w190c3/beavis/fe55/19dec96/0907	641	4b	3.277	3686.8
w190c3/REF	fe55/5894	w190c3/beavis/fe55/19dec96/1036	644	5b	3.277	3682.8
w190c3/REF	fe55/5894	w190c3/beavis/fe55/19dec96/1221	643	7b	3.277	3684.8
w190c3/REF	fe55/5894	w190c3/beavis/fe55/19dec96/1435	302	3b	3.277	3681.6
w190c3/REF	fe55/5894	w190c3/beavis/fe55/19dec96/1635	491	8b	3.277	3686.4
w168c4r/S0	cu/8040	w168c4r/beavis/cu/20dec96/1138	645	4b	3.277	2806
w168c4r/S0	cu/8040	w168c4r/beavis/cu/20dec96/1318	646	2b	3.277	2804.8
w168c4r/S0	cu/8040	w168c4r/beavis/cu/20dec96/1448	641	4b	3.277	2808
w168c4r/S0	cu/8040	w168c4r/beavis/cu/20dec96/1715	631	4b	3.277	2766
w168c4r/S0	cu/8040	w168c4r/beavis/cu/20dec96/1839	647	3b	3.277	2776
w168c4r/S0	cu/8040	w168c4r/beavis/cu/20dec96/1920	324	1b	3.277	2772.4
w190c3/REF	cu/8040	w190c3/beavis/cu/20dec96/1025	649	1b	3.277	2995.6
w190c3/REF	cu/8040	w190c3/beavis/cu/20dec96/1230	645	4b	3.277	3006.4
w190c3/REF	cu/8040	w190c3/beavis/cu/20dec96/1403	647	3b	3.277	3013.6
w190c3/REF	cu/8040	w190c3/beavis/cu/20dec96/1634	649	1b	3.277	2970.4
w190c3/REF	cu/8040	w190c3/beavis/cu/20dec96/1756	650	0n	3.277	2976.8
w190c3/REF	cu/8040	w190c3/beavis/cu/20dec96/1948	99	1b	3.277	2986.4

Table 4.43: w168c4r/S0 CSR Quantum Efficiency Data Sets

Chip	Target/Energy eV	Directory	Accepted Frames	Rejected Frames	Frame Time (seconds)	Counts per Frame
w140c4r/S1	c/277	w140c4r/butthead/c/08mar97/1445	712	3b	3.277	2356
w140c4r/S1	c/277	w140c4r/butthead/c/08mar97/1239	717	3b	3.277	2370.4
w140c4r/S1	c/277	w140c4r/butthead/c/08mar97/1132	706	13b	3.277	2380
w140c4r/S1	c/277	w140c4r/butthead/c/08mar97/1039	712	8b	3.277	2378.4
w140c4r/S1	c/277	w140c4r/butthead/c/08mar97/0624	695	5b	3.277	2426.8
w140c4r/S1	c/277	w140c4r/butthead/c/08mar97/0412	692	6b	3.277	2476.4
w134c4r/S3	c/277	w134c4r/butthead/c/08mar97/1544	524	196b	3.277	2348.4
w134c4r/S3	c/277	w134c4r/butthead/c/08mar97/1341	719	1b	3.277	2356
w134c4r/S3	c/277	w134c4r/butthead/c/08mar97/0921	715	5b	3.277	2390
w134c4r/S3	c/277	w134c4r/butthead/c/08mar97/0835	706	13b	3.277	2400.8
w134c4r/S3	c/277	w134c4r/butthead/c/08mar97/0539	687	3b	3.277	2452.4
w134c4r/S3	c/277	w134c4r/butthead/c/08mar97/0304	687	13b	3.277	2315.6
w140c4r/S1	o/525	w140c4r/butthead/o/07mar97/2337	696	4b	3.277	4804.8
w140c4r/S1	o/525	w140c4r/butthead/o/07mar97/2202	699	1b	3.277	4800.8
w134c4r/S3	o/525	w134c4r/butthead/o/07mar97/2250	616	83b	3.277	4634.8
w134c4r/S3	o/525	w134c4r/butthead/o/07mar97/2108	622	370b	3.277	4656.4
w140c4r/S1	o/525	w140c4r/butthead/o/08mar97/0216	688	2b	3.277	4826.8
w140c4r/S1	o/525	w140c4r/butthead/o/08mar97/0126	699	1b	3.277	4839.2
w134c4r/S3	o/525	w134c4r/butthead/o/08mar97/0240	349	1b	3.277	4676.8
w134c4r/S3	o/525	w134c4r/butthead/o/08mar97/0020	639	60b	3.277	4668.8
w140c4r/S1	f/677	w140c4r/butthead/f/23jan97/2114	647	1b	3.277	2550
w140c4r/S1	f/677	w140c4r/butthead/f/23jan97/2035	649	1b	3.277	2542.8
w140c4r/S1	f/677	w140c4r/butthead/f/23jan97/1830	650	0n	3.277	2552.4
w140c4r/S1	f/677	w140c4r/butthead/f/23jan97/1745	649	1b	3.277	2554
w140c4r/S1	f/677	w140c4r/butthead/f/23jan97/1525	649	1b	3.277	2506
w140c4r/S1	f/677	w140c4r/butthead/f/23jan97/1432	646	2b	3.277	2548
w103c4/REF	f/677	w103c4/butthead/f/23jan97/2202	248	105b	7.226	2220.8
w103c4/REF	f/677	w103c4/butthead/f/23jan97/1913	568	27b	7.227	2220.4
w103c4/REF	f/677	w103c4/butthead/f/23jan97/1612	566	77b	7.227	2220.8
w103c4/REF	f/677	w103c4/butthead/f/23jan97/1302	532	131b	7.226	2222
w140c4r/S1	si/1740	w140c4r/butthead/si/20jan97/1839	325	0n	3.277	2645.2
w140c4r/S1	si/1740	w140c4r/butthead/si/20jan97/1754	649	1b	3.277	2644.8
w140c4r/S1	si/1740	w140c4r/butthead/si/20jan97/1706	619	31b	3.277	2626.4
w140c4r/S1	si/1740	w140c4r/butthead/si/20jan97/1436	614	36b	3.277	2655.6
w140c4r/S1	si/1740	w140c4r/butthead/si/20jan97/1354	650	0n	3.277	2651.6
w140c4r/S1	si/1740	w140c4r/butthead/si/20jan97/1213	650	0n	3.277	2640
w140c4r/S1	si/1740	w140c4r/butthead/si/20jan97/1054	650	0n	3.277	2655.2
w103c4/REF	si/1740	w103c4/butthead/si/20jan97/1909	554	266b	7.227	5355.6
w103c4/REF	si/1740	w103c4/butthead/si/20jan97/1524	557	335b	7.227	5354.8
w103c4/REF	si/1740	w103c4/butthead/si/20jan97/1218	552	371b	7.227	5366
w103c4/REF	si/1740	w103c4/butthead/si/20jan97/0936	538	438b	7.226	5354.8
w140c4r/S1	p/2015	w140c4r/butthead/p/21jan97/2341	648	1b	3.277	2486
w140c4r/S1	p/2015	w140c4r/butthead/p/21jan97/2259	647	1b	3.277	2501.2
w140c4r/S1	p/2015	w140c4r/butthead/p/21jan97/2055	643	3b	3.277	2495.6
w140c4r/S1	p/2015	w140c4r/butthead/p/21jan97/2013	648	1b	3.277	2506
w140c4r/S1	p/2015	w140c4r/butthead/p/21jan97/1932	649	1b	3.277	2510
w140c4r/S1	p/2015	w140c4r/butthead/p/21jan97/1427	648	1b	3.277	2470.4
w140c4r/S1	p/2015	w140c4r/butthead/p/21jan97/1347	646	2b	3.277	2487.2
w140c4r/S1	p/2015	w140c4r/butthead/p/21jan97/1138	649	1b	3.277	2487.2
w140c4r/S1	p/2015	w140c4r/butthead/p/21jan97/1059	648	0n	3.277	2486
w140c4r/S1	p/2015	w140c4r/butthead/p/21jan97/0023	324	0n	3.277	2500
w103c4/REF	p/2015	w103c4/butthead/p/21jan97/2140	357	293b	7.227	3753.6
w103c4/REF	p/2015	w103c4/butthead/p/21jan97/1814	571	244b	7.227	3757.2
w103c4/REF	p/2015	w103c4/butthead/p/21jan97/1222	563	153b	7.226	3713.2
w103c4/REF	p/2015	w103c4/butthead/p/21jan97/0900	562	54b	7.227	3718.4
w103c4/REF	p/2015	w103c4/butthead/p/21jan97/0047	35	163b	7.226	3733.6
w140c4r/S1	ti/4508	w140c4r/butthead/ti/25jan97/2107	649	1b	3.277	2070
w140c4r/S1	ti/4508	w140c4r/butthead/ti/25jan97/2026	648	1b	3.277	2061.2
w140c4r/S1	ti/4508	w140c4r/butthead/ti/25jan97/1802	644	4b	3.277	2064.8
w140c4r/S1	ti/4508	w140c4r/butthead/ti/25jan97/1716	643	5b	3.277	2048.8
w140c4r/S1	ti/4508	w140c4r/butthead/ti/25jan97/1427	648	2b	3.277	2041.2
w140c4r/S1	ti/4508	w140c4r/butthead/ti/25jan97/1345	647	3b	3.277	2036.4
w103c4/REF	ti/4508	w103c4/butthead/ti/25jan97/2154	247	6b	7.227	4697.6
w103c4/REF	ti/4508	w103c4/butthead/ti/25jan97/1847	521	202b	7.226	4694.8
w103c4/REF	ti/4508	w103c4/butthead/ti/25jan97/1514	220	365b	7.227	4693.6
w103c4/REF	ti/4508	w103c4/butthead/ti/25jan97/1226	559	15b	7.226	4697.6
w140c4r/S1	fe55/5894	w140c4r/butthead/fe55/24jan97/1951	323	2b	3.277	2481.2
w140c4r/S1	fe55/5894	w140c4r/butthead/fe55/24jan97/1820	645	5b	3.277	2474.4
w140c4r/S1	fe55/5894	w140c4r/butthead/fe55/24jan97/1738	647	1b	3.277	2475.6
w140c4r/S1	fe55/5894	w140c4r/butthead/fe55/24jan97/1547	649	1b	3.277	2481.6
w140c4r/S1	fe55/5894	w140c4r/butthead/fe55/24jan97/1505	646	2b	3.277	2474.8
w140c4r/S1	fe55/5894	w140c4r/butthead/fe55/24jan97/1218	648	2b	3.277	2470.4
w103c4/REF	fe55/5894	w103c4/butthead/fe55/24jan97/2023	125	NA	7.227	6416.8
w103c4/REF	fe55/5894	w103c4/butthead/fe55/24jan97/1630	432	262b	7.227	6406
w103c4/REF	fe55/5894	w103c4/butthead/fe55/24jan97/1343	524	66b	7.227	6412.4
w103c4/REF	fe55/5894	w103c4/butthead/fe55/24jan97/1058	562	159b	7.226	6418.4

Table 4.44: w140c4r/S1 CSR Quantum Efficiency Data Sets - continued on next page

Chip	Target/Energy eV	Directory	Accepted Frames	Rejected Frames	Frame Time (seconds)	Counts per Frame
w140c4r/S1	cu/8040	w140c4r/butthead/cu/26jan97/2054	647	2b	3.277	837.6
w140c4r/S1	cu/8040	w140c4r/butthead/cu/26jan97/2018	649	1b	3.277	835.6
w140c4r/S1	cu/8040	w140c4r/butthead/cu/26jan97/1933	645	3b	3.277	838.8
w140c4r/S1	cu/8040	w140c4r/butthead/cu/26jan97/1645	649	1b	3.277	839.6
w140c4r/S1	cu/8040	w140c4r/butthead/cu/26jan97/1605	647	2b	3.277	833.2
w140c4r/S1	cu/8040	w140c4r/butthead/cu/26jan97/1510	646	2b	3.277	832.8
w140c4r/S1	cu/8040	w140c4r/butthead/cu/26jan97/1304	645	5b	3.277	837.6
w140c4r/S1	cu/8040	w140c4r/butthead/cu/26jan97/1219	646	3b	3.277	840
w140c4r/S1	cu/8040	w140c4r/butthead/cu/26jan97/1047	648	0n	3.277	838.8
w103c4/REF	cu/8040	w103c4/butthead/cu/26jan97/2137	557	19b	7.226	2464.8
w103c4/REF	cu/8040	w103c4/butthead/cu/26jan97/1805	476	314b	7.226	2469.2
w103c4/REF	cu/8040	w103c4/butthead/cu/26jan97/1305	463	152b	7.227	2468.8
w103c4/REF	cu/8040	w103c4/butthead/cu/26jan97/0922	562	15b	7.227	2478
w140c4r/S1	cu/8040	w140c4r/butthead/cu/27jan97/2009	649	1b	3.277	836.8
w140c4r/S1	cu/8040	w140c4r/butthead/cu/27jan97/1928	649	0n	3.277	829.6
w140c4r/S1	cu/8040	w140c4r/butthead/cu/27jan97/1848	650	0n	3.277	838
w140c4r/S1	cu/8040	w140c4r/butthead/cu/27jan97/1559	646	3b	3.277	830.8
w140c4r/S1	cu/8040	w140c4r/butthead/cu/27jan97/1519	650	0n	3.277	839.2
w140c4r/S1	cu/8040	w140c4r/butthead/cu/27jan97/1438	646	3b	3.277	842
w140c4r/S1	cu/8040	w140c4r/butthead/cu/27jan97/1211	649	1b	3.277	828.8
w140c4r/S1	cu/8040	w140c4r/butthead/cu/27jan97/1128	648	4b	3.277	831.2
w140c4r/S1	cu/8040	w140c4r/butthead/cu/27jan97/1046	648	1b	3.277	834.4
w103c4/REF	cu/8040	w103c4/butthead/cu/27jan97/2104	561	11b	7.227	2490.8
w103c4/REF	cu/8040	w103c4/butthead/cu/27jan97/1654	544	29b	7.227	2493.2
w103c4/REF	cu/8040	w103c4/butthead/cu/27jan97/1300	566	8b	7.227	2494
w103c4/REF	cu/8040	w103c4/butthead/cu/27jan97/0910	330	68b	7.227	2523.2

Table 4.45: w140c4r/S1 CSR Quantum Efficiency Data Sets - continued from previous page

Chip	Target/Energy eV	Directory	Accepted Frames	Rejected Frames	Frame Time (seconds)	Counts per Frame
w182c4r/S2	o/525	w182c4r/butthead/o/18dec96/2221	198	2b	7.148	2303.2
w182c4r/S2	o/525	w182c4r/butthead/o/18dec96/1930	649	1b	7.148	2327.6
w182c4r/S2	o/525	w182c4r/butthead/o/18dec96/1805	647	3b	7.148	2333.2
w182c4r/S2	o/525	w182c4r/butthead/o/18dec96/1244	646	4b	7.148	2399.6
w182c4r/S2	o/525	w182c4r/butthead/o/18dec96/1111	598	2b	7.148	2422
w103c4/REF	o/525	w103c4/butthead/o/18dec96/2225	280	14b	7.227	2316
w103c4/REF	o/525	w103c4/butthead/o/18dec96/2100	577	17b	7.227	2321.2
w103c4/REF	o/525	w103c4/butthead/o/18dec96/1553	576	16b	7.227	2358.8
w103c4/REF	o/525	w103c4/butthead/o/18dec96/1432	561	26b	7.227	2378.4
w103c4/REF	o/525	w103c4/butthead/o/18dec96/0933	512	81b	7.227	2431.2
w182c4r/S2	o/525	w182c4r/butthead/o/19dec96/1527	640	10b	7.148	2258.8
w182c4r/S2	o/525	w182c4r/butthead/o/19dec96/1408	599	1b	7.148	2246
w182c4r/S2	o/525	w182c4r/butthead/o/19dec96/1249	593	7b	7.148	2236
w103c4/REF	o/525	w103c4/butthead/o/19dec96/1709	581	17b	7.227	2232
w103c4/REF	o/525	w103c4/butthead/o/19dec96/1109	577	17b	7.227	2274.8
w103c4/REF	o/525	w103c4/butthead/o/19dec96/0911	587	9b	7.227	2306.8
w182c4r/S2	f/677	w182c4r/butthead/f/19dec96/2131	324	1n	7.148	2155.6
w182c4r/S2	f/677	w182c4r/butthead/f/19dec96/1953	648	2b	7.148	2155.2
w103c4/REF	f/677	w103c4/butthead/f/19dec96/2217	349	10b	7.227	2253.2
w103c4/REF	f/677	w103c4/butthead/f/19dec96/1835	567	22b	7.227	2250.4
w182c4r/S2	f/677	w182c4r/butthead/f/20dec96/1958	698	2b	7.148	2162
w182c4r/S2	f/677	w182c4r/butthead/f/20dec96/1827	697	3b	7.148	2159.6
w182c4r/S2	f/677	w182c4r/butthead/f/20dec96/1531	696	4b	7.148	2154
w182c4r/S2	f/677	w182c4r/butthead/f/20dec96/1137	560	7n	7.148	2168.4
w103c4/REF	f/677	w103c4/butthead/f/20dec96/2131	575	20b	7.226	2259.6
w103c4/REF	f/677	w103c4/butthead/f/20dec96/1704	576	19b	7.227	2260.8
w103c4/REF	f/677	w103c4/butthead/f/20dec96/1401	549	47b	7.227	2261.6
w103c4/REF	f/677	w103c4/butthead/f/20dec96/1015	578	21b	7.226	2264.4
w182c4r/S2	si/1740	w182c4r/butthead/si/21dec96/1829	362	6n	3.277	2516.4
w182c4r/S2	si/1740	w182c4r/butthead/si/21dec96/1747	627	6n	3.277	2521.2
w182c4r/S2	si/1740	w182c4r/butthead/si/21dec96/1659	633	6n	3.277	2523.2
w182c4r/S2	si/1740	w182c4r/butthead/si/21dec96/1442	628	8n	3.277	2523.6
w182c4r/S2	si/1740	w182c4r/butthead/si/21dec96/1403	622	5n	3.277	2518.8
w182c4r/S2	si/1740	w182c4r/butthead/si/21dec96/1152	633	6n	3.277	2520.8
w182c4r/S2	si/1740	w182c4r/butthead/si/21dec96/1109	596	5n	3.277	2517.6
w103c4/REF	si/1740	w103c4/butthead/si/21dec96/1903	196	4b	7.226	5330.8
w103c4/REF	si/1740	w103c4/butthead/si/21dec96/1534	583	13b	7.227	5326
w103c4/REF	si/1740	w103c4/butthead/si/21dec96/1236	584	12b	7.227	5328.4
w103c4/REF	si/1740	w103c4/butthead/si/21dec96/0925	577	19b	7.227	5321.2
w182c4r/S2	p/2015	w182c4r/butthead/p/22dec96/2013	637	7b	3.277	1776
w182c4r/S2	p/2015	w182c4r/butthead/p/22dec96/1933	647	3b	3.277	1777.6
w182c4r/S2	p/2015	w182c4r/butthead/p/22dec96/1705	643	3b	3.277	1773.2
w182c4r/S2	p/2015	w182c4r/butthead/p/22dec96/1626	643	6b	3.277	1772.4
w182c4r/S2	p/2015	w182c4r/butthead/p/22dec96/1420	642	3b	3.277	1772.8
w182c4r/S2	p/2015	w182c4r/butthead/p/22dec96/1341	645	5b	3.277	1768.8
w182c4r/S2	p/2015	w182c4r/butthead/p/22dec96/1054	581	4n	3.277	1776.4
w103c4/REF	p/2015	w103c4/butthead/p/22dec96/2100	556	15b	7.226	3754
w103c4/REF	p/2015	w103c4/butthead/p/22dec96/1755	562	15b	7.227	3754.8
w103c4/REF	p/2015	w103c4/butthead/p/22dec96/1506	550	20b	7.226	3753.6
w103c4/REF	p/2015	w103c4/butthead/p/22dec96/0915	570	19b	7.226	3748.4
w182c4r/S2	ti/4508	w182c4r/butthead/ti/31dec96/2045	646	4b	3.277	2174.4
w182c4r/S2	ti/4508	w182c4r/butthead/ti/31dec96/1842	646	2b	3.277	2170.4
w182c4r/S2	ti/4508	w182c4r/butthead/ti/31dec96/1757	646	4b	3.277	2170.4
w182c4r/S2	ti/4508	w182c4r/butthead/ti/31dec96/1455	623	6b	3.277	2170.4
w182c4r/S2	ti/4508	w182c4r/butthead/ti/31dec96/1214	642	7b	3.277	2168
w182c4r/S2	ti/4508	w182c4r/butthead/ti/31dec96/1131	649	1b	3.277	2170
w103c4/REF	ti/4508	w103c4/butthead/ti/31dec96/2132	167	32b	7.226	4566
w103c4/REF	ti/4508	w103c4/butthead/ti/31dec96/1939	240	9b	7.227	4582.8
w103c4/REF	ti/4508	w103c4/butthead/ti/31dec96/1617	548	24b	7.226	4570.4
w103c4/REF	ti/4508	w103c4/butthead/ti/31dec96/1316	443	125b	7.227	4575.6
w103c4/REF	ti/4508	w103c4/butthead/ti/31dec96/1017	552	22b	7.227	4574.8
w182c4r/S2	fe55/5894	w182c4r/butthead/fe55/30dec96/2132	647	3b	3.277	3386.8
w182c4r/S2	fe55/5894	w182c4r/butthead/fe55/30dec96/1544	587	5n	3.277	3369.2
w182c4r/S2	fe55/5894	w182c4r/butthead/fe55/30dec96/1501	606	6n	3.277	3385.2
w182c4r/S2	fe55/5894	w182c4r/butthead/fe55/30dec96/1256	584	7n	3.277	3385.6
w182c4r/S2	fe55/5894	w182c4r/butthead/fe55/30dec96/1212	562	8n	3.277	3376
w103c4/REF	fe55/5894	w103c4/butthead/fe55/30dec96/2314	99	1b	7.227	6499.2
w103c4/REF	fe55/5894	w103c4/butthead/fe55/30dec96/1714	293	7b	7.227	6512
w103c4/REF	fe55/5894	w103c4/butthead/fe55/30dec96/1341	561	13b	7.226	6515.6
w103c4/REF	fe55/5894	w103c4/butthead/fe55/30dec96/1052	546	23b	7.227	6517.6

Table 4.46: w182c4r/S2 CSR Quantum Efficiency Data Sets - continued on next page

Chip	Target/Energy eV	Directory	Accepted Frames	Rejected Frames	Frame Time (seconds)	Counts per Frame
w182c4r/S2	cu/8040	w182c4r/butthead/cu/02jan97/2212	644	6b	3.277	1360.4
w103c4/REF	cu/8040	w103c4/butthead/cu/02jan97/2256	231	20b	7.227	2372.4
w103c4/REF	cu/8040	w103c4/butthead/cu/02jan97/2103	284	13b	7.227	2363.6
w182c4r/S2	cu/8040	w182c4r/butthead/cu/03jan97/2353	521	4b	3.277	1423.2
w182c4r/S2	cu/8040	w182c4r/butthead/cu/03jan97/2318	520	5b	3.277	1422.4
w182c4r/S2	cu/8040	w182c4r/butthead/cu/03jan97/2112	636	9b	3.277	1416.8
w182c4r/S2	cu/8040	w182c4r/butthead/cu/03jan97/2031	637	6b	3.277	1417.6
w182c4r/S2	cu/8040	w182c4r/butthead/cu/03jan97/1945	643	7b	3.277	1418.8
w182c4r/S2	cu/8040	w182c4r/butthead/cu/03jan97/1737	646	4b	3.277	1420.8
w182c4r/S2	cu/8040	w182c4r/butthead/cu/03jan97/1640	645	5b	3.277	1421.2
w182c4r/S2	cu/8040	w182c4r/butthead/cu/03jan97/1430	645	4b	3.277	1419.6
w182c4r/S2	cu/8040	w182c4r/butthead/cu/03jan97/1349	644	6b	3.277	1421.2
w103c4/REF	cu/8040	w103c4/butthead/cu/03jan97/2158	560	11b	7.227	2440.4
w103c4/REF	cu/8040	w103c4/butthead/cu/03jan97/1821	61	512b	7.227	2452.8
w103c4/REF	cu/8040	w103c4/butthead/cu/03jan97/1521	501	68b	7.226	2455.6
w103c4/REF	cu/8040	w103c4/butthead/cu/03jan97/1132	476	91b	7.225	2452.8
w103c4/REF	cu/8040	w103c4/butthead/cu/03jan97/0034	376	188b	7.227	2430.8
w182c4r/S2	cu/8040	w182c4r/butthead/cu/04jan97/1411	449	1b	3.277	1419.2
w182c4r/S2	cu/8040	w182c4r/butthead/cu/04jan97/1157	648	2b	3.277	1416.8
w103c4/REF	cu/8040	w103c4/butthead/cu/04jan97/1603	423	150b	7.226	2437.2
w103c4/REF	cu/8040	w103c4/butthead/cu/04jan97/1448	480	94b	7.227	2442
w103c4/REF	cu/8040	w103c4/butthead/cu/04jan97/1249	337	NA	7.227	2436.4
w103c4/REF	cu/8040	w103c4/butthead/cu/04jan97/1036	518	51b	7.227	2456.8

Table 4.47: w182c4r/S2 CSR Quantum Efficiency Data Sets - continued from previous page

Chip	Target/Energy eV	Directory	Accepted Frames	Rejected Frames	Frame Time (seconds)	Counts per Frame
w134c4r/S3	c/277	w134c4r/butthead/c/08mar97/0304	687	13b	3.277	2315.6
w134c4r/S3	c/277	w134c4r/butthead/c/08mar97/0539	687	3b	3.277	2452.4
w134c4r/S3	c/277	w134c4r/butthead/c/08mar97/0835	706	13b	3.277	2400.8
w134c4r/S3	c/277	w134c4r/butthead/c/08mar97/0921	715	5b	3.277	2390
w134c4r/S3	c/277	w134c4r/butthead/c/08mar97/1341	719	1b	3.277	2356
w134c4r/S3	c/277	w134c4r/butthead/c/08mar97/1544	524	196b	3.277	2348.4
w140c4r/S1	c/277	w140c4r/butthead/c/08mar97/0412	692	6b	3.277	2476.4
w140c4r/S1	c/277	w140c4r/butthead/c/08mar97/0624	695	5b	3.277	2426.8
w140c4r/S1	c/277	w140c4r/butthead/c/08mar97/1039	712	8b	3.277	2378.4
w140c4r/S1	c/277	w140c4r/butthead/c/08mar97/1132	706	13b	3.277	2380
w140c4r/S1	c/277	w140c4r/butthead/c/08mar97/1239	717	3b	3.277	2370.4
w140c4r/S1	c/277	w140c4r/butthead/c/08mar97/1445	712	3b	3.277	2356
w134c4r/S3	o/525	w134c4r/butthead/o/02feb97/1525	648	2b	3.277	4164.8
w134c4r/S3	o/525	w134c4r/butthead/o/02feb97/1753	650	0n	3.277	4151.6
w134c4r/S3	o/525	w134c4r/butthead/o/02feb97/2030	648	1b	3.277	4164
w134c4r/S3	o/525	w134c4r/butthead/o/02feb97/2249	300	0n	3.277	4130
w203c2/REF	o/525	w203c2/butthead/o/02feb97/1314	628	22b	7.148	2666.4
w203c2/REF	o/525	w203c2/butthead/o/02feb97/1614	645	5b	7.148	2672.4
w203c2/REF	o/525	w203c2/butthead/o/02feb97/1857	625	5b	7.148	2583.6
w203c2/REF	o/525	w203c2/butthead/o/02feb97/2118	623	7b	7.148	2615.2
w203c2/REF	o/525	w203c2/butthead/o/02feb97/2317	623	7b	7.148	2635.2
w134c4r/S3	f/677	w134c4r/butthead/f/03feb97/1438	643	5b	3.277	2504.4
w134c4r/S3	f/677	w134c4r/butthead/f/03feb97/1702	647	0n	3.277	2510
w134c4r/S3	f/677	w134c4r/butthead/f/03feb97/1917	649	1b	3.277	2506
w134c4r/S3	f/677	w134c4r/butthead/f/03feb97/2127	649	1b	3.277	2505.6
w134c4r/S3	f/677	w134c4r/butthead/f/03feb97/2332	649	1b	3.277	2501.2
w203c2/REF	f/677	w203c2/butthead/f/03feb97/1015	646	4b	7.148	1405.6
w203c2/REF	f/677	w203c2/butthead/f/03feb97/1315	645	5b	7.148	1398.4
w203c2/REF	f/677	w203c2/butthead/f/03feb97/1532	645	5b	7.148	1393.6
w203c2/REF	f/677	w203c2/butthead/f/03feb97/1746	646	4b	7.148	1394.4
w203c2/REF	f/677	w203c2/butthead/f/03feb97/2000	647	3b	7.148	1390.8
w203c2/REF	f/677	w203c2/butthead/f/03feb97/2210	646	4b	7.148	1388.4
w203c2/REF	f/677	w203c2/butthead/f/04feb97/0019	644	4b	7.148	1388.4
w203c2/REF	f/677	w203c2/butthead/f/04feb97/0148	649	4b	7.148	1388.4
w203c2/REF	f/677	w203c2/butthead/f/04feb97/0312	647	4b	7.148	1388.4
w134c4r/S3	si/1740	w134c4r/butthead/si/04feb97/0957	648	1b	3.277	5545.6
w134c4r/S3	si/1740	w134c4r/butthead/si/04feb97/1122	649	1b	3.277	5550
w134c4r/S3	si/1740	w134c4r/butthead/si/04feb97/1205	455	1b	3.277	5540
w203c2/REF	si/1740	w203c2/butthead/si/04feb97/0904	615	5b	3.277	4993.6
w203c2/REF	si/1740	w203c2/butthead/si/04feb97/1039	646	2b	3.277	4991.2
w203c2/REF	si/1740	w203c2/butthead/si/04feb97/1239	646	2b	3.277	4992.8
w134c4r/S3	p/2015	w134c4r/butthead/p/04feb97/1427	648	2b	3.277	4560.4
w134c4r/S3	p/2015	w134c4r/butthead/p/04feb97/1738	649	1b	3.277	4560.4
w134c4r/S3	p/2015	w134c4r/butthead/p/04feb97/1833	473	2b	3.277	4564.4
w203c2/REF	p/2015	w203c2/butthead/p/04feb97/1341	646	4b	3.277	3036.4
w203c2/REF	p/2015	w203c2/butthead/p/04feb97/1511	644	6b	3.277	3037.6
w203c2/REF	p/2015	w203c2/butthead/p/04feb97/1732	640	6b	3.277	3030.8
w203c2/REF	p/2015	w203c2/butthead/p/04feb97/1907	680	5b	3.277	3036
w134c4r/S3	ti/4508	w134c4r/butthead/ti/05feb97/0931	646	2b	3.277	4559.2
w134c4r/S3	ti/4508	w134c4r/butthead/ti/05feb97/1027	648	0n	3.277	4594
w203c2/REF	ti/4508	w203c2/butthead/ti/05feb97/0843	357	292b	3.277	4626
w203c2/REF	ti/4508	w203c2/butthead/ti/05feb97/1117	647	2b	3.277	4627.6
w134c4r/S3	fe55/5894	w134c4r/butthead/fe55/04feb97/2047	648	1b	3.277	2832
w134c4r/S3	fe55/5894	w134c4r/butthead/fe55/04feb97/2212	646	1b	3.277	2812
w134c4r/S3	fe55/5894	w134c4r/butthead/fe55/04feb97/2310	646	3b	3.277	2825.2
w134c4r/S3	fe55/5894	w134c4r/butthead/fe55/04feb97/2350	648	0n	3.277	2839.2
w203c2/REF	fe55/5894	w203c2/butthead/fe55/04feb97/2001	640	6b	3.277	3215.6
w203c2/REF	fe55/5894	w203c2/butthead/fe55/04feb97/2130	645	5b	3.277	3212
w203c2/REF	fe55/5894	w203c2/butthead/fe55/05feb97/0116	648	2b	3.277	3214.8
w203c2/REF	fe55/5894	w203c2/butthead/fe55/05feb97/0156	649	0n	3.277	3214.4
w134c4r/S3	cu/8040	w134c4r/butthead/cu/05feb97/2139	646	3b	3.277	2409.2
w134c4r/S3	cu/8040	w134c4r/butthead/cu/05feb97/2221	649	0n	3.277	2392
w203c2/REF	cu/8040	w203c2/butthead/cu/05feb97/2043	643	nun		
w203c2/REF	cu/8040	w203c2/butthead/cu/05feb97/2333	647	nun		
w134c4r/S3	cu/8040	w134c4r/butthead/cu/06feb97/0024	375	0n	3.277	2415.6
w203c2/REF	cu/8040	w203c2/butthead/cu/06feb97/0109	100	0n	3.277	2886.8

Table 4.48: w134c4r/S3 CSR Quantum Efficiency Data Sets

Chip	Target/Energy eV	Directory	Accepted Frames	Rejected Frames	Frame Time (seconds)	Counts per Frame
w457c4/S4	o/525	w457c4/beavis/o/29nov96/2108	692	3b	7.15	3561.6
w457c4/S4	o/525	w457c4/beavis/o/29nov96/1936	690	5b	7.149	3563.2
w457c4/S4	o/525	w457c4/beavis/o/29nov96/1556	698	2b	7.149	3555.2
w457c4/S4	o/525	w457c4/beavis/o/29nov96/1157	598	2b	7.149	3574
w190c3/REF	o/525	w190c3/beavis/o/29nov96/2245	692	3b	7.149	3481.6
w190c3/REF	o/525	w190c3/beavis/o/29nov96/1757	692	3b	7.149	3485.6
w190c3/REF	o/525	w190c3/beavis/o/29nov96/1407	596	4b	7.149	3475.6
w190c3/REF	o/525	w190c3/beavis/o/29nov96/1023	422	2b	7.149	3490.8
w457c4/S4	o/525	w457c4/beavis/o/30nov96/1231	352	5b	7.15	3548
w457c4/S4	o/525	w457c4/beavis/o/30nov96/1037	647	3b	7.149	3550.4
w190c3/REF	o/525	w190c3/beavis/o/30nov96/1401	447	3b	7.149	3483.6
w190c3/REF	o/525	w190c3/beavis/o/30nov96/0857	697	3b	7.149	3488.8
w457c4/S4	f/677	w457c4/beavis/f/30nov96/2112	646	4b	7.149	3903.2
w457c4/S4	f/677	w457c4/beavis/f/30nov96/1822	647	3b	7.149	3896
w457c4/S4	f/677	w457c4/beavis/f/30nov96/1659	648	2b	7.15	3870.8
w190c3/REF	f/677	w190c3/beavis/f/30nov96/2239	648	2b	7.149	3644.8
w190c3/REF	f/677	w190c3/beavis/f/30nov96/1947	648	2b	7.149	3643.2
w190c3/REF	f/677	w190c3/beavis/f/30nov96/1523	647	3b	7.149	3631.2
w457c4/S4	si/1740	w457c4/beavis/si/03dec96/1304	648	2b	3.277	5518.8
w457c4/S4	si/1740	w457c4/beavis/si/03dec96/1216	646	4b	3.277	5520
w457c4/S4	si/1740	w457c4/beavis/si/03dec96/1029	648	2b	3.277	5512.4
w190c3/REF	si/1740	w190c3/beavis/si/03dec96/1359	648	1n	3.277	5468.4
w190c3/REF	si/1740	w190c3/beavis/si/03dec96/1117	647	2b	3.277	5456.8
w190c3/REF	si/1740	w190c3/beavis/si/03dec96/0933	645	4b	3.277	5452.4
w457c4/S4	p/2015	w457c4/beavis/p/03dec96/2120	123	NA	3.277	4600.8
w457c4/S4	p/2015	w457c4/beavis/p/03dec96/1923	643	4b	3.277	4602.8
w457c4/S4	p/2015	w457c4/beavis/p/03dec96/1727	651	2b	3.277	4601.6
w190c3/REF	p/2015	w190c3/beavis/p/03dec96/2217	405	1b	3.277	4555.6
w190c3/REF	p/2015	w190c3/beavis/p/03dec96/2027	633	5b	3.277	4558
w190c3/REF	p/2015	w190c3/beavis/p/03dec96/1825	634	NA	3.278	4554.4
w190c3/REF	p/2015	w190c3/beavis/p/03dec96/1646	644	1b	3.277	4370.4
w457c4/S4	ti/4508	w457c4/beavis/ti/04dec96/2019	648	2b	3.277	5091.6
w457c4/S4	ti/4508	w457c4/beavis/ti/04dec96/1937	642	5b	3.277	5088.4
w457c4/S4	ti/4508	w457c4/beavis/ti/04dec96/1855	646	4b	3.277	5091.6
w190c3/REF	ti/4508	w190c3/beavis/ti/04dec96/2306	64	1b	3.277	5052.8
w190c3/REF	ti/4508	w190c3/beavis/ti/04dec96/2144	435	1b	3.277	5068
w190c3/REF	ti/4508	w190c3/beavis/ti/04dec96/2101	645	5b	3.277	5069.2
w190c3/REF	ti/4508	w190c3/beavis/ti/04dec96/1804	648	2b	3.277	5061.6
w457c4/S4	fe55/5894	w457c4/beavis/fe55/04dec96/1700	150	0n	3.277	3741.2
w457c4/S4	fe55/5894	w457c4/beavis/fe55/04dec96/1440	648	2b	3.277	3744
w457c4/S4	fe55/5894	w457c4/beavis/fe55/04dec96/1344	646	4b	3.277	3744.8
w457c4/S4	fe55/5894	w457c4/beavis/fe55/04dec96/1206	645	4b	3.277	3747.2
w457c4/S4	fe55/5894	w457c4/beavis/fe55/04dec96/1014	648	5b	3.277	3742.4
w190c3/REF	fe55/5894	w190c3/beavis/fe55/04dec96/1737	150	0n	3.277	3731.6
w190c3/REF	fe55/5894	w190c3/beavis/fe55/04dec96/1533	647	3b	3.277	3729.6
w190c3/REF	fe55/5894	w190c3/beavis/fe55/04dec96/1254	645	5b	3.277	3730
w190c3/REF	fe55/5894	w190c3/beavis/fe55/04dec96/1113	641	5b	3.277	3732.4
w190c3/REF	fe55/5894	w190c3/beavis/fe55/04dec96/0925	645	4b	3.277	3734.4
w457c4/S4	cu/8040	w457c4/beavis/cu/05dec96/2017	519	1b	3.277	3209.2
w457c4/S4	cu/8040	w457c4/beavis/cu/05dec96/1646	650	0n	3.277	3198.4
w457c4/S4	cu/8040	w457c4/beavis/cu/05dec96/1549	645	4b	3.277	3201.2
w457c4/S4	cu/8040	w457c4/beavis/cu/05dec96/1343	644	6b	3.277	3202
w457c4/S4	cu/8040	w457c4/beavis/cu/05dec96/1208	645	3b	3.277	3202.4
w190c3/REF	cu/8040	w190c3/beavis/cu/05dec96/2056	514	5b	3.277	3179.2
w190c3/REF	cu/8040	w190c3/beavis/cu/05dec96/1834	644	4b	3.277	3158.4
w190c3/REF	cu/8040	w190c3/beavis/cu/05dec96/1430	646	3b	3.277	3194
w190c3/REF	cu/8040	w190c3/beavis/cu/05dec96/1252	646	6b	3.277	3193.2
w190c3/REF	cu/8040	w190c3/beavis/cu/05dec96/1017	644	3b	3.277	3203.6

Table 4.49: w457c4/S4 CSR Quantum Efficiency Data Sets

Chip	Target/Energy eV	Directory	Accepted Frames	Rejected Frames	Frame Time (seconds)	Counts per Frame
w201c3r/S5	o/525	w201c3r/beavis/o/07dec96/1854	650	NA	7.15	3467.6
w201c3r/S5	o/525	w201c3r/beavis/o/07dec96/1705	650	NA	7.149	3471.2
w201c3r/S5	o/525	w201c3r/beavis/o/07dec96/1513	344	5b	7.15	3475.6
w190c3/REF	o/525	w190c3/beavis/o/07dec96/2026	645	5b	7.149	3416.4
w190c3/REF	o/525	w190c3/beavis/o/07dec96/1532	649	1b	7.149	3366
w190c3/REF	o/525	w190c3/beavis/o/07dec96/1238	646	4b	7.149	3471.6
w201c3r/S5	o/525	w201c3r/beavis/o/08dec96/1525	648	2b	7.15	3445.6
w201c3r/S5	o/525	w201c3r/beavis/o/08dec96/1324	647	3b	7.15	3444.8
w190c3/REF	o/525	w190c3/beavis/o/08dec96/1806	648	2b	7.149	3430.4
w190c3/REF	o/525	w190c3/beavis/o/08dec96/1150	648	2b	7.149	3434.4
w201c3r/S5	f/677	w201c3r/beavis/f/08dec96/2235	399	1b	7.15	3728.8
w190c3/REF	f/677	w190c3/beavis/f/08dec96/2344	198	2b	7.15	3629.6
w190c3/REF	f/677	w190c3/beavis/f/08dec96/2049	84	0n	7.149	3622.4
w201c3r/S5	f/677	w201c3r/beavis/f/09dec96/2219	574	1b	7.15	3714
w201c3r/S5	f/677	w201c3r/beavis/f/09dec96/1806	362	0n	7.15	3716.8
w201c3r/S5	f/677	w201c3r/beavis/f/09dec96/1609	574	1b	7.149	3717.2
w201c3r/S5	f/677	w201c3r/beavis/f/09dec96/1054	649	1b	7.149	3723.6
w190c3/REF	f/677	w190c3/beavis/f/09dec96/1923	562	4b	7.149	3612.4
w190c3/REF	f/677	w190c3/beavis/f/09dec96/1415	572	3b	7.149	3628.8
w190c3/REF	f/677	w190c3/beavis/f/09dec96/1238	572	3b	7.149	3622
w201c3r/S5	si/1740	w201c3r/beavis/si/10dec96/1321	573	2b	3.277	5557.6
w201c3r/S5	si/1740	w201c3r/beavis/si/10dec96/1238	647	3b	3.277	5546.8
w201c3r/S5	si/1740	w201c3r/beavis/si/10dec96/1055	647	NA	3.277	5550
w190c3/REF	si/1740	w190c3/beavis/si/10dec96/1402	575	NA	3.277	5544.8
w190c3/REF	si/1740	w190c3/beavis/si/10dec96/1147	646	2b	3.277	5543.6
w190c3/REF	si/1740	w190c3/beavis/si/10dec96/0921	650	5b	3.277	5536.8
w201c3r/S5	p/2015	w201c3r/beavis/p/10dec96/2123	299	1b	3.277	4542
w201c3r/S5	p/2015	w201c3r/beavis/p/10dec96/2033	642	1n	3.279	4546.4
w201c3r/S5	p/2015	w201c3r/beavis/p/10dec96/1810	644	4b	3.277	4544.4
w201c3r/S5	p/2015	w201c3r/beavis/p/10dec96/1558	648	1b	3.277	4551.2
w190c3/REF	p/2015	w190c3/beavis/p/10dec96/2156	349	1b	3.277	4563.2
w190c3/REF	p/2015	w190c3/beavis/p/10dec96/1858	644	3b	3.277	4566.4
w190c3/REF	p/2015	w190c3/beavis/p/10dec96/1720	650	NA	3.277	4571.6
w190c3/REF	p/2015	w190c3/beavis/p/10dec96/1502	643	4b	3.277	4570.8
w201c3r/S5	ti/4508	w201c3r/beavis/ti/12dec96/1555	147	3b	3.277	5066.8
w201c3r/S5	ti/4508	w201c3r/beavis/ti/12dec96/1456	646	4b	3.277	5068.4
w201c3r/S5	ti/4508	w201c3r/beavis/ti/12dec96/1327	668	7b	3.277	5068.4
w201c3r/S5	ti/4508	w201c3r/beavis/ti/12dec96/1141	637	11b	3.277	5071.2
w190c3/REF	ti/4508	w190c3/beavis/ti/12dec96/1613	399	1b	3.277	5064
w190c3/REF	ti/4508	w190c3/beavis/ti/12dec96/1235	645	3b	3.277	5022.8
w190c3/REF	ti/4508	w190c3/beavis/ti/12dec96/1002	649	1b	3.277	5082.4
w201c3r/S5	fe55/5894	w201c3r/beavis/fe55/11dec96/1730	546	4b	3.277	3714.8
w201c3r/S5	fe55/5894	w201c3r/beavis/fe55/11dec96/1645	639	7b	3.277	3723.2
w201c3r/S5	fe55/5894	w201c3r/beavis/fe55/11dec96/1426	646	4b	3.277	3712
w201c3r/S5	fe55/5894	w201c3r/beavis/fe55/11dec96/1235	646	4b	3.277	3718.4
w201c3r/S5	fe55/5894	w201c3r/beavis/fe55/11dec96/1056	255	2b	3.277	3717.6
w190c3/REF	fe55/5894	w190c3/beavis/fe55/11dec96/1331	460	4b	3.277	3715.6
w190c3/REF	fe55/5894	w190c3/beavis/fe55/11dec96/1141	646	4b	3.277	3711.2
w190c3/REF	fe55/5894	w190c3/beavis/fe55/11dec96/1008	647	1b	3.277	3714.4
w201c3r/S5	cu/8040	w201c3r/beavis/cu/12dec96/2101	643	1b	3.28	2989.6
w201c3r/S5	cu/8040	w201c3r/beavis/cu/12dec96/1923	645	3b	3.277	3002.4
w201c3r/S5	cu/8040	w201c3r/beavis/cu/12dec96/1754	646	1b	3.277	2996.8
w190c3/REF	cu/8040	w190c3/beavis/cu/12dec96/2007	644	6b	3.277	2960.8
w190c3/REF	cu/8040	w190c3/beavis/cu/12dec96/1838	649	NA	3.277	2983.2
w190c3/REF	cu/8040	w190c3/beavis/cu/12dec96/1644	645	4b	3.277	2984.8
w201c3r/S5	cu/8040	w201c3r/beavis/cu/13dec96/2019	400	0n	3.277	3057.2
w201c3r/S5	cu/8040	w201c3r/beavis/cu/13dec96/1940	649	1b	3.277	3052.8
w190c3/REF	cu/8040	w190c3/beavis/cu/13dec96/2054	399	1b	3.277	3028
w190c3/REF	cu/8040	w190c3/beavis/cu/13dec96/1857	643	4b	3.277	3041.6

Table 4.50: w201c3r/S5 CSR Quantum Efficiency Data Sets

Data File	Description
*_rt.evlist	ACIS RV format eventlist
*_rt_bias_avg.fits	mean bias frame
*_bias.000?.fits	sample bias frames
*_frame.000?.fits	sample data frames
*.mca.summary	ascii file summarizing the dataset
*.mca.data	IDL save file including average overclock level, average overclock noise, total number of events, peak location, peak width, and number of events under the peak as a function of frame number.
*.mca.spec	IDL save file including number of events as a function of energy, quadrant, and grade, and an image of the g02346 events under the peak in 32x32 pixel bins.
products/*g0234_img.fits	number density map of detected events in g0234.
products/*g0.qdp	for each quadrant, the pulse height histogram of g0 events.
products/*g0234.qdp	for each quadrant, the pulse height histogram of g0234 events.
products/*g0234_lightcv.qdp	for each quadrant, g0234 count rate as a function of frame number.
prodcuts/*pcf.qdp	for each quadrant, pulse height histograms of each grade.
products/*neighborhist*.qdp	for each quadrant, histograms of corner, top, bottom, left, and right pixel distributions of detected events.

Table 4.51: CSR Database Products

The data products in each directory are summarized in Table 4.51. See MIT ACIS memo PS-71 dated 4 May 1995, by J. Woo (which can be found at http://acis.mit.edu/ttools/acis-analysis.html) for a detailed description of the file formats.

4.7.1.5 IDL Data Products

Each data set in the CSR subassembly calibration database has several files created by and for IDL procedures. These include the .evlist, .mca.data, .mca.summary, and .mca.spec files.

The .evlist file is an RV format event list. See http://acis.mit.edu/ttools/acis-analysis.html for a description of the file format.

The .mca.data file is an IDL file created by the "save" command. The variables saved in this file are biasl, noise, evlog, peaknum, width, peakloc, bad_data, and good_data. biasl is an array that contains the frame number and the average overclock value for each of the four quadrants for each frame. noise is an array that contains the frame number, the standard deviation of the overclocks for each of the four quadrants, the total number of

overclock pixels above the event threshold, the difference between pixels at the top of the image area and those at the bottom of the image area, and the difference between pixels in the image area and pixels in the overclocks for each frame. evlog is an array that contains the number of pixels above threshold, the total number of events, the number of g0234 events in all energies, and the number of g0 events in all energies for each frame. peaknum is an array that contains the total number of counts under the gaussian fit to the main peak of the cumulative g02346 spectrum for each quadrant for each frame. width is an array that contains the width of the gaussian fit to the main peak of the cumulative g02346 spectrum for each quadrant for each frame. peakloc is an array that contains the location in ADU of the gaussian fit to the main peak of the cumulative g02346 spectrum for each quadrant for each frame. bad_data is an array containing the frame number of all unacceptable frames (these frames are not included in the event list). good_data is an array containing the frame number of all acceptable frames.

The .mca.summary file is an ascii file that summarizes the data set. Included in the summary file are the thresholds used, the integration time (msec per frame), the total number of requested frames, the total number of acceptable frames, the total number of frames with unacceptable noise, the total number of frames with overclock pixels over the event threshold, the average overclock level, the average overclock standard deviation, the location (in ADU) of the fitted g02346 peak, the sigma (in ADU) of the fitted g02346 peak, the FWHM (in eV) of the fitted g02346 peak, the total number of counts in the fitted g02346 peak, the number of counts per frame in the fitted g02346 peak, a summary of the total number of events (all energies) in each grade, the branching ratios for each grade, and the counts per frame (all energies) for each grade for each quadrant.

The .mca.spec file is an IDL file created by the "save" command. The variables saved in this file are spectrum, uniplot, and badcol. spectrum is an array that contains the number of events per channel for each quadrant for each grade. uniplot is a 32 x 32 array of the uniformity of the g02346 events under the peak. Each value is the total number of g02346 events under the peak for a 32 x 32 pixel region (in chip coordinates). badcol is an array that contains the total number of events in the g02346 peak per column (in chip coordinates).

4.7.2 Relative Quantum Efficiency Measured at MIT CSR

Here we present results of relative quantum efficiency (QE) measurements made at MIT CSR. In section 4.7.2.1 we discuss spatially-averaged relative quantum efficiency measurements and their internal consistency. In section 4.7.2.2 we discuss spatial variations in relative quantum efficiency.

4.7.2.1 Spatially-averaged Relative Quantum Efficiency Measurements

The results of the relative quantum efficiency measurements described above in Section 4.7.1 are presented in Table 4.52. The mean relative efficiencies given in the table are the centroids obtained from Gaussian fits to histograms of the superpixel ratios in each measurement. These values have been corrected for pileup and are our best estimates for the spatially averaged relative efficiency between the corresponding flight and reference detectors. Listed in parentheses are measurements of the spatial variation (RMS) in efficiency across each chip, obtained by computing the standard deviation of the superpixel ratios. (Note that the RMS variations in efficiency are heavily influenced the framestore cover shielding at the edge of each device. An alternative measure of spatial variation, which is more representative of the majority of the area of each device, is presented and discussed in Figures 4.77–4.86 in section 4.7.2.2.) The name of the reference device used during each measurement is listed in the table, along with the focal plane position of each flight device. Note the QE ratio listed for w140c4r at 525 eV is referenced to w134c4r, a backside chip. No measurement relative to w103c4 was made at this energy because of time constraints. Also, the QE ratio for w134c4r relative to w203c2 at 677 eV was derived from the corresponding ratio for w140c4r relative to w134c4r. This was necessary because reference device w203c2 was misaligned during calibration of w134c4r at this energy.

The correction factors used to correct the count rates at CSR for pileup are presented in Table 4.53. The values listed in parenthesis are the pileup correction factors applied to the count rates from the reference devices.

In Table 4.54 we have used the values given in Table 4.52 to compute QE ratios referenced to w190c3 for each flight device. The results are plotted in Figure 4.76. Most of the relative efficiency points in the upper panel of the figure lie within 5% of unity, and all but two of the points lie within 10%, indicating that at each energy the absolute efficiencies of the eight frontside devices are nearly identical. In the lower panel we see the backside devices are about three times more efficient than the frontside devices at low energies ($<$ 1 keV), but are less efficient than the frontside devices at high energies ($>$ 3–4 keV).

We have computed the mean relative efficiency and the maximum absolute deviation from the mean for each CCD type as a function of energy (see Table 4.55). The largest absolute deviations from the mean ($\sim$10–20%) in the frontside devices are at 525 eV, 677 eV, and 8 keV. The deviations at 525 eV and 677 eV are due to the high relative efficiency of w182c4r at these energies, which in turn is caused by that detector's relatively thin oxide layer. The reason for the large deviations at 8 keV is still unknown.

From the RMS variations listed in Table 4.54 it can be seen that spatial variations in efficiency across the frontside devices are low ($\sim$3–6%). About two-thirds of the RMS variation is the result of shadowing by the framestore covers. Thus, we find the detection efficiencies of the frontside devices are highly uniform within each chip and between the chips.

The spatial variations in efficiency across the backside devices are generally larger ($\sim$5–

Flight Device	Position	Mean (RMS) Relative Efficiency vs. Energy (keV)							Reference Device
		0.525	0.677	1.740	2.015	4.509	5.894	8.040	
		O	F	Si	P	Ti	Fe55	Cu	
w203c4r	I0	0.972 (0.040)	0.992 (0.041)	0.996 (0.046)	0.982 (0.046)	0.994 (0.046)	0.977 (0.045)	0.933 (0.043)	w190c3
w193c2	I1	0.885 (0.045)	0.768 (0.040)	0.980 (0.052)	0.951 (0.049)	1.005 (0.054)	1.034 (0.055)	1.097 (0.060)	w103c4
w158c4r	I2	0.914 (0.040)	0.804 (0.037)	0.986 (0.047)	0.968 (0.045)	1.007 (0.047)	1.029 (0.048)	1.096 (0.055)	w103c4
w215c2r	I3	0.999 (0.041)	1.015 (0.040)	0.997 (0.051)	0.989 (0.050)	0.996 (0.052)	0.980 (0.053)	0.929 (0.046)	w190c3
w168c4r	S0	1.064 (0.042)	1.089 (0.044)	1.004 (0.050)	1.014 (0.050)	0.997 (0.050)	0.972 (0.048)	0.916 (0.047)	w190c3
w182c4r	S2	1.009 (0.042)	0.962 (0.042)	1.003 (0.053)	1.002 (0.052)	1.014 (0.053)	1.067 (0.055)	1.210 (0.064)	w103c4
w457c4	S4	1.020 (0.030)	1.070 (0.043)	1.005 (0.031)	1.020 (0.032)	1.000 (0.031)	0.999 (0.031)	1.000 (0.031)	w190c3
w201c3r	S5	1.004 (0.032)	1.025 (0.034)	1.001 (0.038)	0.991 (0.037)	1.000 (0.039)	1.000 (0.039)	1.005 (0.040)	w190c3
w140c4r	S1	1.030 (0.037)	1.078 (0.038)						w134c4r
			2.507 (0.114)	1.035 (0.050)	1.442 (0.082)	0.934 (0.080)	0.763 (0.054)	0.631 (0.041)	w103c4
w134c4r	S3	3.457 (0.113)	2.955 (0.184)	1.108 (0.061)	1.570 (0.087)	1.014 (0.061)	0.882 (0.054)	0.743 (0.051)	w203c2
w190c3	Ref.	0.890 (0.020)	0.767 (0.017)	0.986 (0.018)	0.949 (0.014)	1.010 (0.014)	1.058 (0.016)	1.164 (0.051)	w103c4
w203c2	Ref.	0.872 (0.016)	0.787 (0.016)	0.979 (0.015)	0.950 (0.015)	1.004 (0.015)	1.009 (0.016)	1.041 (0.021)	w103c4

Table 4.52: Spatially Averaged Relative Detection Efficiency at CSR

8%) than in the frontside devices, but the maximum absolute deviations from the mean of the backside devices are of comparable amplitude to those of the frontside devices. Hence the spatially averaged quantum efficiencies of the two backside devices are in reasonably good agreement with each other.

4.7.2.1.1 Uncertainties in the Cross-calibration of Reference Detectors at 8 keV. The cross-calibration of the two reference detectors w190c3 and w103c4 requires special discussion. The first cross-calibration measurements were made in 1996 April, be-

Flight Device	Position	Flight (Reference) Pileup Correction vs. Energy (keV)							Reference Device
		0.525	0.677	1.740	2.015	4.509	5.894	8.040	
		O	F	Si	P	Ti	Fe55	Cu	
w203c4r	I0	1.053 (1.055)	1.074 (1.075)	1.075 (1.076)	1.097 (1.100)	1.063 (1.064)	1.068 (1.070)	1.169 (1.185)	w190c3
w193c2	I1	1.061 (1.071)	1.031 (1.041)	1.033 (1.076)	1.033 (1.079)	1.026 (1.060)	1.064 (1.146)	1.067 (1.142)	w103c4
w158c4r	I2	1.068 (1.076)	1.032 (1.041)	1.022 (1.050)	1.033 (1.078)	1.027 (1.061)	1.066 (1.151)	1.066 (1.141)	w103c4
w215c2r	I3	1.051 (1.051)	1.075 (1.075)	1.073 (1.074)	1.095 (1.097)	1.066 (1.067)	1.068 (1.070)	1.166 (1.182)	w190c3
w168c4r	S0	1.068 (1.064)	1.074 (1.068)	1.073 (1.074)	1.097 (1.096)	1.067 (1.068)	1.070 (1.073)	1.166 (1.184)	w190c3
w182c4r	S2	1.042 (1.042)	1.039 (1.041)	1.033 (1.075)	1.034 (1.078)	1.026 (1.059)	1.065 (1.143)	1.073 (1.140)	w103c4
w457c4	S4	1.067 (1.066)	1.074 (1.069)	1.078 (1.078)	1.098 (1.096)	1.066 (1.066)	1.073 (1.074)	1.200 (1.201)	w190c3
w201c3r	S5	1.065 (1.065)	1.070 (1.069)	1.078 (1.079)	1.096 (1.098)	1.065 (1.066)	1.072 (1.073)	1.184 (1.184)	w190c3
w140c4r	S1	1.073 (1.072)	1.037 (1.034)						w134c4r
			1.037 (1.040)	1.030 (1.076)	1.048 (1.078)	1.032 (1.061)	1.049 (1.140)	1.018 (1.144)	w103c4
w134c4r	S3	1.063 (1.049)	1.033 (1.031)	1.068 (1.070)	1.096 (1.062)	1.077 (1.060)	1.057 (1.062)	1.057 (1.176)	w203c2
w190c3	Ref.	1.062 (1.070)	1.070 (1.093)	1.067 (1.069)	1.091 (1.097)	1.052 (1.119)	1.078 (1.172)	1.087 (1.166)	w103c4
w203c2	Ref.	1.035 (1.041)	1.031 (1.040)	1.034 (1.078)	1.032 (1.076)	1.026 (1.059)	1.056 (1.127)	1.070 (1.158)	w103c4

Table 4.53: Pileup Correction Factors Applied to Count Rates from CSR

fore we understood how rapidly pileup probability rises with increasing energy. As a result, the fluences used were fairly high ($\sim$ 2000 and $\sim$ 3600 counts per CCD per frametime for w103c4 and w190c3, respectively) and the pileup corrections were large (12% and 23%, respectively). For this reason, the measurements at 8 keV were repeated in 1997 October at fluences about a factor of two lower. The (pileup-corrected) estimates of relative QE (w190c3:w103c4) at 8 keV obtained from these two measurements are substantially different: 1.210 for the earlier, higher-flux measurement, and 1.110 for the later one. Relative QE measurements at 5.9 keV made at these two epochs agree to within 2%.

Flight Device	Position	Mean (RMS) Relative Efficiency vs. Energy (keV)						
		0.525	0.677	1.740	2.015	4.509	5.894	8.040
		O	F	Si	P	Ti	Fe55	Cu
w203c4r	I0	0.972 (0.040)	0.992 (0.041)	0.996 (0.046)	0.982 (0.046)	0.994 (0.046)	0.977 (0.045)	0.933 (0.043)
w193c2	I1	0.994 (0.053)	1.002 (0.054)	0.994 (0.056)	1.002 (0.053)	0.996 (0.055)	0.977 (0.054)	0.942 (0.076)
w158c4r	I2	1.027 (0.048)	1.049 (0.050)	1.000 (0.050)	1.020 (0.050)	0.997 (0.049)	0.972 (0.049)	0.941 (0.073)
w215c2r	I3	0.999 (0.041)	1.015 (0.040)	0.997 (0.051)	0.989 (0.050)	0.996 (0.052)	0.980 (0.053)	0.929 (0.046)
w168c4r	S0	1.064 (0.042)	1.089 (0.044)	1.004 (0.050)	1.014 (0.050)	0.997 (0.050)	0.972 (0.048)	0.916 (0.047)
w182c4r	S2	1.133 (0.052)	1.255 (0.058)	1.017 (0.057)	1.056 (0.056)	1.005 (0.055)	1.008 (0.055)	1.039 (0.083)
w457c4	S4	1.020 (0.030)	1.070 (0.043)	1.005 (0.031)	1.020 (0.032)	1.000 (0.031)	0.999 (0.031)	1.000 (0.031)
w201c3r	S5	1.004 (0.032)	1.025 (0.034)	1.001 (0.038)	0.991 (0.037)	1.000 (0.039)	1.000 (0.039)	1.005 (0.040)
w140c4r	S1	3.487 (0.190)	3.269 (0.154)	1.050 (0.054)	1.519 (0.088)	0.925 (0.080)	0.721 (0.053)	0.542 (0.047)
w134c4r	S3	3.386 (0.139)	3.032 (0.203)	1.100 (0.065)	1.572 (0.093)	1.008 (0.064)	0.841 (0.055)	0.664 (0.062)

Table 4.54: Spatially Averaged Relative Detection Efficiency at CSR—Referenced to w190c3

Device Type	Mean (Max. Abs. Dev.) Relative Efficiency vs. Energy (keV)						
	0.525	0.677	1.740	2.015	4.509	5.894	8.040
	O	F	Si	P	Ti	Fe55	Cu
FI	1.027 (0.106)	1.062 (0.193)	1.002 (0.015)	1.009 (0.046)	0.998 (0.006)	0.986 (0.022)	0.963 (0.076)
BI	3.436 (0.050)	3.151 (0.119)	1.075 (0.025)	1.546 (0.027)	0.967 (0.041)	0.781 (0.060)	0.603 (0.061)

Table 4.55: Mean Relative Detection Efficiencies for FI and BI CCDs at CSR—Referenced to w190c3

A third estimate of the relative efficiency of these two devices is available because

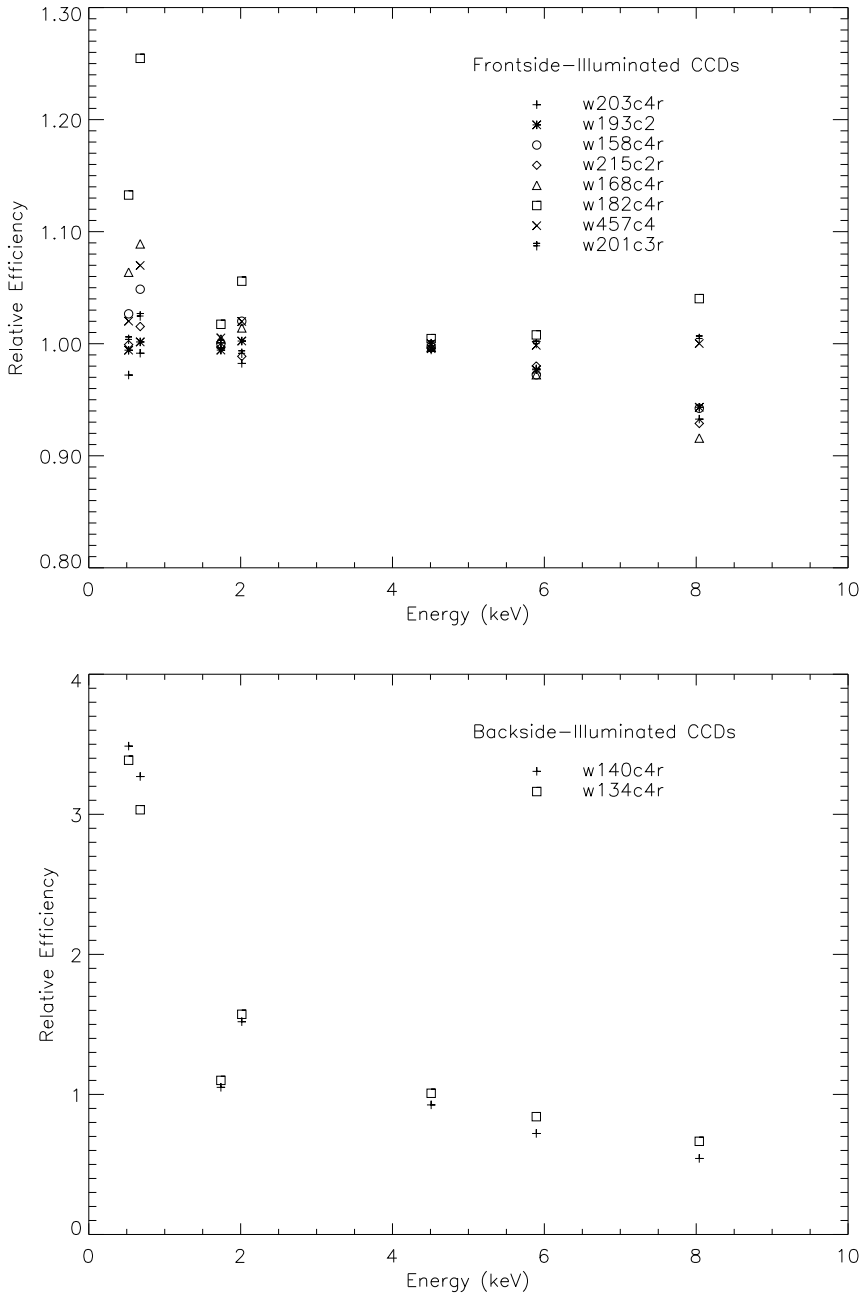

Figure 4.76: Relative detection efficiencies of front-illuminated (upper panel) and back-illuminated (lower panel) ACIS flight CCDs as a function of energy—referenced to w190c3.

one flight detector, I0 (w203c4r), was calibrated against both reference detectors (at relatively low flux). Assuming that the flight detector is stable, we infer a relative QE (w190c3:w103c4) of 1.174 (see Table 4.56).

The cause of this discrepancy is unknown. It is possible, and perhaps plausible, that the pileup corrections are systematically in error for reference detector w103c4 at high energies. This detector has always been operated with an older (non-ACIS) set of analog electronics, which provides lower depletion depth and longer minimum integration times than the ACIS electronics. These differences tend to increase the severity of pileup, particularly at high energies. In spite of these differences, we have used a single pileup model for both detectors.

In the end, we have adopted the unweighted average of the three estimates $((1.110 + 1.210 + 1.174)/3 = 1.164)$ as the relative QE of w190c3:w103c4 at 8 keV. While this number affects our comparison of CSR and XRCF efficiencies, it has no effect on our absolute quantum efficiency model. With our current model, the high energy efficiency is determined entirely by branching ratios at 5.9 keV (see Section 4.6.2).

4.7.2.1.2 Internal Consistency of Relative Quantum Efficiency Measurements made at MIT CSR. As noted above, the flight detector I0 (w203c4r) was calibrated with respect to both w190c3 and w103c4. Since we also cross-calibrated w190c3 and w103c4 with respect to one another, it is possible to check the consistency of these measurements. This comparison is shown in Table 4.56. Excluding the point at 8 keV (which was used in the reference detector cross-calibration), the mean difference is 0.0037 ± 0.0035, consistent with zero, where we have taken the standard deviation of the mean as the error. The RMS about the mean is 0.0085. Assuming each of the 3 relative QE measurement sets has the same error, and that the error is independent of energy, then, to a good approximation, the error in any single measurement is $\sigma_{rqe} = 0.0085/\sqrt{3} = 0.0049$.

Flight Device	Position	Mean Relative Efficiency vs. Energy (keV)							Reference Device
		0.525	0.677	1.740	2.015	4.509	5.894	8.040	
		O	F	Si	P	Ti	Fe55	Cu	
w203c4r	I0	0.972	0.992	0.996	0.982	0.994	0.977	0.933	w190c3 (meas.)
w190c3	Ref.	0.890	0.767	0.986	0.949	1.010	1.058	1.164†	w103c4 (meas.)
w203c4r	I0	0.866	0.760	0.982	0.932	1.004	1.034	1.086†	w103c4 (calc.)
w203c4r	I0	0.848	0.756	0.977	0.940	1.005	1.030	1.095	w103c4 (meas.)
Difference	line 3 − line 4	0.018	0.004	0.005	−0.008	−0.001	0.004	−0.009†	

†Cross-calibration of w190c3 vs. w103c4 uses w203c4r data; see text
Mean Difference, excluding 8 keV point : 0.0037
RMS Difference, excluding 8 keV point : 0.0085

Table 4.56: Reproducibility of Relative Quantum Efficiency Measurement of Detector I0

This level of error, while probably acceptable for ACIS calibration purposes, is one order of magnitude larger than the limiting uncertainty imposed by photon counting statistics.

A number of factors may contribute to this excess error. The two reference detectors used are known to have slightly different pileup characteristics, but the same pileup model was used in the analysis of both data sets. One reference detector (w103c4) was operated with an older (pre-ACIS) generation of electronics that is somewhat noisier than the ACIS electronics; the slight differences in response function may contribute some error. Finally, relative misalignment between flight and reference CCDs can influence low energy ratios (C, O, F) due to the non-uniformity of these sources. (Some misalignment on order 50 pixels seems evident in a few cases, despite the apparent precision achieved with the alignment system.) This is less important for higher energies, which make use of a commercial X-ray tube and have a flatter illumination pattern at the CCD location (primarily due to a larger source-detector separation).

Systematic errors in the modelling of the relative calibration measurements are discussed in detail in Section 4.8.

4.7.2.2 Spatial Variations in Quantum Efficiency

As discussed in section 4.7.1 above, we have measured quantum efficiency (relative to a reference detector) of each ACIS flight device as a function of position. For purposes of presentation, we have binned the relative quantum efficiency into 32-by-32-pixel "super-pixels"; we expect that in typical AXAF observations the celestial image will be dithered over an area of about this size ($\sim$ 15 arcsec) on the ACIS focal plane.

Maps showing the spatial uniformity of the relative quantum efficiency at each measurment energy are presented in Figures 4.77–4.86. Alongside each map is a histogram of the superpixel relative efficiencies. The efficiencies shown in these figures have not been corrected for pileup. The reference CCD count rates used to generate each superpixel relative efficiency have been corrected for cosmetic defects, including the effects of shadowing by the framestore covers used during subassembly calibration at MIT. The flight CCD count rates have not been corrected for cosmetic defects, but have been corrected for shadowing by the subassembly calibration framestore cover. In addition, each uniformity map has been adjusted to reproduce the effect of shadowing by the flight framestore cover. This procedure is intended to produce spatial uniformity maps which replicate the quantum efficiency patterns that will be present in data obtained with the flight CCDs on orbit. The number of rows in each device shadowed by the subassembly and flight framestore covers are listed in Table 4.57.

Histogram legends in Figures 4.77–4.86 indicate the centroid and standard deviation of a Gaussian fit to each histogram. The fitted standard deviation of the histogram provides a good measure of the residual spatial variation in relative quantum efficiency, excluding the effects of the flight framestore shield.

Spatial variations in relative QE are comparable to expected statistical fluctuations for the FI CCDs, except the ratios which are affected by bad or hot columns or pixels and border effects (especially the shadows of frame store covers). These superpixel ratios are

Flight Device	Position	Framestore Cover	
		Subassembly	Flight
w203c4r	I0	4	7
w193c2	I1	6	8
w158c4r	I2	7	7
w215c2r	I3	6	7
w168c4r	S0	6	6
w182c4r	S2	7	6
w457c4	S4	1	5
w201c3r	S5	4	5
w140c4r	S1	6	6
w134c4r	S3	8	5
w190c3	Ref.	10	
w203c2	Ref.	9	
w103c4	Ref.	7	

Table 4.57: Number of CCD Rows Shadowed by the Framestore Covers

generally outliers in the QE ratio histograms, and only weakly affect the Gaussian fit. These effects may be seen in Figures 4.77–4.86. Columns darker than their surrounding regions correspond to either bad columns in the flight CCD or hot columns in the reference CCD, while lighter columns typically correspond to bad columns in the reference CCD. The dark row at the bottom of each relative uniformity map is due to shadowing by the flight framestore cover.

Larger spatial variations are observed in the BI CCDs, and are believed to be caused in part by relatively high charge transfer inefficiency (CTI), exceeding 25% at higher energies. Some provision will need to be developed to characterize this spatial nonuniformity in the two backside flight CCDs (S1 and S3). These variations affect the quality of the Gaussian fit to the histogram of QE ratios.

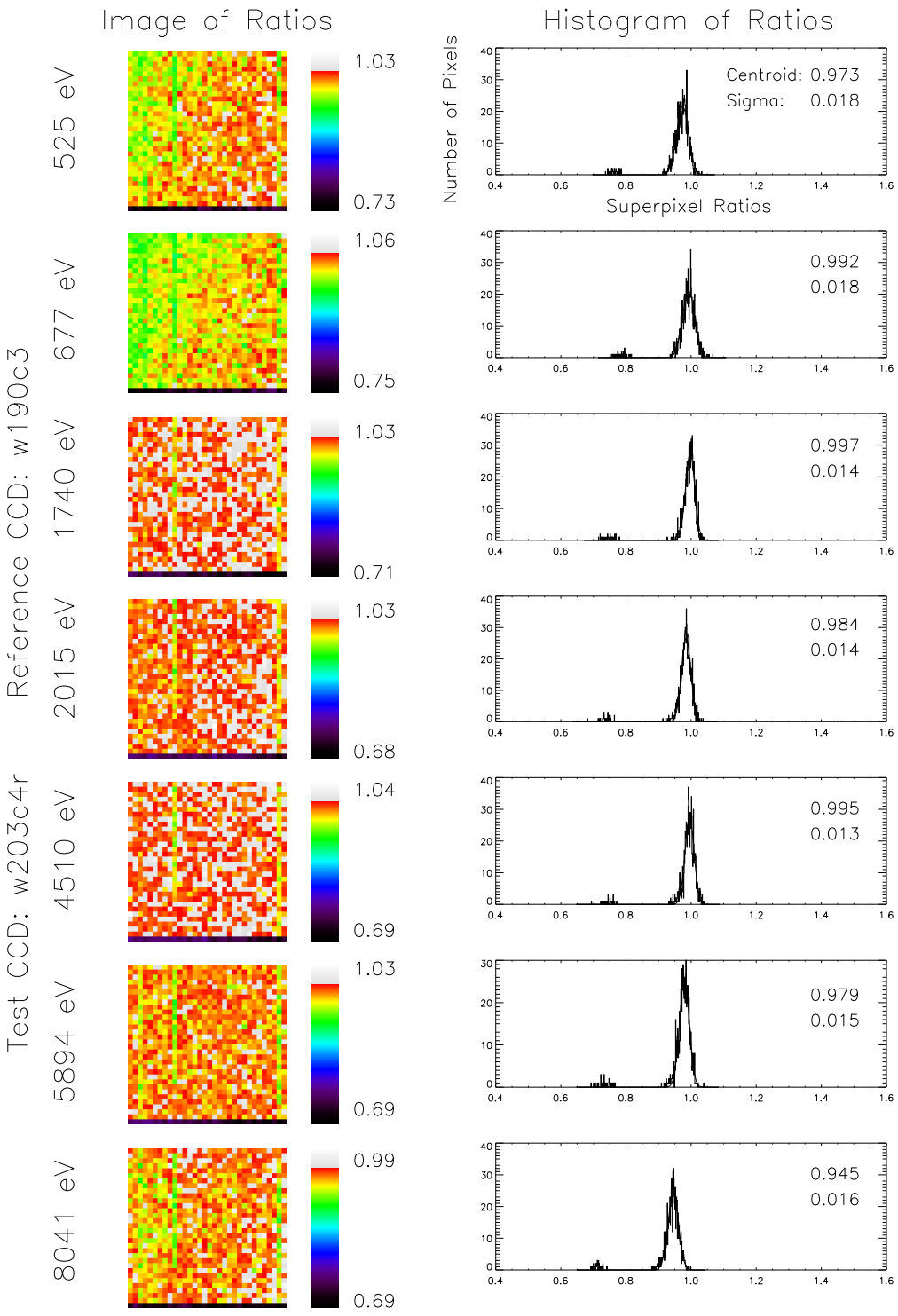

Figure 4.77: Uniformity maps and histograms showing the spatial uniformity of the quantum efficiency of ACIS flight device I0 (w203c4r) relative to reference device w190c3 at seven energies. Each pixel value is the ratio of the raw count rate (i.e. uncorrected for pileup) in a 32×32 pixel subarray of the flight device to the count rate in the corresponding subarray of the reference device.

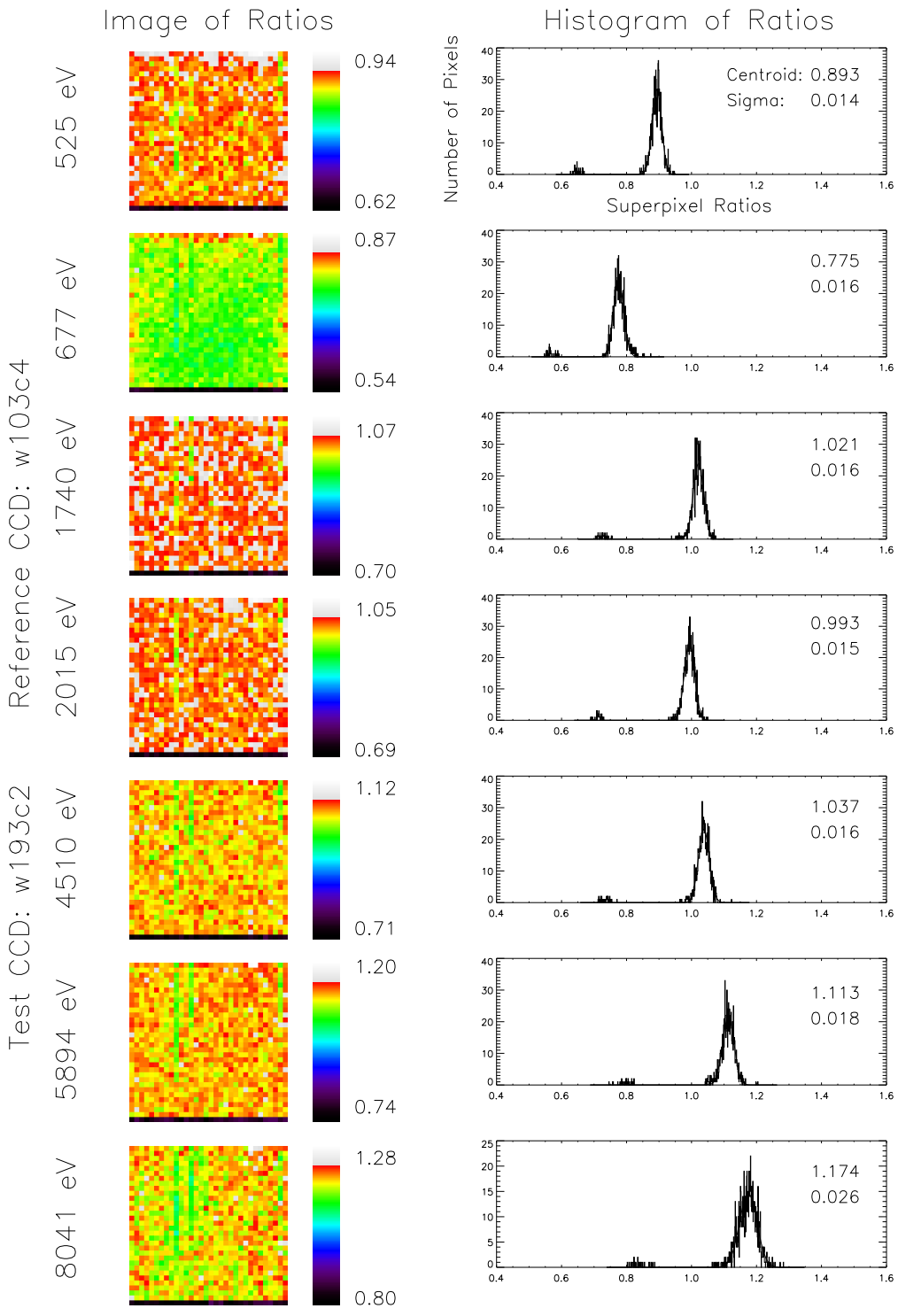

Figure 4.78: Uniformity maps and histograms showing the spatial uniformity of the quantum efficiency of ACIS flight device I1 (w193c2) relative to reference device w103c4 at seven energies. Each pixel value is the ratio of the raw count rate (i.e. uncorrected for pileup) in a 32×32 pixel subarray of the flight device to the count rate in the corresponding subarray of the reference device.

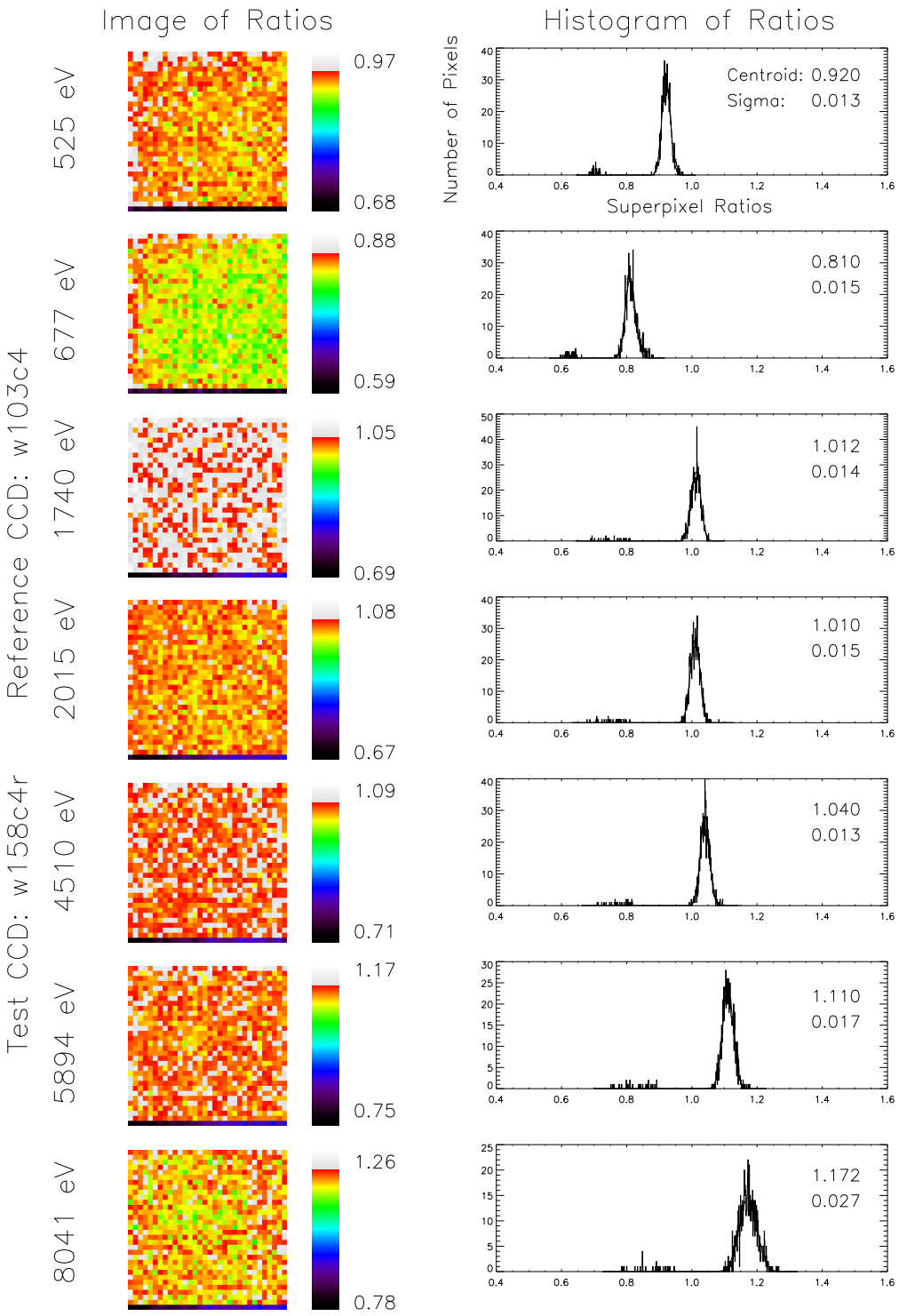

Figure 4.79: Uniformity maps and histograms showing the spatial uniformity of the quantum efficiency of ACIS flight device I2 (w158c4r) relative to reference device w103c4 at seven energies. Each pixel value is the ratio of the raw count rate (i.e. uncorrected for pileup) in a 32 × 32 pixel subarray of the flight device to the count rate in the corresponding subarray of the reference device.

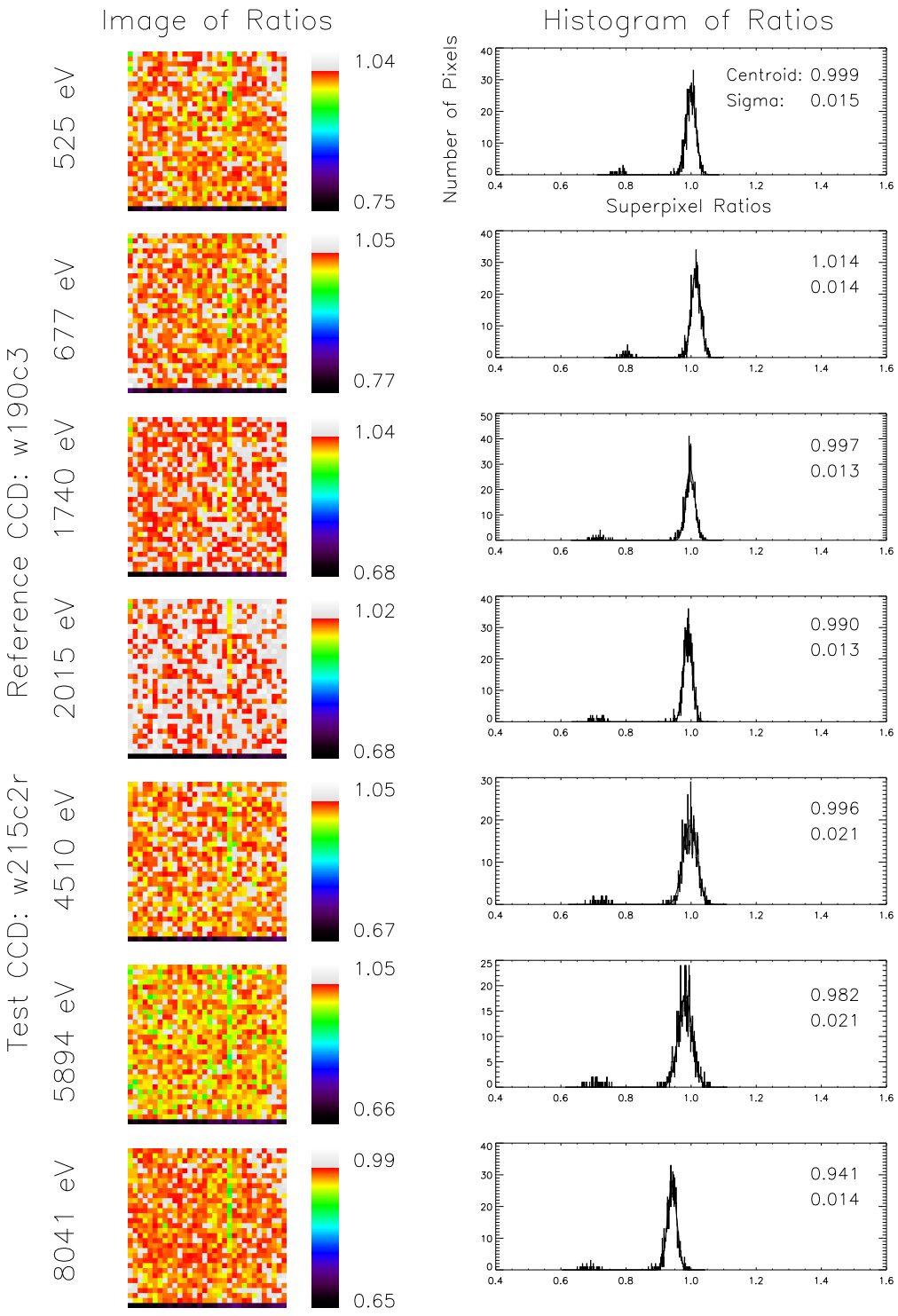

Figure 4.80: Uniformity maps and histograms showing the spatial uniformity of the quantum efficiency of ACIS flight device I3 (w215c2r) relative to reference device w190c3 at seven energies. Each pixel value is the ratio of the raw count rate (i.e. uncorrected for pileup) in a 32×32 pixel subarray of the flight device to the count rate in the corresponding subarray of the reference device.

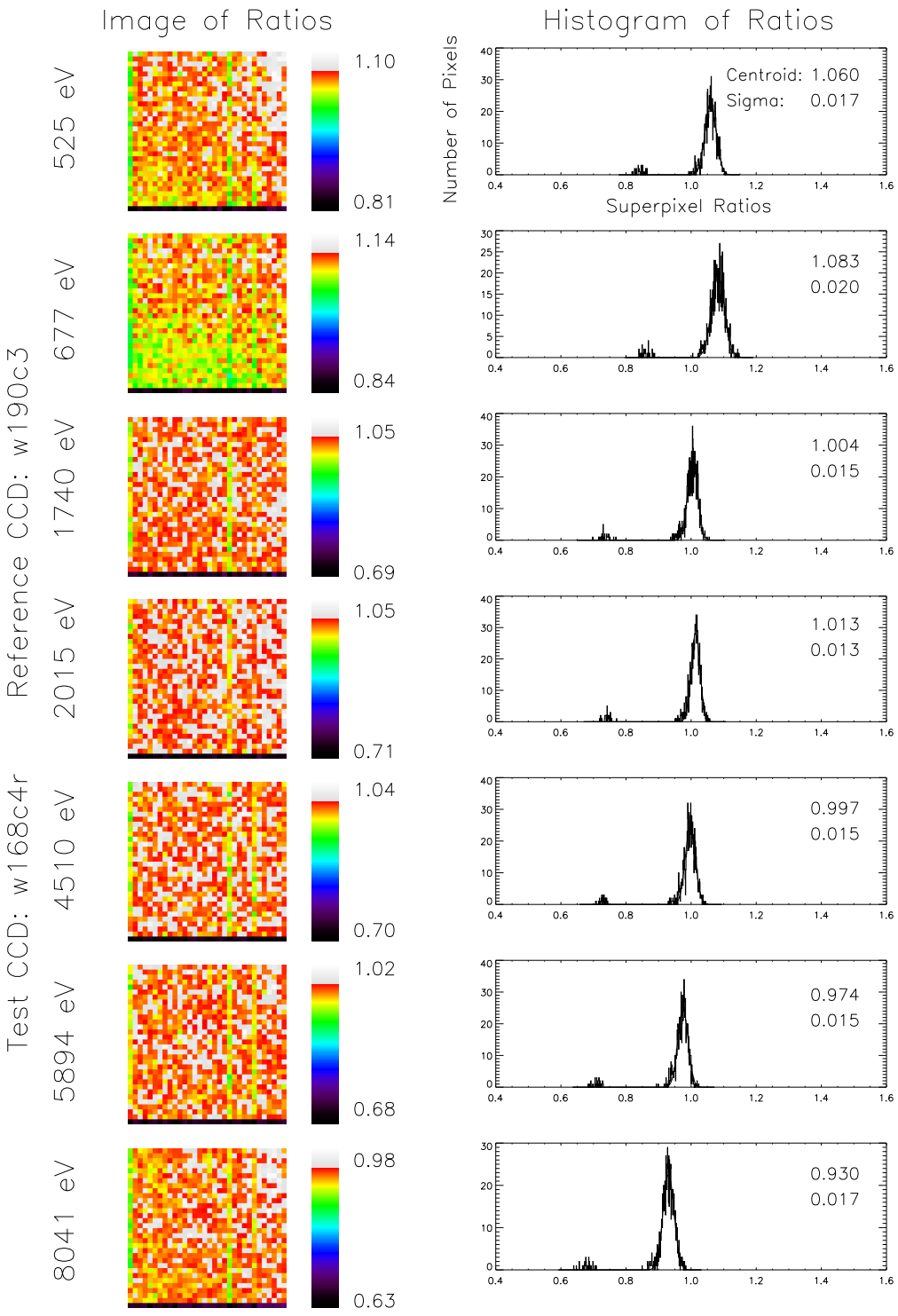

Figure 4.81: Uniformity maps and histograms showing the spatial uniformity of the quantum efficiency of ACIS flight device S0 (w168c4r) relative to reference device w190c3 at seven energies. Each pixel value is the ratio of the raw count rate (i.e. uncorrected for pileup) in a 32 × 32 pixel subarray of the flight device to the count rate in the corresponding subarray of the reference device.

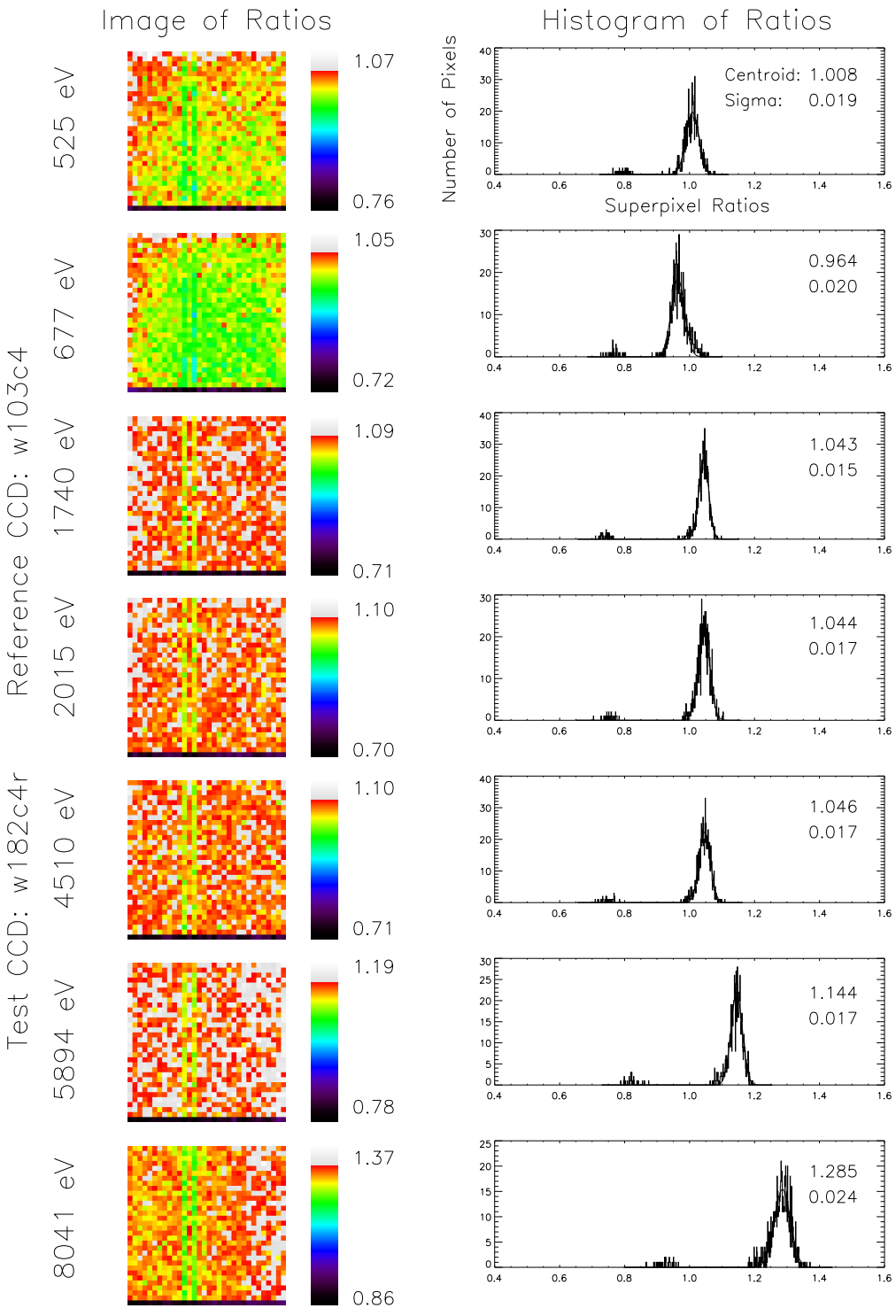

Figure 4.82: Uniformity maps and histograms showing the spatial uniformity of the quantum efficiency of ACIS flight device S2 (w182c4r) relative to reference device w103c4 at seven energies. Each pixel value is the ratio of the raw count rate (i.e. uncorrected for pileup) in a 32 × 32 pixel subarray of the flight device to the count rate in the corresponding subarray of the reference device.

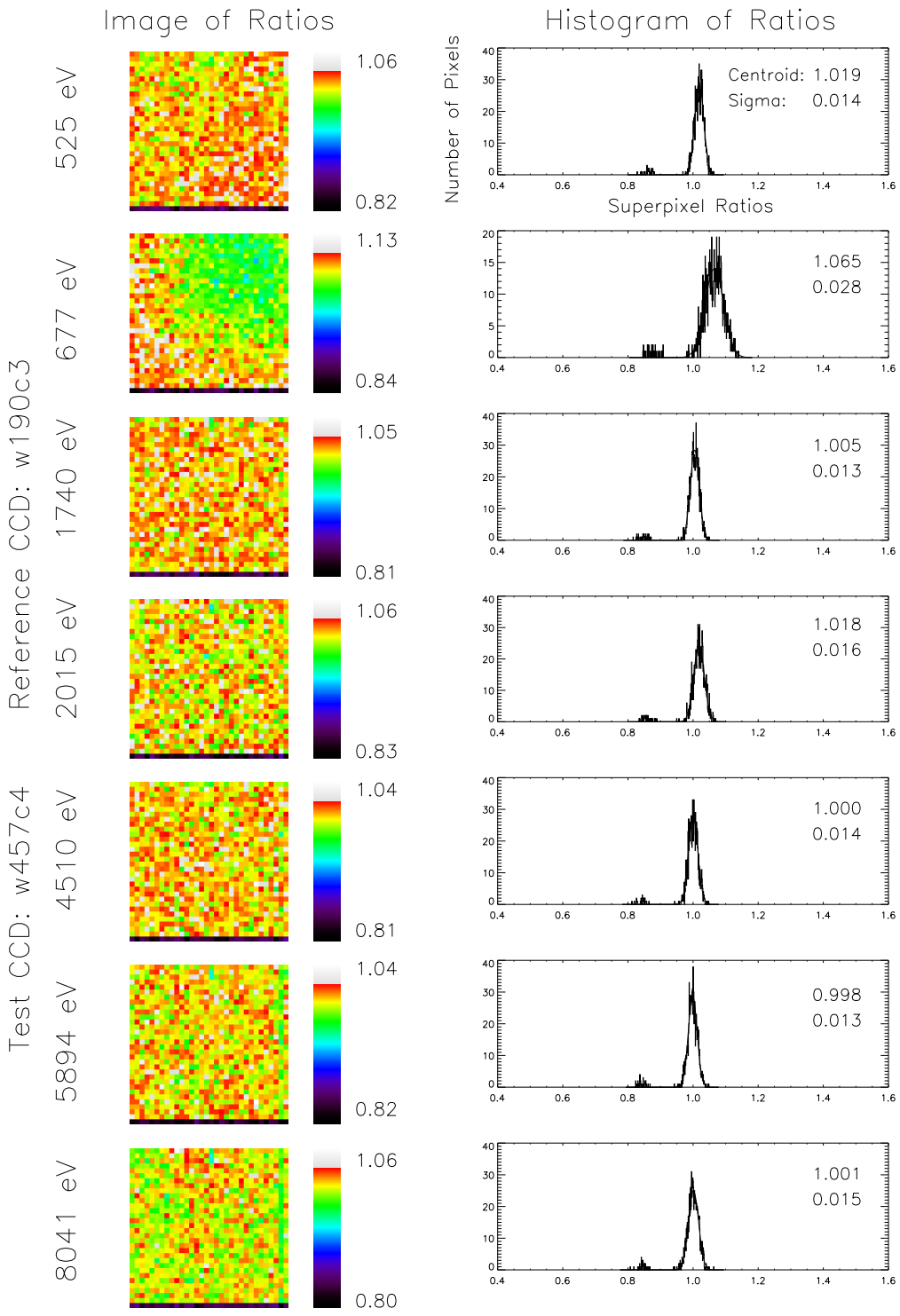

Figure 4.83: Uniformity maps and histograms showing the spatial uniformity of the quantum efficiency of ACIS flight device S4 (w457c4) relative to reference device w190c3 at seven energies. Each pixel value is the ratio of the raw count rate (i.e. uncorrected for pileup) in a 32 × 32 pixel subarray of the flight device to the count rate in the corresponding subarray of the reference device.

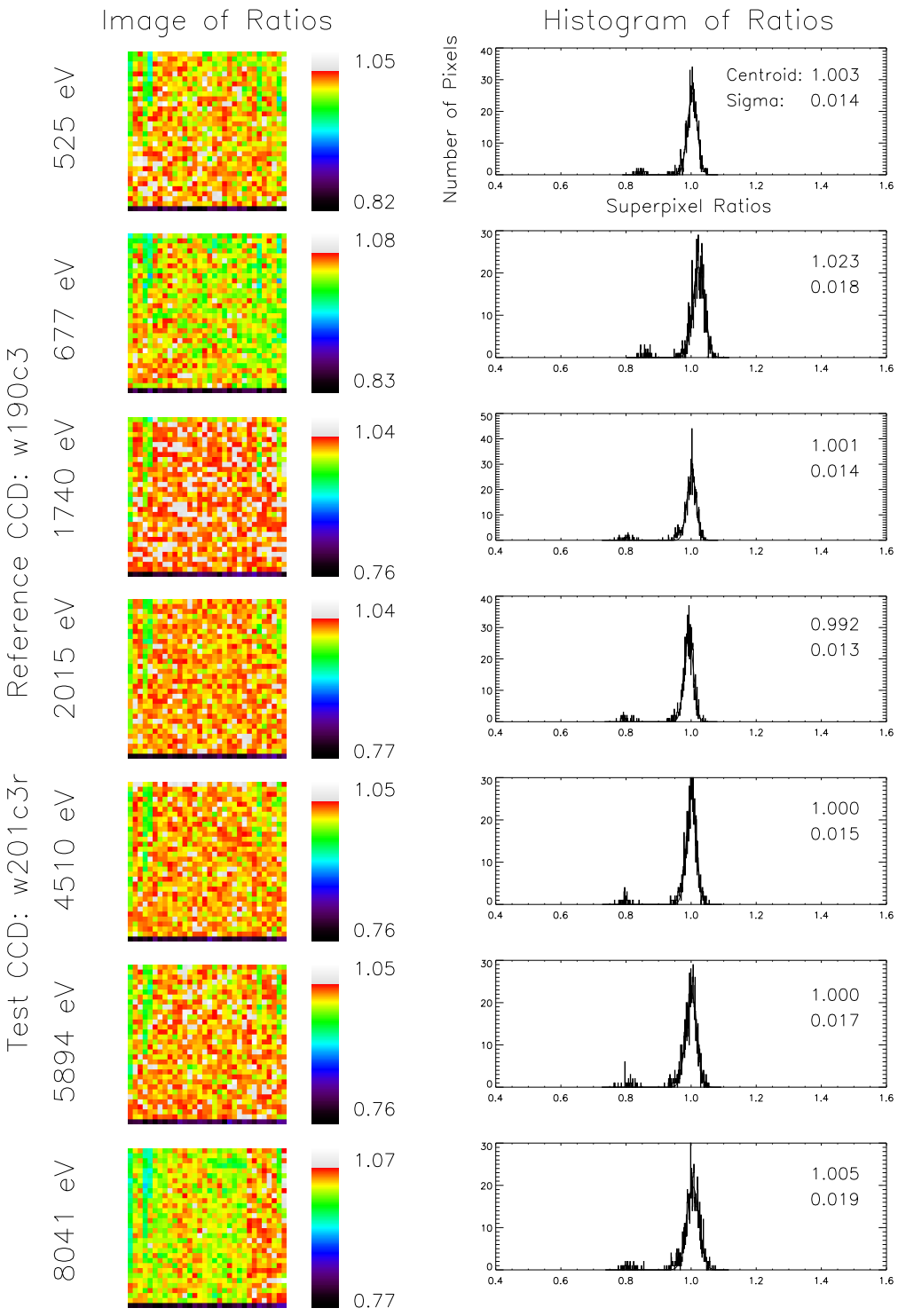

Figure 4.84: Uniformity maps and histograms showing the spatial uniformity of the quantum efficiency of ACIS flight device S5 (w201c3r) relative to reference device w190c3 at seven energies. Each pixel value is the ratio of the raw count rate (i.e. uncorrected for pileup) in a 32 × 32 pixel subarray of the flight device to the count rate in the corresponding subarray of the reference device.

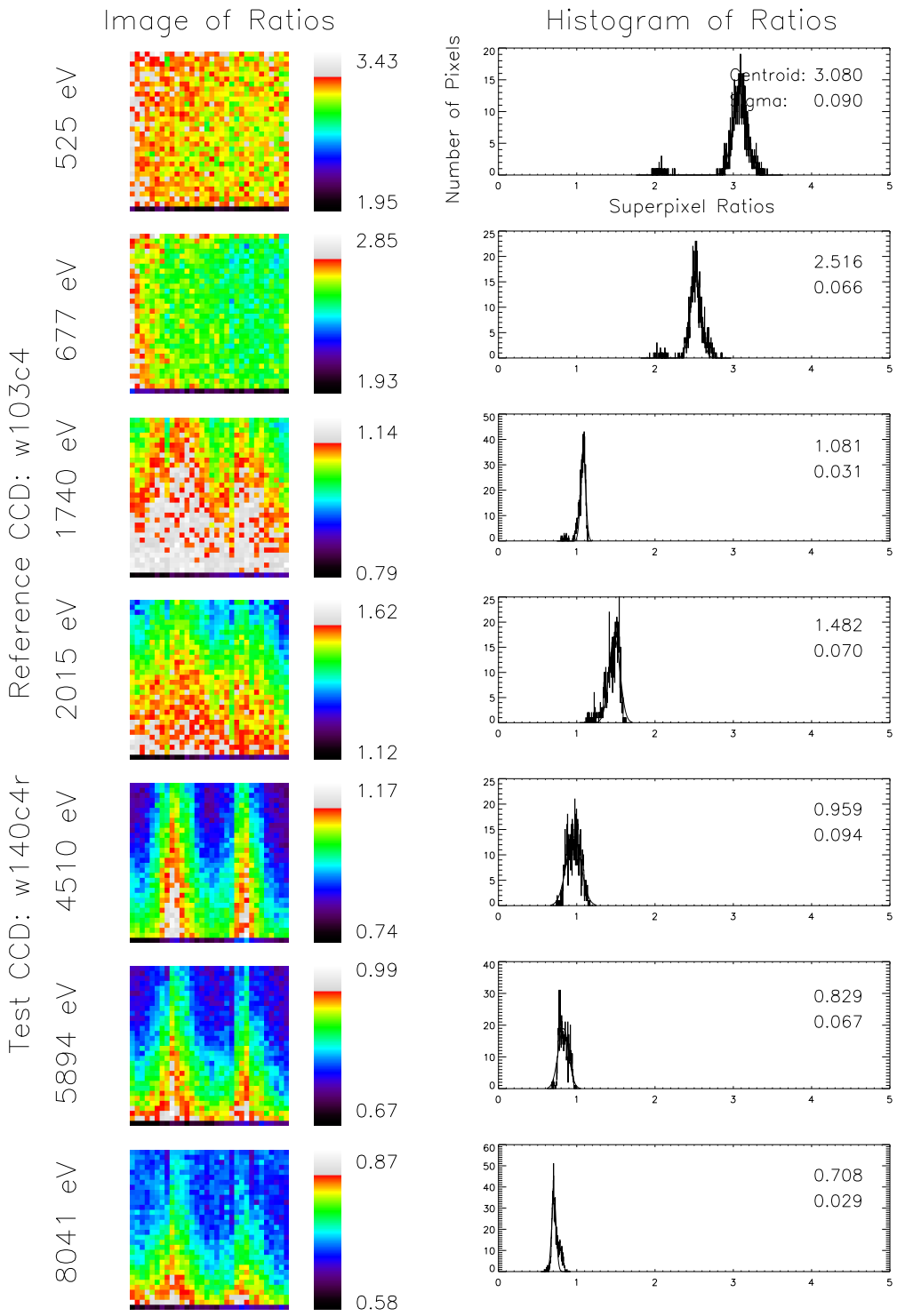

Figure 4.85: Uniformity maps and histograms showing the spatial uniformity of the quantum efficiency of ACIS flight device S1 (w140c4r) relative to reference device w103c4 at seven energies. Each pixel value is the ratio of the raw count rate (i.e. uncorrected for pileup) in a 32 × 32 pixel subarray of the flight device to the count rate in the corresponding subarray of the reference device.

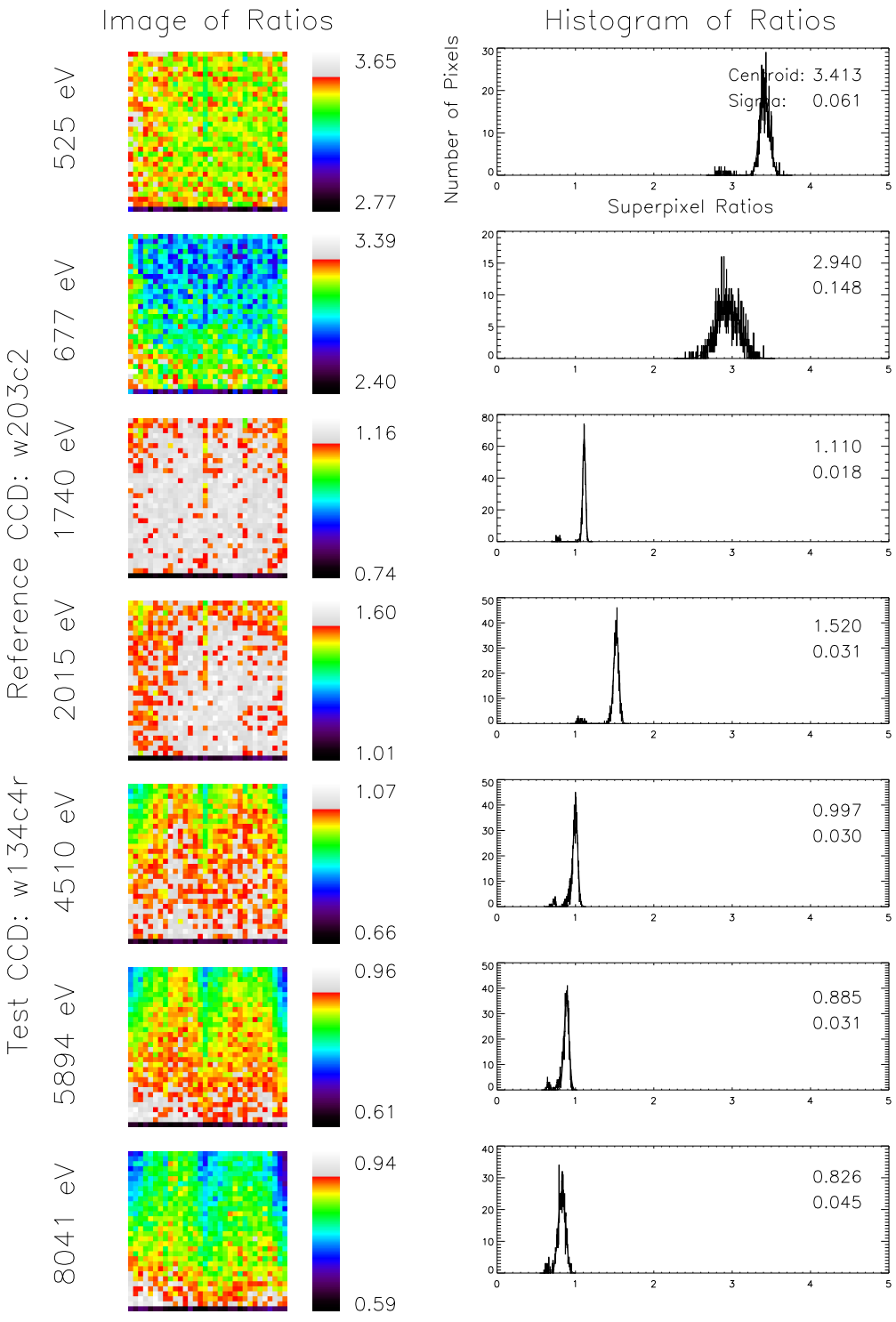

Figure 4.86: Uniformity maps and histograms showing the spatial uniformity of the quantum efficiency of ACIS flight device S3 (w134c4r) relative to reference device w203c2 at seven energies. Each pixel value is the ratio of the raw count rate (i.e. uncorrected for pileup) in a 32 × 32 pixel subarray of the flight device to the count rate in the corresponding subarray of the reference device.

4.7.3 Comparison Between MIT and XRCF (Phase I) Measurements of Relative Quantum Efficiency

To compare measurements of relative quantum efficiency made at MIT's Center for Space Research (CSR) and Marshall Spaceflight Center's X-ray Calibration Facility (XRCF), we have used the data in Table 4.54 to compute relative QE ratios referenced to device S2. The results are presented in Table 4.58. Similarly, we have compiled relative QE ratios referenced to S2 from telemetry data taken at XRCF (see Table 4.59). The telemetry data was taken using windows near the top and bottom of each device to avoid saturating the telemetry stream. The pileup correction factors applied to the XRCF count rates are presented in Table 4.60.

Flight Device	Position	Mean (RMS) Relative Efficiency vs. Energy (keV)						
		0.525	0.677	1.740	2.015	4.509	5.894	8.040
		O	F	Si	P	Ti	Fe55	Cu
w203c4r	I0	0.858 (0.055)	0.790 (0.049)	0.979 (0.071)	0.930 (0.066)	0.990 (0.072)	0.970 (0.074)	0.898 (0.090)
w193c2	I1	0.878 (0.058)	0.798 (0.053)	0.977 (0.073)	0.949 (0.069)	0.991 (0.075)	0.969 (0.077)	0.907 (0.087)
w158c4r	I2	0.906 (0.055)	0.836 (0.051)	0.983 (0.070)	0.966 (0.067)	0.993 (0.071)	0.965 (0.073)	0.906 (0.084)
w215c2r	I3	0.882 (0.056)	0.809 (0.049)	0.980 (0.074)	0.936 (0.069)	0.991 (0.076)	0.972 (0.079)	0.894 (0.092)
w168c4r	S0	0.939 (0.058)	0.868 (0.053)	0.987 (0.074)	0.960 (0.070)	0.992 (0.074)	0.965 (0.076)	0.881 (0.091)
w182c4r	S2	1.000 (0.000)	1.000 (0.000)	1.000 (0.000)	1.000 (0.000)	1.000 (0.000)	1.000 (0.000)	1.000 (0.000)
w457c4	S4	0.901 (0.051)	0.853 (0.052)	0.988 (0.063)	0.966 (0.060)	0.995 (0.064)	0.991 (0.068)	0.963 (0.091)
w201c3r	S5	0.886 (0.051)	0.817 (0.047)	0.984 (0.067)	0.939 (0.061)	0.996 (0.068)	0.992 (0.072)	0.967 (0.095)
w140c4r	S1	3.078 (0.207)	2.606 (0.159)	1.033 (0.074)	1.439 (0.110)	0.921 (0.093)	0.715 (0.066)	0.522 (0.053)
w134c4r	S3	2.989 (0.170)	2.417 (0.187)	1.082 (0.084)	1.489 (0.116)	1.004 (0.082)	0.835 (0.072)	0.640 (0.068)

Table 4.58: Spatially Averaged Relative Detection Efficiency at CSR—Referenced to S2. In each box the mean is given as the top entry; the RMS variation is given in parentheses below it.

Flight Device	Position	Mean Relative Efficiency vs. Energy (keV)								
		0.277	0.525	0.705	1.487	1.740	2.166	4.509	6.399	8.040
		C	O	Fe L	Al	Si	Nb L	Ti	Fe K	Cu
w203c4r	I0		0.842	0.810	0.962	0.982	0.942	0.981	0.948	0.903
w193c2	I1		0.868	0.805	0.965	0.979	0.954	0.985	0.946	0.910
w158c4r	I2		0.909	0.849	0.979	0.996	0.969	0.988	0.951	0.894
w215c2r	I3		0.865	0.807	0.976	0.994	0.961	0.989		0.907
w168c4r	S0	0.687	0.912	0.873	0.979	0.986	0.964	1.002	0.953	0.904
w182c4r	S2	1.000	1.000	1.000	1.000	1.000	1.000	1.000	1.000	1.000
w457c4	S4	0.625	0.897	0.910	0.975	0.991	0.965	1.005	0.980	1.049*
w201c3r	S5	0.625	0.876	0.828	0.966	0.983	0.966	0.999	0.972	1.008
w140c4r	S1	36.619	3.460	3.022	1.071	1.034	1.287	0.847	0.617	0.527
w134c4r	S3	35.679	3.280	3.033	1.115	1.092	1.342	0.949	0.755	0.671

* The XRCF bias for this data point is peculiar.

Table 4.59: Spatially Averaged Relative Detection Efficiency from XRCF Telemetry—Referenced to S2

Flight Device	Position	Pileup Correction vs. Energy (keV)								
		0.277	0.525	0.705	1.487	1.740	2.166	4.509	6.399	8.040
		C	O	Fe L	Al	Si	Nb L	Ti	Fe K	Cu
w203c4r	I0		1.001	1.007	1.049	1.007	1.020	1.017	1.021	1.119
w193c2	I1		1.001	1.007	1.049	1.007	1.020	1.017	1.021	1.117
w158c4r	I2		1.001	1.007	1.050	1.008	1.021	1.009	1.015	1.116
w215c2r	I3		1.001	1.007	1.050	1.008	1.021	1.017		1.116
w168c4r	S0	1.000	1.001	1.002	1.050	1.008	1.021	1.018	1.028	1.139
w182c4r	S2	1.000	1.001	1.007	1.051	1.008	1.022	1.013	1.020	1.140
w457c4	S4	1.000	1.001	1.003	1.050	1.008	1.021	1.011	1.029	1.164
w201c3r	S5	1.000	1.001	1.002	1.049	1.008	1.021	1.018	1.029	1.157
w140c4r	S1	1.001	1.004	1.007	1.044	1.007	1.029	1.019	1.016	1.036
w134c4r	S3	1.001	1.003	1.009	1.046	1.008	1.030	1.016	1.018	1.042

Table 4.60: Pileup Correction Factors Applied to Count Rates from XRCF Telemetry

4.7.3.1 Repeatability and Estimated Errors in Relative Quantum Efficiency Measurements of Front-Illuminated Detectors

In Table 4.61 we have computed the fractional difference (1−XRCF/CSR) between the relative QE measurements made at each site. The relative QE ratios at XRCF for the frontside

devices are in excellent agreement with the ratios obtained at CSR. Indeed, averaged over seven FI chips and the lowest three energies, the mean difference in relative quantum efficiency is $0.27\% \pm 0.24\%$, where the error is the standard deviation about the mean, and the RMS deviation about the mean is 1.1%. If we assume that the CSR and XRCF relative QE measurements in this energy range each have the same random error, and account properly for the normalization of the CSR measurements by the efficiency of S2 required to make this comparison, we infer that the error on a single relative QE measurement is (very nearly) $\sigma_{rqe} = 0.011/\sqrt{3} = 0.006$. This estimate is only slightly larger than the value obtained from internal consistency of the MIT CSR measurements alone ($\sigma_{rqe} = 0.0049$; see section 4.7.2) For purposes of QE model fitting, to be discussed in Section 4.8, we will adopt the larger value as the uncertainty in the relative QE measurement.

Flight Device	Position	Frac. Rel. Eff. Diff. vs. Energy (keV)			
		0.525	1.740	4.509	8.040
		O	Si	Ti	Cu
w203c4r	I0	0.019	−0.003	0.009	−0.006
w193c2	I1	0.011	−0.002	0.006	−0.004
w158c4r	I2	−0.003	−0.013	0.005	0.013
w215c2r	I3	0.019	−0.015	0.002	−0.014
w168c4r	S0	0.029	0.001	−0.010	−0.026
w182c4r	S2	0.000	0.000	0.000	0.000
w457c4	S4	0.004	−0.003	−0.010	*
w201c3r	S5	0.012	0.001	−0.003	−0.042
FI Mean		0.013	−0.005	−0.000	−0.013
FI Std Dev.		0.011	0.006	0.008	0.019
w140c4r	S1	−0.124	−0.001	0.080	−0.010
w134c4r	S3	−0.097	−0.010	0.055	−0.050
BI Mean		−0.111	−0.006	0.068	−0.030
BI Std Dev.		0.019	0.006	0.018	0.028

* This data point was excluded because the XRCF bias for this point was peculiar.

Table 4.61: Fractional Difference (1−XRCF/CSR) between Relative Detection Efficiencies at CSR and XRCF—Referenced to S2

The data at 8 keV require special comment for two reasons. First, the bias obtained from ACIS telemetry for S4 for the 8 keV measurement (ACIS XRCF Science Run 93, TRW ID's I-IAS-SG-1.032 and I-IAS-EA-2.043 through I-IAS-EA-2.048) is peculiar, showing excess charge of order 5 electrons/pixel. The spectral resolution in S4 is severely compromised (FWHM $\sim$ 200 eV) by the bias error, and this in turn affects the measured quantum

efficiency. As a result, a replacement (telemetry) bias was used (taken from ACIS Science Run 89) to compute the relative efficiency listed in Table 4.59. Even with the replacement bias, the spectral resolution was not quite as good as measured at MIT. For this reason, we regard this measurement as suspect, and have quoted statistics in Table 4.61 with this point excluded. The cause of the bias error is not understood. The high-speed tap data obtained for S4 during (a subset of) ACIS XRCF Science Run 93 show no obvious anomalies.

Second, as noted above, the cross-calibration of the two reference detectors w190c3 and w103c4 at MIT is rather uncertain at 8 keV. We require this cross-calibration to compute the response of S2 relative to reference detector w190c3, since S2 was only measured with respect to reference detector w103c4. Formally, the RMS uncertainty of this cross-calibration (derived from the reproducibility of three measurement sets) is about 0.03 (1-sigma). This uncertainty is expected to dominate other errors in the QE, relative to S2, of the five devices (I0, I3, S0, S4 and S5) for which w190c3 is the primary reference standard.

Nevertheless, excluding the S4 point, we find a mean relative quantum efficiency difference of -0.013 ± 0.008, where the error is the standard deviation of the mean, and the RMS deviation of measurements about the mean is 0.019. Thus, whatever the source of the uncertainty in the CSR measurements of the w190c3 vs. w103c4 cross-calibration, the value we have adopted for this cross-calibration is just consistent, at 90% confidence, (i.e., within 1.3%) with the XRCF relative quantum efficiency data.

A related comparison between the best-fit quantum efficiency models and the XRCF data is presented in Section 4.8.

4.7.3.2 Repeatability and Estimated Errors in Relative Quantum Efficiency Measurements of Back-Illuminated Detectors

The agreement between XRCF and CSR is not as good for the backside devices. At 525 eV, both S1 and S3 appear to have been 10–12% more efficient relative to S2 in the XRCF data compared to the CSR data. Discrepancies at the 5% level are also apparent at several other energies. Here we discuss possible origins for these discrepancies.

We have investigated the effects of windowing and spatial variation in the charge transfer inefficiency of the backside devices by averaging the relative efficiency uniformity maps at 525 eV over all columns and plotting the average relative efficiency versus row number. This analysis indicates that the peak-to-peak variation in the relative efficiency of the backside devices, averaged over regions of 1024 columns by 24 rows (similar to the windows used at XRCF), is only $\sim$2–3%. This is too small to account for the differences between the CSR and XRCF relative efficiencies at 525 eV, although this level of variation would constitute a significant fraction of the discrepancies measured at the higher energies.

The spectral redistribution functions of the front- and back-illuminated detectors are significantly different. Moreover, the X-ray sources used at both MIT and XRCF emitted significant and differing continuum fluxes in addition to the intended line flux. In principle, therefore, proper analysis of BI-to-FI relative QE measurements must account for response

function differences. Our analysis to date has ignored these response function differences, and so is subject to several systematic errors as a result. In an effort to bound these errors, we have begun to examine the line-to-continuum ratios of the various sources. We find, for example, that the continuum level of the XRCF source was stronger relative to the emission line at 525 eV than was the case in the CSR source (see Figures 4.87 and 4.88).

We estimate that neglect of the continuum biases the BI-to-FI QE ratio at 525 eV, measured at XRCF, by as much as 15% above the true value. In the CSR measurements, the lower continuum produces a substantially lower bias (about 5%). We also note that one would expect this error to be most serious at the lowest energies, where the BI and FI response functions differ in width by as much as a factor of two; at higher energies, the response function widths differ by 30% or less. Figures 4.89 and 4.90 show that differences in the line-to-continuum ratios at XRCF and CSR were negligible at higher energies.

We conclude that our heretofore inadequate treatment of the redistribution functions and source spectra may well account for the XRCF-to-CSR discrepancies in BI-to-FI relative quantum efficiency measurements. A corollary conclusion is that the CSR measurements of these quantities may be in error by $\sim 5\%$ at low energies.

We have some confidence that suitable modelling of the BI redistribution function and the source spectra will provide us with more accurate estimates of the BI response. The excellent repeatability of the FI results demonstrates that our fundamental measurement procedures are sound. Moreover, each BI measurement was accompanied by a simultaneous or nearly simultaneous measurement of the same source with an FI device. These FI data, and our sound FI models, will provide independent constraints on the source spectra used to characterize the BI detectors. These constraints, in turn, should improve our understanding of the BI-to-FI relative quantum efficiency data.

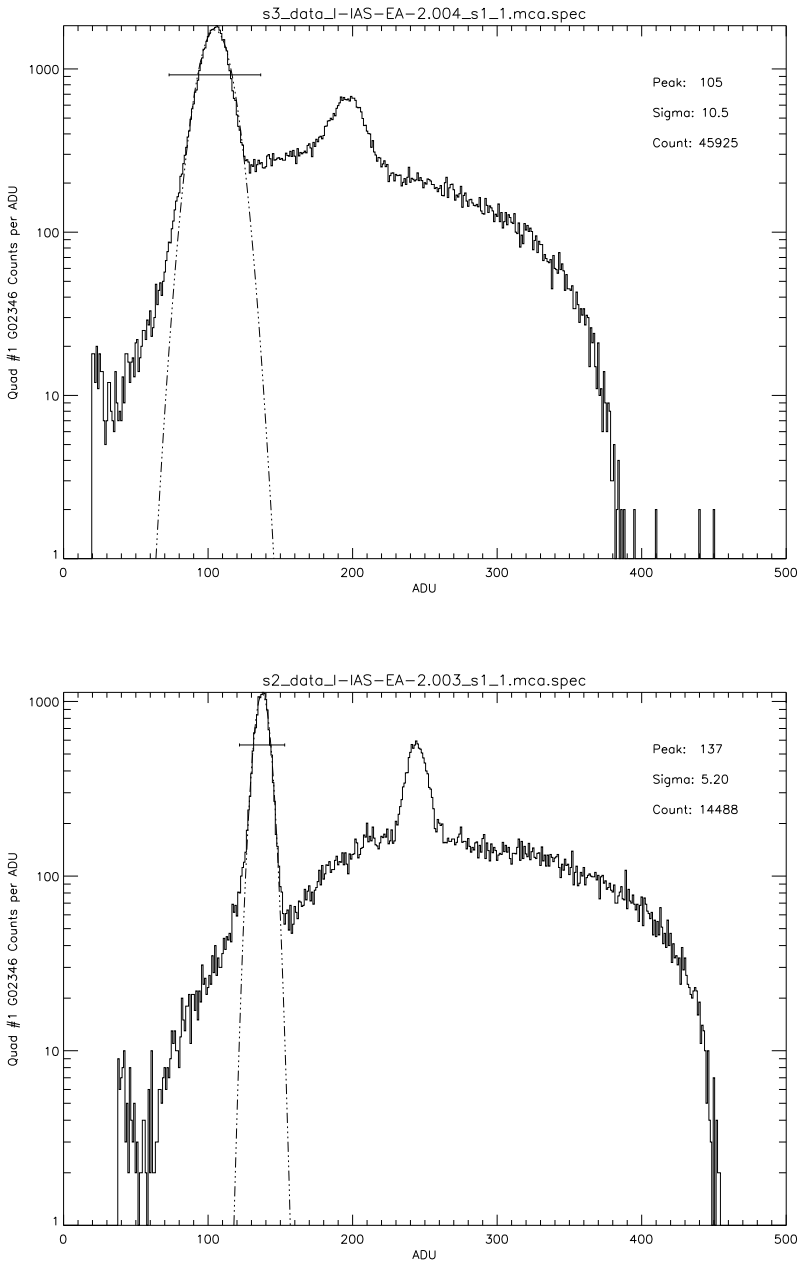

Figure 4.87: O-K spectra for S3 (upper panel) and S2 (lower panel) from XRCF Phase I. The bar in each plot marks the range of channels within 3 sigma of the peak.

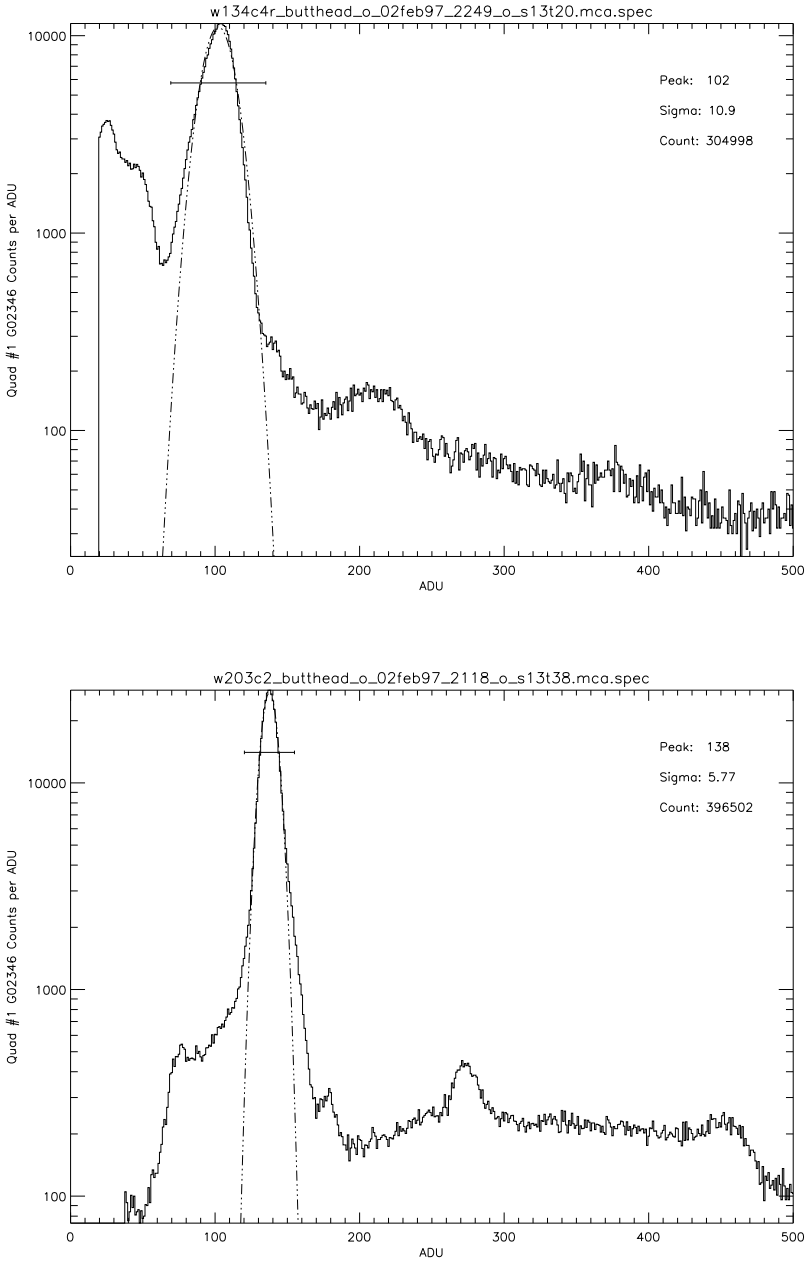

Figure 4.88: O-K spectra for S3 (upper panel) and w203c2 (lower panel) from CSR Subassembly Calibration. The bar in each plot marks the range of channels within 3 sigma of the peak.

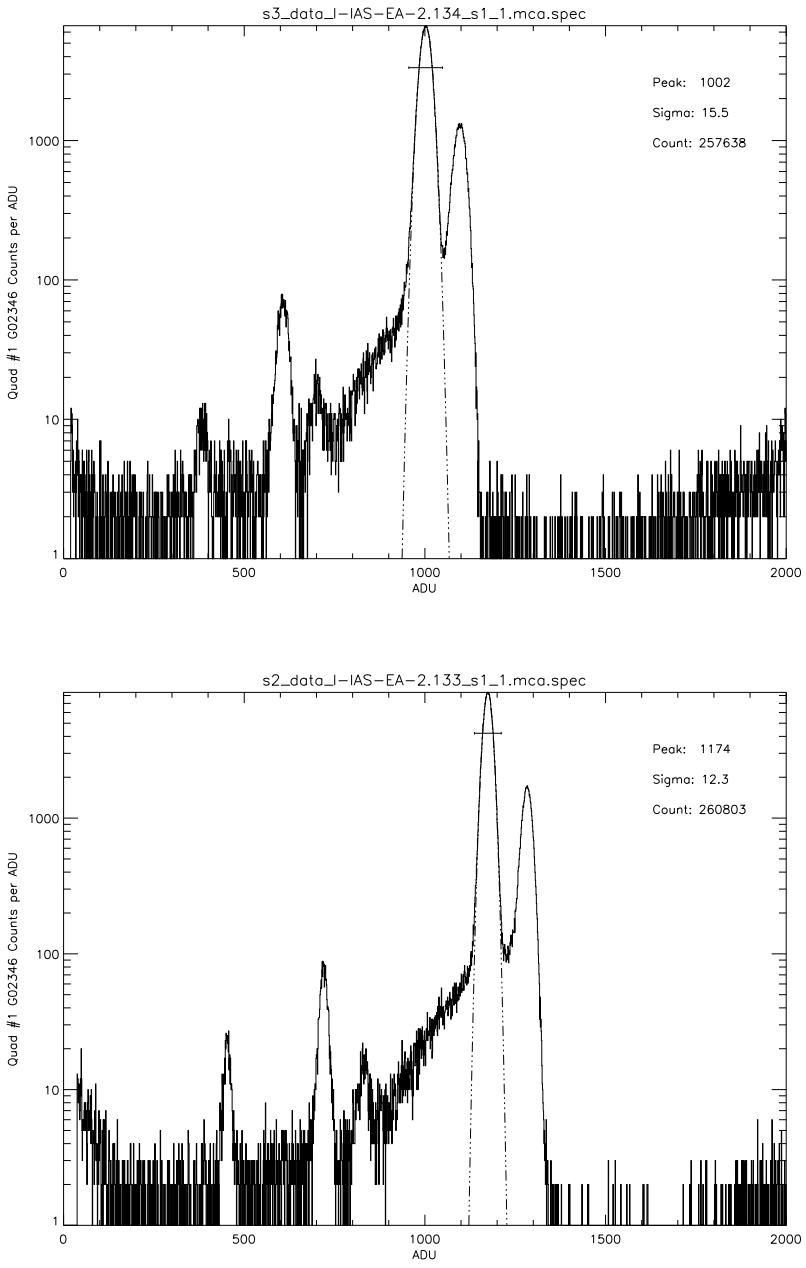

Figure 4.89: Ti-K spectra for S3 (upper panel) and S2 (lower panel) from XRCF Phase I. The bar in each plot marks the range of channels within 3 sigma of the peak.

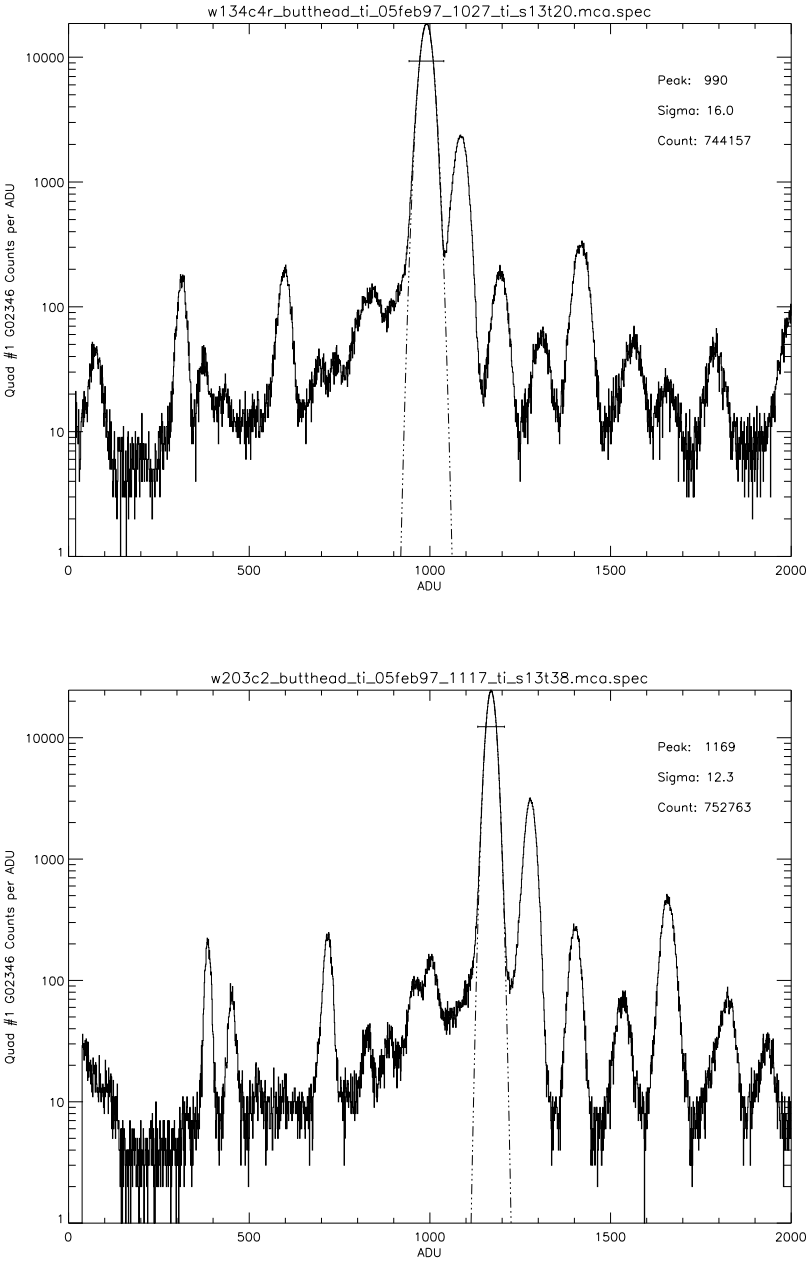

Figure 4.90: Ti-K spectra for S3 (upper panel) and w203c2 (lower panel) from CSR Subassembly Calibration. The bar in each plot marks the range of channels within 3 sigma of the peak.

4.8 Absolute Quantum Efficiency of ACIS Flight Detectors

4.8.1 Quantum Efficiency Model and Fitting Results

In this section we present the best-estimate absolute quantum efficiency, as of this writing, for each flight device. In each case the absolute quantum efficiency has been derived from measurements of the relative quantum efficiency of the flight devices, with respect to reference detectors, described above in section 4.7.2, together with the absolute quantum efficiency models of the reference detectors described in section 4.6.1.

We are confident that we understand the accuracy of quantum efficiency models for the front-illuminated (FI) detectors, and we discuss this subject at some length here. On the other hand, the models we present for back-illuminated (BI) devices are not particularly accurate, and, perhaps worse, the errors in the back-illuminated models are not well characterized. Thus the BI models given here must be regarded as interim products. Fortunately, we have very recently identified the origin of at least a large fraction of the fairly large, (i.e. 10-20%) systematic errors in our current analysis of BI CCD data. In short, we now believe it is essential to use accurate models of both source spectrum and detector spectral redistribution to obtain reliable quantum efficiency measurements for these devices. This more accurate analysis has not been completed at this writing, but we are confident that it can be done. See section 4.7.3 for a brief quantitative discussion of these errors.

We have used the so-called "slab and stop" model of the ACIS CCD gate structure, described in section 4.1, to model detector quantum efficiencies. For clarity, the various slab-and-stop model parameters used in the model of FI detector quantum efficiency are represented in Table 4.62. Note that only four model parameters were varied in fits to measurements made with the flight detectors. The remaining three parameters were constrained by mesh measurements (see section 4.5) or by scanning electron micrograph (SEM) measurements of siblings of the flight devices.

4.8.2 Fitting Methods: FI Device Model Parameters.

The spatially-averaged relative quantum efficiency measurements described in section 4.7.2 were used to constrain slab-and-stop model gate structure parameters for the flight FI devices. For each device, the MIT CSR relative efficiency measurements at 525 eV, 677 eV, 1740 eV and 2015 eV were used to fit for three model parameters: the mean silicon gate thickness, the mean silicon dioxide thickness, and the silicon nitride thickness. In each case, the reference detector quantum efficiency was modelled using the slab and stop model parameters derived from the undispersed synchrotron measurements, as described in section 4.6.1.

Estimates of the errors in the relative quantum efficiency measurements were derived from the comparison of relative efficiency measurements made at MIT CSR to those made

Parameter	Determined from:	See Section:
Poly-silicon gate thickness	Fit to flight-device relative QE data	4.7.2
SiO_2 insulator thickness	Fit to flight-device relative QE data	4.7.2
Si_3N_4 insulator thickness	Fit to flight-device relative QE data	4.7.2
Depletion depth	Fit to flight-device branching ratio data at 5.9 keV	4.6.2
Channel Stop width	Mesh and SEM measurements‡ on sibling devices	4.5
Channel Stop SiO_2 thickness	Mesh and SEM measurements on sibling devices	4.5
Channel Stop Si P^+ thickness	Mesh measurements on sibling devices	4.5

Note: The slab-and-stop model is described in detail in section 4.1

Table 4.62: Model Parameter Determination for Absolute Quantum Efficiency of Front-illuminated Flight Devices

in Phase I (ACIS flat-field) of the XRCF calibration (see section 4.7.3.) Thus, at these energies, for the front-illuminated detectors, we take the standard deviation of the error in each spatially-averaged relative quantum efficiency measurement to be 0.6%, independent of energy. Fitting was performed by minimizing the χ^2 statistic. Best-fit gate-structure model parameters, along with other adopted model parameters, are listed in Table 4.63. In all cases the fits (which had but one degree of freedom each!) were statistically acceptable given the adopted measurement errors.

4.8.2.1 Fitting Methods: BI Device Model Parameters.

The spatially averaged quantum efficiency measurements described in section 4.7.2, together with the best fit absolute quantum efficiency model for detector S2 (w182c4) were used to infer absolute quantum efficiency as a function of energy for each BI device at 525 eV, 677 eV, 1740 eV, 2015 eV, 4509 eV, 5894 eV and 8040 eV. These inferred detection efficiencies exceed unity at three energies (525 eV, 677 eV and 2015 eV) in one or both BI detectors, by amounts ranging from 4% to 7%. Obviously, this result demonstrates the presence of significant systematic errors in our analysis of these data. As discussed above, we believe that one major error in our analysis arises because we do not now correct for the effects of source continuum; since the spectral redistribution functions for the BI and FI chips are quite different, the continuum contributes a larger proportion to the BI counting rate than to the FI counting rate. A preliminary discussion of this effect is presented in section 4.7.3. We have not yet completed a BI device response function model adequate for proper analysis of this data. For purposes of this report we have arbitrarily elected to retain the BI CCD deadlayer model published with the previous of of the ACIS Calibration report (October, 1997). Since continuum effects are expected to be smaller at higher energies (where the resemblance of BI and FI redistribution functions is much closer than

at low energies), we have fit a model to the MIT CSR relative quantum efficiency data to determine the photosenstive thickness of each BI device, given this fixed deadlayer model. Both the fixed deadlayer model and best-fit depletion thicknesses for the BI devices are shown in Table 4.63. The quoted confidence interval for the depletion depth (15%) is based on an assumed relative quantum efficiency error of 5%.

	Model Parameters (μm)							
	Device-Specific Fit				Generic (from sibling devices)			
Location/ Device	Si	SiO_2	Si_3N_4	Depletion Depth	CS Si†	CS SiO_2‡	CS Width⋆	Reference Detector
I0/w203c4r	0.297	0.350	0.022	65	0.35	0.45	4.1	w190c3
I1/w193c2	0.292	0.339	0.024	65	0.35	0.45	4.1	w103c4
I2/w158c4r	0.272	0.319	0.030	65	0.35	0.45	4.1	w103c4
I3/w215c2r	0.291	0.344	0.020	65	0.35	0.45	4.1	w190c3
S0/w168c4r	0.264	0.318	0.024	64	0.35	0.45	4.1	w190c3
S1/w140c4r	0.0001*	0.023*	N/A	30	N/A	N/A	N/A	w134c4r, w103c4
S2/w182c4r	0.270	0.231	0.030	76	0.35	0.45	4.1	w103c4
S3/w134c4r	0.0001*	0.023*	N/A	40	N/A	N/A	N/A	w203c2, w103c4
S4/w457c4	0.244	0.314	0.042	72	0.35	0.45	4.1	w190c3
S5/w203c4r	0.289	0.339	0.021	72	0.35	0.45	4.1	w190c3
1-parameter 90% conf. limits for								
FI Devices:	±0.024	±0.008	±0.010	±1.7	fixed	fixed	fixed	
BI Devices:	fixed	fixed	N/A	±15%	fixed	fixed	fixed	

†: typical one-parameter 90 % confidence range from mesh experiments is $^{+0.06}_{-0.03}\ \mu m$.
‡: typical one-parameter 90 % confidence range from mesh experiments is $^{+0.17}_{-0.11}\ \mu m$.
⋆: typical one-parameter 90 % confidence range from mesh experiments is $^{+0.3}_{-0.4}\ \mu m$.
∗: Deadlayer model parameters for BI devices fixed at approximate values; see text.

Table 4.63: Adopted ACIS Flight Detector Quantum Efficiency Model Parameter Values

4.8.2.2 Results and Data Products

The best-fit model for each flight detector was used to predict quantum efficiency as a function of energy. For historical reasons, our fits of the model to the data (both for the absolute response of the reference detectors, and the relative response of flight detectors) made use of standard (Henke, 1993) mass-absorbtion coefficients. It should be noted, however, that the *predicted* flight detector efficiency curves incorporate our measurements of the absorption edge structure near the nitrogen, oxygen and silicon edges (see section 4.6.4).

As an example, the best-fit quantum efficiency for ACIS detector S2 (the most efficient ACIS FI detector at all energies) is shown in Figure 4.91. The lower panel of the figure shows estimated 90% confidence envelope on the relative error in the model quantum efficiency; these error limits are discussed in detail in the next section.

The adopted quantum efficiency models for the two BI devices are shown in Figures 4.93 and 4.94.

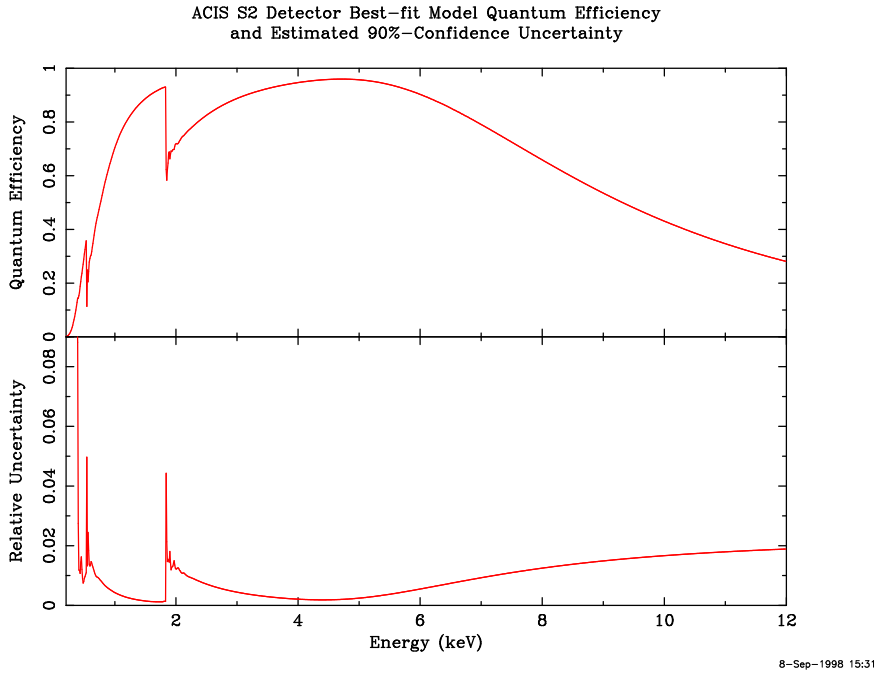

Figure 4.91: Best-estimates for ACIS S2 (Front-illuminated) Detector Quantum Efficiency Model and 90% Confidence Envelope. See text for interpretation of the error envelope.

The best-fit quantum efficiency models for all FI detectors are shown in Figure 4.92. The quantum efficiency of the back-illuminated detector S3 is shown in Figure 4.94

The quantum efficiency of each ACIS flight detector will be made available as an ASCII table file. It is intended that these files be available from the MIT ACIS web page at

`http://acis.mit.edu`.

The files can also be found on the MIT CSR ACIS calibration database in the directory

`/ohno/di/database/rsp/release`.

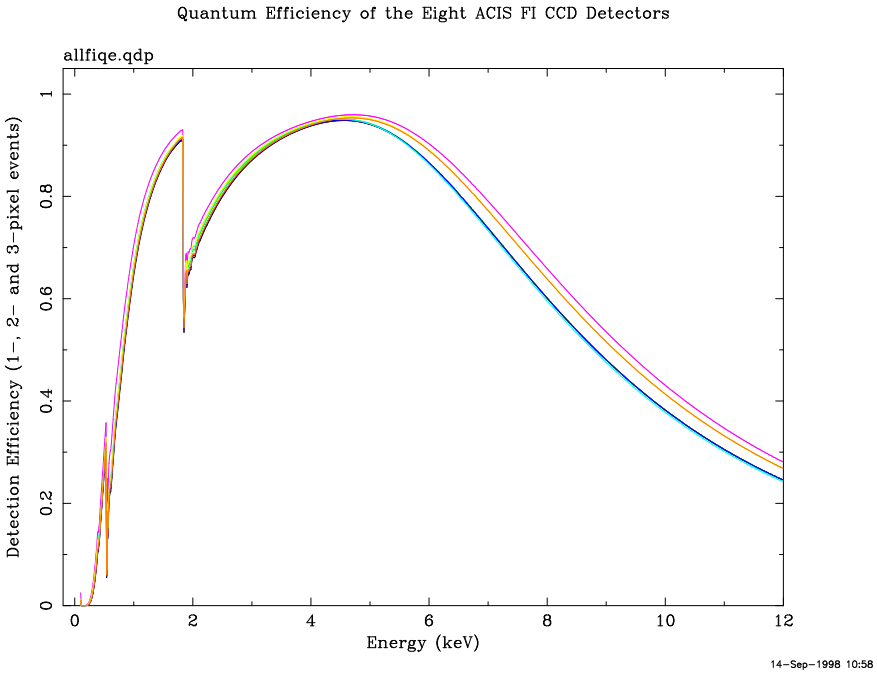

Figure 4.92: Best-fit model quantum efficiency for all ACIS FI Detectors

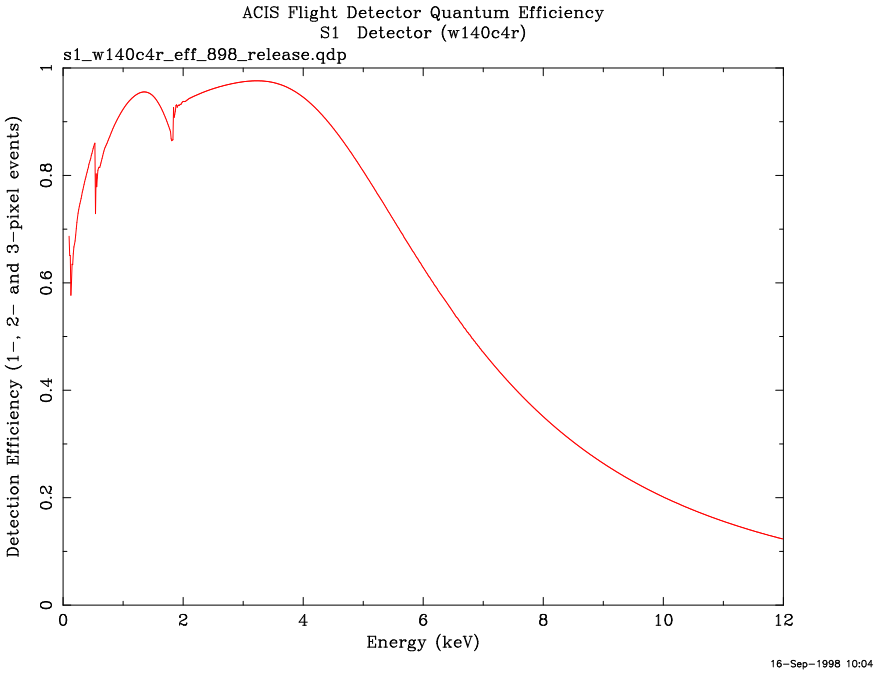

Figure 4.93: Adopted ACIS S1 (Back-illuminated) Detector Quantum Efficiency Model

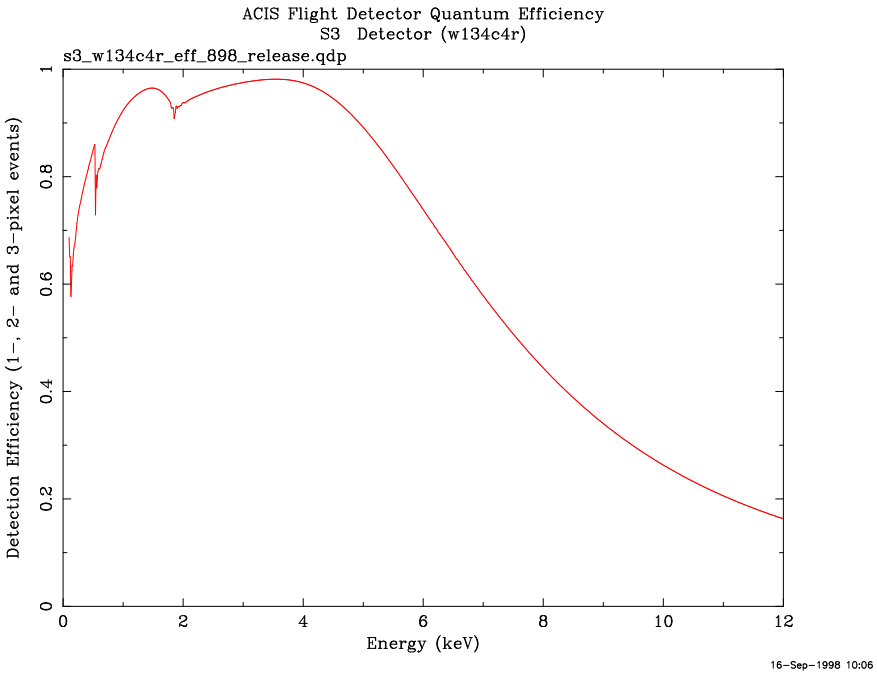

Figure 4.94: Adopted ACIS S3 (Back-illuminated) Detector Quantum Efficiency Model

4.8.3 Uncertainties in Absolute Quantum Efficiency

In this section we attempt to enumerate error sources and, to the extent possible, to quantify the errors in the best-fit model quantum efficiency. It is useful to distinguish at the outset errors arising from the limited precision with which the parameters of the adopted model are constrained by the available data, on the one hand, from those arising from inadequacies in the quantum efficiency model, on the other hand. At the risk of creating some confusion, we choose to say that the former type arise from "measurement errors" since their ultimate origin is the uncertainty in the measured quantities used to constrain the model. Thus we shall sometimes use the phrase "measurement errors" as an abbreviation for "errors in predicted quantum efficiency resulting from errors in measurement." We label the latter error type "modelling errors," intending an analogous ellipsis.

In general, effects of modelling errors are difficult to quantify, and, in any event, not particularly well-bounded at this writing. In contrast, the effects of measurement errors can be quantified using well-known techniques, though it must be emphasized that even these errors must be interpreted carefully. In particular, measurement errors produce quantum efficiency errors which are NOT statistically independent from energy to energy. For many purposes it is therefore much more useful to conceive of the quantum efficiency vs. energy function itself, rather than the quantum efficiency at any particular energy, to be the random variable whose value is constrained by the model fitting.

In this section we first present a straightforward (though incomplete) quantitative analysis of the effects of measurement errors. We then discuss modelling errors. While an effort has been made to quantify modelling errors, more work remains to be done on this problem. As a result, our discussion serves mainly to guide future work.

4.8.3.1 Quantum Efficiency Uncertainties Due to Measurement Errors

To determine the accuracy of our model fits, given that the model is correct, we must define the volume of model parameter space within which model parameter values are consistent, at some level of confidence (we will adopt the 90% confidence level here,) with the data. This parameter space volume is bounded by a surface S_{90}, which we shall call the "90% confidence surface". To each point p on the confidence surface S_{90}, the model assigns a quantum efficiency vs. energy function $f_p(E)$. The ensemble of such functions $\{f_p(E) : p \in S_{90}\}$ is then the set of quantum efficiency functions just allowed, at 90% confidence, by the calibration data. A complete characterization of the quantum efficiency error would include a probability distribution of the allowed values of $f_p(E)$ for all p in the parameter space volume bounded by S_{90}. We do not provide such a characterization here. Instead, we attempt in the following way to estimate the envelope of the functions $f_p(E)$ allowed by the data.

First, we characterize the 90% confidence surface. This surface S_{90} is defined by the property that for any point p on S_{90}, $\chi^2(p) - \chi^2_{min} = \Delta\chi^2_{crit}$, where $\chi^2(p)$ is the value of χ^2

computed for the model $f(p)$ with respect to the data, χ^2_{min} pertains to the best fit model, and $\Delta\chi^2_{crit}$ is a constant depending on the number of model parameters constrained by the fit.

In chosing $\Delta\chi^2_{crit}$, we note that the four fitted parameters belong to two distinct sets. The three gate structure parameters are entirely constrained by the low-energy ($E < 3$ keV) data, while the depletion depth is entirely determined by the high-energy data ($E = 5.9$ keV, in our case). For purposes of bounding the quantum efficiency errors, we can therefore consider the gate structure parameters separately from the depletion depth.

For three interesting parameters (the thicknesses of Si, SiO_2 and $Si3N_4$) at the 90% confidence level, $\Delta\chi^2_{crit} = 6.2$, the 90% confidence limit for a χ^2 distribution with 3 degrees of freedom. We have found the six points on S_{90} which represent the maximum deviations (both positive and negative) of each of the three gate structure parameters from their best-fit values. These are listed in Table 4.64.

Si	SiO_2	Si_3N_4	Remarks
(μm)			
0.235	0.233	0.045	Minimum Si
0.306	0.229	0.016	Maximum Si
0.276	0.220	0.032	Minimum SiO_2
0.264	0.243	0.029	Maximum SiO_2
0.304	0.233	0.015	Minimum Si_3N_4
0.237	0.230	0.045	Maximum Si_3N_4

Table 4.64: Six points on the 90% confidence surface used to determine the uncertainty envelope for FI detector quantum efficiency.

We have evaluated the quantum efficiency model at each of these six points, and then found the extreme values of predicted quantum efficiency (among these six models) at each energy. To determine the envelope at high energy, we have separately varied the depeletion depth through its (single-parameter) 90% confidence interval of $\pm 1.7\mu m$. (Thus we have in fact sampled twelve points in parameter space, *viz.,* the six points listed in table 4.64 at the two extreme values of depletion depth. This error envelope, expressed as a fraction of the best fit model quantum efficiency is plotted as a function of energy for the S2 detector in the lower panel of figure 4.91. The plot shows the absolute value of the 90% confidence limits; positive and negative limits have been calculated, but are nearly identical, and so only the positive limits are shown.

Two limitations of this error analysis must be made clear. First, we have only considered errors resulting from measurement of the flight device quantum efficiency relative to that of the reference detectors. In principle, precisely the same analysis can be performed for the absolute calibration of the reference detectors. In so doing we find that the parameter ranges

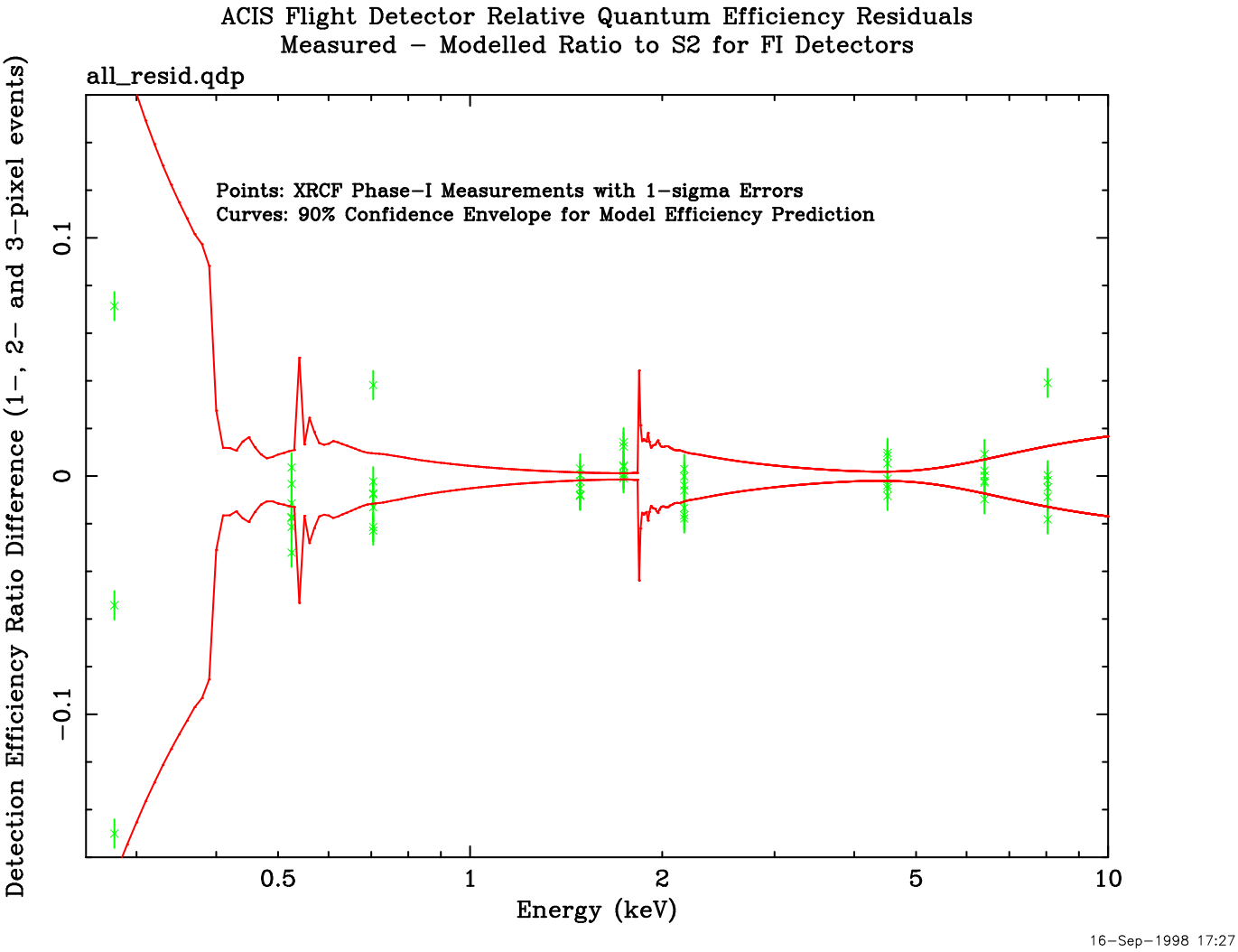

Figure 4.95: Comparison of XRCF Phase I relative quantum efficiency measurements to Model Predictions for front-illuminated detectors. Points are deviations between XRCF quantum efficiency measurements, relative to S2, and lines are estimated 90% confidence intervals for model predictions. Note that the models are based entirely on relative QE measurements made at MIT; the points shown were NOT used to constrain the models. The RMS of the residuals for energies $\geq$ 525 eV is 1.3%.

allowed by fits to the reference detector response to undispersed synchrotron radiation are smaller than those shown in Table 4.64 by factors of three to six. Thus the measurement errors associated with the absolute calibration are in any case small. Moreover, since model parameter errors in the absolute and relative calibrations are presumably statistically independent, their effect on the error envelope is properly accounted for by adding a small

term in quadrature to the envelope derived from the relative data alone. We have therefore chosen to ignore the effect of absolute measurement errors in the present analysis, and estimate that the resulting error in our error envelope is less than 10% of the error envelope.

A much more significant limitation of this error analysis is that we have only included effects of measurement errors on four of the seven model parameters. The three channel stop parameters have not been varied in either the absolute reference detector or relative flight detector measurements. While we have some understanding of the allowed confidence intervals for these parameters (see reference (Pivovaroff et al., 1998)), they are not constrained by measurements on the flight detectors. In principle a joint fit of the flight detector quantum efficiency data and sibling detector mesh experiment data could produce a statistically correct error estimate. We have not yet attempted to perform such a fit.

Neglect of uncertainties in the channel stop parameters may be a significant shortcoming in our error analysis. For example, we find that a 10% increase in the fixed value of each of the three channel stop parameters (the single-parameter 90% confidence limit allowed by the mesh experiments is about 10-15% in each parameter) produces a 0.5% change in the best-fit apparent synchrotron radiation intensity determined by a reference detector, averaged over the 0.4 to 4 keV band. This is comparable to the (spectrally averaged) quantum efficiency error plotted in Figure 4.91.

We believe that a mesh measurement of one of our absolutely calibrated reference detectors would provide us with quantitative information on the effects of channel stop uncertainties on the final model quantum efficiency errors.

As an independent check on these errors (and on the models!), we have compared XRCF measurements of quantum efficiency, relative to detector S2, to the ratio of model predictions for the appropriate detectors. Results are shown for seven FI devices in Figure 4.95. Also shown are the 90% confidence limits for a single model efficiency prediction. (The solid curve is NOT a predicted error envelope for the ratio of two model efficiencies.) The observed residuals are in good qualitative agreement with the quoted error limits, especially considering that the model is based entirely on fits to the MIT CSR data, while the data points come entirely from measurements at XRCF. It is clear that inclusion of XRCF data in model fits is appropriate, and would improve the accuracy of the models further, especially at energies below 0.4 keV.

Quantitative comparison suggests that the observed residuals exceed those expected from the model uncertainties and measurement errors alone, however. Excluding the three measurements at 277 eV, for which the estimated model errors are quite high (and for which the observed residuals are well within expected model errors), the mean residual for 54 measurements shown in figure 4.95 is -0.003, and the RMS deviation about that mean is 0.013. The root mean square residual (about zero, rather the mean) is also 0.013. Ignoring the correlation of model errors at different energies, and assuming that the model errors for different devices are independent, we expect the RMS deviation for the residuals, (accounting for the 0.006 1-sigma measurement errors) to be 0.0095. Thus the observed residuals are larger, by a factor 1.3, than those estimated from the model errors alone.

Several factors may account for this discrepancy. Since most of the variance in the observed residuals comes from 2 of the 54 points, (the S4 point at 705 eV and the S5 point at 8040 eV), it seems likely that some unknown systematic errors (at the 3-4% level) affect these points. With these fairly obvious outliers excluded, the residuals (at 0.009, RMS) are consistent with the model error estimates. In addition, one might expect the internal correlation of errors within any one model to increase the observed variance of the residuals. On the other hand, the model error envelopes do not account for uncertainties in the channel stop parameters, and so must be underestimates at some level.

In any event, we conclude that the our models predict relative quantum efficiency of the ACIS FI detectors with an accuracy better than 1.5%, RMS, over the 0.4 to 8 keV band. Our estimates of the errors in the models are reasonable agreeement with the data, though the errors might be understimated by 30% or so.

4.8.3.2 Quantum Efficiency Uncertainties Due to Modelling Errors

In this section we discuss modelling errors, as defined above, and their effects on both the absolute calibration of reference detectors and the relative calibration of flight detectors with respect to those reference detectors.

4.8.3.2.1 Sources of Modelling Errors in the Absolute Calibration of Reference Detectors. The CCD response model used to analyze the undispersed synchrotron radiation data suffers from a number of shortcomings. The magnitidue of the quantum efficiency errors resulting from these limitations is not well known at present. In principle, simulations comparing the accuracy of the simple models we have used to more realistic (and complicated) models could provide estimates of the magnitude of these errors. Indeed, we have already implemented more elaborate CCD models in our simulations (see section 4.14). The best approach, however, would be to fit these more sophisticated models to the calibration data. There is no technical reason why this could not be done in the near future.

For purposes of guiding such work, we list the major shortcomings of the model we used to establish the absolute response of ACIS reference detectors.

1. *The gate structure model is oversimplified.* The slab and stop model ignores gate overlaps and phase-to-phase variations in gate thickness. The resulting error varies in lowest order as the square of the optical depth of the gate structure, so in the limit that the gates are optically thin, the error vanishes. Conversely, the magnitude of this error is largest just above the absorption edges of oxygen and silicon, and at very low energies. This error can readily be quantified via simulation.

2. *Absorption fine-structure was ignored in determing model parameters.* The undispersed synchrotron radiation data were analyzed using standard Henke (1993) absorption coefficients; these omit edge structure which we have since measured (see

section 4.6.4.) While the spectral resolution of the detector tends to smooth the fine structure, we have not yet established the magnitude of error introduced by neglect of fine structure. The relatively large residuals from the best-fit model (see section 4.6.1) near the absorption edges probably reflect this error. We hope to repeat the reference detector fits with the fine-structure included in the near future.

3. *The redistribution function is oversimplified.* A phenomenological representation of the spectral redistribution function has been used in analysis of synchrotron radiation data. The response to a monochromatic input is modelled as the sum of 2 Gaussians plus a phenomenological low-energy tail. A better, physically-grounded model of the redistribution function is now available (see sections 4.3.2 and 4.14), but has not yet been used to analyze the PTB/BESSY data.

   A more subtle but related difficulty is that aside from the fact that in our current model the channel stop is taken to be a dead volume, there is no allowance for variation of the redistribution function with position within a pixel. A more realistic picture is that the spectral redistribution function for photons absorbed in the channel stops is non-zero but differs markedly from that for the rest of the device. We are now modelling this effect.

4. *Channel stop parameter values have not been measured directly for the reference detectors.* The most reliable measurements of channel stop dimensions are obtained using the mesh technique described in section 4.5, and from (destructive) scanning electron micrographs. Neither of these techniques has been applied to determine the channel stop parameters of the reference detectors themselves. It is hoped that mesh measurements can be made on at least one of the reference detectors.

5. *Spatial variations in quantum efficiency have not been physically modelled.* While the method used to infer depletion depth is simple and apparently reasonbly accurate, it is subject to a number of systematic errors, as has been discussed in section 4.6.2. Of particular note are variations in depletion depth with position in each detector. The branching ratio data show small (several microns out of 65-75 microns) variations in depletion depth from quadrant to quadrant within a detector. Thus the use of spatially averaged quantum efficiency may lead to systematic errors at high energy. Indeed the quantum efficiency maps (see section 4.7) show some modest ($\sim 2-3$) residual variation with detector position at 8 keV; little, if any, such variation is seen at lower energies in the FI devices. While we believe the best interpretation of these variations is that they reflect spatial variation in the depletion depth, this interpretation is speculative.

4.8.3.2.2 Magnitudes of Modelling Errors in the Absolute Calibration of Reference Detectors We have identified several lines of evidence that can supply quantitative bounds on systematic measurement errors, and on some kinds of modelling errors.

Taken together, these checks furnish some confidence that, for front-illuminated devices, the absolute quantum efficiency errors are no larger than 5% in the 0.4 - 4 keV band.

1. *Plausibility of best-fit model parameters.* The best-fit values for synchrotron radiation flux normalizations, relative to the expected value, for three reference detectors discussed in section 4.6.1 are 1.000,0.994, and 0.956, respectively; these numbers each have 90% confidence intervals of approximately ± 0.005. The simplest interpretation of these results is that any residual systematic errors in the broad-band quantum efficiency amount to less than 5%. Moreover, the inferred mean gate structure parameters are in the range (within $\pm 50\%$) expected given the device fabrication process, suggesting that the slab and stop model is providing a reasonable, and therefore probably reliable, representation of the gate structure.

2. *Internal consistency of reference detector quantum efficiencies.* The quantum efficiency models derived for the reference detectors from synchrotron radiation data can be compared to relative efficiency measurements made at MIT CSR. The ratio of the two models agrees quite well with the relative quantum efficiency data: for the five energies measured at MIT within the BESSY passband (0.525 to 4.5 keV), the residuals (measured ratio minus modelled ratio) have a mean of -0.008 and a standard deviation of 0.01. Thus the mean is consistent with 0 at the 2-sigma level, provided the standard deviation is taken to be measure of the random errors in the residuals. The latter assumption is a good one, given that the errors in the relative quantum efficiency measurements are thought to have a standard deviation of 0.6%.

   This result suggests that, although it cannot be ruled out at present, it is unlikely that broadband errors as large as 5% could remain in the absolute quantum efficiency models of the reference detectors, at least in the BESSY passband.

   Of course our internal consistency check cannot rule out all systematic errors. For example, this check would not reveal a geometry error that affected every BESSY measurement identically (though the normalization results described above suggest such an error is highly unlikely.) It is noteworthy, however, that the synchrotron measurements in question were made on different runs separated in time by about a year, and with different sets of electronics.

3. *Comparison to other absolutely calibrated detectors* An extremely valuable check on ACIS absolute efficiency models will be provided by comparisons to absolutely calibrated beam normalization detectors at XRCF. The most suitable detector for this purpose, the solid-state detector (SSD), has been calibrated at the same PTB beamline that was used to calibrate the ACIS reference detectors. As of this writing, the absolute response of the SSD is not yet available, however, so this important check remains to be done.

Nevertheless, since the SSD detector is thought to be fairly well understood at higher energies, and since we have no other external check on our high-energy absolute calibration, we have compared the ACIS flight detector model predictions to ACIS-to-SSD relative QE measurements made at XRCF. The XRCF phase-I results used for this purpose are detailed in table 4.36 in section 4.6.6. If we use the ACIS detector model quantum efficiencies, together with these relative QE data, to infer the detection efficiency of SSD5 at 8.040 keV, we obtain ten estimates of the SSD5 efficiency. The mean value of these estimates is 0.966, and the standard deviation of the estimates is 0.033. For the FI detectors alone (for which the QE model is based on the branching ratio technique), the mean is 0.952, and the standard deviation is 0.018. The a priori expected quantum efficiency of the SSD5 at this energy is 0.997 (according to R. Edgar). This comparison is thus consistent with the supposition that systematic errors in the absolute efficiency of our models for the FI detectors are no more than 5%.

We emphasize that a more precise characterization of ACIS systematic errors, especially at energies above 4 keV, awaits absolute calibration of the XRCF BNDs to an accuracy of order 5% or better. The calibration of SSD5 would be the most useful for this purpose.

4.8.3.2.3 Sources of Modelling Error in the Calibration of Flight Detectors Relative to Reference Detectors. Generally, the relative quantum efficiency measurements are subject to fewer errors, of smaller magnitude than those afflicting the absolute measurements. Nevertheless, the model used to interpret the relative quantum efficiency contains a number of implicit assumptions which are not directly verified by the calibration measurements. Following is a list of some potential "modelling errors" that could affect the accuracy of the relative quantum efficiency model. Future work could, in principle, quantify some of these errors more precisely.

1. *Differences between spectral redistribution functions of flight and reference detectors.* Our model of the relative quantum efficiency measurements implies that differences in efficiency are due to differences in gate structure thickness or depletion depth. Thus we make no correction for differences in the branching ratios or tail amplitudes of the spectral redistribution function (though differences in the spectral resolution are accounted for). For FI-to-FI device relative measurements, the effects of any such differences are minimized because i) we have chosen an event grade set which is known to be substantially independent of energy in the 0.5 - 2.1 keV band, for any given CCD and ii) the sources used are quasi-monochromatic.

   On the other hand, quantum efficiency measurements of back-illuminated flight devices relative to the (front-illuminated) reference detectors are much more sensitive to errors from this source, since the redistribution function is so different for the two

types of detector. Indeed, this difference, coupled with the spectral complexity of the X-ray sources used, is believed to cause significant systematic errors in our current analysis of the relative quantum efficiency data.

At present we have no direct estimate of the size of errors introduced by differences in spectral redistribution functions in FI-to-FI relative efficiency measurements. The consistency of relative quantum efficiency measurements made at MIT and XRCF implies that such errors are not large, at least for the front-illuminated devices. See below.

Errors in BI-to-FI device efficiency arising from this source are discussed in some detail in section 4.7.3. Depending on the source spectrum, such errors can range in size from 5% to 25%.

2. *Spectral complexity in the source.* The current interpretation of relative detection efficiency measurements presumes that the source is monochromatic. In fact, none of the sources used is monochromatic. As discussed above, the error introduced by complexities in the source spectrum is coupled to differences in the response functions of the flight and reference detectors. This error is certainly more important for measurements of back-illuminated flight detectors relative to front-illuminated reference detectors.

   One bound on the magnitude of such errors is provided by a comparison of relative quantum efficiency measurements made at XRCF to those made at MIT CSR, since the "out of band" spectra of the sources at the two sites was generally quite different. In general, the agreement for FI-to-FI detector comparisions is quite good (1.1% RMS below 8 keV), while BI-to-FI detector relative efficiencies are not so reproducible.

3. *Differences in channel stop parameters in the the flight and reference detectors.* The most reliable measurements of channel stop dimensions are obtained using the mesh technique described in section 4.5, and from (destructive) scanning electron micrographs. Neither of these techniques has been applied to determine the channel stop parameters of the flight or reference detectors themselves. Since differences in channel stop parameters are not included in the relative quantum efficiency model, any such differences would be modelled incorrectly. In principle, measurement of channel-stop parameters on a number of siblings of the flight devices (via mesh experiments) could bound the size of errors due to channel stop variations.

4.9 Effects of Instrument Configuration and Environment on Detector Calibration

4.9.1 Effects of Parallel Register Clock Levels on Detection Efficiency

The clock voltages in the image section of a CCD determine the depletion depth of the device. The more positive both levels (low and high) are, the bigger is the depletion depth and, hence, the high energy quantum efficiency. For this reason the standard levels were chosen to be as high as they can safely be, namely, +11 Volts being the high level and +2 Volt the low level. An attempt to further increase the high level voltage above +12 Volts resulted in an increased dark current due to avalanche multiplication of electrons in the channel (so-called "spurious charge" effect). In order to reduce dark current in the frame store section the low clock level there is set to -4.5 Volts. This keeps the surface of silicon under nonintegrating gates in inverted mode, thus suppressing surface generation centers. With the standard levels (+2,+11 Volts) in the image section the depletion depth of the devices varies around a typical value of 70 microns.

For each of the flight devices a measurement was also made with reduced clock levels in the image section. The voltges were chosen to keep nonintegrating gates in inversion with the clock levels at -4.5 and +5 Volts. During calibration the devices did not show any difference in the dark current for the two modes. But the reduced level mode may prove useful when a device undergoes irradiation in space and the level of dark current goes up. The drawback of reducing image clock levels is a reduced depletion depth and, consequently, reduced quantum efficiency at energies above 4 keV. The depletion depth of each flight device was measured in both modes, and results can be found in the Table 4.30 of Section 4.6.2.

In Fig. 4.96 is shown a calculated ratio of quantum efficiencies for the device w193c2 in two different modes. The measured depletion depths for the two modes were found to be 65 and 48 microns, respectively, for standard and reduced voltages. Based on these numbers quantum efficiency was calculated for each mode.

4.9.2 Effects of Focal Plane and Detector Electronics Temperature

4.9.2.1 Detector Electronics Temperature

Prior to delivery to XRCF, the ACIS integrated flight instrument underwent testing at MIT Lincoln Laboratories. Some of these measurements involved operating ACIS with the Detector Electronics Assembly (DEA) at temperatures of -17 C° and 20 C°. These tests were used to map the gain dependence on the electronics temperature. A detailed description and analysis of the gain calibrations are reported in ACIS Memo #143 (Pivovaroff,

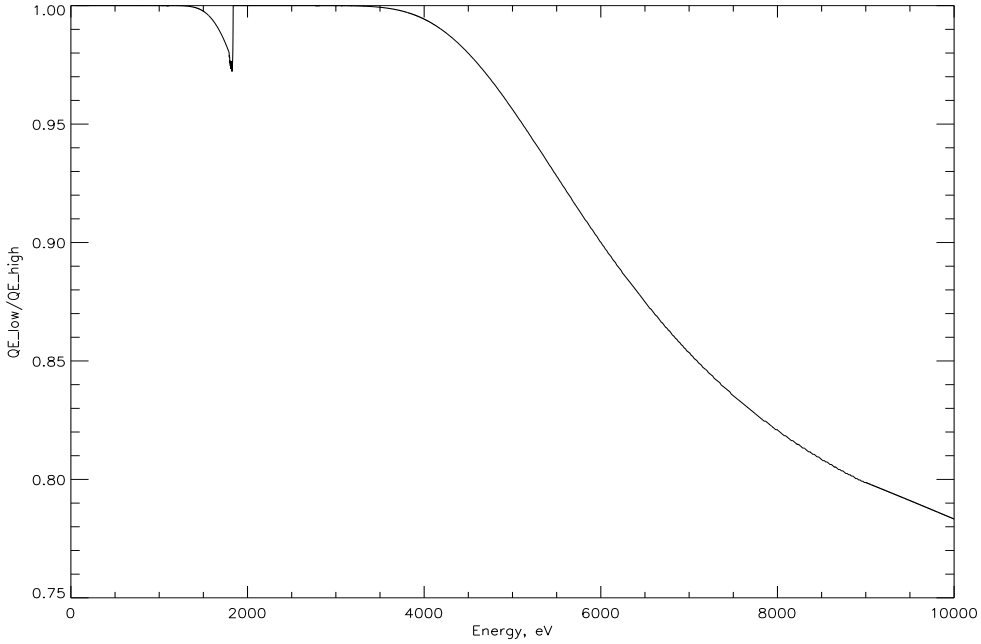

Figure 4.96: The ratio of quantum efficiencies for the device w193c2 with the standard clock levels and the reduced clock levels.

1997c). The main points are summarized below:

–The DEA was stabilized at temperature T_i, (T_i = -17 C°, 20 C°)
–Each chip was independently illuminated with an Al Kα source and an ^{55}Fe source
–The focal plane (FP) temperature during these measurements ranged between -116 and -119 C°
–Gains were calculated by fitting a linear relationship to a gaussian centroid for the Al Kα and the Mn Kα line

Table 4.65 lists the mean gain for each chip for DEA temperatures of 20 C° (hereafter $LLTV_{hot}$) and -17 C° (hereafter $LLTV_{cold}$). Table 4.65 also lists the average chip gains calculated from the XRCF Flat Field ($XRCF_{FF}$), Phase I data. See Section 4.3.1 for the details of these measurements.

It is clear from the data that the gains increase with increasing DEA temperature. In order to quantify this relationship, we have made a linear fit of the gains as a function of temperature. Figure 4.97 shows the linear best-fit plotted against the measured gain values. The hash marks simply indicate the data point and are not representative of errors. The $LLTV_{cold}$ data for I0 and S0 are known to have a problem with drifting biases, so these two data points are suspect[7]. With only three data points to fit, the incorrect $LLTV_{cold}$

[7]This problem is fully characterized in ACIS Memo #143. The jitter.dacs software patch implemented during the XRCF Flat Field measurements eliminates this problem.

	Mean Gain (eV/ADU)		
	$LLTV_{cold}$	$XRCF_{FF}$	$LLTV_{hot}$
FP Location	DEA=$^{-}$17 C° FP=<$^{-}$117.5> C°	DEA=13 C° FP=$^{-}$110 C°	DEA=20 C° FP=<$^{-}$117.5>
I0	3.812	3.827	3.840
I1	3.809	3.849	3.857
I2	3.563	3.592	3.610
I3	3.839	3.882	3.891
S0	3.689	3.797	3.811
S1(BI)	4.405	4.413	4.455
S2	3.724	3.758	3.771
S3(BI)	4.492	4.507	4.574
S4	4.256	4.306	4.319
S5	4.075	4.101	4.119

Table 4.65: Mean gains for ACIS at different operating temperatures

gains greatly influence the fits and skew the slope of the expected lines. Excluding I0 and S0, the data seem to follow the linear relationship quite reasonably. The small deviations from linearity are expected, as only two data were used to define the LLTV gains.

4.9.2.2 Focal Plane Temperature

In addition to being affected by the temperature of the readout electronics, the gain is also dependent on the temperature of the focal plane (FP). Part of the the MIT CSR subassembly calibration efforts included operating each flight chip at off-nominal temperatures to study the influence of this effect on gain. Table 4.66 lists the mean gains and gain variation dependence on chip temperature, as calculated at MIT CSR . Each chip was operated at $^{-}$110 C°, $^{-}$120 C° and $^{-}$130 C° and illuminated with an ^{55}Fe source. Gains were determined by fitting a gaussian to the Mn Kα line and assuming an identically linear (i.e. no offset) relationship between the centroid and 5.895 keV. The differences between the MIT CSR mean gains and the LLTV/XRCF mean gains (Table 4.65) result from not using the flight electronics at MIT CSR.

Before calculating the gain dependence on DEA temperature, we must account for the fact that the FP was operated at slightly different temperatures during the LLTV and XRCF calibrations. Using the ($d\ln(G)/dT_{chip}$) calculated from the MIT measurements, the expected increase in gains from operating the FP at <$^{-}$117.5> C° instead of $^{-}$110 C° is on order of 0.002 ADU/eV. This amount has no affect on the derivation of the gain dependence on DEA temperature. For comparison, .002 ADU/eV corresponds to roughly

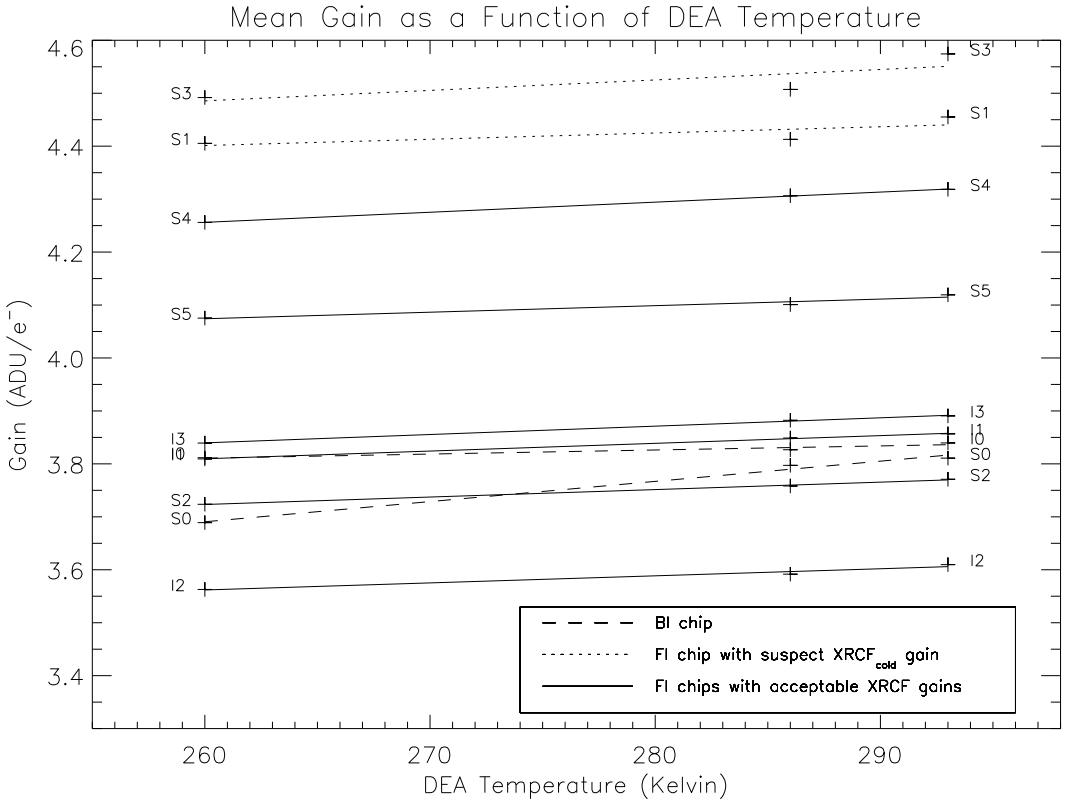

Figure 4.97: ACIS gain variation as a function of DEA temperature.

twice the thickness of a line in in Figure 4.97. If we neglect the very small effect caused by different FP operating temperatures, the DEA temperature dependent variations are determined by the linear fit term divided by the mean gain. These values are also listed in Table 4.66

4.9.3 Long Term Gain Stability

Checking the long term gain stability of the ACIS chips is an important step in the pre-launch calibration. During the course of sub-assembly calibration, the stability in chip gain was firmly established and it is completely expected that ACIS CCD's will share this characteristic. While the earliest gain measurements of the flight instrument date back to March 1997 (LLTV), the first high accuracy (i.e. several characteristic Kα lines used) determination occurred at the XRCF Flat Field (XRCF-FF) calibration in May 1997. The next opportunity to measure the gain came during the first thermal vacuum test at Ball (ISIM-TV1) in October 1997. During this test a significant amount of data was acquired from the External Calibration Source (ExtCalSrc), allowing an accurate gain determination of all ACIS chips. Below, we compare the results of these two calibrations.

Table 4.67 lists the mean gains (all four quadrants of a chip) measured at XRCF-FF

	MIT CSR		**LLTV/XRCF**
FP Location	Mean Gain at chip=$^{-}$120 C° (eV/ADU) (HIREFS)	Gain Temp Variation ($dln(G)/dT_{chip}$) x10^{-5} (C^{-1})	Gain Temp Variation ($dln(G)/dT_{DEA}$) x10^{-4} (C^{-1})
I0	3.990	< 6	2.0
I1	3.972	< 6	3.8
I2	3.865	-10	3.7
I3	4.250	< 6	4.1
S0	4.059	54	10
S1(BI)	5.134	< 6	2.7
S2	4.042	< 6	3.7
S3(BI)	5.109	< 6	4.4
S4	4.375	-8	4.4
S5	4.316	< 6	3.0
mean			**4.2**

Table 4.66: Gain dependence on chip temperature and DEA temperature

and ISIM-TV1. Taking the XRCF-FF values as a baseline, the I-Array chips (imaging CCD's and S2 and S3) have higher gains at ISIM-TV1, while the outer S-Array chips (S0,S1,S4,S5) have approximately the same gains. The gain is known to be dependent on DEA temperature and focal plane temperature. As the effect of the focal plane temperature on the gain is an order of magnitude smaller than that of the electronics temperature, we will focus on the later as a possible explanation of the difference in gains between the two measurements. The mean temperature dependence relationship is: d(ln Gain)/dT=4×10^{-4} (see Section 4.9.2 for details). The thermal conditions for both calibrations were nominally the same: focal plane temperature of -110° C, and DEA -Z plane temperature of +13° C. Allowing for a drift in the DEA temperature of $\sim$ 1° C , we would expect a gain variation on order $\sim$ 0.002, much higher than that observed for the I-array chips. Figure 4.98 plots d(ln Gain) for each quadrant of all ten chips.

Systematic variations, order of a few degrees, are expected in the DEA temperature; the dashed lines indicate the values of d(ln Gain) expected for ΔT=$\pm$5° C. The outer S-Array chips are mostly distributed between this range, indicating that the gains measured with the ExtCalSrc for these chips are stable, within systematic uncertainties. Another dashed line indicates the value of d(ln Gain) for ΔT=25° C; the I-Array chips measured with the ExtCalSrc are tightly grouped abou this line. At this time, the source of the gain shift is not known. However, given the uncertainties in the operating conditions and the thermal

Chip	XRCF-FF	ISIM-TV1	Chip	XRCF-FF	ISIM-TV1
i0	3.827	3.857	s1	4.413	4.398
i1	3.849	3.892	s2	3.757	3.795
i2	3.592	3.632	s3	4.507	4.560
i3	3.882	3.911	s4	4.306	4.308
s0	3.797	3.791	s5	4.101	4.095

Table 4.67: Mean Chip Gain determined at XRCF-FF and ISIM-TV1

environment during the ISIM-TV tests, there exists the distinct possibility that a strong thermal gradient existed inside the DEA unit. This condition can explain the apparantly paradoxical behavior that some of the gains indicate that the DEA -Z plane was in fact $\sim$13° C, while the other chips indicate that the the electronics were $\sim$25° C hotter. This scenario requires that the boards used to read the I-Array chips were in the hottest part of the gradient and furthest from the DEA -Z plane temperature sensor. Further evidence for this hypothesis comes from Internal Calibration Monitor (ICM) data. The ICM can also be used to determine gains, but only for four quadrants. The ICM data was also taken as part of the XRCF-FF tests, as well as during the second ISIM thermal vacuum test, ISIM-TV2[8]. The XRCF-ICM gains (blue symbols in the plot) are also distributed near the $\pm$5° C lines, establishing that the ICM source can provide an accurate gain measurement. During ISIM-TV2, however, the ICM gains (orange symbols in the plot) are also grouped about the 25° C line. The fact that the two ISIM thermal vacuum tests were separated by *more than two months* indicates that whatever condition caused the shift in the ExtCalSrc gains was also present during the subsequent testing. If the mechanism was in fact a thermal gradient, it must have have been stable.

4.9.4 Temperature Dependence on Dark Current

4.9.4.1 Introduction

We report on the ACIS dark current measurements made at Ball in October, 1997 as part of the Integrated Science Instrument Module thermal vacuum tests (ISIM-TV1). Below, we describe the procedure used in calculating the dark current and the dark current values for all ten CCDs at temperatures of -40°, -60° and -90° Celsius. We also discuss the measurements made at -90° C used to check the instrument after a thermal cold soak.

[8]ICM data also exists from the AXAF thermal vacuum tests. While the gains are linear and valid, the thermal conditions during data acquisition are relatively unknown, preventing the inclusion of these points in the current analysis.

4.9.4.2 Procedure

Measurement of dark current requires bias data to be taken using at least two different integration times. During the ISIM TV tests, integration times of 3.3 (short) and 9.9 (long) seconds were used. For each chip eleven frames of data were acquired with the high speed tap (HST) at both the short and long integration times. An average bias frame is created from each set of eleven frames using the `meanbiasclip2` algorithm (/usr/acis/bin/meanbiasclip2). Each of these average bias frames is overclock (OC) corrected before the short average frame is subtracted from the long average frame on a pixel

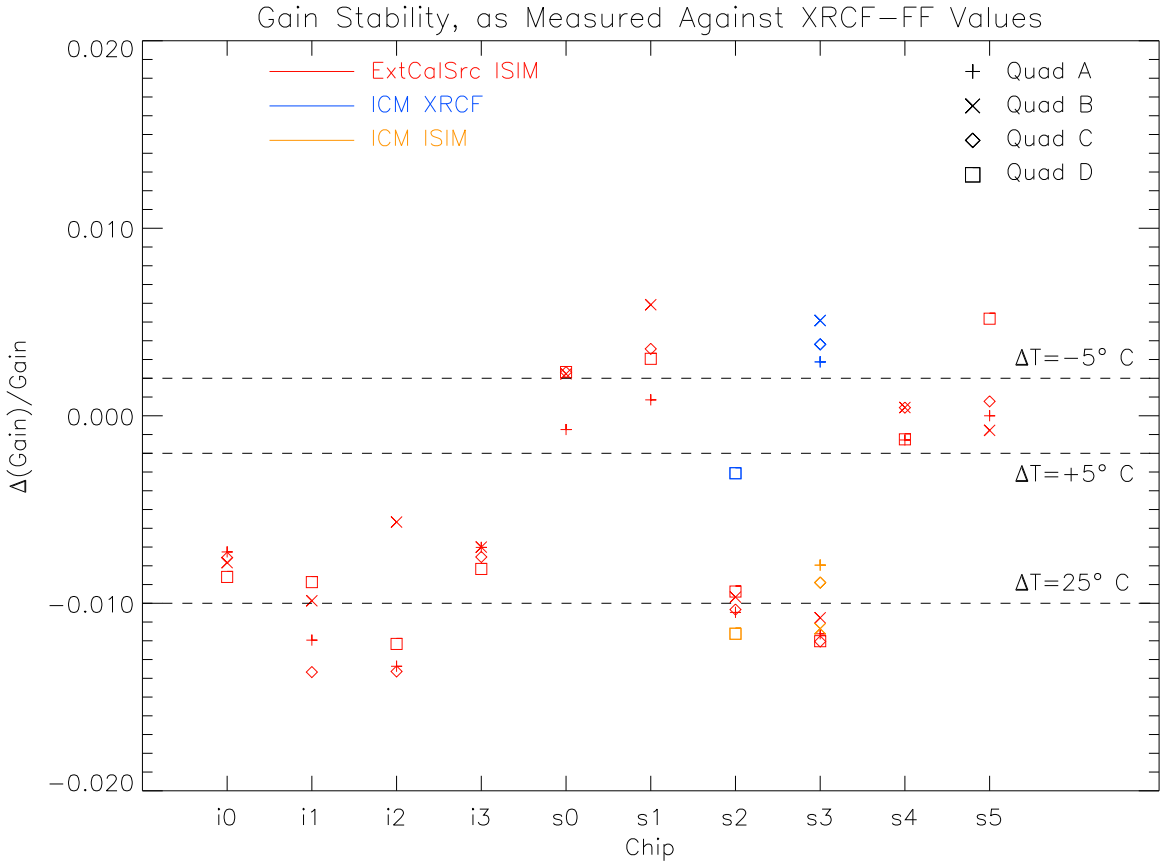

Figure 4.98: The difference in gain measured at XRCF-FF and ISIM-TV1. The figure plots d(ln Gain)=ΔGain/Gain, where the gain from XRCF-FF is taken as a base line. The red points compare the gains calculated from the ExtCalSrc data at ISIM-TV1, the blue points compare the gains calculated from the ICM source at XRCF-FF, and the orange points compare the gains calculated from the ICM source at ISIM-TV2. The dashed lines and labels indicate the change in DEA temperature required to shift the gain by that amount. The ICM source only allows gain measurements for S2 Quad D and S3 Quads A-C.

to pixel basis. Specifically, the distribution of differences D is given by

$$D = \sum_{quad=1}^{4} \sum_{col=1}^{256} \sum_{row=1}^{1024} (Pixel(col,row)_{9.9\ sec} - OC(quad)_{9.9\ sec}) \\ -(Pixel(col,row)_{3.3\ sec} - OC(quad)_{3.3\ sec}).$$

A gaussian function is fit to the distribution D, and the dark current is taken as the center of the gaussian divided by the difference in integration times (6.6 seconds). This procedure was repeated for each chip. Data for chips I0, I1, I2, and I3 were taken with ACIS operating in the I-array configuration. Data for chips S0, S1, S2, S3, S4 and S5 were taken with ACIS operating in the S-array configuration.

4.9.4.3 Data and Analysis

Below, we present the the histograms of the distribution D for each of the ten chips. The smooth, solid line is the gaussian fit to D. Each plot also contains the the dark current (ADU/sec) and width[9] (ADU).

T = -40° C: Figure 4.99 contains the data for the T = -40° C data. The two backside illuminated (BI) chips (S1 and S3) have a considerable number of hot pixels, as evident by the large, extended tail. The frontside illuminated (FI) chips also have a small number of hot pixels. At this relatively warm temperature, such behavior is expected in both the BI and FI chips.

T = -60° C: Figure 4.100 contains the data for the T = -60° C data. With a drop of 20° C, the dark current in the FI chips is reduced about a factor of 20. The FI chips also have fewer hot pixels at this colder temperature. The dark current in the BI chips is also dramatically reduced. S3 continues to have many hot pixels, and while S1 still exhibits a tail, quadrant by quadrant analysis reveals that most of the tail is attributable to quadrant D (the distribution D does not exceed 50 ADU for quadrants A,B, & C).

T = -90° C: Figure 4.101 contains the data for the T = -90° C data. At this temperature, the dark current is effectively zero. The difference distributions D are very gaussian, but often have negative centers. These unphysical dark currents arise due to systematic uncertainties, on order of 1 ADU, in calculating the bias. For the relatively short exposure times used and the systematic uncertainties, we cannot precisely measure the *a priori* low dark current (< 0.1 ADU/sec) expected at a temperature of -90° C. With the exception of the hot pixel tail exhibited by S1 and the slightly large width of both S1 and S3, the BI chips

[9]Here, the width equals σ, where the gaussian is of the form: $e^{-(x-x_0)/2\sigma^2}$.

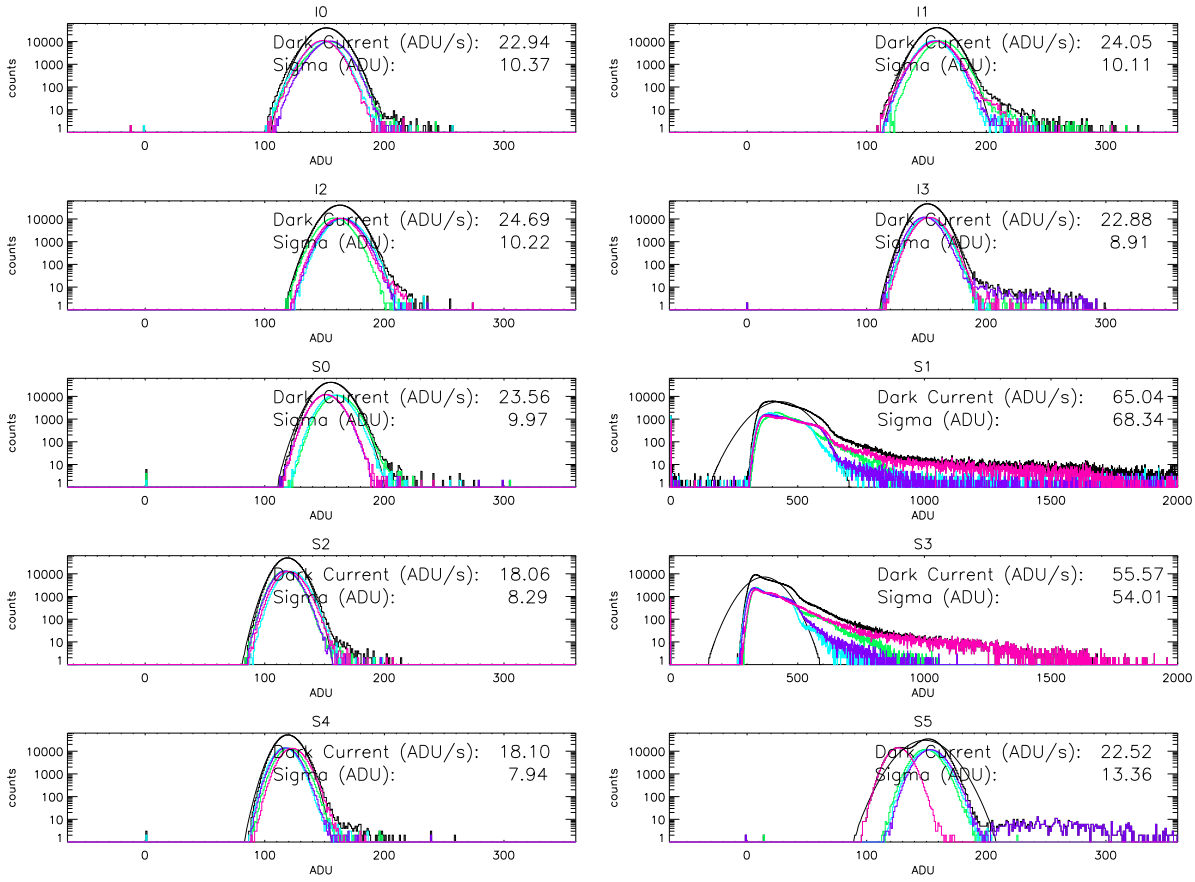

Figure 4.99: ACIS dark current data at T = -40° C.

are virtually indistinguishable from the FI chips. The secondary feature centered around 9 ADU in I0 is due to an instrumental artifact seen in the long (9.9 second) integration data. Examination of the average long frame reveals that the top portion (roughly the first 100 rows) of the bias map is much higher than the rest of the frame. The average short (3.3 second) frame is uniform across the chip. When it is subtracted from the average long frame, the bimodal distribution results. It is suspected that this behavior is due to insufficient settling time between switching ACIS from operation in the the S-array configuration to operation in the I-array configuration.

4.9.4.4 Post Cold Soak Characterizations

One of the procedures performed during the ISIM TV test was to cool the focal plane to T = -129° C. Afterwards, it was important to verify that the cold soak had not damaged ACIS. B. Goeke observed that one way to check for damage to the CCD–to–paddle bond is to measure the dark current. If there is damage, the CCD temperature will rise to the housing temperature (T = -60° C) even if the focal plane is at T = -90° C. Figure 4.102

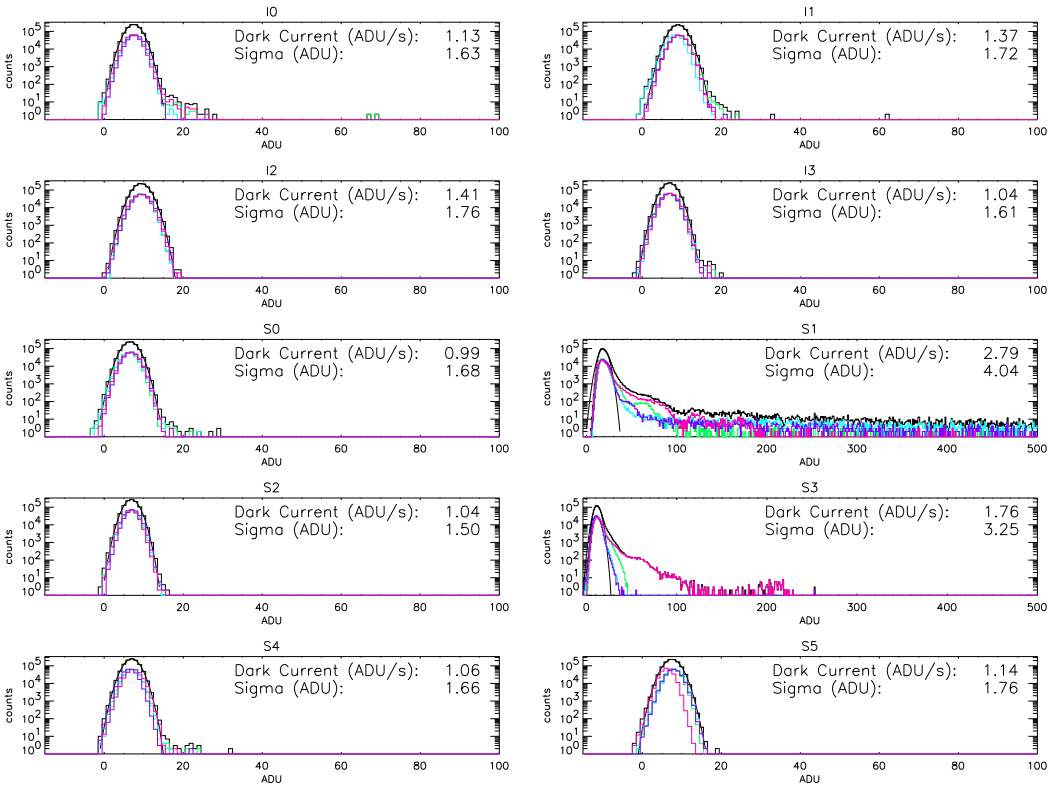

Figure 4.100: ACIS dark current data at T = -60° C.

contains the data taken after the cold soak. The dark current values are entirely consistent with a CCD temperature of T = -90° C, indicating that no damage occured to the bond between the CCDs and the paddle.

4.9.4.5 Summary of Measurements

For future reference, we present the dark current data taken at the ISIM TV test in Table 4.68. Included is the dark current (ADU/sec) and the width (ADU) for each chip.

4.9.5 Effects of CCD Clocking Modes on Detector Peformance

Calibration analyses are based upon data from a timed exposure mode of ccd operation. While this may become the preferred mode of operation it is extremely likely that other operating modes will be used, perhaps even extensively so. Also, most of the analyses, especially of spectral properties such as gain and line shape, are based upon averages of near uniform "flat field" exposures. This type of illumination is not be typical of many sources with the expected telescope point spread function. Illumination and operation mode are closely coupled, the former often dictating the later. Users should consider how

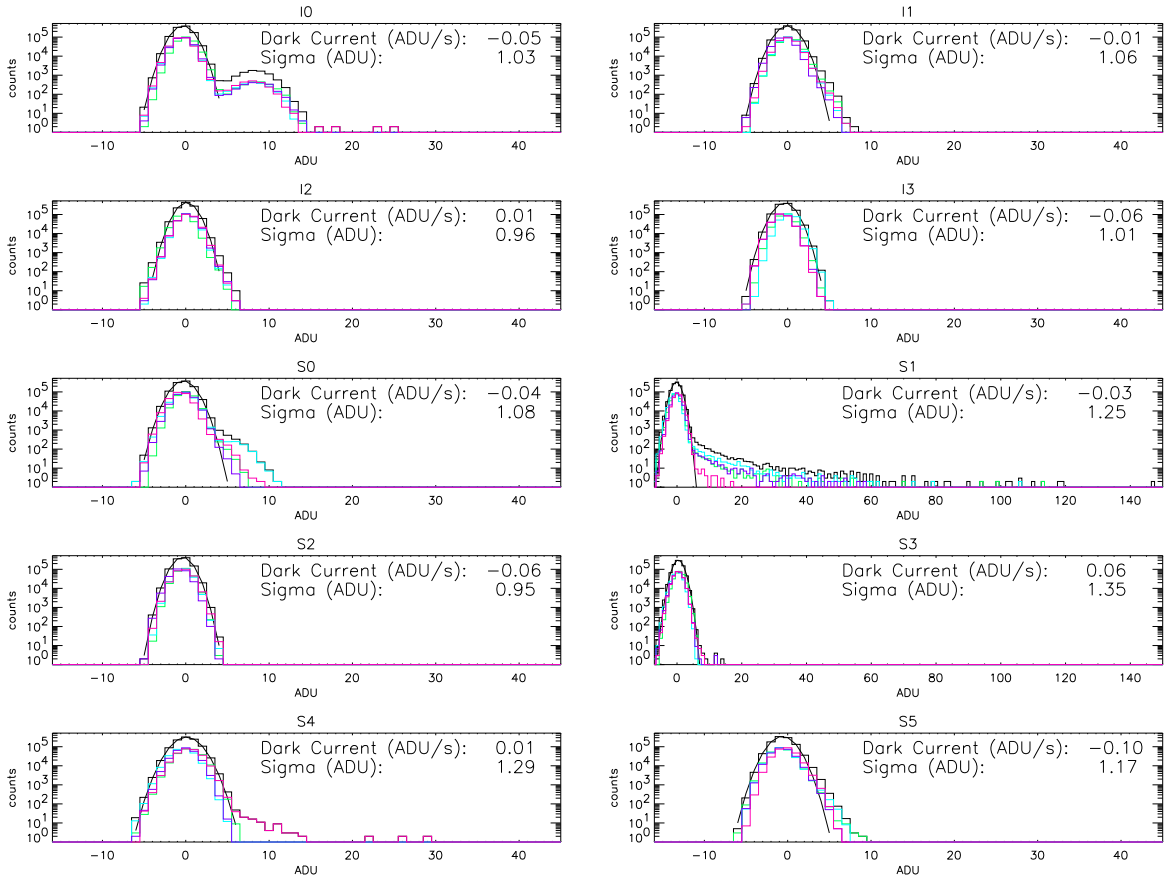

Figure 4.101: ACIS dark current data at T = -90° C.

operation mode will affect application of the calibration results. For this reason a sampling of representative operating modes was tested and the small differences in performance are now described.

Serial 2 pixel summation reduces the gain by approximately 5 percent owing to the necessary shorter integration pulse widths. Because of the peculiar shape of the integrated waveform the relationship between gain and pulse width cannot be predicted. For example, an adjustable gain feature cannot be reliably invoked via the pulse width - halving the pulse width does not halve the gain (it reduces the gain.) Serial summation also modifies the conventional meaning of event grades by promoting some lower grade events (3 pixel and serial split) into higher grades (single split and single pixel.) The pileup correction will also require modification.

Parallel summation of course alters the conventional meaning of event grades, especially of the parallel split events.

Continuous clocking does not seem to require any special consideration.

The window readout shows a peculiar result worthy of mention. This is a mode wherein

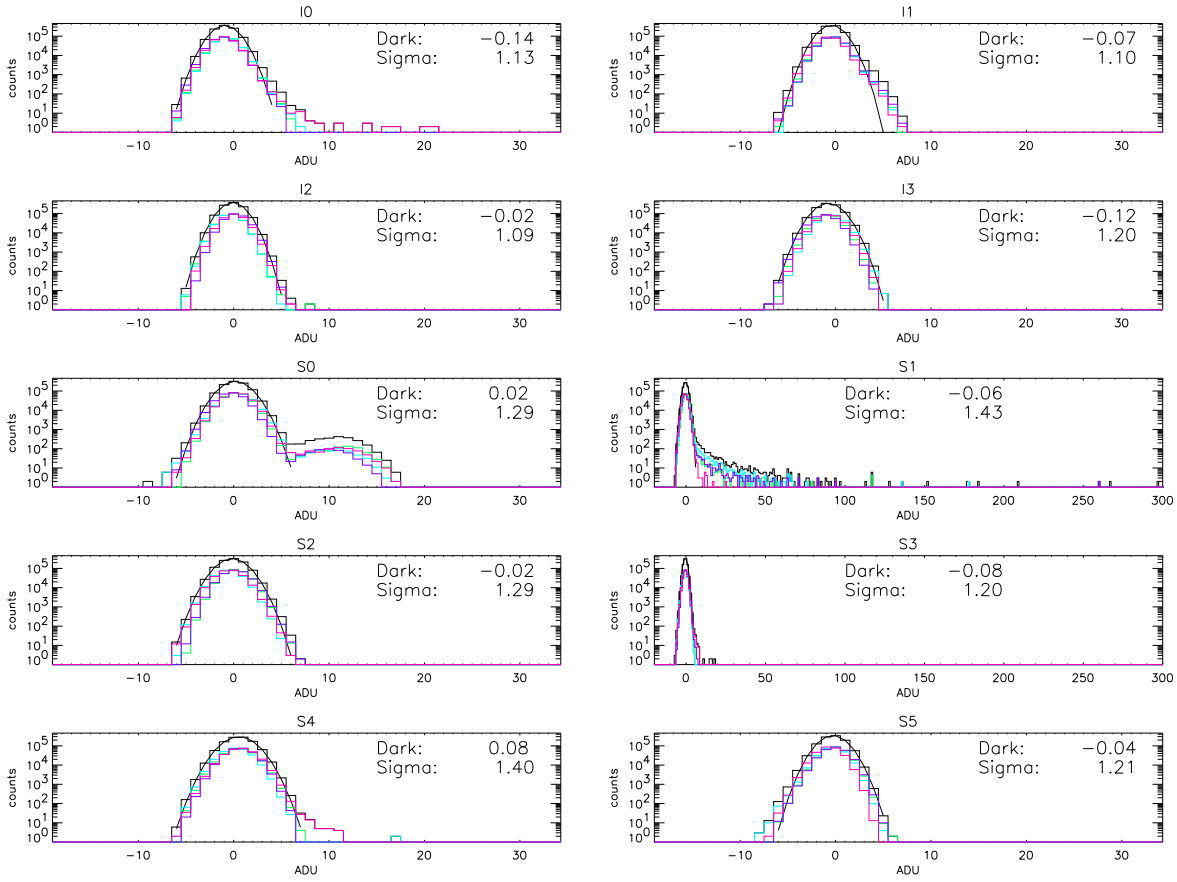

Figure 4.102: Post cold soak ACIS dark current data at T = -90° C.

a fraction of available rows in a timed exposure are actually clocked through and should not be confused with software window sampling wherein all available rows are clocked through but a software mask excludes events not within a virtual window of rows. For testing purposes a window of 100 rows is used with the result that independent of where the 100 rows occur upon the ccd or what monochromatic x-ray energy is used the measured line widths are always narrower than for the full 1024 row readout. Typically the differences is no more than 5 percent. The cause of this change in line width remains a mystery. A leading candidate is the "Elvis-effect", a multilevel disturbance in the bias level which occurs and endures for times comparable to the 100 row readout time. The cause of the Elvis-effect is unknown and it is unclear if it occurs with the flight configured instrument. This is one of a class of bias distortions which would not affect spectra from spatially localised events, but would impact spectra from flat field type illuminations.

The effects of various operating modes are small and occur through the electronics or the meaning of event grades, gain, noise, etc. The description of the ccd model is not affected by choice of operating mode.

	T=-40° C		T=-60° C		T=-90° C			
Chip					pre cold soak		post cold soak	
I0	22.9	10.4	1.13	1.63	-0.05	1.03	-0.14	1.13
I1	24.1	10.1	1.37	1.72	-0.01	1.06	-0.07	1.10
I2	24.7	10.2	1.41	1.76	0.01	0.96	-0.02	1.09
I3	22.9	8.9	1.04	1.61	-0.06	1.01	-0.12	1.20
S0	23.6	10.0	0.99	1.68	-0.04	1.08	0.02	1.29
S2	18.1	8.3	1.04	1.50	-0.06	0.95	-0.02	1.29
S4	18.1	7.9	1.06	1.66	0.01	1.29	0.08	1.40
S5	22.5	13.4	1.14	1.76	-0.10	1.17	-0.04	1.21
S1	65.0	68.3	2.79	4.04	-0.03	1.25	-0.06	1.43
S3	55.6	54.0	1.76	3.25	0.06	1.35	-0.08	1.20

Table 4.68: Dark Current Measured at ISIM TV tests during October, 1997. In each column, the number to the left if the dark current (ADU/sec), the number to the right is the width (ADU) of the gaussian fit.

4.10 Instrumental Background

In this section, we present an analysis of measurements performed during the flat-field tests at XRCF to determine the instrumental background rates and rejection efficiencies of the ACIS flight CCDs. The mean rates and spectral shapes of the instrumental background in the ACIS detectors are presented in Section 4.10.1. Results showing the dependence of background rejection efficiency on event grade selection are reported in Section 4.10.2. The measured background rates from the XRCF data are then used to estimate on-orbit background rates in Section 4.10.3.

4.10.1 Background Rate Measurements at XRCF

Instrumental background measurements at XRCF were performed between flat-field tests, while the energy of the X-ray source was being changed. The data were acquired with the ACIS door in the open position. During each background measurement, the small gate valve where the X-ray beam line enters the thermal vacuum chamber was closed. Occasionally, however, the gate valve was opened by the TRW test director to facilitate tuning of the X-ray source in preparation for the next flat-field test. The background measurements were acquired in 11 science runs performed during the period 1997 May 10–18. For each run, ACIS was operated in either imaging or spectroscopy array mode, with all six detectors in the appropriate array read out. The ACIS telemetry event lists used in this analysis are identified by Science Run Number and TRW ID in Table 4.69.

Science Run	TRW ID	ACIS Array
76	I-BND-BU-2.027	Imaging
85	I-BND-BU-2.025	Spectroscopy
90	I-BND-BU-2.003	Imaging
99	I-BND-BU-2.029	Spectroscopy
105	I-BND-BU-2.013	Imaging
109	I-BND-BU-2.015	Spectroscopy
113	I-IAI-BG-3.001	Imaging
127	I-IAS-BG-3.002	Spectroscopy
150	I-IAS-BG-3.902	Spectroscopy
152	I-IAI-BG-3.901	Imaging
155	I-IAI-BG-3.901A	Imaging

Table 4.69: XRCF Phase I Science Runs Used for the Instrumental Background Analysis

Frames were processed for events by the ACIS electronics using the standard event thresholds for front-illuminated (38 ADU) and back-illuminated (20 ADU) ACIS detectors, along with the standard split threshold of 13 ADU. The exposure time per frame was 3.34 s. Light curves were then plotted showing the number of counts per frame vs. frame number. Periods of time when the gate valve was open were easily identified by the abrupt increase in the number of counts per frame. The range of frame numbers contaminated by X-rays were noted and all events in these frames were removed from the event lists. The events in each list were then sorted into spectra by detector quadrant and event grade.

For each detector, we combined the spectra from all the science runs to increase the signal-to-noise. The total exposure time thus obtained was $\sim$ 63.9 ks for each imaging array detector, and $\sim$ 49.2 ks for each spectroscopy array detector. Detectors S2 and S3 are in both arrays and so had total exposures of $\sim$ 113.1 ks each. To further improve the statistics, we combined the spectra from all eight front-illuminated (FI) flight CCDs. Unfortunately, we could not do the same for the back-illuminated detectors. The ACIS focal plane operating temperature at XRCF was $-110\,^{\circ}$C; this is $10\,^{\circ}$C warmer than the designed operating temperature. Consequently, the background data taken at XRCF with detector S1 were contaminated by an increase in the number of hot pixels and could not be used in the instrumental background analysis.

Rejection of particle-induced events in the ACIS detectors is accomplished using event amplitude and event grade selection criteria (i.e., the sum and distribution of charge in 3×3-pixel events). The passband of the ACIS detectors folded with the HRMA is ~ 0.1–10 keV, so we rejected all events with total pulse-height amplitudes greater than 10 keV. This eliminated 19.5% of the 781,015 events accumulated in the FI detectors and 80.0% of the 26,636 events accumulated in detector S3. We then applied the standard ASCA G02346 event grade selection criteria to the data to reject all events with pixel geometries

that were inconsistent with the physical interaction of X-rays in the ACIS detectors (i.e., ASCA G157 events). The results are presented in Figures 4.103 & 4.104.

The upper panel of Figure 4.103 shows the spectrum from 0.1–10 keV of the background events that were rejected by the ASCA G02346 selection criteria in the FI detectors. The rejected background rises abruptly from zero at low energies to a peak of about 0.32 ct cm^{-2} s^{-1} keV at around 0.65 keV, then decays towards higher energies as a power law with index around -2.2, and finally levels off above 6 keV into a long, flat tail with amplitude $\sim$ 1–2 $\times$ 10^{-3} ct cm^{-2} s^{-1} keV^{-1}. Spectrally-integrated background rates are listed in Table 4.71.

The lower panel of the figure shows the spectrum of the background events in the FI detectors that were not rejected by the event grading scheme. These unrejected background events masquerade as true X-ray events. The spectrum of the unrejected background appears essentially flat from 0.1–10 keV, with the exception of two emission lines. The Mn Kα line at 5.894 keV is due to scattered X-rays from the internal contamination monitor (ICM), while the Au Lα line at 9.671 keV is caused by particle-induced fluorescence in the detector framestore covers.

The spectrum of the rejected background events in detector S3 is shown in the upper panel of Figure 4.104. The spectrum suffers from low counting statistics, but a small peak can be seen around 0.4 keV; the spectrum then drops between 1 keV and 4 keV, before rising with energy in a broad hump that peaks around 13 keV.

The lower panel shows that the unrejected background in S3 is also relatively flat, with the exception of the Au Lα line and a apparent excess in the number of counts below 2 keV. Note there is no sign of an Mn Kα line in the spectrum.

To study the spatial distribution of the Mn Kα line in the focal plane, we have measured the flux of the line in each quadrant. The Mn Kα line fluxes in each detector are listed in Table 4.70, along with the fluxes of the Au Lα line and the unrejected continuum background. The last column contains the mean and RMS deviation of the count rates in the quadrants. The Mn Kα rate varies systematically with position on the focal plane. All of the scattered Mn Kα flux is observed in detectors I0 and I1, and the quadrants of I2 and I3 immediately adjacent to I0 and I1, respectively. The collimator and baffling of the internal contamination monitor was intended to require at least two reflections for a photon to travel from the source itself to the focal plane. The diffuse reflectance of the gold-coated surfaces near the detectors is$\leq$ 2 $\times$ 10^{-5} sr^{-1} at 6 keV. The (unbaffled) brightness of the ICM source itself was about 3 $\times$ 10^{3} ph sr^{-1} during the June 1997 XRCF measurements. Had the ICM baffling requirement been met, the observed flux at the focal plane (some 14 cm from the source) should have been less than 10^{-8} ph cm^{-2} s^{-1}. The observed rate on I0 and I1 suggests that a subtantial fraction of the source flux is arriving at the detectors after a single reflection. The reason for this is not understood. For reference, a diagram showing the ICM, the focal plane, and the intended ICM beam patterns is presented in Figure 4.105.

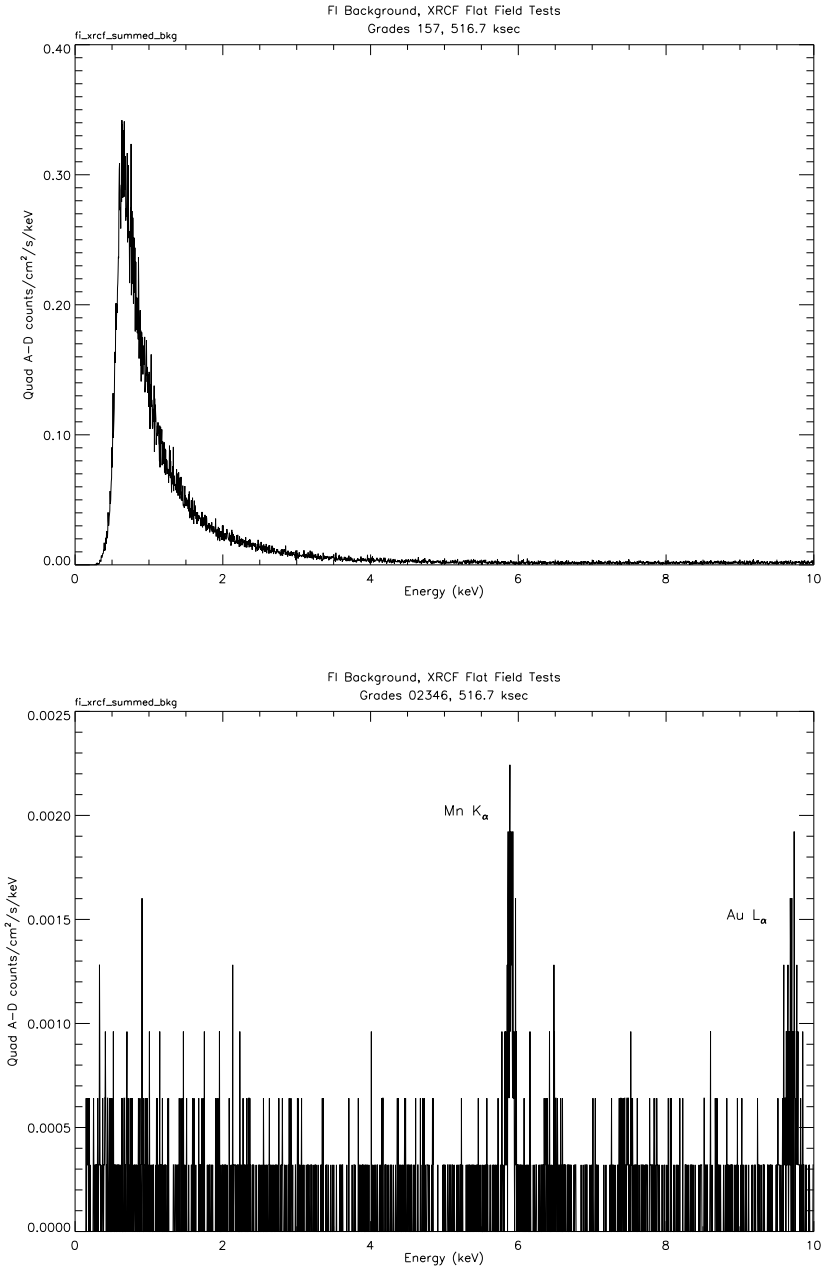

Figure 4.103: Background spectra measured at XRCF in the ACIS front-illuminated flight devices. The spectra have been summed over the four quadrants of all eight front-illuminated flight devices. The upper and lower panels show the spectra of the rejected (ASCA grades 157) and the unrejected (ASCA grades 02346) background events, respectively, in the passband 0.1–10 keV. The lower panel shows Mn K_α line emission due to scattered X-rays from the internal contamination monitor. The Au L_α line is caused by particle-induced fluorescence in the framestore covers.

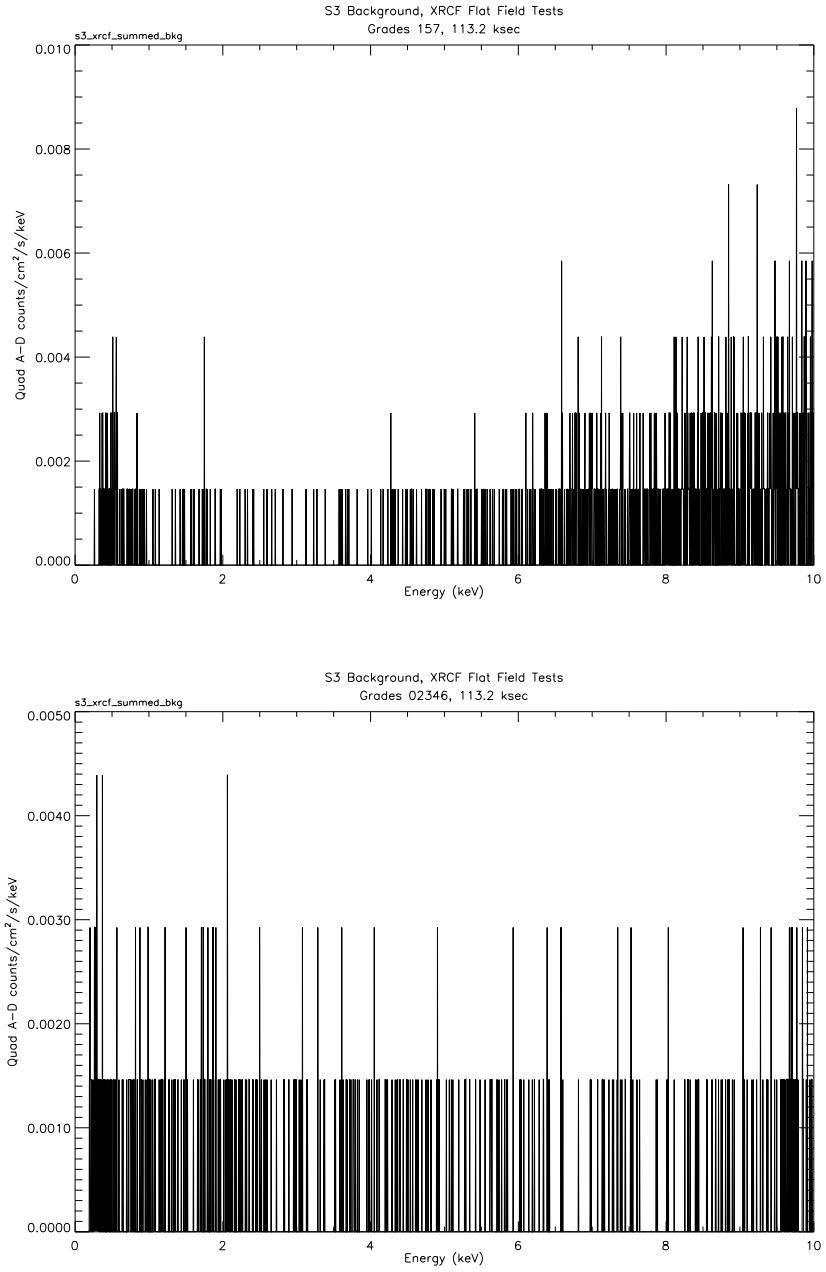

Figure 4.104: Background spectra measured at XRCF in the ACIS back-illuminated flight device S3. The spectra have been summed over all four quadrants. The upper and lower panels show the rejected (ASCA grades 157) and the unrejected (ASCA grades 02346) background spectra, respectively, in the passband 0.1–10 keV.

Flight Device	Source	Quad A	Quad B	Quad C	Quad D	Mean (RMS)
		($\times 10^{-4}$ ct cm^{-2} s^{-1})				
I0	Mn K_α	2.59 ± 0.56	2.07 ± 0.51	2.07 ± 0.51	3.52 ± 0.63	2.56 ± 0.68
	Au L_α	0.93 ± 0.40	1.76 ± 0.49	1.14 ± 0.42	1.24 ± 0.43	1.27 ± 0.35
	Cont.	13.15 ± 1.48	11.50 ± 1.44	12.74 ± 1.44	10.87 ± 1.48	12.06 ± 1.06
I1	Mn K_α	4.04 ± 0.68	3.21 ± 0.62	4.04 ± 0.68	3.62 ± 0.65	3.73 ± 0.40
	Au L_α	1.14 ± 0.42	0.93 ± 0.40	0.93 ± 0.39	1.04 ± 0.40	1.01 ± 0.10
	Cont.	11.60 ± 1.54	14.19 ± 1.57	12.74 ± 1.56	12.63 ± 1.54	12.79 ± 1.06
I2	Mn K_α	3.31 ± 0.61	0.83 ± 0.36	0.00 ± 0.21	0.00 ± 0.21	1.04 ± 1.57
	Au L_α	1.04 ± 0.39	1.86 ± 0.51	1.86 ± 0.50	1.14 ± 0.43	1.48 ± 0.45
	Cont.	10.25 ± 1.43	13.25 ± 1.43	12.73 ± 1.34	13.36 ± 1.32	12.40 ± 1.46
I3	Mn K_α	0.00 ± 0.15	0.10 ± 0.21	1.35 ± 0.43	3.73 ± 0.66	1.29 ± 1.73
	Au L_α	0.73 ± 0.36	1.45 ± 0.44	1.24 ± 0.43	0.41 ± 0.33	0.96 ± 0.47
	Cont.	11.70 ± 1.20	9.43 ± 1.17	11.19 ± 1.34	13.15 ± 1.53	11.37 ± 1.54
S0	Mn K_α	0.00 ± 0.24	0.00 ± 0.19	0.00 ± 0.20	0.00 ± 0.14	0.00 ± 0.00
	Au L_α	0.81 ± 0.43	1.88 ± 0.56	1.88 ± 0.57	2.02 ± 0.59	1.65 ± 0.56
	Cont.	13.72 ± 1.48	9.55 ± 1.37	11.70 ± 1.48	11.97 ± 1.50	11.73 ± 1.71
S2	Mn K_α	0.00 ± 0.16	0.06 ± 0.17	0.23 ± 0.20	0.23 ± 0.20	0.13 ± 0.12
	Au L_α	0.64 ± 0.27	1.46 ± 0.34	0.99 ± 0.31	1.23 ± 0.33	1.08 ± 0.35
	Cont.	13.92 ± 0.98	12.64 ± 0.99	12.87 ± 0.98	12.81 ± 0.99	13.06 ± 0.58
S4	Mn K_α	0.00 ± 0.14	0.27 ± 0.30	0.00 ± 0.24	0.00 ± 0.27	0.07 ± 0.13
	Au L_α	1.35 ± 0.51	1.21 ± 0.49	1.48 ± 0.54	1.08 ± 0.51	1.28 ± 0.17
	Cont.	11.98 ± 1.44	12.92 ± 1.51	16.55 ± 1.67	17.09 ± 1.67	14.63 ± 2.56
S5	Mn K_α	0.40 ± 0.33	0.54 ± 0.36	0.13 ± 0.27	0.00 ± 0.24	0.27 ± 0.25
	Au L_α	1.61 ± 0.52	1.21 ± 0.49	1.08 ± 0.47	1.21 ± 0.49	1.28 ± 0.23
	Cont.	10.36 ± 1.43	11.97 ± 1.49	11.03 ± 1.39	12.51 ± 1.46	11.47 ± 0.96
S1*	Mn K_α	...	...	...	...	...
	Au L_α	...	...	...	...	...
	Cont.	...	...	...	...	...
S3	Mn K_α	0.23 ± 0.24	0.06 ± 0.23	0.00 ± 0.21	0.00 ± 0.20	0.07 ± 0.11
	Au L_α	0.53 ± 0.30	1.58 ± 0.40	0.82 ± 0.35	0.94 ± 0.34	0.97 ± 0.44
	Cont.	22.47 ± 1.23	24.93 ± 1.33	26.80 ± 1.33	22.41 ± 1.23	24.15 ± 2.12

* Background data taken at XRCF for detector S1 were contaminated by an increase in the number of hot pixels as a result of operating the focal plane at $-110°$ C.

Table 4.70: Instrumental Background Fluxes Measured at XRCF in the Passband 0.1–10 keV

The total Mn K_α flux in I0 and I1 is about 3.2×10^{-4} ct cm^{-2} s^{-1}, while the estimated continuum flux under the peak (unrejected) is about 4.1×10^{-5} ct cm^{-2} s^{-1}. Thus, the scattered Mn K_α photons increased the instrumental background in the 5.9 ± 0.06 keV

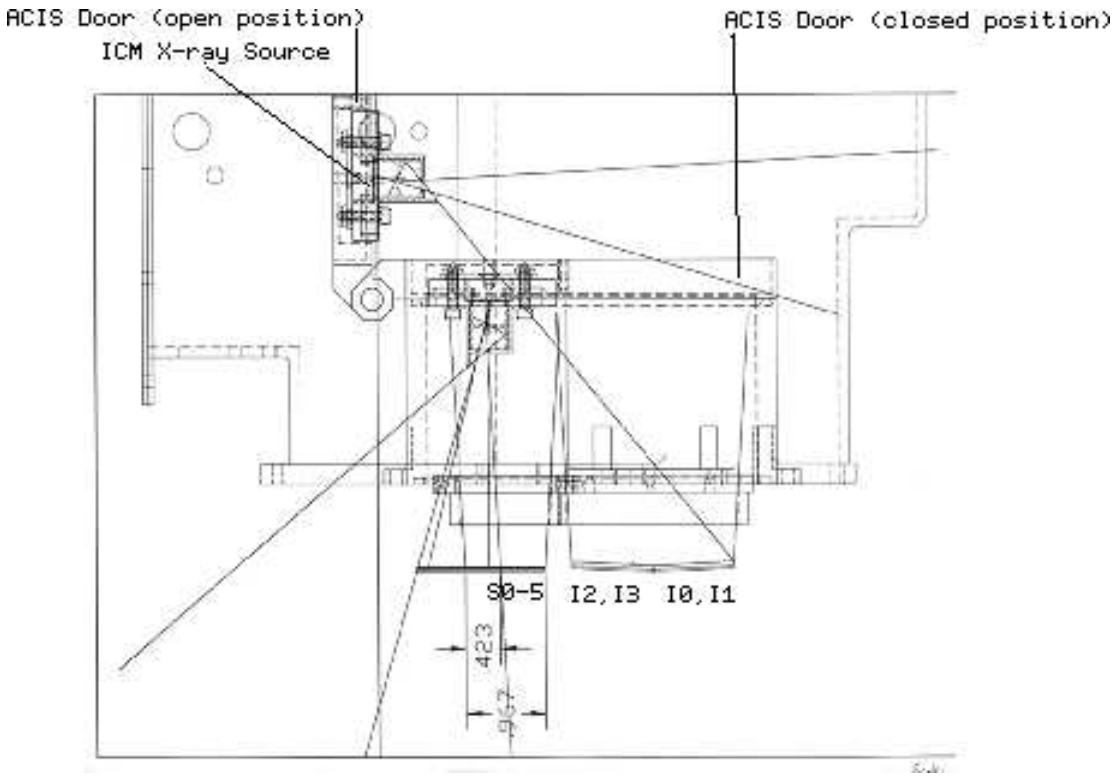

Figure 4.105: Cross-section through the ACIS detector housing showing the internal contamination monitor (ICM) X-ray source, its intended illumination pattern, and the ACIS focal plane. In the drawing the Observatory X-axis is up and the Z axis points to the right. Scattered X-ray flux from the ICM is detected on chips I0 and I1, as well as on high-Z quadrants of chips I2 and I3. The scattering path is unknown. The two dimensions shown are in inches.

spectral band by a factor of ~ 8.6 at XRCF. Assuming AXAF is launched in January or February of 1999, about 20 months will have elapsed since the XRCF measurements were made. Given the 2.7 year half-life of the Fe 55 source in the ICM, the predicted on-orbit rate for the Mn K_α line drop by a factor of about 2/3. Moreover, since the expected amplitude of the on-orbit continuum exceeds that observed at XRCF by about a factor of about 50 (see Section 4.10.3 below), the scattered ICM is expected to increase the on-orbit background by about 10% in the 5.9 ± 0.06 keV band.

Returning to Table 4.70, we see that the Au Lα fluxes and the continuum fluxes are roughly uniform across the focal plane, although a constant model is formally rejected in each case. The mean Au Lα line flux was $(1.25 \pm 0.069) \times 10^{-4}$ ct cm^{-2} s^{-1} in the FI

detectors, and $(0.97 \pm 0.22) \times 10^{-4}$ ct cm^{-2} s^{-1} in S3. This ratio is consistent, within the rather large errors, with the expected relative quantum efficiency of the front- and back-illuminated detectors at 9.7 keV (see section 4.8.) Because the effective area of the ACIS/HRMA is so low at the energy of the Au Lα line, researchers observing faint diffuse sources can easily remove this extra source of background by applying a high-energy cutoff.

The mean background continuum fluxes for ASCA grade G02346 and G157 events are listed in Table 4.71. The errors quoted in the table are the standard deviations of the means. These measurements indicate that the total particle-induced count rate in a frontside device is about 26 times higher than the rate in a backside device, but the rejection efficiency of the frontside device is about 52 times better, so the net result is that the unrejected background rate in a backside device is about twice that of a frontside device.

Flight Device	Unrejected Events (G02346) (ct cm^{-2} s^{-1} keV^{-1})	Rejected Events (G157) (ct cm^{-2} s^{-1} keV^{-1})	Rejection Efficiency (%)
FI	$1.24 \pm 0.29 \times 10^{-4}$	$2.02 \pm 0.05 \times 10^{-2}$	99.4
S3	$2.42 \pm 0.11 \times 10^{-4}$	$5.26 \pm 0.23 \times 10^{-4}$	68.5

Table 4.71: Mean Background Continuum Fluxes Measured at XRCF in the Passband 0.1–10 keV

4.10.2 Dependence of Background Rejection Efficiency on Event Grade Selection

An important consideration in choosing ACIS event selection criteria is the efficiency of background rejection. To illustrate this point, we present in Tables 4.72, 4.73 and 4.74, the fraction of background events in various grades. For conciseness, we list only the standard ASCA grades, and ACIS grade 255. A similar analysis should be performed (presumably by the AXAF Science Center) for all 255 ACIS grades before a final decision is made on the definition of standard ACIS grades. Of course, the raw XRCF background event lists we have compiled are available to ASC for this purpose.

A cursory analysis of these tables shows, for example, that in device I3 91.21% of background events were ACIS bit map grade 255 events (i.e. all eight neighboring pixels were above the split threshold). However, only 4.14% of the background events in S3 were ACIS grade 255 events. Thus, a large majority of the background events in a frontside device could be rejected simply by filtering ACIS grade 255 events, but only a very small percentage of the background events in a backside device would be rejected. If one were to reject only ACIS grade 255 events, the total on-orbit background rate for six devices should be ~ 40 ct s^{-1}, which is about 22% of the telemetry bandwidth.

Flight Device	Event† Grades	Fraction of Events per Event Grade				
		Quad A	Quad B	Quad C	Quad D	Mean
		(%)				
I0	0	0.387	0.395	0.289	0.325	0.349
	1	0.000	0.000	0.000	0.000	0.000
	2	0.139	0.146	0.133	0.121	0.134
	3	0.050	0.052	0.066	0.047	0.054
	4	0.064	0.057	0.076	0.063	0.065
	5	0.144	0.130	0.152	0.173	0.150
	6	0.159	0.120	0.166	0.236	0.170
	7	99.059	99.101	99.118	99.036	99.078
	157	99.202	99.231	99.270	99.209	99.228
	B255	93.677	88.740	89.959	91.731	91.027
I1	0	0.354	0.423	0.355	0.354	0.371
	1	0.000	0.000	0.005	0.000	0.001
	2	0.204	0.146	0.143	0.106	0.150
	3	0.094	0.146	0.069	0.087	0.099
	4	0.077	0.065	0.103	0.087	0.083
	5	0.160	0.173	0.197	0.143	0.168
	6	0.166	0.179	0.172	0.133	0.163
	7	98.945	98.868	98.956	99.090	98.965
	157	99.105	99.041	99.158	99.232	99.134
	B255	91.637	89.269	90.800	91.361	90.767
I2	0	0.343	0.280	0.273	0.230	0.282
	1	0.000	0.004	0.000	0.004	0.002
	2	0.124	0.068	0.104	0.121	0.104
	3	0.057	0.055	0.056	0.042	0.053
	4	0.033	0.093	0.048	0.079	0.063
	5	0.129	0.140	0.164	0.155	0.147
	6	0.114	0.157	0.130	0.113	0.129
	7	99.199	99.202	99.226	99.256	99.221
	157	99.327	99.346	99.390	99.415	99.370
	B255	94.400	90.730	90.750	93.887	92.441
I3	0	0.247	0.197	0.346	0.327	0.279
	1	0.009	0.000	0.000	0.000	0.002
	2	0.085	0.081	0.059	0.163	0.097
	3	0.052	0.031	0.054	0.058	0.049
	4	0.019	0.063	0.069	0.062	0.053
	5	0.190	0.175	0.139	0.125	0.157
	6	0.166	0.103	0.129	0.192	0.148
	7	99.231	99.350	99.204	99.072	99.214
	157	99.430	99.524	99.342	99.197	99.373
	B255	90.273	90.925	90.304	91.679	90.795

† All event grades except B255 are ASCA grades. Here B255 stands for ACIS bit grade code 255 (i.e., all pixels above threshold).

Table 4.72: Fraction of Background Events per Event Grade Measured at XRCF in the Passband 0.1–10 keV for Detectors I0, I1, I2, and I3

Flight Device	Event† Grades	Fraction of Events per Event Grade				
		Quad A	Quad B	Quad C	Quad D	Mean
		(%)				
S0	0	0.195	0.230	0.307	0.263	0.249
	1	0.000	0.000	0.000	0.006	0.001
	2	0.141	0.075	0.080	0.140	0.109
	3	0.060	0.027	0.043	0.053	0.045
	4	0.054	0.016	0.068	0.047	0.046
	5	0.124	0.166	0.141	0.169	0.150
	6	0.135	0.107	0.123	0.105	0.118
	7	99.291	99.379	99.239	99.218	99.282
	157	99.416	99.545	99.380	99.393	99.434
	B255	93.414	90.934	90.052	94.130	92.133
S2	0	0.393	0.298	0.338	0.354	0.346
	1	0.000	0.000	0.000	0.000	0.000
	2	0.179	0.158	0.143	0.156	0.159
	3	0.089	0.084	0.065	0.049	0.072
	4	0.066	0.056	0.068	0.052	0.061
	5	0.241	0.152	0.182	0.192	0.192
	6	0.241	0.155	0.169	0.182	0.187
	7	98.790	99.096	99.034	99.015	98.984
	157	99.031	99.248	99.216	99.207	99.176
	B255	90.966	88.295	88.005	90.258	89.381
S4	0	0.345	0.323	0.411	0.393	0.368
	1	0.000	0.000	0.007	0.008	0.004
	2	0.161	0.232	0.166	0.283	0.210
	3	0.112	0.074	0.151	0.039	0.094
	4	0.032	0.066	0.094	0.063	0.064
	5	0.209	0.182	0.216	0.157	0.191
	6	0.145	0.190	0.144	0.283	0.190
	7	98.996	98.933	98.810	98.774	98.878
	157	99.205	99.115	99.034	98.939	99.073
	B255	92.890	89.010	85.648	89.456	89.251
S5	0	0.222	0.356	0.233	0.415	0.307
	1	0.000	0.000	0.000	0.009	0.002
	2	0.189	0.144	0.141	0.189	0.166
	3	0.072	0.045	0.064	0.028	0.052
	4	0.026	0.083	0.064	0.113	0.072
	5	0.157	0.235	0.162	0.283	0.209
	6	0.091	0.144	0.141	0.217	0.148
	7	99.243	98.991	99.196	98.745	99.044
	157	99.400	99.227	99.358	99.038	99.255
	B255	92.820	88.693	87.609	92.604	90.432

† All event grades except B255 are ASCA grades. Here B255 stands for ACIS bit grade code 255 (i.e., all pixels above threshold).

Table 4.73: Fraction of Background Events per Event Grade Measured at XRCF in the Passband 0.1–10 keV for Detectors S0, S2, S4, and S5

Flight Device	Event† Grades	Fraction of Events per Event Grade				
		Quad A	Quad B	Quad C	Quad D	Mean
		(%)				
S1*	...	...	...	...	...	...
S3	0	5.667	5.579	5.148	5.678	5.518
	1	0.000	0.070	0.071	0.000	0.035
	2	8.000	9.275	9.944	8.754	8.993
	3	2.917	3.138	2.186	2.839	2.770
	4	2.250	2.650	2.680	2.050	2.408
	5	5.250	4.393	4.443	5.836	4.981
	6	14.250	11.018	13.329	12.145	12.685
	7	61.667	63.877	62.200	62.697	62.610
	157	66.917	68.340	66.714	68.533	67.626
	B255	4.333	3.835	4.020	4.180	4.092

† All event grades except B255 are ASCA grades. Here B255 stands for ACIS bit grade code 255 (i.e., all pixels above threshold).
* See note for detector S1 in Table 4.70.

Table 4.74: Fraction of Background Events per Event Grade Measured at XRCF in the Passband 0.1–10 keV for Detectors S1 and S3

4.10.3 Predicted On-orbit Background Rates

To obtain predicted on-orbit instrumental background rates from the rates measured at XRCF, we scaled the XRCF count rates by the ratio of the on-orbit cosmic-ray flux to the cosmic-ray flux at the Earth's surface. As a first step, we analyzed simultaneous high-speed tap and telemetry data from sequence 1 of science runs 113 and 127 for detectors I3 (FI) and S3 (BI), respectively. To determine the cosmic-ray (CR) flux incident on each detector we plotted the ACIS events frame-by-frame, examined the distribution of events by eye, and decided how many cosmic rays were responsible for creating the events. Using this method the observed cosmic-ray flux, averaged over the upper hemisphere, was $(4.08 \pm 0.10) \times 10^{-3}$ CR cm^{-2} s^{-1} sr^{-1} in both I3 and S3.

According to Reinhold Müller-Mellin, principal investigator of the EPHIN instrument on AXAF, the cosmic-ray flux at the Earth's surface is fairly constant over a timescale of a day, with day-to-day variations of less than 1%. Interplanetary transients from solar events (called Forbush decreases) can cause decreases in the flux by 3–10%, while increases of a few percent are sometimes seen due to rare ground-level events. Long-term variations over the 11 year solar cycle result in variations of 15–20%. Thus, we can obtain a reasonably good check on our estimate of the cosmic-ray flux at XRCF by comparing it to the cosmic-ray flux measured by the EPHIN instrument during the AXAF thermal vacuum tests at TRW in 1998 June. Müller-Mellin analyzed 2 hours of EPHIN data on 1998 June 7 and

found the cosmic-ray flux, averaged over the upper hemisphere, to be $(4.04 \pm 0.40) \times 10^{-3}$ CR cm^{-2} s^{-1} sr^{-1}. This is in excellent agreement with the value given above for the cosmic-ray flux measured at XRCF.

The cosmic-ray flux outside the influence of the Earth's magnetic field, (i.e. for eneriges exceeding 50 Mev/nucleon), is approximately 2 CR cm^{-2} s^{-1} (Meyer, 1969). Assuming this were the particle flux incident on the detectors, the predicted on-orbit background rates in ASCA grades 02346 would be $\sim 1.0 \times 10^{-2}$ ct cm^{-2} s^{-1} keV^{-1} in an ACIS frontside device, and $\sim 1.8 \times 10^{-2}$ ct cm^{-2} s^{-1} keV^{-1} in an ACIS backside device.

Estimated On-orbit Background (ASCA Grade 02346 events)		
Estimate	FI chips ct cm^{-2} s^{-1} keV^{-1}	BI chips ct cm^{-2} s^{-1} keV^{-1}
Cosmic ray spectrum	~ 0.010	~ 0.018
SOHO EPHIN based	~ 0.020	~ 0.036

Table 4.75: Estimated On-orbit Background. Top row results from canonical cosmic ray spectrum; bottom row from SOHO EPHIN detector rates.

A second estimate of the AXAF background may be derived from measurements obtained with SOHO and reported by the EPHIN team. The so-called INT channel of EPHIN's sibling on SOHO measures a total flux of 0.38 ct cm^{-2} s^{-1} sr^{-1} in its orbit at L1. This channel integrates all electrons with energies in excess of 8 MeV and all nucleons with energies in excess of $\sim$ 50 Mev/nucleon. If all of these particles interacted with the ACIS as if they were minimum ionizing muons (the dominant cosmic-ray daughter species observed at sea-level), we would expect about twice the background listed above at the ACIS focal plane (i.e., about 2–4 $\times 10^{-2}$ ct cm^{-2} s^{-1} keV^{-1}). We have made no attempt to model the interaction of the actual on-orbit particle spectrum with the instrument. A significant fraction of the high energy protons observed in the INT channel will penetrate directly to the detectors (which are shielded with about 10 g cm^{-2} of Al). If we arbitrarily assume that energetic protons comprise all of the events detected in the INT channel, then the INT rate provides an upper limit to the expected on-orbit ACIS background. To the extent that some INT events are high energy (E $>$ 10 MeV) electrons, this assumption is incorrect.

4.11 In-flight ACIS Calibration Sources

4.11.1 Overview

The Observatory has two radioactive sources solely dedicated to ACIS calibration[10]. The first of these is the Internal Contamination Montior (ICM), located on the underside of the ACIS door. The flux from this tighly collimated source falls primarily on S2 Quad D and S3 Quads A-C. The purpose of the ICM is to allow an accurate measurement of line ratios immediately after launch. The post-launch ratio is then compared to the ratios determined during pre-flight testing. Discrepancies between the pre- and post-launch measurements would indicate the presence of contaminants on the ACIS detectors. Once the door is open, the ICM will not be visible again.

The second radioactive source is the External Calibration Source (ExtCalSrc), viewable by ACIS when the HRC-S is in the Observatory focus. The ExtCalSrc consists of three seperate sources that produce a number of Kα lines and illuminate the entire ACIS focal plane with near uniformity. The ExtCalSource will allow determination of chip gain and monitoring of other performance parameters during the entire lifetime of AXAF.

4.11.2 The Internal Contamination Monitor (ICM)

The Internal Contamination Monitor (ICM) is an ^{55}Fe source located on the inside of the ACIS door. Through electron capture, ^{55}Fe decays to ^{55}Mn through the channel: $^{55}_{26}\mathrm{Fe} + e^{-1} \rightarrow {}^{55}_{25}\mathrm{Mn}^{*} + \nu$. The excited Mn atom may then relax to the ground state through fluorescence of a photon of characteristic energy: ${}^{55}_{25}\mathrm{Mn}^{*} \rightarrow {}^{55}_{25}\mathrm{Mn} + \gamma_{\alpha}$, $\{$ γ_{α}: K_i, L_j, M_k, $\cdots$ $\}$. It is (mostly) the Mn K and L shell photons that are responsible for the observed spectrum.

The main purpose of the ICM is to monitor the potential accumulation of contaminants on the surface of the CCDs. The most probable contaminants are ice or hydrocarbons, and due their large absorption coefficients at the L-line energies ($\sim$ 640 eV), even a relatively thin layer of contamination would result in the attenuation of the L photons. At the K-line energies ($\sim$ 6 keV), however, the photons have a much larger attenuation length and would not be absorbed by the contaminants, much the way that high energy photons pass through the CCD gate structure and insulating layers. As the fluorescent yield of K to L photons from the radioactive source is constant, an increase of the K:L ratio would indicate the the build-up of contamination.

The initial Mn K and L fluorescence lines and additional lines they excite produce a rich spectrum that allows an accurate gain calculation. Thus, the ICM also has served as a gain calibrator during pre-launch calibration efforts and allowed a check of long-term gain stability of those CCDs illuminated by the ICM. Below, we carefully discuss the spectrum

[10] A third source, attached to the HRMA cover, is intended for HRMA calibration and is not discussed here

of the ICM and attempt to identify all the features present. We also measure the K:L ratio from three different measurements spanning over a year.

4.11.2.1 Spectrum

For the following analysis, we have used data from the TRW thermal vacuum tests (also referred to as AXAFTV) at TRW facilities during May-June, 1998. As the TV tests were primarily intended for a systems check of the entire spacecraft, ACIS was given limited time in telemetry format 2, the format used for acquiring science data. Instead, ICM data was collected in graded histogram mode. In this configuration the instrument finds and grades events, disregarding individual frames. Acceptable events (*ASCA* g02346) are written to a histogram, and after a specified number of frames, the histogram is telemetered.

The better response of the FI chip (relative to the BI chip) makes it the best choice for detailed studies of the ICM spectrum. Unless otherwise noted the data is from S2, quadrant D. At the same time, since most of the ICM flux falls on S3, we also discuss the data from the BI chip. In both cases, the data results from a total of 38,400 frames of normal integration (3.3 sec) data. Using a number of easily identified lines (see below), gains and offsets were calculated to convert energy units (ADU) to energy (keV). To facilitate the discussion, the spectral range is divided into three different energy bands, with only descriptive significance given to the names of each band.

Low Energy Band (0-1 keV): An examination of Figure 4.106 reveals a rich diversity of lines below 1 keV. There exists three main complexes of lines. The highest energy complex is clearly due to the three most common Ni L lines. The spectral resolution of the device does not allow separation of the individual lines. Instead, we have computed an average Ni L-line, using the expected intensities of the lines: α_1:α_1:$\beta 1$ 100:10:50. Table 4.76 lists the various low energy lines and computed average line energy for all the low energy features. The next complex, labeled the "L Complex" is centered around 0.67 keV. Although a gaussian nicely fits this feature, two problems exist with identifying it with a single emission line. First, the only line at this energy if F Kα_1 (677 eV) and no fluorine is present in the ICM. Second, the width of the best-fit gaussian to this features is twice as large as that measured for the width of the F Kα_1 during sub-assembly calibration. Thus, we conclude that this feature is a blend of at least two distinct lines, and most probably a combination of the expected Mn and Fe L lines. Referring to Table 4.76 and assuming equal contributions of the average Mn and Fe L lines, the identification of this feature as the "L Complex" becomes clear. Finally, there exists a complex centered around 0.55 keV. Due to the low count rate, a clear identification is not possible. At the same time, the tentative identification of the complex as a blend of O K$\alpha_{1,2}$ and Cr L seems rather reasonable.

The poorer spectral resolution of the BI device and its slight non-linearity in gain blends the low-energy lines together and displaces the features with respect to their expected energy location as seen in Figure 4.107. Instead of the three complexes seen by the FI chip,

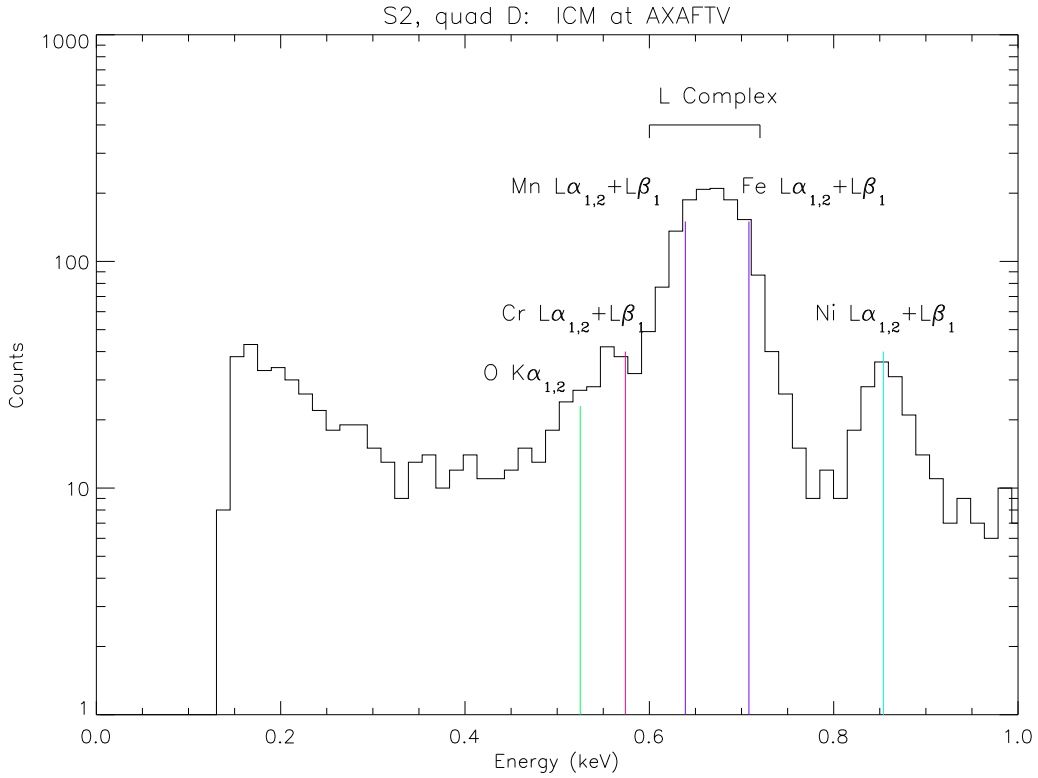

Figure 4.106: FI chip response to the ICM spectrum in the range 0-1 keV.

there are only two visible in the BI chip. The Ni L line feature is still discernible, as is the Mn-Fe L complex, but it now contains the O Kα and Cr L lines. When a functional form is fit to the L complex to determine the K:L fluorescence yield, *what constitutes the L complex will differ between a BI and FI chip*. Thus, even after accounting for the different quantum efficiencies for the BI and FI chip, we expect K:L ratio as determined by the FI, will be higher than the K:L ratio measured by the BI chip.

Line	Energy (keV)	Line	Energy (keV)
O K$\alpha_{1,2}$	0.525		
Cr L$\alpha_{1,2}$	0.571	Fe L$\alpha_{1,2}$	0.704
Cr Lβ_1	0.581	Fe Lβ_1	0.717
<Cr L>	0.574	<Fe L>	0.708
Mn L$\alpha_{1,2}$	0.636	Ni L$\alpha_{1,2}$	0.849
Mn Lβ_1	0.647	Ni Lβ_1	0.866
<Mn L>	0.639	<Ni L>	0.854

Table 4.76: ICM lines in the 0-1 keV band

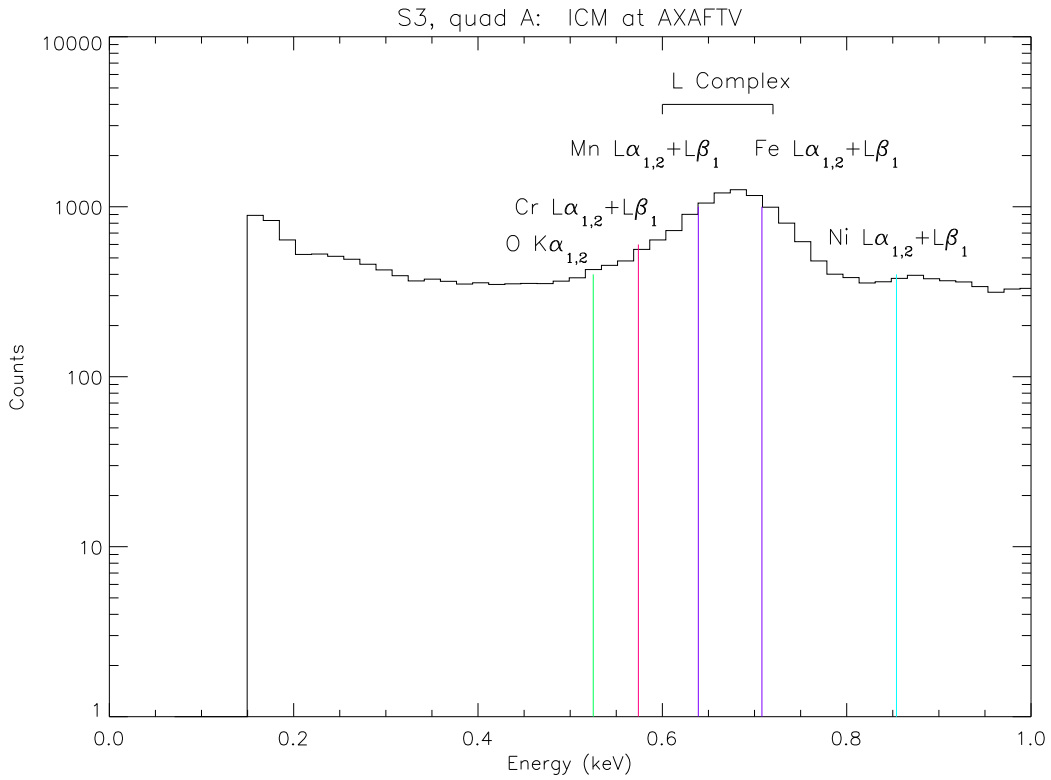

Figure 4.107: BI chip response to the ICM spectrum in the range 0-1 keV.

Middle Energy Band (1-7 keV): Figure 4.108 shows the FI response to the ICM source in the 1-7 keV band. In this energy range Mn emission lines are directly responsible for most of the spectral features. The two brightest lines are Mn K$\alpha_{1,2}$ and Mn Kβ_1. The corresponding escape features of these two lines are also present in the spectrum. The energies of the escape lines equal the emission line energy minus the energy of a Si K$\alpha_{1,2}$ fluorescence photon (1.74 keV). The Si K$\alpha_{1,2}$ fluorescence peak is also clearly visible. The relatively flat continuum at the ~10 count level is the "shoulder" of both the Mn K$\alpha_{1,2}$ and Mn Kβ_1 lines that is due to the incomplete collection of the charge generated by the incident photons.

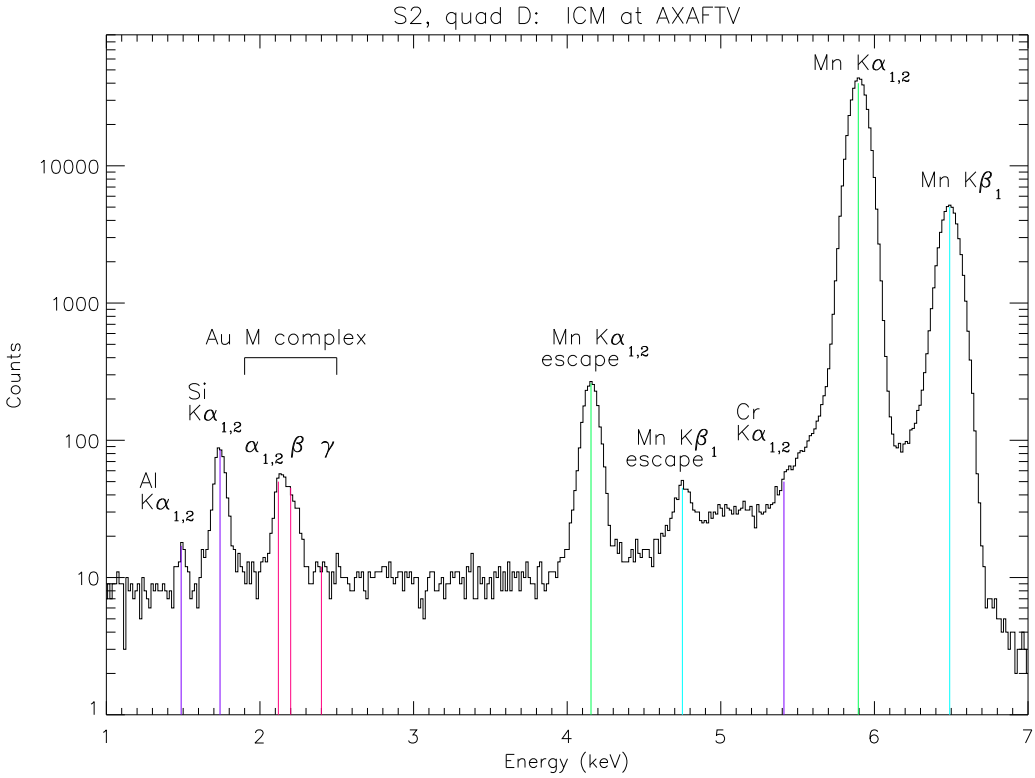

Figure 4.108: FI chip response to the ICM spectrum in the range 1-7 keV.

In addition to the the Mn lines, there is also weak evidence for a Cr K$\alpha_{1,2}$ line at the beginning of the Mn K$\alpha_{1,2}$ shoulder. Taken alone, the existence of the line seems marginal, but when coupled with detection of Cr L lines at lower energies, this identification becomes more secure. Finally, an Al K$\alpha_{1,2}$ line is clearly visible. Table 4.77 lists all the lines and energies for this band.

Line	Energy (keV)	Line	Energy (keV)
<Al K$\alpha_{1,2}$>	1.487	<Mn K$\alpha_{1,2}$> *esc*	4.155
<Si K$\alpha_{1,2}$>	1.740	Mn Kβ_1 *esc*	4.750
Au M$\alpha_{1,2}$	2.112	<Cr K$\alpha_{1,2}$>	5.411
Au Mβ	2.205	<Mn K$\alpha_{1,2}$>	5.895
Au Mγ	2.410	Mn Kβ_1	6.490

Table 4.77: ICM lines in the 1-7 keV band

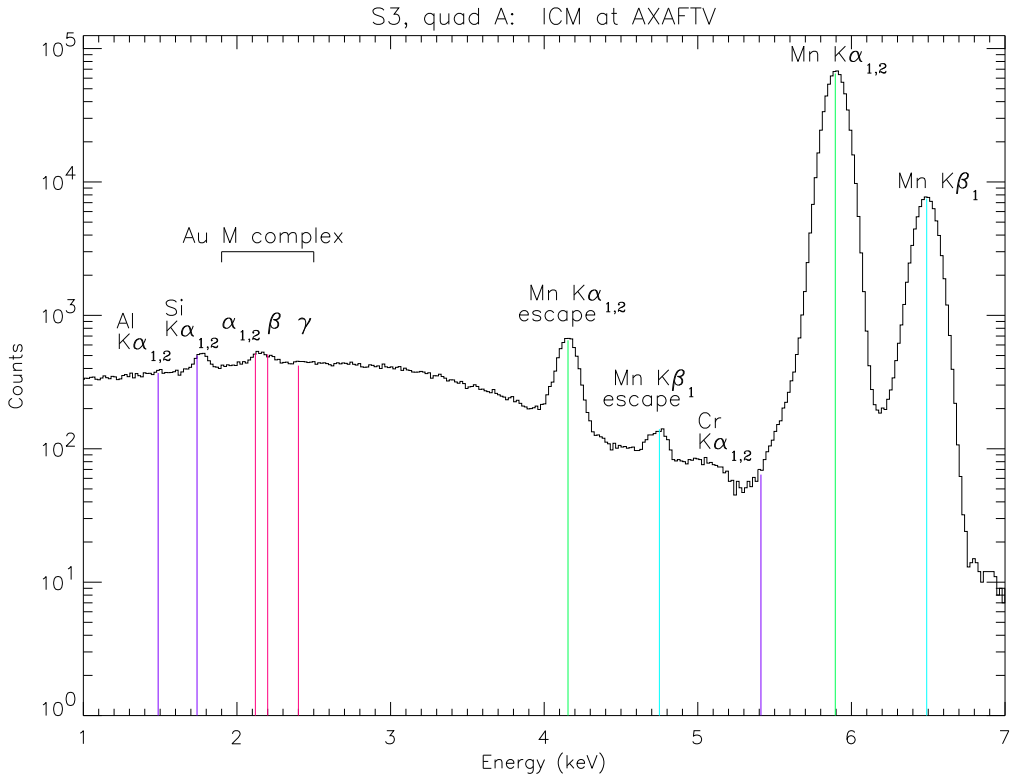

Figure 4.109: BI chip response to the ICM spectrum in the range 1-7 keV.

Figure 4.109 shows the BI response to the ICM source in the 1-7 keV band. In addition to the increased width of the spectral lines, the continuum level for the BI chip is much higher (a factor of ∼20) and has a slow energy dependence. Due to the high continuum level, the Al K$\alpha_{1,2}$ line is not visible in the BI spectrum, and the Si K$\alpha_{1,2}$ line and Au M complex are just above the continuum level.

High Energy Band (7-15.5 keV): Figure 4.110 shows the FI response to the ICM source in the 7-15.5 keV band. Since this band begins at an energy above that of the highest Mn K emission line, we *a priori* expect 1) few events and 2) that those events will have

an unusual origin. The rich spectral features arise from three distinct processes: pile-up, excitation by cosmic rays, and instrumental saturation. Pile-up results when charge from

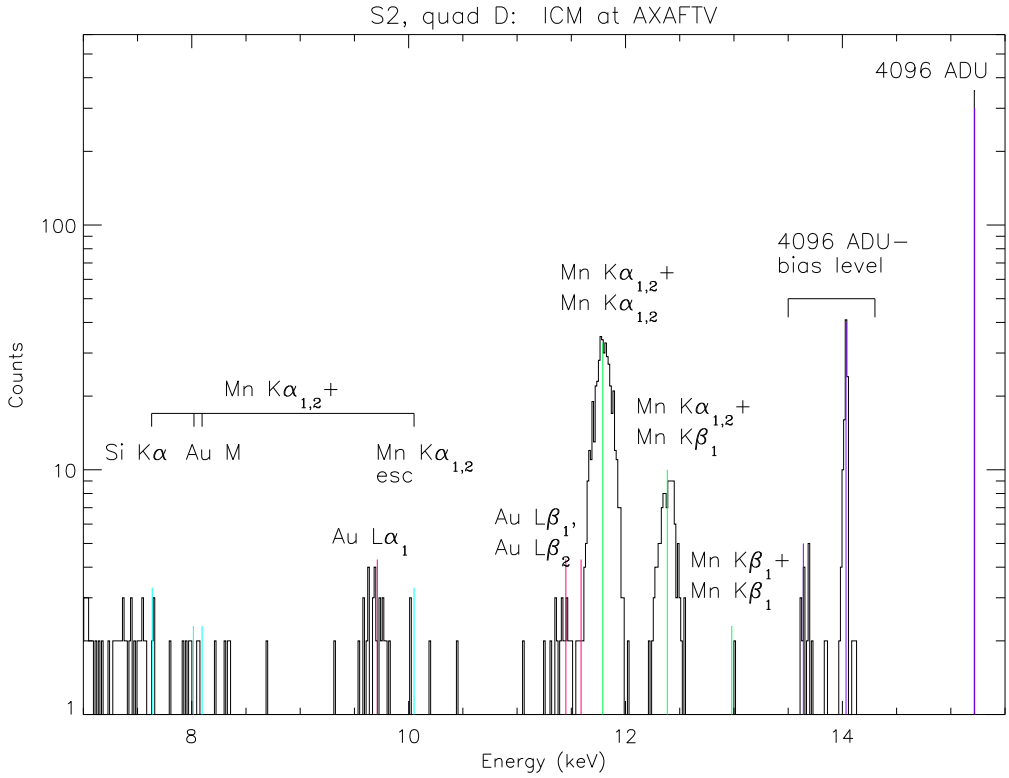

Figure 4.110: FI chip response to the ICM spectrum in the range 7-15.5 keV

two or more absorbed photons are collected in the same pixel during a single integration time. Since Mn K$\alpha_{1,2}$ is the most abundant line, it is not surprising that all but one of the pile-up "lines" involves the summation of a Mn K$\alpha_{1,2}$ with another line. Table 4.78 lists the seven most probable pile-up lines in this band and their energies. The counting statistics are too low to absolutely resolve all of the lines listed (Au M + Mn K$\alpha_{1,2}$, for example), but given a sufficiently long integration, their existence would be obvious. A completely different mechansim is responsible for the Au L lines. These lines arise not from the ICM source, but from cosmic rays that are absorbed by the Au covering of the frame store. The origin of these lines is confirmed by the existence of Au L and Au M lines in the spectrum of *all* CCDs, including ones that are not directly illuminated by the ICM. This means that every spectrum will contain some level of Au M and Au L contamination. The highest energy features are due to the saturation of the digital chain. The spike at 15.22 keV corresponds to the highest analog-to-digital (ADU) value allowed (4096). The spikes at ∼14.1 keV and ∼13.7 keV correspond to 4096 ADU minus the bias level. The extremely narrow width of these line clearly indicates a non-emission origin. As the gain and bias level varies quadrant to quadrant, these features will occur at a range of energies.

Table 4.78 also lists all the instrumental and cosmic-ray produced lines and energies.

Line	Energy (keV)	Line	Energy (keV)
Mn K$\alpha_{1,2}$ + Si K$\alpha_{1,2}$	7.635	Au Lβ_2	11.52
Mn K$\alpha_{1,2}$ + Au M$\alpha_{1,2}$	8.007	Mn K$\alpha_{1,2}$ + Mn K$\alpha_{1,2}$	11.79
Mn K$\alpha_{1,2}$ + Au Mβ	8.095	Mn K$\alpha_{1,2}$ + Mn Kβ_1	12.39
Au Lα_1	9.711	Mn Kβ_1 + Mn Kβ_1	12.98
Mn K$\alpha_{1,2}$ + Mn K$\alpha_{1,2}$ *esc*	10.05	4096 ADU - bias	13.6−14.2†
Au Lβ_1	11.44	4096 ADU	15.22†

†: these energies are dependent on the gain and bias levels and will vary from chip to chip

Table 4.78: ICM lines in the 7-15.5 keV band

Figure 4.111 shows the BI response to the ICM in the high energy band. In general, there is very little difference between the BI and FI spectra at the these energies. In addition to the discrete pile-up features, a flat continuum (few count level) extends from 7 keV up to highest pile-up line, a result of the summation of Mn K$\alpha_{1,2}$ photons with the low-energy tail from the Mn K lines. The energy response in the BI chips is higher than the FI chips ($\sim$ 18 keV versus $\sim$ 16 keV) due to the higher gain in the BI. The different gain and bias levels shifts the saturation features to higher energies than in the FI chip.

4.11.2.2 Illumination Pattern

Before calculating the K:L ratio, it is necessary to check that the ICM source has not moved with respect to the focal plane. While the FI chips are flat, that is they show virtually no variations in QE or spectral response across their surface, the BI chips do have noticable spatial variations. If the area illuminated by the ICM changed from measurement to measuremnt, we might see variations in the K:L ratio. Figure 4.112 shows the illumination pattern of the ICM source on the focal plane. The map was made by selecting Mn K$\alpha_{1,2}$ events. Data was binned into 16 pixel×16 pixel cells to smooth the Poisson fluctuations The chips were then normalized with respect to the maximum cell values. The spatial variations in the BI chip S3 are clearly visible as a general reduction in detection efficiency near the Quad A/Quad B boundary and the small fluctuations over Quads B & C. As long as the illumination pattern remains stable with time, however, these spatial variations will be normalized out of K:L ration calculation. Figure 4.113 shows the normalized contours of the Mn K$\alpha_{1,2}$ events from three different measurements: XRCF-I calibration from 1997 June, ISIM-TV measurements in 1998 January, and AXAF-TV measurements in 1998 May. Due to a lack of sufficient low temperature HST data, there are no intensity contours for

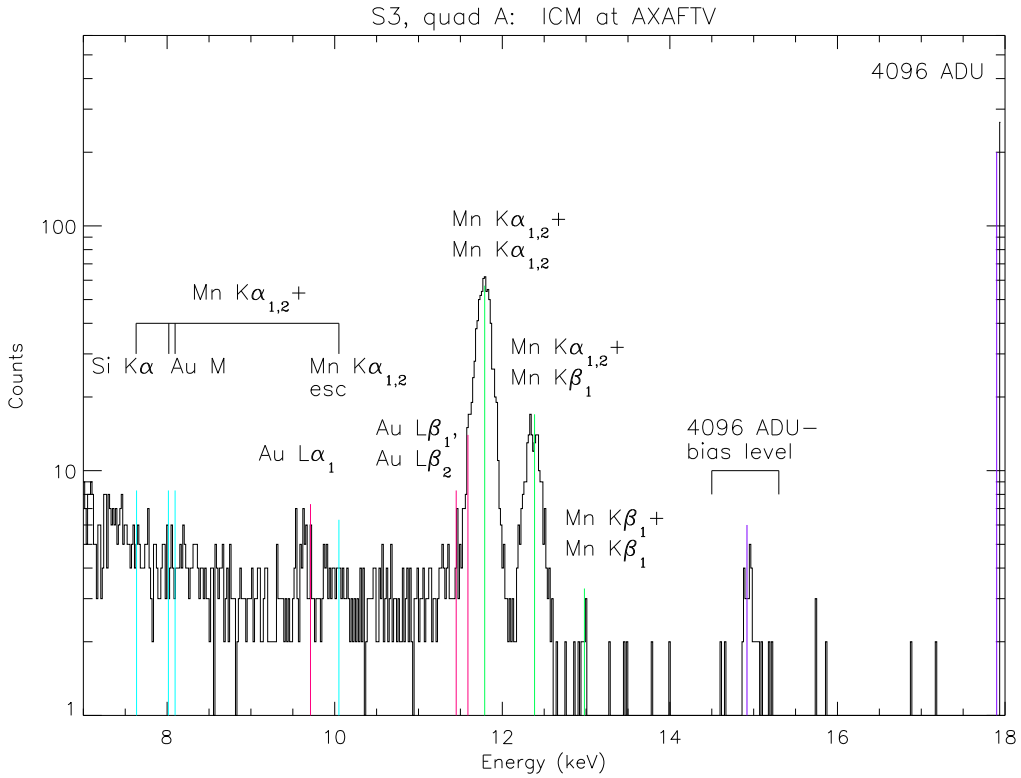

Figure 4.111: BI chip response to the ICM spectrum in the range 7-18 keV

S2 from AXAFTV. Nonetheless, it is clear that ICM position is stable with respect to the focal plane.

4.11.2.3 Mn K$\alpha_{1,2}$:L complex ratio

Code was written to ensure that the K:L would be calculated the same way for each additional measurement. For the FI chip S2 this involves fitting a gaussian model to the Mn K$\alpha_{1,2}$ line and a gaussian model to the combined Mn−Fe L feature. The K:L ratio is simply the ratio of the gaussian areas. For the BI chip S3 a gaussian was also fit to the Mn K$\alpha_{1,2}$ line. The poorer low energy spectral response required a more complicated function to accurately fit the L complex: a gaussian model with constant, linear and quadratic terms. The K:L ratio is still the ratio of the gaussian areas.

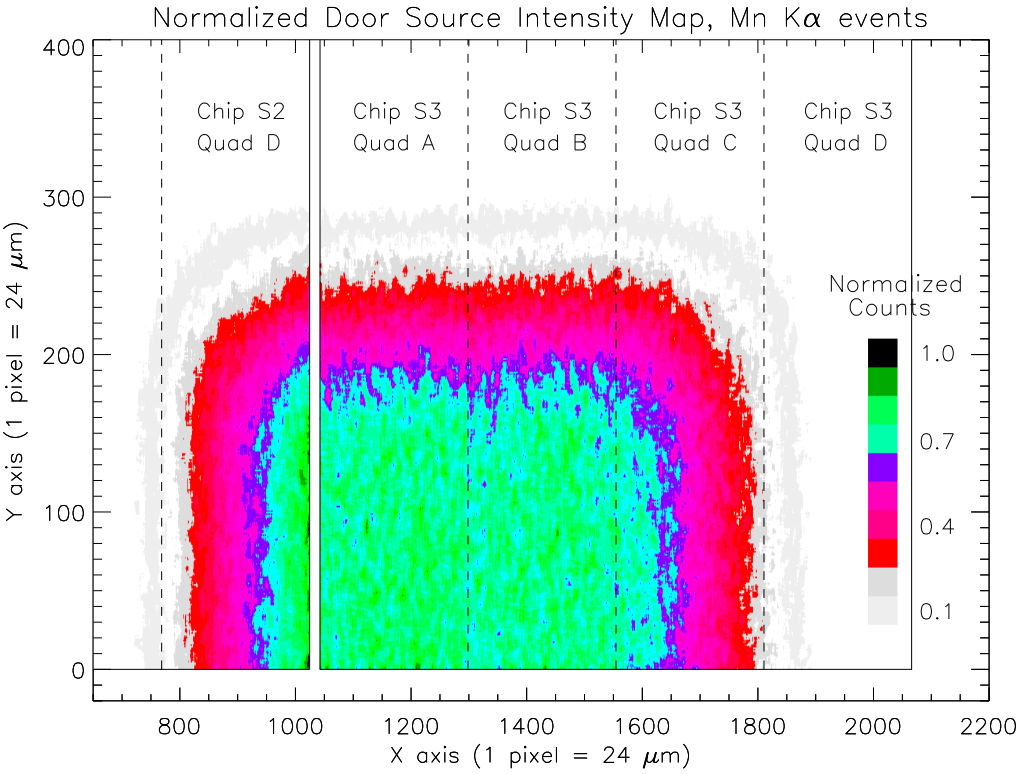

Figure 4.112: Illumination pattern of Mn K$\alpha_{1,2}$ events from the ICM as measured at XRCF-I

Table 4.79 presents the ratios for one S2 quadrant and three S3 quadrants from three different measurements. The quoted errors are 1 σ Poisson errors. For S2, the ratios are consistent within the errors, while for S3 the values show a larger than statistical variation. The mean and standard deviation of the nine points are 106.6 ± 5.16, clearly demonstrating that there is some unaccounted for systematic effect. If we disregard the highest and lowest values, the mean and standard deviation are 106.0 ± 2.30, closer to, but still higher than statistical fluctuations. The large difference between the BI and FI ratio is due to the BI's higher low energy quantum efficiency. Since we know the QE of both chips, the intrinsic K:L ratio can be calculated from both sets of data and compared as an additional check. We measure

$$R_{FI} = \frac{QE^{FI}_{MnK\alpha}}{QE^{FI}_{Lcomplex}} \times \frac{K}{L} \quad \& \quad R_{BI} = \frac{QE^{BI}_{MnK\alpha}}{QE^{BI}_{Lcomplex}} \times \frac{K}{L}$$

where R_i is the K:L ratio for the BI or FI chip, QE^i_j is the quantum efficiency for the i^{th} chip at energy j, and $\frac{K}{L}$ is the intrinsic Mn K$\alpha_{1,2}$ to Mn$-$Fe L complex ratio. Since the L complex is a blend of lines, we approximate the low energy QE as the average of the mean QE's at Mn L and Fe L, which themselves are weighted averages of the various L lines. Table 4.80 lists the appropriate quantum efficiencies, the measured ratios, and the

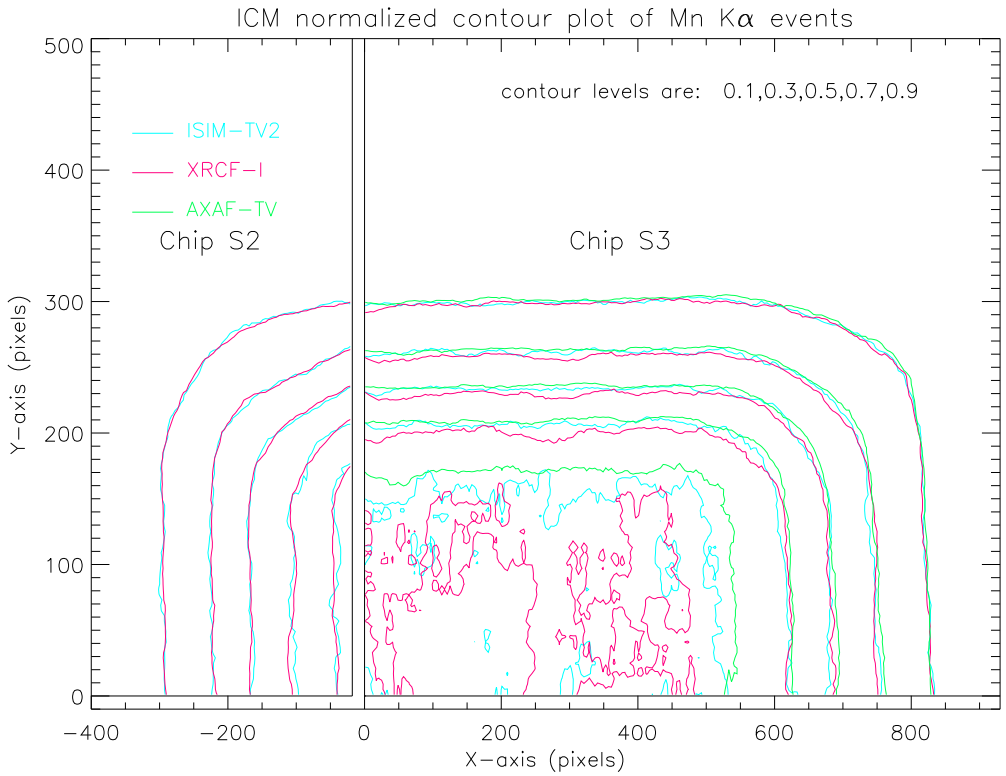

Figure 4.113: Contour map of ICM Mn K$\alpha_{1,2}$ events from three different measurements.

calculated intrinsic ratios. While the ratios are much closer to agreeing, there is still a ∼15% discrepancy. If we then consider that BI $\frac{K}{L}$ value should be higher, due to the addition of the O Kα and Cr L flux in the L complex (see Section 2 for details), the discrepancy becomes larger. At the same time, however, our approximation laden method clearly over-simplifies the situation. Our averaging of discrete QE values over a wide energy pass band introduces errors into the low energy QE. Also, our simplistic gaussian + background model of the L complex cannot account for the complicated spectral redistribution function of the BI. A reliable, exact comparison demands that an accurately modeled ICM source spectrum be folded through both the BI and FI response matrices.

4.11.3 The External Calibration Source (ExtCalSrc)

The External Calibration Source (hereafter abbreviated ExtCalSrc) consists of three separate radioactive sources held in a common holder. While all three sources contain ^{55}Fe, they each predominately produce lines of different energies. Two widely collimated sources use the Mn Kα and Mn Kβ photons to fluoresce either Ti or Al and excite those characteristic K emission lines. The third source does not fluoresce another metal and mainly emits only Mn K and L photons. Some of the Mn photons pass through the Al and Ti sources without being absorbed, so these sources also produces Mn K and L lines. The ExtCalSrc

		S2	S3		
Location	Date	Quad D	Quad A	Quad B	Quad C
XRCF-I	01Jun97	293.9 ± 5.82	109.1 ± 1.04	103.8 ± 0.97	105.7 ± 1.20
ISIM-TV2	16Jan98	278.8 ± 9.65	104.3 ± 1.74	108.9 ± 1.85	117.8 ± 2.55
AXAF-TV	16May98	287.3 ± 3.81	106.5 ± 0.68	99.33 ± 0.62	103.6 ± 0.80

Table 4.79: Mn K$\alpha_{1,2}$:Mn–Fe L complex ratios

	Quantum Efficiency		Measured	Intrinsic
Chip	<0.674 keV >	5.895 keV	Ratio (R)	Ratio ($\frac{K}{L}$)
FI	0.365	0.910	287	115
BI	0.952	0.747	106	135

Table 4.80: The intrinsic strength of the Mn K$\alpha_{1,2}$ line to the L complex

illuminates the ACIS focal plane only when the HRC-S instrument is in the telescope focus position. The various emission lines produced by the ExtCalSrc will allow an accurate gain measurement for each node of each ACIS CCD. With sufficiently long integrations, the ratio of the Mn Kα flux to the Mn L-Fe L flux can be measured and used to monitor the potential accumulation of contaminants on ACIS (see Section 4.11.2 for the details of this technique). Below, we discuss the spectrum of the ExtCalSrc, the expected count rate in the Al, Ti and Mn Kα lines, and the spatial distribution of the flux.

4.11.3.1 Spectrum

Figure 4.114 shows the spectrum of the ExtCalSrc from S2. The data consists of a 9.2 ks exposure of HST data. After accounting for the different gains of each quadrant, the data from each output was summed together to increase the signal. The most obvious features are the easily discernible Kα and Kβ lines needed for accurate gain measurements. A number of other, well-understood features are present and are discussed below. The lowest energy complex is a blend of Mn Lα, Mn Lβ, Fe Lα, and Fe Lβ lines. The CCD resolution does not allow differentiation between the Mn and Fe lines (ΔE $\approx$ 60 eV apart) and they appear as a single line. See Section 4.11.2.1 for a detailed discussion on the characteristics of the L complex. The next feature is the Al Kα emission line with its very well defined low-energy shoulder. Right above that is the Si Kα fluorescence line. These photons are produced when an incident photon of higher energy interacts inside the CCD and produces a Si Kα photon. If the photon travels far enough from the interaction sight in the proper direction, it can be detected. Regardless on whether the Si Kα photon is detected, if it travels sufficiently far from the initial absorption site, the charge deposited at that site will equal the energy of the incident photon - 1740 eV (Si Kα energy). These feature are the

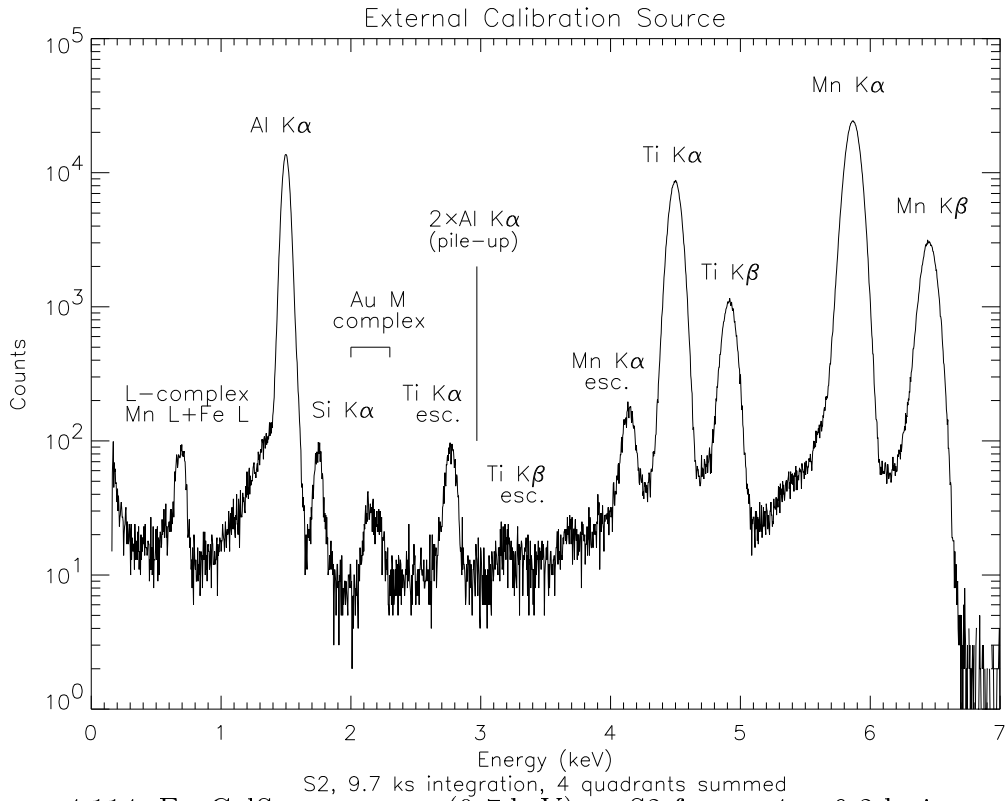

Figure 4.114: ExtCalSrc spectrum (0-7 keV) on S2 from a 4 × 9.2 ks integration

escape features of an emission line. Both the Mn and Ti Kα escape features are clearly present and nearly gaussian. Ti Kβ escape is also present, but with fewer events. Mn Kβ escape is also present, but is hidden by the Ti Kβ line. The well-defined, but irregularly shaped feature around 2.2 keV is the Au M complex, a number of closely spaced Au M lines. The lines are produced by fluorescence of the gold coating on the outer surface of the radioactive sources. Finally, we have indicated where the pile-up line of Al Kα would occur. There is a hint of counts above the background at the appropriate energy, but low statistics prevents a firm detection. Certainly, pile-up is always present at some level, but the incidence for the ExtCalSrc is small and will only decrease as the ^{55}Fe decays. For a discussion of the features present above 7 keV, we again refer the reader to detailed discussion in Section 4.11.2.1. Table 4.81 lists the lines and energies of all the labeled features in Figure 4.114.

4.11.3.2 Count Rate

It is important to accurately measure the count rate of the largest emission features of the ExtCalSrc, mainly the Al, Ti, and Mn Kα lines for two reasons. First, the accuracy of the gain calculations needed for continual ACIS calibration depends on how well the line

Line	Energy (keV)	Line	Energy (keV)
Mn L$\alpha_{1,2}$	0.636	<Ti K$\alpha_{1,2}$> *esc*	2.768
Mn Lβ_1	0.647	2 × <Al K$\alpha_{1,2}$>	2.974
Fe L$\alpha_{1,2}$	0.704	Ti Kβ_1 *esc*	3.191
Fe Lβ_1	0.717	<Mn K$\alpha_{1,2}$> *esc*	4.155
<Al K$\alpha_{1,2}$>	1.487	<Ti K$\alpha_{1,2}$>	4.508
<Si K$\alpha_{1,2}$>	1.740	Mn Kβ_1 *esc*	4.750
Au M$\alpha_{1,2}$	2.112	Ti Kβ_1	4.931
Au Mβ	2.20	<Mn K$\alpha_{1,2}$>	5.895
Au Mγ	2.410	Mn Kβ_1	6.490

Table 4.81: ExtCalSrc lines in the 0-7 keV band

centers are measured, which in turn depends on the number of counts in the peak. With an accurate count rate in hand, we can calculate the time needed to collect the counts for the desired level of gain accuracy. Second, knowing the count rates will allow adjustment of the spatial windows to avoid saturating telemetry and to maximize the amount of calibraiton data.

The ExtCalSrc was carefully measured on 23 October 1997 during the first ISIM thermal vaccuum testing (ISIM-TV1). Because both spatial and spectal information were desired and full-frame data on six chips would have saturated telemetry, we acquired a mininum of ∼1500 HST frames for each chip. Gaussian lines were then fit to the Kα peaks, and the count rates simply equal the gaussian area/integration time. Table 4.82 present the count rates and errors, where the errors are the 1 σ Poisson noise.

Two general facts are immediate noticable. First, the ratio of Mn Kα:Ti Kα:Al Kα is ∼4:1:1 for the FI chips and ∼2:1:1 for the BI chips. The large difference in the ratio and the differences in the actual count rates are due to the general variations in quantum efficiences between BI and FI chips. Second, the fluctuation in count rate between FI chips is much larger than the stastical errors. In some cases this is at least partially attributable to slightly different QEs, but the largest contributor to this effect is the physical distribution of incident photons (see the section below on spatial uniformities).

The observed flux from the ExtCalSrc will exponentially decrease with time as the source ^{55}Fe radioactively decays. Using the published half-life value $T_{1/2}$ = 2.73 yr, we have calculated what the count rates for the three primary lines will be during the early days of AXAF's orbital operation. Table 4.83 lists the count rates for a typical FI chip and both BI chips.

Chip	Mn Kα (cnt s^{-1} chip^{-1})	Ti Kα (cnt s^{-1} chip^{-1})	Al Kα (cnt s^{-1} chip^{-1})
I0	89.69 $\pm$ 0.13	25.65 $\pm$ 0.07	25.86 $\pm$ 0.07
I1	89.44 $\pm$ 0.13	26.02 $\pm$ 0.07	25.89 $\pm$ 0.07
I2	90.57 $\pm$ 0.19	26.93 $\pm$ 0.10	26.48 $\pm$ 0.10
I3	89.58 $\pm$ 0.13	27.29 $\pm$ 0.07	26.38 $\pm$ 0.07
S0	87.34 $\pm$ 0.13	24.54 $\pm$ 0.07	25.55 $\pm$ 0.07
S2	92.08 $\pm$ 0.13	28.10 $\pm$ 0.07	27.14 $\pm$ 0.07
S4	89.48 $\pm$ 0.13	28.77 $\pm$ 0.07	26.36 $\pm$ 0.07
S5	87.61 $\pm$ 0.13	28.40 $\pm$ 0.07	24.98 $\pm$ 0.07
S1	59.12 $\pm$ 0.11	22.14 $\pm$ 0.06	29.46 $\pm$ 0.07
S3	72.98 $\pm$ 0.08	27.45 $\pm$ 0.05	31.04 $\pm$ 0.05

Table 4.82: Observed Counting Rate from the External Cal Source on 23 October 1997

Chip	Mn Kα (cnt s^{-1} chip^{-1})	Ti Kα (cnt s^{-1} chip^{-1})	Al Kα (cnt s^{-1} chip^{-1})
<FI>	62.1	18.7	18.1
S1	41.0	15.4	20.5
S3	50.7	19.1	21.6

Table 4.83: Predicted Count Rate for 01 April 1999

4.11.3.3 Spatial Distribution

While the spatial distribtuion of ExtCalSrc flux does not directly influence the gain calculation, it is intimately tied to the detected count rate of the Kα lines. Two types of variation are observed. First, for a given source, there will be a certain pattern expected from its collimation beam and a reduction of intensity as the distance from the source axis increases. Second, since the photons for each flavor of Kα lines come from a seperate source, we expect that intensity patterns will vary source to source. The housing for the ExtCalSrc contains locations for four individual sources (only three are occupied). Looking down on the focal plane such that S0 is in the lower left and I1 in the upper right (see Figures below), the Al source is in the upper left, the Ti source is in the upper right, and the Mn source is in lower left. Figures 4.115, 4.116, & 4.117 contain the intensity maps for each Kα line. To account for chip-to-chip differences in quantum efficiency, all the chips have been normalized to the QE of S2 at each energy. For example, if S0 is only 90% as efficient as S2 at Al Kα, the observed Al Kα intensity for S0 is multiplied by 1.0/0.9. Each

1024×1024 CCD image was binned into a 64 × 64 array (16 pixels×16 pixels/cell). For the typical 4800 sec exposures taken during ISIM-TV1, the total counts in a single cell is approximately equal to the count rates in Table 4.82. Since the Poisson noise was rather large (19%, 17%, and 10% for Al, Ti, and Mn) the images were smoothed with a 5×5 box car function to reduce 1 σ statistical fluctuations to the ∼5% level. Finally, the map was normalized with respect to the mean intensity of S2 (i.e. the mean intensity of S2 is unity for all the maps).

The most obvious of the macroscopic features is the patchy nature of the maps that results from Poisson fluctuations. The BI chips also contain significant banded structure along the quadrant boundaries and the top (row 1024) of the chip. This structure results from using a global value for the quantum efficiency, rather than accounting for the measured spatial variations in QE. This effect is most notable in chip S1 at Ti and Mn[11]. Finally, the intensity distribution is discernable. For example, at Mn chips S4 and S5 have less flux, consistent with the placement of the bare ^{55}Fe source in the lower left of the ExtCalSrc holder. The Ti intensity dramatically dereases at the outer edge of S0, while the Al intensity drops dramatically at the egde of S5. Both of these structures also agree with placement of the Ti source in upper right holder position (farthest from S0) and the Al source in the upper left holder position (farthest from S5).

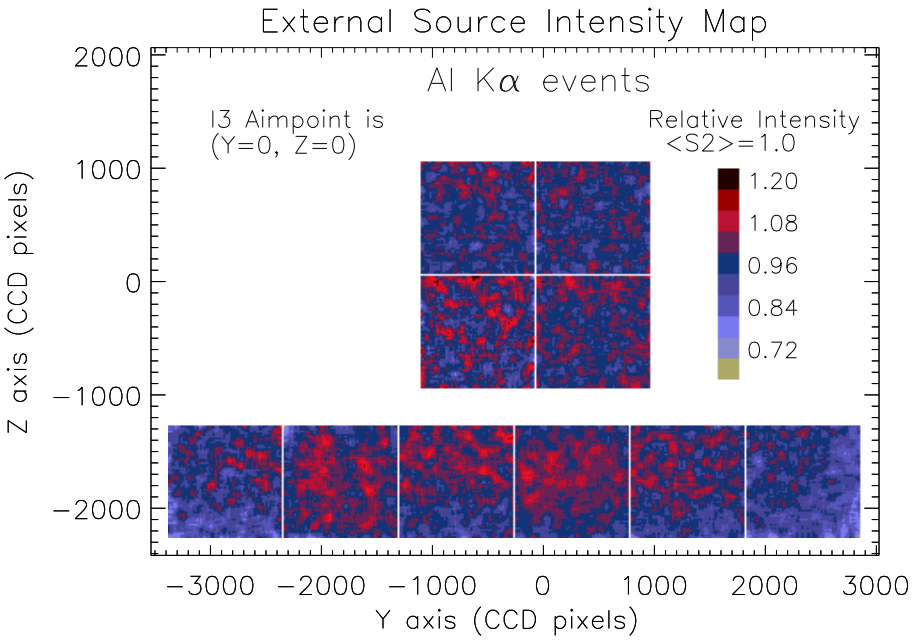

Figure 4.115: Relative intensity map of ExtCalSrc Al Kα. Quantum efficiencies have been normalized with respect to S2. Intensities were then normalized with resepct to S2.

[11]In the future, a spatially dependent QE map will be used to correct for the large QE variations across the BI chips. This measure will eliminate the banding and related structure in these intensity maps.

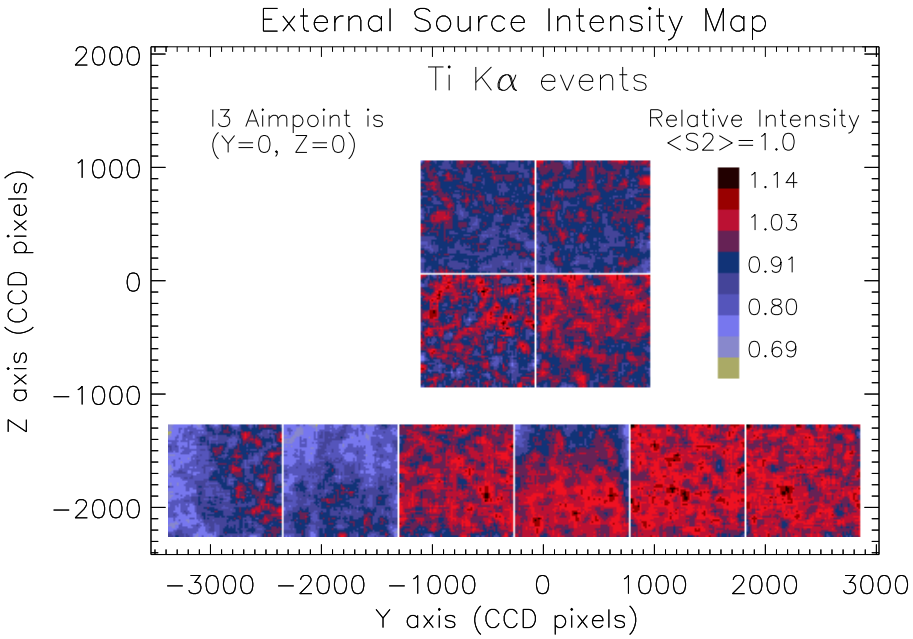

Figure 4.116: Relative intensity map of ExtCalSrc Ti Kα. Quantum efficiencies have been normalized with respect to S2. Intensities were then normalized with resepct to S2.

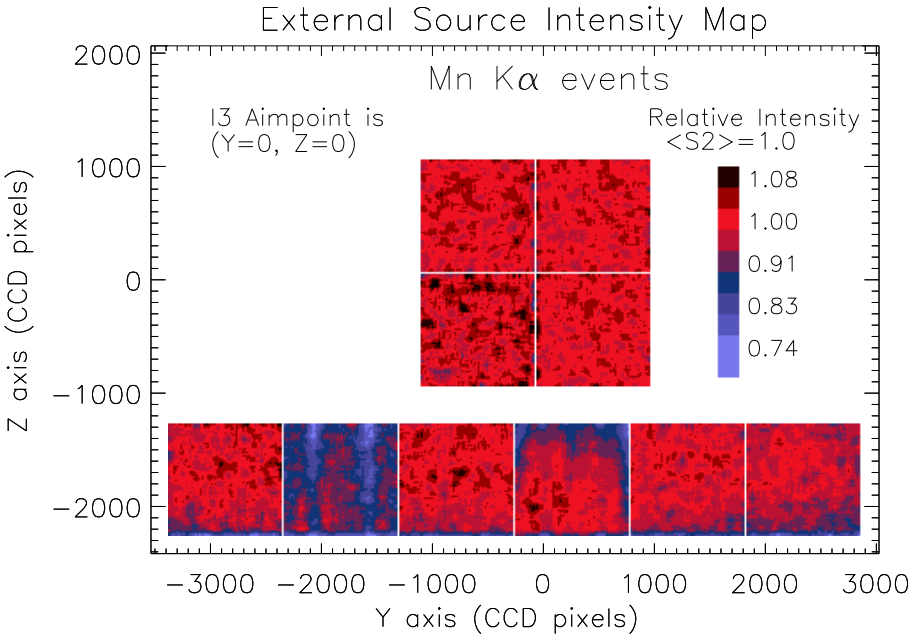

Figure 4.117: Relative intensity map of ExtCalSrc Mn Kα. Quantum efficiencies have been normalized with respect to S2. Intensities were then normalized with resepct to S2.

4.12 ACIS Sensitivity to Visible-Band Radiation

Light detection efficiency tests of the ACIS flight instrument have been made using four different light sources. At the Lincoln Lab instrument thermal vacuum test external 880 and 660 nm as well as internal 660 nm LED sources were used. At XRCF the internal (LED) source and an external "flashlight" were used. At ISIM and TRW thermal vacuum testing only the internal source was used.

Qualitatively all the tests produce the same pattern of spatial response nonuniformity across the focal plane. This is especially true for the 660 nm light source(s). There is no indication that the instrument response to light at 660 nm has changed in any way between April 1997 and May 1998. Because the spatial response features reproduce under all test scenarios (at least for 660 nm) the inference is that these features are not caused by nonuniformities of the light source. However, uncertainties in illumination pattern and intensity introduce a considerable error in determination of numeric result. ACIS memo PS-136 and PS-137 describe the Lincoln Lab test which is the source of the quantitative results.

Figure 4.118 shows the responsivity (in electrons per pixel per incident photon at 660 nm) measured during the ACIS instrument thermal vacuum test at MIT Lincoln Laboratories in April, 1997.

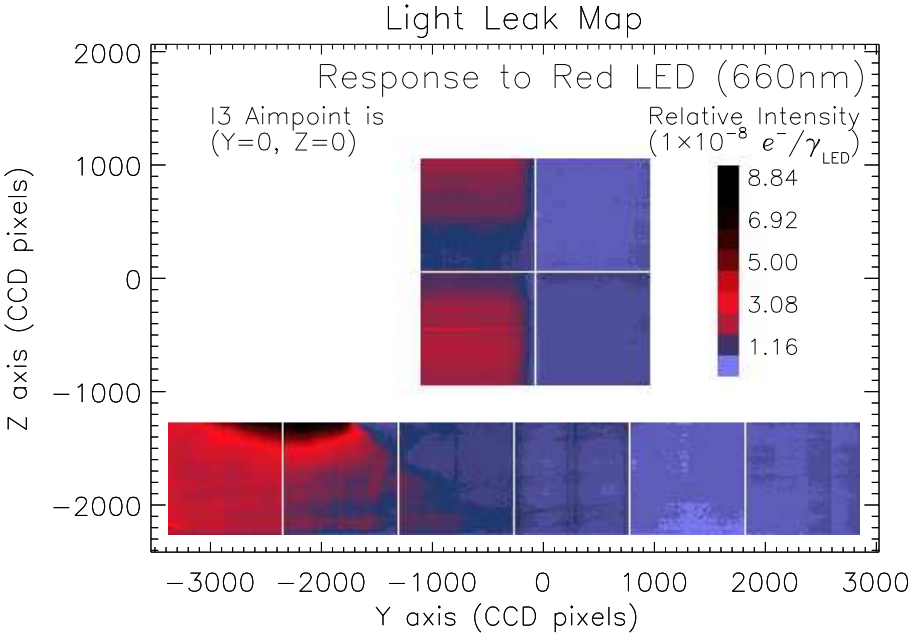

Figure 4.118: ACIS Responsivity at 660 nm as measured at the Lincoln Laboratory Thermal Vacuum Test

Figure 4.119 shows the spatial variation in light sensitivity observed in various tests. The most noticeable feature in this figure is a "leak" in the region between S0, S1 and I2

with an order of magnitude enhanced response. Also evident, especially in the S array, are features clearly attributable to wrinkles in the blocking filter. Another constant result is the relative insensitivity of I1 and I3 relative to adjacent I0 and I2.

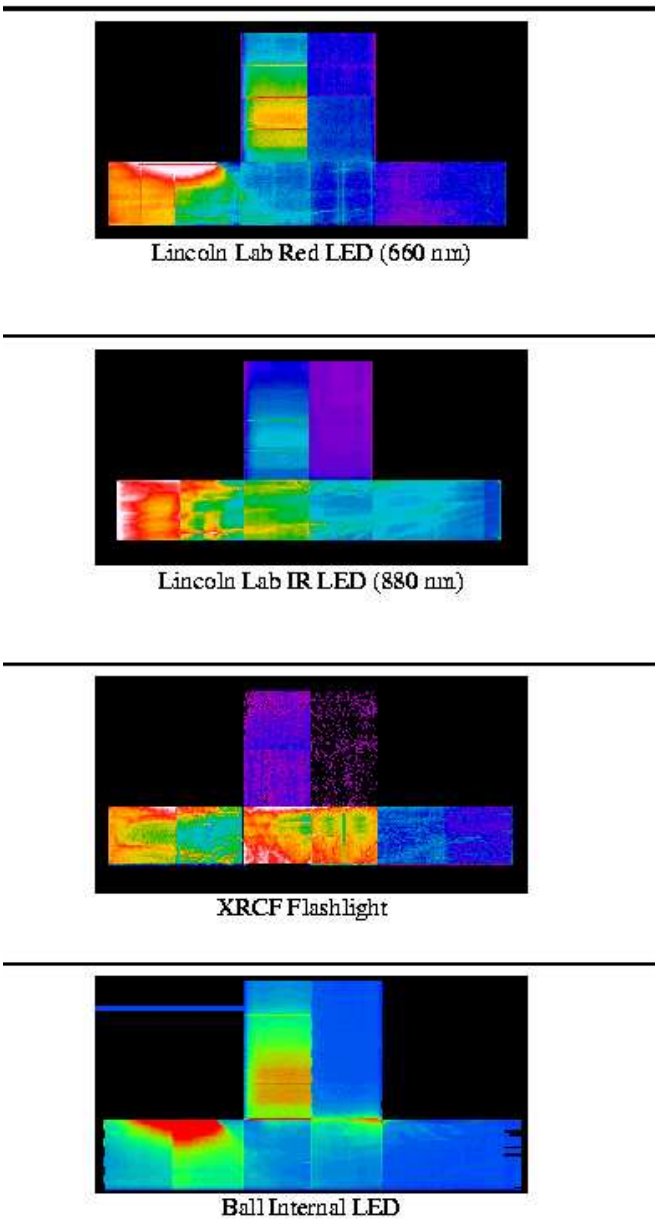

Figure 4.119: Focal plane composite images for various light leak tests. Color scale is for qualitative comparison only. Note similarity of all 660 nm LED images (both external and internal mounted sources).

4.13 ACIS CCD Sensitivity to Ionizing and Non-Ionizing Radiation

Preliminary radiation damage tests of ACIS front illuminated CCDs have been performed with two types of ionizing radiation sources. The Fe-55 X-ray source is expected to produce damage in the oxide layer and bulk oxide interface causing increased surface dark current and flat band voltage shifts. Because of the anticipated exceptional focusing of the HRMA this type of test is pertinent to the issue of overexposure and "burn-in" caused by bright X-ray sources. The high energy proton beam at the Harvard Cyclotron represents a class of radiation that primarily cause damage through collisions with silicon atoms. This displacement damage can result in trapping centers resulting in increased CTI and bulk dark current.

4.13.1 Ionizing Dose Effects

The X-ray ionizing dose test was made by placing an Fe-55 source in proximity to an engineering front illuminated CCID-17 with a geometrical baffle that limited exposure to a small section of the image array. No part of the frame store or serial register output node was exposed. The exposed region experienced a flux of 7 counts per pixel per second for 10 hours for a total equivalent dose of 900 rads. This exposure was made while the CCD was at room temperature in vacuum. The standard calibration timed exposure readout method was employed for all testing.

The most noticeable result of this test was the production of an area of enhanced dark current directly coincident with the exposed region (see figure 4.120). The dark current was uniform on small distance scales and no exceptionally hot pixels were seen. The enhanced dark current could only be measured for operating temperatures above -80 C. At the standard -120 C operating temperature no enhanced dark current could be measured even for exceptionally long integration times. Furthermore no increase in CTI was seen at any temperature. Long periods of high temperature bakeout (20 hours at +80 C) had no affect upon the damaged region, which appears to be a permanent feature. Experience with overexposure to X-rays at BESSY-PTB, XRCF-2CACIS and SES confirms the enduring nature of this type of radiation damage.

A similar X-ray ionizing dose experiment was made with a back illuminated CCD which yielded qualitatively similar results. A special overexposure of focussed bare carbon anode radiation on the backside w134c4 S3 was made as part of the XRCF testing. At -40 C an apparent spot of increased dark current can be seen but at lower temperatures this feature is not evident.

4.13.2 Effects of Energetic Protons

High-energy proton dose tests were made at the Harvard Cyclotron Laboratory where an engineering front illuminated CCID-17 was exposed to a well-characterized proton beam with 40 MeV peak energy. Exposures were made at room temperature in ambient air with a lead aperture that allowed irradiation of a controlled section of the image array. Irradiation occurred in incremental steps to a final total of 400 Rads. A minimum 48 hour period at ambient condition elapsed between exposure and all subsequent characterization. While there is evidence to suggest changes in post radiation behavior immediately following exposure with time scales of hours no changes were seen following the 2 day period - all damage features appear permanent and unaffected by subsequent temperature cycles.

As with the X-ray test the most noticeable result of proton beam exposure was the production of an area of enhanced dark current coincident with the exposed region. This dark current could not be measured for temperatures below -90 c. No flickering or hot pixels were detected at any temperature.

Proton damage is expected to produce traps whose presence can be seen by an increase in CTI, and indeed a gradual increase in CTI at a rate of 2 x 10-5 per kRad was seen when tested with a spatially uniform 25 count/sec/output Fe-55 source. A clocking method was used to create an adjustable line of charge in the image array. At -120 c this sacrificial charge technique only influenced pixels in the next few rows suggesting a detrapping time of order 100 microseconds. At -90 c the CTI is four times greater and the utility of the charge injection method more pronounced although improvements of any performance measure such as CTI or resolution could never be increased beyond levels achieved by normal operation at -120 c. Additional proton irradiation of just the frame store area had no affect upon the measured CTI but did continue to degrade the gain and resolution of the device. This is a consequence of the way in which CTI is measured.

Figure 4.121 shows the observed variation of CTI with proton dose.

4.13.3 Search for Effects of Short Exposure to Low-Earth Orbit on ACIS CCD Peformance

Two calibrated ACIS CCID17 units were flown aboard Space Shuttle Discovery for a 12 day mission in August 1997. (STS 85, OV-103) The devices, w157c1 and w147c3 (back illuminated) were in the normal input-shorted storage configuration in the standard shipping container which was stowed in the pressurized crew compartment.

Testing immediately before and after flight showed no change in performance for either device. Neither an increase in the number of hot or flickering pixels nor any CTI increase due to radiation exposure was seen.

Pre- and post-flight mean dark current maps for the two test devices are compared in figures reffig:w157dc and reffig:w147dc. These images are averages of at least ten individual exposures, each of 18 seconds. All except the pre-flight image of w157c1 (the

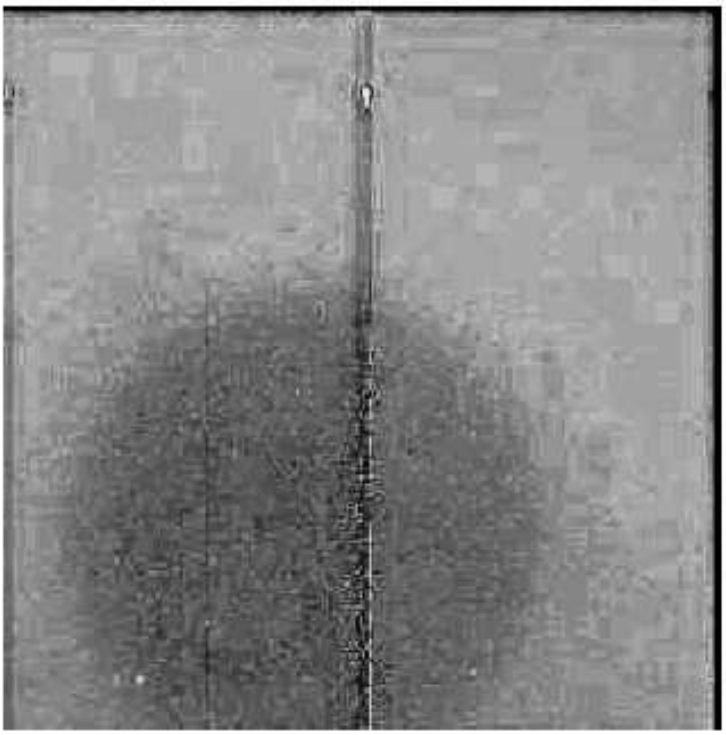

Figure 4.120: Dark current map showing circular area of exposure to 5.9 keV photons. Total dose was 900 rads (Si); this map was obtained with the device at -60C. At nominal operating temperature (-120C) no increase in dark current is measurable. Device quadrants 0-3 are from left to right; the serial register is toward the top of the picture.

front-illuminated device) were obtained with the detector temperature at -120C; the pre-flight image of w157c1 was obtained at -60C. The front illuminated device w157c1, which had a small edge glow and a bright defect prior to flight, showed no evidence of either feature during any post-flight testing. This change may have been a consequence of handling and may have nothing to do with the shuttle orbital environment. We conclude that low earth orbit shuttle cabin environment has no impact upon CCD performance for 1 week exposures.

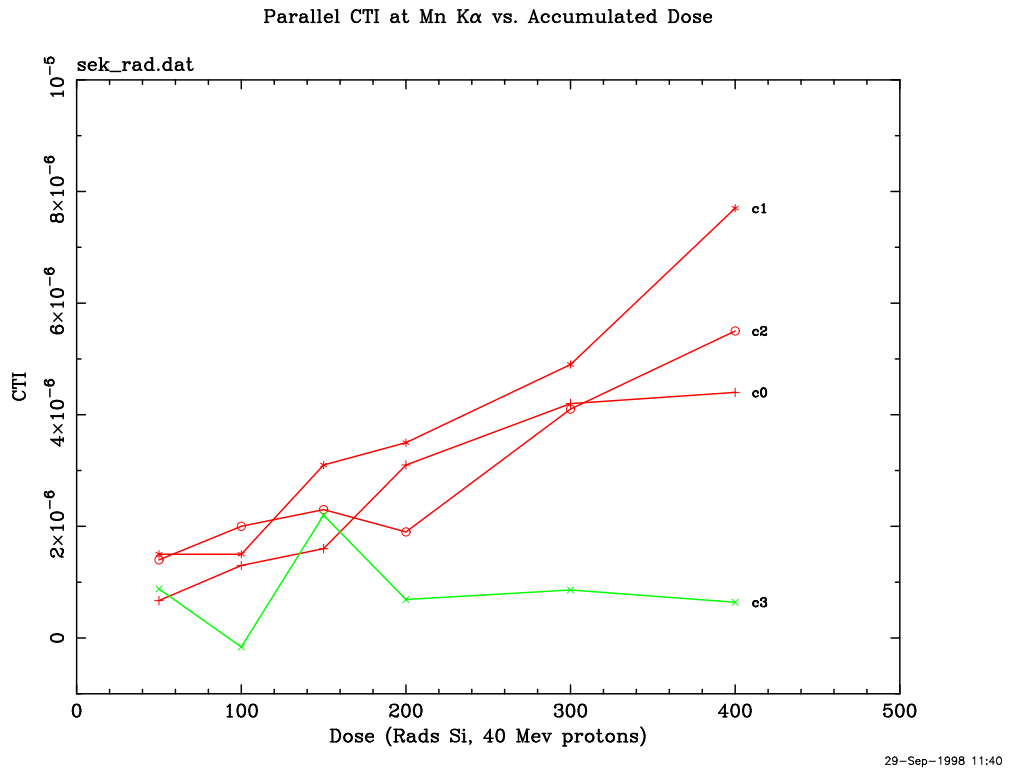

Figure 4.121: Charge transfer inefficiency (CTI) vs. accumulated ionizing dose of 40 MeV protons for a front-illuminated ACIS CCD. The curves labelled c0,c1, and c2 pertain to exposed areas of the device. The curve labelled c3 pertains to an area well-shielded from proton radiation.

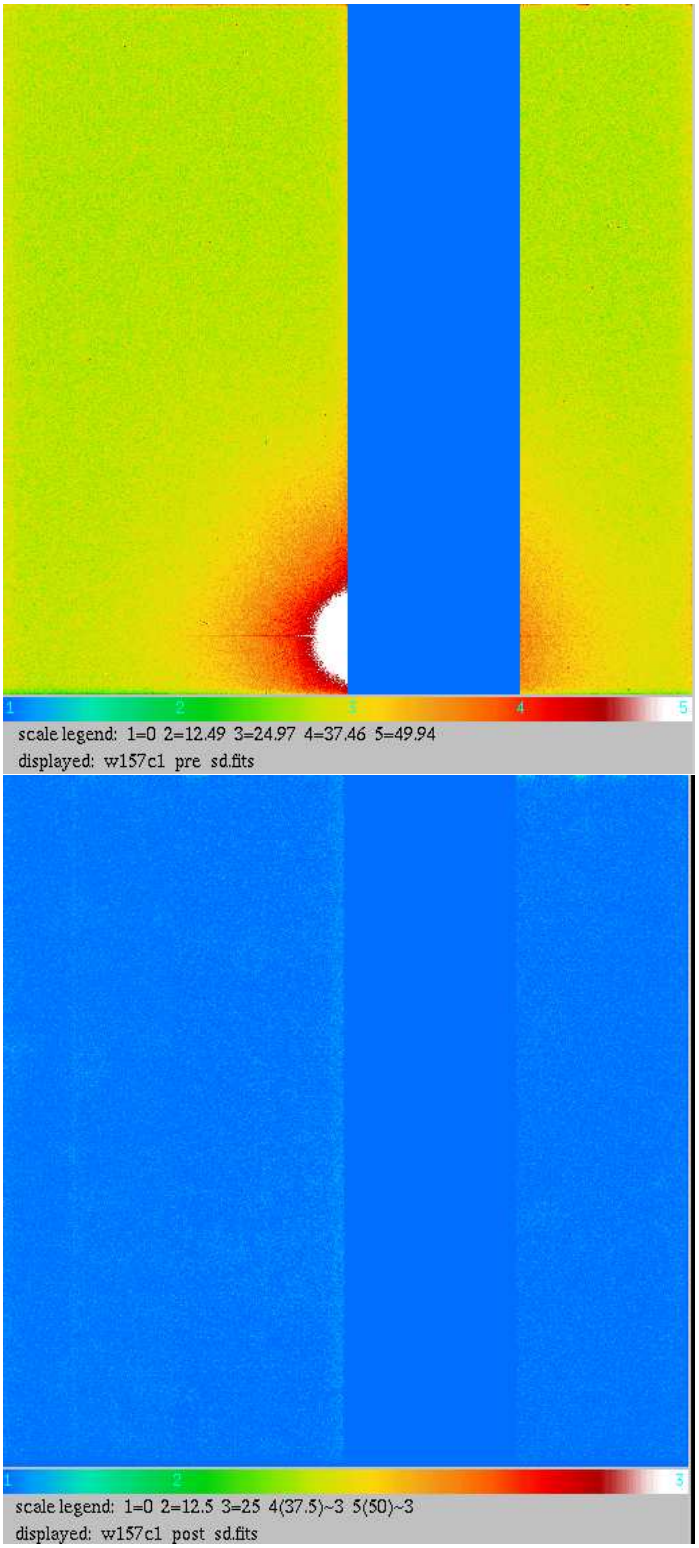

Figure 4.122: Dark current for the front-illuminated device w157c1 before (top) and after (bottom) its flight on STS-85. The preflight image was obtained at -60C and the postflight image at -120C. The bright defect was invisible at any temperature after the shuttle flight. The images are shown with identical colors scales; the signal level, in electrons per pixel per 18 s, is shown. Quadrant C was defective before and after the flight.

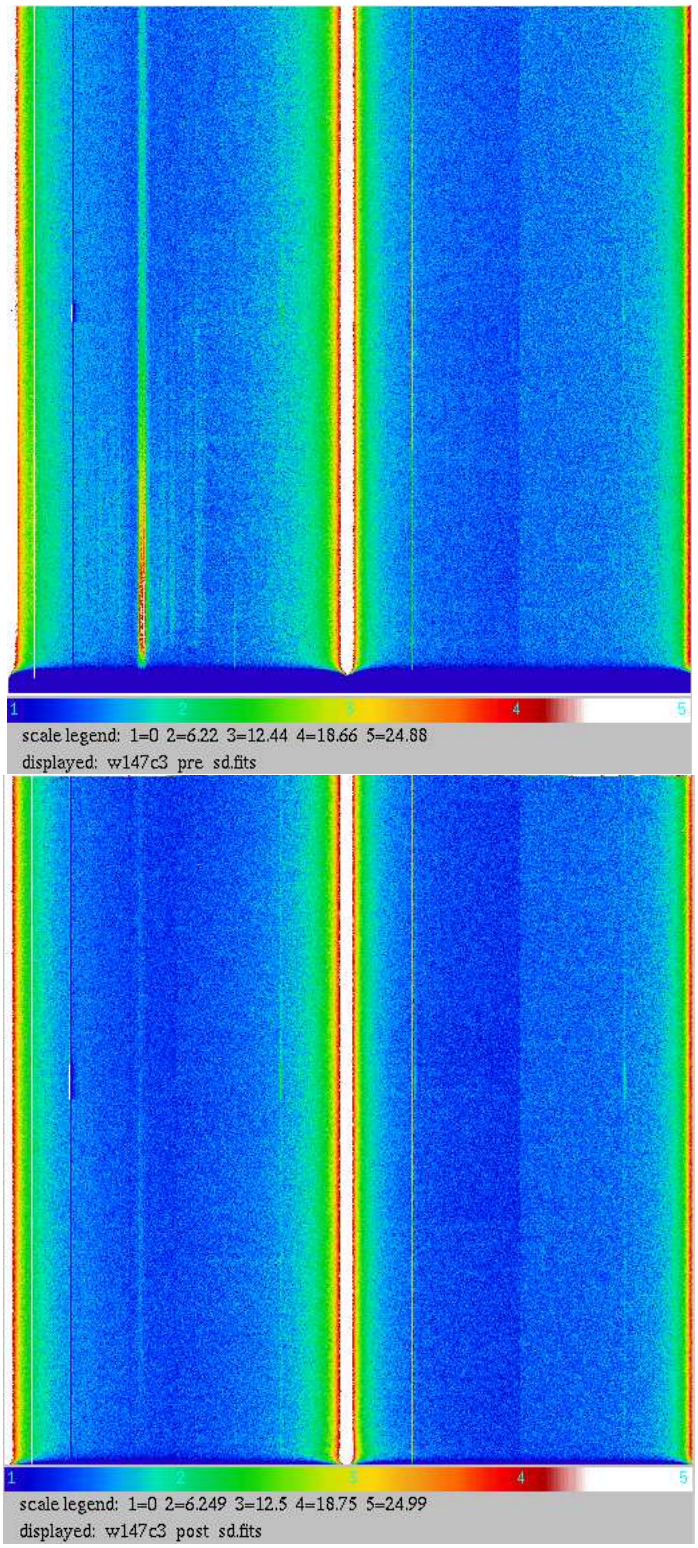

Figure 4.123: Dark current for the back-illuminated device w147c3 before (top) and after (bottom) its flight on STS-85. There is no apparent increase in the dark current. Both images were obtained at -120C. The same color scale is used for the two images; the signal level, in electrons per pixel per 18 s, is shown on the color bar.

4.14 The MIT Model of the ACIS CCD

We have developed a detailed model of the frontside illuminated CCD response to the X-ray illumination. The model is based on the Monte-Carlo technique. Photons of given energy are thrown into the random positions on the CCD surface and the device reaction is calculated for each individual photon. The most important new features of our model are discussed below.

4.14.0.1 Absorption in the gate structure

X-ray photon can be absorbed in any material with an exponentially distributed (depthwise) probability of interaction. To model this process the simulation program generates an exponentially distributed random number R. If $R > \frac{d}{\lambda}$ we assume that the photon have passed the layer of thicknness d with characteristic absorption length λ without being absorbed. Otherwise the photon is absorbed inside the layer.

The cross section of the gate structure of the ACIS CCD along the direction of charge transfer is shown schematically on Fig. 4.124. Another cross-section, perpendicular to the

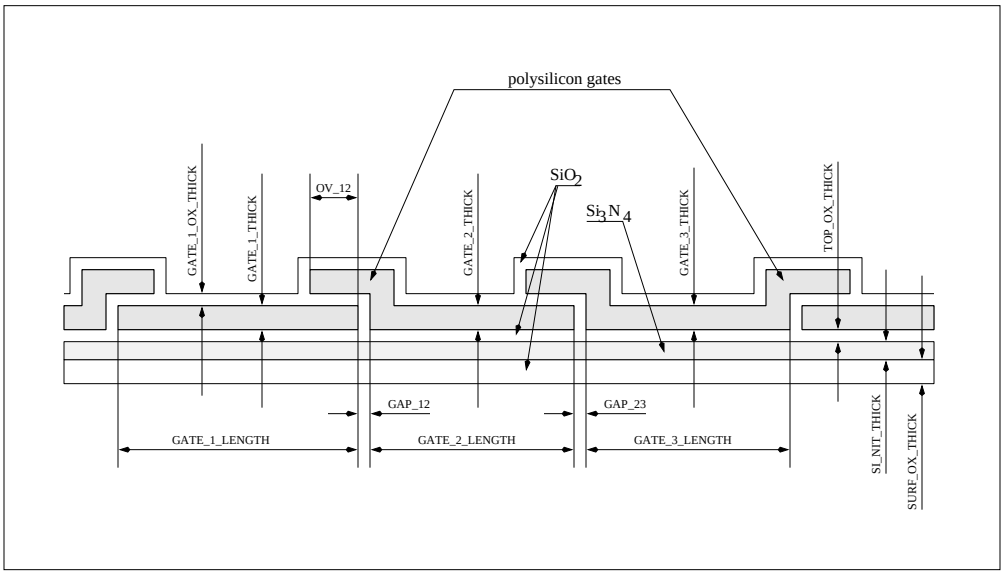

Figure 4.124: Cross section of the gate structure of the CCD along the transfer channel.

direction of the charge transfer is shown on Fig. 4.125. Electron microscope photographs clarifying the real life details of both cross-sections are shown on the Figures 4.43 and 4.44.

Absorption of X-rays in the gates becomes a very significant factor at low energies (below 1 keV) and immediately above silicon edge. Our model simulates all the details of the gate structure such as gate overlaps, oxide walls at the edges of the polysilicon gates, triangular shape of the wings of the oxide layer above the channel stop regions.

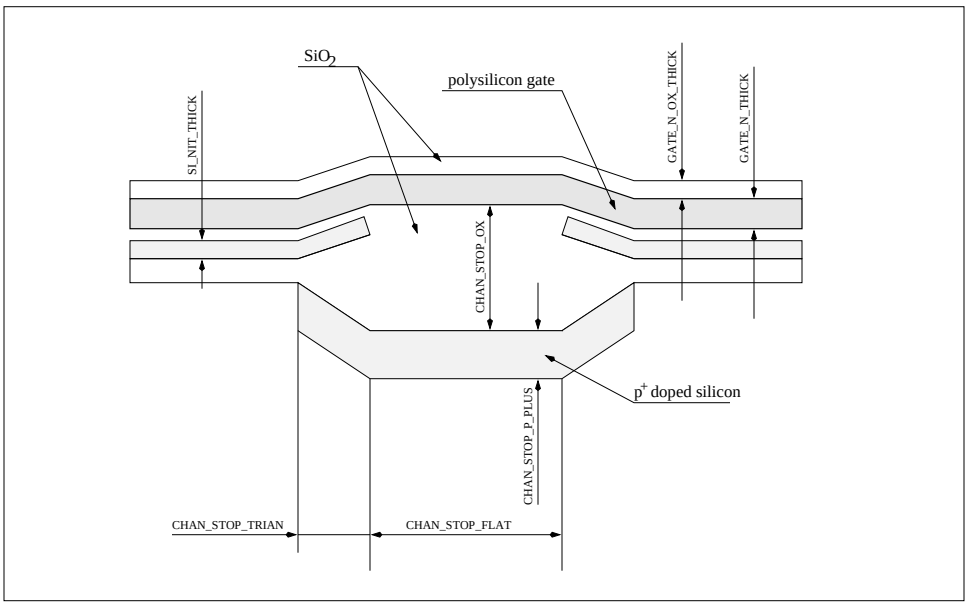

Figure 4.125: Cross section of the gate structure of the CCD perpendicular to the transfer channel.

Characteristic absorption lengths for all the constituent layers are calculated based on the high precision measurements of the thin films of the corresponding materials performed at synchrotron beamlines (see subsection 4.6.4). As a result the model can very accurately predict quantum efficiency of the device in the entire energy range. It has a capability to show the distribution of the intensity of the detected fluxs across the pixel, which can be important for the subpixel resolution studies (see Chapter 6). Figures 4.126 and 4.127 demonstrate variations in sensitivity inside the pixel at the energies immediately below and above oxygen absorption edge for a pixel cross-section along the transfer channel.

Slightly different gate thicknesses (the values were obtained in the mesh experiment, see section 4.5) result in different intensity under different gates. Sharp drops in the sensitivity can be seen in the regions where adjacent gates overlap. Silicon dioxide is less opaque than silicon below oxygen absorption edge and more opaque immediately above the edge. Because of this jumps in sensitivity corresponding to oxidized edges of the gates inside overlap regions go in opposite directions at the two energies.

4.14.0.2 Fluorescence events

Simulating CCD response we assume that for each photon with energy greater than the silicon absorption K edge (1839 eV) absorbed inside silicon, there is a 0.043 probability to emit a fluorescent photon with the characteristic energy of 1.739 keV. We neglect the fluorescence from other elements (oxygen and nitrogen) as well as L-shell fluorescence of silicon due to a very small probabilities of these events. The fluorescent photons are emitted

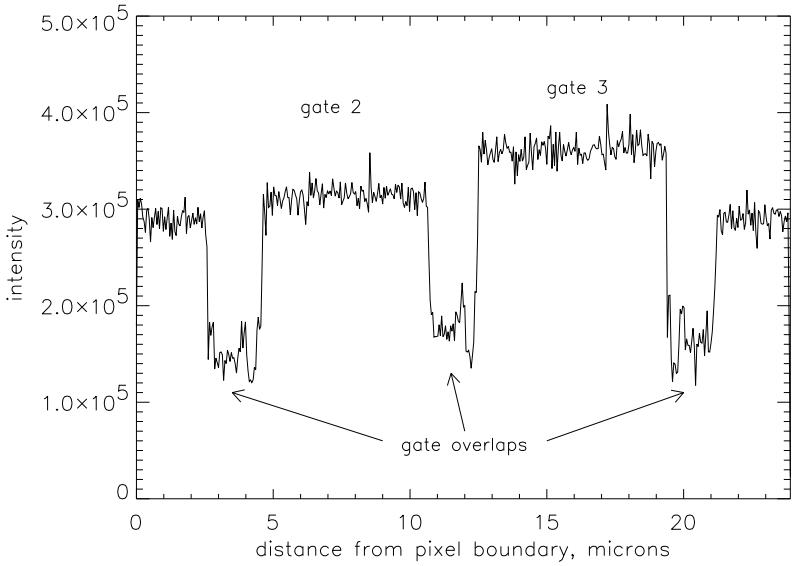

Figure 4.126: Number of detected events as a function of coordinate inside a single pixel. Energy of the incident photons is 525 eV.

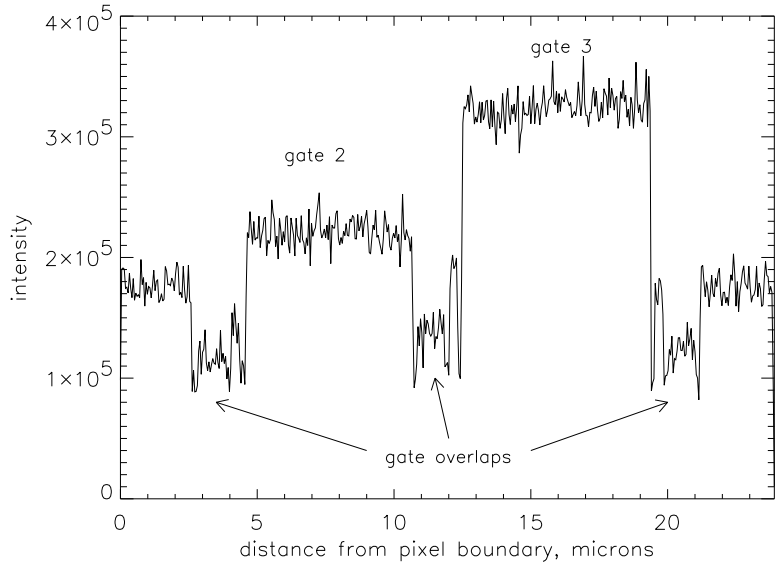

Figure 4.127: Number of detected events as a function of coordinate inside a single pixel. Energy of the incident photons is 539 eV, right above oxygen K edge. Notice a different behavior inside overlap regions

uniformly in all directions and the program calclulates the spatial angles using a random number generator. After that the absorption probability for the fluorescent photons is calculated in the same manner as for a regular photon. If the fluorescent photon leaves silicon substrate or interacts several pixels away from the site of interaction of the primary photon, an escape event will be detected. The model makes an accurate prediction of the

escape peak amplitude.

An amplitude of the fluorescent peak was much harder to reproduce. The key to the correct model of the flourescent peak, especially at energies close to the Si absorption edge, is taking into account fluorescence from the gates. Immediately above Si edge absorption in the polysilicon gates becomes a significant factor. Of the absorbed photons 4.3% produce a fluorescent photon and roughly half of them goes into the bulk of silicon and gets detected, while another half is emitted into the upper hemisphere and is lost. Unlike flourescent photons that are emitted from the bulk silicon, the leftover charge corresponding to the difference in energy between primary and fluorescent photon cannot be detected when it is formed in the polysilicon gate. This means that approximately half of the photons fluoresced from the gates will be found in the fluorescent peak, while only a tiny fraction of the ones from the bulk will end up in the fluorescent peak. Because of this flourescence from the gates is by far a dominant factor in forming the flourescence peak. On Fig. 4.128 are shown the amplitudes of the escape and flourescence peaks both from experimental data and simulated eventlists. The experimental data had been collected at a synchrotron ring at BESSY using Crystal Monochromator Beamline with a device w102c3.

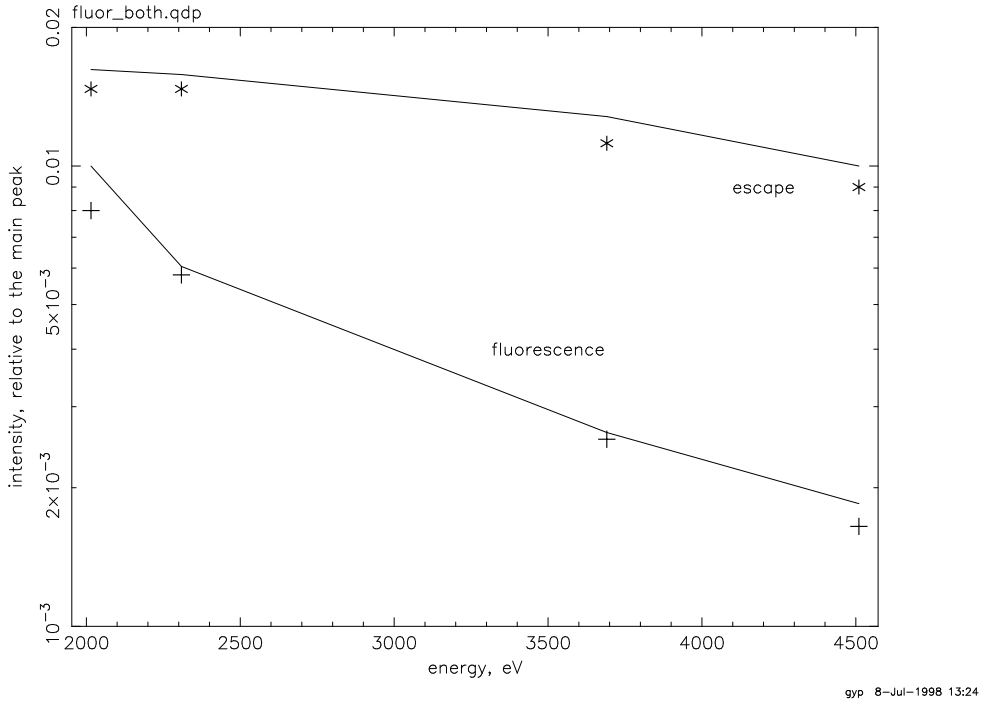

Figure 4.128: Intensities of experimentally measured escape (*) and fluorescence (+) features as a function of energy. Solid lines are the model predictions.

Solid lines on Fig. 4.128 show the model predictions. An agreement between the data and the model is good. A discrepancy in the amplitudes of the fluorescence peak reported previously in the Preliminary Calibration Report is now resolved. It was caused mostly by

not taking into account fluorescence from the gate structure.

4.14.0.3 Formation and diffusion of the electron cloud

When the photon interacts with a silicon atom in a detector an electron cloud is formed. If the interaction occured in the depleted layer, the electrons are pulled by the electric field and the cloud drifts into CCD potential wells, while spreading wider due to diffusion processes at the same time. If the cloud was formed in the undepleted bulk of silicon, the electrons diffues without a drifting component, where only the electrons that reach the border with the depleted region are carried by the electric field into the potential wells of the CCD. The final cloud size is an important parameter which determines how the charge of the cloud is split between adjacent pixels. We use the most common approach and calculate the final cloud radius r according to the formula $r = \sqrt{r_i^2 + r_d^2}$, where r_i is the initial cloud radius, r_d is the cloud radius after the diffusion process. To calculate the diffusion radius for charge generated both in depleted and undepleted bulk we follow the paper of Hopkinson (Hopkinson, 1987). For the initial cloud radius we use the results of Scholze&Ulm (Scholze and Ulm, 1994) if the interaction of the photon with the silicon atom did not occur near the $Si - SiO_2$ interface. Events which originate within a small distance from the surface lose some charge to the oxide layer and form a low energy tail of the response function. The treatment of such events is described in the subsection 4.3.2, the original cloud radius for them being much smaller than for the bulk events.

A different procedure is used for the charge clouds that are formed in the doped area of the channel stops. We have shown (see (Prigozhin, 1998)) that events originating in the p^+ region of the channel stop suffer a charge loss and as a result form a shoulder on the low energy side of the main peak. Since the majority of the events in the channel stops is split between two adjacent pixels, this effect is most pronounced for the horizontally split events. A histogram of the horizontally split events (ASCA grades 3 and 4) at 1487 eV is shown in Fig. 4.129. We have measured a fraction of the events in the shoulder relative to the total number of counts in the horizontally split histogram as a function of energy. The corresponding plot is shown on Fig. 4.130. It indicates that all the lossy events in the channel stop area come from a shallow region about 0.3 microns deep.

To take this phenomenon into account in our model for all charge clouds having their centers inside this region we introduce a loss which is a function of the cloud charge and the cloud center location. As a result our model can reproduce the low energy tail of the horizontally split events reasonably well.

4.14.0.4 Splitting of charge between pixels

Once the cloud sizes and cloud centers are known, the final calculations are fairly common for this kind of model. The cloud is split between adjacent pixels assuming gaussian distribution of charge density in the cloud. This implies a very simple routine for evaluation

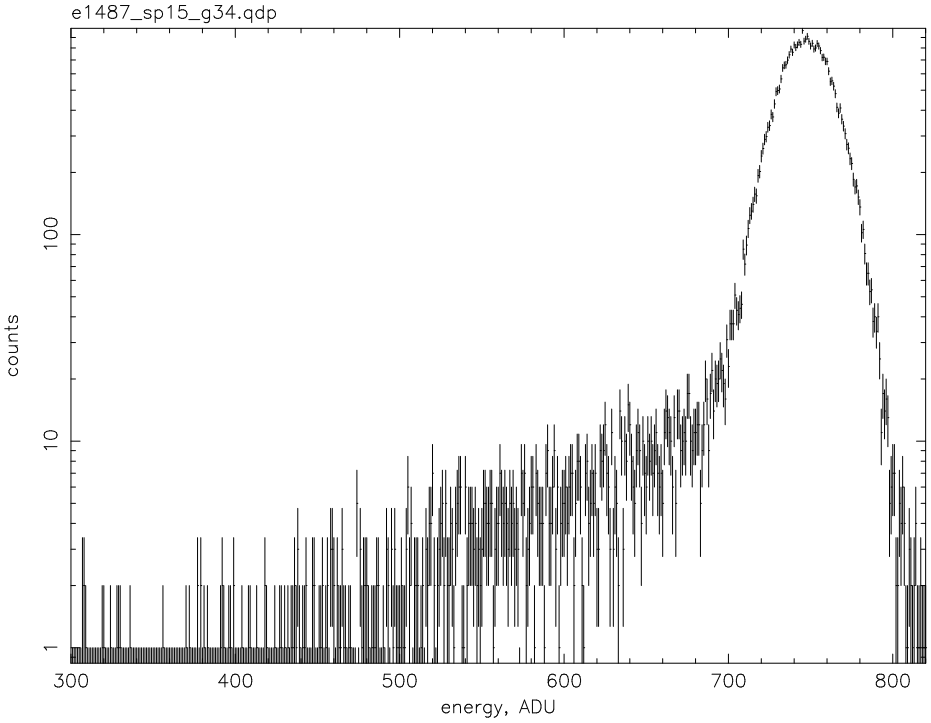

Figure 4.129: Histogram of the horizontally split events at 1487 eV

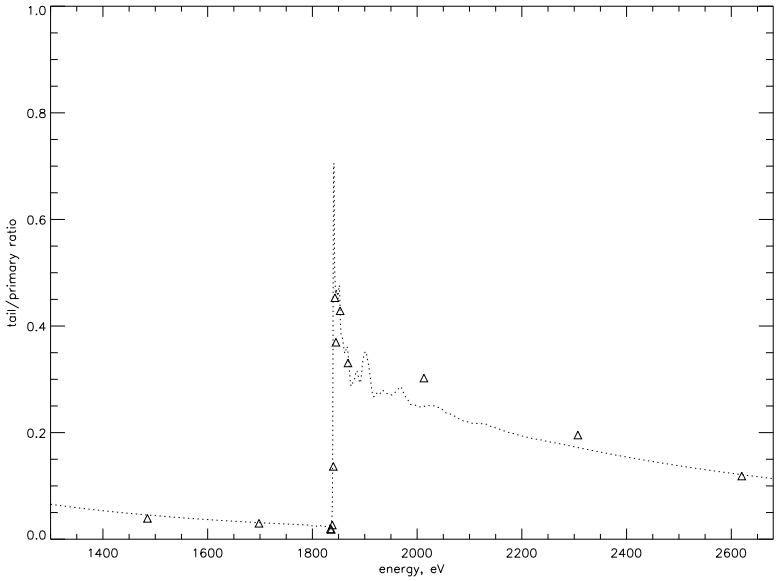

Figure 4.130: Ratio of the number of events in the shoulder to the total number of events in the horizontally split event histogram (triangles). Dotted line shows the calculated ratio assuming these events come from a layer of silicon 0.3 microns thick.

of the signal amplitude in pixels adjacent to the cloud center. After that readout noise with a gaussian distribution is added to each pixel and a gain factor is introduced to adjust the

amplitude of the signal to that of the paticular device that is being modeled. The last stage is an event finding routine - a procedure similar to the one used in data analysis software to determine whether the amplitude of an event is great enough to be included into an eventlist. The output of the program is a standard eventlist which is entirely compatible with numerous software tools available for the real data analysis. In Figure 4.131 are shown standard grade histograms for experimental data taken under monochromatic illumination at 4510 eV and the histograms of simulated data for the same energy. While there are some small discrepancies, all the important features of the response, such as escape and fluorescent peaks, low energy peak, low energy tail, peculiar shape of the low energy tail of the horizontaly split events, are reflected in the model, and agreement between the model and the data in general is good.

4.15 Unresolved Issues

4.15.1 Bias Stability

An unexplained bias distortion invariably beginning at the start of a science run and enduring for hundreds of readout frame times has resulted in much consternation over worthless data and the current implementation of the prophylactic regimen with the charming sobriquet "jitter-dacs" which has become a permanent feature of the flight software. The distortion is clearly produced by an excess of charge which only accrues when the parallel clock low level does not go below some near 0 volt level for a period of time equal to or greater than a single frame readout cycle. It is possible to believe that the sources of the charge are surface states lying directly under the gates, or at the gate-silicon junctures. Bringing the gate voltage low (or more precisely, jittering the voltage many times between high and low) depletes these states once and for all time. While this may be difficult to believe it is indisputable that without jitter-dacs neither useful data or bias can be acquired for a long time after the start of a science run.

It should be noted that apparent bias instabilities have occasionally been observed after the installation of the "jitter-dacs" feature in the ACIS flight software. One such example, alluded to in section 4.7.3 occurred in ACIS XRCF Science Run 93 (TRW ID's I-IAS-SG-1.032 and I-IAS-EA-2.043 through I-IAS-EA-2.048) and affected the bias of detector S4. The cause of this instability is unknown. It may be relevant that S4 is unique among ACIS detectors in having framestore parallel clock levels equal to the imaging area clock levels at $(+2, +11\text{V})$. All other detectors have framestore clock levels of $(-4.5, +5\text{V})$.

4.15.2 Long-term Gain Stability

As indicated in section 4.9, between XRCF Phase I and Ball ISIM Thermal Vacuum tests, the mean detector gains, after correction for effects of CCD and electronics temperature,

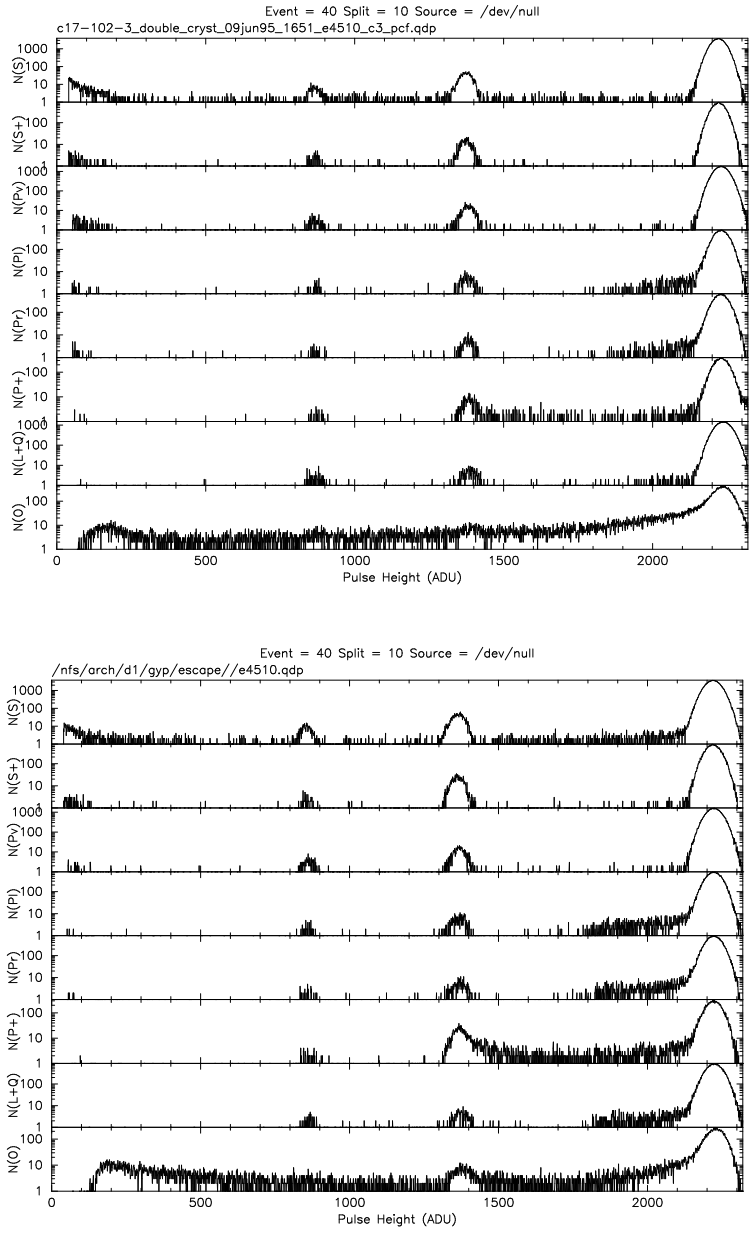

Figure 4.131: Standard graded histograms comparing experimental data with simulated data. Data collected for a monochromatic source at 4510 eV. (top) Data; (bottom) Simulation

changed by a mean (for 10 detectors, 40 output nodes) of 0.5%; the RMS fluctuation about this mean was 0.6% per measurement CCD. This is considerably larger than the expected

level of about 0.1% per output node (0.05% per CCD). The gain change residuals apper to fall in two groups. In one group (detectors I1,I2,S2 and S3) the mean gain change (XRCF Phase I - Ball ISIM Thermal Vac) is about -1%; in the other group, the mean gain change is less than -0.2%.

The source of these residual gain changes is unknown. It may be that different analog signal chains have different slightly different temperature coefficients of gain. Evidently the effect of DEA temperature, and other factors, on gain must be better understood if long-term gain stability better than 0.5% is to be achieved.

Chapter 5

Optical Blocking Filter Performance

5.1 ACIS UV/Optical Blocking Filter Transmission Function

The ACIS-I and S arrays are covered by UV/Optical blocking filters (OBF). These filters are necessary because CCD's are sensitive to UV and optical radiation (see Lumb et al., 1991). The ACIS filters consist of polyimide, a polycarbonate plastic with a chemical composition of $C_{22}H_{10}O_4N_2$, with a layer of aluminum coated on each side to provide optical light blocking. The x-ray transmission properties of the ACIS OBFs were measured in the energy range of 260 to 3000 eV at the National Synchrotron Light Source at Brookhaven Laboratories, by a team headed by George Chartas. Additional measurements probing the fine structure near the edges of C, N, O, and Al, were made at the Advanced Light Source at Berkeley, by George Chartas.

The main purpose of the calibration was to determine model transmission functions for the ACIS OBF's in the energy range of 0.05 to 10 keV with an accuracy of better than 1%. We present a model transmission function that fits the data to better than 1% in the measured energy band of 260 to 3000 eV. The transmission above 3 keV is expected to vary smoothly and is predicted by the model from the measured filter parameters. Detailed fine energy scans above the Al-K and C-K absorption edges revealed the presence of fine oscillations of the X-ray transmission. These features are most likely extended X-ray absorption fine structure (EXAFS). The amplitude of the EXAFS oscillations above the Al absorption edge is about 5% of the mean value of the X-ray transmission. The ACIS OBF's were measured at room temperature while the on orbit temperature of the filters is expected to be about -60 C. We predict that the amplitude of the EXAFS will increase by less than 0.5% when the filters are in orbit at normal operating temperatures.

Optical transmission measurements on a multilayer filter composed of Al/Polyimide/Al = 340Å/2020Å/357Å were made at PSU and Denton Vacuum, Inc., by Gordon Garmire, Leisa Townsley and Pat Broos. We have used the results from the optical measurements

to determine the optical constants for polyimide in the measured wavelength band and to predict the optical transmission performance of the flight filters.

5.1.1 Brookhaven Experimental Configuration

The 0.26 to 3 keV X-ray transmission of the ACIS OBFs was measured at the National Synchrotron Light Source (NSLS) at Brookhaven National Laboratories. The use of the NSLS synchrotron source for the calibration was necessitated by the required high accuracy for these measurements. The NSLS provided a monochromatic X-ray beam allowing us to measure the transmission of the ACIS filters at fine energy steps with sufficient intensity for good counting statistics and fair beam stability to allow accurate detector normalization corrections.

The X-ray ring at NSLS in normal operation mode accelerates electrons to energies of about 2.5 GeV for optimized X-ray emission in the range of 1 to 10 keV. A table of the operating parameters of the NSLS X-ray storage ring is provided at their Web site (http://www.nsls.bnl.gov/). Our experiment was setup on beamline X8A, one of 56 X-ray beamlines attached to the X-ray storage ring. The beam energy incident on the filters was selected by adjusting the orientation of the crystal element of a double crystal monochromator located upstream from the vacuum chamber. Each crystal element spans a certain energy range. In particular a W/Si multilayer covers the energy range 0.26-2.0 keV with energy resolution ($\Delta E/E$) of $2\text{x}10^{-2}$, a Si(111) crystal covers the range 2.1-5.9 keV with a resolution of $5\text{x}10^{-4}$, and a Beryl(1010) crystal covers the range from 0.8-2.0 keV with a resolution of $8\text{x}10^{-4}$. In Table 5.1, we list the energies surveyed and the monochromator crystal elements used for the transmission measurements of the ACIS-I and ACIS-S UV/Optical blocking filters. Detailed fine energy scans were performed above the absorption K edges of C, N, O, and Al to investigate extended X-ray absorption fine structure (EXAFS) and shifts in the location of the Al-K edge due to possible Al_2O_3 contamination.

The configuration of the test setup is shown in Figure 5.1. Witness samples made with the ACIS filters were placed into the UC/SAO spectrometer-reflectometer chamber and mounted onto a mechanical fixture. The fixture was made to support both image and spectrometer filters and was mounted on a rotary stage that allowed for the selection of the portion of the filter to be intercepted by the X-ray beam. The X-ray beam was collimated with a set of vertical and horizontal entrance slits to a size of 2 mm by 2 mm. The beam flux was monitored using a detector that was moved in and out of the X-ray beam with a computer controlled actuator.

5.1.2 Calibration Strategy

The transmission of the filters is determined by moving the filter in and out of the beam and using a "measurement" detector to measure the X-ray flux attenuated and non-attenuated

Energy Range eV	Step Size eV	Monochromator	Beam Filter	Absorption Edge
260-360	1	W/Si Multilayer	Titanium	C-K(284eV)
300-600	5	W Si Multilayer	Chromium	N-K(401.6eV)
500-660	5	W/Si Multilayer	Nickel	O-K(543.1eV)
660-860	20	W/Si Multilayer	Nickel	
800-1300	25	W/Si Multilayer	Magnesium	
1200-1600	20	W/Si Multilayer	Aluminum	Al-K(1559eV)
1450-1700	30	W/Si Multilayer	Nickel	Al-K(1559eV)
1700-2000	40	W/Si Multilayer	Nickel	Si-K(1838.9eV)
1450-1700	2	Beryl(1010)	Titanium	Al-K(1559eV)
1540-1590	0.5	Beryl(1010)	Titanium	Al-K(1559eV)
1700-2000	2	Beryl(1010)	Titanium	Si-K(1838.9eV)
2000-2600	20	Si(111)	Titanium	
2600-3000	5	Si(111)	Titanium	Cl-K(2833.0eV)

Table 5.1: Energies surveyed and the monochromator crystal elements used for the transmission measurements of the ACIS I and ACIS S UV/Optical blocking filters.

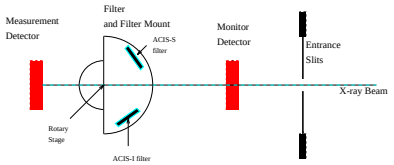

Figure 5.1: Schematic of the test configuration for the measurement of the X-ray transmission of the ACIS filters.

by the filter respectively. The purpose of the monitor detector measurements is to take into account possible flux variations of the beam between the time the filter is in vs. when it is out of the beam. Both detectors are silicon PIN photodiodes. One detector is exposed to the X-ray beam at a time allowing a simultaneous background signal level measurement from the other unexposed detector. If $I_{i,j}$ represents a measured signal from the i'th detector (i=0 for the monitor and i=1 for the measurement detector), taken when the filter is located in the j'th position (j=in, for filter in beam, j=out, for filter out of beam), then the X-ray transmission at the X-ray energy E is determined using the expression,

$$T(E) = \frac{I_{1,in} - B_{1,in}}{I_{1,out} - B_{1,out}} \frac{I_{0,out} - B_{0,out}}{I_{0,in} - B_{0,in}} \tag{5.1}$$

where $B_{i,j}$ is the background measurement of detector i with a filter in the j position.

Measurements with the filters out of the beam provide cross calibration of the monitor and measurement detector at all energies selected for the transmission measurements. A cross calibration between measurement and monitor detectors was performed before and after each transmission measurement. As an estimate of the errors in our measurements, we took the percent change in the two cross calibration runs. For the data points considered in the present analysis the percent change in normalization was below 0.5%. There is a delay of about 20 sec between measurements from each detector and one expects there to be an additional calibration error due to changes in the beam intensity, shape and direction that could occur during that time interval.

5.1.3 Modeling the Transmission Data and Determining an X-ray Transmission Function.

A method commonly used to model the X-ray transmission of filters assumes that the absorption through a multilayer filter with constituent compounds i is described by the equation,

$$\frac{I}{I_o} = \prod e^{-\mu_i \rho_i}, \tag{5.2}$$

where μ_i is the mass absorption coefficient of constituent compound i and ρ_i is the mass per unit area of the constituent compound i. μ_i can be expressed as a function of the compound's constituent elements j as,

$$\mu_i = \sum \mu_j w_j, \tag{5.3}$$

where μ_j is the mass absorption coefficients of element j, and w_j is the fraction by weight of element j. Tabulated values for the mass absorption coefficients for elements with atomic weights ranging from Z = 1 to Z = 92 may be found in Henke et al. (1993).

We initially performed a least squares fit to the transmission data of the Imager and Spectroscopy filters using the function given in equation 5.2 while considering a multilayer filter structure of the form Al_2O_3/Al:Si/Polyimide/Al:Si/Al_2O_3. Free parameters for this fit were the mass per unit area of Polyimide ($C_{22}H_{10}O_4N_2$) and Al. The large values for χ^2 obtained in these fits make them formally unacceptable. The residuals to these fits indicate that most of the discrepancy between the model and data occurs above the absorption edges of C, N, O, and Al. The transmission data clearly show oscillations above the absorption edges that extend up to several hundred eV. Such structures are commonly known as extended X-ray absorption fine structure and occur only when atoms are in condensed matter. The oscillations arise from interference of the scattered electron wavefunction outgoing from a central atom, i, with the backscattered electron wavefunctions from nearby atoms, j. A detailed review of EXAFS theory and applications may be found in Stern and Heald (1983).

In our next attempt to fit the transmission data we excluded energies corresponding to EXAFS and used the same function as in the previous model. The values obtained for reduced χ^2 of ~ 0.2 (for 442 degrees of freedom) indicate a significant improvement in the fit. We obtain values for the mass per unit area for the Imager filter, for Polyimide of 2.734×10^{-05} gr cm^{-2} and Al of 4.071×10^{-05} gr cm^{-2} and for the Spectroscopy filter Polyimide of 2.632×10^{-05} gr cm^{-2} and Al of 3.068×10^{-05} gr cm^{-2}.

For the purpose of determining a function that fits the transmission data well, we used a very simplistic EXAFS model that incorporates features from the independent particle model developed by Stern 1978, Lee and Pendry 1975, and Stern et al. 1975. Our model considers only interference effects from the nearest atomic shell.

The EXAFS component $\chi(k)$ is defined as the oscillating part of the mass absorption coefficient and is given by,

$$\chi(k) = \frac{\mu - \mu_0}{\Delta\mu_0} \tag{5.4}$$

where μ_0 is the smoothly varying part of the mass absorption coefficient corresponding to an isolated atom, $\Delta\mu_0$ is the change in the mass absorption coefficient over the absorption edge, and k is the wavenumber of the scattered photoelectron given by,

$$k = \frac{\sqrt{2m(E - E_{edge})}}{\hbar} \tag{5.5}$$

The model used to fit the oscillatory component of the transmission has the form,

$$\begin{aligned}\xi_j(E) = a_0(E - E_{j,edge})^{-\frac{1}{2}} step(E_{j,edge}, E_{j,4}) \mathrm{e}^{(-\mathrm{a}_1(\mathrm{E}-\mathrm{E}_{\mathrm{j,edge}}))} \sin(a_2(E - E_{j,edge})^{\frac{1}{2}} + a_3) step(E_{j,2}, E_{j,4}) \\ + a_4 \sin(a_5 E^{\frac{1}{2}} + a_6) step(E_{j,1}, E_{j,2}) \\ + (a_7 E + a_8) step(E_{j,3}, E_{j,4})\end{aligned} \tag{5.6}$$

The term $a_2(E - E_{j,edge})^{-\frac{1}{2}}$ represents the phase shift of a photoelectron as it traverses the distance 2R, where R is the interatomic separation, a_3 and $\exp(-a_1(E - E_{j,edge}))$ account for phase shifts in the presence of potentials, disorders and thermal vibrations of atoms about their average distance R from the central atom. Near edge structure in our transmission data is modeled with the term $a_4 \sin(a_5 E^{\frac{1}{2}} + a_6)$. Equation 5.6 does not take into account the nonlinear dependence of the phase shift and the dependence of the backscattering amplitude on k. A more physical model will be presented in a future publication.

For our modeling purposes j takes the values j=0 for the Al-K edge and j=1 for the C-K edge. We define the function $step(E_{j,1},E_{j,2})$ as follows,

$$step(E_{j,1}, E_{j,2}) = 0, \text{for } E_{j,1} > E \text{ or } E_{j,2} < E \tag{5.7}$$

$$step(E_{j,1}, E_{j,2}) = 1, \text{for } E_{j,1} < E < E_{j,2}$$

In Figure 5.2 and Figure 5.3 we show fits of our simple EXAFS model to the regions above the Al-K and C-K edges. Because of the limitations of the multilayer monochromator the EXAFS above the N-K and O-K edge were not resolved. In Figure 5.2 we also show the relevant energy boundaries used in our model. $E_{j,edge}$ defines the energy of the absorption K edge, ($E_{j,2}$, $E_{j,4}$) , ($E_{j,1}$,$E_{j,2}$), ($E_{j,3}$,$E_{j,4}$), define the boundaries of the first, second and third term of equation (5.6) respectively.

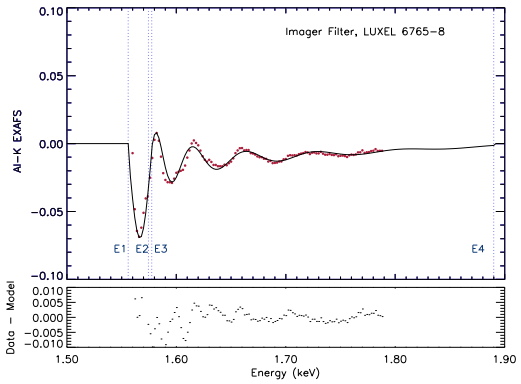

Figure 5.2: Top Panel; Al-K EXAFS with model fit. Lower Panel; Difference between data and model .

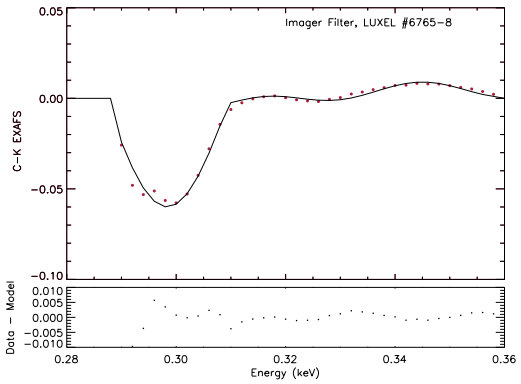

Figure 5.3: Top Panel; C-K EXAFS with model fit. Lower Panel; Difference between data and model .

The total transmission function of the ACIS filters is finally described by the following expression,

$$f(E) = \prod e^{-\mu_j \rho_j} + \sum \xi_j(E) step(E_{j,1}, E_{j,4}) \tag{5.8}$$

For energies excluding the EXAFS regions the transmission function $f(E)$ is given by the fit of our model described by Equation 5.8 that incorporates the atomic scattering factors f_1 and f_2 as tabulated by Henke et al., (1993). For energies within the EXAFS regions our model function $f(E)$ includes in addition the best fit model to the EXAFS regions. The values for all the relevant parameters that enter equation (5.8) are listed in Table 5.2.

The transmission data for the Imager and Spectroscopy filters together with the model transmission function and the percent difference between the model and data are presented in Figure 5.4 and Figure 5.5.

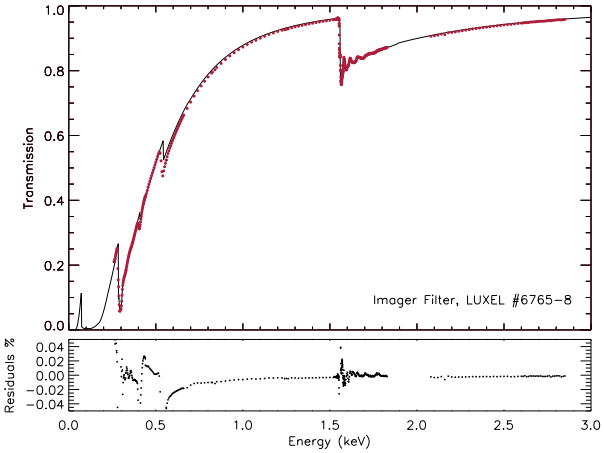

Figure 5.4: Top Panel; X-ray transmission data of Imager filter with best fit transmission model. Lower Panel; Percent difference between model fit and data.

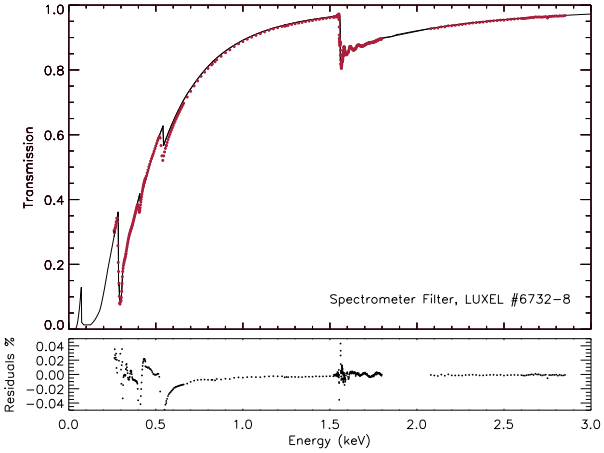

Figure 5.5: Top Panel; X-ray transmission data of Spectrometer filter with best fit transmission model. Lower Panel; Percent difference between model fit and data.

5.1.4 ACIS UV/Optical Blocking Filter Calibration at the Advanced Light Source

The transmission of the ACIS optical blocking filters between 50 and 700eV was measured at the Advanced Light Source at Berkeley Labs. The measurements were performed on beamline 6.3.2 which contains a variable-line spaced plane grating monochroator that provides high resolution ($E/\Delta E \sim 2000$ at 550 eV with 50μm exit slit and 1200 l/mm grating) and a triple mirror "order-suppressor" that in combination with filters provides

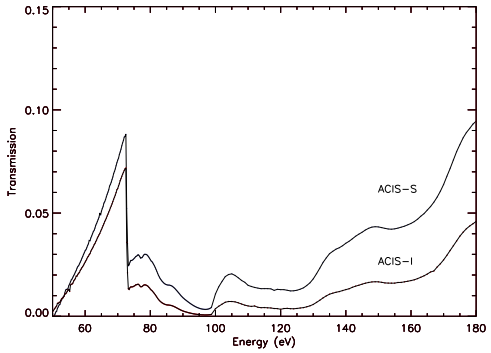

Figure 5.6: Al-L XAFS .

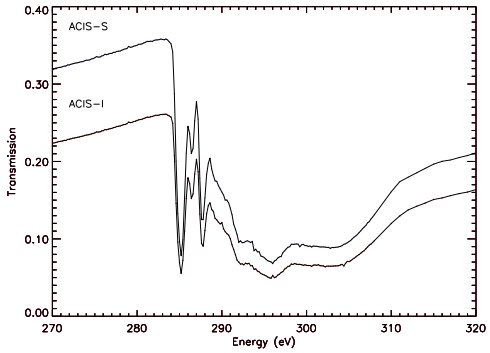

Figure 5.7: C-K XAFS .

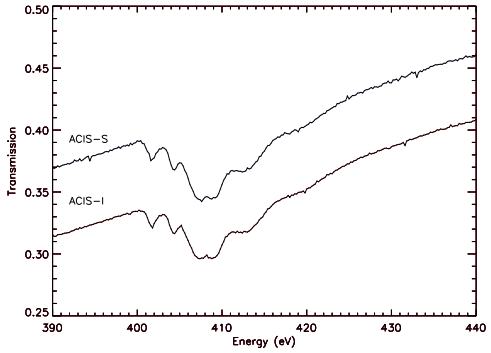

Figure 5.8: N-K XAFS .

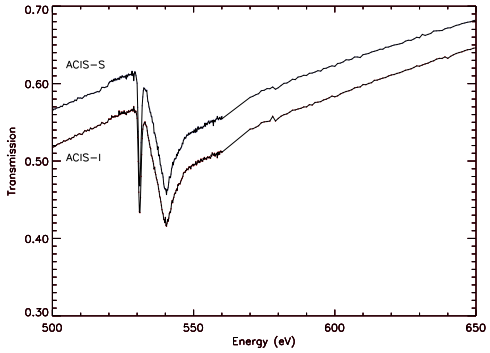

Figure 5.9: O-K XAFS .

high spectral purity.

The high flux levels obtainable ($\sim 1 \times 10^{12}$ photons/sec/0.1% BW) on this beamline were comparable to the levels obtained at NSLS. Additionally, the stability of the source beam, the high spectral purity and wavelength accuracy at the ALS allowed us to obtain high quality transmission data which clearly resolve the near and extended absorption fine structure of the Al-L, C-K, N-K and O-K absorption edges (see Figures 5.6 - 5.9).

As an indicator of the absolute accuracy of the transmission values a comparison of the ALS and NSLS transmission values away from absorption edges indicates differences of less than 1% of the measured value. Figure 5.10 shows the X-ray transmission function of the ACIS-I and S filters between 0.05 and 3 keV. Transmission values below 0.7 keV are from the ALS measurements, transmission values between 0.7 and 1.8 keV are from the NSLS measurements.

We have created a transmission function of the ACIS OBF's between the energies 0.05-10 keV as a composite of measurements and models. (Fig 5.10) In particular in the energy range between 0.05 - 0.7 keV we use the X-ray transmission values derived from the mea-

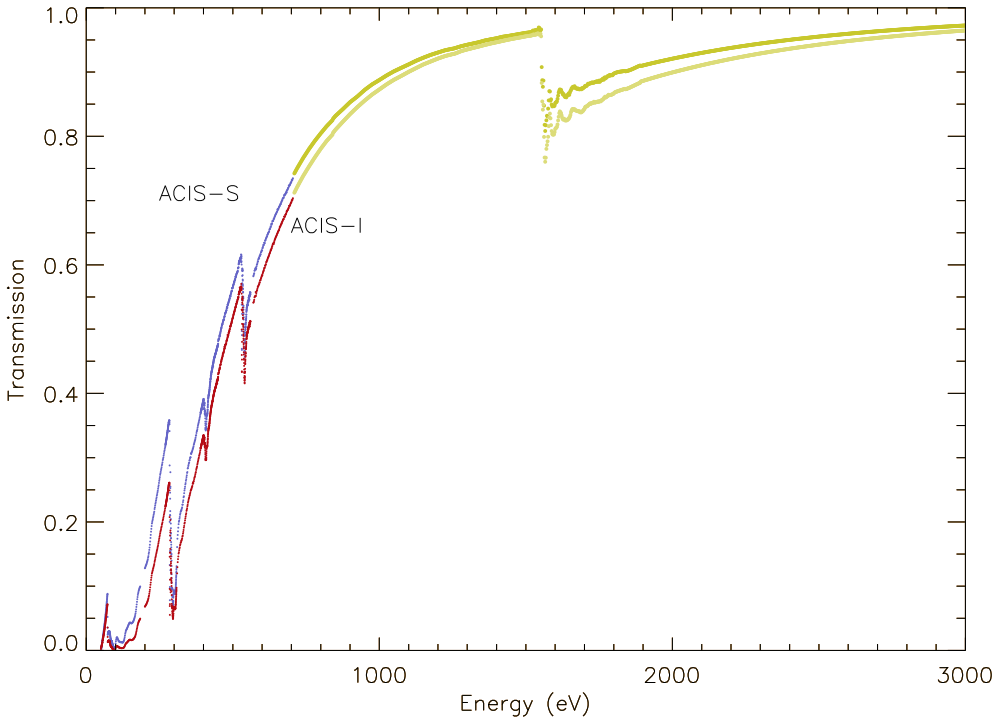

Figure 5.10: X-ray transmission of the ACIS filters in the 0.05-3keV band.

surements of the OBF's at the ALS at Berkeley Laboratories, in the energy range 0.7 - 1.8 keV we use the transmission values obtained at the NSLS at Brookhaven Laboratories and between 1.8 - 10 keV we have used a model that incorporates results from fits to the measured transmission data.

Witness Sample	Fitted Parameters for Smooth Component gr cm^{-2}	Fitted Parameters for ξ_{al}(E) Component	Fitted Parameters for ξ_c(E) Component
Imager, 6765-8	$\rho_{Polyimide} = 2.73400 \times 10^{-5}$ $\rho_{al} = 4.07111 \times 10^{-5}$ $\rho_{Al_2O_3} = 7.2 \times 10^{-7}$	$a_0 = 0.00391$ $a_1 = 8.58072$ $a_2 = 71.89980$ $a_3 = 3.48600$ $a_4 = 0.05499$ $a_5 = 400.001$ $a_6 = 0.39964$ $a_7 = 0.04000$ $a_8 = -0.07724$ $E_{0,1} = 1.556$ $E_{0,2} = 1.5775$ $E_{0,3} = 1.558$ $E_{0,4} = 1.89$ $E_{0,edge} = 1.56$	$a_0 = 0.00009895$ $a_1 = -39.49626$ $a_2 = 97.56914$ $a_3 = 3.02784$ $a_4 = 0.05998$ $a_5 = 150.00030$ $a_6 = 4.46030$ $a_7 = 0.199918$ $a_8 = -0.06410$ $E_{1,1} = 0.29$ $E_{1,2} = 0.3095$ $E_{1,3} = 0.3095$ $E_{1,4} = 0.3600$ $E_{1,edge} = 0.2842$
Spectrometer,6732-8	$\rho_{Polyimide} = 2.63186 \times 10^{-5}$ $\rho_{al} = 3.06826 \times 10^{-5}$ $\rho_{Al_2O_3} = 7.2 \times 10^{-7}$	$a_0 = 0.00263$ $a_1 = 5.00026$ $a_2 = 71.79978$ $a_3 = 3.49500$ $a_4 = 0.04000$ $a_5 = 400.00003$ $a_6 = 0.40503$ $a_7 = 0.03200$ $a_8 = -0.06001$ $E_{0,1} = 1.556$ $E_{0,2} = 1.5775$ $E_{0,3} = 1.5580$ $E_{0,4} = 1.89$ $E_{0,edge} = 1.56$	$a_0 = 0.00013$ $a_1 = -39.99043$ $a_2 = 97.99200$ $a_3 = 3.00020$ $a_4 = 0.08000$ $a_5 = 145.00028$ $a_6 = 0.88018$ $a_7 = 0.34000$ $a_8 = -0.11108$ $E_{1,1} = 0.29$ $E_{1,2} = 0.3098$ $E_{1,3} = 0.3098$ $E_{1,4} = 0.36$ $E_{1,edge} = 0.2842$

Table 5.2: Values for parameters of ACIS Imager and Spectrometer transmission function that enter equation (5.8)

5.1.5 Optical Characterization of the ACIS UV/Optical Blocking Filters.

5.1.5.1 Optical/UV Experimental Configuration

As a check on the optical transmission measurements made at PSU and to extend the filter transmission data into the UV, filter samples were taken to Denton Vacuum, Inc. in Moorestown, NJ. Leisa Townsley and Patrick Broos worked with Ian Stevenson there to measure the transmission on two samples: just polyimide (2015 Å) and polyimide + aluminum (Al/Polyimide/Al = 340Å/2020Å/357Å). Both samples were measured in the UV, optical, and NIR, from 200nm to 1500nm in steps of 2nm. The polyimide + aluminum sample used a thinner aluminum coating than the flight filters because the instrument used to measure the transmission was unable to detect transmission below about 10^{-6}, so no optical constants could be inferred from a flight-like sample (with transmission about 10^{-8}).

The instrument used to measure the transmission was a Perkin Elmer Lambda 900 UV/VIS/NIR Spectrometer and Reflectometry System. This is a double beam, double monochromator, ratio recording spectrometer controlled by a PC. It uses a photo-multiplier tube for the 200-800nm range and a lead sulfide detector for the 800-1500nm range. The system was calibrated by measuring the beam intensity with the empty filter holder in place (to reproduce the stray light conditions present for this geometry). Next, each filter was placed in the holder and the beam intensity measured. The entire cycle was repeated to assess system stability and measure detector noise.

5.1.5.2 Optical/UV Transmission of ACIS Filters

Measurements, at PSU and Denton Vacuum, of the optical transmission of a multilayer filter composed of Al/Polyimide/Al = 340Å/2020Å/357Å (values of multilayer thicknesses reported by LUXEL corporation) were used to constrain the optical constants for polyimide. To infer the real and imaginary parts of the refractive index from the transmission measurements we constructed a model transmission function with optical constants for polyimide parameterized as:

$$n(\lambda) = A + \frac{B}{(\lambda - C)^2} + \frac{D}{(\lambda - C)^4}$$

$$k(\lambda) = E + \frac{F}{(\lambda - G)^2} + \frac{H}{(\lambda - G)^4}$$

where n and k are the real and imaginary parts of the refractive index for polyimide.

The optical transmission of the ACIS multilayer filters was calculated using the matrix method described in Born and Wolf, 1997. By solving Maxwell's equations for the total electric and magnetic field with boundary conditions at the filter interfaces one finds that

the relation between the incident and exiting electromagnetic fields can be written in matrix notation as :

$$\begin{pmatrix} \mathrm{E}_I \\ \mathrm{H}_I \end{pmatrix} = [\mathrm{M}] \times \begin{pmatrix} \mathrm{E}_{II} \\ \mathrm{H}_{II} \end{pmatrix} \tag{5.9}$$

$$\mathrm{M} = \begin{vmatrix} \cos(k_0) & i\sin(k_0 h)/Y_1 \\ Y_1 i \sin(k_0) & \cos(k_0) \end{vmatrix} \tag{5.10}$$

where M is the characteristic matrix of the stratified medium.

A least squares fit of a model transmission function, incorporating the above parameterization of n and k, to the measured optical transmission data provided the optical constants for polyimide which were then used to predict the optical transmission performance of the flight filters. In Figure 5.11 we present a fit of our model transmission function to the polyimide data.

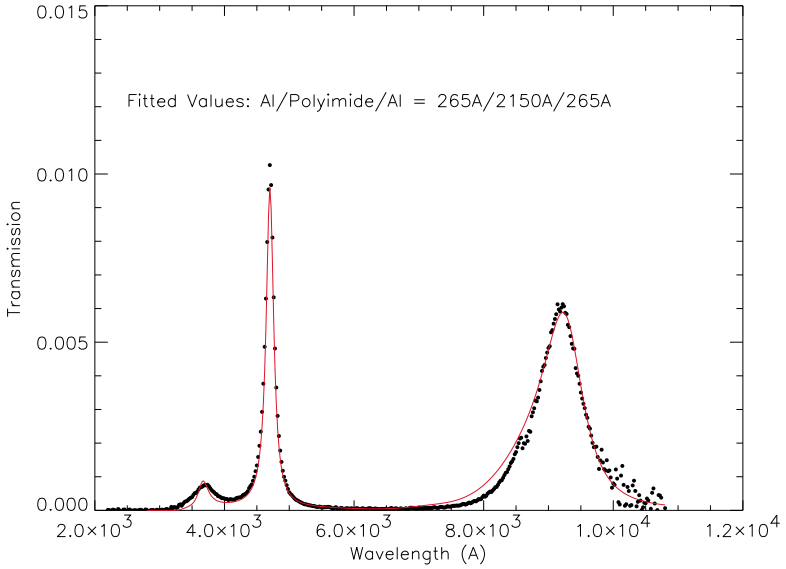

Figure 5.11: A fit of an optical transmission model to measured optical transmission of an aluminized polyimide sample.

Figure 5.12 shows the real part of the refractive index for polyimide resulting from the fit of our model to the optical transmission data for the polyimide sample.

We incorporated the derived optical constants of polyimide into a transmission model for the ACIS-I and ACIS-S flight multilayer filters. For the simulations of the ACIS I and S transmissions we assumed the following thicknesses:

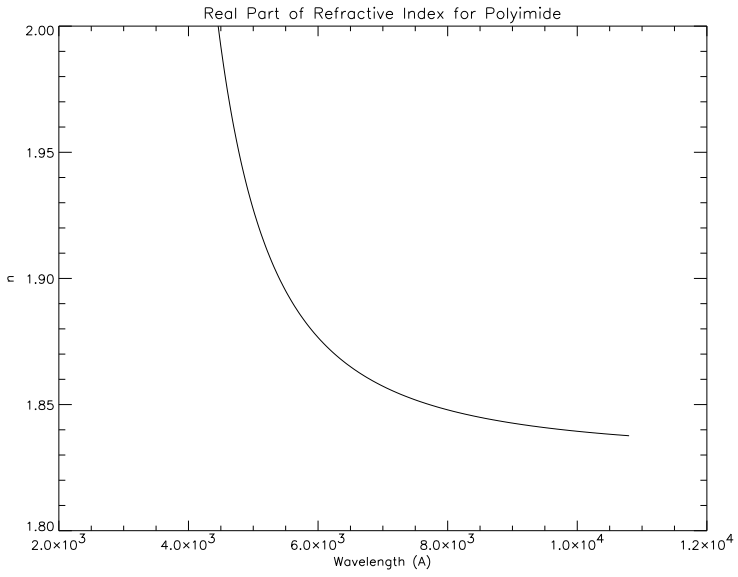

Figure 5.12: Real part of refractive index for polyimide.

ACIS-I : Al/Polyimide/Al = 1200Å/2000Å/400Å
ACIS-S : Al/Polyimide/Al = 1000Å/2000Å/300Å

Figure 5.13 and Figure 5.14 show the predicted optical transmission of the ACIS-I and ACIS-S OBF's respectively. Peaks appear in the transmittance, one at about 4500 Å and the other at about 8700 Å. The two peaks in the transmission curve shift toward smaller wavelengths as the incident photon angle is increased.

The amplitude of the transmission does not change significantly in the 3-7 degree range (the angle of incidence of rays at the HRMA focal point is expected to range from 3 to 7 degrees), however, for large incident angles ($>$ 60 degrees) the transmission at 8000 Å is expected to increase by about one order of magnitude (with respect to the normal incidence case). This effect may need to be considered, especially if a large scattered optical light component is present.

The diffuse transmission through the ACIS UV/Optical filters was calculated using the expression:

$$T_{diff}(\lambda) = \frac{\sum(w(\theta_{n-1},\theta_n) * T(\theta_{n-1},\theta_n,\lambda))}{\sum(w(\theta_{n-1},\theta_n))} \tag{5.11}$$

where $w(\theta_{n-1},\theta_n) = cos(\theta_{n-1}) - cos(\theta_n)$, is a weighting function that takes into account the differential solid angle that the filter 'sees' for incident photon angles between θ_n and θ_{n-1}.

$T(\theta_{n-1},\theta_n,\lambda)$ is the transmission for rays incident at an angle of θ_{n-1}. $T(\theta_{n-1},\theta_n,\lambda)$

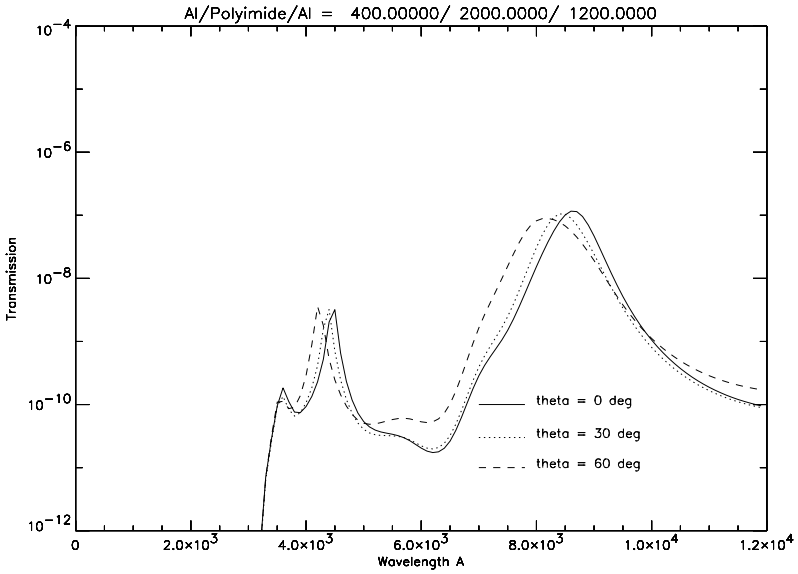

Figure 5.13: Predicted Optical Transmission for the ACIS I OBF for angles between photon direction and normal to CCD of 0, 30 and 60deg.

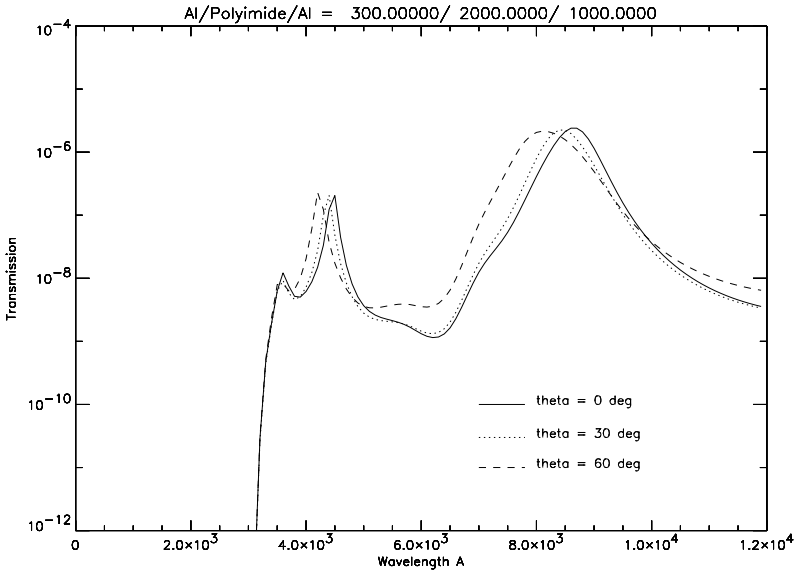

Figure 5.14: Predicted Optical Transmission for the ACIS S OBF for angles between photon direction and normal to CCD of 0, 30 and 60deg.

was calculated for incident angles of 0,1,2,...89 degrees. Figure 5.15 and Figure 5.16 show the predicted transmission including interference effects for diffuse light for the ACIS I and S OBF's respectively.

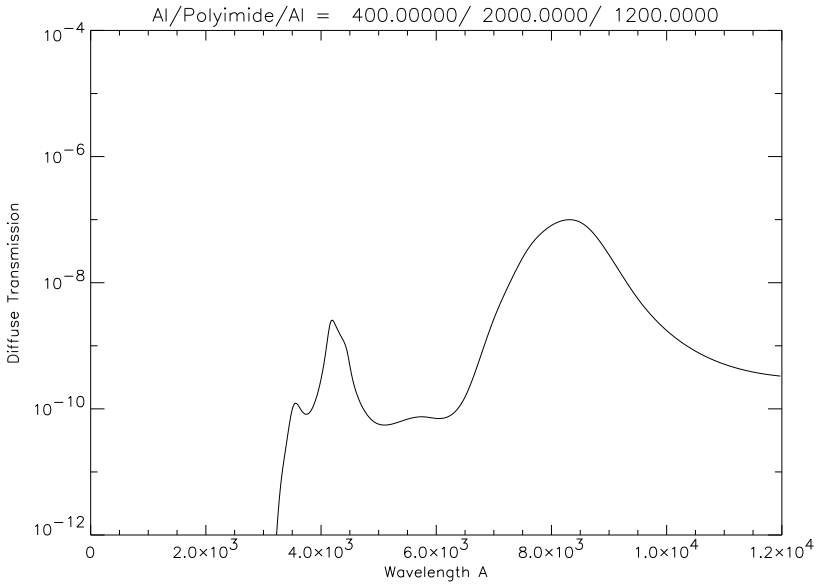

Figure 5.15: Predicted Optical transmission for the ACIS I OBF for diffuse illumination.

5.1.6 Temperature Dependence of Filter Properties

An issue that may be relevant to the accurate determination of the filter transmission on orbit is the temperature dependence of the amplitude of EXAFS. According to EXAFS theory the amplitude of the EXAFS oscillations are a function of temperature. This dependence arises from the fact that thermal vibrations of the atoms in a solid produce a phase mismatch of the backscattered electron wave function. The transmission properties of the ACIS filters were measured at room temperatures (∼20 C) while the on orbit filter temperature is expected to be about -60 C. The temperature dependence of the EXAFS component is incorporated in a Debye-Waller type term Q(k,T) (Stern et al., 1975). For thermally induced disorders of atoms and for deviations about the average shell distance of R_j which follow a Gaussian distribution, Q(k,T) is given by,

$$Q(k,T) = e^{-2k^2\sigma^2} \tag{5.12}$$

where σ is the mean square deviation about the average value R_j. For the Einstein model of lattice vibrations, where motions between adjacent atoms are uncorrelated σ^2 has the

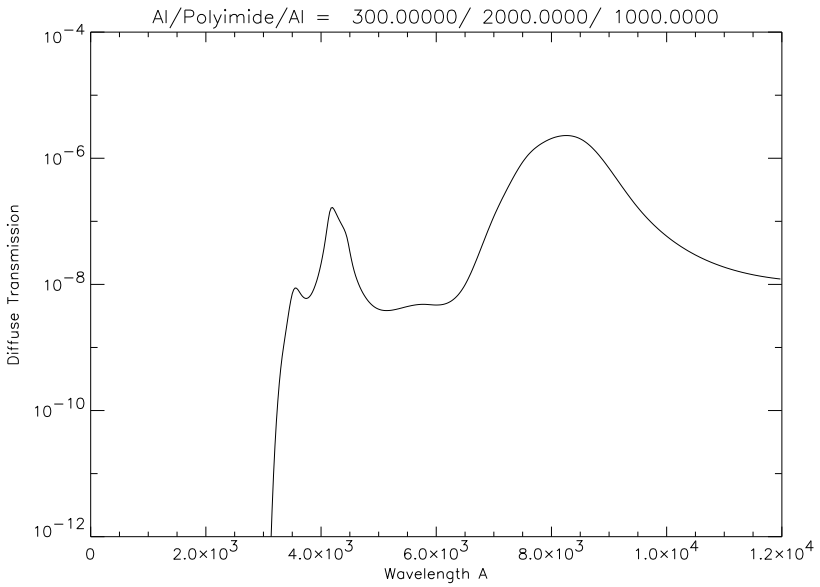

Figure 5.16: Predicted Optical transmission for the ACIS S OBF for diffuse illumination.

form:

$$\sigma^2 = \frac{\hbar}{M_r \omega} \frac{1}{e^{\frac{\hbar\omega}{kT}} - 1} \tag{5.13}$$

where M_r is the reduced mass and ω is the frequency of vibration of the atoms and is related to the Einstein temperature of the solid through the expression:

$$\omega = \frac{T_{ein} k}{\hbar} \tag{5.14}$$

To derive the temperature dependence of the filter transmission we assume that $\chi(k) = C(k)Q(k,T)$. If we define f_{sm} as the smooth component of the transmission function, and f_{tot} as the total transmission function, we obtain,

$$\frac{f_{tot}(T)}{f_{sm}(T)} \; = \; e^{-\rho(\mu-\mu_0)} \; = \; e^{-\rho\mu_0\chi(k)} \; = \; e^{-\rho\mu_0 C(k) Q(k,T)} \tag{5.15}$$

and solving for C(k) we have:

$$C(k) = -\frac{1}{\rho\mu_0} \frac{\ln\left(\frac{f_{tot}(T_{gr})}{f_{sm}}\right)}{Q(k,T_{gr})} \tag{5.16}$$

The on orbit transmission at temperature T_{orb} is expressed as a function of the transmission as measured on ground at temperature T_{gr} by the expression,

$$\frac{f_{tot}(T_{orb})}{f_{tot}(T_{gr})} = e^{-C(k)\rho\mu_0[Q(k,T_{orb}) - Q(k,T_{gr})]} \tag{5.17}$$

In Figure 5.17 we show the percent change in filter transmission above the Al-K absorption edge for an expected on orbit filter temperature of -60 C.

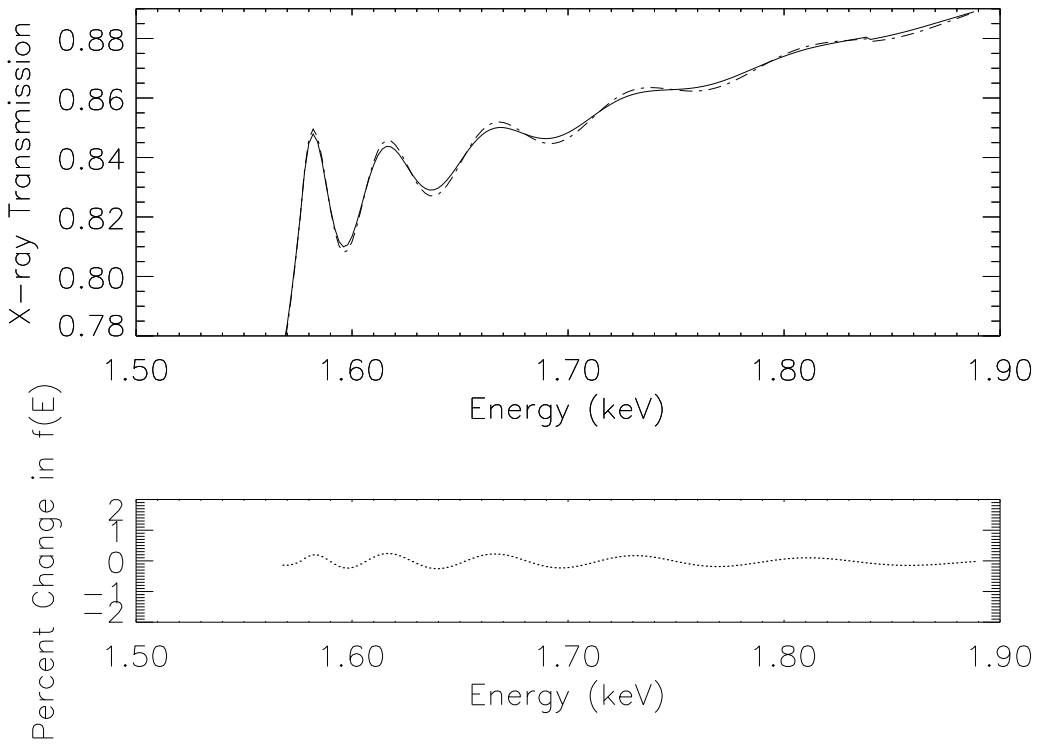

Figure 5.17: Top Panel; Filter transmission of Spectrometer filter above the Al-K absorption edge at 20 and -60 C. Lower Panel; Percent change in filter transmission between 20 and -60 C

5.1.7 Summary and Conclusions

The X-ray transmission of the ACIS-I and ACIS-S flight-like filters was measured at NSLS in the energy range between 0.26 and 3 keV. We have presented a means of constructing an X-ray transmission function for the ACIS Imager and Spectrometer filters that can be expressed as a function of atomic scattering factors and EXAFS effects. The transmission function follows the data to better than 0.5% in non-EXAFS regions and better than 1% in the C-K and Al-K EXAFS regions. For energies within several eV of the absorption edges, larger deviations of a few percent are observed. These can be explained as a combination of the limits in the resolving power of the monochromator used in our measurements, the uncertainties in the atomic scattering factors near absorption edges and to the presence of resonance lines and narrow near edge X-ray absorption structure within several eV of the absorption edges. A detailed investigation of the spatial uniformity of the ACIS filter performed by Townsley et al. 1996 show the ACIS filter X-ray transmission uniformity to be better than 2% over the entire filter area, down to spatial scales of $\sim$1 mm (see below). Finally as our future scientific goals for X-ray observations become even more demanding, subtle effects such as temperature dependence of EXAFS will need to be considered. We presented a simple model to describe the change in the X-ray transmission of a filter with temperature and estimated a change of less than 0.5% in the amplitude of the Al-K EXAFS for the ACIS filters for temperatures ranging from 20 C to -60 C.

5.2 Transmission Maps of the ACIS UV/Optical Blocking Filters

As mentioned above, ACIS uses polyimide/aluminum meshless films placed above the two CCD arrays to filter optical and ultraviolet light, so that the CCDs see only X-radiation. It is necessary to calibrate these filters by mapping their soft X-ray transmission on fine spatial scales, so that the filter response can be removed from the CCD data and a more accurate estimate of the true sky recovered. Different OBFs are used for each array, with the ACIS-S OBF having a thinner aluminum coating, since light falling on the spectroscopy array will often be dispersed by transmission gratings which can be placed in front of the ACIS-S array.

We measured engineering and flight versions of these filters and witness samples of the filter material at the University of Wisconsin Synchrotron Radiation Center (SRC) between June 1995 and January 1997. For all data, better than one percent accuracy in transmission as a function of energy was maintained over the entire filter area. The resulting transmission maps reveal spatial non-uniformities in the filters of about 0.5% to 2%. These transmission maps provide the finest spatial calibration ever achieved on such filters.

5.2.1 Measurements

Many ACIS OBFs manufactured by Luxel Corporation were calibrated at the SRC Multilayer Beamline. The technique was established and tested using Lexan-based engineering filters, then all flight-candidate Lexan filters were mapped. In the summer of 1996, we discovered that the Lexan-based filters suffered light leaks after acoustic testing, which led to the current polyimide-based filter design. We mapped the final suite of polyimide-based flight-candidate filters in December 1996. Several witness samples were mapped then and in January 1997, for use in other transmission tests.

The Multilayer Beamline is ideally suited for these measurements due to its ability to access several energies in the 200-2000 eV range and its built-in, computer-controlled x-z stage, which allows us to map the filters automatically with excellent spatial resolution. Complete transmission maps were obtained on all filters at 273 eV, 522 eV, and 775 eV, with a spatial resolution of 0.76mm x 0.76mm, roughly 32 ACIS pixels (15 arcseconds) square. Additionally, small swaths of the filters were mapped at 1330 eV and 1860 eV, in an attempt to measure the filter thicknesses by fitting transmission curves to points at many energies.

These energies were chosen because they spanned the wavelength range of interest, they bracketed absorption edges of important elements (carbon, oxygen, and aluminum), and because they were readily accessible with existing beamline hardware. The spatial resolution was chosen to match the planned aspect dither amplitude of the spacecraft and to yield a complete map of each filter in a reasonable time (6-8 hours). Coincidentally, this pixel size was well-matched to the size of the striations in the filters, oversampling them adequately. We searched the Lexan-based filters for variations on finer spatial scales (0.2mm x 0.4mm) but saw none. The pixel size we used is too coarse to reveal pinholes in the filters, which are usually only a few microns in size.

5.2.2 Transmission Maps

The reduced data consist of images (transmission maps) of the filters in 273 eV, 522 eV, and 775 eV light and estimates of the filter thicknesses for all pixels that were mapped at all five energies, based on fits to the transmissions at these energies. The 273 eV images usually show small (1–2%) gradients in the aluminum deposition across the filter. Subtle striations in the polyimide are visible at the 0.5–1% level in some filters (see the 522 and 775 eV images). The 522 eV images were obtained mainly to verify the results at 273 eV and 775 eV. They should show a combination of the properties evident at 273 eV and 775 eV, and indeed they always do. Since the filters are so thin, the features revealed by the transmission maps never correlate with macroscopic wrinkles or other visible features on the filters.

The transmission maps are presented in Figures 5.18 and 5.19. All maps are displayed in a range of $\pm 2\%$ of the median value in the map, around that median. See the figure

captions for specific comments about each filter. Imperfect data reduction is apparent in the transmission variations that show up as horizontal lines. These features are not real; they result because the data are acquired by scanning across the filter one row at a time. If the unattenuated intensity measured for that row is not exactly correct or if the beam intensity changes across a row in an unexpected manner, the calculated transmission reflects these errors and yields horizontal features.

To test the reproducibility of the data, a single row of pixels was scanned multiple times and the results compared pixel-wise. This was repeated for several isolated rows throughout the mapping at each energy. The transmission values for each pixel are usually reproducible to approximately 0.1%, based on a comparison of these scans. The dominant source of error in the system appears to be beam instability. Our pixel size is closely matched to the spatial extent of the synchrotron beam for our three lower energies, thus very slight beam motion produces measureable transmission fluctuations.

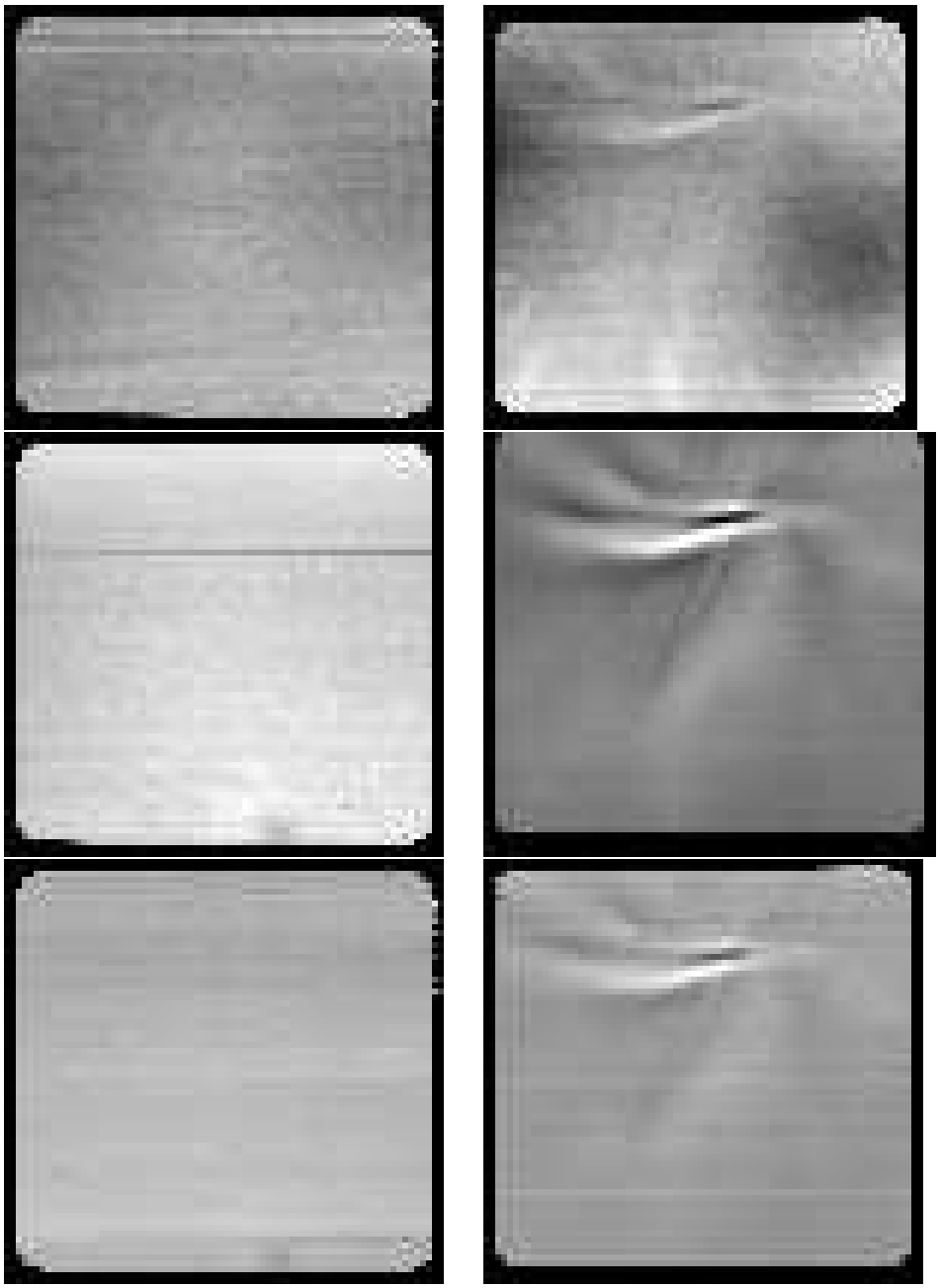

Figure 5.18: Imaging Array Filters 009 (left) and 019 (right). The top images show the filter transmission at 273 eV (Filter 009: $T \sim 24.8\%$; Filter 019: $T \sim 27.8\%$); the middle images are 522 eV maps (Filter 009: $T \sim 50.5\%$; Filter 019: $T \sim 53.1\%$); the bottom images are 775 eV maps (Filter 009: $T \sim 75.3\%$; Filter 019: $T \sim 77.1\%$). The left filter (009) was chosen as the imaging array flight unit. It is quite uniform at all energies mapped, implying that both the polyimide substrate and the aluminum coatings have uniform thickness and will contribute minimally to artifacts in ACIS images. The 273 eV map of filter 019 shows smooth but substantial variation in the aluminum thickness, although some "pinwheel" striations due to spinning out the polyimide are detectable in this image as well as in the higher-energy maps. These complex curved features correlate well row-to-row within a given image and between images, confirming that they are not artifacts of the data collection.

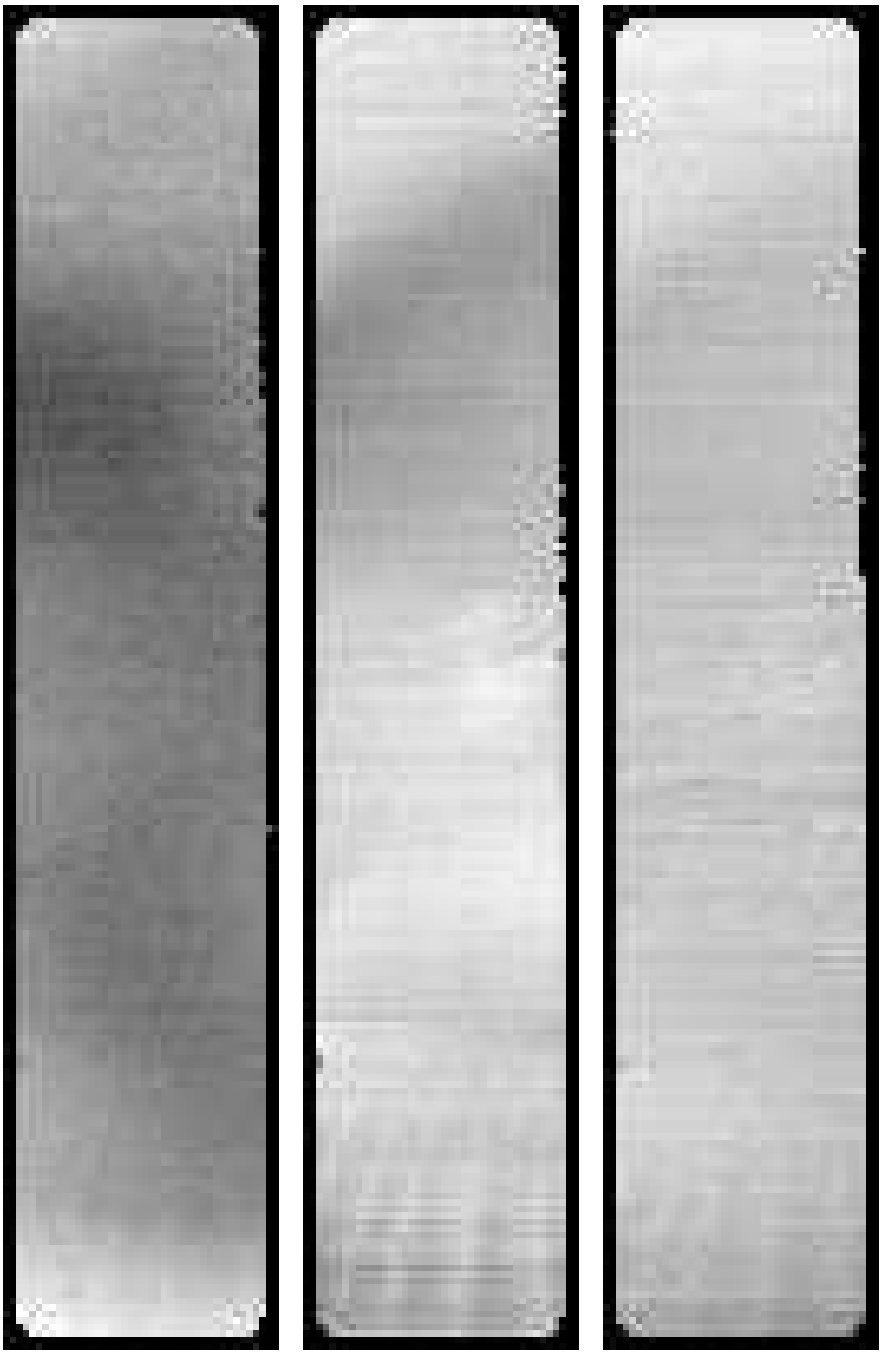

Figure 5.19: Spectroscopy Array Filter 003, with the 273 eV map ($T \sim 34.9\%$) at the left, the 522 eV map ($T \sim 56.5\%$) in the middle, and the 775 eV map ($T \sim 79.0\%$) at the right. The smooth transmission gradient at low energies is presumably due to slight nonuniformities in the aluminum coatings. The diverging striations visible in the 522 and 775 eV maps are from the polyimide substrate. This is the most uniform of the polyimide-based spectroscopy array filters.

5.2.3 Transmission Profiles

The ultimate goal of these calibrations is to obtain a transmission "spectrum" for each pixel, that is, an estimate of the filter transmission as a function of energy in the range 0.1-10 keV, the bandpass of the telescope. Below 0.1 keV the CCDs have virtually no response; the filter transmission goes to unity above 3 keV. Thus we present our estimates of the filter transmission profiles in this range. We performed non-linear least squares fits to the data using a model based on laboratory transmission data for common elements by Henke et al. (1993). The algorithm was supplied by George Chartas.

Example transmission profiles are given in Figure 5.20. The left panel shows the profile for one pixel in an imaging array filter; the right panel shows a similar single-pixel profile for a spectroscopy array filter. For all fits, we assumed that the filters were coated on each surface with 20 Å of aluminum oxide.

For all SRC data, the nominal energies are (in eV): [273, 522, 775, 1330, 1860] but the energies that yielded the best fit are a little different. This is not surprising, given that the beamline energy is set mechanically (not computer-controlled). The filters were measured one at a time, stepping through the energies. The energy repeatability is no better than (in eV, matching the energies given above): [10,10,3,10,10]. For imaging array filter 009, the best-fit energies are [283, 512, 778, 1320, 1850]. For spectroscopy array filter 003, the best-fit energies are [283, 512, 778, 1340, 1850].

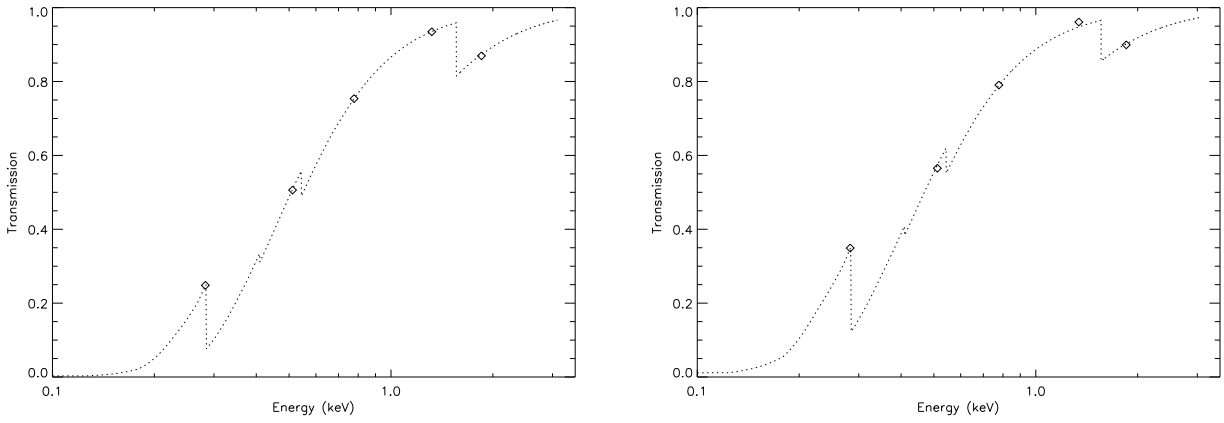

Figure 5.20: Example transmission profiles. An example fit to one pixel on an imaging array filter is shown on the left; a fit to one pixel on a spectroscopy array filter is on the right.

These fits yield an estimate of the areal density of the filter material at each pixel position. Given a volume density for the material, one can calculate the filter thickness. We calculated the polyimide and aluminum thicknesses in this way for an example pixel on each flight filter to compare our results to those provided by Luxel Corporation. Luxel

estimates the filter material thicknesses by a completely different technique.

Luxel measures the thickness of the polyimide film and the metallic coatings using a Tencor Profilometer which is calibrated at regular intervals. Several measurements are taken and averaged to arrive at the thickness measurement that is given on the Filter Certification.

The results are presented in Table 5.3. The volume densities assumed are 1.44 gm/cm^3 for polyimide and 2.5 gm/cm^3 for aluminum. As mentioned above, the Al_2O_3 thickness is fixed in the fit to be 20Å; its density is assumed to be 3.6 gm/cm^3. We also assumed that the silicon thickness was 1% of Luxel's value for the aluminum thickness, since it is doped at 1%. The assumed Si density is 2.32 gm/cm^3.

Table 5.3: A comparison of SRC and Luxel filter thickness estimates

Filter ID	SRC Polyimide Thickness (Å)	Luxel Polyimide Thickness (Å)	SRC Al Thickness (Å)	Luxel Al Thickness (Å)
spectroscopy 003	2084 ± 34	2000 ± 100	1262 ± 19	1330 ± 58
imaging 009	2357 ± 39	2055 ± 100	1696 ± 27	1660 ± 59

5.2.4 Summary

Using a synchrotron light source and a translation stage, we have mapped a suite of flight candidate UV/optical blocking filters for ACIS, in five energies and with high spatial resolution. The maps show the filters to be quite uniform, with deviations no larger than about 2%.

Based on these data and Luxel's specifications, the filters were ranked for their suitability for flight. The best imaging array filter (009) and spectroscopy array filter (003) are now installed in the ACIS flight focal plane. The other filters are maintained in a clean environment and will be reserved as backups for the flight filters and for future tests.

5.3 ACIS Sensitivity to Optical Light from Stars

The ACIS CCDs are extremely sensitive to optical frequencies. Further, the HRMA is capable of focusing incident optical photons as well as the X-ray photons. In order to use the CCD camera on AXAF to study X-ray emission from normal stars, which have X-ray to optical flux ratios ranging from 10^{-3} to 10^{-6}, the OBF must block the visible light with high efficiency while at the same time transmitting a high proportion of the X-ray flux. Most non-stellar objects that emit X-rays have a ratio of optical to X-ray flux that is close to unity, so optical light from these objects can easily be ignored if the OBF is satisfactory for stellar X-ray sources.

As the HRMA forms a good image in the optical band as well as the X-ray band, optical light from stars in the ACIS field of view will be well focused on the detector after attenuation by the aluminum in the OBF. The attenuation of the filter over ACIS-I is not uniform with wavelength, but averages about 10^{-8} (Figure 5.13). The filter over ACIS-S employs a thinner coating of aluminum, as the optical light will be diffracted far from the CCDs for most spectroscopic observations. The spectroscopic array can be used as an imager when the transmission gratings are not in place behind the mirrors. In this case the thinner aluminum places greater restrictions on the ratio of optical to X-ray signal (Figure 5.14).

5.3.1 Starlight Sensitivity Calculation

The sensitivity of ACIS to starlight is computed using realistic stellar atmosphere emission. The models of Kurucz (1991) have been used as the input spectrum for a range of temperatures. In all cases dwarf stellar gravity values have been assumed. The form of the computations is to integrate the radiation flux times the blocking filter transmission and the CCD optical detection efficiency over the full energy range and compare this to the same spectrum put through a standard V filter, for example, with a unit efficiency detector of one square centimeter. Putting this into an equation we have

$$OF = \int_0^\infty F_{star}(\lambda) \cdot T_{bf}(\lambda) \cdot QE_{CCD}(\lambda) \cdot A_{tel}(\lambda) d\lambda \tag{5.18}$$

where the OF refers to the optical flux, the quantity $\mathrm{F}_{star}(\lambda)$ is the flux computed using the Kurucz model spectrum for a star at temperature T, as a function of wavelength; $\mathrm{T}_{bf}(\lambda)$ is the transmission of the filter at wavelength λ; $\mathrm{QE}_{CCD}(\lambda)$ is the quantum detection efficiency for photons at wavelength λ, and $\mathrm{A}_{tel}(\lambda)$ is the area of the AXAF telescope for visible light at a wavelength λ. The telescope area was taken as the geometrical area, 1029 cm^2, times a function describing the fraction of the diffracted light that falls into one pixel with the telescope axis at the center of the pixel. This function was computed by the expressions found in Born and Wolfe . (See Appendix C for details.) The value of OF was then multiplied by 3.3 to include the exposure time.

The integral above was computed using standard numerical integration techniques. Although stellar atmosphere data exists for many more temperatures than computed here, the variation with temperature appears to be slowly varying, so that adding more points seems unnecessary.

The effect of optical contamination is to introduce photoelectrons which are unrelated to X-ray interactions. Thus if the X-ray frame bias is calculated without the star's optical light the X-ray photon energy will be miscalculated due to these additional electrons. If accurate X-ray photon energies are important to the analysis, then the observer should refrain from observing stars brighter than a certain limit. The results of the computation (assuming that one electron per pixel is the threshold for concern) are shown in Table 5.4. Observing with

shorter integration times (by using subframe readout or continuous clocking), or willingness to tolerate greater uncertainty in the X-ray energies will move the threshold toward brighter stars.

Stellar Temperature (K)	BI Chip in S-Array (V-magnitude)	FI Chip in I-Array (V-magnitude)
4000	5.76	2.07
5000	5.16	1.44
6500	4.76	1.00
10000	4.29	0.36
20000	4.18	0.16

Table 5.4: Stellar Magnitude required to produce one photoelectron per 3.3 second frame in the central pixel at the focus of AXAF for a range of stellar temperatures

Since many observations of bright stars will be performed with the objective gratings in place, the optical transmission of samples of the grating facets were measured as a function of wavelength. The results of these measurements are illustrated in Appendix C. The transmission curves were used in the integral above to compute the limiting magnitude with the grating in place. The HEG and MEG gratings were taken to cover 33% and 67% of the mirror area respectively, the MEG covering the outer two shells and the HEG covering the inner two shells. Table 5.5 gives the corresponding limit for optical contamination when the gratings are in place.

Stellar Temperature (K)	BI Chip in S-Array (V-magnitude)	FI Chip in I-Array (V-magnitude)
4000	2.13	-1.52
5000	1.49	-2.16
6500	1.04	-2.62
10000	0.41	-3.27
20000	0.21	-3.48

Table 5.5: Stellar Magnitude required to produce one photoelectron per 3.3 second frame in the central pixel at the focus of AXAF for a range of stellar temperatures with MEG/HEG grating in place

Table 5.4 shows that most observations proposed using ACIS will not suffer from optical light contamination, since the optical emission for most X-ray emitting objects are fainter than these limiting magnitudes. Only those observations in which bright stars fall within the ACIS array will a background signal be produced and only when the image is nearly on-axis. (The off-axis PSF grows rapidly, spreading the optical light over many more pixels, and hence reducing the number of optical photoelectrons per pixel.)

The optical photoelectron signal will behave differently from a signal induced by X-rays in that the photon level will build up linearly with time for stars brighter than the limiting ones in Table 5.4. X-rays, on the other hand will produce discrete packets of electrons in a pixel that either appear or are zero; they do not increase the charge in a pixel in a linear manner with accumulation time.[1]

Even if contamination is present, it can be removed just as a bias offset can be removed, but at the cost of an increase in the noise level in the detected electrons generated by the fluctuations in the light signal. For spectroscopic observations, the grating will attenuate the optical light by a factor of about thirty-three, or increase the magnitude limit by 3.8 magnitudes. Only the very brightest stars should be a problem when the gratings are in place.

[1]Unless the target is so bright in X-rays that pileup occurs. Even then the increase in number of electrons produced by X-ray photons occurs in such large packets that it is easy to distinguish from optical photon induced signal.

Chapter 6

ACIS/HRMA Performance Prediction

6.1 ACIS XRCF Measurement Plan

6.1.1 Introduction

The ACIS calibration plan was to perform ground-based measurements on the ACIS camera, HRMA mirrors and the combined HRMA-ACIS system so as to verify the models of the sub-assembly and assembled system performance. The critical part of that process was conducted at the Marshall Space Flight Center X-Ray Calibration Facility (XRCF), using a carefully constructed set of tests.

This is the entire ACIS XRCF Measurement Plan, including ACIS-2C data from Phase F and Phase G as well as ACIS flight camera data from Phase H. Each class of tests is mentioned, with a brief narrative description of the intent of the set of measurements. We also present tables summarized from the "as-requested" CMDB (Calibration Measurement DataBase) for each type of test; these tables represent our best current record of the data obtained at XRCF, grouped according to the calibration goal that they satisfy.

As we describe the types of tests we list the descriptions for each test according to the TRW ID, and supplementary descriptive entries from the CMDB. The columns for all tables are defined below. These definitions were taken from the CMDB Web page; please refer there for more complete definitions (http://asc.harvard.edu/cal/expander/expander.cgi).

- **TRW ID** – A string uniquely identifying an XRCF measurement.
- **source** – The source used to generate X-rays for this test.
- **energy** – The specific energy you wish to be using, in keV.
- **FP_Rate, Total_Cts** – The estimated rate of detected counts in the focal plane, per second; the total number of counts expected for the whole test.

- **Int_time** – The integration time for this test, in seconds.
- **mult** – Multiplicity, the number of distinct XRCF configurations sampled in this test (e.g. the number of monochromator settings for each DCM test).
- **pitch** – The angular rotation of the HRMA about the XRCF Z axis, with positive numbers increasing "down," in arcminutes.
- **yaw** – The angular rotation of the HRMA about the XRCF Y axis, with positive numbers increasing "left" (also known as "south"), in arcminutes.
- **yoff** – The linear offset of the FAM in the XRCF Y direction (+Y is "south"), in units of mm.
- **zoff** – The linear offset of the FAM in the XRCF Z direction (+Z is "up"), in units of mm.
- **Defocus** – The linear offset of the FAM in the XRCF X direction (+X is towards the X-ray source), in units of mm.
- **Focal** – Focal plane choice, the detector in the focal plane for this test.
- **HST** – The ACIS chip monitored by the high-speed tap.
- **frametime** – The approximate amount of time in each ACIS exposure (the integration time, between CCD readouts), in seconds.
- **proc_mode** – The mode of ACIS processing.
- **rows** – The number of rows in the ACIS readout window.
- **frames** – The number of ACIS data frames taken during the measurement integration.

6.1.2 Shutter Focus

Shutter Focus tests are designed to find rapidly the focal spot of the HRMA and to develop estimates of where to move the ACIS or ACIS-2C by FAM motions to find the prime focal spot and place it at the desired pixel location. This test is iterated, changing X until the minimum diameter 10% power level is found. Note: due to gravitational distortion effects on telescope blur the blur was deformed in Y and Z. The actual criterion was minimum image width in the Y (grating dispersion) direction.

TRW_ID	source	energy	FP_Rate,Total_Cts	Int_time	mult	pitch	yaw	yoff	zoff	Defocus	Focal	HST	frametime	proc_mode	rows	frames
F–I2C–SF–1.003	Al–Ka	1.486	164.7,20000	485.73	4	0	0	0	0	0	2C1	–	0.66	INTEG	114	21
F–I2C–SF–1.004	Al–Ka	1.486	191.62,20000	417.49	4	0	0	0	0	0	2C0	–	0.66	INTEG	114	18
F–I2C–SF–3.001	Al–Ka	1.486	260,15600	240	4	0	0	0	0	0	2C0	–	0.66	INTEG	114	11
F–I2C–SF–3.002	Al–Ka	1.486	260,15600	240	4	0	0	−8.04	−11.112	0	2C0	–	0.66	INTEG	114	11
F–I2C–SF–3.003	Al–Ka	1.486	260,15600	240	4	0	0	−8.04	11.088	0	2C0	–	0.66	INTEG	114	11
F–I2C–SF–3.004	Al–Ka	1.486	260,15600	240	4	0	0	14.16	11.088	0	2C0	–	0.66	INTEG	114	11
F–I2C–SF–3.005	Al–Ka	1.486	260,15600	240	4	0	0	14.16	−11.112	0	2C0	–	0.66	INTEG	114	11
F–I2C–SF–3.006	Al–Ka	1.486	223.47,13408.2	240	4	0	0	0	0	0	2C1	–	0.66	INTEG	114	11
F–I2C–SF–3.007	Al–Ka	1.486	223.47,13408.2	240	4	0	0	12	−4.8	0	2C1	–	0.66	INTEG	114	11
F–I2C–SF–3.008	Al–Ka	1.486	223.47,13408.2	240	4	0	0	12	15.53	0	2C1	–	0.66	INTEG	114	11
F–I2C–SF–3.009	Al–Ka	1.486	223.47,13408.2	240	4	0	0	−8.4	15.53	0	2C1	–	0.66	INTEG	114	11
F–I2C–SF–3.010	Al–Ka	1.486	223.47,13408.2	240	4	0	0	−8.4	−4.8	0	2C1	–	0.66	INTEG	114	11
H–IAS–SF–3.002	Al–Ka	1.486	9.9790,598.74	240	4	0	0	0	0	1	S3	S3	3.3	INTEG	1024	19
H–IAI–SF–2.001	DCM	2.5	9.0588,2500	1103.9	4	0	0	0	0	0	I3	I3	0.5	INTEG	100	552
H–IAS–SF–2.002	DCM	2.5	9.9194,2500	1008.13	4	0	0	0	0	0	S3	S3	3.3	INTEG	1024	77
G–I2C–SF–31.008	Mg–Ka	1.254	397.2818,10000	100.68	4	0	0	0	0	0	2C1	–	0.11	INTEG	18	5

Table 6.1: Shutter Focus Tests

6.1.3 Plate Focus

Plate Focus tests are designed to measure precisely the focus of the HRMA on the ACIS or ACIS-2C, and to relate the integration mode data to single photon counting data and to the in-flight focus data.

TRW_ID	source	energy	FP_Rate,Total_Cts	Int_time	mult	pitch	yaw	yoff	zoff	Defocus	Focal	HST	frametime	proc_mode	rows	frames
F–I2C–dF–2.003	Al–Ka	1.486	9.69,29070	3000	1	0	0	0	0	−0.25	2C1	–	0.113	PH_CNT	18	521
F–I2C–dF–2.004	Al–Ka	1.486	9.69,29070	3000	1	0	0	0	0	0	2C1	–	0.113	PH_CNT	18	521
F–I2C–dF–2.005A	Al–Ka	1.486	9.69,29070	3000	1	0	0	0	0	0.25	2C1	–	0.113	PH_CNT	18	521
F–I2C–dF–2.008	Al–Ka	1.486	9.42,28260	3000	1	0	0	0	0	−1	2C0	–	0.113	PH_CNT	18	521
F–I2C–dF–2.009	Al–Ka	1.486	9.42,28260	3000	1	0	0	0	0	−0.5	2C0	–	0.113	PH_CNT	18	521
F–I2C–dF–2.010	Al–Ka	1.486	9.42,28260	3000	1	0	0	0	0	−0.25	2C0	–	0.113	PH_CNT	18	521
F–I2C–dF–2.011	Al–Ka	1.486	9.42,28260	3000	1	0	0	0	0	0	2C0	–	0.113	PH_CNT	18	521
F–I2C–dF–2.012	Al–Ka	1.486	9.42,28260	3000	1	0	0	0	0	0.25	2C0	–	0.113	PH_CNT	18	521
F–I2C–dF–2.013	Al–Ka	1.486	9.42,28260	3000	1	0	0	0	0	0.5	2C0	–	0.113	PH_CNT	18	521
F–I2C–dF–2.014	Al–Ka	1.486	9.42,28260	3000	1	0	0	0	0	1	2C0	–	0.113	PH_CNT	18	521
F–I2C–dF–99.024	Al–Ka	1.486	9.69,29070	3000	1	0	0	0	0	−0.5	2C1	–	0.113	PH_CNT	18	521
F–I2C–dF–99.027	C–Ka	0.277	11.46,3000	261.77	1	0	0	0	0	0	2C0	–	0.113	PH_CNT	18	46
F–I2C–dF–99.028	C–Ka	0.277	11.46,3000	261.77	1	0	0	0	0	−1	2C0	–	0.113	PH_CNT	18	46
F–I2C–dF–99.029	C–Ka	0.277	11.46,3000	261.77	1	0	0	0	0	1	2C0	–	0.113	PH_CNT	18	46
F–I2C–dF–63.011	Cu–Ka	8.030	11.79,3000	254.45	1	0	0	0	0	0	2C0	–	0.113	PH_CNT	18	45
F–I2C–dF–63.012	Cu–Ka	8.030	11.79,3000	254.45	1	0	0	0	0	1	2C0	–	0.113	PH_CNT	18	45
F–I2C–dF–63.013	Cu–Ka	8.030	11.79,3000	254.45	1	0	0	0	0	−1	2C0	–	0.113	PH_CNT	18	45
F–I2C–dF–63.014	Cu–Ka	8.030	11.79,3000	254.45	1	0	0	0	0	−0.5	2C0	–	0.113	PH_CNT	18	45
F–I2C–dF–63.015	Cu–Ka	8.030	11.79,3000	254.45	1	0	0	0	0	0.5	2C0	–	0.113	PH_CNT	18	45
F–I2C–dF–64.011	Cu–Ka	8.030	11.86,3000	252.95	1	0	0	0	0	0	2C1	–	0.113	PH_CNT	18	44
F–I2C–dF–64.012	Cu–Ka	8.030	11.86,3000	252.95	1	0	0	0	0	1	2C1	–	0.113	PH_CNT	18	44
F–I2C–dF–64.012a	Cu–Ka	8.030	11.86,3000	252.95	1	0	0	0	0	1	2C1	–	0.113	PH_CNT	18	44
F–I2C–dF–64.013	Cu–Ka	8.030	11.86,3000	252.95	1	0	0	0	0	−1	2C1	–	0.113	PH_CNT	18	44
F–I2C–dF–64.014	Cu–Ka	8.030	11.86,3000	252.95	1	0	0	0	0	−0.5	2C1	–	0.113	PH_CNT	18	44
F–I2C–dF–64.015	Cu–Ka	8.030	11.86,3000	252.95	1	0	0	0	0	0.5	2C1	–	0.113	PH_CNT	18	44
F–I2C–dF–62.001	O–Ka	0.525	11.69,3000	256.63	1	0	0	0	0	0	2C0	–	0.113	PH_CNT	18	45
F–I2C–dF–62.002	O–Ka	0.525	11.69,3000	256.63	1	0	0	0	0	1	2C0	–	0.113	PH_CNT	18	45
F–I2C–dF–62.003	O–Ka	0.525	11.69,3000	256.63	1	0	0	0	0	−1	2C0	–	0.113	PH_CNT	18	45
F–I2C–dF–62.004	O–Ka	0.525	11.69,3000	256.63	1	0	0	0	0	−0.5	2C0	–	0.113	PH_CNT	18	45
F–I2C–dF–62.005	O–Ka	0.525	11.69,3000	256.63	1	0	0	0	0	0.5	2C0	–	0.113	PH_CNT	18	45
F–I2C–dF–63.001	O–Ka	0.5249	10.97,3000	273.47	1	0	0	0	0	0	2C0	–	0.113	PH_CNT	18	48
F–I2C–dF–63.002	O–Ka	0.5249	10.97,3000	273.47	1	0	0	0	0	1	2C0	–	0.113	PH_CNT	18	48
F–I2C–dF–63.003	O–Ka	0.5249	10.97,3000	273.47	1	0	0	0	0	−1	2C0	–	0.113	PH_CNT	18	48

continued on next page

continued from previous page

TRW_ID	source	energy	FP_Rate,Total_Cts	Int_time	mult	pitch	yaw	yoff	zoff	Defocus	Focal	HST	frametime	proc_mode	rows	frames
F–I2C–dF–63.004	O–Ka	0.5249	10.97,3000	273.47	1	0	0	0	0	−0.5	2C0	–	0.113	PH_CNT	18	48
F–I2C–dF–63.005	O–Ka	0.5249	10.97,3000	273.47	1	0	0	0	0	0.5	2C0	–	0.113	PH_CNT	18	48
F–I2C–dF–64.001	O–Ka	0.5249	11.8,3000	254.23	1	0	0	0	0	0	2C1	–	0.113	PH_CNT	18	45
F–I2C–dF–64.002	O–Ka	0.5249	11.8,3000	254.23	1	0	0	0	0	1	2C1	–	0.113	PH_CNT	18	45
F–I2C–dF–64.003	O–Ka	0.5249	11.8,3000	254.23	1	0	0	0	0	−1	2C1	–	0.113	PH_CNT	18	45
F–I2C–dF–64.004	O–Ka	0.5249	11.8,3000	254.23	1	0	0	0	0	−0.5	2C1	–	0.113	PH_CNT	18	45
F–I2C–dF–64.005	O–Ka	0.5249	11.8,3000	254.23	1	0	0	0	0	0.5	2C1	–	0.113	PH_CNT	18	45

Table 6.2: Plate Focus Tests

6.1.4 Point Spread Function

Point Spread Function (PSF) tests measure the core (PI) and wings (PW) of the PSF on-axis and at several off-axis positions, at the point of ideal focus determined by the Shutter focus/Plate focus measurements (X=0). Two types of data are collected: the core PSF is done in single photon mode in the core of the PSF; the wings PSF is done with higher fluxes, which produces photon mode in the wings but integration mode data in the core. Note that the shutter focus test data at X=0 are identical to the PSF core test for Al, so we do not repeat that test. Measurements are made at medium (Al K), high (Cu K), and low (O K) energy. We changed from the rehearsal energy of Fe to Cu because of the higher response above 6 keV of the HRMA versus the TMA. The Al K inner core test is deleted because the plate focus at X=0 provides the same data. C K is included for an ultra-low energy point for the BI chips. Tests were also made to estimate the PSF using the ACIS and ACIS-2C continuous readout mode.

Sub-pixel position measurements were also performed as part of the PSF test suite. We moved the PSF by sub-pixel amounts to sample the digitization error resulting from pixel size undersampling of the PSF and to test split X-ray event reconstruction models of sub-pixel interaction location. For FI chips, tests were performed at high (Cu K) and low (O K) energy to test for differing split event fractions. For BI chips, Cu K was also used as the high-energy test, but C K was chosen for the low-energy test for differing split event fractions.

TRW_ID	source	energy	FP_Rate,Total_Cts	Int_time	mult	pitch	yaw	yoff	zoff	Defocus	Focal	HST	frametime	proc_mode	rows	frames
F–I2C–PI–1.001	Al–Ka	1.486	283.59,28359	100	1	0	0	0	0	0	2C1	–	0.66	PH_CNT	114	17
F–I2C–PI–2.001	Al–Ka	1.486	296.95,29695	100	1	0	0	0	0	0	2C0	–	0.66	PH_CNT	114	17
F–I2C–PI–5.001	Al–Ka	1.486	98.88,148320	1500	1	0	0	0	0	90	2C1	–	6	PH_CNT	1024	251
H–IAI–PI–4_25.001	Al–Ka	1.486	19.5190,10000	512.32	1	0	0	0	0	0	I3	I3	0.0032	PH_CNT	1	156
H–IAI–PI–4_25.002	Al–Ka	1.486	19.5190,10000	512.32	1	0	0	0	0	0	I3	I3	0.0032	PH_CNT	1	156
H–IAI–PI–4_25.005	Al–Ka	1.486	94.8024,10000	105.48	1	0	0	0	0	0	I3	I3	0.0032	PH_CNT	1	32
H–IAI–PI–4_25.006	Al–Ka	1.486	94.8024,10000	105.48	1	0	0	0	0	0	I3	I3	0.0032	PH_CNT	1	32
H–IAI–PI–4_25.009	Al–Ka	1.486	393.3634,10000	25.42	1	0	0	0	0	0	I3	I3	0.0032	PH_CNT	1	8
H–IAI–PI–4_25.010	Al–Ka	1.486	393.3634,10000	25.42	1	0	0	0	0	0	I3	I3	0.0032	PH_CNT	1	8
H–IAI–PI–3.001	Al–Ka	1.486	4.8569,9713.8	2000	1	0	0	0	0	0	I3	I3	0.8	PH_CNT	100	2501
H–IAI–PI–3.003	Al–Ka	1.486	4.8362,9672.4	2000	1	−7.49	0	0	−21.576	0.023	I3	I3	0.8	PH_CNT	100	2501
H–IAI–PI–3.006	Al–Ka	1.486	187.3,93673	500	1	−7.49	0	0	−21.576	0.023	I3	I3	0.8	PH_CNT	100	626
H–IAS–PI–7.010	Al–Ka	1.486	4.6749,9349.8	2000	1	−3.7	1.6	−4.511	−10.751	0	S3	S3	0.5	PH_CNT	100	4001
H–IAS–PI–7.015	Al–Ka	1.486	186.1531,93076.6	500	1	−3.7	1.6	−4.511	−10.751	0	S3	S3	0.5	PH_CNT	100	1001
H–IAS–PI–7.011	Al–Ka	1.486	4.7921,9584.2	2000	1	−3.7	−5.9	16.992	−10.751	0	S3	S3	0.5	PH_CNT	100	4001

continued on next page

continued from previous page

TRW_ID	source	energy	FP_Rate,Total_Cts	Int_time	mult	pitch	yaw	yoff	zoff	Defocus	Focal	HST	frametime	proc_mode	rows	frames
H–IAS–PI–7.016	Al–Ka	1.486	175.6272,87813.6	500	1	–3.7	–5.9	16.992	–10.751	0	S3	S3	0.5	PH_CNT	100	1001
H–IAI–PI–7.002	Al–Ka	1.486	4.5,9000	2000	1	–7.5	–7.5	21.5	–21.576	0	I3	I3	0.5	PH_CNT	100	4001
H–IAI–PI–7.005	Al–Ka	1.486	194.4,97200	500	1	–7.5	–7.5	21.5	–21.576	0	I3	I3	0.5	PH_CNT	100	1001
H–IAS–PI–4_25.003	Al–Ka	1.486	19.0917,10000	523.78	1	0	0	0	0	0	S3	S3	0.0032	PH_CNT	1	159
H–IAS–PI–4_25.004	Al–Ka	1.486	19.0917,10000	523.78	1	0	0	0	0	0	S3	S3	0.0032	PH_CNT	1	159
H–IAS–PI–4_25.007	Al–Ka	1.486	92.7270,10000	107.84	1	0	0	0	0	0	S3	S3	0.0032	PH_CNT	1	33
H–IAS–PI–4_25.008	Al–Ka	1.486	92.7270,10000	107.84	1	0	0	0	0	0	S3	S3	0.0032	PH_CNT	1	33
H–IAS–PI–4_25.011	Al–Ka	1.486	384.7521,10000	25.99	1	0	0	0	0	0	S3	S3	0.0032	PH_CNT	1	8
H–IAS–PI–4_25.012	Al–Ka	1.486	384.7521,10000	25.99	1	0	0	0	0	0	S3	S3	0.0032	PH_CNT	1	8
H–IAS–PI–3.008	Al–Ka	1.486	4.6749,9349.8	2000	1	3.73	1.57	–4.511	10.751	0.006	S3	S3	0.8	PH_CNT	100	2501
H–IAS–PI–3.009	Al–Ka	1.486	4.7921,9584.2	2000	1	3.73	–5.89	16.992	10.752	0.02	S3	S3	0.8	PH_CNT	100	2501
H–IAS–PI–3.013	Al–Ka	1.486	186,93076.6	500	1	3.73	1.57	–4.511	10.751	0.006	S3	S3	0.8	PH_CNT	100	626
H–IAS–PI–3.014	Al–Ka	1.486	175,87813.6	500	1	3.73	–5.89	16.992	10.752	0.02	S3	S3	0.8	PH_CNT	100	626
F–I2C–PI–2.004	C–Ka	0.277	9.44,28320	3000	1	0	0	0	0	0	2C0	–	0.113	PH_CNT	18	521
F–I2C–PI–1.004	Cu–Ka	8.030	9.63,28890	3000	1	0	0	0	0	0	2C1	–	0.113	PH_CNT	18	521
F–I2C–PI–1.005	Cu–Ka	8.030	280.54,28054	100	1	0	0	0	0	0	2C1	–	0.66	PH_CNT	114	17
F–I2C–PI–1.008	Cu–Ka	8.030	280.54,28054	100	1	0	0	0	0	0	2C1	–	6	PH_CNT	1024	17
F–I2C–PI–2.002	Cu–Ka	8.030	9.84,29520	3000	1	0	0	0	0	0	2C0	–	0.113	PH_CNT	18	521
F–I2C–PI–2.003	Cu–Ka	8.030	286.77,28677	100	1	0	0	0	0	0	2C0	–	0.66	PH_CNT	114	17
F–I2C–PI–2.008	Cu–Ka	8.030	286.77,28677	100	1	0	0	0	0	0	2C0	–	6	PH_CNT	1024	17
F–I2C–PI–3.001	Cu–Ka	8.030	4.96,1488	300	1	0	0	–0.009	0	0	2C1	–	0.113	PH_CNT	18	53
F–I2C–PI–3.002	Cu–Ka	8.030	4.96,1488	300	1	0	0	–0.006	0	0	2C1	–	0.113	PH_CNT	18	53
F–I2C–PI–3.003	Cu–Ka	8.030	4.96,1488	300	1	0	0	–0.003	0	0	2C1	–	0.113	PH_CNT	18	53
F–I2C–PI–3.004	Cu–Ka	8.030	4.96,1488	300	1	0	0	0	0	0	2C1	–	0.113	PH_CNT	18	53
F–I2C–PI–3.005	Cu–Ka	8.030	4.96,1488	300	1	0	0	0.003	0	0	2C1	–	0.113	PH_CNT	18	53
F–I2C–PI–3.006	Cu–Ka	8.030	4.96,1488	300	1	0	0	0.006	0	0	2C1	–	0.113	PH_CNT	18	53
F–I2C–PI–3.007	Cu–Ka	8.030	4.96,1488	300	1	0	0	0.009	0	0	2C1	–	0.113	PH_CNT	18	53
F–I2C–PI–3.008	Cu–Ka	8.030	4.96,1488	300	1	0	0	0.012	0	0	2C1	–	0.113	PH_CNT	18	53
F–I2C–PI–3.009	Cu–Ka	8.030	4.96,1488	300	1	0	0	0	–0.015	0	2C1	–	0.113	PH_CNT	18	53
F–I2C–PI–3.010	Cu–Ka	8.030	4.96,1488	300	1	0	0	0	–0.01	0	2C1	–	0.113	PH_CNT	18	53
F–I2C–PI–3.011	Cu–Ka	8.030	4.96,1488	300	1	0	0	0	–0.005	0	2C1	–	0.113	PH_CNT	18	53
F–I2C–PI–3.012	Cu–Ka	8.030	4.96,1488	300	1	0	0	0	0	0	2C1	–	0.113	PH_CNT	18	53
F–I2C–PI–3.013	Cu–Ka	8.030	4.96,1488	300	1	0	0	0	0.005	0	2C1	–	0.113	PH_CNT	18	53
F–I2C–PI–3.014a	Cu–Ka	8.030	4.96,1488	300	1	0	0	0	0.01	0	2C1	–	0.113	PH_CNT	18	53
F–I2C–PI–4.001	Cu–Ka	8.030	3.33,999	300	1	0	0	–0.009	0	0	2C0	–	0.113	PH_CNT	18	53
F–I2C–PI–4.002	Cu–Ka	8.030	3.33,999	300	1	0	0	–0.006	0	0	2C0	–	0.113	PH_CNT	18	53
F–I2C–PI–4.003	Cu–Ka	8.030	3.33,999	300	1	0	0	–0.003	0	0	2C0	–	0.113	PH_CNT	18	53
F–I2C–PI–4.004	Cu–Ka	8.030	3.33,999	300	1	0	0	0	0	0	2C0	–	0.113	PH_CNT	18	53
F–I2C–PI–4.005	Cu–Ka	8.030	3.33,999	300	1	0	0	0.003	0	0	2C0	–	0.113	PH_CNT	18	53
F–I2C–PI–4.005	Cu–Ka	8.030	3.42,1026	300	1	0	0	0.003	0	0	2C0	–	0.113	PH_CNT	18	53
F–I2C–PI–4.006	Cu–Ka	8.030	3.42,1026	300	1	0	0	0.006	0	0	2C0	–	0.113	PH_CNT	18	53
F–I2C–PI–4.006	Cu–Ka	8.030	3.33,999	300	1	0	0	0.006	0	0	2C0	–	0.113	PH_CNT	18	53
F–I2C–PI–4.007	Cu–Ka	8.030	3.33,999	300	1	0	0	0.009	0	0	2C0	–	0.113	PH_CNT	18	53
F–I2C–PI–4.008	Cu–Ka	8.030	3.33,999	300	1	0	0	0.012	0	0	2C0	–	0.113	PH_CNT	18	53
F–I2C–PI–4.009	Cu–Ka	8.030	3.33,999	300	1	0	0	0	–0.015	0	2C0	–	0.113	PH_CNT	18	53
F–I2C–PI–4.010	Cu–Ka	8.030	3.33,999	300	1	0	0	0	–0.01	0	2C0	–	0.113	PH_CNT	18	53
F–I2C–PI–4.011	Cu–Ka	8.030	3.33,999	300	1	0	0	0	–0.005	0	2C0	–	0.113	PH_CNT	18	53
F–I2C–PI–4.012	Cu–Ka	8.030	3.33,999	300	1	0	0	0	0	0	2C0	–	0.113	PH_CNT	18	53
F–I2C–PI–4.013	Cu–Ka	8.030	3.33,999	300	1	0	0	0	0.005	0	2C0	–	0.113	PH_CNT	18	53
F–I2C–PI–4.014	Cu–Ka	8.030	3.33,999	300	1	0	0	0	0.01	0	2C0	–	0.113	PH_CNT	18	53
G–I2C–PI–1.001	Cu–Ka	8.030	4.9674,496.74	2800	28	0	0	0	0	0	2C1	–	0.113	PH_CNT	18	486
H–IAI–PI–12.001	Cu–Ka	8.030	5.4502,8720.32	1600	1	0	0	0	0	0	I3	I3	0.1	PH_CNT	38	485
H–IAS–PI–12.002	Cu–Ka	8.030	5.4626,8740.16	1600	1	0	0	0	0	0	S3	S3	0.1	PH_CNT	38	485
H–IAI–PI–2.001	DCM	3.5	2.9769,9526.08	3200	1	1.2	1.19	–3.439	3.457	0.001	I0	I0	0.8	PH_CNT	100	4001
H–IAI–PI–2.002	DCM	3.5	2.8335,9067.2	3200	1	8.68	8.67	–24.992	25.027	0.063	I0	I0	0.5	PH_CNT	100	6401
H–IAI–PI–2.003	DCM	3.5	2.5633,8202.56	3200	1	8.68	1.19	–3.438	25.033	0.032	I0	I0	0.8	PH_CNT	100	4001
H–IAI–PI–2.007	DCM	3.5	2.9810,9539.2	3200	1	1.2	0	0	3.459	0	I1	I1	0.8	PH_CNT	100	4001
H–IAI–PI–2.008	DCM	3.5	2.8996,9278.72	3200	1	8.68	–7.47	21.522	25.022	0.054	I1	I1	0.5	PH_CNT	100	6401
H–IAI–PI–2.009	DCM	3.5	2.6413,8452.16	3200	1	1.22	–7.47	21.533	3.53	0.024	I1	I1	0.5	PH_CNT	100	6401
H–IAI–PI–2.013	DCM	3.5	2.9811,9539.52	3200	1	0	1.19	–3.43	0	0	I2	I2	0.8	PH_CNT	100	4001
H–IAI–PI–2.014	DCM	3.5	2.8988,9276.16	3200	1	–7.49	8.68	–25.006	–21.585	0.055	I2	I2	0.5	PH_CNT	100	6401
H–IAI–PI–2.015	DCM	3.5	2.5696,8222.72	3200	1	–0.02	8.67	–24.991	–0.069	0.031	I2	I2	0.5	PH_CNT	100	6401
H–IAI–PI–2.019	DCM	3.5	2.9909,9570.88	3200	1	0	0	0	0	0	I3	I3	0.1	PH_CNT	38	970
H–IAI–PI–2.020	DCM	3.5	2.9706,9505.92	3200	1	–7.48	–7.47	21.522	–21.567	0.046	I3	I3	0.5	PH_CNT	100	6401
H–IAI–PI–2.021	DCM	3.5	2.6468,8469.76	3200	1	–7.49	0	0	–21.576	0.023	I3	I3	0.8	PH_CNT	100	4001
H–IAI–PI–2.022	DCM	5.2	2.8131,9001.92	3200	1	0	0	0	0	0	I3	I3	0.1	PH_CNT	38	970
H–IAI–PI–2.023	DCM	5.2	2.8172,9015.04	3200	1	–7.48	–7.47	21.522	–21.567	0.046	I3	I3	0.5	PH_CNT	100	6401

continued on next page

continued from previous page

TRW_ID	source	energy	FP_Rate,Total_Cts	Int_time	mult	pitch	yaw	yoff	zoff	Defocus	Focal	HST	frametime	proc_mode	rows	frames
H–IAI–PI–2.024	DCM	5.2	2.8815,9220.8	3200	1	−7.49	0	0	−21.576	0.023	I3	I3	0.8	PH_CNT	100	4001
H–IAI–PI–21.001	DCM	3.5	18.0892,9044.6	500	1	−12.95	23.92	−68.939	−37.322	0.31	I	S0	3.3	PH_CNT	1024	152
H–IAI–PI–21.002	DCM	3.5	19.7738,9886.9	500	1	−12.95	15.41	−44.407	−37.322	0.169	I	S1	3.3	PH_CNT	1024	152
H–IAI–PI–21.003	DCM	3.5	2.6402,2640.2	1000	1	−12.95	6.9	−19.876	−37.321	0.09	I	S2	3.3	PH_CNT	1024	304
H–IAI–PI–21.004	DCM	3.5	2.7709,2770.9	1000	1	−12.95	−1.61	4.645	−37.32	0.071	I	S3	3.3	PH_CNT	1024	304
H–IAI–PI–21.005	DCM	3.5	18.1784,9089.2	500	1	−12.95	−10.13	29.197	−37.322	0.113	I	S4	3.3	PH_CNT	1024	152
H–IAI–PI–21.006	DCM	3.5	19.9045,9952.25	500	1	−12.95	−18.64	53.718	−37.322	0.215	I	S5	3.3	PH_CNT	1024	152
H–IAS–PI–2.031	DCM	3.5	2.9441,9421.12	3200	1	−3.73	10.24	−29.517	−10.751	0.049	S2	S2	0.5	PH_CNT	100	6401
H–IAS–PI–2.032	DCM	3.5	2.9441,9421.12	3200	1	3.73	10.24	−29.517	10.751	0.049	S2	S2	0.8	PH_CNT	100	4001
H–IAS–PI–2.035	DCM	3.5	2.6830,8585.6	3200	1	3.73	1.57	−4.511	10.751	0.006	S3	S3	0.8	PH_CNT	100	4001
H–IAS–PI–2.036	DCM	3.5	2.5128,8040.96	3200	1	3.73	−5.89	16.992	10.752	0.02	S3	S3	0.8	PH_CNT	100	4001
H–IAS–PI–2.037	DCM	3.5	2.6830,8585.6	3200	1	−3.73	1.57	−4.511	−10.751	0.006	S3	S3	0.5	PH_CNT	100	6401
H–IAS–PI–2.038	DCM	3.5	2.5128,8040.96	3200	1	−3.73	−5.89	16.992	−10.752	0.02	S3	S3	0.5	PH_CNT	100	6401
H–IAS–PI–2.043	DCM	3.5	2.8044,8974.08	3200	1	0	0	0	0	0	S3	S3	0.1	PH_CNT	38	970
H–IAS–PI–2.044	DCM	5.2	2.7940,8940.8	3200	1	0	0	0	0	0	S3	S3	0.1	PH_CNT	38	970
F–I2C–PI–1.002	Fe–Ka	6.4	9.43,28290	3000	1	0	0	0	0	0	2C1	–	0.113	PH_CNT	18	521
F–I2C–PI–1.003	Fe–Ka	6.4	285.55,28555	100	1	0	0	0	0	0	2C1	–	0.66	PH_CNT	114	17
H–IAI–PI–1.005	Fe–Ka	6.4	5.8984,9437.44	1600	1	8.68	−7.47	21.522	25.022	0.054	I1	I1	0.5	PH_CNT	100	3201
H–IAI–PI–1.014	Fe–Ka	6.4	5.7031,9124.96	1600	1	−0.02	8.67	−24.991	−0.069	0.031	I2	I2	0.5	PH_CNT	100	3201
H–IAI–PI–1.021	Fe–Ka	6.4	5.7607,9217.12	1600	1	0	0	0	0	0	I3	I3	0.1	PH_CNT	38	485
H–IAS–PI–1.029	Fe–Ka	6.4	5.4902,8784.32	1600	1	−3.73	10.24	−29.517	−10.751	0.049	S2	S2	0.5	PH_CNT	100	3201
H–IAS–PI–1.041	Fe–Ka	6.4	5.7342,9174.72	1600	1	0	0	0	0	0	S3	S3	0.1	PH_CNT	38	485
H–IAI–PI–1.023	Fe–La	0.705	5.7773,9243.68	1600	1	0	0	0	0	0	I3	I3	0.1	PH_CNT	38	485
H–IAS–PI–1.042	Fe–La	0.705	5.5768,8922.88	1600	1	0	0	0	0	0	S3	S3	0.1	PH_CNT	38	485
G–I2C–PI–1.002	Mg–Ka	1.254	4.7774,477.74	2800	28	0	0	0	0	0	2C1	–	0.113	PH_CNT	18	486
F–I2C–PI–1.006	O–Ka	0.5249	9.64,28920	3000	1	0	0	0	0	0	2C1	–	0.113	PH_CNT	18	521
F–I2C–PI–1.007	O–Ka	0.5249	298.3,29830	100	1	0	0	0	0.144	0	2C1	–	0.66	PH_CNT	114	17
F–I2C–PI–2.006	O–Ka	0.5249	9.86,29580	3000	1	0	0	0	0	0	2C0	–	0.113	PH_CNT	18	521
F–I2C–PI–2.007	O–Ka	0.5249	281.32,28132	100	1	0	0	0	0	0	2C0	–	0.66	PH_CNT	114	17
F–I2C–PI–3.015	O–Ka	0.5249	3.33,999	300	1	0	0	−0.009	0	0	2C1	–	0.113	PH_CNT	18	53
F–I2C–PI–3.016	O–Ka	0.5249	3.33,999	300	1	0	0	−0.006	0	0	2C1	–	0.113	PH_CNT	18	53
F–I2C–PI–3.017	O–Ka	0.5249	3.33,999	300	1	0	0	−0.003	0	0	2C1	–	0.113	PH_CNT	18	53
F–I2C–PI–3.018	O–Ka	0.5249	3.33,999	300	1	0	0	0	0	0	2C1	–	0.113	PH_CNT	18	53
F–I2C–PI–3.019	O–Ka	0.5249	3.33,999	300	1	0	0	0.003	0	0	2C1	–	0.113	PH_CNT	18	53
F–I2C–PI–3.020	O–Ka	0.5249	3.33,999	300	1	0	0	0.006	0	0	2C1	–	0.113	PH_CNT	18	53
F–I2C–PI–3.021	O–Ka	0.5249	3.33,999	300	1	0	0	0.009	0	0	2C1	–	0.113	PH_CNT	18	53
F–I2C–PI–3.022	O–Ka	0.5249	3.33,999	300	1	0	0	0.012	0	0	2C1	–	0.113	PH_CNT	18	53
F–I2C–PI–3.023	O–Ka	0.5249	3.33,999	300	1	0	0	0	−0.015	0	2C1	–	0.113	PH_CNT	18	53
F–I2C–PI–3.024	O–Ka	0.5249	3.33,999	300	1	0	0	0	−0.01	0	2C1	–	0.113	PH_CNT	18	53
F–I2C–PI–3.025	O–Ka	0.5249	3.33,999	300	1	0	0	0	−0.005	0	2C1	–	0.113	PH_CNT	18	53
F–I2C–PI–3.026	O–Ka	0.5249	3.33,999	300	1	0	0	0	0	0	2C1	–	0.113	PH_CNT	18	53
F–I2C–PI–3.027	O–Ka	0.5249	3.33,999	300	1	0	0	0	0.005	0	2C1	–	0.113	PH_CNT	18	53
F–I2C–PI–3.028	O–Ka	0.5249	3.33,999	300	1	0	0	0	0.01	0	2C1	–	0.113	PH_CNT	18	53
F–I2C–PI–4.015	O–Ka	0.5249	3.28,984	300	1	0	0	−0.009	0	0	2C0	–	0.113	PH_CNT	18	53
F–I2C–PI–4.016	O–Ka	0.5249	3.28,984	300	1	0	0	−0.006	0	0	2C0	–	0.113	PH_CNT	18	53
F–I2C–PI–4.017	O–Ka	0.5249	3.28,984	300	1	0	0	−0.003	0	0	2C0	–	0.113	PH_CNT	18	53
F–I2C–PI–4.018	O–Ka	0.5249	3.28,984	300	1	0	0	0	0	0	2C0	–	0.113	PH_CNT	18	53
F–I2C–PI–4.019	O–Ka	0.5249	3.28,984	300	1	0	0	0.003	0	0	2C0	–	0.113	PH_CNT	18	53
F–I2C–PI–4.020	O–Ka	0.5249	3.28,984	300	1	0	0	0.006	0	0	2C0	–	0.113	PH_CNT	18	53
F–I2C–PI–4.021	O–Ka	0.5249	3.28,984	300	1	0	0	0.009	0	0	2C0	–	0.113	PH_CNT	18	53
F–I2C–PI–4.022	O–Ka	0.5249	3.28,984	300	1	0	0	0.012	0	0	2C0	–	0.113	PH_CNT	18	53
F–I2C–PI–4.023	O–Ka	0.5249	3.28,984	300	1	0	0	0	−0.015	0	2C0	–	0.113	PH_CNT	18	53
F–I2C–PI–4.024	O–Ka	0.5249	3.28,984	300	1	0	0	0	−0.01	0	2C0	–	0.113	PH_CNT	18	53
F–I2C–PI–4.025	O–Ka	0.5249	3.28,984	300	1	0	0	0	−0.005	0	2C0	–	0.113	PH_CNT	18	53
F–I2C–PI–4.026	O–Ka	0.5249	3.28,984	300	1	0	0	0	0	0	2C0	–	0.113	PH_CNT	18	53
F–I2C–PI–4.027	O–Ka	0.5249	3.28,984	300	1	0	0	0	0.005	0	2C0	–	0.113	PH_CNT	18	53
F–I2C–PI–4.028	O–Ka	0.5249	3.28,984	300	1	0	0	0	0.01	0	2C0	–	0.113	PH_CNT	18	53
F–I2C–PW–13.001	Al–Ka	1.486	9.14,27420	3000	1	−2	0	−0.96	0	0.00174	2C1	–	0.113	PH_CNT	18	521
F–I2C–PW–13.001a	Al–Ka	1.486	9.14,27420	3000	1	−2	0	−0.96	0	0.00174	2C1	–	0.113	PH_CNT	18	521
F–I2C–PW–13.002	Al–Ka	1.486	9.8,29400	3000	1	−4	0	−0.96	0	0.007	2C1	–	0.113	PH_CNT	18	521
F–I2C–PW–13.003	Al–Ka	1.486	9.43,28290	3000	1	−6	0	−0.96	0	0.0156	2C1	–	0.113	PH_CNT	18	521
F–I2C–PW–13.004	Al–Ka	1.486	9.61,28830	3000	1	−10	0	−0.96	0	5.6	2C1	–	0.23	PH_CNT	38	522
F–I2C–PW–13.005	Al–Ka	1.486	9.44,28320	3000	1	−15	0	−0.96	0	12.1	2C1	–	0.66	PH_CNT	114	506
F–I2C–PW–13.006	Al–Ka	1.486	9.11,27330	3000	1	−20	0	−0.96	0	20.7	2C1	–	6	PH_CNT	1024	501

continued on next page

continued from previous page

TRW_ID	source	energy	FP_Rate,Total_Cts	Int_time	mult	pitch	yaw	yoff	zoff	Defocus	Focal	HST	frametime	proc_mode	rows	frames
F–I2C–PW–13.007	Al–Ka	1.486	280.8,28080	100	1	–2	0	–0.96	0	0.00174	2C1	–	0.66	PH_CNT	114	17
F–I2C–PW–13.008	Al–Ka	1.486	298.13,29813	100	1	–4	0	–0.96	0	0.007	2C1	–	0.66	PH_CNT	114	17
F–I2C–PW–13.009	Al–Ka	1.486	289.73,28973	100	1	–6	0	–0.96	0	0.0156	2C1	–	0.66	PH_CNT	114	17
F–I2C–PW–13.010	Al–Ka	1.486	295.31,29531	100	1	–10	0	–0.96	0	0.0434	2C1	–	0.66	PH_CNT	114	17
F–I2C–PW–13.011	Al–Ka	1.486	290.03,29003	100	1	–15	0	–0.96	0	0.0977	2C1	–	0.66	PH_CNT	114	17
F–I2C–PW–13.012	Al–Ka	1.486	298.78,29878	100	1	–20	0	–0.96	0	0.1736	2C1	–	0.66	PH_CNT	114	17
F–I2C–PW–13.025	Cu–Ka	8.030	9.38,28140	3000	1	–2	0	–0.96	0	0.5	2C1	–	0.113	PH_CNT	18	521
F–I2C–PW–13.026	Cu–Ka	8.030	9.53,28590	3000	1	–4	0	–0.96	0	1	2C1	–	0.113	PH_CNT	18	521
F–I2C–PW–13.027	Cu–Ka	8.030	9.46,28380	3000	1	–6	0	–0.96	0	2.2	2C1	–	0.113	PH_CNT	18	521
F–I2C–PW–13.028	Cu–Ka	8.030	9.46,28380	3000	1	–10	0	–0.96	0	5.6	2C1	–	0.23	PH_CNT	38	522
F–I2C–PW–13.029	Cu–Ka	8.030	8.51,25530	3000	1	–15	0	–0.96	0	12.1	2C1	–	0.66	PH_CNT	114	506
F–I2C–PW–13.030	Cu–Ka	8.030	9.66,28980	3000	1	–20	0	–0.96	0	20.7	2C1	–	6	PH_CNT	1024	501
F–I2C–PW–13.031	Cu–Ka	8.030	297.73,29773	100	1	–2	0	–0.96	0	0.5	2C1	–	0.66	PH_CNT	114	17
F–I2C–PW–13.032	Cu–Ka	8.030	299.53,29953	100	1	–4	0	–0.96	0	1	2C1	–	0.66	PH_CNT	114	17
F–I2C–PW–13.033	Cu–Ka	8.030	297.14,29714	100	1	–6	0	–0.96	0	2.2	2C1	–	0.66	PH_CNT	114	17
F–I2C–PW–13.034	Cu–Ka	8.030	297.13,29713	100	1	–10	0	–0.96	0	5.6	2C1	–	0.66	PH_CNT	114	17
F–I2C–PW–13.035	Cu–Ka	8.030	297.06,29706	100	1	–15	0	–0.96	0	12.1	2C1	–	0.66	PH_CNT	114	17
F–I2C–PW–13.036	Cu–Ka	8.030	298.28,29828	100	1	–20	0	–0.96	0	20.7	2C1	–	6	PH_CNT	1024	17
H–IAI–PW–12.003	Cu–Ka	8.030	181.2993,108780	600	1	0	0	0	0	0	I3	I3	0.1	PH_CNT	38	182
H–IAS–PW–12.004	Cu–Ka	8.030	181.7113,109027	600	1	0	0	0	0	0	S3	S3	0.1	PH_CNT	38	182
H–IAI–PW–2.004	DCM	3.5	175.3786,87689.3	500	1	1.2	1.19	–3.439	3.457	0.001	I0	I0	0.8	PH_CNT	100	626
H–IAI–PW–2.005	DCM	3.5	137.4065,68703.2	500	1	8.68	8.67	–24.992	25.027	0.063	I0	I0	0.5	PH_CNT	100	1001
H–IAI–PW–2.006	DCM	3.5	151.0153,75507.6	500	1	8.68	1.19	–3.438	25.033	0.032	I0	I0	0.8	PH_CNT	100	626
H–IAI–PW–2.010	DCM	3.5	175.6191,87809.6	500	1	1.2	0	0	3.459	0	I1	I1	0.8	PH_CNT	100	626
H–IAI–PW–2.011	DCM	3.5	140.6113,70305.6	500	1	8.68	–7.47	21.522	25.022	0.054	I1	I1	0.5	PH_CNT	100	1001
H–IAI–PW–2.012	DCM	3.5	155.6065,77803.2	500	1	1.22	–7.47	21.533	3.53	0.024	I1	I1	0.5	PH_CNT	100	1001
H–IAI–PW–2.016	DCM	3.5	175.6240,87812	500	1	0	1.19	–3.43	0	0	I2	I2	0.8	PH_CNT	100	626
H–IAI–PW–2.017	DCM	3.5	140.5722,70286.1	500	1	–7.49	8.68	–25.006	–21.585	0.055	I2	I2	0.5	PH_CNT	100	1001
H–IAI–PW–2.018	DCM	3.5	151.3838,75691.9	500	1	–0.02	8.67	–24.991	–0.069	0.031	I2	I2	0.5	PH_CNT	100	1001
H–IAI–PW–2.025	DCM	3.5	176.2056,88102.8	500	1	0	0	0	0	0	I3	I3	0.1	PH_CNT	38	152
H–IAI–PW–2.026	DCM	3.5	144.0505,72025.2	500	1	–7.48	–7.47	21.522	–21.567	0.046	I3	I3	0.5	PH_CNT	100	1001
H–IAI–PW–2.027	DCM	3.5	155.9328,77966.4	500	1	–7.49	0	0	–21.576	0.023	I3	I3	0.8	PH_CNT	100	626
H–IAI–PW–2.028	DCM	5.2	270.1269,135063	500	1	0	0	0	0	0	I3	I3	0.1	PH_CNT	38	152
H–IAI–PW–2.029	DCM	5.2	219.1243,109562	500	1	–7.48	–7.47	21.522	–21.567	0.046	I3	I3	0.5	PH_CNT	100	1001
H–IAI–PW–2.030	DCM	5.2	249.0239,124512	500	1	–7.49	0	0	–21.576	0.023	I3	I3	0.8	PH_CNT	100	626
H–IAS–PW–2.033	DCM	3.5	142.7686,71384.3	500	1	–3.73	10.24	–29.517	–10.751	0.049	S2	S2	0.5	PH_CNT	100	1001
H–IAS–PW–2.034	DCM	3.5	142.7686,71384.3	500	1	3.73	10.24	–29.517	10.751	0.049	S2	S2	0.8	PH_CNT	100	626
H–IAS–PW–2.039	DCM	3.5	158.0632,79031.6	500	1	3.73	1.57	–4.511	10.751	0.006	S3	S3	0.8	PH_CNT	100	626
H–IAS–PW–2.040	DCM	3.5	148.03089,74019.5	500	1	3.73	–5.89	16.992	10.752	0.02	S3	S3	0.8	PH_CNT	100	626
H–IAS–PW–2.041	DCM	3.5	158.0632,79031.6	500	1	–3.73	1.57	–4.511	–10.751	0.006	S3	S3	0.5	PH_CNT	100	1001
H–IAS–PW–2.042	DCM	3.5	148.03089,74019.5	500	1	–3.73	–5.89	16.992	–10.752	0.02	S3	S3	0.5	PH_CNT	100	1001
H–IAS–PW–2.045	DCM	3.5	165.2153,82607.7	500	1	0	0	0	0	0	S3	S3	0.1	PH_CNT	38	152
H–IAS–PW–2.046	DCM	5.2	268.2930,134146	500	1	0	0	0	0	0	S3	S3	0.1	PH_CNT	38	152
H–IAI–PW–1.009	Fe–Ka	6.4	199.1651,99582.6	500	1	8.68	–7.47	21.522	25.022	0.054	I1	I1	0.5	PH_CNT	100	1001
H–IAI–PW–1.018	Fe–Ka	6.4	192.5703,96285.2	500	1	–0.02	8.67	–24.991	–0.069	0.031	I2	I2	0.5	PH_CNT	100	1001
H–IAI–PW–1.025	Fe–Ka	6.4	141.3478,70673.9	500	1	0	0	0	0	0	I3	I3	0.1	PH_CNT	38	152
H–IAS–PW–1.031	Fe–Ka	6.4	185.3794,92689.7	500	1	–3.73	10.24	–29.517	–10.751	0.049	S2	S2	0.5	PH_CNT	100	1001
H–IAS–PW–1.043	Fe–Ka	6.4	185.2342,92617.1	500	1	0	0	0	0	0	S3	S3	0.1	PH_CNT	38	152
H–IAI–PW–1.027	Fe–La	0.705	193.9209,96960.4	500	1	0	0	0	0	0	I3	I3	0.1	PH_CNT	38	152
H–IAS–PW–1.044	Fe–La	0.705	192.4921,96246.1	500	1	0	0	0	0	0	S3	S3	0.1	PH_CNT	38	152
F–I2C–PW–13.013	O–Ka	0.5249	9.59,28770	3000	1	–2	0	–0.96	0	0.5	2C1	–	0.113	PH_CNT	18	521
F–I2C–PW–13.014	O–Ka	0.5249	9.26,27780	3000	1	–4	0	–0.96	0	1	2C1	–	0.113	PH_CNT	18	521
F–I2C–PW–13.015	O–Ka	0.5249	9.9,29700	3000	1	–6	0	–0.96	0	2.2	2C1	–	0.113	PH_CNT	18	521
F–I2C–PW–13.016	O–Ka	0.5249	9.07,27210	3000	1	–10	0	–0.96	0.144	5.6	2C1	–	0.23	PH_CNT	38	522
F–I2C–PW–13.017	O–Ka	0.5249	9.93,29790	3000	1	–15	0	–0.96	0.144	12.1	2C1	–	0.66	PH_CNT	114	506
F–I2C–PW–13.018	O–Ka	0.5249	9.61,28830	3000	1	–20	0	–0.96	0	20.7	2C1	–	6	PH_CNT	1024	501
F–I2C–PW–13.019	O–Ka	0.5249	299.8,29980	100	1	–2	0	–0.96	0.144	0.5	2C1	–	0.66	PH_CNT	114	17
F–I2C–PW–13.020	O–Ka	0.5249	289.49,28949	100	1	–4	0	–0.96	0.144	1	2C1	–	0.66	PH_CNT	114	17
F–I2C–PW–13.021	O–Ka	0.5249	297.28,29728	100	1	–6	0	–0.96	0.144	2.2	2C1	–	0.66	PH_CNT	114	17
F–I2C–PW–13.022	O–Ka	0.5249	283.69,28369	100	1	–10	0	–0.96	0.144	5.6	2C1	–	0.66	PH_CNT	114	17
F–I2C–PW–13.023	O–Ka	0.5249	298.05,29805	100	1	–15	0	–0.96	0.144	12.1	2C1	–	0.66	PH_CNT	114	17
F–I2C–PW–13.024	O–Ka	0.5249	297.35,29735	100	1	–20	0	–0.96	0	20.7	2C1	–	6	PH_CNT	1024	17

Table 6.3: Point Spread Function Tests

6.1.5 Effective Area

Effective Area (EA) tests measure the total effective collecting area over the PSF at many energies in photon counting mode. We performed this test at many energies due to the need for detailed sampling of energy space. The tests were done with the system substantially defocused, to minimize photon loss due to pileup. Measurements were made on-axis and at several off-axis positions.

TRW_ID	source	energy	FP_Rate,Total_Cts	Int_time	mult	pitch	yaw	yoff	zoff	Defocus	Focal	HST	frametime	proc_mode	rows	frames
F–I2C–EA–1.003	Al–Ka	1.486	49.55,20000	403.63	1	0	0	−0.96	0	40	2C1	–	6	PH_CNT	1024	68
F–I2C–EA–11.013	Al–Ka	1.486	49.33,20000	405.43	1	−2	0	−0.96	0	40	2C1	–	6	PH_CNT	1024	68
F–I2C–EA–11.014	Al–Ka	1.486	47.61,20000	420.08	1	−4	0	−0.96	0	40	2C1	–	6	PH_CNT	1024	71
F–I2C–EA–11.015	Al–Ka	1.486	45.81,20000	436.58	1	−6	0	−0.96	0	40	2C1	–	6	PH_CNT	1024	73
F–I2C–EA–11.016	Al–Ka	1.486	46.69,20000	428.35	1	−10	0	−0.96	0	40	2C1	–	6	PH_CNT	1024	72
F–I2C–EA–11.017	Al–Ka	1.486	45.86,20000	436.11	1	−15	0	−0.96	0	40	2C1	–	6	PH_CNT	1024	73
F–I2C–EA–11.018	Al–Ka	1.486	49.18,20000	406.66	1	−20	0	−0.96	0	40	2C1	–	6	PH_CNT	1024	68
F–I2C–EA–12.031	Al–Ka	1.486	46.49,20000	430.2	1	−2	0	0	0	40	2C0	–	6	PH_CNT	1024	72
F–I2C–EA–12.032	Al–Ka	1.486	49.86,20000	401.12	1	−4	0	0	0	40	2C0	–	6	PH_CNT	1024	67
F–I2C–EA–12.033	Al–Ka	1.486	47.97,20000	416.92	1	−6	0	0	0	40	2C0	–	6	PH_CNT	1024	70
F–I2C–EA–12.034	Al–Ka	1.486	48.89,20000	409.08	1	−10	0	0	0	40	2C0	–	6	PH_CNT	1024	69
F–I2C–EA–12.035	Al–Ka	1.486	48.02,20000	416.49	1	−15	0	0	0	40	2C0	–	6	PH_CNT	1024	70
F–I2C–EA–12.036	Al–Ka	1.486	46.34,20000	431.59	1	−20	0	0	0	40	2C0	–	6	PH_CNT	1024	72
F–I2C–EA–2.003	Al–Ka	1.486	46.69,20000	428.35	1	0	0	−0.96	0	40	2C0	–	6	PH_CNT	1024	72
H–IAS–EA–21.001	Al–Ka	1.486	73.1706,20000	273.33	1	0	23.86	−68.491	0	40.237	S3	S0	3.3	PH_CNT	1024	83
H–IAS–EA–21.002	Al–Ka	1.486	76.8710,20000	260.17	1	0	15.18	−43.583	0	40.096	S3	S1	3.3	PH_CNT	1024	79
H–IAS–EA–21.003	Al–Ka	1.486	77.1033,20000	259.39	1	0	−10.84	31.132	0	40.049	S3	S4	3.3	PH_CNT	1024	79
H–IAS–EA–21.004	Al–Ka	1.486	75.6216,20000	264.47	1	0	−19.52	56.051	0	40.159	S3	S5	3.3	PH_CNT	1024	81
F–I2C–EA–12.043	C–Ka	0.277	25.11,20000	796.49	1	−2	0	0	0	40	2C0	–	6	PH_CNT	1024	133
F–I2C–EA–12.044	C–Ka	0.277	26.68,20000	749.62	1	−4	0	0	0	40	2C0	–	6	PH_CNT	1024	125
F–I2C–EA–12.045	C–Ka	0.277	25.67,20000	779.12	1	−6	0	0	0	40	2C0	–	6	PH_CNT	1024	130
F–I2C–EA–12.046	C–Ka	0.277	25.89,20000	772.49	1	−10	0	0	0	45	2C0	–	6	PH_CNT	1024	129
F–I2C–EA–12.047	C–Ka	0.277	25.23,20000	792.7	1	−15	0	0	0	−30	2C0	–	6	PH_CNT	1024	133
F–I2C–EA–12.048	C–Ka	0.277	26.03,20000	768.34	1	−20	0	0	0	−20	2C0	–	6	PH_CNT	1024	129
F–I2C–EA–2.008	C–Ka	0.277	25.24,20000	792.39	1	0	0	−0.96	0	40	2C0	–	6	PH_CNT	1024	133
H–IAI–EA–23.001	C–Ka	0.277	36.6972,10000	272.5	1	4.95	4.93	−14.163	14.225	40.02	I3	I0	3.3	PH_CNT	1024	83
H–IAI–EA–23.002	C–Ka	0.277	37.3086,10000	268.030	1	4.95	−3.74	10.733	14.225	40.016	I3	I1	3.3	PH_CNT	1024	82
H–IAI–EA–23.003	C–Ka	0.277	37.3140,10000	267.99	1	−3.76	4.93	−14.163	−10.781	40.016	I3	I2	3.3	PH_CNT	1024	82
H–IAI–EA–23.004	C–Ka	0.277	30.4067,10000	328.87	1	−3.76	−3.74	10.733	−10.781	40.011	I3	I3	3.3	PH_CNT	1024	100
H–IAS–EA–23.005	C–Ka	0.277	33.8649,10000	295.29	1	−13.2	7.03	−20.181	−37.895	40.093	S2	S2	3.3	PH_CNT	1024	90
H–IAS–EA–23.006	C–Ka	0.277	30.1858,10000	331.28	1	−13.2	−1.64	4.716	−37.896	40.073	S3	S3	3.3	PH_CNT	1024	101
H–IAS–EA–23.007	C–Ka	0.277	35.7706,10000	279.55	1	0	23.86	−68.491	0	40.237	S0	S0	3.3	PH_CNT	1024	85
H–IAS–EA–23.008	C–Ka	0.277	39.1692,10000	255.3	1	0	15.18	−43.583	0	40.096	S1	S1	3.3	PH_CNT	1024	78
H–IAS–EA–23.009	C–Ka	0.277	37.0765,10000	269.71	1	0	6.51	−18.675	0	40.017	S2	S2	3.3	PH_CNT	1024	82
H–IAS–EA–23.010	C–Ka	0.277	38.5090,10000	259.68	1	0	0	0	0	40	S3	S3	3.3	PH_CNT	1024	79
H–IAS–EA–23.011	C–Ka	0.277	38.2031,10000	261.75	1	0	−2.17	6.224	0	40.002	S3	S3	3.3	PH_CNT	1024	80
H–IAS–EA–23.012	C–Ka	0.277	37.4382,10000	267.1	1	0	−10.84	31.132	0	40.049	S4	S4	3.3	PH_CNT	1024	81
H–IAS–EA–23.013	C–Ka	0.277	36.8342,10000	271.48	1	0	−19.52	56.051	0	40.159	S5	S5	3.3	PH_CNT	1024	83
F–I2C–EA–1.001	Cu–Ka	8.030	28.39,20000	704.47	1	0	0	−0.96	0	40	2C1	–	6	PH_CNT	1024	118
F–I2C–EA–11.001	Cu–Ka	8.030	27.67,20000	722.8	1	−2	0	−0.96	0	40	2C1	–	6	PH_CNT	1024	121
F–I2C–EA–11.002	Cu–Ka	8.030	28.12,20000	711.23	1	−4	0	−0.96	0	40	2C1	–	6	PH_CNT	1024	119
F–I2C–EA–11.002a	Cu–Ka	8.030	28.12,20000	711.23	1	−4	0	−0.96	0	40	2C1	–	6	PH_CNT	1024	119
F–I2C–EA–11.003	Cu–Ka	8.030	27.89,20000	717.1	1	−6	0	−0.96	0	40	2C1	–	6	PH_CNT	1024	120
F–I2C–EA–11.004	Cu–Ka	8.030	27.89,20000	717.1	1	−10	0	−0.96	0	45	2C1	–	6	PH_CNT	1024	120
F–I2C–EA–11.005	Cu–Ka	8.030	27.88,20000	717.36	1	−15	0	−0.96	0	−30	2C1	–	6	PH_CNT	1024	120
F–I2C–EA–11.006	Cu–Ka	8.030	27.72,20000	721.5	1	−20	0	−0.96	0	−20	2C1	–	6	PH_CNT	1024	121
F–I2C–EA–12.001	Cu–Ka	8.030	47.9,20000	417.53	1	−2	0	0	0	40	2C0	–	6	PH_CNT	1024	70
F–I2C–EA–12.002	Cu–Ka	8.030	48.67,20000	410.93	1	−4	0	0	0	40	2C0	–	6	PH_CNT	1024	69
F–I2C–EA–12.003	Cu–Ka	8.030	48.29,20000	414.16	1	−6	0	0	0	40	2C0	–	6	PH_CNT	1024	70
F–I2C–EA–12.004	Cu–Ka	8.030	48.28,20000	414.25	1	−10	0	0	0	45	2C0	–	6	PH_CNT	1024	70
F–I2C–EA–12.005	Cu–Ka	8.030	48.27,20000	414.33	1	−15	0	0	0	−30	2C0	–	6	PH_CNT	1024	70
F–I2C–EA–12.006	Cu–Ka	8.030	46.69,20000	428.35	1	−20	0	0	0	−20	2C0	–	6	PH_CNT	1024	72
F–I2C–EA–2.001	Cu–Ka	8.030	49.15,20000	406.91	1	0	0	−0.96	0	40	2C0	–	6	PH_CNT	1024	68
H–IAI–EA–24.007	Cu–Ka	8.030	15.9156,10000	628.31	1	4.95	4.93	−14.163	14.225	40.02	I3	I0	3.3	PH_CNT	1024	191

continued on next page

continued from previous page

TRW_ID	source	energy	FP_Rate,Total_Cts	Int_time	mult	pitch	yaw	yoff	zoff	Defocus	Focal	HST	frametime	proc_mode	rows	frames
H–IAI–EA–24.008	Cu–Ka	8.030	16.8230,10000	594.42	1	4.95	−3.74	10.733	14.225	40.016	I3	I1	3.3	PH_CNT	1024	181
H–IAI–EA–24.009	Cu–Ka	8.030	16.8311,10000	594.13	1	−3.76	4.93	−14.163	−10.781	40.016	I3	I2	3.3	PH_CNT	1024	181
H–IAI–EA–25.002	Cu–Ka	8.030	19.2976,10000	518.19	1	0	0	10.8	−2.7	40	I3	I3	3.3	PH_CNT	1024	158
H–IAS–EA–24.028	Cu–Ka	8.030	16.4785,10000	606.85	1	0	6.51	−18.675	0	40.017	S2	S2	3.3	PH_CNT	1024	184
H–IAS–EA–24.029	Cu–Ka	8.030	19.3415,10000	517.02	1	0	0	0	0	40	S3	S3	3.3	PH_CNT	1024	157
F–I2C–EA–1.007	Cu–La	0.9297	47.68,20000	419.46	1	0	0	−0.96	0	40	2C1	–	6	PH_CNT	1024	70
H–IAI–EA–25.005	Cu–La	0.9297	37.3716,10000	267.58	1	0	0	10.8	−2.7	40	I3	I3	3.3	PH_CNT	1024	82
H–IAI–EA–3.001	Cu–La	0.9297	37.5746,10000	266.13	1	4.95	4.93	−14.163	14.225	40.02	I3	I0	3.3	PH_CNT	1024	81
H–IAI–EA–3.002	Cu–La	0.9297	38.2039,10000	261.75	1	4.95	−3.74	10.733	14.225	40.016	I3	I1	3.3	PH_CNT	1024	80
H–IAI–EA–3.003	Cu–La	0.9297	38.2096,10000	261.71	1	−3.76	4.93	−14.163	−10.781	40.016	I3	I2	3.3	PH_CNT	1024	80
H–IAS–EA–18.021	Cu–La	0.9297	37.9650,10000	263.4	1	0	6.51	−18.675	0	40.017	S2	S2	3.3	PH_CNT	1024	80
H–IAS–EA–18.022	Cu–La	0.9297	36.8636,10000	271.27	1	0	0	0	0	40	S3	S3	3.3	PH_CNT	1024	83
F–I2C–EA–23.001	DCM	1.7	43.37,10000	230.57	1	−0	−0	0	0	0	2C1	–	6	INTEG	1024	39
F–I2C–EA–23.003	DCM	1.7	42.84,10000	233.42	1	−0	−0	0	0	0	2C0	–	6	INTEG	1024	39
F–I2C–EA–3.002	DCM	1.8425	40.31,20000	2976.93	6	0	0	0	0	40	2C0	–	6	PH_CNT	1024	497
F–I2C–EA–3.004	DCM	1.885	48.66,20000	2055.08	5	0	0	0	0	40	2C0	–	6	PH_CNT	1024	343
F–I2C–EA–5.001b	DCM	2.62	47.23,20000	5081.52	12	0	0	−0.96	0	40	2C1	–	6	PH_CNT	1024	847
F–I2C–EA–5.003	DCM	2.54999	46.25,20000	2162.16	5	0	0	−0.96	0	40	2C1	–	6	PH_CNT	1024	361
F–I2C–EA–5.004	DCM	2.16	45.25,20000	2209.94	5	0	0	−0.96	0	40	2C1	–	6	PH_CNT	1024	369
F–I2C–EA–5.005	DCM	2.09	47.43,20000	2108.37	5	0	0	−0.96	0	40	2C1	–	6	PH_CNT	1024	352
F–I2C–EA–6.001	DCM	1.575	48.89,20000	2454.48	6	0	0	0	0	40	2C1	–	6	PH_CNT	1024	410
F–I2C–EA–6.002	DCM	4.75	43.61,20000	4586.1	10	0	0	−0.96	0	40	2C1	–	6	PH_CNT	1024	765
F–I2C–EA–6.003	DCM	6.75	20.18,20000	9910.79	10	0	0	−0.96	0	40	2C1	–	6	PH_CNT	1024	1652
F–I2C–EA–6.004	DCM	1.575	49.53,20000	2422.77	6	0	0	0	0	40	2C0	–	6	PH_CNT	1024	404
F–I2C–EA–6.005	DCM	4.75	43.09,20000	4641.45	10	0	0	−0.96	0	40	2C0	–	6	PH_CNT	1024	774
F–I2C–EA–6.006	DCM	6.75	21.14,20000	9460.74	10	0	0	−0.96	0	40	2C0	–	6	PH_CNT	1024	1577
F–I2C–EA–72.001	DCM	3.25	46.87,10000	640.06	3	0	0	−0.96	0	23.5	2C1	–	6	PH_CNT	1024	107
G–I2C–EA–41.002	DCM	1.83	1105.0602,165759	150	1	0	0	0	0.144	23.4	2C1	–	0.66	PH_CNT	114	26
G–I2C–EA–41.008	DCM	1.88	66.3701,9955.51	900	6	0	0	0	0.144	23.4	2C1	–	0.66	PH_CNT	114	152
H–IAI–EA–2.001	DCM	6	72.4814,20000	1931.53	7	4.95	4.93	−14.666	14.731	40.021	I3	I0	3.3	PH_CNT	1024	586
H–IAI–EA–2.002	DCM	6	75.3108,20000	1858.96	7	4.95	−3.74	11.114	14.73	40.016	I3	I1	3.3	PH_CNT	1024	564
H–IAI–EA–2.003	DCM	6	75.3361,20000	1858.34	7	−3.76	4.93	−14.667	−11.164	40.016	I3	I2	3.3	PH_CNT	1024	564
H–IAI–EA–2.004	DCM	6	78.5836,20000	1781.54	7	−3.76	−3.74	11.115	−11.164	40.012	I3	I3	3.3	PH_CNT	1024	540
H–IAI–EA–2.005	DCM	6	77.7692,20000	1800.2	7	−13.2	7.03	−20.899	−39.243	40.096	I3	S2	3.3	PH_CNT	1024	546
H–IAI–EA–2.006	DCM	6	77.9840,20000	1795.24	7	−13.2	−1.64	4.884	−39.244	40.076	I3	S3	3.3	PH_CNT	1024	545
H–IAI–EA–2.020	DCM	6	73.1412,20000	1914.11	7	0	0	10.8	−2.7	40	I3	I3	3.3	PH_CNT	1024	581
H–IAS–EA–2.007	DCM	6	55.8527,20000	2506.59	7	0	23.86	−70.927	0	40.246	S3	S0	3.3	PH_CNT	1024	760
H–IAS–EA–2.008	DCM	6	75.8731,20000	1845.19	7	0	15.18	−45.133	0	40.099	S3	S1	3.3	PH_CNT	1024	560
H–IAS–EA–2.009	DCM	6	73.5752,20000	1902.82	7	0	6.51	−19.339	0	40.018	S3	S2	3.3	PH_CNT	1024	577
H–IAS–EA–2.010	DCM	6	72.4895,20000	1931.31	7	0	0	0	0	40	S3	S3	3.3	PH_CNT	1024	586
H–IAS–EA–2.011	DCM	6	78.3540,20000	1786.76	7	0	−2.17	6.445	0	40.002	S3	S3	3.3	PH_CNT	1024	542
H–IAS–EA–2.012	DCM	6	72.1441,20000	1940.56	7	0	−10.84	32.239	0	40.05	S3	S4	3.3	PH_CNT	1024	589
H–IAS–EA–2.013	DCM	6	72.3609,20000	1934.75	7	0	−19.52	58.045	0	40.164	S3	S5	3.3	PH_CNT	1024	587
F–I2C–EA–1.002	Fe–Ka	6.4	27.04,20000	739.64	1	0	0	−0.96	0	40	2C1	–	6	PH_CNT	1024	124
F–I2C–EA–11.007	Fe–Ka	6.4	29.07,20000	687.99	1	−2	0	−0.96	0	40	2C1	–	6	PH_CNT	1024	115
F–I2C–EA–11.008	Fe–Ka	6.4	29.92,20000	668.44	1	−4	0	−0.96	0	40	2C1	–	6	PH_CNT	1024	112
F–I2C–EA–11.009	Fe–Ka	6.4	27.21,20000	735.02	1	−6	0	−0.96	0	40	2C1	–	6	PH_CNT	1024	123
F–I2C–EA–11.010	Fe–Ka	6.4	29.01,20000	689.41	1	−10	0	−0.96	0	45	2C1	–	6	PH_CNT	1024	115
F–I2C–EA–11.011	Fe–Ka	6.4	28.48,20000	702.24	1	−15	0	−0.96	0	−30	2C1	–	6	PH_CNT	1024	118
F–I2C–EA–11.012	Fe–Ka	6.4	27.21,20000	735.02	1	−20	0	−0.96	0	−20	2C1	–	6	PH_CNT	1024	123
F–I2C–EA–12.007	Fe–Ka	6.4	48.01,20000	416.58	1	−2	0	0	0	40	2C0	–	6	PH_CNT	1024	70
F–I2C–EA–12.008	Fe–Ka	6.4	49.41,20000	404.77	1	−4	0	0	0	40	2C0	–	6	PH_CNT	1024	68
F–I2C–EA–12.009	Fe–Ka	6.4	44.94,20000	445.03	1	−6	0	0	0	40	2C0	–	6	PH_CNT	1024	75
F–I2C–EA–12.010	Fe–Ka	6.4	49.82,20000	401.44	1	−10	0	0	0	45	2C0	–	6	PH_CNT	1024	67
F–I2C–EA–12.011	Fe–Ka	6.4	48.91,20000	408.91	1	−15	0	0	0	−30	2C0	–	6	PH_CNT	1024	69
F–I2C–EA–12.012	Fe–Ka	6.4	49.93,20000	400.56	1	−20	0	0	0	−20	2C0	–	6	PH_CNT	1024	67
F–I2C–EA–2.002	Fe–Ka	6.4	49.63,20000	402.98	1	0	0	−0.96	0	40	2C0	–	6	PH_CNT	1024	68
H–IAI–EA–25.006	Fe–Ka	6.4	18.2752,10000	547.19	1	0	0	10.8	−2.7	40	I3	I3	3.3	PH_CNT	1024	166
H–IAI–EA–3.013	Fe–Ka	6.4	19.3036,10000	518.030	1	4.95	4.93	−14.163	14.225	40.02	I3	I0	3.3	PH_CNT	1024	157
H–IAI–EA–3.014	Fe–Ka	6.4	18.1770,10000	550.14	1	4.95	−3.74	10.733	14.225	40.016	I3	I1	3.3	PH_CNT	1024	167
H–IAI–EA–3.015	Fe–Ka	6.4	18.1842,10000	549.92	1	−3.76	4.93	−14.163	−10.781	40.016	I3	I2	3.3	PH_CNT	1024	167
H–IAS–EA–18.035	Fe–Ka	6.4	19.8577,10000	503.58	1	0	6.51	−18.675	0	40.017	S2	S2	3.3	PH_CNT	1024	153
H–IAS–EA–18.036	Fe–Ka	6.4	19.3990,10000	515.49	1	0	0	0	0	40	S3	S3	3.3	PH_CNT	1024	157
F–I2C–EA–1.017	Fe–La	0.705	45.44,20000	440.14	1	0	0	−0.96	0	40	2C1	–	6	PH_CNT	1024	74
F–I2C–EA–11.025	Fe–La	0.705	45.21,20000	442.38	1	−2	0	−0.96	0	40	2C1	–	6	PH_CNT	1024	74
F–I2C–EA–11.026	Fe–La	0.705	48.51,20000	412.28	1	−4	0	−0.96	0	40	2C1	–	6	PH_CNT	1024	69

continued on next page

continued from previous page

TRW_ID	source	energy	FP_Rate,Total_Cts	Int_time	mult	pitch	yaw	yoff	zoff	Defocus	Focal	HST	frametime	proc_mode	rows	frames
F–I2C–EA–11.027	Fe–La	0.705	46.67,20000	428.54	1	–6	0	–0.96	0	40	2C1	–	6	PH_CNT	1024	72
F–I2C–EA–11.028	Fe–La	0.705	47.53,20000	420.78	1	–10	0	–0.96	0	45	2C1	–	6	PH_CNT	1024	71
F–I2C–EA–11.029	Fe–La	0.705	42.1,20000	475.05	1	–15	0	–0.96	0	–30	2C1	–	6	PH_CNT	1024	80
F–I2C–EA–11.030	Fe–La	0.705	40.34,20000	495.78	1	–20	0	–0.96	0	–20	2C1	–	6	PH_CNT	1024	83
F–I2C–EA–12.013	Fe–La	0.705	27.1,20000	738	1	–2	0	0	0	40	2C0	–	6	PH_CNT	1024	124
F–I2C–EA–12.014	Fe–La	0.705	26.17,20000	764.23	1	–4	0	0	0	40	2C0	–	6	PH_CNT	1024	128
F–I2C–EA–12.015	Fe–La	0.705	25.18,20000	794.28	1	–6	0	0	0	40	2C0	–	6	PH_CNT	1024	133
F–I2C–EA–12.016	Fe–La	0.705	25.38,20000	788.02	1	–10	0	0	0	45	2C0	–	6	PH_CNT	1024	132
F–I2C–EA–12.017	Fe–La	0.705	27.21,20000	735.02	1	–15	0	0	0	–30	2C0	–	6	PH_CNT	1024	123
F–I2C–EA–12.018	Fe–La	0.705	26.07,20000	767.16	1	–20	0	0	0	–20	2C0	–	6	PH_CNT	1024	128
F–I2C–EA–2.005	Fe–La	0.705	27.24,20000	734.21	1	0	0	–0.96	0	40	2C0	–	6	PH_CNT	1024	123
H–IAI–EA–24.013	Fe–La	0.705	38.3593,10000	260.69	1	4.95	4.93	–14.163	14.225	40.02	I3	I0	3.3	PH_CNT	1024	79
H–IAI–EA–24.014	Fe–La	0.705	39.0007,10000	256.4	1	4.95	–3.74	10.733	14.225	40.016	I3	I1	3.3	PH_CNT	1024	78
H–IAI–EA–24.015	Fe–La	0.705	39.0064,10000	256.36	1	–3.76	4.93	–14.163	–10.781	40.016	I3	I2	3.3	PH_CNT	1024	78
H–IAI–EA–25.003	Fe–La	0.705	31.0882,10000	321.66	1	0	0	10.8	–2.7	40	I3	I3	3.3	PH_CNT	1024	98
H–IAS–EA–24.035	Fe–La	0.705	38.7572,10000	258.01	1	0	6.51	–18.675	0	40.017	S2	S2	3.3	PH_CNT	1024	79
H–IAS–EA–24.036	Fe–La	0.705	37.0485,10000	269.91	1	0	0	0	0	40	S3	S3	3.3	PH_CNT	1024	82
F–I2C–EA–1.009	Mg–Ka	1.254	47.21,20000	423.63	1	0	0	–0.96	0	40	2C1	–	6	PH_CNT	1024	71
F–I2C–EA–1.029	Mg–Ka	1.254	40.8,20000	490.19	1	0	0	0	0	40	2C0	–	6	PH_CNT	1024	82
G–I2C–EA–1.010	Mo–La	2.293	45.2022,20000	442.45	1	0	0	–0.96	0	40	2C1	–	6	PH_CNT	1024	74
F–I2C–EA–2.012	Ni–La	0.852	29.19,20000	685.16	1	0	0	–0.96	0	40	2C0	–	6	PH_CNT	1024	115
F–I2C–EA–2.020	Ni–La	0.852	49.53,20000	403.79	1	0	0	0	0	40	2C1	–	6	PH_CNT	1024	68
F–I2C–EA–1.005	O–Ka	0.5249	41.31,20000	484.14	1	0	0	–0.96	0	40	2C1	–	6	PH_CNT	1024	81
F–I2C–EA–11.037	O–Ka	0.5249	41.1,20000	486.61	1	–2	0	–0.96	0	40	2C1	–	6	PH_CNT	1024	82
F–I2C–EA–11.038	O–Ka	0.5249	43.66,20000	458.08	1	–4	0	–0.96	0	40	2C1	–	6	PH_CNT	1024	77
F–I2C–EA–11.039	O–Ka	0.5249	42,20000	476.19	1	–6	0	–0.96	0	40	2C1	–	6	PH_CNT	1024	80
F–I2C–EA–11.040	O–Ka	0.5249	42.36,20000	472.14	1	–10	0	–0.96	0	45	2C1	–	6	PH_CNT	1024	79
F–I2C–EA–11.041	O–Ka	0.5249	41.28,20000	484.49	1	–15	0	–0.96	0	–30	2C1	–	6	PH_CNT	1024	81
F–I2C–EA–11.042	O–Ka	0.5249	45.72,20000	437.44	1	–20	0	–0.96	0	–20	2C1	–	6	PH_CNT	1024	73
F–I2C–EA–12.025	O–Ka	0.5249	28.14,20000	710.73	1	–2	0	0	0	40	2C0	–	6	PH_CNT	1024	119
F–I2C–EA–12.026	O–Ka	0.5249	27.17,20000	736.1	1	–4	0	0	0	40	2C0	–	6	PH_CNT	1024	123
F–I2C–EA–12.027	O–Ka	0.5249	29.05,20000	688.46	1	–6	0	0	0	40	2C0	–	6	PH_CNT	1024	115
F–I2C–EA–12.028	O–Ka	0.5249	29.59,20000	675.9	1	–10	0	0	0	45	2C0	–	6	PH_CNT	1024	113
F–I2C–EA–12.029	O–Ka	0.5249	29.13,20000	686.57	1	–15	0	0	0	–30	2C0	–	6	PH_CNT	1024	115
F–I2C–EA–12.030	O–Ka	0.5249	28.2,20000	709.22	1	–20	0	0	0	–20	2C0	–	6	PH_CNT	1024	119
F–I2C–EA–2.007	O–Ka	0.5249	28.29,20000	706.96	1	0	0	–0.96	0	40	2C0	–	6	PH_CNT	1024	118
H–IAI–EA–24.001	O–Ka	0.5249	37.3352,10000	267.84	1	4.95	4.93	–14.163	14.225	40.02	I3	I0	3.3	PH_CNT	1024	82
H–IAI–EA–24.002	O–Ka	0.5249	37.9586,10000	263.44	1	4.95	–3.74	10.733	14.225	40.016	I3	I1	3.3	PH_CNT	1024	80
H–IAI–EA–24.003	O–Ka	0.5249	37.9641,10000	263.4	1	–3.76	4.93	–14.163	–10.781	40.016	I3	I2	3.3	PH_CNT	1024	80
H–IAI–EA–24.004	O–Ka	0.5249	38.6796,10000	258.53	1	–3.76	–3.74	10.733	–10.781	40.011	I3	I3	3.3	PH_CNT	1024	79
H–IAI–EA–25.001	O–Ka	0.5249	30.4905,10000	327.97	1	0	0	10.8	–2.7	40	I3	I3	3.3	PH_CNT	1024	100
H–IAS–EA–24.021	O–Ka	0.5249	37.7219,10000	265.09	1	0	6.51	–18.675	0	40.017	S2	S2	3.3	PH_CNT	1024	81
H–IAS–EA–24.022	O–Ka	0.5249	36.6008,10000	273.21	1	0	0	0	0	40	S3	S3	3.3	PH_CNT	1024	83
H–IAI–EA–25.004	Si–Ka	1.739	39.6983,10000	251.9	1	0	0	10.8	–2.7	40	I3	I3	3.3	PH_CNT	1024	77
H–IAI–EA–3.007	Si–Ka	1.739	39.7868,10000	251.34	1	4.95	4.93	–14.163	14.225	40.02	I3	I0	3.3	PH_CNT	1024	77
H–IAI–EA–3.008	Si–Ka	1.739	36.4065,10000	274.67	1	4.95	–3.74	10.733	14.225	40.016	I3	I1	3.3	PH_CNT	1024	84
H–IAI–EA–3.009	Si–Ka	1.739	36.4118,10000	274.63	1	–3.76	4.93	–14.163	–10.781	40.016	I3	I2	3.3	PH_CNT	1024	84
H–IAS–EA–18.028	Si–Ka	1.739	36.1793,10000	276.4	1	0	6.51	–18.675	0	40.017	S2	S2	3.3	PH_CNT	1024	84
H–IAS–EA–18.029	Si–Ka	1.739	37.9455,10000	263.53	1	0	0	0	0	40	S3	S3	3.3	PH_CNT	1024	80
F–I2C–EA–1.004	Ti–Ka	4.51	29.13,20000	686.57	1	0	0	–0.96	0	40	2C1	–	6	PH_CNT	1024	115
F–I2C–EA–11.019	Ti–Ka	4.51	28.61,20000	699.05	1	–2	0	–0.96	0	40	2C1	–	6	PH_CNT	1024	117
F–I2C–EA–11.020	Ti–Ka	4.51	27.46,20000	728.33	1	–4	0	–0.96	0	40	2C1	–	6	PH_CNT	1024	122
F–I2C–EA–11.021	Ti–Ka	4.51	29,20000	689.65	1	–6	0	–0.96	0	40	2C1	–	6	PH_CNT	1024	115
F–I2C–EA–11.022	Ti–Ka	4.51	28.33,20000	705.96	1	–10	0	–0.96	0	45	2C1	–	6	PH_CNT	1024	118
F–I2C–EA–11.023	Ti–Ka	4.51	28.72,20000	696.37	1	–15	0	–0.96	0	–30	2C1	–	6	PH_CNT	1024	117
F–I2C–EA–11.024	Ti–Ka	4.51	27.73,20000	721.24	1	–20	0	–0.96	0	–20	2C1	–	6	PH_CNT	1024	121
F–I2C–EA–12.019	Ti–Ka	4.51	48.58,20000	411.69	1	–2	0	0	0	40	2C0	–	6	PH_CNT	1024	69
F–I2C–EA–12.020	Ti–Ka	4.51	46.63,20000	428.9	1	–4	0	0	0	40	2C0	–	6	PH_CNT	1024	72
F–I2C–EA–12.021	Ti–Ka	4.51	49.24,20000	406.17	1	–6	0	0	0	40	2C0	–	6	PH_CNT	1024	68
F–I2C–EA–12.022	Ti–Ka	4.51	48.12,20000	415.62	1	–10	0	0	0	45	2C0	–	6	PH_CNT	1024	70
F–I2C–EA–12.023	Ti–Ka	4.51	48.77,20000	410.08	1	–15	0	0	0	–30	2C0	–	6	PH_CNT	1024	69
F–I2C–EA–12.024	Ti–Ka	4.51	47.09,20000	424.71	1	–20	0	0	0	–20	2C0	–	6	PH_CNT	1024	71
F–I2C–EA–2.004	Ti–Ka	4.51	49.47,20000	404.28	1	0	0	–0.96	0	40	2C0	–	6	PH_CNT	1024	68

continued on next page

continued from previous page

TRW_ID	source	energy	FP_Rate,Total_Cts	Int_time	mult	pitch	yaw	yoff	zoff	Defocus	Focal	HST	frametime	proc_mode	rows	frames
F–I2C–EA–12.049	Ti–La	0.4522	49.04,20000	407.83	1	−2	0	0	0	40	2C0	–	6	PH_CNT	1024	68
F–I2C–EA–12.050	Ti–La	0.4522	47.35,20000	422.38	1	−4	0	0	0	40	2C0	–	6	PH_CNT	1024	71
F–I2C–EA–12.051	Ti–La	0.4522	45.56,20000	438.98	1	−6	0	0	0	40	2C0	–	6	PH_CNT	1024	74
F–I2C–EA–12.052	Ti–La	0.4522	46.41,20000	430.94	1	−10	0	0	0	45	2C0	–	6	PH_CNT	1024	72
F–I2C–EA–12.053	Ti–La	0.4522	45.68,20000	437.82	1	−15	0	0	0	−30	2C0	–	6	PH_CNT	1024	73
F–I2C–EA–12.054	Ti–La	0.4522	49.14,20000	407	1	−20	0	0	0	−20	2C0	–	6	PH_CNT	1024	68
F–I2C–EA–2.009	Ti–La	0.4522	28.02,20000	713.77	1	0	0	−0.96	0	40	2C0	–	6	PH_CNT	1024	119

Table 6.4: Effective Area Tests

6.1.6 Count-Rate Linearity

Count-rate Linearity (Pileup) tests measure the effect of increasing the level of photons per pixel on the PSF, the EA, source centroiding, and photon detection. We used two methods to vary photon density: longer readout times for constant beam flux, and brighter beam flux at constant readout times. The data are being compared to see if the pileup is different between these two methods. For FI chips, this test was repeated at medium energy (Al K) for minimum event splitting and at high energy (Cu K) for maximum event splitting. For BI chips, it was repeated at medium energy (Al K) for minimum event splitting and high energy (Cu K) for comparison with FI; we added low energy (O K) and ultra low energy (C K) for maximum BI event splitting. It was important to repeat these tests separately for each chip because the results depend intimately on the event splitting characteristics of the chip.

TRW_ID	source	energy	FP_Rate,Total_Cts	Int_time	mult	pitch	yaw	yoff	zoff	Defocus	Focal	HST	frametime	proc_mode	rows	frames
F–I2C–CR–1.001	Al–Ka	1.486	9.04,20000	2212.39	1	0	0	0	0	0	2C1	–	0.113	PH_CNT	18	384
F–I2C–CR–1.002	Al–Ka	1.486	9.04,20000	2212.39	1	0	0	0	0	0	2C1	–	0.227	PH_CNT	38	390
F–I2C–CR–1.003	Al–Ka	1.486	9.04,20000	2212.39	1	0	0	0	0	0	2C1	–	0.318	PH_CNT	54	387
F–I2C–CR–1.004	Al–Ka	1.486	9.04,20000	2212.39	1	0	0	0	0	0	2C1	–	0.66	PH_CNT	114	373
F–I2C–CR–1.005	Al–Ka	1.486	2.74,20000	7299.27	1	0	0	0	0	0	2C1	–	0.113	PH_CNT	18	1267
F–I2C–CR–1.006	Al–Ka	1.486	28.82,20000	693.96	1	0	0	0	0	0	2C1	–	0.113	PH_CNT	18	121
F–I2C–CR–1.007	Al–Ka	1.486	54.23,20000	368.8	1	0	0	0	0	0	2C1	–	0.113	PH_CNT	18	64
F–I2C–CR–1.015a	Al–Ka	1.486	0.95,10000	21052.6	2	0	0	0	0	0	2C1	–	0.113	PH_CNT	18	3654
F–I2C–CR–2.001a	Al–Ka	1.486	9.16,20000	2183.41	1	0	0	0	0	0	2C0	–	0.113	PH_CNT	18	379
F–I2C–CR–2.002	Al–Ka	1.486	9.16,20000	2183.41	1	0	0	0	0	0	2C0	–	0.227	PH_CNT	38	385
F–I2C–CR–2.003	Al–Ka	1.486	9.16,20000	2183.41	1	0	0	0	0	0	2C0	–	0.318	PH_CNT	54	382
F–I2C–CR–2.004	Al–Ka	1.486	9.16,20000	2183.41	1	0	0	0	0	0	2C0	–	0.66	PH_CNT	114	368
F–I2C–CR–2.005	Al–Ka	1.486	2.87,20000	6968.64	1	0	0	0	0	0	2C0	–	0.113	PH_CNT	18	1210
F–I2C–CR–2.006	Al–Ka	1.486	27.16,20000	736.37	1	0	0	0	0	0	2C0	–	0.113	PH_CNT	18	128
F–I2C–CR–2.007	Al–Ka	1.486	56.79,20000	352.17	1	0	0	0	0	0	2C0	–	0.113	PH_CNT	18	62
F–I2C–CR–2.029	Al–Ka	1.486	18.32,10000	1091.7	2	0	0	0	0	0	2C0	–	0.113	PH_CNT	18	190
H–IAI–CR–1.001	Al–Ka	1.486	2.9392,20000	6804.57	1	0	0	0	0	0	I3	I3	0.1	PH_CNT	38	2062
H–IAI–CR–1.003	Al–Ka	1.486	9.3359,20000	2142.27	1	0	0	0	0	0	I3	I3	0.1	PH_CNT	38	650
H–IAI–CR–1.005	Al–Ka	1.486	29.7500,20000	672.26	1	0	0	0	0	0	I3	I3	0.1	PH_CNT	38	204
H–IAI–CR–1.007	Al–Ka	1.486	55.9798,20000	357.27	1	0	0	0	0	0	I3	I3	0.1	PH_CNT	38	109
H–IAS–CR–1.002	Al–Ka	1.486	2.9340,20000	6816.63	1	0	0	0	0	0	S3	S3	0.1	PH_CNT	38	2066
H–IAS–CR–1.004	Al–Ka	1.486	9.1315,20000	2190.21	1	0	0	0	0	0	S3	S3	0.1	PH_CNT	38	664
H–IAS–CR–1.006	Al–Ka	1.486	29.0987,20000	687.31	1	0	0	0	0	0	S3	S3	0.1	PH_CNT	38	209
H–IAS–CR–1.008	Al–Ka	1.486	54.7544,20000	365.26	1	0	0	0	0	0	S3	S3	0.1	PH_CNT	38	111
F–I2C–CR–2.022	C–Ka	0.277	9.2,20000	2173.91	1	0	0	0	0	0	2C0	–	0.113	PH_CNT	18	378
F–I2C–CR–2.023	C–Ka	0.277	9.2,20000	2173.91	1	0	0	0	0	0	2C0	–	0.227	PH_CNT	38	384
F–I2C–CR–2.024	C–Ka	0.277	9.2,20000	2173.91	1	0	0	0	0	0	2C0	–	0.318	PH_CNT	54	380
F–I2C–CR–2.025	C–Ka	0.277	9.2,20000	2173.91	1	0	0	0	0	0	2C0	–	0.66	PH_CNT	114	366
F–I2C–CR–2.026	C–Ka	0.277	2.88,20000	6944.44	1	0	0	0	0	0	2C0	–	0.113	PH_CNT	18	1206

continued on next page

continued from previous page

TRW_ID	source	energy	FP_Rate,Total_Cts	Int_time	mult	pitch	yaw	yoff	zoff	Defocus	Focal	HST	frametime	proc_mode	rows	frames
F–I2C–CR–2.026a	C–Ka	0.277	2.88,20000	6944.44	1	0	0	0	0	0	2C0	–	0.113	PH_CNT	18	1206
F–I2C–CR–2.026b	C–Ka	0.277	2.88,20000	6944.44	1	0	0	0	0	0	2C0	–	0.113	PH_CNT	18	1206
F–I2C–CR–2.027	C–Ka	0.277	26.78,20000	746.82	1	0	0	0	0	0	2C0	–	0.113	PH_CNT	18	130
F–I2C–CR–2.027a	C–Ka	0.277	26.78,20000	746.82	1	0	0	0	0	0	2C0	–	0.113	PH_CNT	18	130
F–I2C–CR–2.027b	C–Ka	0.277	26.78,20000	746.82	1	0	0	0	0	0	2C0	–	0.113	PH_CNT	18	130
F–I2C–CR–2.027c	C–Ka	0.277	26.78,20000	746.82	1	0	0	0	0	0	2C0	–	0.113	PH_CNT	18	130
F–I2C–CR–2.028a	C–Ka	0.277	58.26,20000	343.28	1	0	0	0	0	0	2C0	–	0.113	PH_CNT	18	60
F–I2C–CR–2.028b	C–Ka	0.277	58.26,20000	343.28	1	0	0	0	0	0	2C0	–	0.113	PH_CNT	18	60
F–I2C–CR–2.028c	C–Ka	0.277	58.26,20000	343.28	1	0	0	0	0	0	2C0	–	0.113	PH_CNT	18	60
F–I2C–CR–2.028d	C–Ka	0.277	58.26,20000	343.28	1	0	0	0	0	0	2C0	–	0.113	PH_CNT	18	60
F–I2C–CR–1.008	Cu–Ka	8.030	9.33,20000	2143.62	1	0	0	0	0	0	2C1	–	0.113	PH_CNT	18	372
F–I2C–CR–1.009	Cu–Ka	8.030	9.33,20000	2143.62	1	0	0	0	0	0	2C1	–	0.227	PH_CNT	38	378
F–I2C–CR–1.010	Cu–Ka	8.030	9.33,20000	2143.62	1	0	0	0	0	0	2C1	–	0.318	PH_CNT	54	375
F–I2C–CR–1.011	Cu–Ka	8.030	9.33,20000	2143.62	1	0	0	0	0	0	2C1	–	0.66	PH_CNT	114	361
F–I2C–CR–1.012	Cu–Ka	8.030	2.93,20000	6825.94	1	0	0	0	0	0	2C1	–	0.113	PH_CNT	18	1185
F–I2C–CR–1.013	Cu–Ka	8.030	27.7,20000	722.02	1	0	0	0	0	0	2C1	–	0.113	PH_CNT	18	126
F–I2C–CR–1.014	Cu–Ka	8.030	57.91,20000	345.36	1	0	0	0	0	0	2C1	–	0.113	PH_CNT	18	60
F–I2C–CR–1.016	Cu–Ka	8.030	0.91,10000	21978	2	0	0	0	0	0	2C1	–	0.113	PH_CNT	18	3814
F–I2C–CR–2.008	Cu–Ka	8.030	9.54,20000	2096.44	1	0	0	0	0	0	2C0	–	0.113	PH_CNT	18	364
F–I2C–CR–2.009	Cu–Ka	8.030	9.54,20000	2096.44	1	0	0	0	0	0	2C0	–	0.227	PH_CNT	38	370
F–I2C–CR–2.010	Cu–Ka	8.030	9.54,20000	2096.44	1	0	0	0	0	0	2C0	–	0.318	PH_CNT	54	367
F–I2C–CR–2.011	Cu–Ka	8.030	9.54,20000	2096.44	1	0	0	0	0	0	2C0	–	0.66	PH_CNT	114	353
F–I2C–CR–2.012	Cu–Ka	8.030	2.99,20000	6688.96	1	0	0	0	0	0	2C0	–	0.113	PH_CNT	18	1161
F–I2C–CR–2.013	Cu–Ka	8.030	28.31,20000	706.46	1	0	0	0	0	0	2C0	–	0.113	PH_CNT	18	123
F–I2C–CR–2.014	Cu–Ka	8.030	59.2,20000	337.83	1	0	0	0	0	0	2C0	–	0.113	PH_CNT	18	59
F–I2C–CR–2.030	Cu–Ka	8.030	0.94,10000	21276.6	2	0	0	0	0	0	2C0	–	0.113	PH_CNT	18	3692
F–I2C–CR–2.015	O–Ka	0.5249	8.5,20000	2352.94	1	0	0	0	0	0	2C0	–	0.113	PH_CNT	18	409
F–I2C–CR–2.016	O–Ka	0.5249	8.5,20000	2352.94	1	0	0	0	0	0	2C0	–	0.227	PH_CNT	38	415
F–I2C–CR–2.017	O–Ka	0.5249	8.5,20000	2352.94	1	0	0	0	0	0	2C0	–	0.318	PH_CNT	54	412
F–I2C–CR–2.018	O–Ka	0.5249	8.5,20000	2352.94	1	0	0	0	0	0	2C0	–	0.66	PH_CNT	114	397
F–I2C–CR–2.019	O–Ka	0.5249	2.72,20000	7352.94	1	0	0	0	0	0	2C0	–	0.113	PH_CNT	18	1276
F–I2C–CR–2.020	O–Ka	0.5249	27.39,20000	730.19	1	0	0	0	0	0	2C0	–	0.113	PH_CNT	18	127
F–I2C–CR–2.021	O–Ka	0.5249	56.71,20000	352.67	1	0	0	0	0	0	2C0	–	0.113	PH_CNT	18	62
H–IAI–CR–1.009	O–Ka	0.5249	2.7596,20000	7247.43	1	0	0	0	0	0	I3	I3	0.1	PH_CNT	38	2197
H–IAI–CR–1.011	O–Ka	0.5249	9.7710,20000	2046.87	1	0	0	0	0	0	I3	I3	0.1	PH_CNT	38	621
H–IAS–CR–1.010	O–Ka	0.5249	2.8086,20000	7120.99	1	0	0	0	0	0	S3	S3	0.1	PH_CNT	38	2158
H–IAS–CR–1.012	O–Ka	0.5249	9.3034,20000	2149.75	1	0	0	0	0	0	S3	S3	0.1	PH_CNT	38	652

Table 6.5: Count-rate Linearity Tests

6.1.7 Spatial Linearity

The Spatial Linearity tests consist of moving the PSF across chips to determine that the desired motion converts properly from the spatial domain to the CCD pixel domain. Also look for PSF variation indicating that the CCD chips are tilted with respect to the HRMA axis.

TRW_ID	source	energy	FP_Rate,Total_Cts	Int_time	mult	pitch	yaw	yoff	zoff	Defocus	Focal	HST	frametime	proc_mode	rows	frames
H–IAI–SL–1.001	O–Ka	0.5249	5.7696,1730.88	1900	1	0	0	0	0	0	I3	I3	3.3	PH_CNT	1024	576
H–IAS–SL–1.002	O–Ka	0.5249	5.6467,1694.01	900	1	0	0	0	0	0	S3	S3	3.3	PH_CNT	1024	273

Table 6.6: Spatial Linearity Tests

6.1.8 Flight Contamination Monitor

In the Flight Contamination Monitor tests, we position the ACIS or ACIS-2C at infinite conjugate focus and observe the Forward Contamination Cover sources (Mn K and Ag L)

reflecting off the mirrors over both BI and FI chips. This allowed the facility to monitor the HRMA for contamination buildup throughout XRCF testing and baselines the radiation source spectra for on-orbit contamination monitoring.

TRW_ID	source	energy	FP_Rate,Total_Cts	Int_time	mult	pitch	yaw	yoff	zoff	Defocus	Focal	HST	frametime	proc_mode	rows	frames
F–I2C–RC–72.001	Al–Ka	1.486	9297.08,2789124	3000	10	–0	–0	–3.17	0	195	2C0	–	6	PH_CNT	1024	501
H–IAS–RC–1.001	Al–Ka	1.486	70133,1.122e+08	1600	1	0	0	0	0	200	S3	I3	3.3	PH_CNT	1024	485
F–I2C–RC–72.002	Cu–Ka	8.030	905.52,271656	3000	10	–0	–0	–3.17	0	195	2C0	–	6	PH_CNT	1024	501
F–I2C–RC–72.044	Cu–Ka	8.030	1018.72,305616	3000	10	–0	–0	–3.17	0	195	2C0	–	6	PH_CNT	1024	501
G–I2C–RC–72.044	Cu–Ka	8.030	1018.7211,305616	3000	10	0	0	–3.17	0	195	2C0	–	6	PH_CNT	1024	501
H–IAS–RC–1.005	Cu–Ka	8.030	69509,2.0853e+08	3000	1	0	0	0	0	200	S3	I3	3.3	PH_CNT	1024	910
H–IAS–RC–1.004	Fe–La	0.705	18461,5.538e+07	3000	1	0	0	0	0	200	S3	I3	3.3	PH_CNT	1024	910
H–IAI–RC–8.002	HIREF–W	0.68877	88.8022,266407	3000	1	0	0	0	0	40	I	I3	3.3	PH_CNT	1024	910
H–IAS–RC–8.001	HIREF–W	0.68877	88.8022,266407	3000	1	0	0	0	0	40	S3	S3	3.3	PH_CNT	1024	910
F–I2C–RC–72.004	Mg–Ka	1.254	5299.79,1589937	3000	10	–0	–0	–3.17	0	195	2C0	–	6	PH_CNT	1024	501
G–I2C–RC–72.004	Mg–Ka	1.254	5299,1.589e+06	3000	10	0	0	–3.17	0	195	2C0	–	6	PH_CNT	1024	501
G–I2C–RC–72.046	Mo–La	2.293	2368.7061,710612	3000	10	0	0	–3.17	0	195	2C0	–	6	PH_CNT	1024	501
F–I2C–RC–72.022	Ni–La	0.852	42.22,12666	3000	10	–0	–0	–3.17	0	195	2C0	–	6	PH_CNT	1024	501
F–I2C–RC–72.008	O–Ka	0.5249	0,0	3000	10	–0	–0	–3.17	0	195	2C0	–	6	PH_CNT	1024	501
F–I2C–RC–72.042	O–Ka	0.5249	9969.84,2990952	3000	10	–0	–0	–3.17	0	195	2C0	–	6	PH_CNT	1024	501
F–I2C–RC–72.006	Si–Ka	1.739	149.44,44832	3000	10	–0	–0	–3.17	0	195	2C0	–	6	PH_CNT	1024	501
F–I2C–RC–72.016	Ti–Ka	4.51	432.76,129828	3000	10	–0	–0	–4.38	5.64	195	2C1	–	6	PH_CNT	1024	501

Table 6.7: Flight Contamination Monitor Tests

6.2 HRMA/ACIS Effective Area and Energy Resolution

Using an automated event filtering software package developed at PSU, we have analyzed a subset of the XRCF calibration data to investigate the dependence of the effective area and energy response of ACIS/HRMA as a function of grade selection, split event threshold, CCD and CCD amplifier, off-axis angle and region of interest on the ACIS focal plane. The main goal of this study is to facilitate selection of the appropriate ACIS parameters that optimize a desired feature in an observed ACIS spectrum. This work may also guide observers in selecting the appropriate CCD for the observation. Optimizing a particular feature in an ACIS observation in general may require making a trade-off between effective area and energy resolution of AXAF/ACIS. The present analysis will facilitate the selection of the appropriate grades, CCD, CCD amplifier and split event thresholds needed to attain the optimal point. As an illustration of the effectiveness of this approach we will present several case studies of typical astrophysical source spectra in which we enhance a particular scientific feature in the observed ACIS spectrum by the appropriate selection of ACIS parameters.

6.2.1 Analysis Technique

An effective area measurement entails determining the ratio of the X-ray line count rate R_{FP} measured by the ACIS focal plane detector to the X-ray line flux F_{BND} incident on the HRMA as measured by a beam normalization detector.

We define as the effective area A_{eff} of the HRMA/ACIS combination the quantity:

$$A_{eff} = \frac{R_{FP}}{R_{BND}} A_{BND}$$

where A_{BND} is the area of the BND normalization detector.

The effective area measurements performed at the XRCF were made in a defocused mode with ACIS moved approximately 40 mm away from the optimal focus position in the direction of the X-ray source. Operating in the defocused mode resulted in the reduction of pileup by means of spreading the X-ray image over many CCD pixels. In several measurements the image was defocused onto 2 adjacent segments of a CCD that were read out by different CCD amplifiers. Because of slight differences in the properties of the CCD amplifiers, the spectra corresponding to each amplifier were analyzed separately and the results combined to produce the total detected ACIS event rate over the selected spatial region of interest (ROI).

In the present analyses we have made use of incident source spectra produced by electron impact point sources (EIPS) for photon energies below 3 keV. For photon energies of 3 keV and above we have incorporated incident source spectra produced by the combination of the EIPS with a double crystal monochromator (DCM). The extraction of the X-ray line count rate detected by ACIS simply entails determining the number of counts in a region of interest around the X-ray line. The incident X-ray flux levels were high enough to produce noticeable pile-up in the ACIS spectra despite defocusing. Pile-up occurs whenever two or more photons are incident within either adjacent CCD pixels or with only one empty pixel between events, and are detected within a single CCD readout cycle. In such an instance the ACIS electronics will regard these as a single event with an amplitude given by the sum of the charge in the 3x3 neighborhood of the pixel with the maximum detected charge. The manifestation of pile-up in the ACIS spectra is the appearance of "pile-up lines" at energies that are multiples of the incident line energy. In addition to these lines a portion of the charge from the multiple events will not be recorded in the 3x3 island resulting in tails below the pile-up lines. Another consequence of pile-up is grade migration. In grade migration the X-ray events are detected, but the grade distribution is altered by the effects of multiple photons in close proximity.

For the analysis of ACIS spectra we have considered ROI's that include the Si escape peak (if present), the main X-ray line and pile-up lines. The number of events, $N_{pile-up,n}$ detected in the n'th pile-up line are multiplied by n+1. We estimate the detected ACIS

count rate with the expression:

$$R_{ACIS} = \frac{N_{escape} + N_{line} + \sum (n+1) * N_{pile-up,n}}{t_{live}} \tag{6.1}$$

where t_{live} in the total integration time. Due to dropped CCD frames t_{live} is determined as the product of the frame readout time of 3.341 sec and the number of processed CCD frames. For the present analysis we have not made any corrections for grade migration due to pile-up.

6.2.2 Filtering of ACIS Events

The effective area of the HRMA/ACIS combination at a given energy does not have a unique value but in general is a function of several parameters, the values of which are selected based on the scientific goals of a particular ACIS observation and the nature of the observed spectrum. As an example, in some situations an observer may wish to sacrifice energy resolution for increased effective area by accepting a larger number of ACIS grades. We therefore have determined the effective area and energy resolution (FWHM) of ACIS as a function of split event threshold, CCD grade, and off-axis angles.

For the reduction of ACIS data acquired at XRCF we have made use of the interactive tool named Event Browser (EB) and an automated event filtering tool named AcisFilter based on EB. The interactive tool is used to initially inspect each event file to be processed and to determine the spectral ROI's, the good time intervals and the centroid of the focussed beam on the CCD. The automated event filtering tool is used to filter ACIS events by grade, time, split event thresholds, and circular or rectangular spatial regions for a given amplifier of a given CCD. It also computes the CCD ontime, t_{live}, for filtered events.

To reduce the data processing time and to allow the addition of possible future enhancements without having to manually repeat all the steps we have incorporated the various input parameters (ie. ACIS event filenames, split event thresholds, grade selections, ROI's in spectral, spatial and time domain) in parameter files that are read in by the event filtering software tool.

6.2.3 X-ray Line Flux Density at HRMA Entrance

As described in section 6.2.1 an absolute effective area measurement requires a normalization to the X-ray flux density at the HRMA entrance. For DCM measurements in the 3 to 10 keV range the X-ray beam incident on the HRMA was measured to be non-uniform at approximately the 10% level. We have estimated the incident flux by taking the average of the four BND's at the HRMA location. Higher spectral orders from the DCM are not expected to be present in the 3 to 10 keV range. The quantum efficiency values and open areas for the BND counters were provided by SAO.

For the present reduction of the BND spectra we have chosen a region of interest approach. The extracted X-ray line count rate is divided by the quantum efficiency of the BND at the X-ray line energy.

6.2.4 Effective Area and Energy Resolution vs. Grade Selection; Pre-launch Results

The HRMA/ACIS effective area and energy resolution were calculated for the ASCA grade selections g0, g01, g012, g0123, g01234, g012345, g02346.[1] We also considered the special case of including all grades except ACIS grade 255. ACIS 255 (which corresponds to all eight neighbors of the central pixel being above the Split Event Threshold) is considered to contain mostly events that result from interactions of cosmic ray particles with ACIS (and not X-ray photons). Figure 6.1 and figure 6.2 show the dependence of effective area with grade selection for ACIS CCD's I1 and S3. Tables 6.8 and 6.9 provide numerical forms of the results.

The effective area measurements for the FI and BI devices presented here were made with HRMA (Pitch,Yaw) values of (5',-3.7') and (0,0) respectively. For the purpose of comparing FI with BI performance we present in Table 6.10 a list of HRMA effective area correction factors for converting the off-axis (5',-3.7') FI effective areas to on-axis ones.

Energy keV	HRMA EA off-axis cm^2	HRMA EA on-axis cm^2	Correction Factor
0.277	766.71863	812.18695	0.9440
0.525	737.62781	781.42084	0.9440
0.93	740.83380	784.86621	0.9439
1.4867	732.67267	776.44696	0.9436
3	418.14990	445.54376	0.9385
4	432.86209	465.34161	0.9302
5	379.03247	417.80930	0.9072
6	251.41301	295.91565	0.8496
7	144.60548	190.16235	0.7604

Table 6.10: HRMA Effective Area (EA) Correction Factors for a HRMA Pitch Angle of 5 arcmin and a HRMA Yaw Angle of -3.7 arcmin.

The HRMA effective area off-axis correction factor is defined as the ratio of the off-axis effective area to the on-axis value.

[1]Event grades are a characteristic of each event recognized by the ACIS software. They are critically important for separating X-ray produced events from non-X-ray events. The full ACIS grade information is reported as an eight-bit integer (0-255), but typically users analyze data by combining the grades into larger categories. Commonly used are the grade categories defined by the ASCA satellite processing.

Fuller descriptions of grades can be found in Appendix A, a document on ACIS Grades by Kenny Glotfelty of the ASC, and the ACIS Operations Manual, SOP-01. (See also http://www.astro.psu.edu/xray/docs/sop/.)

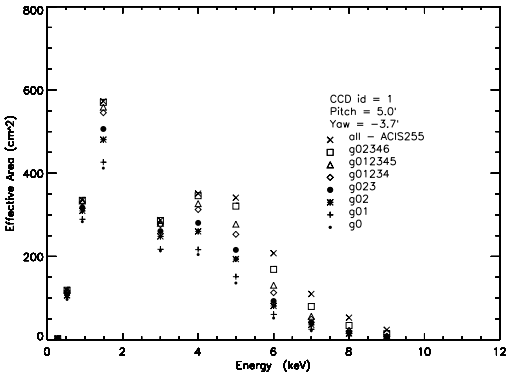

Figure 6.1: Effective Area vs. Energy and Grade Selection for ACIS CCD I1 calculated for grade selections of g0, g01, g02, g023, g01234, g012345, g02346, all grades - ACIS255

Energy	Effective Area							
	g0	g01	g02	g023	g01234	g012345	g02346	all - ACIS(255)
keV	cm^2	cm^2	cm^2	cm^2	cm^2	cm^2	cm^2	cm^2
0.277	2.33	2.33	2.37	2.37	2.38	2.38	2.38	2.38
0.525	96.82	101.15	106.49	109.60	117.11	118.37	118.87	118.96
0.93	283.51	289.22	309.47	317.53	330.60	333.30	334.75	335.31
1.4867	412.15	426.40	480.60	506.20	545.22	558.62	570.06	572.62
3	213.56	217.10	248.15	260.79	276.30	279.77	286.28	287.23
4	204.53	216.40	260.17	280.58	312.61	326.90	345.91	351.00
5	136.17	151.35	193.68	215.76	253.12	277.71	320.80	341.08
6	51.96	60.69	81.09	92.91	112.95	130.95	168.88	207.70
7	21.77	25.13	35.76	40.97	49.48	56.26	79.82	109.90
8	8.93	9.98	14.83	17.05	20.28	22.62	34.23	52.95
9	3.60	4.03	6.00	6.96	8.34	9.00	14.44	23.77

The effective area values listed in this table apply for **CCD ID = 1**, a HRMA Pitch angle of 5 arcmin, a HRMA Yaw angle of -3.7 arcmin, and a split event threshold of 13 adu. Events within the entire CCD were considered.

Table 6.8: Effective Area vs. Energy and Grade Selection for CCD I1

The first significant result is that the HRMA/ACIS effective area varies considerably with grade selection for both front illuminated (FI) and back illuminated (BI) CCD's. A possible use of this effect is in the analysis of grating observations of faint objects where CCD energy resolution only influences the separation of overlapping spectral orders. The exclusion of only ACIS grade 255 will result in a relatively high effective area and a higher signal to noise spectrum of the faint object.

Figure 6.3 and figure 6.4 show the dependence of energy resolution with grade selection for ACIS CCD's I1 and S3. (Tables 6.11 and 6.12 give numeric values of this data.) The energy resolution for FI chips is fairly insensitive to grade selection in the 3-6 keV range. For energies above 6 keV the exclusion of grades begins to improve energy resolution for FI chips. In the energy range of 3-9 keV investigated so far, the energy resolution for back

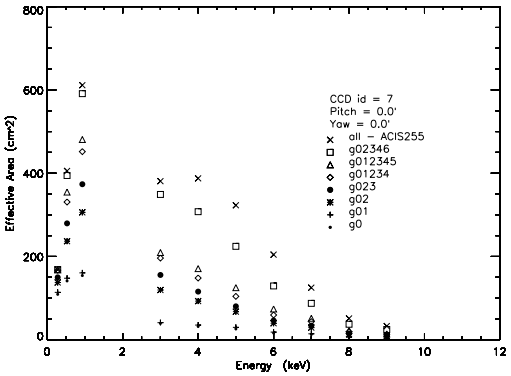

Figure 6.2: Effective Area vs. Energy for ACIS CCD S3 calculated for grade selections of g0, g01, g02, g023, g01234, g012345, g02346, all grades - ACIS255

Energy	Effective Area							
	g0	g01	g02	g023	g01234	g012345	g02346	all - ACIS(255)
keV	cm^2	cm^2	cm^2	cm^2	cm^2	cm^2	cm^2	cm^2
0.277	109.09	113.72	137.46	149.75	166.9	167.65	168.43	168.49
0.522	141.25	147.66	236.67	279.46	330.76	354.62	394.43	405.34
1.4867	154.10	160.54	305.89	373.49	451.76	480.94	591.09	611.30
3	39.15	40.90	119.42	155.51	196.07	209.37	348.93	380.83
4	32.02	35.22	92.73	115.54	148.12	170.75	307.53	387.58
5	26.06	29.64	67.36	80.18	104.11	125.00	224.27	322.95
6	15.96	18.27	39.48	46.06	59.37	73.77	129.18	204.34
7	12.68	14.15	29.06	33.79	43.54	51.44	87.31	125.03
8	5.98	6.42	13.10	14.90	19.23	22.23	37.13	51.08
9	3.50	3.77	8.14	9.22	12.11	14.01	24.54	32.72

The effective area values listed in this table apply for **CCD ID = 7**, a HRMA Pitch angle of 0 arcmin, a HRMA Yaw angle of 0 arcmin, and a split event threshold of 13 adu. Events within the entire CCD were considered.

Table 6.9: Effective Area vs. Energy for CCD S3

sided CCD's improves significantly with the exclusion of grades.

A possible astrophysical observation in which this effect may be exploited is ACIS imaging of a bright source with the BI chip. For bright sources imaged on a BI chip it may be desirable to sacrifice source counts for spectral resolution by selecting only single events.

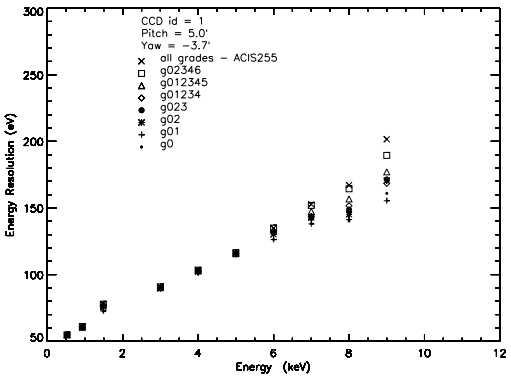

Figure 6.3: Energy Resolution (FWHM) vs. Energy for ACIS CCD I1 calculated for grade selections of g0, g01, g012, g0123, g01234, g012345, g02346, all grades - ACIS255

Energy	Energy Resolution							
	g0	g01	g012	g0123	g01234	g012345	g02346	all - ACIS(255)
keV	eV	eV	eV	eV	eV	eV	eV	eV
3	89.40	89.86	90.10	90.08	89.78	90.03	90.59	90.19
4	100.80	101.57	103.14	103.17	103.00	102.81	103.59	103.67
5	115.21	114.78	115.44	115.92	116.01	116.19	116.50	116.52
6	126.29	126.06	129.75	130.70	132.07	133.08	134.67	134.44
7	137.47	138.59	141.74	142.48	143.12	146.60	151.75	151.84
8	139.43	141.91	146.13	148.93	152.01	154.79	164.02	165.79
9	158.36	154.01	165.58	167.14	168.19	175.50	188.22	196.76

The energy resolution (FWHM) values listed in this table apply for **CCD ID = 1**, a HRMA Pitch angle of 5 arcmin, a HRMA Yaw angle of -3.7 arcmin, and a split event threshold of 13 adu. Events within the entire CCD were considered.

Table 6.11: Energy Resolution vs. Energy for CCD I1

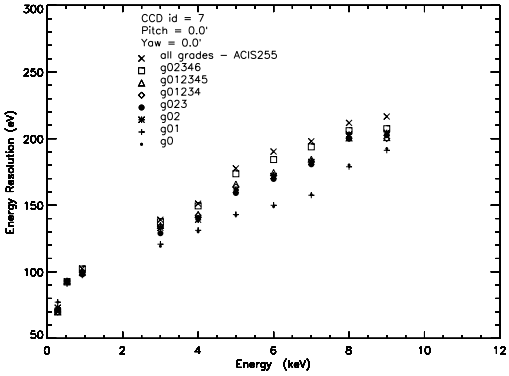

Figure 6.4: Energy Resolution (FWHM) vs. Energy for ACIS CCD S3 calculated for grade selections of g0, g01, g02, g023, g01234, g012345, g02346, all grades - ACIS255

Energy	Energy Resolution							
	g0	g01	g02	g023	g01234	g012345	g02346	all - ACIS(255)
keV	eV	eV	eV	eV	eV	eV	eV	eV
0.277	77.18	77.22	73.07	71.20	69.84	69.89	70.07	69.96
0.525	90.86	90.86	92.83	93.11	93.12	93.20	92.34	92.70
1.4867	98.11	97.41	99.14	98.0	99.66	99.93	102.10	102.43
3	119.18	120.74	133.01	128.95	133.87	134.82	137.55	139.11
4	130.11	131.13	139.07	140.48	142.43	143.16	149.48	151.17
5	142.36	142.98	161.41	159.14	163.89	165.92	173.58	177.65
6	148.95	149.94	171.94	169.68	172.56	174.57	184.27	190.27
7	157.89	157.48	182.49	180.67	183.12	184.56	193.79	197.96
8	180.15	178.86	203.08	200.06	200.22	200.50	205.97	211.79
9	192.39	191.20	204.37	202.54	200.05	200.75	207.44	216.57

The energy resolution (FWHM) values listed in this table apply for **CCD ID = 7**, a HRMA Pitch angle of 0 arcmin, a HRMA Yaw angle of 0 arcmin, and a split event threshold of 13 adu. Events within the entire CCD were considered.

Table 6.12: Energy Resolution vs. Energy for CCD S3

6.2.5 Effective Area and Energy Resolution vs. Split Event Threshold

The HRMA/ACIS effective area and energy resolution were also evaluated for split event thresholds of 5 to 15 adu in steps of 2 adu.

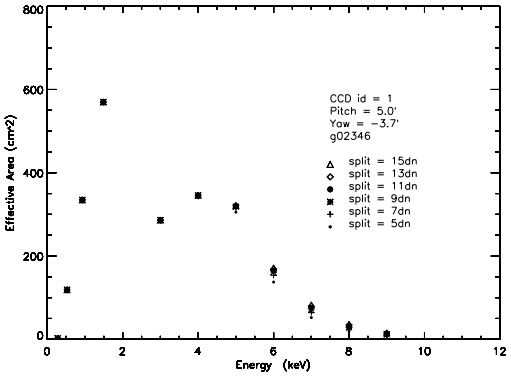

Figure 6.5: Effective Area vs. Energy for ACIS CCD I1 calculated for split event thresholds of 5, 7, 9, 11, 13 and 15 ADU

Energy	Effective Area					
	5adu	7adu	9adu	11adu	13adu	15adu
keV	cm^2	cm^2	cm^2	cm^2	cm^2	cm^2
0.277	2.37	2.38	2.38	2.38	2.38	2.38
0.525	118.42	118.84	118.92	118.90	118.87	118.88
0.93	334.65	334.73	334.84	334.80	334.75	334.78
1.4867	569.80	570.06	570.10	570.06	570.06	570.03
3	284.07	286.06	286.15	286.31	286.28	286.3
4	339.75	344.87	345.65	345.87	345.91	346.14
5	305.37	315.73	318.24	319.62	320.80	321.60
6	137.45	153.44	161.07	165.56	168.88	171.71
7	52.08	63.97	71.07	75.96	79.82	82.86
8	19.66	25.06	28.67	31.63	34.23	36.31
9	8.12	10.19	11.75	13.13	14.44	15.63

The effective area values listed in this table apply for **CCD ID = 1**, a HRMA Pitch angle of 5 arcmin, a HRMA Yaw angle of -3.7 arcmin, and grade selection of g02346. Events within the entire CCD were considered.

Table 6.13: Effective Area vs. Split Threshold for CCD I1

Figure 6.5 and figure 6.6 show the dependence of effective area with split event threshold for ACIS CCD's I1 and S3. Tabular versions of the data are listed in Tables 6.13 and 6.14. Figures 6.7 and 6.8 show the dependence of energy resolution with split event threshold for ACIS CCD's I1 and S3. Tabular versions of the data are listed in Tables 6.15 and 6.16.

These results indicate that the HRMA/ACIS effective area and energy resolution do not vary considerably with split event threshold for FI CCD's, whereas the BI chip performance is significantly different, showing a significant dependence on split event threshold.

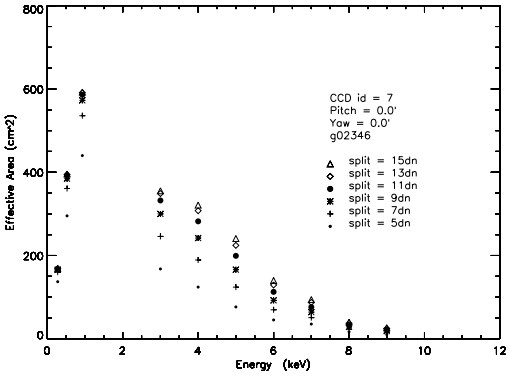

Figure 6.6: Effective Area vs. Energy for ACIS CCD S3 calculated for split event thresholds of 5, 7, 9, 11, 13 and 15 ADU

Energy	Effective Area					
	5adu	7adu	9adu	11adu	13adu	15adu
keV	cm^2	cm^2	cm^2	cm^2	cm^2	cm^2
0.277	137.02	159.79	165.75	167.60	168.43	169.10
0.525	295.19	360.90	384.35	391.97	394.43	395.79
0.93	439.99	535.67	572.61	586.07	591.09	592.62
3	167.70	245.80	299.84	332.17	348.93	355.37
4	124.12	189.12	241.82	282.05	307.53	321.12
5	76.47	124.05	165.86	199.18	224.27	240.84
6	45.15	69.54	92.15	112.64	129.18	140.04
7	35.28	50.68	63.98	76.14	87.31	94.09
8	16.70	22.91	28.42	33.20	37.13	39.94
9	10.29	14.86	18.51	21.87	24.54	26.58

The effective area values listed in this table apply for **CCD ID = 7**, a HRMA Pitch angle of 0 arcmin, a HRMA Yaw angle of 0 arcmin, and grade selection of g02346. Events within the entire CCD were considered.

Table 6.14: Effective Area vs. Split Threshold for CCD S3

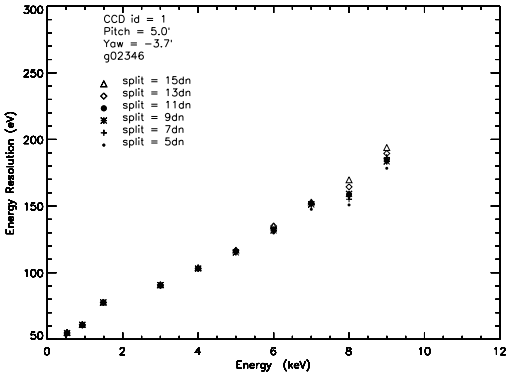

Figure 6.7: Energy Resolution (FWHM) vs. Energy for ACIS CCD I1 calculated for split event thresholds of 5, 7, 9, 11, 13 and 15 ADU

Energy	Energy Resolution					
	5adu	7adu	9adu	11adu	13adu	15adu
keV	eV	eV	eV	eV	eV	eV
0.277	45.97	46.30	44.86	45.33	45.68	44.85
0.525	55.59	55.42	54.64	54.64	54.73	55.19
0.93	60.38	60.25	60.83	60.58	60.98	61.22
1.4867	77.29	77.43	77.61	77.57	77.79	77.92
3	91.21	90.05	90.60	90.25	91.82	91.00
4	103.57	103.24	102.99	103.16	103.27	103.87
5	116.07	115.49	115.20	116.24	116.43	117.01
6	129.83	131.17	131.70	132.58	134.95	135.17
7	147.54	151.02	151.19	152.15	151.91	153.10
8	150.85	155.08	159.14	158.46	164.41	169.73
9	178.35	186.48	183.48	184.22	189.48	193.95

The energy resolution values listed in this table apply for **CCD ID = 1**, a HRMA Pitch angle of 5 arcmin, a HRMA Yaw angle of -3.7 arcmin, and grade selection of g02346. Events within the entire CCD were considered.

Table 6.15: Energy Resolution vs. Split Threshold for CCD I1

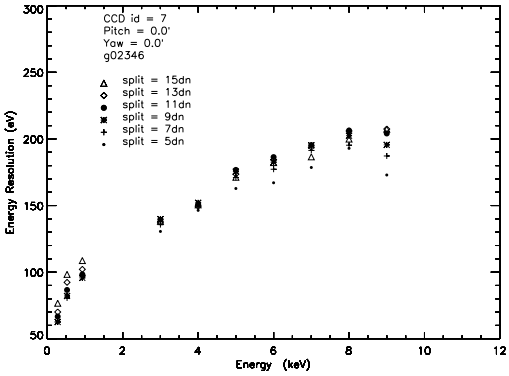

Figure 6.8: Energy Resolution (FWHM) vs. Energy for ACIS CCD S3 calculated for split event thresholds of 5, 7, 9, 11, 13 and 15 ADU

Energy	Energy Resolution					
	5adu	7adu	9adu	11adu	13adu	15adu
keV	eV	eV	eV	eV	eV	eV
0.277	43.35	62.63	62.57	66.68	70.07	76.64
0.525	83.09	80.60	82.10	86.62	92.34	98.31
0.93	99.03	96.89	95.71	98.30	102.10	108.68
3	130.55	135.66	139.76	139.35	137.55	138.21
4	146.38	150.33	152.01	150.78	149.48	150.50
5	162.78	171.01	175.40	176.75	173.58	171.24
6	167.08	177.24	182.56	186.36	184.27	182.22
7	178.56	191.37	195.14	195.39	193.79	186.53
8	192.94	195.28	202.41	206.32	205.97	199.89
9	172.92	187.21	195.52	204.09	207.44	207.28

The energy resolution values listed in this table apply for **CCD ID = 7**, a HRMA Pitch angle of 0 arcmin, a HRMA Yaw angle of 0 arcmin, and grade selection of g02346. Events within the entire CCD were considered.

Table 6.16: Energy Resolution vs. Split Threshold for CCD S3

6.2.6 Scientific Applications

We provide examples of the use of these results on effective area and energy resolution in the design of specific observations.

6.2.6.1 Case Study 1 : ACIS/HEG Observation of Fe-K_α line profile in the Seyfert Galaxy NGC 4151

The improved energy resolution of ACIS/HEG at 6.4 keV (compared to previously attainable ASCA SIS resolution of about 180 eV) is needed to identify the presence of gravitational and Doppler effects and verify whether or not multiple reprocessors contribute to the broadening of the Fe-K_α line. For grating observations the intrinsic energy resolution of a CCD is mostly used to separate spectral orders. For this case study we have sacrificed intrinsic spectral resolution for increased effective area by excluding only ACIS grade 255 events resulting in an effective area at 6.4kev of about 30 cm^2. We considered a model for the incident spectrum of NGC 4151 in the vicinity of the Fe line based on ASCA observations, (see Table 6.17) and convolved it with the expected grating energy resolution of about 25 eV at 6.4 keV and added Poisson noise. The expected dependence of the effective area of the ACIS/HEG combination between 5 and 7 keV with grade is shown in figure 6.9. In figure 6.10a we show a simulation of the incident spectrum of NGC 4151 in the vicinity of the Fe-Kα line. By excluding only grade 255 events in the analysis of the ACIS/HEG observation of NGC4151 we maximize the effective area without compromizing the spectral resolution. Figure 6.10b shows a simulation of an ACIS/HEG observation of NGC 4151 analyzed with different grade selection schemes.

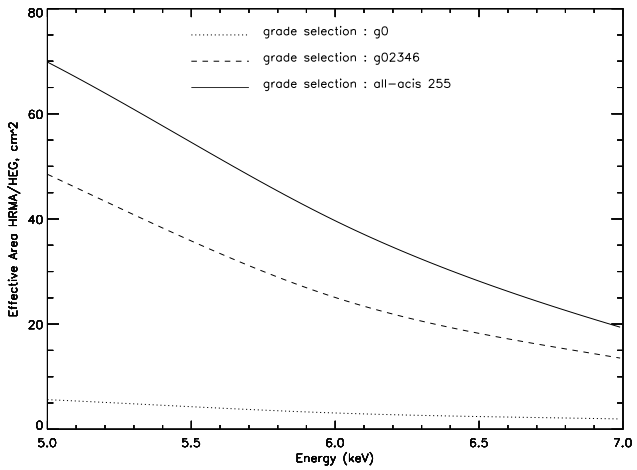

Figure 6.9: Expected dependence of the effective area of the ACIS/HEG combination between 5 and 7 keV with grade selection.

Case Study 1: NGC4151

Target	z	$N_H(Gal)$ $cm^{-2}\times10^{20}$	$logL_x^a$ erg s^{-1}	Γ	$W_{K\alpha}$ eV	i
NGC 4151	0.003	2.2	42.97	1.52	290	21

[a] Logarithm of X-ray luminosity from 2-10keV

Table 6.17: Spectral Parameters of NGC 4151

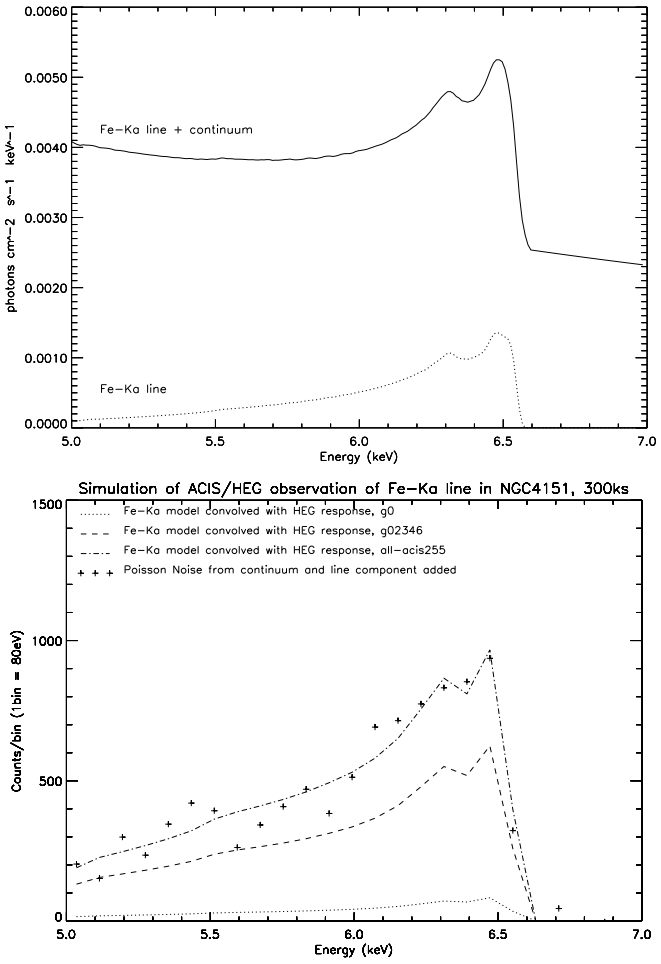

Figure 6.10: (a) Simulation of the incident spectrum of NGC 4151 in the vicinity of the Fe-Kα line. (b) Simulation of an ACIS/HEG observation of NGC 4151 analyzed with different grade selection schemes.

6.2.6.2 Case Study 2 : ACIS-BI Observation of a Warm Absorber

We investigated whether an appropriate selection of grades and split threshold could lead to improvements in resolving absorption features in quasar spectra. We considered an ionizing incident quasar continuum transmitted through a warm absorber. The warm absorber model used in this study consists of a simple power law spectrum incident on the absorber with a photon index $\alpha_\nu = 1.2$. We chose an absorber with an ionization parameter of 0.3, a column density of $5.\times10^{22}$ cm^{-2} and a total hydrogen density of $8.\times10^{3}$ cm^{-3}. We convolved the simulated absorbed quasar spectrum with two different spectral resolution functions. The first resolution function was created using the grade selection g0 and a split threshold of 6 ADU. The second spectral resolution function was created using the grade selection g02346 and a split threshold of 13 ADU. A slight improvement in resolving the absorption features is achieved when selecting only single events and low split thresholds, with the loss however of considerable effective area. Figure 6.11 shows the modeled spectrum of an absorbed quasar convolved with the two different spectral resolution functions mentioned above.

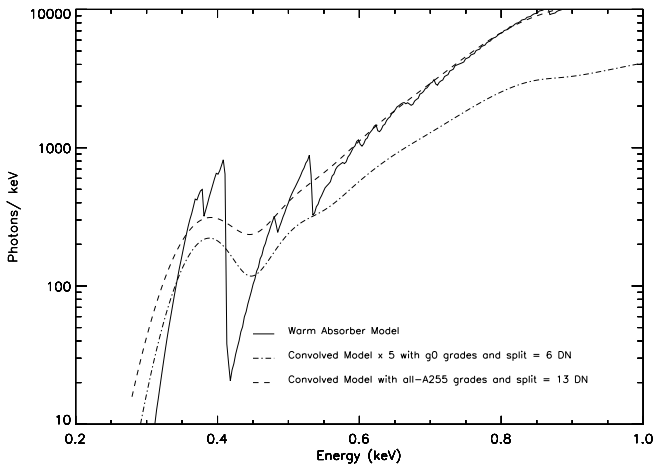

Figure 6.11: By selecting only single events and low split thresholds a slight improvement is achieved in resolving the absorption features in an absorbed quasar spectrum.

6.3 ACIS/HRMA Point Spread Function

In order to recover an accurate representation of the sky sampled by AXAF using ACIS, we must understand how the combined HRMA + ACIS spatially redistributes the incoming photons. This spatial redistribution function (the so-called point spread function, or PSF) is a combination of the HRMA PSF and the ACIS instrument's pixelization and detection efficiency. The HRMA + ACIS combined PSF is a function of energy (or input spectrum), off-axis angle, subpixel position, count rate (i.e. pileup), grade selection, ACIS operating mode, and perhaps other quantities.

Given the complexity of this problem, the ACIS team has concentrated on the issues specific to ACIS, attempting to assess how ACIS modifies the HRMA PSF. We must, then, rely on the efforts of the Mission Support Team to define the HRMA PSF and stay in close communication with them, reporting our ACIS modeling and data analysis results and receiving updated HRMA model output. We acknowledge that ACIS and ACIS-2C data from XRCF may be useful in refining the HRMA model but we do not propose to take this as the primary goal of our data analysis.

Clearly the goal of PSF data analysis and modeling is to generate a model that predicts the on-orbit HRMA + ACIS PSF. We will use the XRCF calibration data to refine and improve our models of ACIS, then rely on MST's on-orbit HRMA model to predict HRMA + ACIS on-orbit PSFs. We will strive to create a PSF generator, an engine that produces a PSF for a point source falling at any position on any ACIS pixel, given the aimpoint (to determine off-axis angle), the subpixel position of the point source, the source spectrum and energy bandwidth, the count rate, and a list of acceptable event grades. The format of this model PSF should be the same as the dataset being modeled, namely an event list. The ideal system would allow a user to assemble a set of point sources to approximate an extended source.

6.3.1 XRCF Measurements of ACIS/HRMA PSF

Each XRCF Phase H PSF observation consists of photon-counting-mode data from an approximately monochromatic source. The FAM was positioned so that the bulk of the PSF is contained within the boundaries of one ACIS amplifier, so that most PSF photons have the same gain. The system was fully cooled and focused before PSF measurements were made. The PSF was measured at several energies, both on-axis and at several off-axis locations (thus the PSF dataset involves all ACIS CCDs). The inner core of the PSF was sampled using a low flux rate (the "PI" tests); separate tests were made to populate the PSF wings (the "PW" tests) in a reasonable amount of time by increasing the flux. These PW tests sacrifice information about the PSF core due to heavy pile-up.

It is useful to note that other XRCF tests can be used in PSF analysis; the count rate linearity tests and some focusing measurements also serve as PSF samples. In fact, the lowest-flux count rate linearity tests represent the best available PSF-core measurements,

as they suffer the least pile-up of the entire dataset. A summary of all XRCF PSF data is presented in Section 6.1.4.

6.3.2 The ACIS Model

Modeling the ACIS device consists of estimating the spatially-dependent spectral transmission function of the ACIS UV/optical blocking filters (OBFs) and simulating the output of the CCD detectors. The OBFs are described above (Sec. 5.1). The CCDs are simulated using a Monte Carlo technique and assuming a slab model of the devices. Details of the basic model used at PSU are described in Section 7.1.

As mentioned above, the SAOSAC HRMA model serves as the basis for our PSF analysis; thus we are dependent on the fidelity of this model for comparison to XRCF data and for predicting on-orbit results. We chose to use SAOSAC for the PSF simulations because it is the most comprehensive model of the HRMA; the subtle features and interesting azimuthal structure of the PSF is not modeled by MARX. The PSU CCD simulator "*acis_sim*" (described in detail in Section 7.1) was designed to interface with MARX to exploit the excellent modeling capabilities of the MARX package. We chose to preserve this design for the PSF simulations; thus we use MARX to read the SAOSAC rayfiles and propagate the rays to the surface of the ACIS chips, relying on MARX to supply the appropriate geometric transformations and to account for the tilts and spacing of the chips in the ACIS camera. The *acis_sim* program uses the ray positions at the chip surfaces and the direction cosines to project the rays to their interaction points in each CCD. It generates event lists, which have been processed in this analysis with the Event Browser package (see Section 7.2).

6.3.3 Tuning Parameters

There are several quantities used in the simulators that must be tuned in order to get the simulations to reproduce adequately the XRCF PSF data.

- **Focus** – can be adjusted to match the data fairly well just by examining the rays (we used the "dataset_2d" tool, part of the TARA package, and the MARX output files "xpixel.dat" and "ypixel.dat"), since this parameter is controlled by MARX.
- **Flux** – tuning the flux is crucial for reproducing XRCF data, since this is the way to reproduce and explore pile-up. The current analysis suffers from a lack of flux tuning capability, but this will hopefully be available in the next MARX release. For now, we have forced the simulator to the idealized state of exactly one photon per frame.
- **FAM orientation (CHIPX & CHIPY offsets, rotation)** – we have implemented the ability to adjust the position of the PSF in CHIPX and CHIPY, but have not yet explored the possibility of rotation.

- **Others?** – As we tune the above parameters and improve the simulator, we may discover other parameters whose tuning allows us to reproduce the data more accurately. We remain alert for such potential adjustments.

6.3.4 Limitations

Our ability to reproduce the data is limited by several factors, many of which will soon be ameliorated. The current SAOSAC rays for XRCF ACIS data presume that the source is at a finite distance, but to achieve the best possible simulated results they also need to account for the finite size of the source (the rays currently assume a point-like source). These improved rays should be available soon. The SAOSAC rays are also monochromatic, whereas the sources are not. This is probably not a major concern for the PSF simulations at present. As mentioned above, our strongest current limitation is the inability to adjust the source flux. We anticipate that the next version of MARX will relieve this constraint. The *acis_sim* program also has a long list of planned revisions (see Section 7.1), some of which may affect the simulated PSF. The most critical change to be made in the transition from XRCF data to on-orbit predictions is the inclusion of aspect errors. Existing simulator components give us the ability to randomize photon positions by a given amount, but no more detailed prescription of aspect errors has been attempted.

6.3.4.1 Example: H-IAI-CR-1.001

As a test case, we chose the count rate linearity test H-IAI-CR-1.001, sampling the on-axis in-focus PSF at Al Kα (1.486 keV). This test is purported by the CMDB to have the lowest flux of any Phase H ACIS test; since we are unable to simulate pile-up at present, this test is the best comparitor due to its minimal pile-up. Even so, some pile-up is present, as illustrated by Figure 6.12. At Al Kα, most of the photons produce single-pixel events, so pile-up acts to suppress mainly the height of the central pixel in the PSF peak. The height of this central pixel is the main difference between the simulated and real PSF for this test, as shown below. So even modest pile-up acts to degrade the spatial resolution of AXAF – a fact that should not be lost by the user in the rush to worry about spectral degradation due to pile-up.

6.3.4.2 Rays and Events

The first step in the simulation is to pass SAOSAC rays (generated and supplied for each XRCF test by Diab Jerius of the Mission Support Team) through the MARX package, which propagates them to the appropriate ACIS focus via two special parameters that configure MARX for XRCF use (supplied by Michael Wise): SourceDistance = 537.583 and DetOffsetX = -194.872. These parameters serve to inform MARX that the source is at

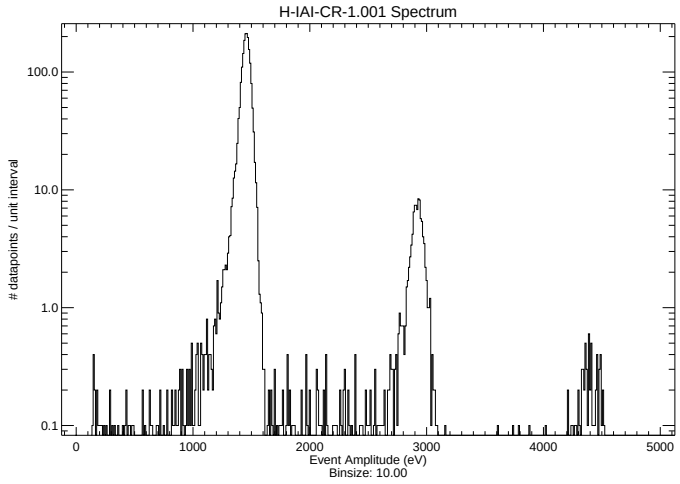

Figure 6.12: The spectrum of the PSF spot in the XRCF test H-IAI-CR-1.001. No grade filtering was applied, in an effort to illustrate the pile-up present in this test. The data were spatially filtered to include only a 10×10 pixel region around the PSF centroid, so spurious cosmic ray events do not contribute strongly to this spectrum. A light curve shows the ACIS count rate to be approximately 2.5 counts/sec. Even at such a modest flux (by XRCF standards), the 2-photon and 3-photon pile-up peaks are discernable. This spectrum also shows that the source spectrum is quite clean, so this example analysis was carried out with no grade or spectral filtering.

a finite distance and that ACIS is not at the default focus used by the rays. These supplied values were not adjusted in this analysis.

The virtual photons generated in this process were then allowed to interact with the CCD via the *acis_sim* program. Before we compare the simulated CCD output to the XRCF data, a useful aside is to compare the rays incident upon the CCD to the set of events generated by the interaction of those rays with the CCD. This illustrates the degradation of the PSF by convolving it with the quantized detector picture elements.

Figure 6.13 shows the SAOSAC rays configured to match the geometry of the XRCF for test H-IAI-CR-1.001. In order to facilitate comparison between the rays and the simulated CCD events, Figure 6.14 and Figure 6.15 show the rays grouped into 1×1 pixel bins beside the CCD simulator output. Because Al Kα photons often produce single-pixel events, the simulated output very closely resembles the binned rays. This is not to be expected at higher energies, where split events are more prevalent. The "lego" plots (Figure 6.15) better illustrate the PSF broadening due to pixelization.

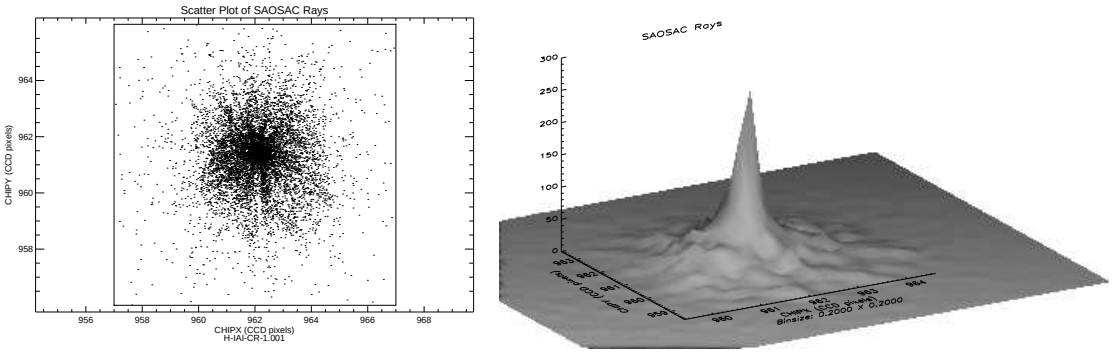

Figure 6.13: The left-hand panel shows a scatter plot of the rays for test H-IAI-CR-1.001. The right-hand panel shows the same rayfile, displayed as a surface and binned arbitrarily at 0.2 pixels.

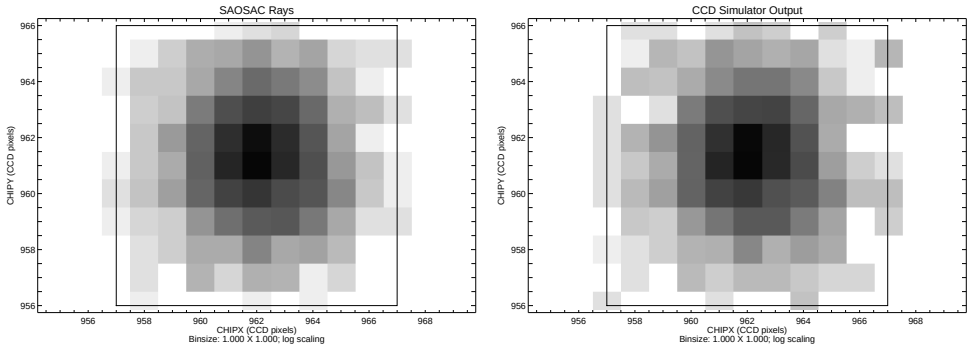

Figure 6.14: The left-hand panel shows an image of the rays for test H-IAI-CR-1.001, grouped in 1×1 pixel bins. The right-hand panel shows the simulated CCD events binned similarly.

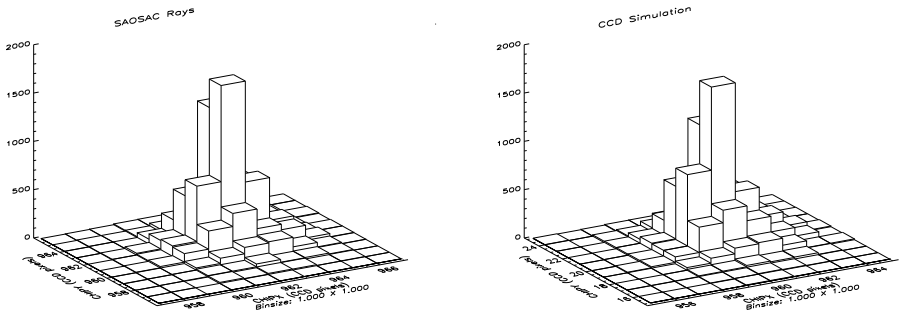

Figure 6.15: The left-hand panel shows a 2-dimensional histogram ("lego plot") of the rays for test H-IAI-CR-1.001, grouped in 1×1 pixel bins. The right-hand panel shows the simulated CCD events binned similarly.

6.3.5 PSF Simulation Metrics

In order to test the models, we must find physically meaningful and appropriate metrics to characterize both the simulated and actual event lists. As mentioned above, the HRMA + ACIS PSF depends on the input photon energy, the subpixel position of the source, the grade selection scheme used (which implies assumptions regarding the best split event threshold and gain conversion for each of 40 CCD amplifiers), the count rate at ACIS and the degree of pileup, and possibly other quantities.

For on-axis sources, some simple PSF core metrics are the centroid and its second moments, cuts through the centroid pixel, and fits to those cuts. The PSF wings can be characterized by the radial surface brightness and encircled energy, but these quantities yield no azimuthal information. The PSFs of off-axis sources lose the simple centrally-peaked geometry enjoyed by on-axis sources (see the MST Phase 1 report). Other, more complicated metrics must be employed here, such as width of the pincushion caustics and major and minor axes of the extended lobes. Again we must work closely with MST to characterize these features, generating a common set of metrics to facilitate comparison.

"Standard" analysis products like radial histograms and encircled energies must be treated with care when the bulk of the PSF is contained in a single pixel. Most algorithms to calculate these quantities yield inaccurate results when the PSF is undersampled, as is the case with ACIS at XRCF. Since the point of this test was to explore the details of the PSF core, we will use comparitors that are more appropriate for this region.

The simplest and most obvious metric is an image. Figure 6.16 shows a greyscale image of the data PSF core and one of the simulation, on the same scale. The number of events is the same (19428). The simulation was tuned by moving the "virtual FAM," i.e. by adjusting the subpixel position of the entire rayfile. The offsets used here are (chipx, chipy) = (+0.1, -0.3). Since the data are affected by pile-up but the simulation is not, the number of events in the central pixel is not a good metric. Instead, we used the number of events in the neighboring pixels, examining all the neighbors in a 5×5 pixel region around the central pixel.

By examining the difference image (Figure 6.17), we can get a sense for the accuracy of the offsets, although we must keep in mind the pile-up and other factors, such as the pointlike nature of the current rayfile and the fact that we have not attempted to apply any rotation. This difference image implies that the offsets might need further adjusting – either a slight rotation or a smaller offset in CHIPX.

Figure 6.18 illustrates another way to view the 2-dimensional datasets, as lego plots. These help illustrate the fact that the central pixel in the simulation has more events than in the data (because of pile-up) and the neighboring pixel at (962,962) has a similar number of extra events – a fact that will require further investigation.

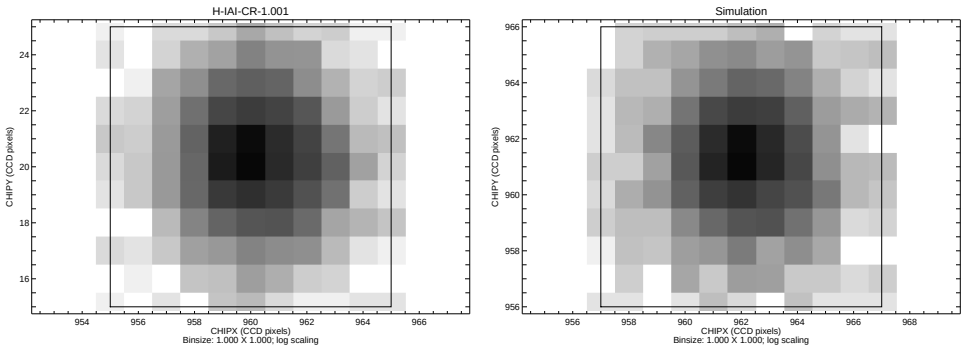

Figure 6.16: The left image shows the data for test H-IAI-CR-1.001; the right shows the simulation.

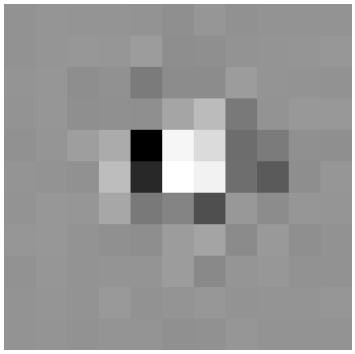

Figure 6.17: Difference image, simulation - data. The image scaling is between the minimum and maximum values in the difference image (black = -349 counts, white = +254 counts). There are 19428 counts in each dataset. The PSF is centered on the white pixel, where the simulation has more counts because it is unaffected by pile-up.

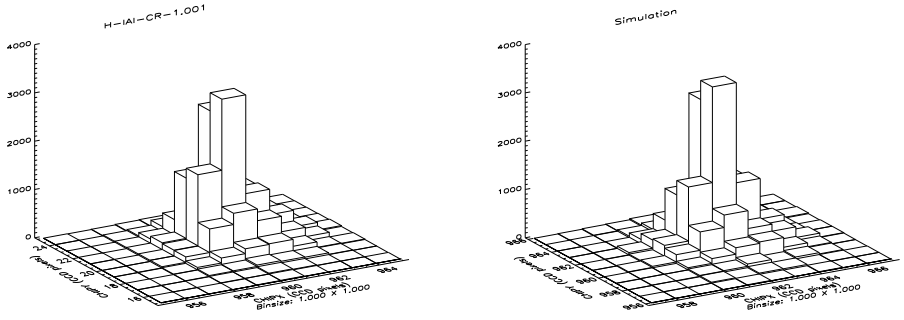

Figure 6.18: The left 2-dimensional histogram ("lego plot") shows the data for test H-IAI-CR-1.001; the right shows the simulation.

One-dimensional metrics are also useful, supplying a simpler means of comparing the datasets (with, of course, a corresponding loss of information over 2-dimensional methods). These are illustrated in Figure 6.19, showing vertical and horizontal cuts through the centroids of both the data and the simulation, and Figure 6.20, showing x and y marginal sums.

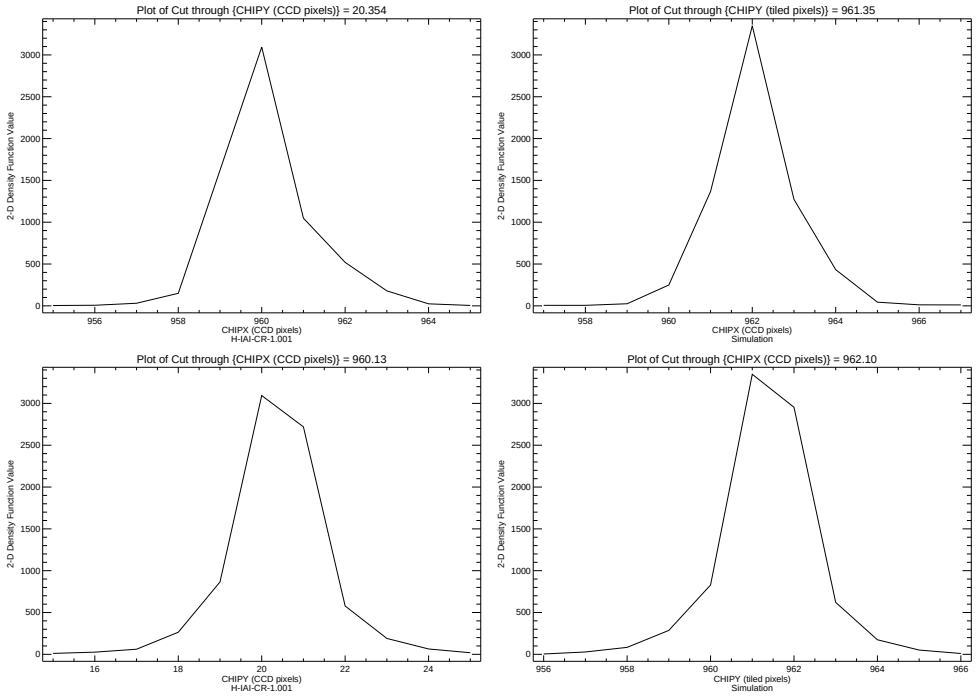

Figure 6.19: Horizontal and vertical cuts through the centroid of the PSF from the data (left) and the simulation (right).

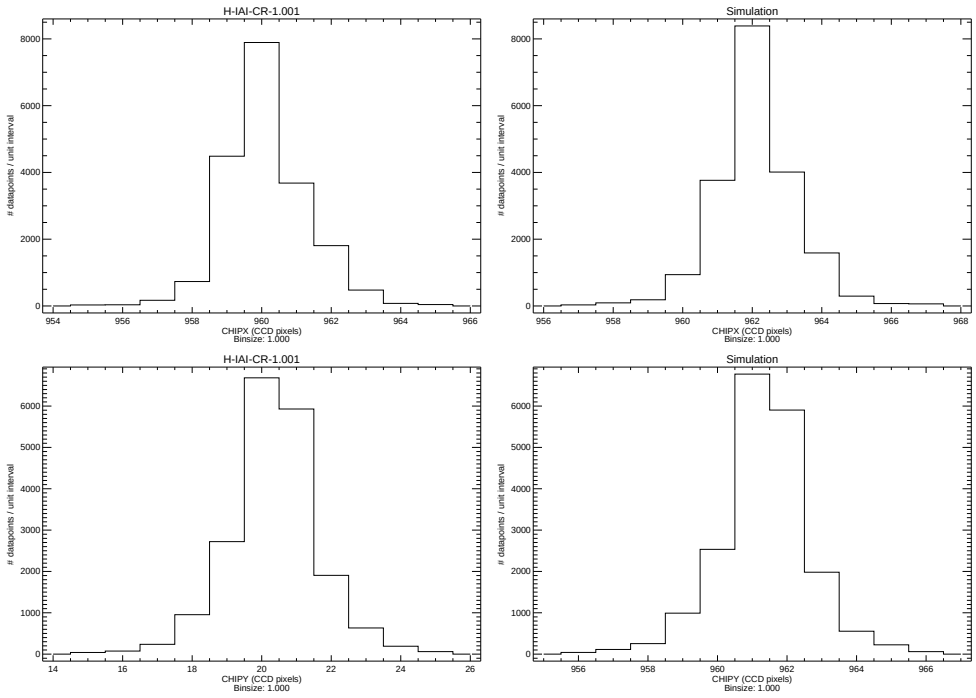

Figure 6.20: Marginal sums of the PSF from the data (left) and the simulation (right).

6.3.6 On-Orbit Simulations

It is important to keep in mind that these comparisons of the model suite to XRCF data serves only to refine and validate these models – their real purpose is to predict the behavior of AXAF on-orbit. Although we expect the CCDs to behave on-orbit very much the same as they did at XRCF, the HRMA will be somewhat different. SAOSAC already produces on-orbit rays so we can predict the on-orbit performance of the HRMA-ACIS system, but we must be careful to include the concept of spacecraft dither and the resulting aspect solution. Real events from ACIS on-orbit will not be delivered to the user in integer chip coordinates – rather they will have an aspect solution applied, with necessary errors, and be returned in real-valued "sky" coordinates. This added complexity will render some of the metrics used for XRCF comparison irrelevant and we must be careful to anticipate important changes to our assumptions. For example, the XRCF PSF is clearly undersampled by the ACIS pixels, at least marginally. Once aspect error is added, however, the PSF will broaden and it is likely that ACIS will achieve critical sampling of this more realistic PSF.

6.4 Focal plane geometry

In order to compute a joint HRMA-ACIS simulation we must be able to relate the rays produced by the HRMA simulators and propagate them back to the point of contact with the ACIS CCD detectors. The problem we want to solve consists of the following: given a photon emerging from the HRMA from a given direction, we want to determine which CCD the photon will hit and the pixel coordinates of the event. Our input information is the direction of the incoming photons (in terms of three direction cosines) from an arbitrary point outside the mirror. This information will be provided by the ASC program SAOSAC (see the XRCF Phase 1 report). The problem consists of finding the (unique) intersection of the ray trajectory with the CCD surface, taking into account the tilt of the latter with respect to the HRMA optical axis. The MARX program, provided by the ASC, is a convenient tool which includes this calculation.

6.4.1 CCD geometry

We first summarize the coordinate systems used for formulating the ray tracing problem. For a more comprehensive description of the various coordinate systems of the mission, we refer to the "ASC Coordinate System".

The coordinate systems we will use below are:

- Chip Physical Coordinates (CPC), which give the physical position of an event on the active surface of the CCD: X_{CPC}, Y_{CPC}, Z_{CPC}, in mm. The Y_{CPC}, Z_{CPC} axes describe the plane of the CCD, with origin in its lower-left corner. The X_{CPC} axis completes a right-handed set;

- Local Science Instrument (LSI). This system is fixed for each instrument in the SIM. The origin is in the instrument, the +X axis runs toward the mirror aperture, the +Z axis coincides with the upward translation direction of the instrument table. The Y axis completes a right-handed system.

Note that, since the output from SAOSAC is provided in the XRCF coordinate system, a transformation of the event coordinates into LSI will be necessary.

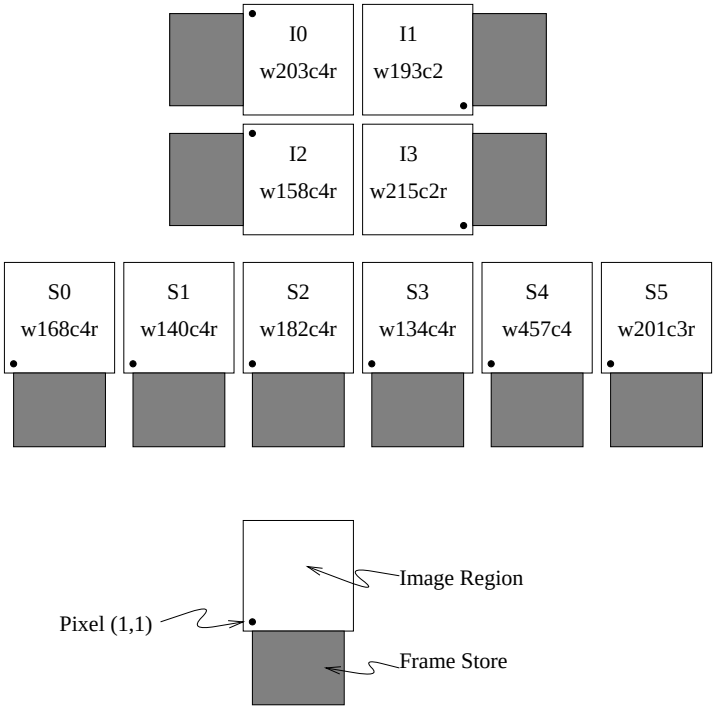

Figure 6.21: Locations and orientations of chips chosen for ACIS flight focal plane. (Figure courtesy of K. Glotfelty, ASC.)

While the LSI is unique for the instrument, every CCD in both ACIS-I and ACIS-S has its own CPC system, where the plane of the CCD defines the (Y_{CPC}, Z_{CPC}) plane. This is illustrated in Figure 3 of the "ASC Coordinate System". To transform from CPC to LSI we need a rotation and a translation, so that a generic point r on the plane is described in the LSI system by:

$$\mathbf{r} = \mathbf{p_0} + Y_{CPC}\mathbf{e_Y} + Z_{CPC}\mathbf{e_Z} \tag{6.2}$$

where $\mathbf{p_0}$ is the origin of the CPC coordinates (the lower-left corner of the chip being refered to; this is shown as pixel (1,1) in Fig. 6.21.) and $\mathbf{e}_Y$, $\mathbf{e}_Z$ are the unit vectors of the CPC Y, Z axes. The latter, as well as p_0, are determined from the coordinates of the CCD

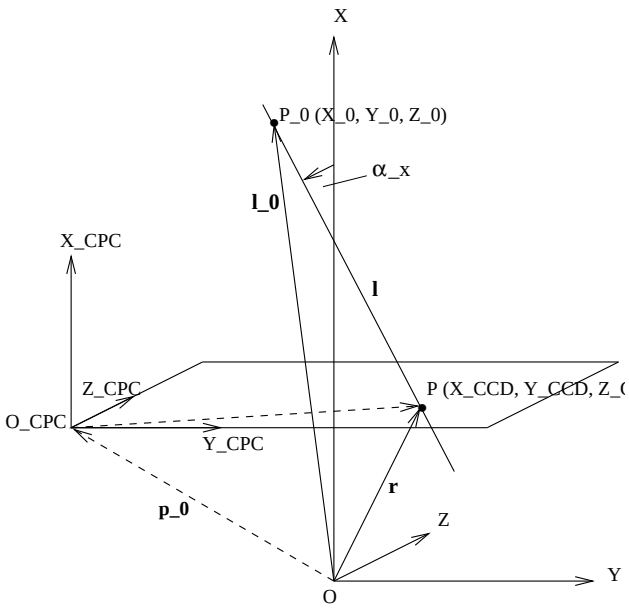

Figure 6.22: Projecting rays on ACIS. Case A: plane of the CCD orthogonal to the HRMA axis.

corners in LSI coordinates, specifically, from Eq. (15) and Table 4 of the "ASC Coordinate System".

6.4.2 Ray projection on ACIS

Lets assume the trajectory of the emergent ray is described by the following equation:

$$\mathbf{r} = \mathbf{l_0} + \mathrm{t}\mathbf{l} \tag{6.3}$$

where $\mathbf{l_0}$ is an arbitrary point on the ray trajectory with LSI coordinates (X_0, Y_0, Z_0), $\mathbf{l}$ is the ray direction (specified by the three direction cosines α_X, α_Y, α_Z), and t is a parameter which describes the position of the point on the line. Intersecting the line with the CCD translates into the geometrical problem of determining t such that the point lies on the CCD plane.

We will distinguish two cases: **A: The CCD plane is orthogonal to the HRMA axis.** Let P be the intersection of the ray with the CCD plane, and (X_{CCD}, Y_{CCD}, Z_{CCD}) its coordinates in the LSI system on the CCD. The geometry is summarized in Figure 6.22. By imposing that P lies on the line, i.e., its coordinates satisfy eq. (6.3), we derive t:

$$t = \frac{X_{CCD} - X_0}{\alpha_X} \tag{6.4}$$

and thus the position of P on the CCD:

$$Y_{CCD} = Y_0 + \frac{X_{CCD} - X_0}{\alpha_X}\alpha_Y \tag{6.5}$$

$$Z_{CCD} = Z_0 + \frac{X_{CCD} - X_0}{\alpha_X}\alpha_Z \tag{6.6}$$

One needs to know *a priori* X_{CCD}, which is just the distance of the CCD from the LSI coordinate origin (Fig. 6.22).

B: The CCD plane is tilted with respect to the HRMA axis. In this case we will use the general expression of a point on the CCD plane in LSI system, given by eq. (6.2), and impose that the point belongs to the ray trajectory, eq. (6.3). Figure 6.23 visualizes the situation.

By equating eqs. (6.2) and (6.3), we derive:

$$t\mathbf{l} = (\mathbf{p_0} - \mathbf{l_0}) + Y_{CCD}\mathbf{e_Y} + Z_{CCD}\mathbf{e_Z}. \tag{6.7}$$

We now take the dot product of both sides of the equation with the normal $\mathbf{e_X}$ of the CCD (i.e., we project the vector $t\mathbf{l}$ along the tilted X_{CCD} axis) and derive t:

$$t = \frac{(\mathbf{p_0} - \mathbf{l_0}) \cdot \mathbf{e_X}}{\mathbf{l} \cdot \mathbf{e_X}}. \tag{6.8}$$

Indeed, as Figure 6.22 shows, in the case of no tilt, $\mathbf{p_0} \cdot \mathbf{e_X} = X_{CCD}$, $\mathbf{l_0} \cdot \mathbf{e_X} = X_0$, and $\mathbf{l} \cdot \mathbf{e_X} = \alpha_X$, so that eq. (6.7) becomes eq. (6.4). To derive the coordinates of the point in the LSI system we project P on the CCD axes, i.e.,

$$Y_{CCD} = (\mathbf{r} - \mathbf{p_0}) \cdot \mathbf{e_Y} \tag{6.9}$$

$$Z_{CCD} = (\mathbf{r} - \mathbf{p_0}) \cdot \mathbf{e_Z} \tag{6.10}$$

The ASC program SAOSAC provides the necessary information about the ray trajectory, specifically the three coordinates of $\mathbf{l_0}$ and the direction cosines defining $\mathbf{l}$. Since these coordinates are in the XRCF system, we will need to do the appropriate transformation into LSI coordinates before using the above formulas.

The above algorithms were incorporated in an IDL program. The output (a FITS file) is used directly for the CCD simulator and, eventually, for comparison with the calibration data. We can use the complete simulation system (SAO-sac + ray projection + CCD simulator) to estimate the orientation of the ACIS focal plane in XRCF coordinates, by fixing the chip spacing and tilts and other measured geometric quantities of the instrument/FAM combination, then comparing the photon positions inferred from the simulation with actual XRCF data. We can also use this system to obtain better estimates of the spacing and tilt of individual chips in the ACIS focal plane, iterating between XRCF data and the models

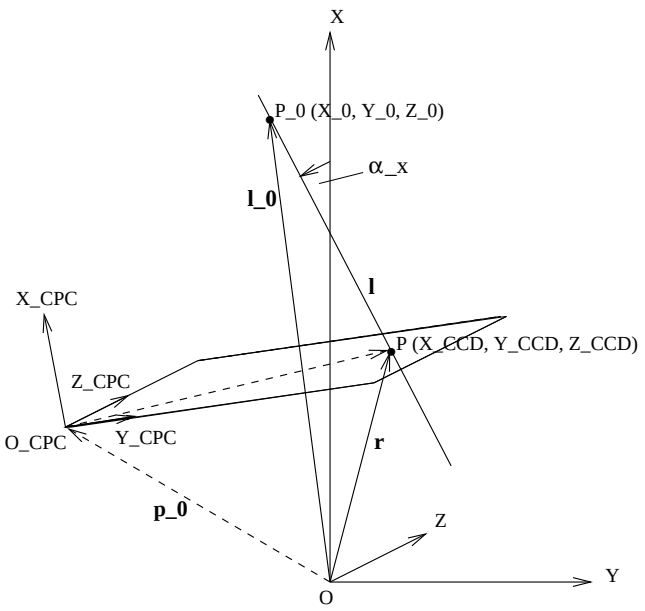

Figure 6.23: Projecting rays on ACIS. Case B: plane of the CCD tilted with respect to the HRMA axis.

to improve our picture of ACIS geometry. Ultimately, we will use this exercise to guide us in designing the most effective on-orbit tests to fix the geometry of ACIS in the spacecraft coordinate system, to be performed in the early calibration phase of on-orbit operations.

6.5 Sub-pixel Photon Position Detection

The FWHM of the HRMA PSF is roughly 0.5 arcsec, the same size as a pixel in ACIS. In order to reconstruct the PSF and obtain source positions accurate to less than 0.5 arcsec, we would like to locate individual photon interaction sites on a subpixel scale. We have explored this goal by using the intrinsically larger event splitting tendencies of back-illuminated (BI) CCDs at moderate (1 keV) X-ray energies.

A theoretical model ACIS BI CCD was modeled using the CCD simulator described in Chapter 7. We placed 4000 1-keV photons on a simulated ACIS BI 1024×1024 array, with the subpixel position fixed but the depth and array position random. This was done 121 times for 121 subpixel positions, mapping out a pixel in 0.1-pixel increments.

Each output image was run through an event-finding algorithm to generate a list of event energies and grades, and a histogram of the distribution of grades. Events are detected by considering a 3×3 pixel subarray centered on a bright pixel. For clarity, the pixels in this subarray are assigned numbers as given in the array below. Here, pixel number 4 is the brightest pixel in the subarray. (Note: this pixel numbering is *not* the same as used in ACIS flight or calibration event neighborhood coding.)

6	7	8
3	4	5
0	1	2

Table 6.18: Pixel numbering for grade subarrays

The grades used are defined in Table 6.19, which refers to the pixels by the numbers given above. The cryptic grades S+, P+, and Other are equivalent to the ASCA grades of the same name and refer to the few unusual events that contain diagonal pixels or don't fit into any of the other shape catagories.

event type	*constituent pixels*	*grade*	*probability maximum*
single	4	0	(0,0)
S+	4 + others	1	—
up vertical	4,7	2	(0,0.4)
down vertical	1,4	3	(0,-0.4)
left horizontal	3,4	4	(-0.4,0)
right horizontal	4,5	5	(0.4,0)
P+	4 + others	6	—
down left L	1,3,4	7	(-0.3,-0.3)
down right L	1,4,5	8	(0.3,-0.3)
up left L	3,4,7	9	(-0.3,0.3)
up right L	4,5,7	10	(0.3,0.3)
down left quad	0,1,3,4	11	(-0.4,-0.4)
down right quad	1,2,4,5	12	(0.4,-0.4)
up left quad	3,4,6,7	13	(-0.4,0.4)
up right quad	4,5,7,8	14	(0.4,0.4)
Other	4 + others	15	—

Table 6.19: Grade definitions and subpixel positions of probability maxima

Dividing the grade distribution histogram by the total number of detected events then gives a fractional grade distribution. One of these was generated for each subpixel position. Of the 16 possible grades, all but S+, P+, and Other are useful in determining event positions. These three grades were not used because there were too few events in each grade to yield a meaningful event position probability distribution (see below). Trimming these left a 13-element vector of fractional grade distribution. The normalization occurred before these grades were removed. The event-finding algorithm used an event detection threshold of 50 electrons and a split-event threshold of 20 electrons – these thresholds do affect the splitting.

We can assemble all the 13-element vectors for each subpixel position into a 13-plane-deep 3-D array, each plane representing the fractional grade distribution of a given grade

across the pixel. Examples of these planes are given in Figures 6.24 through 6.27. The peaks of the distributions are marked in the figures and given in Table 6.19 for each plane. We can treat these planes as probability distributions for each grade, showing the likelihood that a photon impinging at a certain subpixel position will yield an event of the shape (grade) being considered.

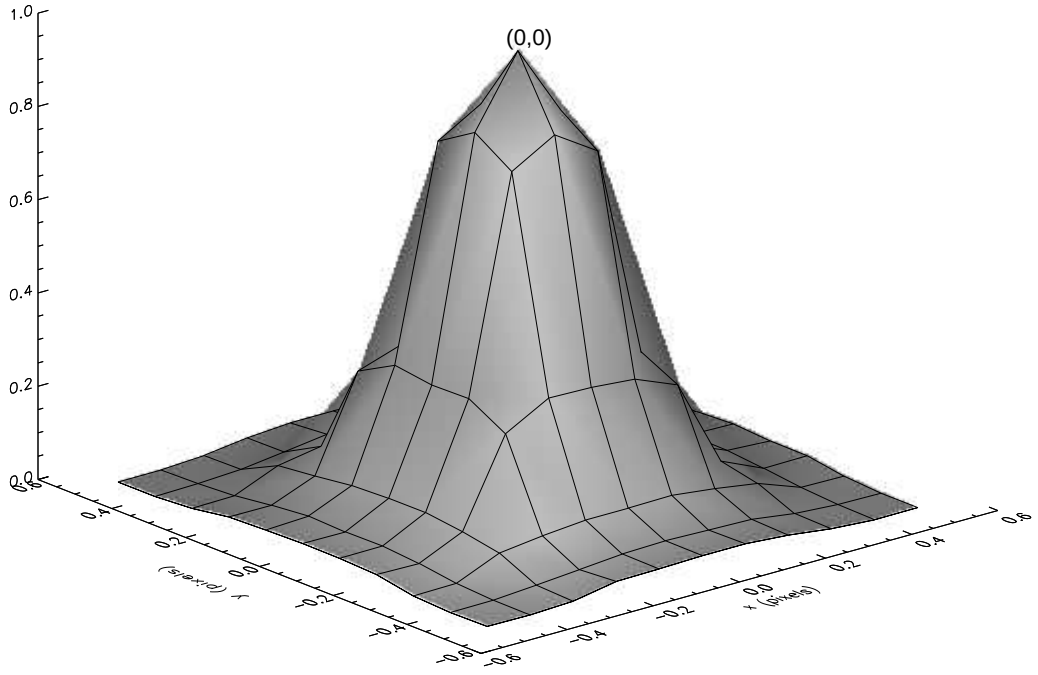

Figure 6.24: Single-pixel event position probability distribution

Note the bimodality in these distributions – the upwards single-split distribution shown in Figure 6.25, for example. Some events that occurred near the *lower* edge of the pixel were detected as *up* splits – this is because enough of the charge clouds from these events were detected in the adjacent (lower) pixel that they were detected as upward splits. This illustrates the fact that we cannot *know* in which pixel the event really occurred, we can only *assume* that it occurred in the brightest pixel, and this assumption is not always right. Note also that, by replicating these single-pixel distributions for adjacent pixels, a consistent probability distribution appears, shaped similarly to the single-pixel distribution but centered on different subpixel coordinates ((0.3,-0.3) for the L-shaped events shown in Figure 6.26, instead of (0,0) for the single-pixel events) and having somewhat different widths. This implies that, if we are given an event's grade, we have a distribution showing the likelihood that the event came from a certain subpixel position.

Returning to the simulations, we deposited 4000 photons at the same subpixel position

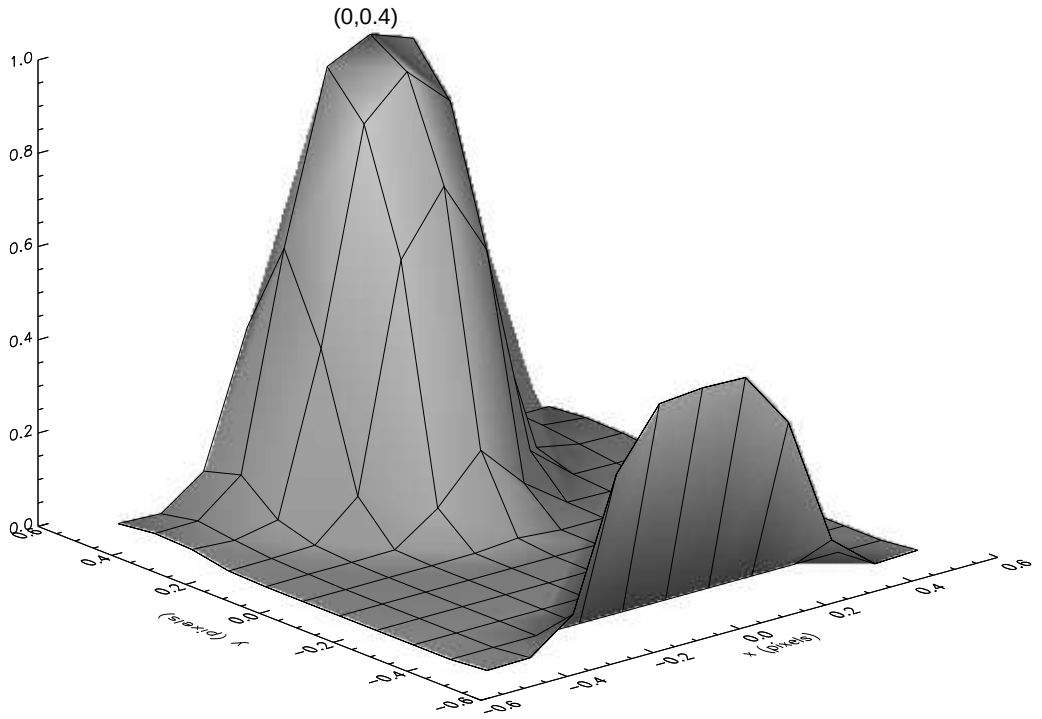

Figure 6.25: Two-pixel event position probability distribution

and came up with a distribution of grades. We want to use that distribution of grades to estimate the position of this ensemble of events. We have probability distributions of positions for each event, but how do we combine these to yield the best-estimate position for the ensemble?

As an initial step, we chose the simplest conceivable mapping. We assumed that a given grade came from a photon which interacted at the most likely subpixel position for that grade, i.e. wherever the peak is in the plots mentioned above. The subpixel coordinates of the peak are given as the third column of Table 6.19. Then we just averaged these positions to get the most likely subpixel position for the ensemble.

We computed ensemble position estimates as above for each subpixel position. Then to test the accuracy of the method, we generated a "distortion map" by subtracting the true position from the estimated position (separately for x and y), then computing a radial distortion. Figure 6.28 shows this distortion map. This map is intended to illustrate the degree to which this simple algorithm is able to recover positions. Note that there are regions on the pixel where the algorithm works well, and regions where it does not. This

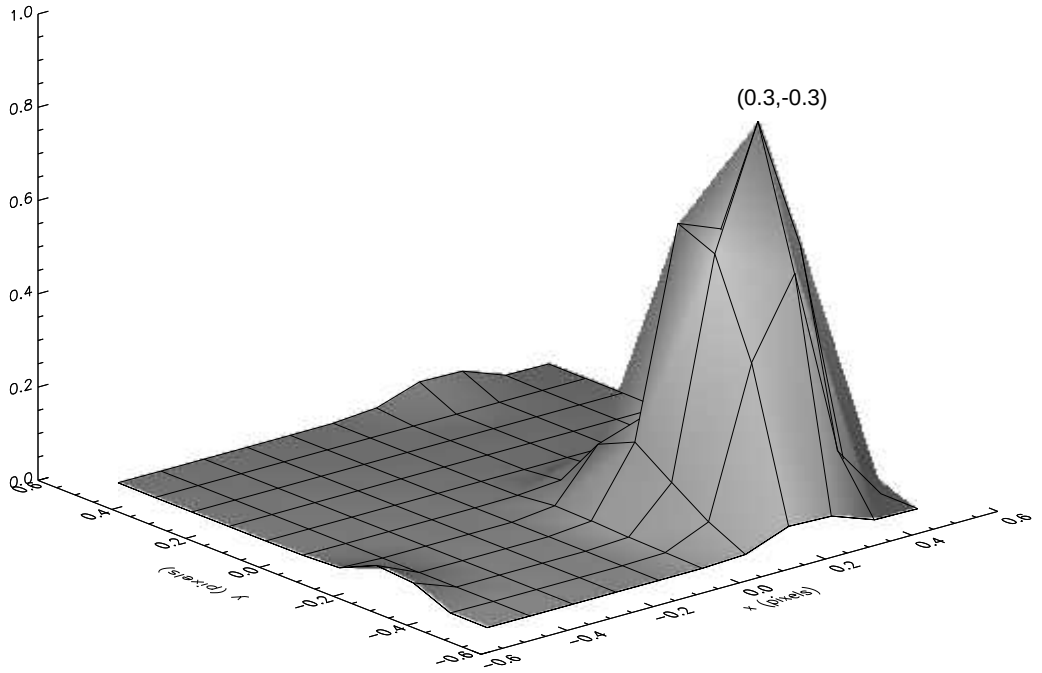

Figure 6.26: Three-pixel (L-shaped) event position probability distribution

leads to ambiguities in a photon's true subpixel position and indicates that this algorithm provides accurate subpixel positioning to about 1/16 pixel.

A more relevant test of the algorithm is the degree to which it can recover an accurate subpixel position of a point source smeared by a PSF. To simulate this, we generated photons with a two-dimensional Gaussian distribution about some pre-determined subpixel position. We deposited these photons on simulated CCD frames one at a time, then simulated frame readout and event detection and grading. This rate of one photon per source per frame is consistent with the readout rate expected for modest sources with AXAF. Using each event's grade as above, and ignoring events with grades S+, P+, and Other, we assigned to the event a subpixel position (the most likely position for that grade). Once we had accumulated an ensemble of events, we computed the simple average and standard deviation for the x and y positions separately and compared these estimates of the source's position and the PSF widths to the input values. We also made these estimates using only integer pixel positions for each photon and using the true subpixel positions for each photon, for comparison. Since the positions and PSF widths obtained from the true sub-

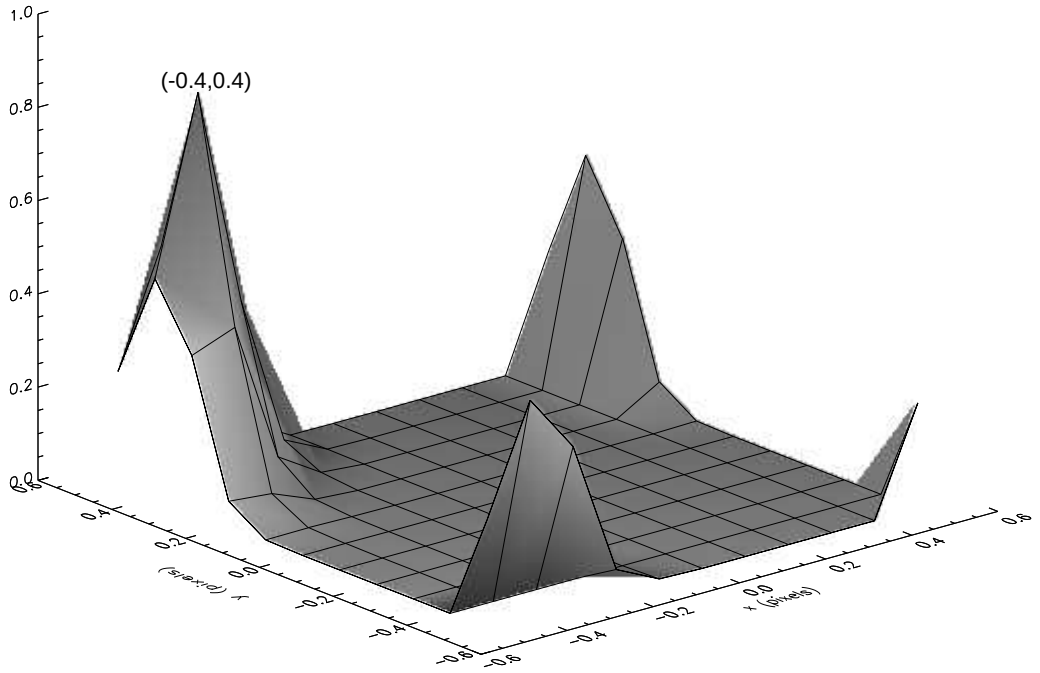

Figure 6.27: Four-pixel (square-shaped) event position probability distribution

pixel positions of the photons are the best estimates we can make given the finite sample size, the fairest comparison is between these results and those for the two algorithms in question, not between the input values and the results for the two algorithms. The results are summarized in Table 6.20. Note that some source positions were deliberately located at subpixel positions that suffered large distortions in the earlier tests (see Figure 6.28).

energy (eV)	number of photons	true PSF				estimate using integer pixel positions				estimate using mapped subpixel positions				estimate using real photon positions			
		x	y	σ_x	σ_y	x	y	σ_x	σ_y	x	y	σ_x	σ_y	x	y	σ_x	σ_y
1000	3000	5.30	5.00	0.85	0.85	5.30	5.00	0.90	0.89	5.30	5.00	0.85	0.86	5.30	5.00	0.85	0.85
1000	3000	5.38	5.35	0.85	0.85	5.37	5.34	0.90	0.89	5.37	5.34	0.85	0.85	5.37	5.34	0.84	0.85
1000	3000	5.20	5.50	0.85	0.85	5.18	5.48	0.90	0.91	5.18	5.49	0.85	0.87	5.18	5.49	0.84	0.86
1000	500	5.20	5.50	0.85	0.85	5.21	5.51	0.89	0.90	5.20	5.52	0.84	0.87	5.20	5.52	0.83	0.86
1000	100	5.20	5.50	0.85	0.85	5.31	5.45	0.94	0.83	5.25	5.51	0.86	0.80	5.25	5.50	0.88	0.80
1000	1000	5.05	5.35	0.85	0.85	5.03	5.30	0.88	0.90	5.07	5.30	0.84	0.86	5.06	5.30	0.84	0.86
500	1000	5.05	5.35	0.85	0.85	4.96	5.31	1.02	1.03	4.97	5.30	1.00	1.01	5.02	5.37	0.85	0.85
5000	1000	5.05	5.35	0.85	0.85	5.08	5.33	0.91	0.89	5.10	5.34	0.88	0.86	5.09	5.34	0.86	0.85
1000	1000	5.03	5.35	0.10	0.10	5.18	5.50	0.47	0.00	5.05	5.38	0.13	0.16	5.05	5.38	0.10	0.10
5000	1000	5.03	5.35	0.10	0.10	5.18	5.50	0.47	0.00	5.04	5.30	0.12	0.18	5.05	5.35	0.10	0.10
1000	1000	5.05	5.35	0.40	0.40	5.07	5.36	0.51	0.49	5.07	5.35	0.40	0.42	5.07	5.35	0.40	0.41
1000	20	5.05	5.35	0.40	0.40	5.00	5.45	0.51	0.51	5.02	5.48	0.42	0.40	5.08	5.43	0.37	0.40
1000	5	5.05	5.35	0.40	0.40	5.30	5.50	0.45	0.71	5.30	5.42	0.35	0.48	5.27	5.35	0.30	0.47

Table 6.20: Results of subpixel position testing using a PSF-convolved point source

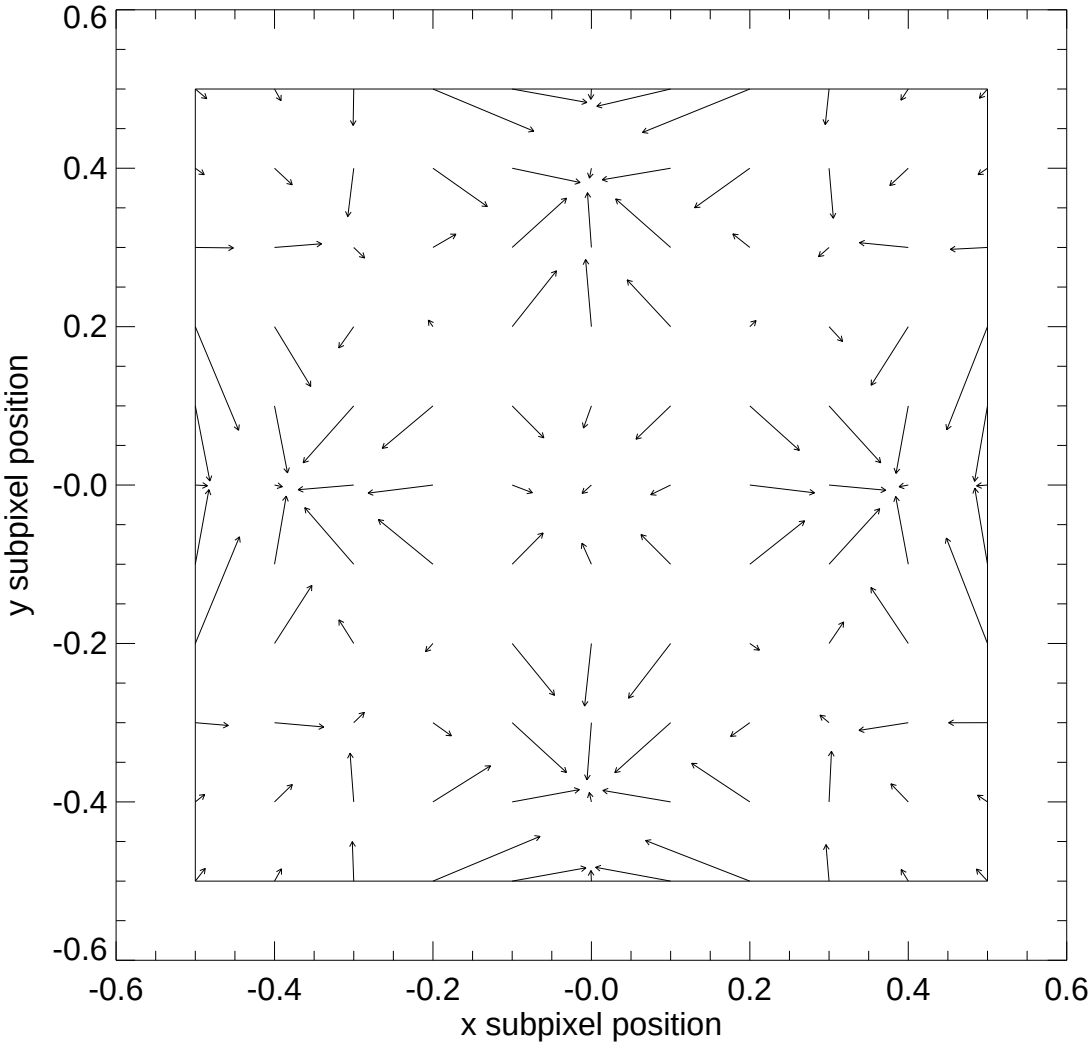

Figure 6.28: Radial distortion map for one pixel, showing the difference between the true and reconstructed positions for 121 sample positions in a pixel. Each arrow starts at the true subpixel position and points to the position estimated by the algorithm.

These results confirm that the subpixel position mapping algorithm described above does a better job of recovering the source position than integer pixel positioning, when the PSF is small compared to the pixel size. Not surprisingly, the algorithms converge when the PSF is comparable to the pixel size (as we approach critical sampling). The results of the grade-based algorithm are affected by energy since the splitting is affected by energy – as fewer events are split, the subpixel position mapping algorithm collapses to integer pixel positioning. Subpixel position mapping appears to perform marginally better than integer

pixel positioning for small numbers of photons.

6.6 Spatial linearity

Spatial linearity tests, including the effects of sub-pixel structure on that linearity, were conducted using the ACIS-2C instrument with the HRMA at XRCF. The tests were performed in two sessions with slightly different modes of operations.

In the first session both front- and back-illuminated chips of the ACIS-2C instrument have been used. They were exposed to the Cu K-alpha (8.04 keV) and O K-alpha (0.53 keV) photons.

The FAM was being moved in either horizontal (FAM Y) or vertical (FAM Z) directions with increments of 5 μm. At each position data were collected for 300 seconds, so that the total number of X-ray events detected was about 1000 for oxygen K-α and about 300 for copper. The total motion of the FAM in both directions was 20-30 μm.

In the second session FAM steps were nominally 27 μm, which resulted in a total path of $\sim$440 μm in the horizontal direction and $\sim$300 μm in the vertical direction. This mode improved dramatically the FAM mechanical performance and repeatability of the data. The ACIS-2C front-illuminated chip was exposed to Mg K_α(1.25 keV) and Mo L_α (2.29 keV) X-rays in this session, with 50 sec data collection at each step, so that the total number of detected events at each point was about 200.

6.6.1 Linearity between FAM and ACIS positions

We consider data for a front-illuminated device exposed to 2.29 keV photons as a typical case. Correlation between the ACIS measured positions and the FAM Y values for horizontal displacement of the FAM is shown at Fig. 6.29. Mean scatter of the experimental points (standard deviation) is 1.79 μm. Here we should take into account that an error in FAM positioning is not less than 1 μm, which results in a formal ACIS error of less than 1.5 μm.

Results shown in Fig. 6.29 demonstrate that accompanying the FAM movement in the horizontal direction there is also a change in the vertical positions of ACIS. That means that the ACIS-2C camera was installed with a rotation angle of 18 arc min around the FAM X axis.

6.6.2 Size of ACIS-2C pixels

In the preceding subsection we assumed that both the FAM relative spatial motion in Y and Z, and the size of the CCD pixel are exactly as predicted. Using the above subpixel test data it is possible to cross-check these assumptions. To do this we divided the stated total motion of the FAM (440 μm) into dummy pixels of size differing from the fabrication

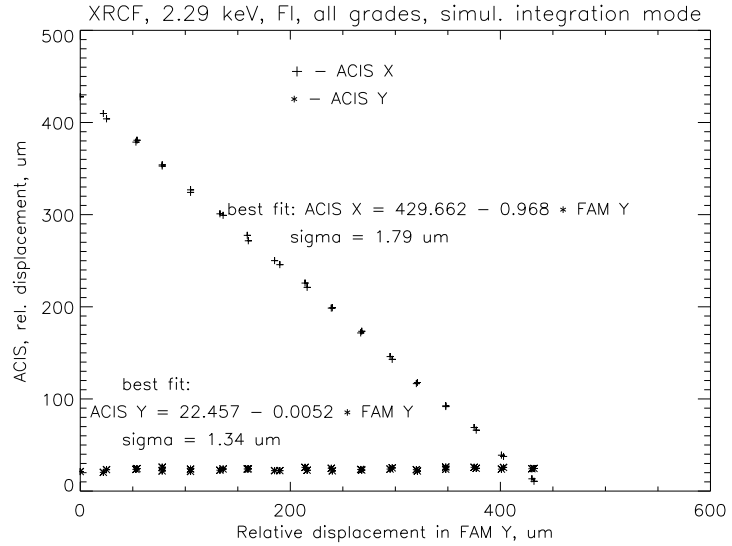

Figure 6.29: Plot of centroid of ACIS Y,Z positions vs. FAM Y,Z

goal of 24 μm. In the ideal case there should be a linear correlation between the position of a beam inside an ACIS pixel and that of trial FAM pixels.

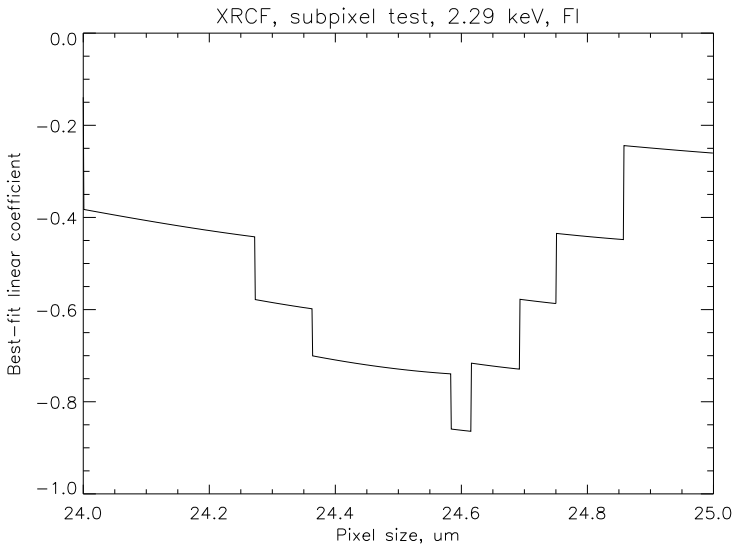

Figure 6.30: Plot of correlation coefficient vs. assumed size of ACIS CCD pixel

Values of the linear coefficient for different sizes of FAM 'pixels' are shown in Fig. 6.30. It is clearly seen that only a narrow region of 24.60 +/- .025 μm pixel size exists where the data converge and give good statistics.

The value of 24.6 μm is 2.5% bigger than the nominal value of 24 μm for ACIS pixels, and measured with a high precision - 250 Å - by this method. This deviation is considerably larger than allowed by the measurements of the total CCD active area for 1024 pixels. The probable explanation for this difference is that the FAM scale itself is compromised and the true displacement is really 390 μm when readings show 400 μm.

6.7 Pileup for PSF concentrated measurements

When more than one X-ray photon interaction with the CCD places charge in the same or neighboring pixels, the ACIS event processing software has difficulties reconstructing the energy, grade, or even number of photons. The effect of these multiple photon charge cloud combinations is called 'pileup'. As discussed in Chapter 4, the case of uniform illumination pileup removal is reasonably well modelled for moderate incident flux levels.

At XRCF, and in flight when point sources are being observed, the HRMA produces a highly non-uniform illumination of the CCD chips in ACIS. This focussed beam is sharply peaked in the core of the HRMA PSF, with additional flux in wings of the PSF (especially off-axis), and with corrections resulting from the pixelization effects of the CCD and internal charge cloud spreading.

In the standard processing of ACIS data the event lists are generated by summing the charge found in 3x3 pixel regions of the CCD. This approach assumes that the probability of a 3x3 pixel detection cell containing charge from more than one photon is insignificant, which is true for most astrophysical sources. When bright ($> 100\mu$Crab) sources are observed, however, photons can pile up on top of each other, i.e. a significant number of detection cells can be contaminated by charge from nearby photons. This so-called *pile-up effect* can lead to several types of error(ASC, 1997).

- *Spectral distortion:* A detection cell containing charge from a secondary photon nearby will overestimate the energy of the primary photon.
- *Grade migration:* The spatial distribution of charge among the nine pixels in a detection cell (an event's *grade*) is an important event property that is used during data analysis. When extra charge is added to a detection cell, the grade is often changed.
- *Raw event rate underestimation:* The raw event rate can be underestimated because closely spaced photons are detected as a single event.
- *Clean event rate corruption:* If an event list is filtered using the corrupted energy or grade properties, then the resulting number of "clean" events will be inaccurate. Some grade filtering is always applied to reduce the number of events associated with the particle background.
- *Point spread function (PSF) distortion:* The severity of pile-up depends on the surface brightness of the incident photon distribution. Thus the core of the PSF suffers more pile-up, and loss of events, than the wings do.

Data to evaluate these pileup effects on ACIS performance were collected at the X-ray Calibration Facility (XRCF) in 1997 February and April during Phases F and H of the calibration operations. The primary goals were to investigate possible trends of pileup with source flux and grade selection, and to compare in detail the measured pileup fraction with

current theoretical models, in order to assess the general validity of the latter for predicting pileup for in-flight observations.

In the following sections we present our efforts to understand and correct or ameliorate pileup effects.

6.7.1 Flux correction via the ROI method

In this section we examine the XRCF data to develop empirical measures for correcting the inferred flux for pileup in the case of focussed illumination emerging from the HRMA and striking ACIS. Data for this situation were collected as part of the Count-Rate Linearity tests (cf. Table 6.5).

If the HRMA Point Spread Function (PSF) were infinitely narrow, then a simplified treatment of pileup would consist of the following simple algorithm. The spectrum of a mono-energetic incident flux would appear in the CCD as a series of peaks, each separated by the energy of the individual photons. The number of events found at the incident energy, $\mathrm{E_L}$, would be the number of frames containing a single photon. The number of events seen at the apparent energy of $2 \times \mathrm{E_L}$ would be the number of frames with two piled-up photons. The number of events at $3 \times \mathrm{E_L}$ is the number of frames with three piled-up photons, and so on. Thus to extract the true number of incident photons one could integrate over each peak in the observed CCD spectrum and sum them, after weighting by how many photons occur in each peak. Expressed as an equation:

$$n = \sum_{i=1}^{\infty} i \cdot c_i \tag{6.11}$$

where

$$c_i = \int_{i\cdot \mathrm{E_L}-\Delta E}^{i\cdot \mathrm{E_L}+\Delta E} I(E)dE \tag{6.12}$$

I(E) is the observed CCD spectrum and ΔE is the energy halfwidth of the line.

Unfortunately this simple algorithm is insufficient for complete correction. Fig. 6.31 shows the result of fitting Gaussian profiles to each peak in the countrate linearity measurements at 1.486 keV (Al-Kα). The circles are the number of counts per second in the single photon peak alone, while the diamonds are the inferred rate based on equation 6.11. Only events falling into the ASCA grades 02346 were included.

If the same algorithm is applied, but instead calculating the number of events by integrating the total number of counts with a region of interest (ROI) starting at the top of the lower order pileup peak, going up to the top edge of the given pileup peak, then the pileup correction for the same data looks like Fig. 6.32. The pileup correction is clearly still not correcting for all events (otherwise the diamonds would fall on a straight line, indicating direct proportionality between the CCD inferred rate and the BND rate), but using an ROI detects significantly more events than Gaussian fits to the peaks. The implication is that

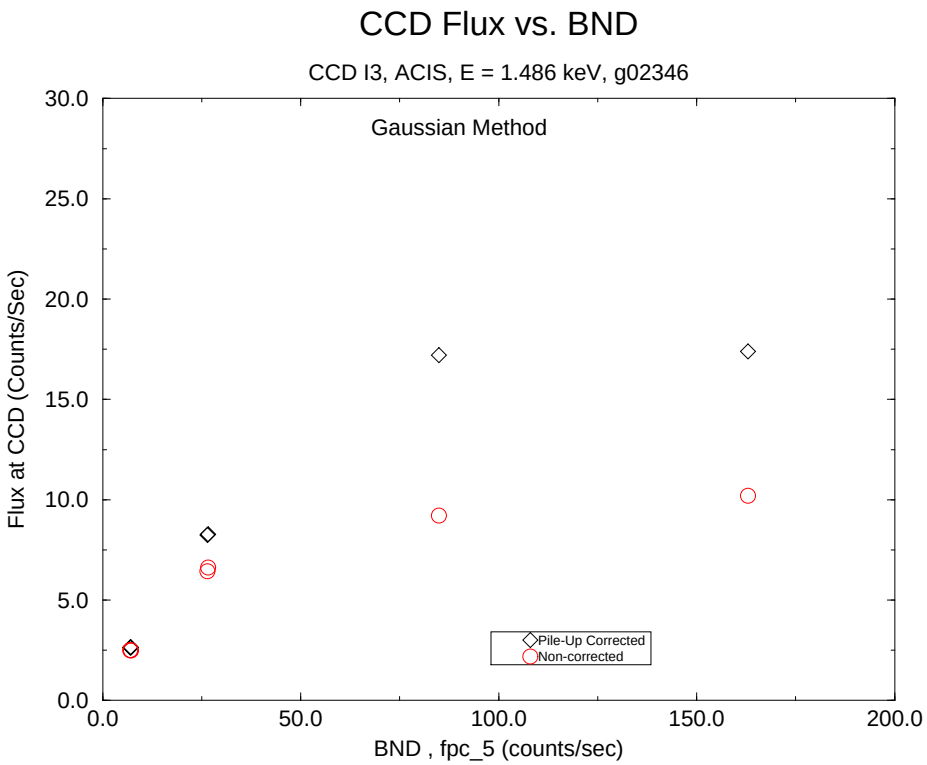

Figure 6.31: Plot of CCD detected flux vs. BND count rate; circles are CCD flux in single photon peak alone - diamonds are CCD flux corrected for higher order pileup peaks.

the interaction between multiple charge clouds produce event spatial distributions which cause a loss of charge (to the event reconstruction algorithm). This is not implausible if we consider that the HRMA PSF is not perfect, but causes photons to be distributed with a ∼0.5 arc second FWHM over the CCD (roughly a pixel). Thus succeeding photons do not always strike the same pixel, but frequently strike neighboring pixels. When this occurs further charge splitting results in some charge outside the 3x3 event reconstruction neighborhood, and thus causing loss of charge. For the succeeding plots we use the ROI method when reconstructing events.

In the Count-Rate Linearity tests the number of photons per frame was regulated in two ways: the X-ray beam intensity was increased at a single frame time (0.11 second); and the X-ray beam intensity was held constant while the CCD frame times were increased (0.11, 0.22, 0.33, 0.66 second). In principle the relevant quantity describing the pileup behavior should be the number of photons per frame (which is the product of the frame time times the rate of photons per frame). To check this we plot the 'Pile Up Fraction' versus counts per frame with constant frame time (filled circles) and with constant incident X-ray flux (stars; Fig. 6.33).

The 'Pile Up Fraction' is defined as the ratio of the number of events inferred in the

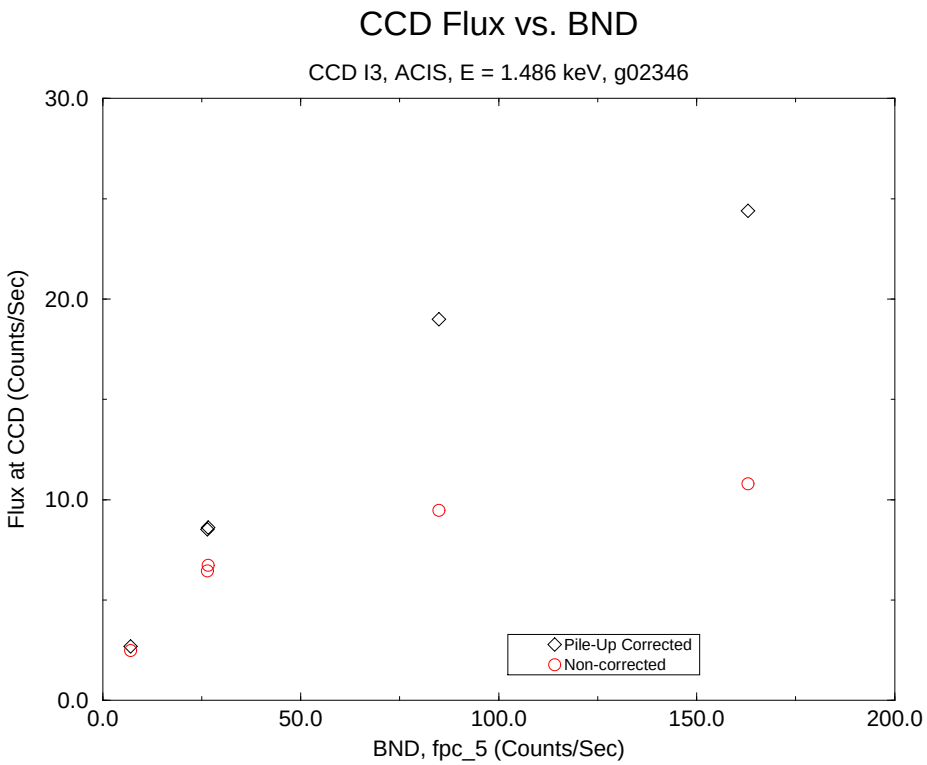

Figure 6.32: Plot of CCD detected flux vs. BND count rate using ROI; circles are CCD flux in single photon peak alone - diamonds are CCD flux corrected for higher order pileup peaks.

$n = 2$ and higher peaks divided by the total number of events, including the $n = 1$ peak. The two sets of points are in good agreement, leading us to conclude that the pileup effect can be treated as a function of the total counts per frame (within the PSF), independent of the frametime.

If, instead of using the standard grade selection (g02346), we accept all events regardless of grade, then the pileup correction of equation 6.11 becomes much better. Figure 6.34 shows the correlation of the total ACIS rate (all grades) after pileup correction versus the incident beam (as determined by the BND counting rate). Note that the circles form a nearly straight line, indicating that the pileup corrected CCD rate is proportional to the BND rate, and hence the incident flux. Even if some X-rays are not being counted, the linearity and proportionality shows that we will be able to calibrate a conversion factor to correct piled-up photons into incident X-ray flux.

Unfortunately the total rate expected from background events in orbit will saturate the telemetry if no grade selection is applied. A significant reduction in charged particle events can be achieved by merely excluding the ACIS grade 255 events (i.e. all eight neighbors of the central pixel exceed the split event threshold). The proportionality of the CCD

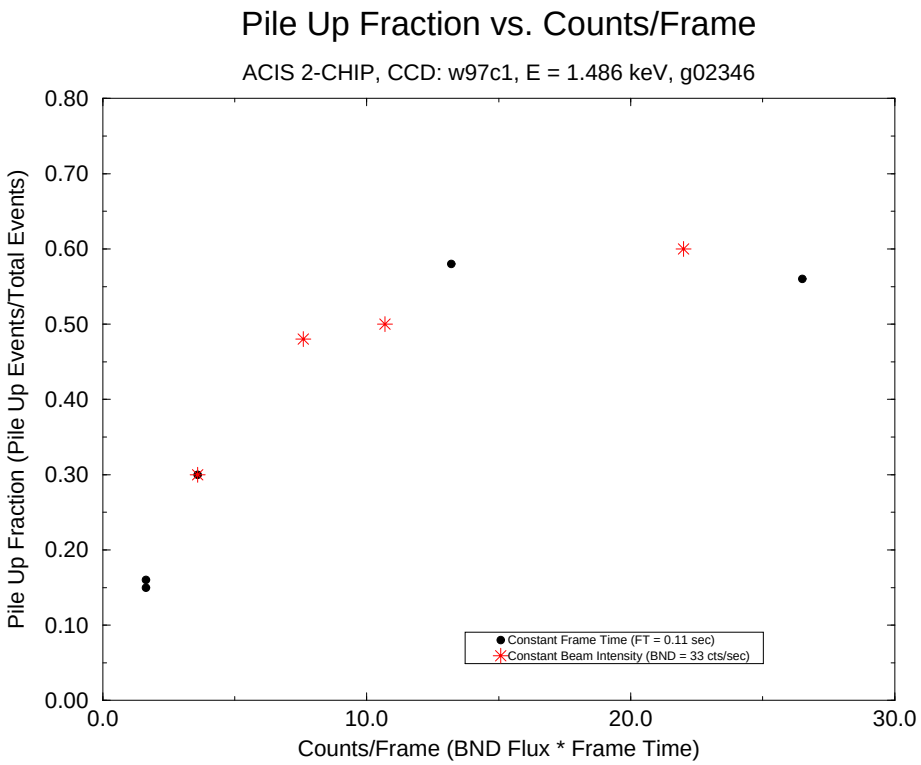

Figure 6.33: Plot of Pile Up Fraction vs. number of counts per frame; Circles: CCD frame time is held constant at 0.11 seconds, while beam intensity is varied; Stars: CCD frame time varies, while beam intensity is constant.

corrected rate to the BND rate remains, indicating that exclusion of grade 255 still allows flux pile-up correction.

The success of the pileup correction in this monochromatic case does not mean that the pileup problem is solved in general. In astrophysical spectra the usual case is a distribution of many photon energies. When multiple photons are combined we lose the ability to individually recognize them. Moreover as the incident energy changes so to does the event spreading, which means that the monochromatic case will need to be explored at differing energies.

The next section describes analysis of the measurements made at the XRCF which were intended to test the effects of pileup.

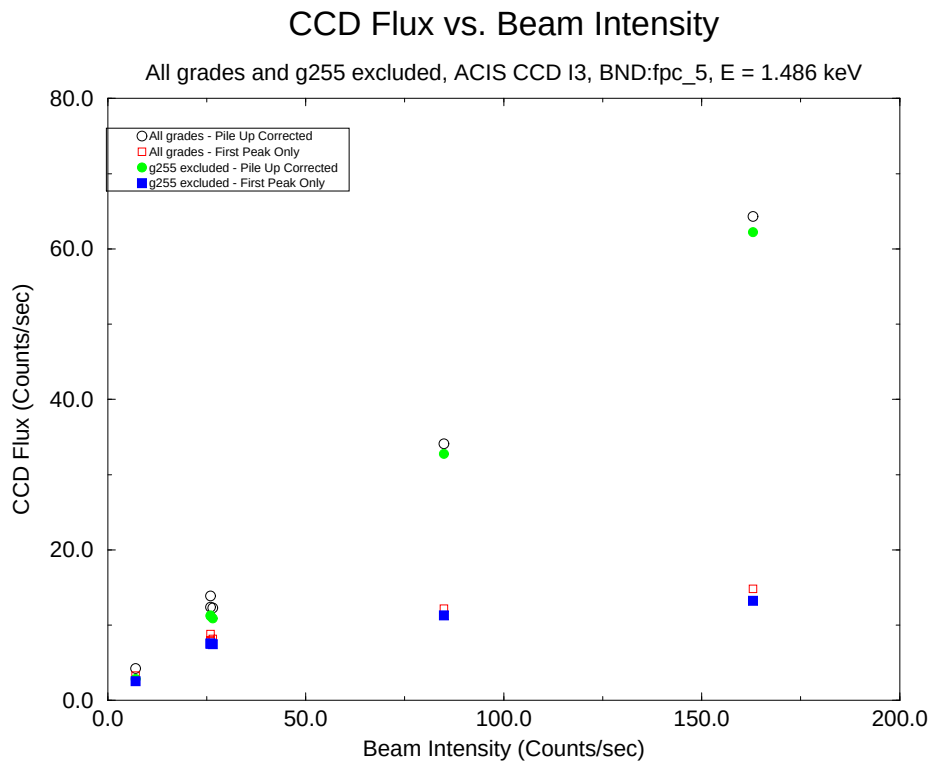

Figure 6.34: Plot of pileup corrected CCD flux with all grades (with and without ACIS grade 255) - Open symbols: all grades, including ACIS 255; Filled symbols: all grades, excluding ACIS 255.

6.7.2 XRCF experiments on pileup effects

6.7.2.1 Phase H data

We first analyzed data collected during Phase H (i.e., ACIS + the High Resolution Mirror Assembly). We considered only data with high signal-to-noise ratio beam normalization spectra, and analyzed only the ACIS telemetry mode observations; the High Speed Tap data lead to similar results (e.g., Kastner, Allen, & Glotfelty 1998).

Table 6.21 lists the Phase H data used in this study, in order of increasing source flux. Data from both chip I3 of ACIS-I, corresponding to a Front-Illuminated (FI) CCD, and from chip S3 of ACIS-S (Back-Illuminated, BI, CCD), were considered. Data from FI and BI chips are listed in Table 6.21a and 6.21b, respectively. The TRW IDs of the tests are listed in column 1, while columns 2 and 3 list the energy of the source (Al-Kα, 1.486 keV; O-Kα, 0.525 keV) and the exposures. The latter correspond to the net integration times after screening of the data, and after removing intervals of data dropouts. All the data in Table 6.21 were accumulated in staggered mode with only 38 rows centered on the aimpoint

being read out. All data were taken with a well collimated, in focus beam.

Test Name	Energy (keV)	Exposure (s)	BND Flux (counts s^{-1} cm^{-2})	Predicted ACIS counts/frame [a] All–255	G02346	G023	G0
a) Front-illuminated CCD							
H-IAI-CR-1.001	1.486	7555	0.0045	0.321	0.319	0.283	0.231
H-IAI-CR-1.003	1.486	2624	0.0166	1.194	1.187	1.150	0.859
H-IAI-CR-1.005	1.486	818	0.0530	3.807	3.784	3.363	2.739
H-IAI-CR-1.007	1.486	595	0.1017	7.435	7.370	6.566	5.348
H-IAI-CR-1.009	0.525	7145	0.0342	0.489	0.489	0.452	0.369
H-IAI-CR-1.011	0.525	2248	0.0987	1.417	1.415	1.306	1.152
b) Back-illuminated CCD							
H-IAS-CR-1.002	1.486	7459	0.0037	0.323	0.312	0.202	0.115
H-IAS-CR-1.004	1.486	2419	0.0129	1.129	1.089	0.702	0.402
H-IAS-CR-1.006	1.486	932	0.0432	3.834	3.700	2.236	1.366
H-IAS-CR-1.008	1.486	533	0.0838	7.344	7.084	4.570	2.616
H-IAS-CR-1.010	0.525	2910	... [b]	...	...	...	...
H-IAS-CR-1.012	0.525	7215	0.0065	0.344	0.335	0.239	0.124

Table 6.21: XRCF Phase H Pileup Data

a=Predicted unpiled ACIS count rate per frame as a function of grade (see text);
b=Poor quality data.

We define the frametime t_f as the time during which the CCD is integrating data during one frame:

$$t_f = \frac{T}{f} - t \times n \tag{6.13}$$

where T is the net exposure (in seconds), f is the number of frames during the exposure, t is the frame transfer time (41 ms), and n is the fraction of rows that are read out ($n = 0.0371$ in 38 row staggered mode). For the data in Table 6.21, we find $t_f = 0.1153$ s for all cases except test I-HAS-CR-1.006, where $t_f = 0.1167$ s.

Columns 4 of Table 6.21 reports the source flux at the HRMA entrance, determined from the beam normalization detectors (BND). Columns 5–8 list the predicted incident (unpiled) ACIS counts/frame for different grade selections: unbinned ACIS grades excluding grade 255 whose events are most likely due to cosmic rays, and the ASCA-like grades G02346, G0234, and G0. The counts/frame were derived by multiplying the BND fluxes for the timeframe t_f and a factor including the effective area of the mirror, the detector quantum efficiency, and the filter transmission. The detector quantum efficiency is grade-dependent (Chartas et al. 1998), so we list the counts/frame corresponding to each grade selection; for reference, for G02346 and at Al-Kα the HRMA/ACIS effective

area is 619.45 cm^2 for FI chips and 733.18 cm^2 for BI chips, and at O-Kα it is 124.3 cm^2 for FI and 446.8 cm^2 for BI. The effective areas were obtained from the Telescope Scientist Team web page: http://hea-www.harvard.edu/MST/mirror/www/home.html (Note that the effective areas provided at this site are the result of scaling the XRCF calibration data to the raytrace effective area curve. Calibration data differ from raytrace as much as 15%.) The ACIS I3 and S3 CCD quantum efficiencies were derived from the MIT Web pages: http://acis.mit.edu/cal/w215c2r_eff_897.qdp for the FI chip, and http://acis.mit.edu/cal/w134c4r_eff_pre_997.qdp for the BI chip. The transmission data for the ACIS OBF's are taken from the PSU anonymous FTP site ftp.astro.psu.edu in /pub/gc/filters/acis_i.data for the Imager, and in /pub/gc/filters/acis_s.data for the Spectrometer. The quantum efficiencies for the BND detectors were taken from the SAO Web page http://hea-www.harvard.edu/MST/simul/xrcf/HXDS/index.html. Relatively large systematic errors of up to 10% remain between the model fits and the measured BND quantum efficiencies. The newly released BND quantum efficiencies differ considerably from the values used in earlier papers (e.g., Kastner et al. 1997).

Tests H-IAI-CR-1.001, 1.003, and 1.005 were previously analyzed by Kastner et al. (1998). Among the tests done with ACIS-S in Table 1b, test H-IAS-CR-1.010 provided a spectrum of poor quality, and will not be considered any further.

6.7.2.2 Methodology and pileup definition

Analysis of the spectra was done using the `TARA` package developed at Penn State (v. 3.1). We accumulated events within a circle centered on the source and of radius 10.5 pixels for the brighter sources and 6.9 pixels for the fainter ones, excluding photons that were contained in the Charge Transfer Trail. We estimate that the latter are at most a few percent (2–3%) of the total flux. We inspected the light curves for flux variability, and found that, in general, the flux remained constant during the observations. In two cases (tests H-IAI-CR-1.003 and 1.009), during the exposure the source was moved to be centered in the middle of the spatial window; since apparent variability is produced in the light curve, we filtered the light curves for the longest stable exposure.

It is well known that, in the case of a monochromatic source, the primary spectral effect of pileup is producing secondary peaks at integer multiples of the primary peak energy, and with decreasing amplitude (e.g., Kastner et al. 1998).

We have previously given an empirical definition of pileup fraction. However, in order to allow a proper comparison between the data and the theoretical models, in the remainder of this section we will adopt a different pileup definition. We will define *the pileup fraction* as the *the fraction of one or more events detected in the secondary peaks*; in symbols,

$$\frac{N_1 + N_2 + ... + N_p}{N_0 + N_1 + N_2 + ... + N_p} \tag{6.14}$$

where N_i is the number of events in each detected peak, with $i = 0$ being the primary

peak. Note that the definition in eq. 6.14 differs from the definition given elsewhere in the Calibration Report in the sense that the correction factors for the multiple-event peaks are neglected here. (This definition follows that used by Brian McNamara's work at the ASC described in Section 6.7.2.4.1.)

As pileup is dependent upon the grade filtering of the data (Kastner et al. 1998), our analysis will need to be performed for different grade selections to compare calibration data to flight data, or even between different sets of flight data if the grade selections are changed. At this time (pre-launch) we expect to use as a standard grade selection one to the two following selections: a) all events, excluding grade 255, and b) all events falling into ASCA-type grades: G0, G023, or G02346, for both FI and BI detectors.

The number of counts in each spectral peak was evaluated simply by counting the events falling in a given "Region of Interest" across the peak energy. This region may contain part of the adjacent continuum, which is formed by piled events: in fact, a portion of the charge produced from multiple events may not be recorded in the 3x3 event island resulting in tails below the pile-up lines. (See Section 6.7.1.)

For tests H-IAI-CR-1.001, 1.003, and 1.005, our analysis thus yields a higher number of events in each peak than in the work by Kastner et al. 1998) who used much narrower spectral regions around the peaks, excluding the nearby continuum.

6.7.2.3 Pileup trends with source flux and grade selection

Table 6.22 lists the results of our pileup analysis of Phase H data. Column 2 reports the fraction of total events detected for grade selection All–255, defined as the ratio of the total counts detected in the observed spectrum to the expected incident counts from Table 6.21. The following three columns list the counts detected in the primary peak (col. 3), the sum of all the counts detected in the piled peaks (col. 4), and the pileup fraction (col. 5), according to eq. 6.14. In the following, we will refer to the pileup fraction estimated from the XRCF data as the "measured" pileup fraction. The same information is contained in the following columns of Table 6.22 for grade selections G02346, G023, and G0.

From Table 6.22 a number of features are apparent. For increasing source flux, the pileup fraction increases, although in a non-linear fashion, as expected due to the Poisson nature of the pileup phenomenon. This is illustrated in Figures 6.35 and 6.36, where the pileup is plotted versus the incident counts/frame as a function of grade selections for FI and BI chips, respectively.

For a fixed source flux, the pileup fraction decreases when the higher grades are discarded, as illustrated in Figures 6.35 and 6.36. The decrease in pileup is more dramatic for BI chips than for FI at comparable source fluxes, as expected because of the way the BI chips work. Note also in Figure 6.36 the "cutoff" of the pileup at higher fluxes for the BI chip, which is particularly evident for grades G023 and G0. This is possibly related to grade migration at higher fluxes.

The decrease in pileup is accompanied by a loss of total detected events, i.e., going from

Test Name	Detected Events for All - 255				Detected Events for G02346				Detected Events for G023				Detected Events for G0			
	Frac. of Events	Peak1	Piled Peaks	Pileup Frac.	Frac. of Events	Peak1	Piled Peaks	Pileup Frac.	Frac. of Events	Peak1	Piled Peaks	Pileup Frac.	Frac. of Events	Peak1	Piled Peaks	Pileup Frac.
a) Front-illuminated CCD																
H-IAI-CR-1.001	0.93	18446	1054	0.054	0.90	18004	774	0.041	0.95	17581	575	0.033	0.95	14242	140	0.010
H-IAI-CR-1.003	0.77	17160	3639	0.175	0.68	15826	2500	0.136	0.64	14932	1809	0.108	0.66	12499	434	0.034
H-IAI-CR-1.005	0.51	8218	5563	0.403	0.37	6958	2972	0.300	0.35	6514	1763	0.213	0.30	5404	336	0.059
H-IAI-CR-1.007	0.35	6459	6844	0.514	0.21	5328	2546	0.32	0.18	5021	1235	0.197	0.16	4183	168	0.038
H-IAI-CR-1.009	0.77	21792	1520	0.065	0.74	21061	1321	0.059	0.78	20860	1079	0.052	0.87	19630	295	0.015
H-IAI-CR-1.011	0.66	15191	3079	0.169	0.59	13842	2438	0.150	0.61	13707	1841	0.118	0.60	12835	531	0.041
b) Back-illuminated CCD																
H-IAS-CR-1.002	0.89	17461	1161	0.062	0.86	16911	530	0.030	0.85	10936	158	0.014	0.61	4508	11	0.002
H-IAS-CR-1.004	0.76	14355	3553	0.198	0.65	13226	1573	0.106	0.62	8651	473	0.05	0.41	3446	42	0.012
H-IAS-CR-1.006	0.47	7924	6554	0.453	0.28	6554	1935	0.228	0.24	4007	414	0.094	0.14	1484	29	0.020
H-IAS-CR-1.008	0.32	4779	6048	0.559	0.15	3755	1009	0.212	0.11	2201	135	0.058	0.06	776	9	0.012
H-IAS-CR-1.012	0.77	15573	920	0.056	0.75	15147	512	0.033	0.85	12397	264	0.021	0.85	6552	31	0.005

Table 6.22: Pileup Analysis for Phase H Data

G02346 to G0 more and more photons are thrown away. For example, at the Al-Kα energy and for a source incident flux of ~ 0.05 counts s^{-1} cm^{-2} (test H-IAI-CR-1.005), from Tables 6.21 and 6.22a we can see that for the FI chip the pileup is reduced from $\sim 40\%$ to 6% going from no grade selection to G0, with a loss of 58% of detected photons. At a slightly lower source flux for the BI chip of ~ 0.04 counts s^{-1} cm^{-2} (test H-IAS-CR-1.006), the pileup is reduced from $\sim 45\%$ to 2%, losing a larger fraction of events, 89%. We thus conclude that, at least for the FI chip, grade selection can be used for bright sources to reduce efficiently the pileup and still retain enough photons to do some simple spectral analysis.

6.7.2.4 Observed versus predicted pileup

6.7.2.4.1 Analytical model by B. McNamara An analytical treatment of pileup has been performed by McNamara (1997). He defines the pileup fraction as the *ratio of number of frames with two or more events to the number of frames with one or more events*, consistent with our definition above in eq. 6.14. The model does not include any grade selection effects, and we will thus compare its prediction with the measured pileup for All-255 grades in Table 6.22. In addition, the model predictions hold for the Al-Kα energy only.

Figure 6.37 shows the plot of the difference between the predicted pileup fraction from McNamara's model and the observed pileup as a function of the source counts per frame, at the Al-Kα energy and for All-255 grade selection. The predicted pileup fraction was extrapolated from the plot in Figure 2 of McNamara (1997). assuming an encircled energy fraction of 0.7, as appropriate for the XRCF data. Figure 6.37 shows that the analytical model always overstimates the measured pileup. The maximum discrepancy (30%) is obtained for the FI chip at large source fluxes. For our fiducial flux of 1 count/frame, the pileup is overestimated by 24% for the FI chip and 10% for the BI chip.

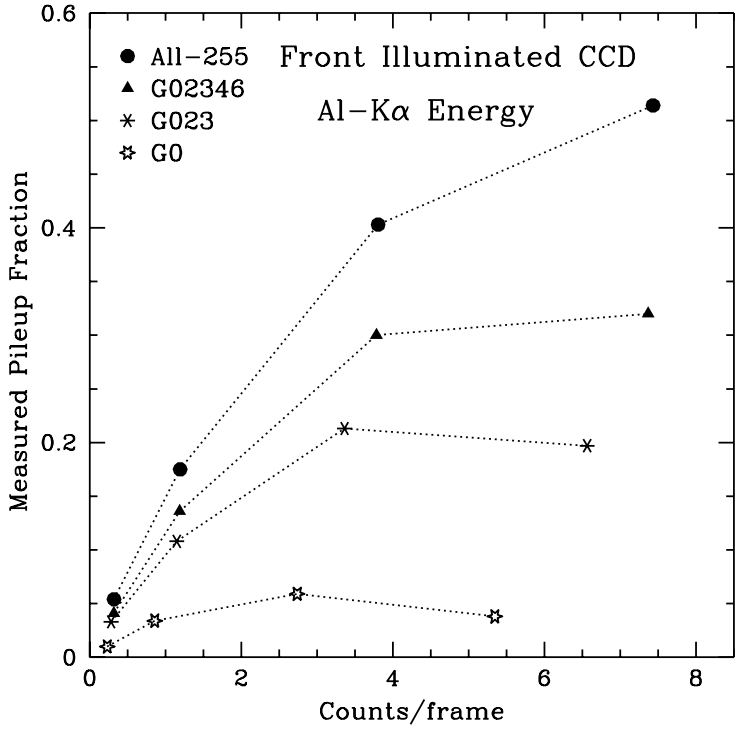

Figure 6.35: Plot of the measured pileup fraction from Phase H data for chip I3 of ACIS-I, versus source flux incident on the HRMA entrance (Table 6.20a). Different grade selections are shown. The dotted curves simply connect the datapoints and are plotted to guide the eye. For increasing source flux the pileup fraction increases, with a non-linear trend. For a fixed source flux, the pileup decreases when events related to the higher grades are discarded. This also corresponds to throwing away an increasingly larger fraction of total detected events (Table 6.20a).

We conclude that the analytical model provided by McNamara (1997) can be used to obtain a conservative upper limit for the pileup for both FI and BI detectors, for a monoenergetic sources and no grade selection.

6.7.2.4.2 MARX simulations The Model of AXAF Response to X-rays `MARX` (Wise et al. 1997) is widely used to simulate AXAF data in detail. The `MARX` associated tool `pileup` allows simulations of the pileup effects (for a description of the `pileup` tool, see the `MARX` manual). We used `MARX` v.2.0 to simulate the pileup fraction for Phase H data taken with ACIS-I (Table 6.22a), since the code presently supports only FI chips. `MARX` provides a more flexible tool to predict pileup than the analytical model of McNamara (1997), since it incorporates a more realistic physical description of the CCDs, allowing for grade selection.

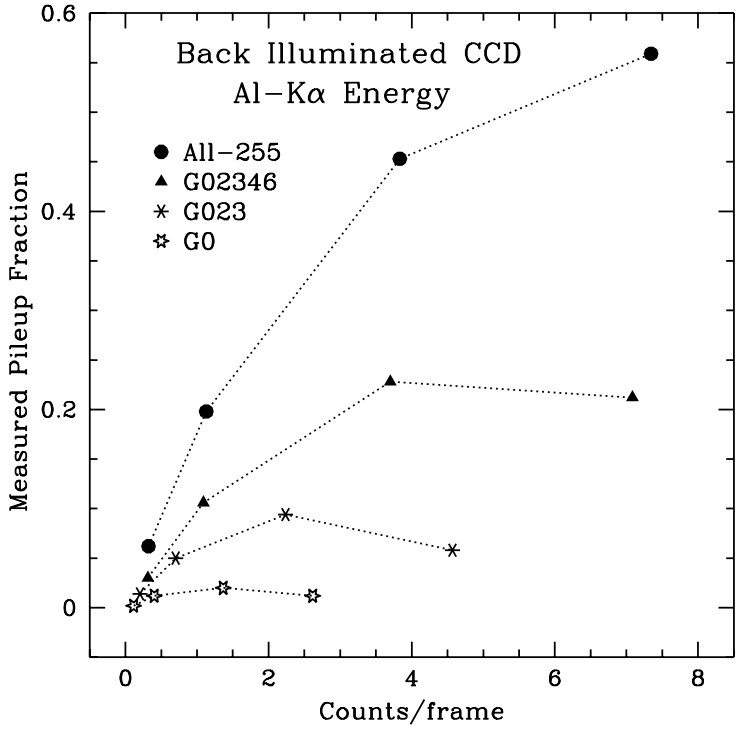

Figure 6.36: Plot of the measured pileup fraction from Phase H data for chip S3 of ACIS-S, versus source flux incident on the HRMA entrance (Table 6.20b), as a function of grade selection. The dotted curves simply connect the datapoints and are plotted to guide the eye. As for FI chip (see Figure 6.23), there is a non-linear trend of increasing pileup for increasing source flux. Discarding the events corresponding to the higher grades lead to a significant reduction of the pileup at the expense of a drastic loss of total events (cfr. Table 6.20b).

Note that the currently available `MARX` version has incorrect values of the encircled energy at energies > 4 keV, whose effect is to broaden the PSF and thus affect the pileup analysis at those energies. We thus restrict ourselves here to using `MARX` at the lower energies.

We first simulated the source spectrum assuming a monochromatic emission line at 1.486 keV for the Al-Kα tests and at 0.525 keV for the O-Kα tests, normalized to the source flux as derived from the analysis of the BND data and integrated over the same net exposures (Table 6.21). The parameter "DetIdeal" in the `marx.par` parameter file was set equal to `yes`, as recommended. The staggered mode of Phase H data was simulated by activating only 38 rows centered on the nominal I3 aimpoint in the `acis.par` parameter file, and adjusting the frametime to the observed value (see above). The split and event thresholds were fixed at 13 and 38 adu, respectively, as appropriate for an FI detector. The

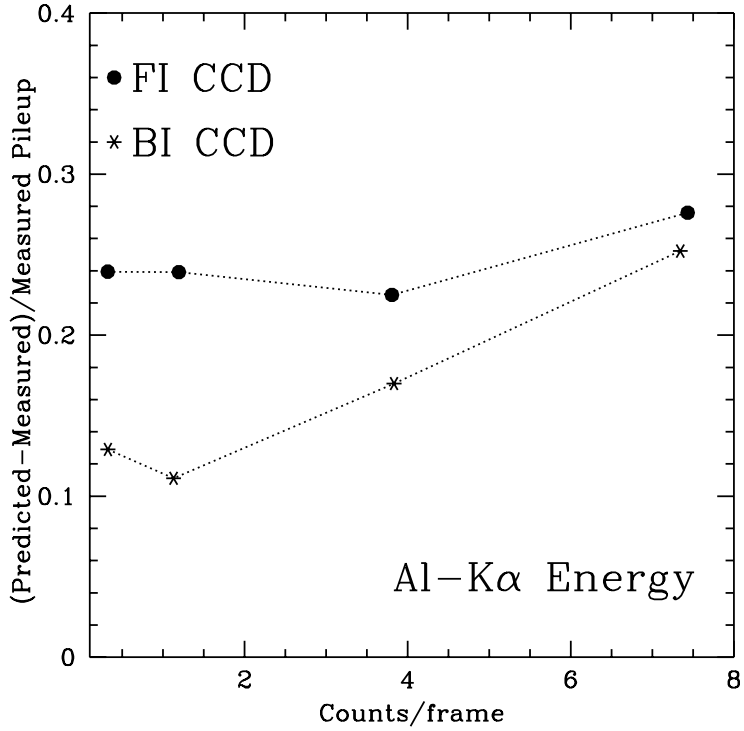

Figure 6.37: Plot of the percent difference between the pileup predicted by the analytical model of McNamara (1997) and the pileup measured for Phase H data (Table 2), versus incident source flux. Only data for grade selection All–255 and for the Al-Kα energy (where the model is defined) are used. It is apparent that the model overestimates the pileup fraction, especially at high source fluxes.

"MeanNoise" and "SigmaNoise" parameters were fixed at their default values (2.0 and 1.0, respectively).

Table 6.23 reports the results of the `MARX` pileup simulations. Column 2 lists the total number of photons detected by the `pileup` tool, while column 3 gives the fraction of total counts that were collected. The following columns give the number of events detected in the primary and piled peaks, and the corresponding pileup fraction (according to the definition in eq. 6.14). The latter was derived in the *same* regions of interest as for the XRCF data. *Note: No grade selection is considered here, since the order of the pixels in the 3x3 island in the* `FITS` *files produced by* `MARX` *is different than in the XRCF data.*

The results are shown in Figure 6.38, where the percent difference of the `MARX` predicted pileup and the fraction measured for the Phase H data is plotted versus incident count/frame. Only data taken at the Al-Kα energy are plotted. The Figure shows that for every event detection rate the predicted pileup by `MARX` is lower than the measured pileup.

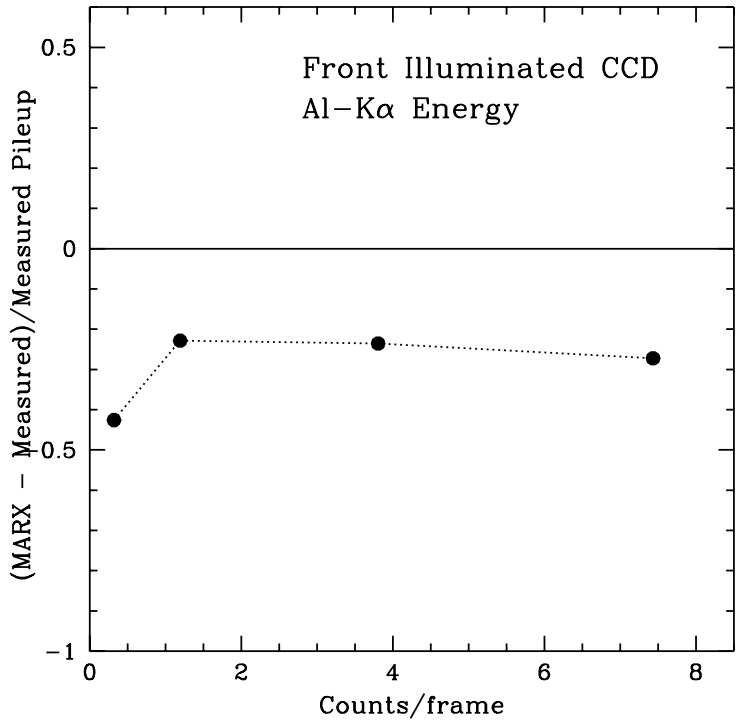

Figure 6.38: Comparison between the pileup fraction predicted with MARX and measured for Phase H data for All-255 (see text). MARX underestimates the measured pileup at all observed event detection rates.

		# Events for All - 255			
Test Name	Detected Events	Frac. of Events	Peak1	Piled Peaks	Pileup Frac.
H-IAI-CR-1.001	13528	0.99	13089	419	0.031
H-IAI-CR-1.003	19052	0.99	16439	2572	0.135
H-IAI-CR-1.005	14601	0.99	10077	4491	0.308
H-IAI-CR-1.007	15721	0.99	9807	5852	0.374
H-IAI-CR-1.009	13199	1.00	12434	765	0.058
H-IAI-CR-1.011	9643	1.00	8291	1352	0.140

Table 6.23: MARX Pileup Simulations for Phase H Data

6.7.2.5 Reducing pileup with subframing mode

As discussed above, pileup depends (non-linearly) on the source flux (Table 6.22): for a given exposure and frametime, decreasing the source flux leads to a smaller pileup fraction, essentially because the number of events per frame is lower. In a realistic astrophysical situation, the observer does not have the option to vary the source flux; however, if a

Test Name	Frametime	# of Rows	Pileup Fraction	
			All–255	G02346
F-I2C-CR-2.001a	0.113	18	0.260	0.105
F-I2C-CR-2.002	0.227	38	0.410	0.172
F-I2C-CR-2.003	0.318	54	0.487	0.180
F-I2C-CR-2.004	0.660	114	0.580	0.186

Table 6.24: XRCF Phase F Pileup Data

method can be found to reduce the number of detected *events per frame*, the observed pileup will be lower. This method is called "subframing" and consists of reading out only a fraction of the CCD rows centered on the aimpoint. Since the CCD is sitting on the source for less time, the number of photons detected during each frame will be lower.

A few tests during the Phase F of the XRCF calibration operation were indeed performed in subframe mode, giving us a chance to test this method to control pileup. Table 6.24 reports the Phase F tests that were used here. They corresponds to data acquired with the BI chip (w97c1) for a fixed source flux of 0.0133 c/s/cm^2 and exposure 2183.41 s at the Al-Kα energy. (Similar tests with the FI chip could not be used because the energy switched to another value after the first two tests.) The number of rows, and corresponding frametimes, were varied as reported in Table 6.24.

We accumulated spectra and analyzed them in the way described above. Table 6.24 lists the measured pileup fraction for two reference grade selections, G02346 (the most commonly used for the in-flight data) and the unbinned ACIS grades All–255, for comparison. The pileup fraction defined in eq. 6.14 was used. It is apparent that subframing mode can be used to control pileup. For the tests in Table 6.24, the pileup is reduced by 55% in the case of no grade selection, and by 44% for G02346.

We conclude that subframe mode can be used to effectively control pileup in most astrophysical situations when a bright point-like source of a given flux is observed. Of course the penalty paid for sub-framing is a reduced field of view because only a portion of the CCD is being processed for X-ray events. Thus there will be a smaller sky coverage when subframe mode is used.

6.7.2.6 Reducing pileup with Continuous Clocking mode

ACIS is primarily designed to study faint X-ray sources (F$\leq\sim 10^{-13}$ ergs-cm^2-sec). From the initial selection of targets through the first GTO and GO proposal rounds, it is clear that many of the favorite AXAF targets were discovered by previous X-ray missions, and are much brighter than the AXAF limiting source sensitivity.

In order to study these very bright sources we must accomodate the effects of pile-up, as described in the preceeding sections. If the objective is to obtain a spectrum of such a bright target, by using one of the transmission gratings, then pileup is not a problem, as

pile-up effects will be greatest on the highest counting rate in the image (which is typically the zeroth order image). The critical quantity to be determined for the analysis of the dispersed spectrum is the centroid of this zeroth order image. Pileup effects will not affect the centroid determination of the zero order position of the spectrum. The grating has the property of dispersing the X-rays over a large portion of the ACIS-S array, so the projected flux in the dispersed spectrum is much lower than the zeroth order (as only a small portion of the spectrum falls on a single pixel).

If instead the intent is to obtain a spectrum of a very bright target, either integrated over time, or for time variable targets, to carry out phase dependent or time dependent spectroscopy, then by using the continuous clocking mode it is possible to reduce the pile-up substantially, since the effective exposure time is only 3.2 msec. (Note that the source must be bright, because the lack of timed exposures makes the incident photon's position ambiguous in one dimension. If we assume all photons detected originate from the target, then this loss of information about position doesn't matter.)

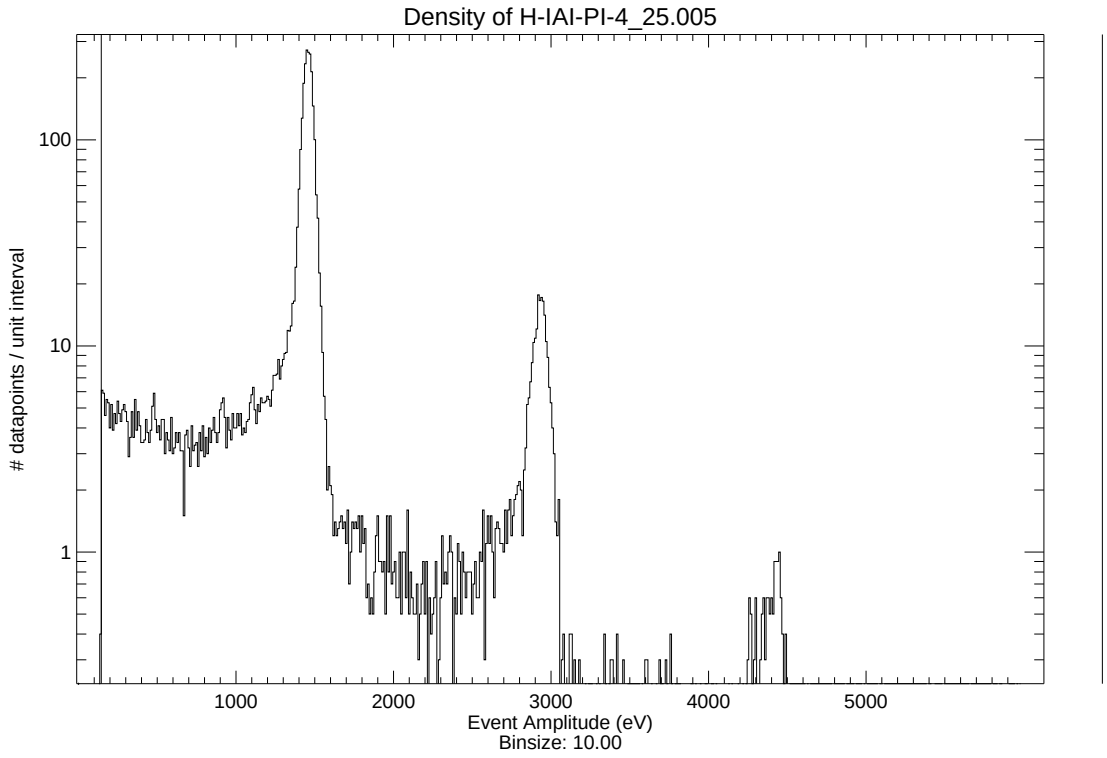

Figure 6.39: Al Kα spectrum taken in Continous Clocking mode using 3x1 event processing (incident flux produced a rate of 96.3 events/sec).

In the future, should high time resolution become important for certain classes of observations, it is possible to reduce the exposure time to about 0.1 msec. The spectral fitting

of data obtained from continuous clocking may not be as reliable as in normal faint mode operation, since the on-board event reconstruction currently does not use all eight adjacent pixels to the event pixel. Instead only a 3x1 region is examined for split threshold crossings. Because some split events result in charge in vertically adjacent pixels, split events are confused with single events in 3x1 event recognition. A spectrum collected using 3x1 event data exhibits low energy tails as compared to data processed by 3x3 event recognition. Figure 6.39 shows the observed spectrum of an Al Kα line spectrum collected in continuous clocking mode at XRCF.

Another effect of using 3x1 event recognition is multiple events produced by a single photon. In the data shown in Figure 6.39, for example, adding up only the peaks and multiplying by the number of piled-up events in each peak results in 26,562 events. The total number of events inferred from the flux measured by the Beam Normalization Detectors (BND) times the area times the time gives 27,742 events. On the other hand, the result of fitting the peaks and the continuum and multiplying by the number of piled-up events is to infer 36,368 events. The reason that total event rate exceeds the correct rate is that one event can be counted as many as three times, as it can split along both directions of the readout path.

Future software patches to the flight software will include the 3x3 event processing of each isolated event in contiuous clocking mode, so that the normal response matrices for spectral analysis should work and the inferred incident rate should accurately reflect the incident photon rate.

6.7.2.7 Reducing pileup with Off-axis Pointing

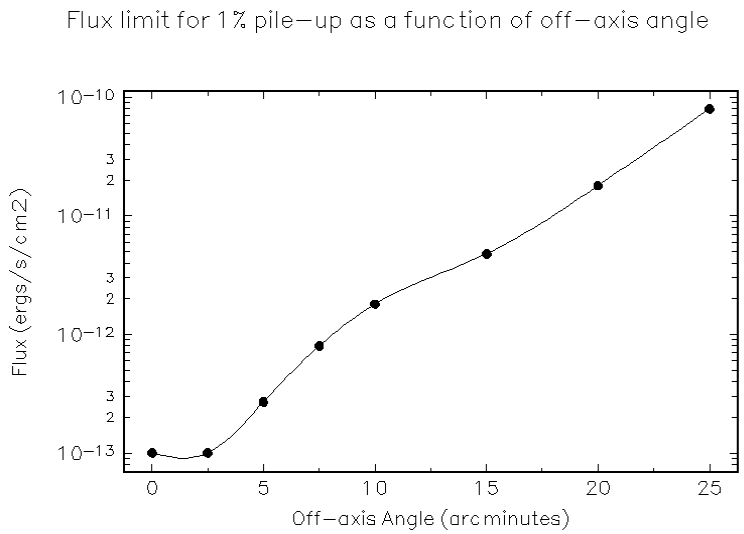

Figure 6.40: Flux limit for 1% pile-up as a function of off-axis angle.

In planning observations it is possible to reduce pile-up effects by pointing the axis of the telescope away from the target of interest by a small amount. As the PSF gets larger with increasing off-axis angle the detected flux from a point source will be spread over many more pixels, hence decreasing the probability of photon pileup within a single CCD frametime. Naturally the telescope used off-axis has degraded spatial resolution, so this technique is best used for relatively isolated point sources. Note also that the effective area of the HRMA decreases with off-axis angle, but in these cases the desire is to limit the rate of photons detected, so the area decline is not usually a problem. The user should also take care that the offset pointing does not place the target within the 'gaps' between CCDs, or off the active chip array.

Figure 6.40 shows the off-axis angle required to lower the pile-up fraction to 1% versus incident flux. By using this figure, an observer can request an off-axis angle which reduces the source flux at which pile-up occurs by two orders of magnitude.

6.7.2.8 Conclusions from XRCF pileup analysis

The primary results from the pileup analysis for a subset of Phase F and H data taken at the Al-Kα and O-Kα energies with ACIS-I and ACIS-S in focus, and comparison to model predictions, are as follows:

- The measured pileup fraction increases with the source intrinsic flux, as expected, with a non-linear trend.
- The pileup is a function of grade selection, decreasing significantly when only grade G0 is considered (Figures 6.35 and 6.36). For bright sources and for the FI chip, grade filtering could provide an effective method to control pileup without losing the capability of doing some (modest) spectral analysis.
- The analytical model proposed by McNamara (1997) overestimates the true pileup. This model should thus be used to derive a conservative upper limit for the pileup.
- The `MARX` tool `pileup` underestimates the true pileup by as much as 50% at lower source fluxes and for no grade selection (see above).
- Subframing (i.e., reading out a reduced number of CCD rows centered on the aim-point) can be used to control pileup. Available calibration observations show that pileup can be reduced by 44% for grades G02346 by going from 114 to 18 rows.
- For extremely bright sources either the gratings should be used, or Continuous Clocking mode used (or both).
- In cases where spatial resolution is not critical, it is possible to avoid pileup problems by intentionally positioning the source off-axis.

6.7.3 Pile-up Mitigation

Although there are a number of observing strategies that will raise the threshold flux level at which pile-up becomes a significant problem (ASC, 1997), some piled-up ACIS observations will nevertheless be performed. We hope that an algorithm for correcting a piled-up spectrum will eventually be developed. In the meantime, however, we are investigating simple analysis strategies that will separate reliable events from corrupted events, allowing the observer to discard the corrupted ones.

Here we describe an obvious technique suitable for isolated point sources: **Since pile-up is related to the surface brightness of the incident photon distribution, an event's position in the source PSF is related to the probability that the event is corrupted. So, one can reduce pile-up effects to any desired level by discarding a sufficient number of events from the PSF core.**

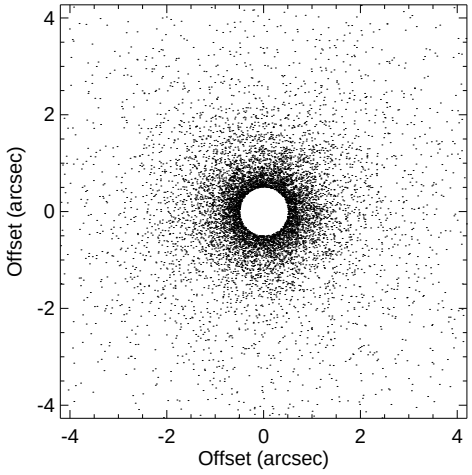

Figure 6.41: Mask applied to aspect-corrected events.

We choose to discard events by applying a circular mask centered on the PSF, as depicted in Figure 6.41. Our investigation explores the relationships between the photon flux level, the size of the mask, and the magnitude of the spectral distortion remaining in the unmasked events. Since both the CCD behavior and the AXAF PSF are energy dependent, we simulated on-axis (aimpoint of the I-array) monochromatic point sources at three different energies – Oxygen (525 eV), Aluminum (1.49 keV), and Copper (8.03 keV).

6.7.3.1 Simulation Results

Photons were generated using the MARX (Wise et al., 1997) package and Monte-Carlo simulations of the CCD physics were performed by software developed at Penn State. In order to meet the schedule for this report, these simulations had to be performed using MARX version 2.04, which uses PSF models which are known to differ significantly from the measured AXAF PSF. **Thus, this work should be considered as a demonstration of an idea rather than as a calibrated recipe for pileup mitigation in ACIS.** The ACIS team will repeat this analysis using a proper HRMA simulation when the corrected MARX version becomes available.

The relative motion that will occur between ACIS and the sky ("dither" (ASC, 1997))

and the expected error in measuring that motion (aspect error[2]) are simulated. Events with grade 255 are discarded[3]. Each simulated event list contained $\sim 50,000$ detected events.

For each of the three energies, the following eight simulations were performed:

- A *Reference Simulation* put exactly one photon on the CCD per frame, representing the behavior of the system with no pile-up (very low flux).
- A *base flux* level, F_B, which produced ~ 0.067 detected events per frame was determined empirically.
- With photons allowed to arrive randomly, seven simulations were run at the following flux levels: $F_B, 2F_B, 4F_B, 8F_B, 16F_B, 32F_B,$ & $64F_B$.

The width of the spectral line was measured in each reference event list: $\sigma \approx$ 20eV (O-Kα), 30eV (Al-Kα), 70eV (Cu-Kα). The event lists were filtered to extract those events which fell within 5σ of the line peak and which had grades normally considered acceptable (ASCA grades 02346), producing eight *in-band* event lists. Each of these was then spatially filtered using various circular masks centered on the source, producing a large set of in-band event lists which explore the (flux, exclusion radius) parameter space. The fraction of photons detected in-band was calculated for each event list and those data are shown in Figure 6.42. The curves plainly demonstrate that many in-band events are lost at high fluxes when no masking is done (exclusion radius = 0) but that, for a given flux level, if you increase the exclusion radius you can approach the results of the reference simulation, i.e. reduce pile-up. The overall differences in the range of the Y axes and shape of the curves between the three energies reflects the energy dependence of the ACIS quantum efficiency and AXAF PSF size.

To quantify the reduction in pile-up effects that can be achieved by discarding events, a measure of pile-up effects is needed. Here, we concentrate on quantifying the spectral distortion effect remaining after an event list has been spatially masked by defining a "quality" metric in an obvious way: **The "quality", Q, of an event list that has been filtered (e.g. by grade, spatial mask, etc.) is defined to be the number of events remaining divided by the number of events that would remain if the same photons had arrived at a very low rate (no pile-up) and the resulting events had been filtered in the same way.** In our context, Q is the number of in-band events divided by the number of in-band events produced by a reference simulation (one photon per frame) that used the same number of incident photons. In Figure 6.42 dividing each of the seven curves by the reference curve (solid line) produces a plot of Q versus exclusion radius. For this study, we arbitrarily adopt a quality goal of 0.90 and plot the exclusion radius required to achieve this goal versus the relative flux level in Figure 6.43-left.

[2]The predicted AXAF aspect errors are gaussian, $\sigma \approx 0.17''$ (ASC, 1997).

[3]In normal operation ACIS discards events with the grade 255 morphology since their origin is likely to be cosmic rays rather than X-ray photons.

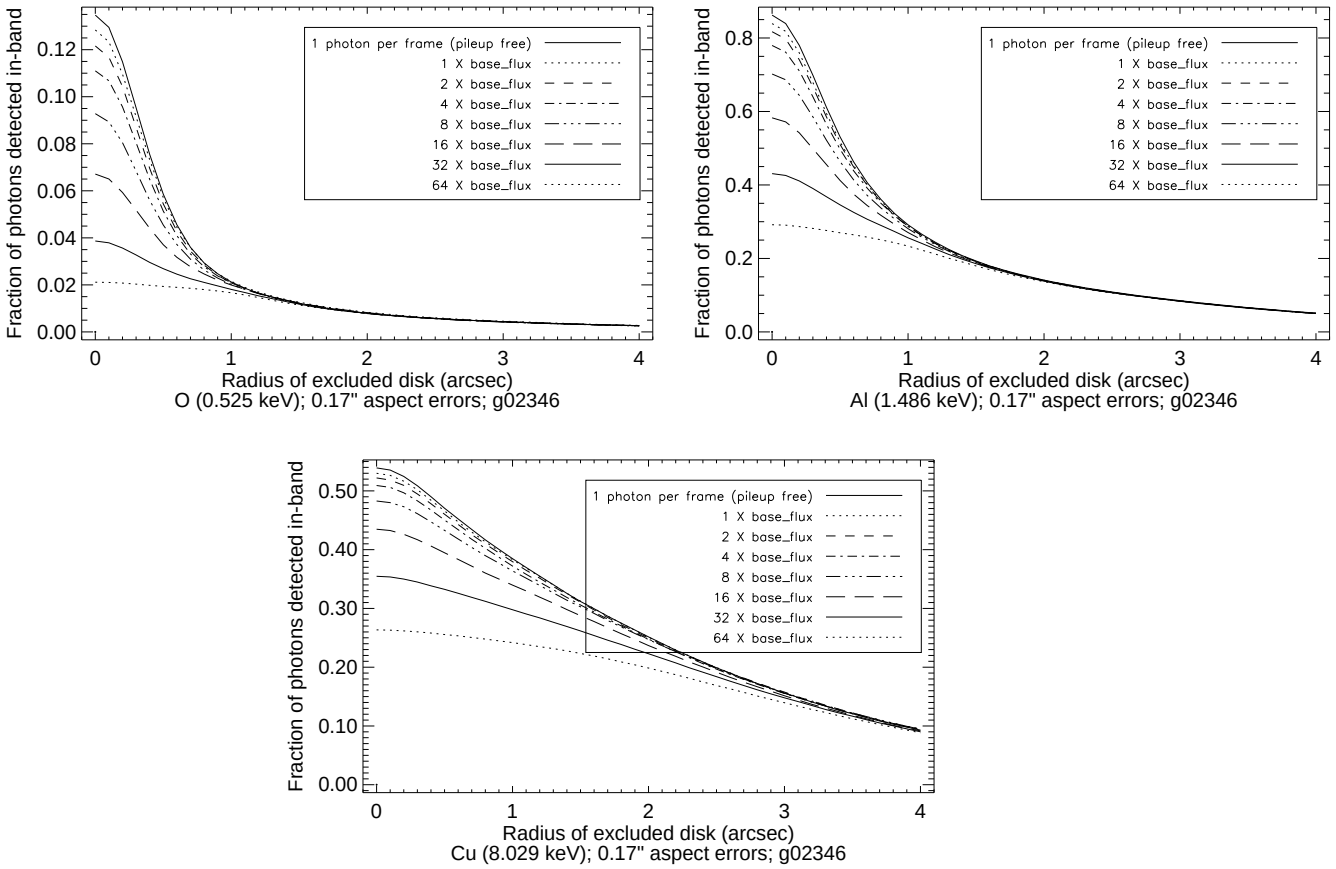

Figure 6.42: In-band events with PSF core excluded for eight flux conditions. The Base Flux level produced ~ 0.067 detected events per frame.

If the exclusion radii shown in Figure 6.43-left are applied, then the quantum efficiency of ACIS will, of course, be reduced. The relative efficiency of the masked ACIS compared to a hypothetical ACIS that suffered no pile-up effects is shown in Figure 6.43-right. These values were determined empirically by computing the fraction of events from the Reference Simulation that survived the appropriate mask. An equivalent way to compute the relative efficiency would be to blur the AXAF mirror point spread function to account for aspect errors, then integrate the resulting PSF outside the exclusion radius. Figure 6.44 shows the results of applying the masking technique to the three most piled-up simulations ($\times 64$ flux level).

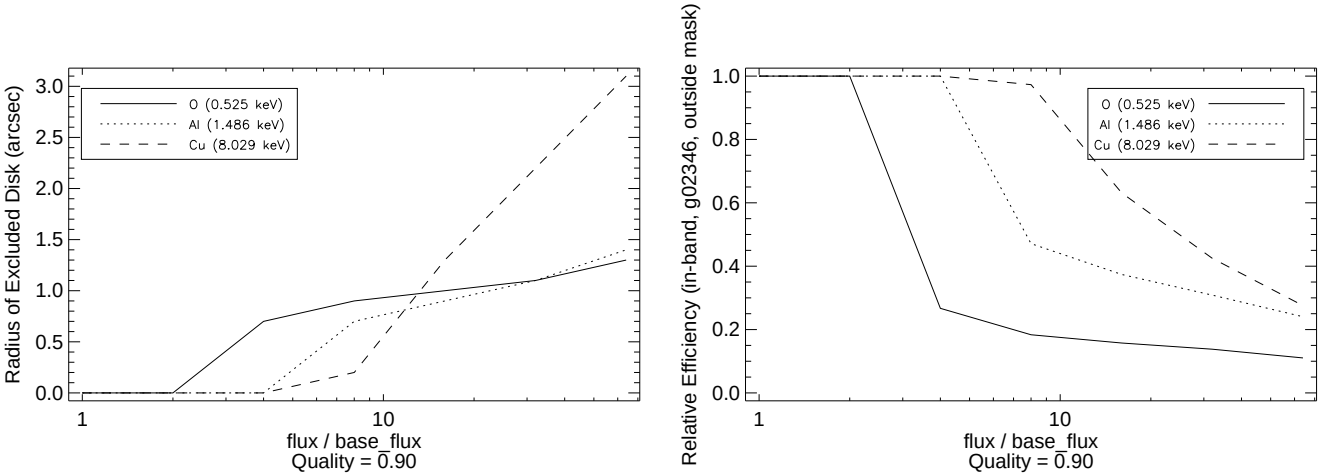

Figure 6.43: Core masking (left) and efficiency reduction (right) required to achieve quality metric, $\frac{\#\,in{-}band\,events}{\#\,reference\,in{-}band\,events}$, of 0.90.

6.7.3.2 A Recipe for Pile-up Mitigation?

These simulation results, while illustrative of the concept of masking to improve piled-up spectra, do not provide a recipe for pile-up mitigation that can be blindly followed. Pile-up effects clearly depend on the incident spectrum, and no astrophysical spectrum looks like the lines we've simulated. Furthermore, the quality metric we've used is not defined for a polychromatic spectrum.

Nevertheless, an observer could use these results either to estimate the masking a proposed observation will require or to roughly clean up an actual observation. Assuming a point source on axis, the steps would be:

- From the observed event list, measure either the raw event rate, the g02346 event rate, or the raw event rate outside of a $1''$ circle centered on the source. These quantities all serve as proxies for the incident photon flux, which is unknown.
- Using curves similar to those in Figure 6.45 find the O, Al, & Cu simulations that produced the same flux proxy value.
- For O, Al, & Cu, look up the exclusion radius that achieves the desired quality level.
- Use the largest of those radii to filter the events (i.e. assume all photons from the source are at the "worst" of the three energies).
- Adjust the AXAF effective area curve by the relative efficiency shown in Figure 6.43-right. Obviously one would want to compute the relative efficiency more accurately and at more energies than was done here.

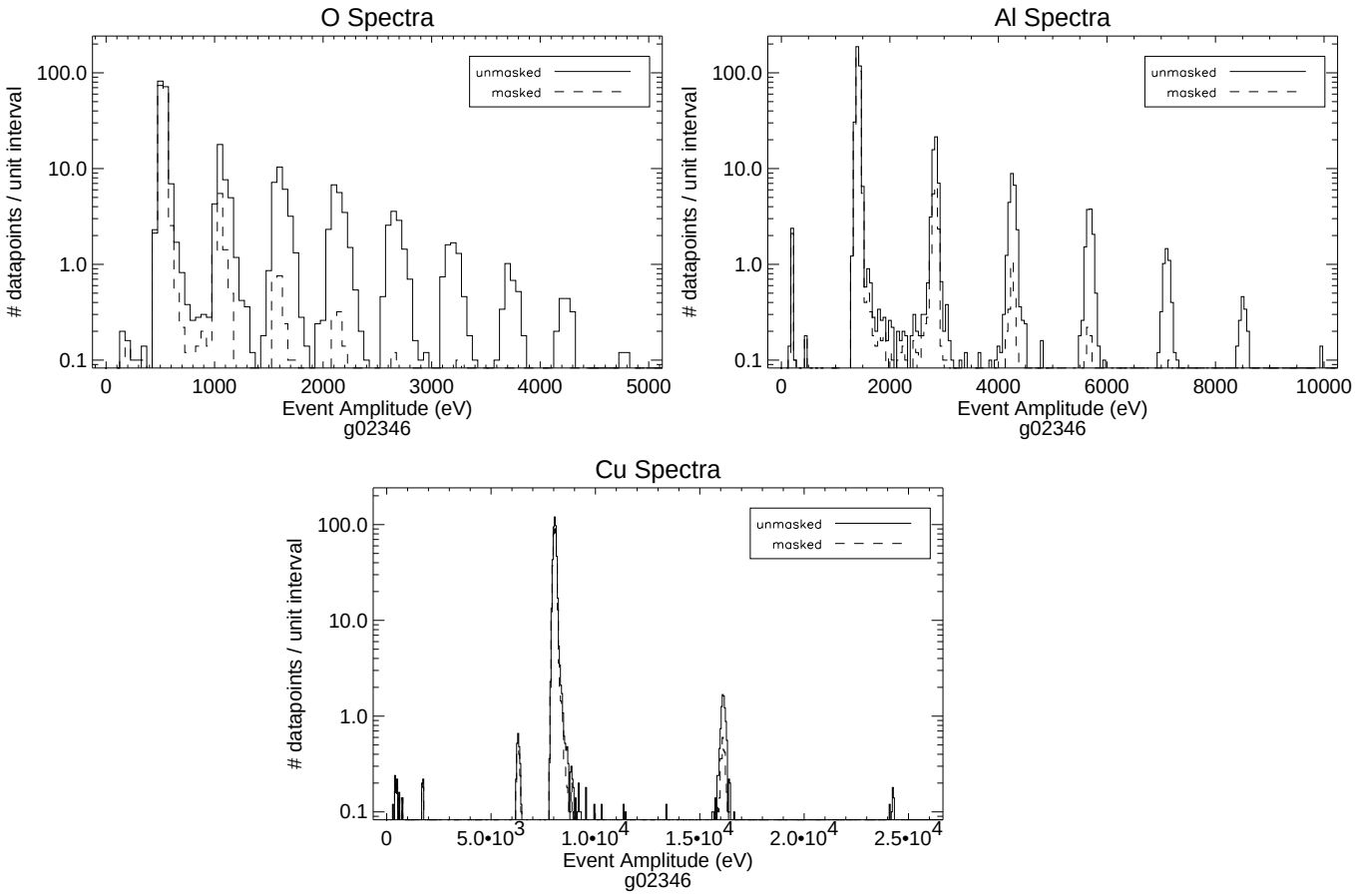

Figure 6.44: Grade-filtered piled-up spectra (×64 flux level) shown both with no masking, and with masking that achieves a quality level of 0.90.

6.7.3.3 Comments on the Use of Masking

All observers must choose a spatial region over which the light from a source will be integrated. Traditionally this region has been shaped like a circle and the radius is a compromise between wanting to include as much signal as possible and wanting to include as little background as possible. The technique discussed here is simply an extension of this idea to an annular shaped region. The choice of the inner radius is again a compromise between desirable signal (the unpiled events) and undesirable background (the piled-up events).

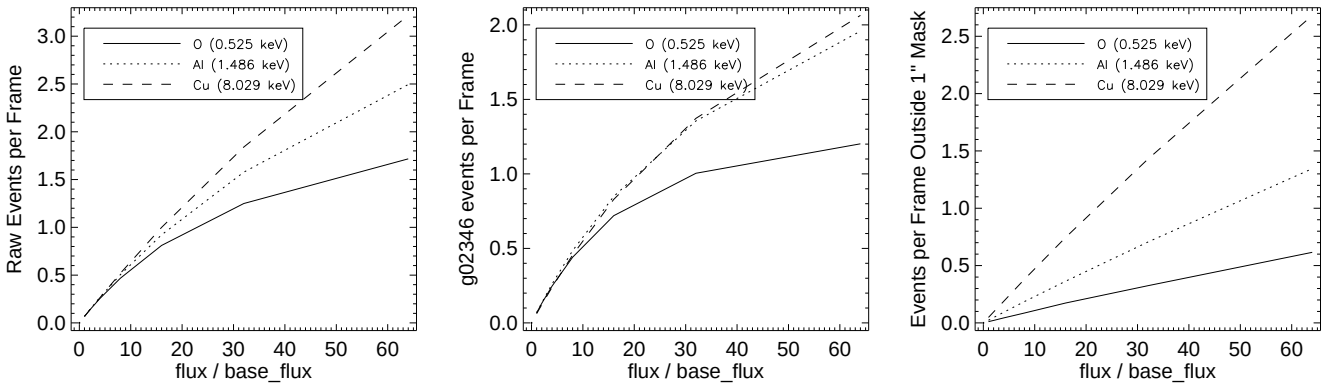

Figure 6.45: Flux proxies for seven simulations

6.8 Radiation Damage from HRMA Focussed X-rays

The ACIS CCDs are sensitive to exposure to X-rays as well as to protons and particles with greater charges. Radiation tests with tungsten X-rays show that 200 krads is sufficient to change the operating point of a CCD by 2 Volts, which renders the CCD inoperative. In the case of AXAF with a focused beam of X-rays, a small voltage shift can create a pocket that can change the charge transfer efficiency in a given column of a CCD. The physical mechanism that creates this condition is the ionization of silicon dioxide atoms and silicon nitride atoms in the layer separating the gate structure from the buried channel in the CCD (see cross section below). This charge is trapped in the dielectric and can not be discharged, hence the buildup is cumulative. If sufficient charge accumulates over time, the charge transfer efficiency of the CCD is affected. For this reason, some precautions must be used in the exposure of ACIS to bright X-ray sources on orbit. The charging of the dielectric layer is a function of x-ray energy, being strongest at low energy in the front illuminated (FI) CCDs. The back illuminated (BI) CCDs are less sensitive to charging because the layer of silicon that is about 40 microns thick, overlays the insulation layer and provides shielding for this layer. A gate thickness of only about 0.6 μm shields the FI CCDs from the charging effect.

To compute the radiation damage from cosmic sources it is necessary to assume a spectrum for the source - or use a measured spectrum. To define the problem take the photon number spectrum to be given by N(E)dE, the absorption coefficient for silicon as $\mu_{Si}(E)$, the absorption coefficient for SiO_2 as $\mu_{SiO_2}(E)$, and the absorption coefficient for Si_3N_4 as $\mu_{Si_3N_4}(E)$, the densities of three components as ρ_x, and the pixel area to be A_{pixel}. The cross section of the CCD containing two pixels is shown in Figure 6.46. X-rays from the focusing optics, which are located at the top of the page, can be imagined as directing a stream of X-rays down onto the pixel from above. The gate structure absorbs a

fraction of the X-rays depending upon the energy, and the rest pass through with a small fraction absorbed in the Si_3N_4 layer and another fraction absorbed in the SiO_2. For a back illuminated CCD the X-rays are flowing upward on the page into the pixel where a significant fraction is absorbed in the Depleted Silicon region before it reaches the oxide layer separating the gates from the depleted silicon.

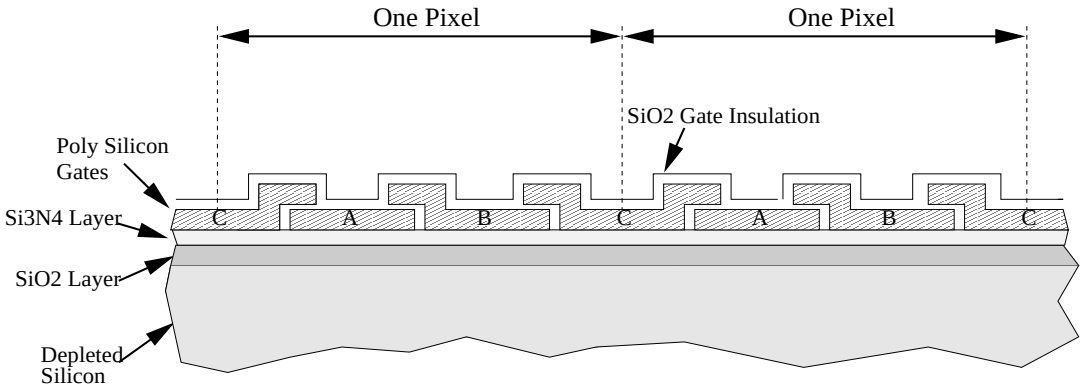

Figure 6.46: Cross section of two CCD pixels showing the different layers of absorbing material. The overlapping portion of the gate structure is exaggerated.

In order to compute the amount of ionizing radiation deposited in the insulating layer between the depleted silicon and the gate structure, it is necessary to integrate over the incoming spectrum. The following integral serves to illustrate the dose of ionizing radiation received by the SiO_2.

$$D = Abs/Area \tag{6.15}$$

where

$$\begin{aligned} Abs = \int_0^\infty A(E) \cdot f(E) \cdot N(E) \exp(-\mu_{Al}(E)\rho_{Al}x_{Al} - \mu_{poly}\rho_{poly}x_{poly}) \\ \cdot \exp(\mu_{SiO_2}(E)\rho_{SiO_2}x_{SiO_2}) \exp(\mu_{gates}(E)\rho_{gates}x_{gates}) \\ \cdot \exp(-\mu_{Si_3N_4}(E)\rho_{Si_3N_4}x_{Si_3N_4}) \cdot (1 - \exp(-\mu_{SiO_2}x_{SiO_2}))EdE \end{aligned} \tag{6.16}$$

$$Area = A_{pixel}\rho_{SiO_2}100 \int_0^\infty N(E)dE \tag{6.17}$$

The first term in 6.16 is the area of the telescope, the second term the fraction of the flux into a single pixel for the on-axis position (Fig. 6.47), the third term is the input photon number flux after the absorption by the interstellar medium has been included, the fourth term is the absorption in the aluminum/polyimide optical blocking filter, the fifth term the absorption in the SiO_2 overcoating, the sixth term the silicon in the gate structure, the seventh term the silicon nitride insulation layer and finally, the absorption in the silicon dioxide insulation layer. The actual gate structure is used in the calculation, but the fourth term with a gates subscript is a placeholder to represent this term. The divisor converts

the absorbed energy into the absorbed energy in units of 100 ergs per gram of material in the pixel which is the dose in rads, D.

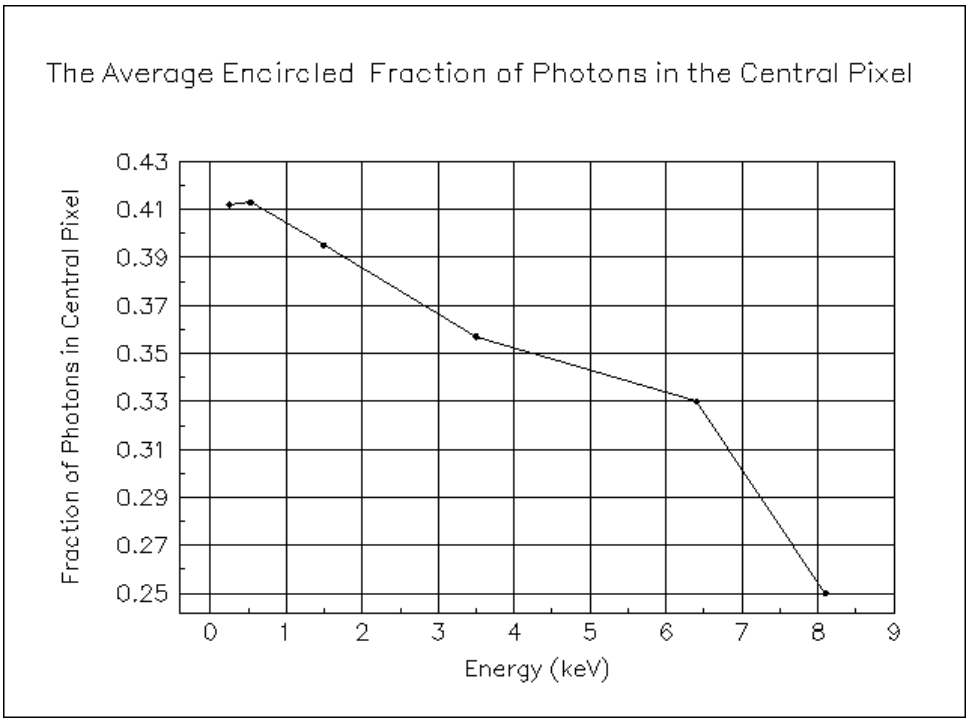

Figure 6.47: Fraction of incident X-ray flux falling within central pixel (averaged over all sub-pixel positions).

The following figures (6.48-6.51) present the results of computations for a range of input spectral parameters. The input spectrum has been normalized to one photon cm^{-2}-s^{-1}, as seen at the top of the Earth's atmosphere.

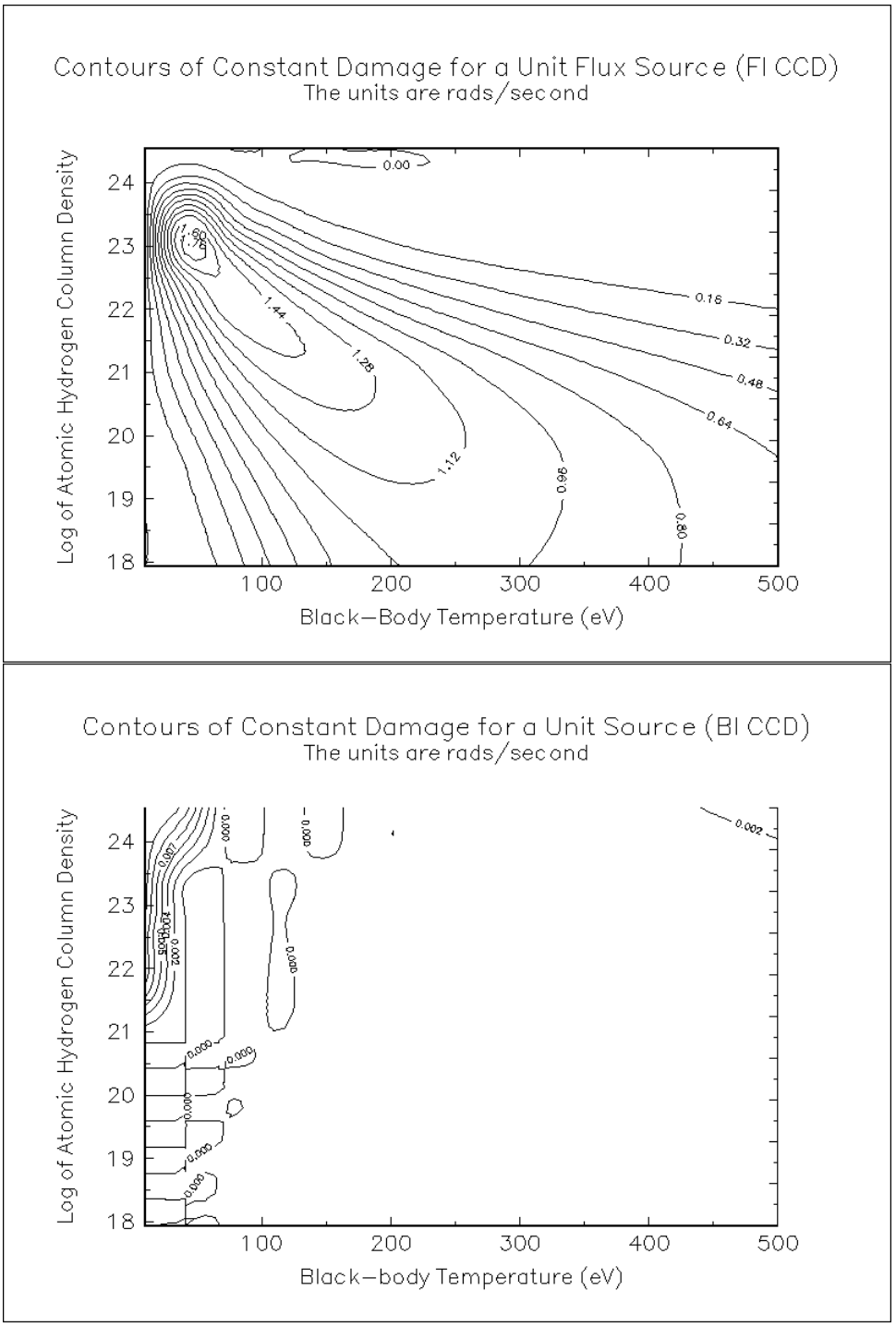

Figure 6.48: Expected radiation damage from a 1 photon/cm^2-s blackbody source incident at the HRMA aperture. Top: FI chip; Bottom: BI chip.

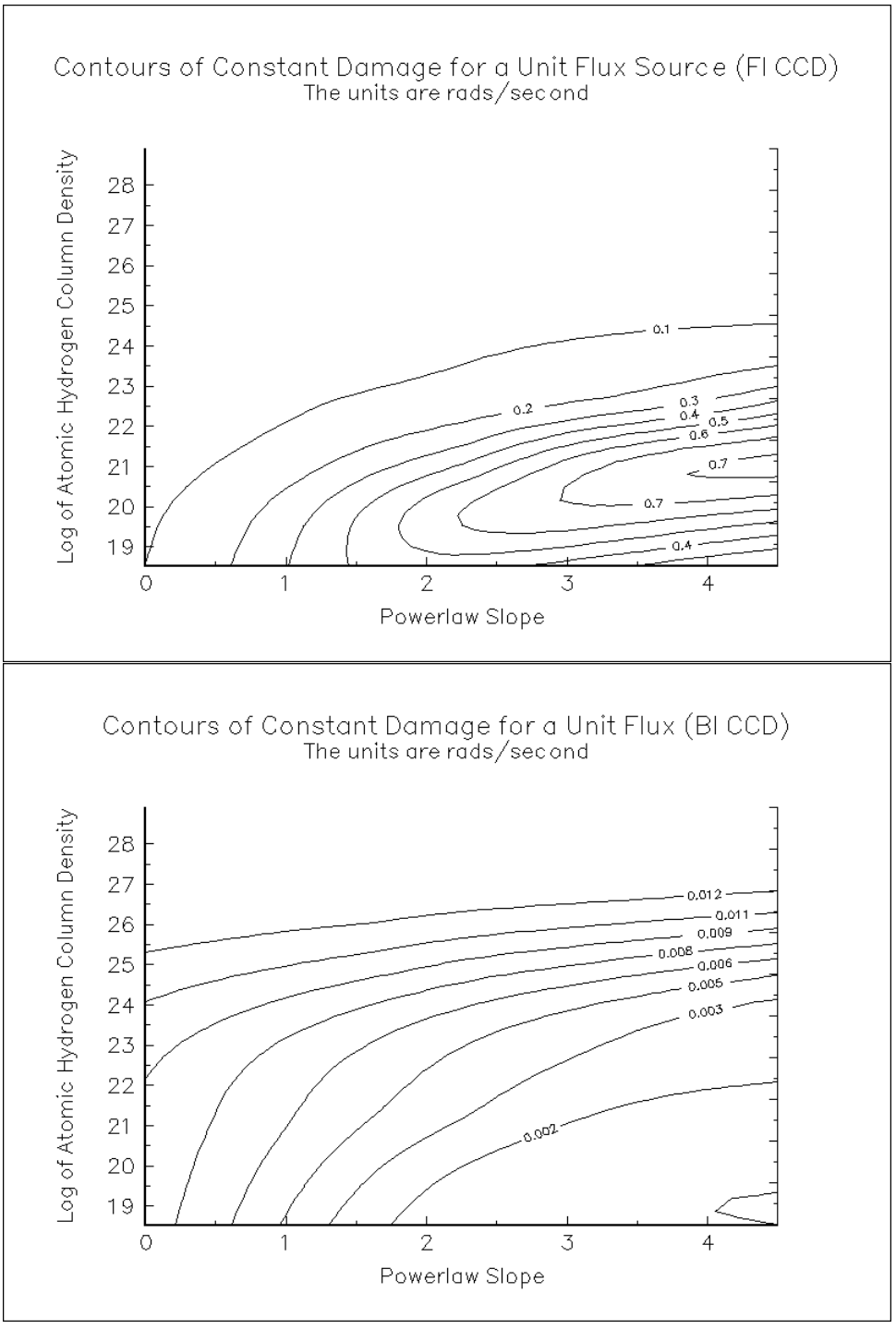

Figure 6.49: Expected radiation damage from a 1 photon/cm^2-s power law source incident at the HRMA aperture. Top: FI chip; Bottom: BI chip.

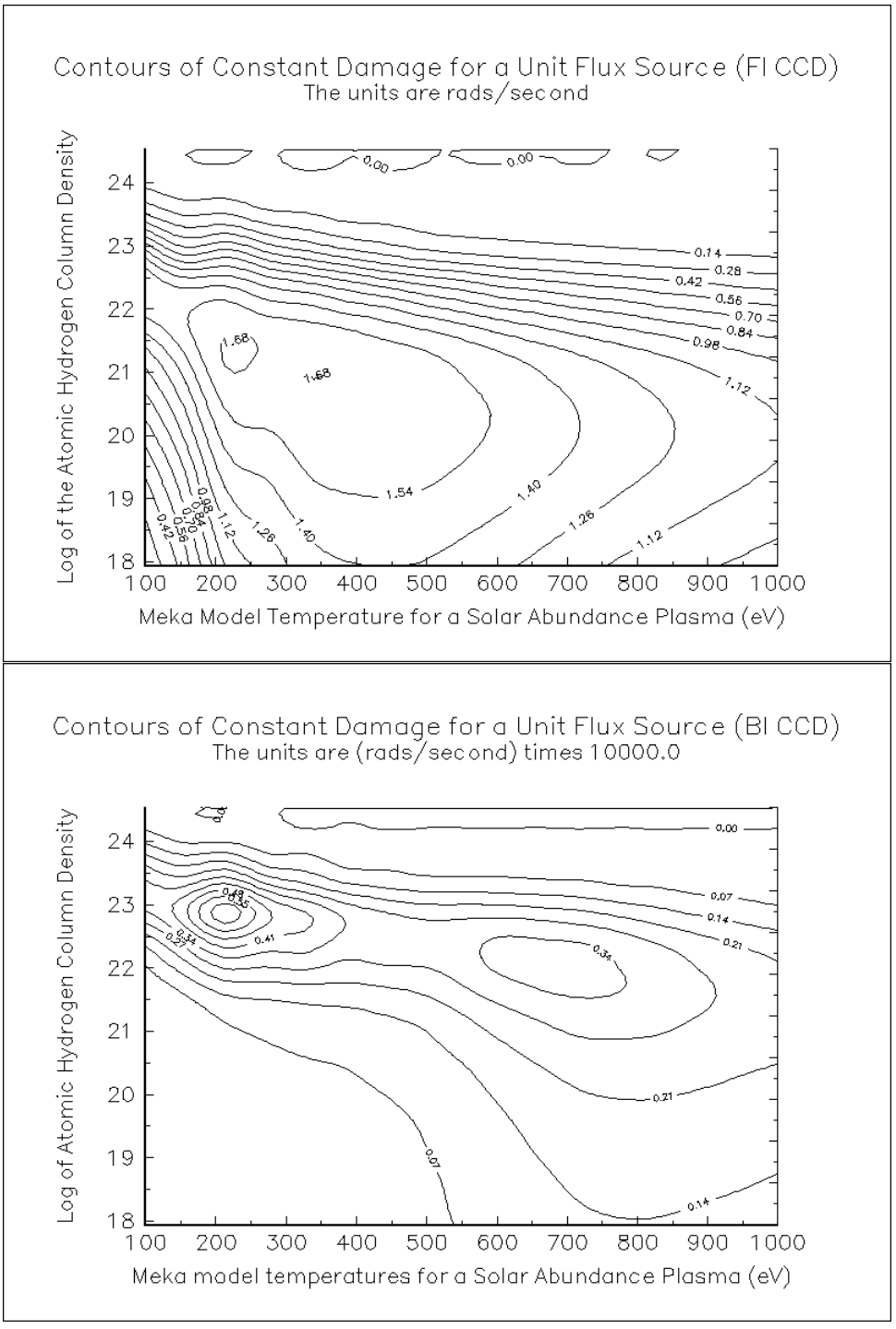

Figure 6.50: Expected radiation damage from a 1 photon/cm^2-s thermal plasma source incident at the HRMA aperture. Top: FI chip; Bottom: BI chip.

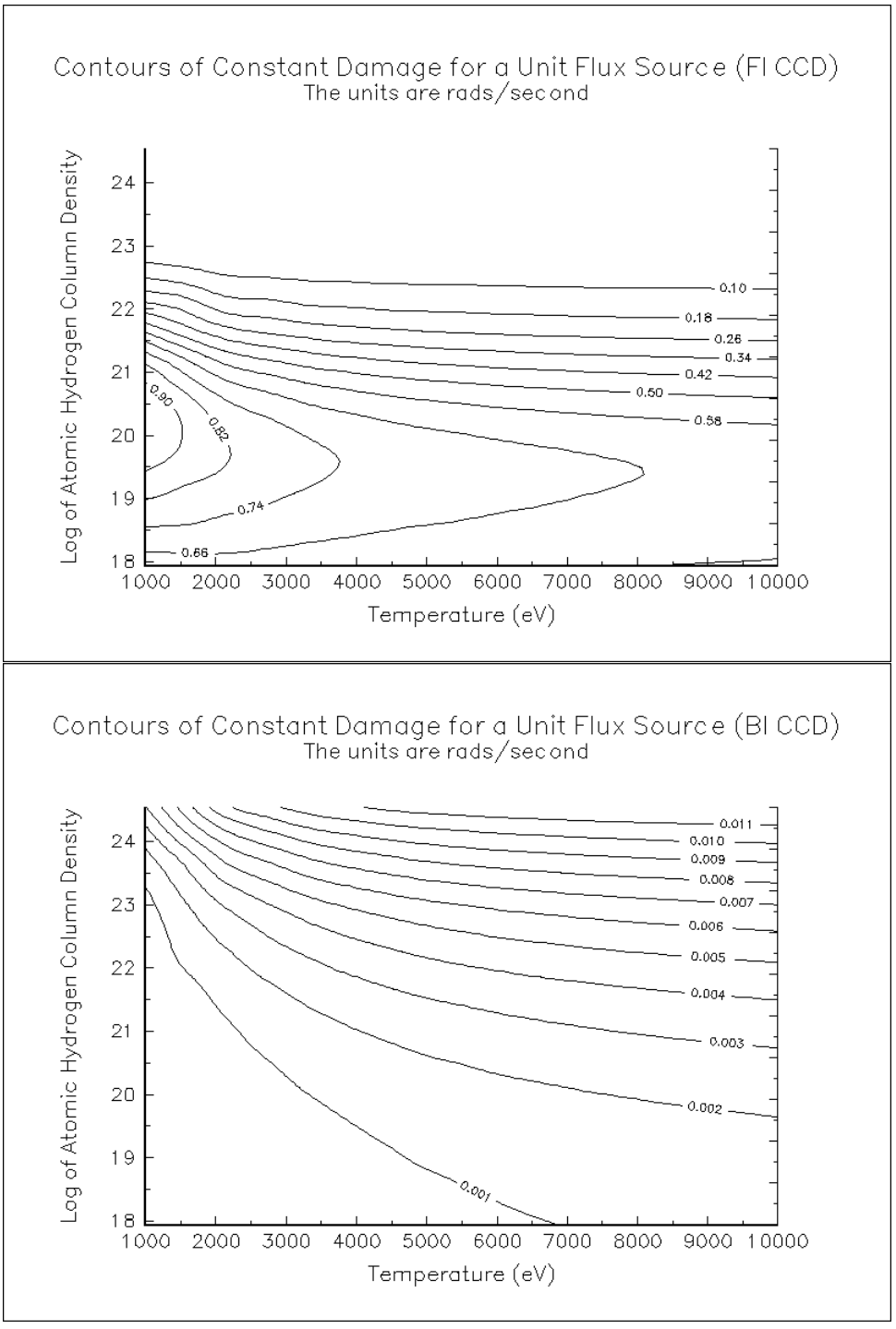

Figure 6.51: Expected radiation damage from a 1 photon/cm^2-s thermal bremsstrahlung source incident at the HRMA aperture. Top: FI chip; Bottom: BI chip.

6.9 On-orbit Performance Prediction

The data collected at the XRCF cannot be directly applied to prediction of in-orbit performance because several significant effects influence the ground data which will be different in orbit. The source at XRCF is not located at an infinite distance from the ACIS, the XRCF source has a finite size which is resolved by the HRMA in measurements near the optical axis, the gravitational effects of loading on the HRMA structure cannot be perfectly removed by the HRMA mounting fixture, and the ACIS operating temperature differs slightly from the expected in-orbit values. Thus we must use the data collected at XRCF and the sub-assembly results to refine and validate a model of the HRMA/ACIS response.

The preceeding sections describe the status of the testing and validation of the model. Then, given raytrace models of the HRMA which are appropriate to zero-gravity and infinite source distance, we apply our ACIS models to obtain predictions of the in-orbit performance.

For this report (January, 1999) we have not received the exact ray-trace results for the XRCF tests. Approximate SAOSAC ray files exist, which incorporate finite-distance XRCF effects and on-orbits predictions, but we still lack ray files with the effect of finite-source-size. We will in future reports obtain the ray-traces and produce user-friendly summaries of the expected HRMA/ACIS performance.

Chapter 7

Calibration Products

The ACIS team produced various highly useful items which may be of interest to people wanting to extend or apply the calibration results listed in this document. As many of these items are dynamic, in the sense that continuing work is leading to improvements, expansions and corrections, what we present here are descriptions of these products. We anticipate that the ACIS team will maintain these in Internet accessible forms for the duration of the ACIS team support. We hope that the ASC will also support the accessibility of these materials.

7.1 ACIS_SIM: Simulations of CCD Response to X-rays

Due to the difficulties and expense associated with collecting X-ray CCD data, astronomers have relied on simulations of such devices almost as long as they have used the devices themselves. Every X-ray CCD group has its own simulation code; that code is usually subject to rapid and radical change as the physics of these devices becomes better understood and the devices themselves evolve. Under this paradigm, the ACIS partnership between PSU and MIT has seen the development of two virtually independent ACIS simulators. Each one has strengths and weaknesses; each invokes different aspects of the physics to explain the data. Both are under active development. The following descriptions and results pertain only to the PSU version. (See Chapter 4 for a discussion of results based on the MIT CCD simulator.)

7.1.1 The Generic CCD Simulator

A Monte Carlo algorithm has been implemented in order to model and predict the response of X-ray CCDs to photons and minimally-ionizing particles. This algorithm draws on

empirical results and predicts the response of three basic types of CCD devices: back-illuminated, epitaxial front-illuminated, and bulk front-illuminated. Each type of device is assumed to consist of a stack of slabs, each slab having different properties. The three types of CCDs are modeled by arranging these slabs in the appropriate order. The user specifies the device to be modeled by supplying the thickness of each layer. Both ACIS BI and FI (bulk type) chips can be modeled using this technique.

In a back-illuminated device, the top layer is a damage or surface layer, in which liberated charge is not efficiently propagated and is largely lost to recombination. Photons which interact in this layer may only have a fraction of their charge propagated to the depletion layer. Below this damaged or "modified substrate" layer is a field-free layer, which acts as a reflecting layer and prevents charge from the depletion region from leaking out into the modified substrate and generating dark current. The surface and field-free layers sit on top of the depletion layer, which ends in the buried channel and gate structure at the bottom of the device.

An epitaxial front-illuminated device is similar to an inverted back-illuminated device. The top layer is the gate structure, modeled simply as a uniform slab of absorbing material (a "dead" layer). Beneath this is the depletion (field) region, followed by a field-free region, then a bulk silicon substrate. A bulk front-illuminated device (such as the ACIS FI chips) has the same dead layer on top of a depletion layer, but this is simply followed by a bulk substrate.

In order to simulate X-ray photon detection by these devices, a random interaction depth is generated for each simulated photon, based on the absorption coefficient appropriate to that photon's energy. The photon is allowed to interact with the device and produce a cloud of charge. This charge spreads through the layers of the device, with the spreading rate and the charge reflection and absorption dependent on the properties of each layer. Once the charge reaches the buried channel, it is "detected" by recording an appropriate number of electrons in each pixel over which the charge spread. The degree to which a given photon's charge cloud is split across pixels depends on the photon's energy, its interaction depth, and the proximity of the interaction to pixel boundaries (channel stops).

The simulation accounts for the possibility of secondary fluorescent photon generation (both Kα and Kβ) from the silicon, if the initial photon energy is above 1839 eV. Fluorescent photons from other elements in the device (such as oxygen) may occur, but with a lower probability, so they have not been included in the simulation at this time. As the charge cloud propagates through the field-free regions of the device, some of the charge may recombine and be lost. Charge spreading and recombination has been modeled by solving the diffusion equation for each slab of the device.

The output of the simulation is a rectangular CCD frame, with the size determined by the user. It is in units of electrons and contains photon events, readout and other noise, and minimally-ionizing particle events. These particle events were modeled similarly to photon events; the track of a particle through the detector is randomly generated, then simulated by allowing the detector to absorb energy from the particle every time it traverses one

micron in depth through the device. The charge cloud generated at each interaction point is propagated just as photon charge clouds are propagated.

Figure 7.1 shows the output for a back-illuminated device with 1000 1keV photon events and 10 particle events, assuming the uniform illumination one would expect in subassembly calibrations. Note that most of the photon events are spread among several pixels at this energy. For comparison, consider Figure 7.2, which also contains 1000 1keV photon event and 10 particle events, but detected by a front-illuminated device. Most of the photon events are contained in a single pixel. Note how much more the particle events have bloomed – this is a result of the thick substrate assumed for this device.

Figure 7.1: Example of a simulated back-illuminated CCD frame, containing 1000 1keV photon events and 10 particle events

Radiation damage can also be included in the model, at the user's option. The effect of this damage is manifested by increased charge transfer inefficiency. This effect is assumed

Figure 7.2: Example of a simulated front-illuminated CCD frame, containing 1000 1keV photon events and 10 particle events

to have a power-law dependence with energy. The code allows the user to supply this power-law index and the CTI.

7.1.2 Specifics of the ACIS CCD Simulator

A User's Guide to the Penn State CCD Simulator can be found in Appendix B. All parameters, including device geometry and tuning parameters, necessary to run the simulator are encapsulated in an input parameter file. There is a different parameter file for each ACIS CCD.

All absorption coefficients are from Henke data (no EXAFS included anywhere). We are currently working on improved modelling which incorporates the effect of variation in interaction depth, based on detailed absorption cross-sections which include EXAFS. These

EXAFS improved models are not yet ready for this report. For now we will presume that either the main part of the CCD's silicon is too nonuniform to produce EXAFS or that the EXAFS measured in the gate structure samples by Prigozhin et al. are not applicable to this thick crystal. The consequence of this assumption is that the only applicable absorption coefficients available to us, for photon interactions below the gate structure (i.e. in the main part of the device), are the Henke data. We currently do not simulate the complex geometry of the gate structure (unlike the MIT model – see Chapter 4).

Our model is tuned to match XRCF Phase H and I data *from the I3 and S3 chips only*, at 21 energies unevenly sampling the range 277–9000 eV. The XRCF dataset is much smaller than the MIT lab dataset; the PSU model is tuned to fewer test events than the MIT model in all cases, sometimes to very few (< 10000) events.

The XRCF data were filtered to contain only ASCA "g02346" events prior to tuning the simulator to match them. This helped to remove contamination in the data from pileup, cosmic rays, and some of the source continuum spectrum. It is likely that some source continuum is still present in these filtered data, especially at energies below that of the main peak. We cannot guarantee that our tuning is not somewhat corrupted by the presence of this extraneous source spectrum masquerading as the CCD energy redistribution function.

A thin SiO_2 layer under the gates is invoked to explain the small feature at the lowest energies (usually $\sim 150eV$) in the XRCF FI data and to explain the background counts, based on ideas from the MIT ACIS team (Prigozhin et al. (1998b)). We do not see the energy-dependent low-energy peak described in this MIT document in the XRCF data. So, although the mechanism for including this feature is in place in the simulator, this feature is not modeled.

A model for the channel stops is used to account for the soft shoulder of the main peak in the FI data. We currently assume that photons interacting in the SiO_2 layer of the channel stop are completely lost. Those that interact in the p+ silicon suffer splitting of their charge clouds; we assume that the charge is quickly swept to the right or left side of the channel stop, and that the fraction swept to each side depends on the interaction distance from each side. Each separated charge cloud is assumed to propagate from a new x position (at the edge of the channel stop) through the depletion region as a normal photon would, using an initial charge cloud radius calculated from the original photon's energy. This model is motivated by the overabundance of right- and left-hand split events (ASCA-like grades 3 and 4) present in the soft shoulders of the XRCF data. We include a special location-dependent loss mechanism and an extra noise term for this process, necessary to reproduce the offset in the mean of the soft shoulder from the main peak mean and to reproduce the width of the soft shoulder.

As noted above, the PSU simulator allows for Si Kβ as well as Si Kα fluorescence and escape peaks. This is a very small effect and contributes insignificantly, given the low probabilities involved. For that reason, fluorescence of other elements present in the device (oxygen, for example) remains unmodeled.

We include explicit temperature-dependence for the parameters where laboratory exper-

iments have provided an analytical form for such dependence. This constrains us to model only those devices with acceptor concentrations less than $\sim 10^{14}$ cm^{-3}. Conveniently, the ACIS devices satify this criterion.

The PSU model is NOT to be used to infer CCD quantum efficiency, due to the way it is coded in these simulations and the fact that its QE predictions have not been compared to calibration data.

Work continues on attempting to include more effects in the simulation. Of significance is the effect of CTI on especially the BI chip performance. We will make available our results when we feel we can understand the phenomena reliably.

7.1.3 Tuning Parameters

There are seven energy-dependent tuning parameters used in the simulator to get its output to match XRCF data. They are necessary because the simulator does not incorporate all the device physics required to predict the data exactly; in effect, the existence of a tuning parameter represents an inadequacy in the model. We continue to improve the physics in the model. As we do so, these tuning parameters will change or, in some cases, disappear altogether.

For now, the tuning parameters can be grouped into those that affect the main peak, those that affect the size of the charge clouds, those that pertain to the SiO_2 layer between the gates and the depletion region, and those that pertain to the channel stops. They are described in detail below.

- Main Peak Parameters

  gain_fudge adjusts the mean of the main peak to match the data at a given energy – represents non-linearities in the gain

  linewidth_fudge increases the width of the main peak to match the data

- Charge Cloud Radius Parameters

  rdsat_fudge increases the size of the charge cloud in the depletion region to achieve the observed grade distribution (branching ratios); note that this parameter is tuned only so the simulation reproduces the observed percentage of g0 events (i.e. no conscious effort is made to get the percentages to come out right in the other grades)

- SiO_2 Insulating Layer Parameters

  rioxide_fudge adjusts the size of the charge cloud in the SiO_2 insulating layer under the gates; this affects the background level and the sharpness of the low-energy feature

q0_oxide defines the charge contained in events that contribute to the low-energy feature – this sets the energy of that feature to match what is seen in XRCF data – it does not model the feature seen by MIT in the lab data and described by Jones et al. since this feature was not apparent in XRCF data

- Channel Stop Parameters

cslinewidth_fudge increases the width of the soft shoulder of the main peak

csloss_fudge adjusts the mean energy of the soft shoulder of the main peak

Figure 7.3 shows the values of all the tuning parameters for CCD I3, as a function of energy. For simulating photons with energies not measured at XRCF, the code performs a linear interpolation between the two closest measured values. When forced to extrapolate (for simulated energies beyond the range measured at XRCF), the code uses the tuning parameter values appropriate for the closest measured energy.

7.1.4 Future Plans

We need to instantiate the gate structure, incorporating the correct geometry and calculating the absorption coefficients appropriate for the gate structure materials using the data of Prigozhin et al. (1998d). This will make our code more applicable to quantum efficiency tuning and simulation.

Effects of CTI are seen in the calibration data, especially for the BI chips. We will make available our results when we feel we can understand the phenomena reliably.

In spite of its limitations, the current incarnation of the frame simulator is useful for addressing timely issues in CCD characterization. The code has been used to develop an algorithm to determine sub-pixel positions of photons and to assess the problems associated with photon pile-up from bright uniform beams and bright point sources. It has been used in conjunction with SAOSAC and MARX to model the XRCF PSF (see Chapter 6). Event lists generated by this simulator are being used by the ASC to generate ACIS response matrices.

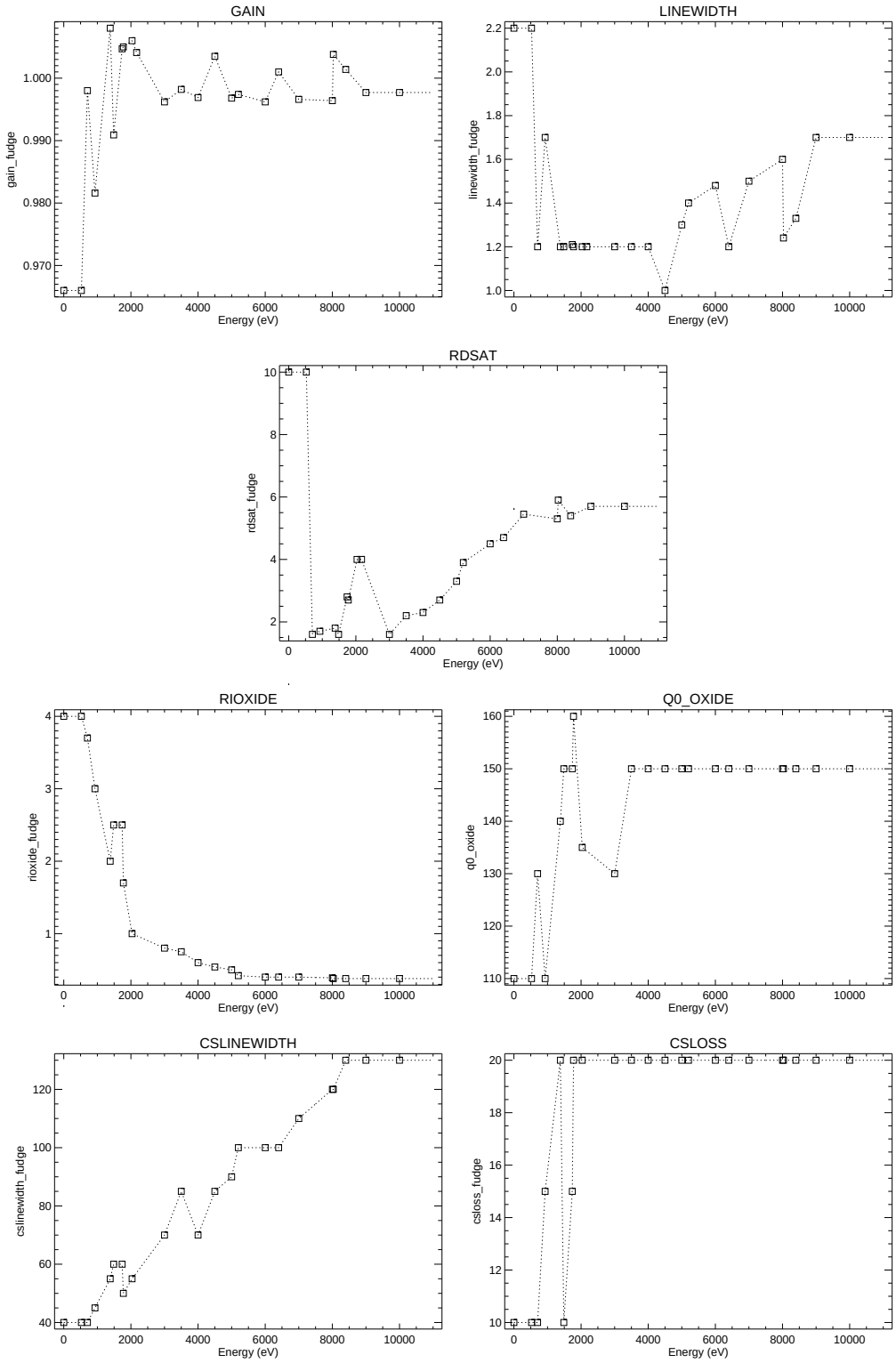

Figure 7.3: Plots of the seven tuning parameters, using the values for the I3 chip. The squares are the data points; the dashed lines show the interpolated values for other (unmeasured) energies.

7.1.5 Comparing Simulated Output to XRCF Data

7.1.5.1 Spectral Simulation

To illustrate the fidelity of the model, below is an typical example of simulated output compared to XRCF FI data. The model was tuned according to the prescriptions given above to match the data as closely as possible. Figure 7.4 gives a spectrum from the I3 chip of 4.5 keV photons produced by a Double Crystal Monochromator at the XRCF. Figure 7.5 is the corresponding simulation. The peak at about 1.2 keV in the data is not reproduced by the simulator – it is likely due to a complex of Ge L lines intrinsic to the spectrum produced by the DCM source and not due to redistribution in the CCD. Table 7.1.5.1 compares the branching ratios of the data to the simulated event list. Again, the tuning metric used was the number of g0 events only.

ASCA-like grade	Data (%)	Simulation (%)
0	63.1	62.3
2	16.5	15.5
3	6.2	7.9
4	6.0	8.0
6	8.2	6.3

Table 7.1: A comparison of real and simulated grade distributions (branching ratios) for the I3 chip at 4.5 keV.

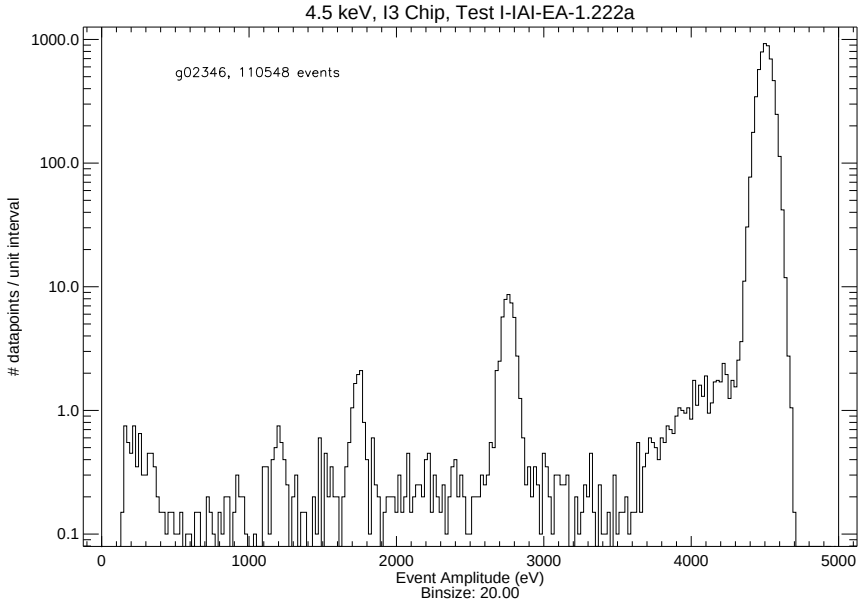

Figure 7.4: Spectrum of XRCF Phase I data.

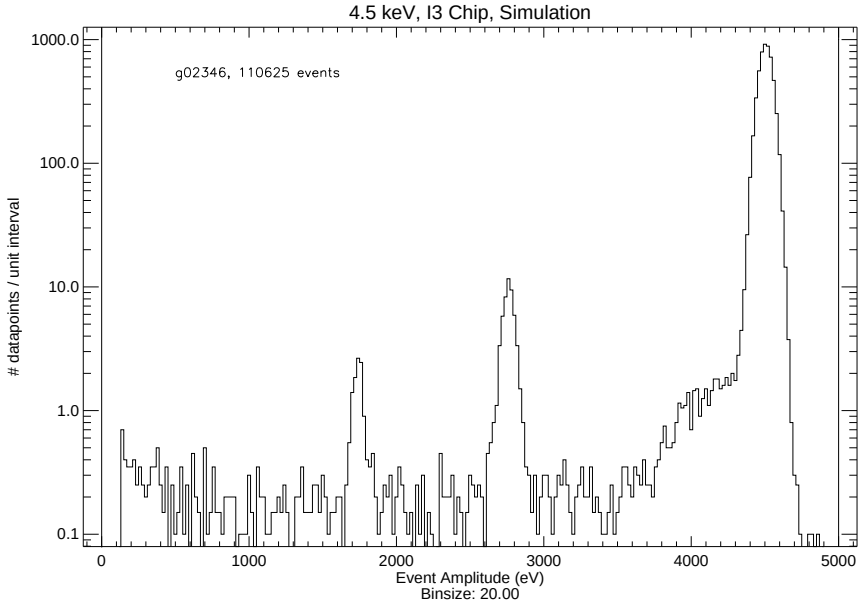

Figure 7.5: Spectrum of simulated data, tuned to match the above test.

7.1.5.2 Gain Determination & Uncertainty

The value of the simulator can be demonstrated by the following example. Allyn Tennant of the MSFC Project Science team analyzed XRCF data from ACIS which was taken with a continuum source dispersed across the ACIS-S array. These data provided an excellent check of the ACIS intrinsic energy resolution, because by separating the image into separate spectra, one can get effectively an incident monochromatic beam, with the incident energy slowly increasing with position.

The surprise that appeared was that the 'gain', as measured by fitting a Gaussian peak to the ACIS spectra at each point, showed a jump at the Silicon K edge energy. (See Figure 7.6.) This is surprising because the CCD should have no intrinsic gain within the detector, and the analog and digital electronics should have no special sensitivity to the Si K edge (as the electronics are only seeing a charge packet).

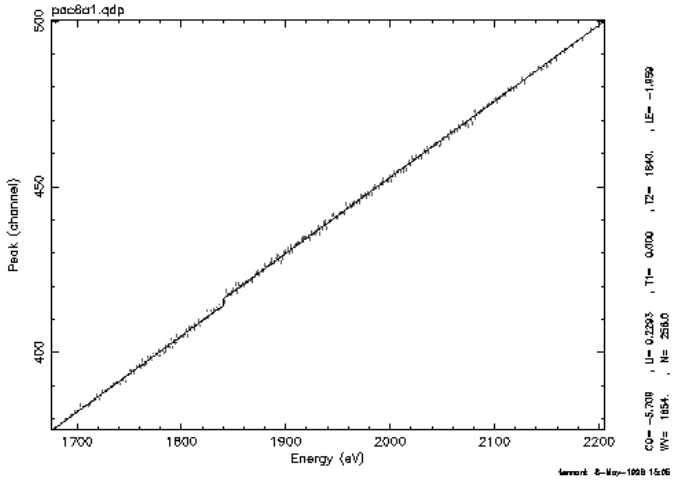

Figure 7.6: Peak of a Gaussian fit to CCD spectra extracted from a grating dispersed incident spectrum. The abscissa gives the energy of the incident photons inferred from the grating dispersion equation. Note the apparent 'break' in slope near 1.84 keV. [Data & analysis by MSFC Project Science].)

While the CCD should have no significant gain change at the Si K edge, the energy resolution function shows an abrupt change across the edge. First, in FI devices, photons above the K edge can create fluorescent Si Kα photons at 1.74 keV due to absorptions in the gates, which cause reabsorbed photon detections of Si Kα in the depletion region. Second, photons just above the K edge have very shallow penetration depths into the CCD, so, proportionally, a much high proportion of these photons interact in the channel stops than photons with energy just below the K edge. (In this case the lower energies penetrate more, and so many can pass right through the stop and interact normally in the depletion level below.)

The combined effect of Si K fluorescent photons and more channel stop photons is to build up an apparent low energy wing onto the energy response function. We have run our CCD simulation program and find about a factor of ten higher soft shoulder for photons above the K edge, than for photons below it.

To see how much this shoulder affects fits, we created simulated datasets at 1830 eV (just below the K edge) and 1860 eV (just above the edge). (See Fig. 7.7.) Then, simple Gaussian models were fit to the data. In the first case only a single Gaussian was used (which is what we believe was done by MSFC Project Science). Next, two or three Gaussians were used (one for the main peak, one broad and lower energy for the channel stop events, and one [for the 1860 eV case] for the fluorescent peak at 1740 eV). The results were:

Ratio of fitted energy in main peak to true energy			
Energy	1 Gaussian	2 Gaussians	3 Gaussians
1830 eV	0.9956	0.9967	-
1860 eV	1.003	0.9989	0.9989

Table 7.2: Comparison of apparent peak shifts when fitting one, two or three Gaussians to ACIS spectra.

Note that for the single Gaussian fit the mean of the primary peak 'jumps' upward by 1.003-0.9956 = 0.74%. This is very similar to the jump that MSFC Project Science found of 2.5/415 channels = 0.6%. We believe that the discontinuity in 'gain' results from a discontinuity in the instrument energy response profile at the Si K edge, and not in either a gain jump in the Si of the CCD or the CCD camera electronics and processing. Approximating the CCD response by a single Gaussian is inexact and the effect of this inaccuracy is to induce this non-linearity at the edge when the energy response changes rapidly.

It is interesting to observe how adding a low energy shoulder onto a Gaussian peak can *raise* the mean of the peak. What seems to happen is that the fit results in a larger sigma to accomodate the soft shoulder, which results in a *higher* mean because the high energy tail of the Gaussian model simply ignores the data. (There are more channels better fit by the single Gaussian model on the soft side of the peak, so the model chooses that over fitting the hard side and ignoring the soft.)

Note that using 2 or 3 Gaussians to approximate the response is better (the jump decreases from 0.74% to 0.21%), but it is not perfect. To reach accuracies significantly better than 1% will require treating the energy response by using the full simulation distribution or an accurate high order empirical approximation. Alternatively we can make approximations using simpler functions (single or multiple Gaussians) but then we need to calibrate them using the full simulator (i.e. fit the simulation results to the simple functions, and determine a calibration relation between the simple functions and the true values).

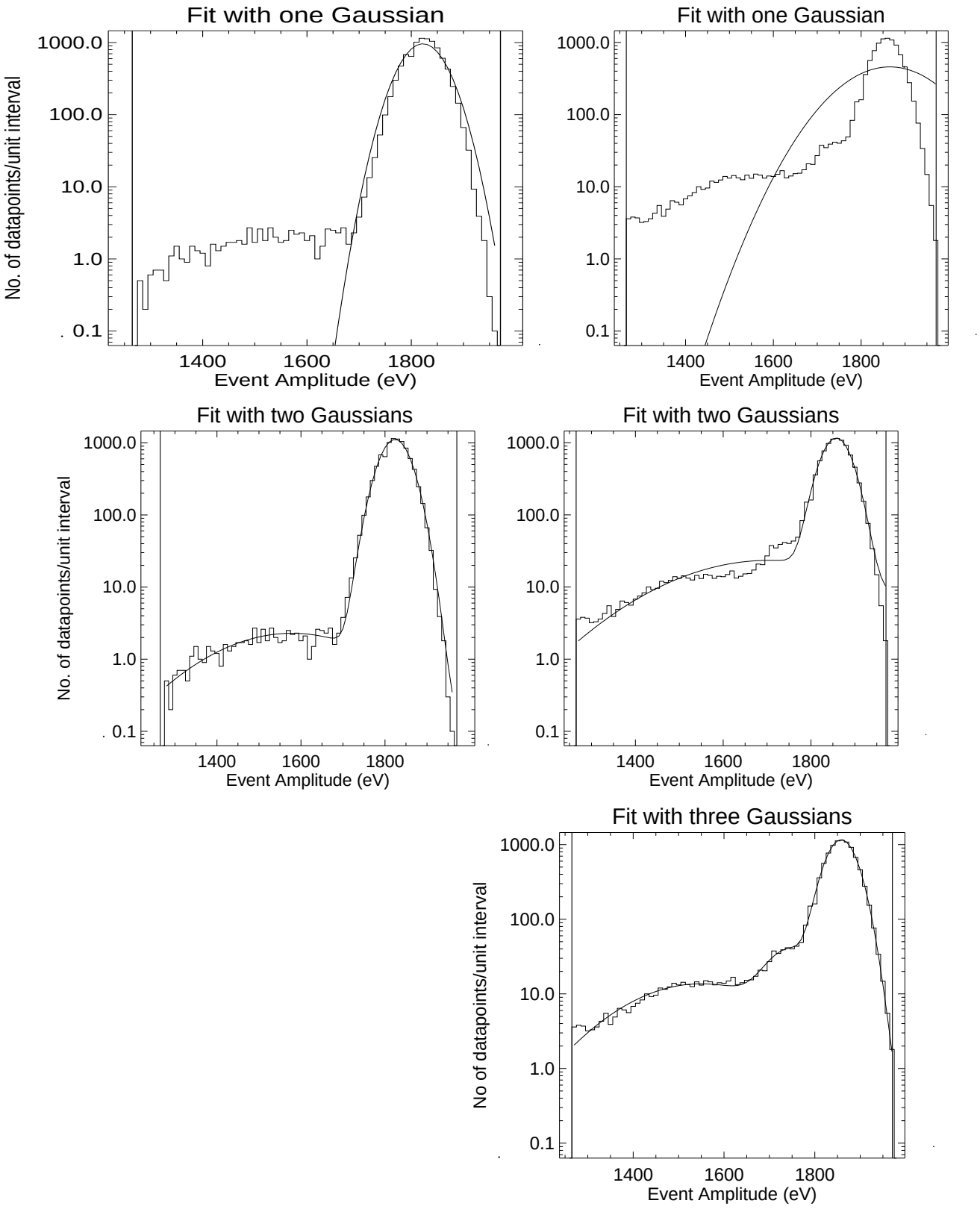

Figure 7.7: ACIS simulations of 1830 eV (left) and 1860 eV (right) incident photons. Solid lines are model fits of 1, 2, or 3 Gaussian components. Note that the scale is logarithmic, and the soft shoulder is ten times higher in 1860 eV simulation than 1830 eV.

Currently, the determination of X-ray energies from ACIS data is based on laboratory calibration measurements done at MIT, as described in Chap. 4. These calibrations apply multi-Gaussian fits to the lab data, and so are presumably no more accurate than the results shown in Table 7.2. Thus we suggest that the knowledge of the ACIS energy is accurate to a level better than 1%, but that these systematic effects must be limiting the accuracy to no better than 0.2%.

7.2 Tools for ACIS Real-time Analysis (TARA)

At Penn State inspection of the XRCF data and some analyses were performed using the IDL program *Event Browser*[1]. This program offers a graphical user interface for performing standard visualization and analysis tasks on FITS event lists. The set of events that is of interest may be constrained spatially, spectrally, morphologically (by grade), and temporally. Standard visualizations, such as spectra (in DN or eV), light curves and images, are provided. Basic analysis capabilities, such as fitting a spectral peak to a gaussian model, are provided.

Figure 7.8 shows a light curve plot in Event Browser. The user has control over the histogram binning, error bar display, axis styles (linear or log), axis ranges, titles, symbol & line styles, and color.

Figure 7.9 shows a spectrum plot. The vertical lines depict a region-of-interest (ROI) defined by the user and a gaussian model of the data in the ROI has been overplotted.

Figure 7.10 shows a grey-scale image that depicts the spatial distribution of an event list from a defocussed effective area test. The user may plot cuts through the image, compute the centroid, and plot radial profiles about the centroid.

Figure 7.11 shows the same dataset with an annular spatial filter applied to select events from one of the four mirror shells.

Figure 7.12 shows a region-of-iterest (ROI) defined on a plot of event energy verses exposure number for a DCM scanning test. The user may configure the ROI so that it acts as a filter that selects only events from one DCM energy dwell.

Other filtering tools allow grade selection, selection by CCD amplifier, etc. One of the strengths of Event Browser is that redefinitions of the filters, changes to the input dataset itself, or changes to various parameters of the reduction (such as the split threshold) produce automatic updates to all the displays (such as spectrum plots). For example it is easy to plot a spectrum with one set of grades, then change the grade filter and overplot the new spectrum for comparison.

Filtered event lists may be saved as FITS event lists or as XSPEC spectral files. Since the user has direct control over plot scaling, titles, colors, and styles, production of presentation-quality plots is straight-forward.

[1]See http://www.astro.psu.edu/xray/docs/

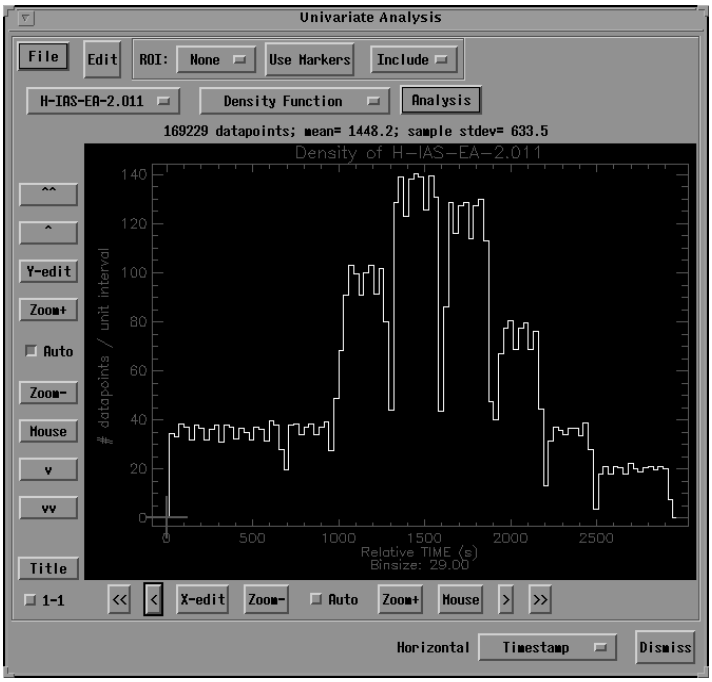

Figure 7.8: Event Browser Light Curve

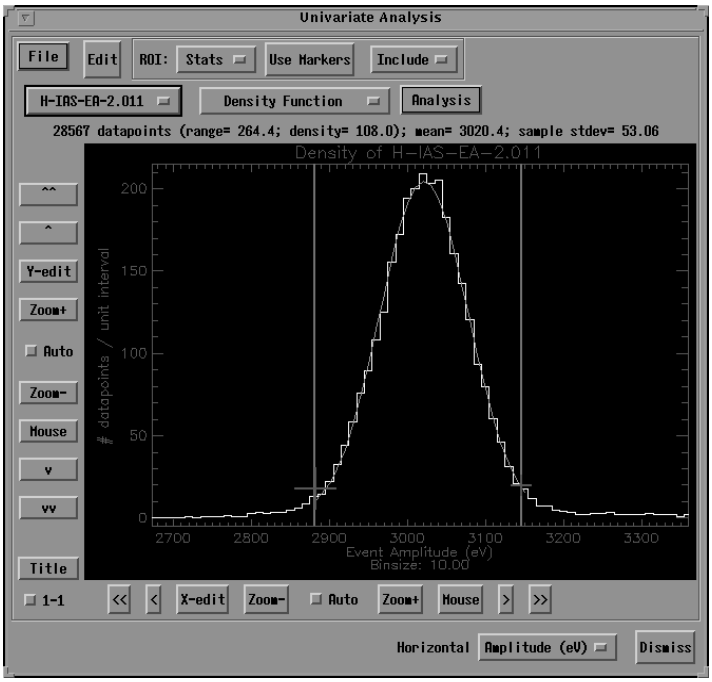

Figure 7.9: Event Browser Spectrum

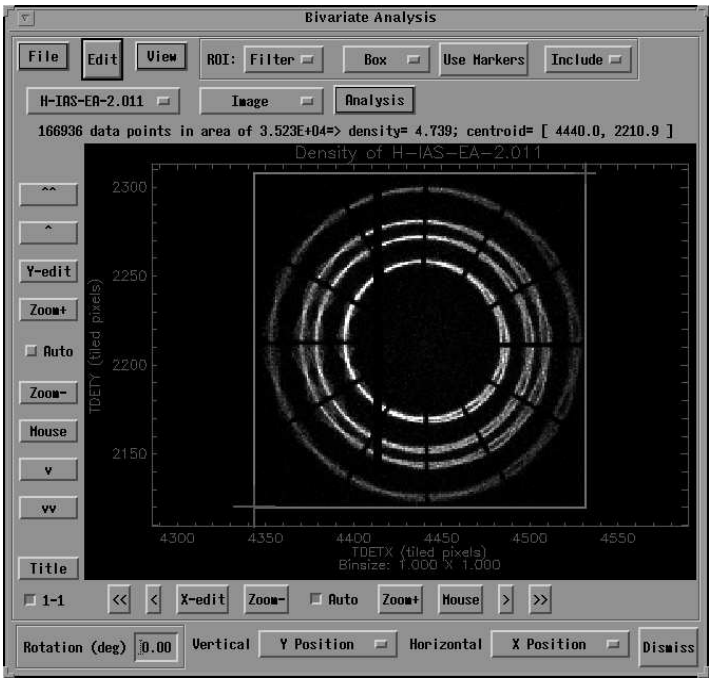

Figure 7.10: Event Browser Image

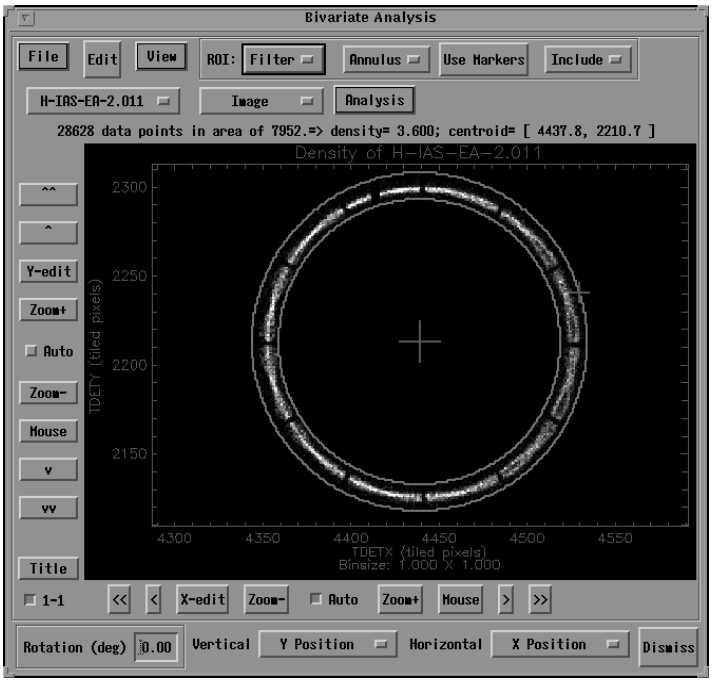

Figure 7.11: Event Browser Spatial Filter

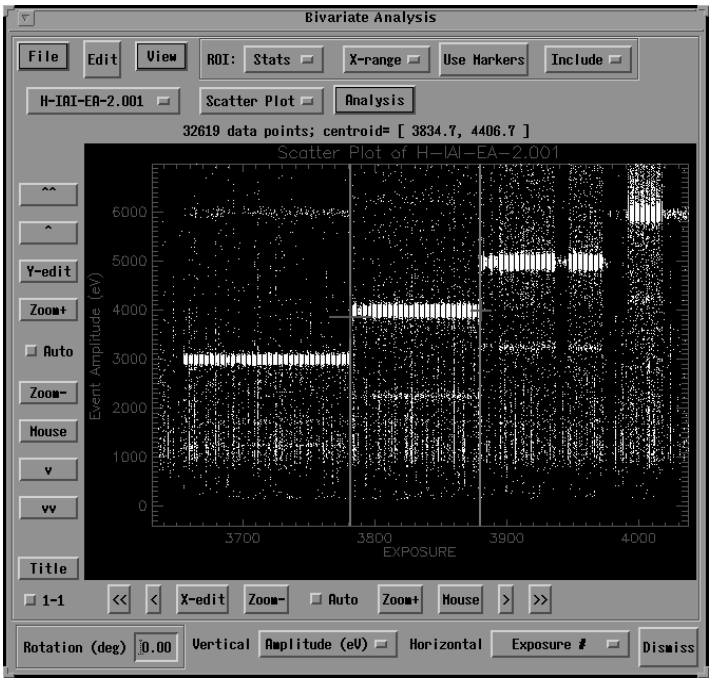

Figure 7.12: Event Browser Property/Property Filter

Bibliography

Arnold, D. and Ulm, G.: 1992, *Rev. Sci. Instrum.* 63

ASC: 1997, *AXAF Proposers' Guide*, AXAF Science Center

Born, M. and Wolf, E.: 1997, *Principles of Optics*, Cambridge University Press, Cambridge, 6th edition

Burke, B., Gregory, J., M.Bautz, Prigozhin, G., Kissel, S., Kosicki, B., Loomis, A., and Young, D.: 1997, *IEEE Transactions on Electron Devices* 44

Burke, B., Mountain, R. W., Daniels, P. J., Cooper, M. J., and Dolat, V. S.: 1993, *Proc. SPIE* 2006

Canali, C., Martini, M., Ottaviani, G., and Quaranta, A.: 1972, *IEEE Transactions on Nuclear Science* NS-19(4)

Ford, P. and Francis, J.: 1997, *ACIS Science Instrument Software Requirements Specification*, Massachusetts Institute of Technology, DR SDM02

Gendreau, K.: 1995, *X-ray CCDs for Space Applications: Calibration, Radiation Hardness, and Use for Measuring the Spectrum of the Cosmic X-ray Background*, PhD Thesis, MIT

Henke, B. L., Gullikson, E. M., and Davis, J. C.: 1993, *Atomic Data and Nuclear Data Tables* 54(2)

Hopkinson, G.: 1987, *Opt. Eng.* 29(8)

Janesick, J., Elliott, T., Collins, S., Daud, T., Campbell, C., Dingizian, A., and Garmire, G.: 1986, *SPIE Proc.* 597

Jones, S., Bautz, M., Kissel, S., and Pivovaroff, M.: 1996, *Proc. SPIE* 2808

Jones, S., Prigozhin, G., Bautz, M., Ricker, G., and Kraft, S.: 1997, *AAS HEAD meeting*

Kurucz, R.: 1991, in L. Crivelari, I. Hubeny, D. Hummer, and I. Howarth (eds.), *Stellar Atmospheres - Beyond the Classical Models*, Kluwer

Lechner, P. and Struder, L.: 1995, *Nucl. Inst. Methods A* 354

Lee, P. A. and Pendry, J. B.: 1975, *Phy. Rev.* B11(2795)

Lumb, D., Berthiaume, G. D., Burrows, D. N., Garmire, G. P., and Nousek, J. A.: 1991, *Experimental Astronomy* 2(179)

McDowell, J.: 1997, *ASC Coordinates*, AXAF Science Center

Meyer, P.: 1969, *Ann.Rev.Astron.Astrophysics* 7

Pivovaroff, M.: 1997a, *BESSY Integration Times*, Massachusetts Institute of Technology, ACIS Memo #135

Pivovaroff, M.: 1997b, *Data Analysis of BESSY Wavelength Shifter measurements*, Massachusetts Institute of Technology, ACIS Memo #142

Pivovaroff, M.: 1997c, *Gain Calculation from LLTV–Phase Two Measurements*, Massachusetts Institute of Technology, ACIS Memo #143

Pivovaroff, M., Jones, S., Bautz, M., Kissel, S., Prigozhin, G., Ricker, G., Tsunemi, T., and Miata, E.: 1998, *IEEE Transactions on Nuclear Science* 45

Pivovaroff, M., Kissel, S., Bautz, M., Prigozhin, G., Isobe, T., Woo, J., and Gregory, J.: 1996, *Proc. SPIE* 2808

Prigozhin, G.: 1998, *X-ray detection in channel stops*, Massachusetts Institute of Technology, ACIS Memo #150

Prigozhin, G., Jones, S., Bautz, M., and Ricker, G.: 1998a, *Proc.* 8^{th} *European Symposium on Semiconductor Detectors*

Prigozhin, G., Jones, S., Bautz, M., and Ricker, G.: 1998b, *Nucl. Inst. Methods*, submitted

Prigozhin, G., Woo, J., Gregory, J., Loomis, A., Bautz, M., Ricker, G., and Kraft, S.: 1998c, *SPIE Proc.* 3301

Prigozhin, G., Woo, J., Gregory, J., Loomis, A., Bautz, M., Ricker, G., and Kraft, S.: 1998d, *Opt. Eng.* 37(10)

Rasmussen, A.: 1995a, *BESSY Data Pileup Monitor and Correction*, Massachusetts Institute of Technology, ACIS Memo #93

Rasmussen, A.: 1995b, *Building Response Matrices: using RSPGEN*, Massachusetts Institute of Technology, ACIS Memo #73

Riehle, F. and Wende, B.: 1986, *Metrologia* 22

Scholze, F., Rabus, H., and Ulm, G.: 1996, *Proc. SPIE* 2808

Scholze, F. and Ulm, G.: 1994, *Nucl. Instrum. Meth. A* 339

Schwinger, J.: 1949, *Phys. Rev.* 75

Stern, E. A. and M., H. S.: 1983, *Handbook on Synchrotron Radiation*, 1B, ERNST-ECKHARD KOCH

Tsunemi, H., Yoshita, K., and Kitamoto, S.: 1997, *Jpn. J. Appl. Phys.* 36

Weaver, J., Olson, C., and Lynch, D.: 1977, *Phys. Rev. B* 15

Wise, M., Davis, J., Huenemoerder, D., Houck, J., Dewey, D., Flanagan, K., and Baluta, C.: 1997, *MARX 2.0 User Guide*, AXAF Science Center

Appendix A

ACIS Grades

ACIS candidate X-ray events are assigned to grades based on the number and orientation of the pixels neighboring the central candidate pixel which exceed the split event threshold. This grade is helpful in distinguishing between X-ray events and non-X-ray events.

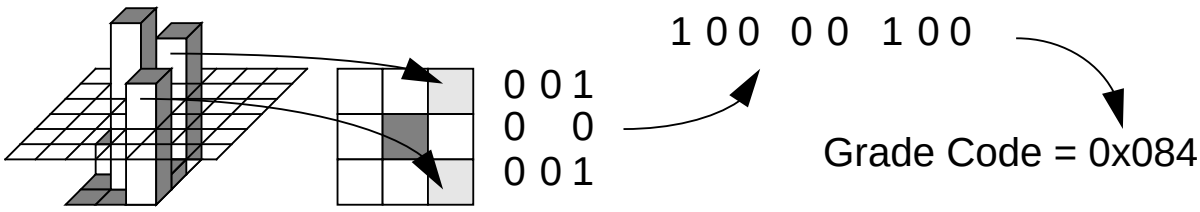

Figure A.1: 3x3 Event Grading Illustration

The grade is computed by the BEP (Back-End Processor) by comparing the corrected pulse heights of the eight outer edge pixels of the event to the "Split Threshold" specified in the Timed Exposure Parameter Block. Each pixel corresponds to a "bit" in the grade code. If a pixel's pulse height is greater than or equal to the threshold, the corresponding bit is marked as a "1". If a pixel's pulse height is less than the threshold, the bit is marked as a "0". Since there are eight pixels on the edge of a 3x3 event, this leads to an 8-bit grade code. There are 256 possible "grades" for a 3x3 event. Figure A.1 illustrates an example 3x3 event, with pixel pulse heights drawn as vertical bars and the split threshold drawn as a grid. The pixels whose pulse height is above the threshold are shown to the right as lightly shaded areas. Since the center pixel has been selected on the basis of being a local maximum, it will always be the pixel with the highest signal. (It is shown using a darker shade in the diagram.)

A complete list of the ACIS grades with a diagram illustrating the split event threshold crossings is given in Table A.1. Please note that ACIS grades and ASCA grades do not use

the same numbering convention. ACIS grades run from 0 to 255, while ASCA grades run from 0 to 7. ACIS grade 0 is identical to ASCA grade 0 (a single, isolated event without any neighboring split threshold crossings), but all other ASCA grades are sums of many ACIS grades. Also note that when ACIS operates in "Graded Mode" only the total reconstructed energy of the X-ray event is telemetered to the ground. The total energy is computed by summing all pixels which exceed the split event threshold. On ASCA the corresponding mode ('Bright Mode') sums pixels regardless of whether the split threshold is crossed. The result is that some ASCA grade 5 and 7 event total energy values cannot be calculated from ACIS grade and energy information alone.

The commonly used ASCA grades are g0 (which are single events and the same as ACIS Grade 0), g0234 (which are the singles plus vertical and horizontal split events, and correspond to the combination of ACIS Grades 0, 2, 8, 16, 64, and twelve other rare ACIS grades), and g02346 (which corresponds to the preceeding plus ASCA grade 6). ASCA grade 6 has the n=3 and n=4 events which are compact (i.e. form small 'L'-shaped or 2x2 square-shaped regions).

Table A.1: ACIS Grade Description

Appendix B

CCDSIM User Guide

B.1 Introduction

The Penn State ACIS simulator is analogous to the *pileup* tool in the MARX system – a physical simulation of ACIS CCD's is performed using a MARX simulation as the source of photons. The output of the simulator is a FITS event list compatible with Event Browser.

B.2 Running the MARX Simulation

You can have MARX use an SAOSAC ray file instead of its internal HRMA model, however the timestamps assigned to SAOSAC photons are spaced by exactly one second, which is relevant for simulations where pileup is present.

We use MARX as a source of photons because it provides the user with convenient control over the spatial, spectral, and timing characteristics of the photons. Re-implementing all the cool current features of MARX, and the future ones too, sounded like no fun at all! Detailed information on MARX parameters is, of course, in the MARX User's Guide.

As described in Section 6.3 of the MARX User's Guide, you should set the MARX parameter *DetIdeal* **to "yes" when the MARX output will be used by a CCD simulator.** Also, do not forget that MARX has the unfortunate habit of modifying its parameter file *marx.par* based on the command-line options you specify.

Note that fluxes in MARX are specified by the parameter *SourceFlux* in photons/sec/cm^2 at the entrance to the HRMA. **Choosing a flux appropriate to your investigation can make your brain hurt** due to several complications. (Yes, maximizing "complicating details" was one of our design goals!)

- The easiest case would seem to be where your actual goal is to simulate a specific astrophysical source flux. You *should* be able to simply convert your source flux to photons/sec/cm^2 units and use that for the MARX *SourceFlux* parameter. Unfortunately, the transmission of the optical blocking filter (OBF) in ACIS is not currently

simulated by the Penn State ACIS simulator and MARX will not simulate the OBF when *DetIdeal* is "yes". Thus, you must deal with the OBF transmission yourself.

Note also that the PSU CCD simulator does not attempt to simulate the precise values of gates transmissions, including the effects of EXAFS. Thus, again, this simulator should not be applied where precision quantum efficiency estimates are required. Use the MIT supplied values incorporated into the ASC response matrices in these cases.

- If you are trying to achieve a specific photon rate incident on the CCDs, then you're going to have to perform a short test run of MARX, see what you get, then scale the MARX *SourceFlux* parameter accordingly. Determine the MARX output rate by counting the photons MARX produced

  ```
  marx --dump dir/time.dat | wc
  ```

  and figuring out how many seconds the MARX simulation covered

  ```
  marx --dump dir/time.dat | tail
  ```

  You can also determine the MARX output rate by looking at the keyword FLUX (photons per frame) in the event list file produced by the Penn State ACIS simulator. Note that the MARX output omits photons that survive the HRMA and OBF, but then miss the CCD's that MARX is simulating.

- If you are trying to achieve a specific event rate out of ACIS, then you'll have to count the events that come out of the simulator and determine the length of the simulation. The tricky part here is making sure you have a clear idea of what "event rate" means. You could just count the raw events that come out of the simulator

  ```
  fverify dir.evt
  ```

  but grade 255 events may contaminate the count – ACIS will normally throw away grade 255 events. A better method would be to filter the event list (using Event Browser) to match whatever grades are implied by the definition of your target event rate. The moral is that "event rate" is a vague term.

  To determine the length of the simulation execute

  ```
  fverify dir.evt
  ```

  and read off the range of the TIME column. There are 3.34 seconds per exposure.

  Note that you will often choose to simulate a small region of an ACIS CCD to speed things along, so you'll see an event rate slightly lower than the larger physical CCD

would produce because photons way out in the PSF wings miss the virtual CCD you are simulating. Of course, the real ACIS also produces a small number of un-rejected background events. The CCD simulator can simulate a particle background, but you probably don't want to get into that.

MARX can use SAOSAC rays, rather than its own HRMA model, in a simulation. The Penn State ACIS simulator will accept such an SAOSAC-derived MARX simulation, however **the flux level in the CCD simulation will not be what you specified in the MARX run**. The problem is that MARX 2.04 does not assign appropriate timestamps to SAOSAC photons. In the future, either MARX will be fixed or the Penn State ACIS simulator will be hacked to work around this problem.

You may find it convenient to run MARX from some type of script (csh, perl, etc.). If you decide to use IDL as your scripting language, you'll find the following IDL code interesting. (Change the reference to /bulk/pkg/asc/marx_2.04-dist to the appropriate MARX directory on your machine.)

```
spawn, '/bin/cp /bulk/pkg/asc/marx_2.04-dist/marx.par .'

spawn, 'echo "MARX LOG" > marxlog.txt'

num_events = 1000
flux       = ...
dir        = "my_sim"
energy     = 1.486

f='("marx ExposureTime=0 NumRays=",I0," SourceFlux=",F0," OutputDir=",A,' +$
  '" MinEnergy=",F0," MaxEnergy=",F0," DetIdeal=yes  >> marxlog.txt")'

cmd = string(num_events, flux, dir, energy, energy, F=f)
print, cmd
spawn, 'echo "' + cmd + '" >> marxlog.txt '
spawn, cmd
```

B.3 Running the Penn State ACIS Simulator

The top-level simulator program is called *rain_on_acis* and is in the default IDL path (try *findpro, 'rain_on_acis'* at the IDL prompt). The rain_on_acis program has two required parameters.

- A list of CCD parameter files for the CCD's you wish to simulate.
- The name of a MARX simulation directory.

The ten ACIS CCD's are described by FITS parameter files ccd0.par ... ccd9.par are available with the simulator distribution. You should copy the parameter files you need to your local directory. The FITS keywords found in the parameter file are shown in Figure B.1.

```
COMMENT CCD device parameters for use in Penn State simulation system.
CCD_ID  =                     3 / CCD position in ACIS instrument, [0..9]
ILLUM   = 'bulk    '            / CCD style: "back", "bulk", or "epi"
NUMCOLS =                  1024 / width of sub-frame simulated
NUMROWS =                  1024 / height of sub-frame simulated
FIRSTCOL=                     1 / first col of sub-frame in 1-based CHIPX system
FIRSTROW=                     1 / first row of sub-frame in 1-based CHIPY system
XPIXSIZE=                    24 / X-size of pixel (microns)
YPIXSIZE=                    24 / Y-size of pixel (microns)
SPLASH  =                     7 / max footprint of a photon; MUST BE ODD NUMBER!
DEAD    =                     1 / dead layer thickness (microns)
EPIFF   =                     0 / epitaxial field-free layer thickness (microns)
DEPLN   =                    65 / depletion layer thickness (microns)
SUBSTFF =                   460 / bulk field-free layer thickness (microns)
NA      =                1.0e13 / dopant concentration (# per cc)
TEMP    =                   163 / operating temperature of CCD (Kelvins)
S_NOISE =                     2 / "system noise" (electrons)
DARK    =                     0 / dark signal (electrons)
NUMPART =                     0 / average number of particles per frame
CTI     =                1.0e-6 / charge transfer inefficiency
RADPOWER=                     0 / power term for power law radiation damage model
COMMENT ev-to-DN linear model quoted by MIT
COMMENT Pulse Height(ADU) = Slope x Energy(eV)  + Intcpt
SLOPE_A =                0.2582
SLOPE_B =                0.2588
SLOPE_C =                0.2542
SLOPE_D =                0.2592
INTCPT_A=                  1.19
INTCPT_B=                  1.25
INTCPT_C=                  1.25
INTCPT_D=                  1.09
THRESHLD=                    38 / event threshold
```

Figure B.1: FITS keywords in Penn State ACIS simulator parameter file

The parameter files in the archive setup a simulation of an entire CCD, which is generally NOT what you want because it's VERY slow. Normally, you would figure out where all

the action is on the CCD,

```
marx --dump dir/xpixel.dat dir/ypixel.dat
```

then edit the CCD parameter file to simulate a rectangular region around most of the photons. The relevant keywords in the parameter file are NUMCOLS, NUMROWS, FIRSTCOL, & FIRSTROW; (FIRSTCOL,FIRSTROW) is the lower-left corner of the active region, in 1-based CHIP coordinates. Use the FTOOL *fv* to edit these keywords.

Normally, the CCD frames are simulated until all the MARX photons are used up. However, the rain_on_acis keyword NUM_PHOTONS can be used to shorten the simulation.

If the keyword DITHER is set, then rain_on_acis will, for each CCD frame, randomly offset the photons from their MARX positions (simulating spacecraft dither), let the photons interact with the CCD, detect events, then adjust the event positions by the offset applied to the photons (simulating perfect aspect correction). A gaussian aspect error may be simulated by passing the standard deviation of the gaussian **in units of ACIS pixels, not arcseconds,** in the keyword ASPECT_ERROR. MARX suggests 0.17 arcseconds = 0.35 pixels as a plausible aspect error model.

If the keyword ONE_PHOTON_PER_FRAME is set then photon timestamps are ignored and exactly one photon lands on each CCD frame.

A typical call to the CCD simulator would be

```
rain_on_acis, 'ccd3.par', 'my_marx', /DITHER, ASPECT_ERROR=0.35
```

assuming you have the parameter file ccd3.par and a MARX simulation my_marx in your current directory.

You may find it convenient to put the IDL statements necessary to run MARX and the CCD simulator in an IDL batch file or program, then run IDL in the background overnight. For example, if you have a batch file named *runsims* containing IDL statements then you could issue the unix command

```
nohup nice idl < runsims >& log &
```

log out, and go home to more interesting pursuits. What would normally be printed to the screen will be in the file *log*. If you want to watch the output for a while, execute

```
tail -f log
```

If you have written an IDL procedure, *runsims.pro*, which spawns MARX jobs and drives the simulator for you, then issue the unix command

```
nohup echo runsims | nice idl >& log &
```

and go home.

Once you have the simulator running, if the UNIX utility *top* shows that the IDL process is receiving less than 90 percent of the CPU (45 percent on a two-processor machine), then you may be page faulting due to a shortage of memory. Either find a better computer or simulate a smaller region of the CCD.

B.4 FITS Output of the Simulator

The simulator produces a FITS event list named *acis.evt* in the MARX directory and copies the CCD parameter files to the MARX directory. You can supply an alternate name for the event file with the rain_on_acis keyword EVENT_FILE. Some of the interesting FITS keywords found in the binary table header are:

- PARFILE?: the name of a CCD parameter file used by the simulator.
- PHOTONS: the number of photons simulated.
- FLUX: the number of photons simulated divided by the number of exposures simulated.

The FITS binary table used to store the event list always includes the following columns.

- TIME: The MARX timestamp in seconds corresponding to the midpoint of the CCD frame.
- EXPOSURE: The CCD exposure number, starting at zero.
- CCD_ID: The CCD that detected the event, obtained from the CCD_ID keyword in the parameter file.
- AMP_ID: The amplifier, numbered 0..3, associated with the central pixel of the event.
- QUALCODE: An 8-bit quality code computed for each event. Bit 2 is set (value = 4) if the central pixel exceeds 4095 DN.
- CHIPX/CHIPY: The 1-based integer position of the event.
- TDETX/TDETY: The position of the event in the "tiled coordinate system AXAF-ACIS-2.2" defined by Jonathan McDowell at the ASC.
- PHAS: A 9 element vector containing the event island pixel values corrected for bias. The relationship between this 9-vector and the 3x3 event island is shown in Figure B.2.

If the rain_on_acis keyword DITHER is set, then the TDETX & TDETY columns are corrected for the dither, i.e. an aspect correction with optional aspect error is applied. The CHIPX & CHIPY columns however are NOT aspect-corrected – they contain the integer positions of the dithered events. **You should examine dithered events in the TDETX/TDETY coordinate system, not the CHIPX/CHIPY system.** When DITHER is set, the FITS columns DITHER_X and DITHER_Y are added, specifying the random offsets that were added to the MARX photon positions.

If the rain_on_acis keyword ONE_PHOTON_PER_FRAME is set, then FITS columns RAY_X and RAY_Y are included, specifying the real-valued position (in CHIP coordinates) of the photon which lead to the corresponding event.

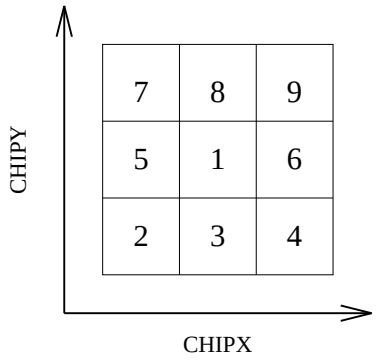

Figure B.2: Ordering of PHAS vector

Appendix C

Optical Light Contamination from HRMA Focussed Stars

The HRMA focusses optical light in a very similar manner as X-ray light (with the difference that the longer wavelength of optical light makes diffraction effects much more important). The Optical Blocking Filters (OBF) are designed to reject the optical and UV light, but allow a maximum of X-ray flux to pass through and be detected by the CCDs. The design of the OBFs reflected a tradeoff between thinner filters which maximized the soft X-ray efficiency, and thicker filters which rejected more unwanted optical light.

The largest problem of optical light contamination occurs for point sources which emit large amounts of optical light, but relatively few X-rays – namely stars. As discussed in Section 5.3 we provide estimates of the optical magnitudes of stars (as a function of stellar temperature) at which the optical contributions begin to become of concern. The details of the calculations are presented here.

C.1 Calculation without Gratings

The AXAF telescope mirrors consist of four shells of zerodur coated with 350 /AA of iridium that reflect electromagnetic radiation at grazing incidence angles of about 0.44° to 0.84°. The mirrors are constructed in such a way as to present concentric annuli to incoming radiation. The dimensions of the four annuli are given in the following table (van Speybroeck, private communication).

In order to compute the intensity of optical light for an on-axis source, the Airy function for each mirror was computed at two wavelengths: 450 nm and 850 nm, corresponding to the peak transmission wavelengths of the optical blocking filters. The reflectivity in the optical band at these grazing angles of incidence is very high, ∼99%, based on the optical constants found by Weaver (1977). The contributions to the Airy function from each mirror annulus were added incoherently, as no effort was made during fabrication to align

Mirror Number	Front Radius (mm)	Back Radius (mm)
1	612.69	600.34
3	493.41	483.47
4	435.63	426.85
6	323.82	317.29

Table C.1: AXAF Mirror Parameters

the mirrors to the accuracy necessary to maintain coherence. An example of the results of the calculation for the two wavelengths is shown in Figures C.1, C.2, and C.3. The fraction of the encircled energy for the pixel at the on-axis point was taken to be 0.03 and 0.06 at 850 nm and 450 nm respectively. In the integration over the bandpass carried out to compute the optical fraction transmitted, OF (see Equation 5.18), the encircled energy was computed at a number of wavelengths and interpolated linearly with wavelength.

The encircled energy is included in the term $A_{tel}(\lambda)$.

Figure C.1 shows the point spread function of the telescope computed at 450 nm. The small 'dips' are interference effects. This curve was multiplied by $2\pi\theta d\theta$, where θ is the off-axis angle variable of integration and integrated to a specific off-axis angle to produce the results shown in Figure C.2. The same procedure was used to produce the results at 850 nm, shown in Figure C.3.

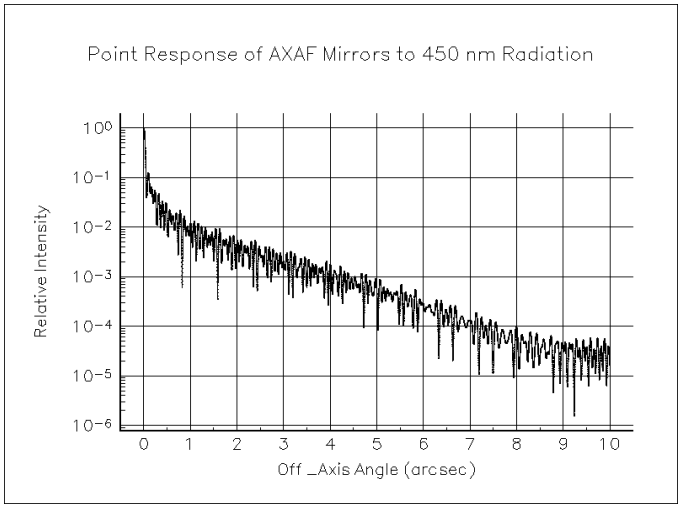

Figure C.1: The point spread function of the AXAF mirrors at 450 nm as a function of off-axis angle in arc seconds.

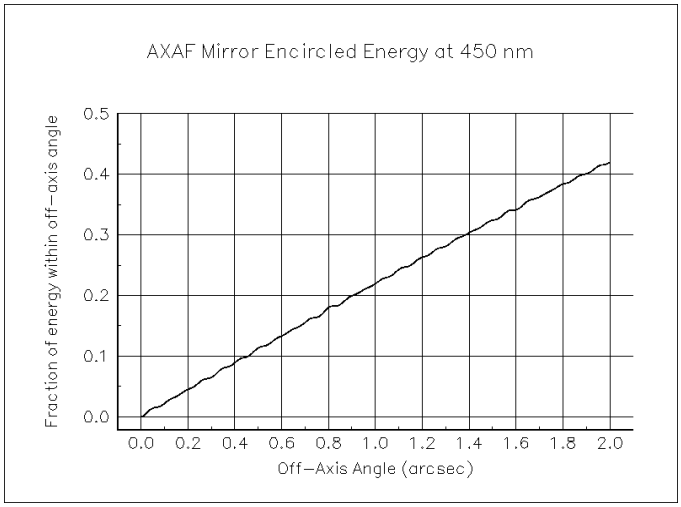

Figure C.2: The encircled energy as a function of off-axis angle for the AXAF mirrors at 450 nm.

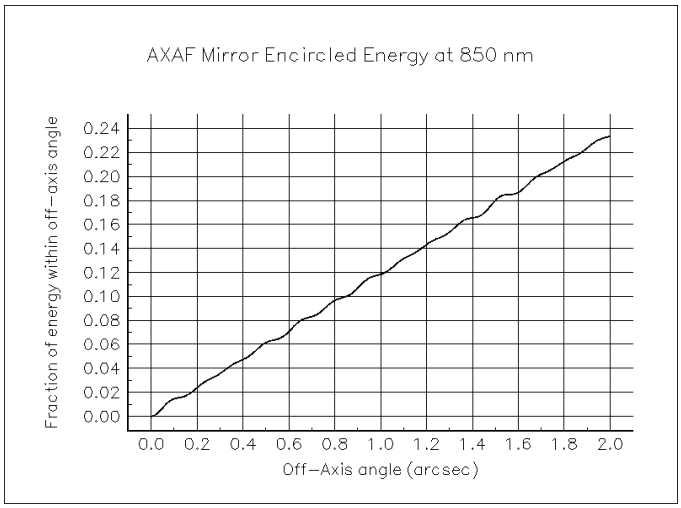

Figure C.3: The encircled energy as a function of off-axis angle for the AXAF mirrors at 850 nm.

C.2 Calculation with Gratings

The ACIS instrument can be complemented by the introduction of transmission gratings into the light path emerging from the aft end of the HRMA. These gratings disperse the optical light as well as the X-ray photons (and to much larger dispersion angles because the optical wavelengths are so much longer than the X-ray ones). Thus when the gratings are in place the only concern is for optical light leakage which is collected in the zeroth

order (or undiffracted) image.

A facet of each of the MEG and HEG gratings was provided by Dr. Dan Dewey of the Grating team for measurement of the optical transmission of the grating as a function of wavelength. The grating facet was placed in an f8 convergent beam of light to approximate the AXAF mirror configuration. The light source was a standard 10 watt tungsten lamp manufactured by the Oriel Corp. which was focused by an f8 lens through the grating and onto the slit of an Oriel Corp. 1/8 m monochromator. The monochromator output was then focused onto a photodiode and readout with a Keithley digital ammeter. The results of these measurements are shown in Figures C.4 and C.5.

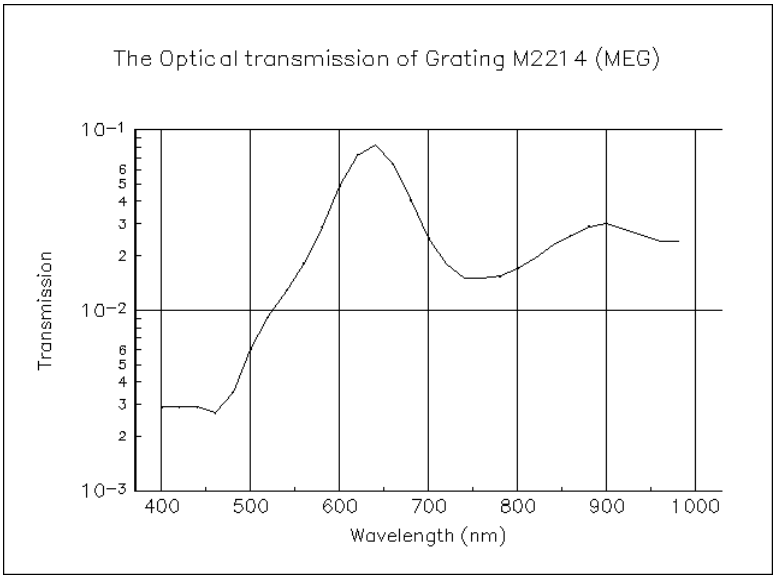

Figure C.4: Transmission of an MEG facet focused with an f8 beam of light onto a monochromator slit as a function of wavelength

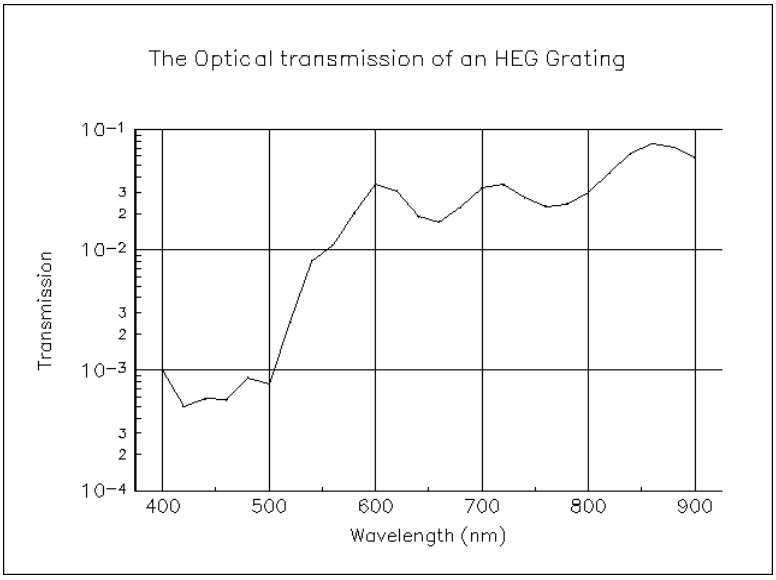

Figure C.5: Transmission of an HEG facet focused with an f8 beam of light onto a monochromator slit as a function of wavelength

Appendix D

Glossary of Acronyms

ACIS AXAF CCD Imaging Spectrometer, one of two focal plane instruments aboard AXAF, consisting of two arrays of CCD chips supporting imaging and transmission spectroscopy. It provides simultaneous imaging and non-dispersive moderate resolution spectroscopy.

ACIS-I Term referring to Imaging CCD array.

ACIS-S Term referring to Spectroscopic CCD array, which supports the use of the AXAF transmission gratings.

ADC Analog-to-Digital Converter, provides digital equivalent to analog signals.

ADU Analog-to-Digital Unit, unit defining integer values resulting from an analog to digital conversion.

AQLC ACIS Quick Look Computer, one of two computers used at the X-ray Calibration Facility to assess ACIS data. The AQLC reduces and displays data in near real time to evaluate the scientific validity of the data.

ASC AXAF Science Center, center for the analysis of AXAF data and general scientific support and analysis in the post-launch AXAF phase.

ADS Two meanings based on context:

1. Aspect Determination System, AXAF system determining the satellite pointing and orientation,
2. Astrophysics Data System, NASA Astrophysics Division supported system for the access, dissemination and utilization of archival astrophysical data.

AXAF Advanced X-ray Astrophysical Facility, the spacecraft carrying the ACIS experiment and the high resolution X-ray telescopes.

BESSY The Berlin synchrotron light source used to establish the reference calibration of CCDs used during the MIT pre-assembly calibration measurements to achieve an absolute quantum efficiency calibration.

BEP Backend Processor, digital signal processor and control processor which packetizes data for downlink and controls the CCDs.

BI Backside Illuminated, term applied to a type of CCD chip, in which the normal thick silicon substrate is removed and X-rays illuminate the back of the device. BI chips have good low energy quantum efficiency.

BND Beam Normalization Detector, an X-ray counter used at the XRCF to measure the intensity of the incident X-ray beam, and hence allow normalization of any measurements made at the XRCF.

BNL Brookhaven National Laboratory, site of a synchrotron used as an X-ray source during ACIS filter calibration.

CCD Charged Coupled Device, the active detector elements in ACIS.

CDR Critical Design Review, formal meeting certifying the start of full production of the overall hardware and software design.

CEI Contract End Item, item specified in the NASA contract which must be delivered by the ACIS team.

CIT Calibration Implementation Team, a group combining the CTT, MSFC Project and support staff, and TRW, which will implement the XRCF calibration of AXAF.

CMDB Calibration Measurement DataBase, a database containing all parameters needed to describe the measurements conducted at the XRCF.

CTE Charge Transfer Efficiency, ratio of charge remaining after one pixel clocking to the charge before clocking.

CTI Charge Transfer Inefficiency, deviation of CTE from unity. Convenient because CTE is often very close to one.

CTT Calibration Task Team, a scientifically oriented group drawn from the Project and Science Instrument teams, charged with the responsibility for planning AXAF calibration.

CTUE Command Telemetry Unit Emulator, a piece of ground support equipment which emulates the spacecraft command and telemetry unit. This unit transmits commands from the spacecraft to the instruments and packages instrument data into the telemetry major frames.

DA Detector Assembly, houses CCD arrays, fiducial lights and an X-ray calibration source. Functionally equivalent to term 'CCD Camera'.

DEA Digital Electronics Assembly, ACIS digital signal processing section.

DPA Digital Processing Assembly, ACIS analog signal processing section.

DPS Detector & Processor Subsystem, subsystem dedicated to the detection and processing of X-rays, consisting of the DA, DEA and DPA.

DR Data Requirement, a formal NASA specification for required documentation format, content and delivery dates.

EGSE Electronic Ground Support Equipment, one of two computers used at the X-ray Calibration Facility to assess ACIS data. The EGSE generates commands and monitors housekeeping data to assure the health and safety of the instrument.

EMI Electro-Magnetic Interference, electro-magnetically induced noise appearing on electrical signal wires. Usually referred to in the context of eliminating or shielding to prevent EMI.

FAM Five-Axis Mount, mounting stage for the AXAF instruments at XRCF which controlled the x, y, z, pitch and yaw orientations of the instruments with respect to the facility coordinate system.

FEP Frontend Processor, digital signal processor, part of the DPA which does initial processing on raw CCD pixel data.

FI Frontside Illuminated, a traditional CCD chip design where the chip is illuminated from the front layer, which requires the X-rays to traverse the electronic gate structures. The low energy quantum efficiency of FI chips is low, but the energy resolution is superior to BI chips.

FP Focal Plane, the sub-assembly portion of the ACIS experiment which holds the CCD chips.

FWHM Full Width at Half Maximum, a measure of the width of a distribution, frequently used to describe the resolving power of the CCD for spectral emission lines.

GSE Ground Support Equipment, auxiliary equipment needed to operate the ACIS experiment during assembly and ground testing.

HETG High Energy Transmission Gratings, used to provide dispersed X-ray spectra appropriate to the higher energy X-rays collected by the HRMA. The HETG uses the ACIS as its prime detector system.

HRC High Resolution Camera, the other focal plane instrument on AXAF, based on a micro-channel plate X-ray detector.

HRMA High Resolution Mirror Assembly, the AXAF X-ray telescope mirror assembly, consisting of four nested confocal Wolter I optical systems.

HST High Speed Tap, a high speed data path providing raw CCD pixel data into the ACIS EGSE computers. These data are similar to the sub-assembly calibration data, and form a direct check on the flight telemetry format data. The HST also offers a much higher bandwidth data path valuable during ground calibration. The HST will not be available during flight.

ICD Interface Control Document, documents defining the observatory interfaces.

IPI Instrument Principal Investigator, scientist in charge of the development of the instrument and leader of the team submitting the proposal and executing the task. For ACIS the IPI is Prof. Gordon Garmire.

kbs kilobit per second, a data transfer rate measured in thousands of bits per second.

LMA Lockheed Martin Astronautics, sub-contractor providing some of the fabrication of the ACIS instrument, formerly named MMAG.

LETG Low Energy Transmission Gratings, disperse X-ray spectra appropriate to the lower energy X-rays collected by the HRMA. The LETG uses the HRC as its prime detector system.

MCC Master Control Computer, central coordinating computer at the XRCF facilty during AXAF calibration.

MMAG Martin Marietta Aerospace Group, sub-contractor providing the fabrication of the ACIS instrument, name now changed to LMA.

MIT Massachusetts Institute of Technology, home institution of ACIS CCD development work and camera design.

MSFC Marshall Space Flight Center, the home institution for the AXAF Project.

NaN Not a Number, a computing expression for bit strings in numeric fields which do not interpret as numbers. It can be encountered by invalid calculations or used as a flag to prevent use of invalid values where no proper value exists.

NSLS National Synchrotron Light Source, a synchrotron used as a light source in measuring the X-ray transmission of the ACIS filters.

OBC On-Board Computer, the AXAF spacecraft computer which transmits commands to ACIS and which receives telemetry data for transmission to the ground.

OBDS On-Board Data System, the computing system for ACIS on-board the satellite.

OV Orbital Verification, the first period of orbital operations, in which the instruments and spacecraft are turned on and proper operations are verified.

PDR Preliminary Design Review, formal meeting reviewing the overall hardware and software design.

PRAM Program Random-Access Memory, radiation resistant on-board non-volatile memory which is used to store instructions for CCD readout.

PSMC Power Supply and Mechanism Controller, supplies power and mechanism control to ACIS.

PSU Penn State University, home institution for the ACIS Principal Investigator and ground software development.

PTS Power & Thermal control Subsystem, ACIS subsystem which delivers power and maintains thermal control of the experiment.

RCTU Remote Command and Telemetry Unit, TRW supplied interface box supplying connection to spacecraft data and power busses.

SDS Software Design Specification, document specifying the software design for each build of the ground software.

SEU Single Event Upset, single bit errors introduced into memory or processors, resistance to which reflects more robust processor performance in a space environment.

SIM Science Interface Module, a translational mechanical structure which moves to allow insertion of either the HRC and ACIS into the telescope focal plane, and to shift between the ACIS-I and S arrays.

SIN Science Instrument Notebook, ASC reference document on all AXAF Science Instruments.

SOP01 Science Instrument Operations Manual, http://www.astro.psu.edu/xray/docs/sop/, required deliverable for the ACIS team, presenting the information needed to properly operate the ACIS experiment.

SRAM Sequencer Random-Access Memory, highly radiation resistant memory used to store instructions for the ACIS CCD readout.

SRR Software Requirements Review, formal meeting reviewing the adequacy and accuracy of the Software Requirements.

SRS Software Requirements Specification, document specifying the ACIS software requirements.

SRC Synchrotron Radiation Center, a synchrotron facility run by the University of Wisconsin, Madison, used for ACIS flight filter calibration.

ST STatus information, information ancillary to the scientific data which is appended to the science analysis data.

SWG Science Working Group, the team of scientists, consisting of the Instrument PIs, the Telescope Scientist, the Interdisciplinary Scientists and the Project Scientist, who work as a top-level advisory team to assure the AXAF Project remains faithful to the scientific goals of the program.

TBS, TBR, TBD To Be Supplied, Revised, Determined, terms holding space for specific numbers or text which are to be supplied, revised or determined at a later time.

VVA Vent Valve Assembly, provides a commandable opening and closing path to vent the inside of ACIS.

WBS Work Breakdown Structure, management document and numbering scheme for formalizing and categorizing the various tasks associated with this project into a tiered hierarchy with associated dependencies to enable the efficient identification and tracking of progress on the assigned goals.

XRCF X-ray Calibration Facility, the X-ray facility built at Marshall Space Flight Center to support AXAF calibration of the joint HRMA-Science Instrument system.